

AD-787 546

PROCEEDINGS OF THE FLUIDIC STATE-OF-THE-ART  
SYMPOSIUM HELD AT NAVAL ORDNANCE LABORATORY,  
WHITE OAK, MARYLAND ON 30 SEPTEMBER -  
3 OCTOBER, 1974  
VOLUME I

HARRY DIAMOND LABORATORIES

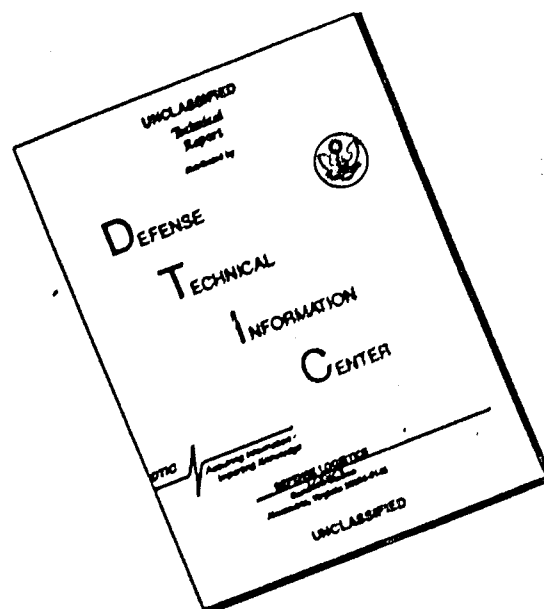
1974

DISTRIBUTED BY:

**NTIS**

National Technical Information Service  
U. S. DEPARTMENT OF COMMERCE

# DISCLAIMER NOTICE



THIS DOCUMENT IS BEST QUALITY AVAILABLE. THE COPY FURNISHED TO DTIC CONTAINED A SIGNIFICANT NUMBER OF PAGES WHICH DO NOT REPRODUCE LEGIBLY.



AD 787546

FLUIDIC  
STATE-OF-THE-ART

SUMMER SIMUL

1974

30 SEPTEMBER - OCTOBER

DDC  
RECEIVED  
OCT 23 1974  
RECEIVED  
D.



Reproduced by  
NATIONAL TECHNICAL  
INFORMATION SERVICE  
U S Department of Commerce  
Springfield VA 22151

VOLUME I

U.S. Army Materiel Command  
Harry Diamond Laboratories  
Washington, D.C.

DISTRIBUTION STATEMENT A

Approved for public release;  
Distribution Unlimited

REPORT DOCUMENTATION PAGE		READ INSTRUCTIONS BEFORE COMPLETING FORM
1. REPORT NUMBER	2. GOVT ACCESSION NO.	3. RECIPIENT'S CATALOG NUMBER
4. TITLE (and Subtitle) Proceedings of the Fluidic State-of-the-Art Symposium, 30 Sep - 3 Oct 74, Vol. 1		5. TYPE OF REPORT & PERIOD COVERED Technical Report
7. AUTHOR(s)  Various		6. PERFORMING ORG. REPORT NUMBER <del>ND 3023</del>
9. PERFORMING ORGANIZATION NAME AND ADDRESS		8. CONTRACT OR GRANT NUMBER(s)  HDL Proj.NO. 302531
11. CONTROLLING OFFICE NAME AND ADDRESS		10. PROGRAM ELEMENT, PROJECT, TASK AREA & WORK UNIT NUMBERS
14. MONITORING AGENCY NAME & ADDRESS (if different from Controlling Office)		12. REPORT DATE
		13. NUMBER OF PAGES 605
		15. SECURITY CLASS. (of this report)  Unclassified
		15a. DECLASSIFICATION/DOWNGRADING SCHEDULE
16. DISTRIBUTION STATEMENT (of this Report)  Unlimited		
<div style="border: 1px solid black; padding: 5px; text-align: center;"> <b>DISTRIBUTION STATEMENT A</b>            Approved for public release            Distribution Unlimited         </div>		
17. DISTRIBUTION STATEMENT (of the abstract entered in Block 20, if different from Report)		
18. SUPPLEMENTARY NOTES		
19. KEY WORDS (Continue on reverse side if necessary and identify by block number) Fluierics, fluidics; vortex diode; vortex triode, turbulence amplifier; lamainar proportional amplifier; wall-attachment fluid amplifiers; bistable fluidic amplifiers		
20. ABSTRACT (Continue on reverse side if necessary and identify by block number)  This volume contains twelve papers for a total of 605 pages.		

## FOREWORD

A major goal of this Symposium has been to assemble in one place a comprehensive volume on the state-of-the-art of fluidics. As reading of these papers will show, we have been highly successful in meeting this goal and I wish to express my deep appreciation to the authors many of whom spent a great many hours and put a tremendous amount of effort into preparing their papers.

I would also like to take this opportunity to thank the HDL staff of reviewers who helped me to read the papers: R. Deadwyler, T. Drzewiecki, N. Eisenberg, J. Iseman, S. Katz, and R. Woods.

In particular I would like to thank Mrs. E. Janifer and Ms D. Perry for their typing and other secretarial help often way beyond the call of duty and T. Drzewiecki for help in taking care of many of the details involved in preparing for and organizing this Symposium.

Finally in behalf of the Harry Diamond Laboratories I would like to express my deep appreciation to the Naval Ordnance Laboratory for the use of the NOL auditorium and specifically to Mrs. R. S. Kahne for her helpful cooperation.

*Joseph M. Kirshner*

JOSEPH M. KIRSHNER

*ial*

## WELCOME TO THE HDL FLUIDICS STATE-OF-THE-ART SYMPOSIUM

by

B. M. Horton  
Technical Director

On 2 March 1960, the Harry Diamond Laboratories disclosed the concepts of fluid amplification and a wave of interest began that within a very few years involved individuals and organizations around the world in efforts to use the devices and in trying to solve the difficult but intriguing problems associated with them. This initial period was unfortunately marked by exaggerated predictions for the growth of fluidics inspired by overenthusiasm and failure to grasp the enormous technical difficulties involved.

Inevitably this initial enthusiasm died as the technical problems made themselves obvious. A large factor in this disillusionment was the attempted application of fluidics for uses that the then available components could not possibly accomplish.

Fortunately, there were those who carefully sought out applications which matched the available components, and there were those who continued to battle the frontiers of knowledge in an effort to improve the devices and to develop analyses of devices and systems.

Analysis techniques began to gel about 1969-1970, and in quick succession complete first order theories for the more important fluidic active components began to appear thereby making it possible to analytically consider the trade-offs in geometry necessary to obtain desired characteristics. This was an important milestone in fluidics and has set the stage for a more rapid growth of the technology.

This decade has also seen advances in development. The devices have continually been improved and the range of possible applications has been appreciably increased. Of great significance is the fact that many systems have now been operating trouble free for several years thereby verifying early predictions on the reliability of fluidics.

This symposium provides a means of gathering together many of the individuals who are responsible for the generation and growth of the technology. It and the proceedings will provide a means for gathering together information on the current technical status of fluidics.

We hope that by providing this opportunity for all of us to get together and to learn where the technology now stands, we will have added an additional stimulus to the growth of fluidics.

# Volume I

<i>A Review of Vortex Diode and Triode Static and Dynamic Design Characteristics</i>	
D. N. Wormley, MIT, Cambridge, Massachusetts . . . . .	1
<i>Vortex Diodes</i>	
S. S. Fineblum, Bell Labs, Whippany, New Jersey . . . . .	45
<i>The Turbulence Amplifier</i>	
A. Bell, State University of New York at Buffalo, Buffalo, New York . . . . .	81
<i>Analytical Design of Laminar Proportional Amplifiers</i>	
Francis M. Manion, Harry Diamond Laboratories, Washington, D.C.	
Tadeusz M. Drzewiecki, Harry Diamond Laboratories, Washington, D.C. . . . .	149
<i>Experimental Design of Laminar Proportional Amplifiers</i>	
Richard F. Hellbaum, NASA-Langley, Langley, Virginia . . . . .	235
<i>Jet Deflection Proportional Amplifier</i>	
A. J. Healey, University of Texas, Austin, Texas . . . . .	269
<i>Fluidic Proportional Amplifiers for Very Low Reynolds Numbers</i>	
R. H. Bellman, Corning Glass Works, Corning, New York . . . . .	351
<i>Design Characteristics of a New Liquid Laminar Jet Fluidic Element</i>	
S. B. Friedman, Wm. Rainey Harper College, Illinois	
H. R. Martin, University of Waterloo, Canada . . . . .	383
<i>The Effect of Geometric and Fluid Parameters on the Static Performance of Wall-Attachment Type Fluid Amplifiers</i>	
H. L. Moses, Virginia Polytechnic Institute and State University, Blacksburg, Virginia	
R. A. Comparin, Newark College of Engineering . . . . .	403
<i>The Design of Fluidic, Turbulent Wall-Attachment Flip-Flops</i>	
T. Drzewiecki, Harry Diamond Laboratories, Washington, D.C. . . . .	433

*Effects of a Splitter and Vents on a Reattaching Jet  
and its Switching in Wall-Reattachment Fluidic Devices*  
T. Wada, M. Takagi, and T. Shimizu, Okayama University,  
Okayama, Japan . . . . . 499

*Splitter Switching in Bistable Fluidic Amplifiers*  
C. J. William, University of Windsor, Canada  
W. G. Colborne . . . . . 555

A REVIEW OF VORTEX DIODE AND TRIODE  
STATIC AND DYNAMIC DESIGN TECHNIQUES

D. N. Wormley\*

Abstract

Vortex diode and triode amplifiers and their operating characteristics are described. Experimental and analytical studies of the essential characteristics of vortex chamber flow fields are briefly reviewed. Data and design techniques developed for the static design of diodes and triodes are summarized, and methods to estimate the small signal and global dynamic response of diodes and triodes are reviewed. Finally, studies describing the application of vortex diodes and triode amplifiers in engineering systems are cited.

---

\*Associate Professor of Mechanical Engineering, Massachusetts Institute of Technology, Cambridge, Massachusetts.

# NOMENCLATURE

$A_c$	control port area
$A_e$	exit port area
$A_s$	supply port area
BLC	boundary layer coefficient defined in (20)
BLC*	modified boundary layer coefficient: $(\lambda) \cdot (\text{BLC})$
$c_c$	control port discharge coefficient
$c_e$	exit port discharge coefficient
$c_s$	supply port discharge coefficient
$D_i$	diodicity
e	exponential function
f	friction coefficient defined in (20)
$f_1$	side wall friction coefficient
$f_2$	end wall friction coefficient
G	parameter defined in (15)
h	vortex chamber height
$k_h$	high resistance diode loss coefficient
$k_L$	low resistance diode loss coefficient
$K_c, K_o, K_u$	constants defined in (28) and (29)
$K_1, K_2$	constants defined in (30)
N	number of exit ports
$P_a$	ambient pressure
$P_c$	control port pressure
$P_{cc}$	cutoff control port pressure
$P_e$	pressure at radius $r_e$
$P_o$	pressure at radius $r_o$
$P_s$	supply port pressure
$\bar{Q}$	average volume flow through chamber
QP	quiescent power drain ratio
r	radial position in chamber



$r_e$	exit port radius
$r_o$	chamber radius
$R_r$	Reynolds number: $u_o r_o \rho / \mu$
$R_w$	maximum flow Reynolds number: $W_m / 2\pi r_o \mu$
$s$	LaPlace operator
$T_D$	delay time
$T_f$	fill time defined in (27)
$T_L$	lag time
$T_r$	response time
$TR$	turndown ratio
$\bar{u}$	average flow velocity through a diode
$u$	radial velocity in chamber
$v$	tangential velocity in chamber
$w$	axial velocity in chamber
$W_c$	control flow rate
$W_{cc}$	cutoff control flow rate
$W_m$	maximum flow rate
$W_s$	supply flow rate
$W_o$	total flow rate
$\Delta$	increment of a quantity
$Y$	parameter defined in (13)
$\Gamma$	circulation: $vr$
$\epsilon$	inlet jet recovery factor
$\mu$	fluid viscosity
$\lambda$	swirl: $v_o / u_o$

## INTRODUCTION

Pure fluid devices which employ confined vortex flows have been of engineering interest for more than fifty years. Studies have described effort to develop cyclone separators [1]\*, confined vortex gaseous reactors [2,3], Ranque-Hilsch tubes [4,5], thrust vector controllers [6], temperature [7] and flow rate [8,9] measuring instruments, oscillators [10], angular rate sensors [11,12], vortex diodes [13,14], and vortex triode amplifiers [15,16]. A summary of publications concerning vortex devices has been compiled by Mayer [17]. In this paper discussion is focused on the vortex diode and the triode amplifier.

The vortex diode is of particular interest, since in studies [18, 19] of the comparative performance of common types of pure fluid diodes, vortex diodes have been shown to have the highest ratio of forward to reverse flow resistance.

The vortex triode amplifier is of interest because of the pure fluid devices considered to date, including beam deflection amplifiers, turbulence amplifiers and impact modulators [20,21], it is the only device which has the ability to modulate the total output power from a source. It is useful in power-level types of applications similar to classical open-center valves and has been employed in a number of hydraulic and gaseous flow modulation applications [20--24].

## BASIC DESCRIPTION OF THE VORTEX TRIODE AND DIODE

### Triode Geometry and Functional Characteristics

A sketch of a conceptual vortex triode amplifier is shown in Fig. 1. The amplifier consists of a short cylindrical chamber (i.e., the chamber height  $h$  to chamber radius  $r_0$  ratio  $h/r_0$  is usually less than 1.0) with three types of ports: an outlet port in the chamber end plates, a supply inlet port through which radially directed flow enters the chamber and a control inlet port through which tangentially directed flow enters the chamber. While Fig. 1 illustrates only single inlet and outlet ports, in practice a number of both supply and control inlet ports or annular port configurations may be used to obtain a more uniform flow distribution in the chamber, and outlet ports may be used either in one or in both chamber end walls. The principal types of triode configurations including single, multiple and annular, button-type

\*Numbers in [ ] refer to references listed in the Bibliography.

supply port, and both single and multiple control and exit port geometries are described in [20--32].

In a triode when the tangential control flow is zero, the primary or supply flow proceeds radially from the supply to the exit port with negligible pressure drop across the chamber. In this condition the triode delivers its nominal maximum flow which is determined principally by the supply and exit port characteristics and the supply and exit pressures. When control flow is injected into the chamber, a tangential velocity component is imparted to the fluid at the outer radius of the chamber. As the fluid flows toward the center of the chamber, a vortex is formed between the inlet and outlet ports in the chamber. The vortex flow field creates a radial pressure gradient in the chamber which in effect increases the resistance to flow and thus decreases the supply flow rate. Since a relatively small tangential control flow is required to modulate the relatively large supply flow, the triode is essentially a flow amplifier in which total flow (supply plus control flow) is reduced as the control flow is increased. A minimum in total flow for fixed supply and exit pressures, called the cutoff flow, is obtained when the supply flow is reduced to zero and the total flow equals the control flow.

Typically, the static characteristics of a triode are presented as total exit flow versus control flow or control pressure, for constant supply and exhaust pressures. In Fig. 2 sketches of triode characteristics are plotted nondimensionally, where the normalizing flow is the maximum flow  $W_m$  obtained with  $W_c = 0$  and the normalizing pressure is the fixed supply-exhaust pressure difference across the triode  $P_s - P_e$ . Depending upon triode geometry and operating fluid properties either a proportional characteristic in which total flow is a single valued function of control flow and pressure or a bistable characteristic in which multiple values of total flow exist for certain ranges of control pressure or flow may be obtained.

Several figures of merit defined for triodes are illustrated in Fig. 2, including:

- (1) The turndown ratio--a measure of the total flow modulation capability defined as:

$$TR = W_m / W_{cc} = 1 / \bar{W}_{cc}$$

where  $W_{cc}$  is the control flow required to cutoff the supply flow.

- (2) The cutoff control pressure ratio---a measure of the maximum control pressure to the supply pressure defined as:

$$\bar{P}_{cc} = \frac{(P_{cc} - P_a)}{(P_s - P_a)}$$

where  $P_{cc}$  is the control pressure corresponding to  $W_{cc}$ .

- (3) The quiescent power drain ratio---a measure of the quiescent to the maximum power consumption of triode for operation on an incompressible fluid which is defined as:\*

$$QP = \bar{P}_{cc} / TR = \bar{P}_{cc} \bar{W}_{cc}$$

In a number of studies these performance indices have been discussed for a variety of triode geometries operating with compressible [24, 25] and incompressible [26--31] fluids. Turn-down ratio values of  $TR = 22$  for  $\bar{P}_{cc} = 4.0$  [27], of  $TR = 20$  for  $\bar{P}_{cc} = 3.0$  [26] and of  $TR = 8$  with  $\bar{P}_{cc} = 2.0$  [25] have been reported.

The studies cited have indicated for all the triode geometries described that operation of a triode over its full range requires  $\bar{P}_{cc} > 1.0$ . The requirement that the control pressure exceed the supply pressure is one of the principal disadvantages of classical vortex triodes. Studies described in [32] and [33] have described triode geometries in which it is possible to operate the triode over a portion of its characteristic using a control pressure less than the supply pressure,  $\bar{P}_{cc} < 1.0$ . In [32] an assymetric single supply and control jet triode<sup>cc</sup> developed for application in large scale water distribution control systems is described for which the total flow can be reduced to 32% of the maximum flow with the control pressure head less than or equal to the fixed supply pressure head. The triode utilizes supply, control and exit areas which are nearly comparable and takes advantage of the effects of the mixed control-supply jet attachment to the chamber wall.

An axial triode matched to a coanda unit is described in [33] in which the flow may be reduced to 80% of its maximum value

\*In [25] a power index is defined in terms of enthalpy for compressible flow through triodes.

with  $\bar{P}_{cc} < 1.0$ .

For systems in which large values of  $\bar{P}_{cc} > 1.0$  are available, the use of a triode coupled to an ejector which uses primary flow from the control source to eject flow from the triode exhaust to form the total inlet control flow to the triode can improve triode turndown ratio. In [34] a triode with an initial turndown ratio of 8 was shown to have an effective turndown ratio of 35 when combined with an ejector since the ejector recycled the triode outlet flow through the control inlet and reduced the total flow delivered to load at the triode outlet.

For classical triode designs which employ no external devices to augment the turndown ratio and are not designed to exploit jet attachment effects associated with asymmetry, carpet maps of TR and  $\bar{P}_{cc}$  are presented in [27], [28] and [29] as a function of triode geometry so that a maximum quiescent power drain ratio  $QP = \bar{P}_{cc}/TR$  may be determined as a function of geometry.

While the figures of merit cited describe the gross characteristics of vortex triodes, for a specific application detailed characteristics are required so that in proportional applications, the gain and region of linearity and in bistable devices the switching points may be determined. To completely describe a triode in addition to the transfer characteristics of Fig. 2, additional characteristics are required, including the supply and control port input and output port exit impedance relationships.

#### Diode Geometry and Characteristics

The vortex diode is similar to the vortex triode and consists of a short cylindrical chamber with a tangential inlet port or ports and an exit port or ports in the chamber end walls. When flow passes through the diode from the tangential port to the end wall exit port, a vortex is formed in the chamber and a high flow resistance is obtained while when the flow is reversed and enters through the port in the chamber end wall and passes through the chamber to exit through the tangential port no vortex is formed and a relatively low flow resistance path is formed. A typical diode configuration is sketched in Fig. 3 with forward and reverse flow characteristics presented from the data in [18].

A figure of merit for the diode is defined in terms of the ratio of the flow resistance coefficients in the low  $k_L$  and high  $k_h$  resistance flow directions. The diodicity  $D_1$  is:

$$D_1 = k_h/k_L$$

where  $k$  is flow resistance loss coefficient defined as:

$$k = 2\Delta P / \rho \bar{u}^2$$

with  $\Delta P$  the pressure drop across the diode,  $\bar{u}$  the average flow velocity and  $\rho$  the fluid density.

Values of  $D_1$  have been reported for the vortex diodes tested by Paul [18] ranging from 5 to 43. Heim [13] and Zobel [14] have also described geometries which yield values of  $D_1$  in excess of 40. In comparative studies of vortex, scroll, nozzle and diffuser diodes Paul [18] and Baker [19] have reported achieving higher values of diodicity with vortex diodes than with the other diodes tested.

### VORTEX CHAMBER FLOW FIELD

#### The Chamber Regions

To provide a basis for understanding the performance characteristics of both vortex triodes and diodes, some knowledge of the physical phenomena occurring in the vortex chamber is required. A number of experimental and analytical studies [35--46] of confined vortex flow fields have been conducted. These studies have considered the following three flow regions in a vortex chamber:

- (1) an inlet flow mixing region
- (2) a main chamber region
- (3) an exit region

First, inviscid models of the three regions are discussed, and then the influence of viscous effects in the three regions are described.

#### An Inviscid Model

A model for a vortex triode or for the high resistance flow path in a diode can be formulated in a simple form for each region if incompressible, inviscid flow is considered.

### Inlet Region

In the inlet mixing region the supply  $W_s$  and control  $W_c$  flows are assumed to be described by quadratic orifice relationships

$$W_s = c_s A_s \sqrt{2\rho(P_s - P_o)} \quad (1)$$

$$W_c = c_c A_c \sqrt{2\rho(P_c - P_o)} \quad (2)$$

where:

$A_s$  = supply port area

$A_c$  = tangential control port area

$c_s (c_c)$  = supply (control) area discharge coefficient

$P_o$  = pressure at radius  $r_o$ , the edge of the inlet mixing region

If the supply and control flows mix completely in an inlet mixing region which is concentrated in a thin annulus at the outer radius of the chamber, then at radius  $r_o$ , the radial velocity  $u_o$  may be computed from mass conservation as:

$$u_o = \frac{W_o}{2\pi r_o h \rho} \quad (3)$$

where the total flow  $W_o$  is:

$$W_o = W_c + W_s \quad (4)$$

By conservation of angular momentum, the tangential velocity  $v_o^+$  under lossless mixing conditions at radius  $r_o$  is:

$$v_o^+ = \frac{W_c^2}{\rho c_c A_c W_o} \quad (5)$$

### Main chamber region

In the main chamber region, if the fluid is assumed to be uniformly distributed axially, inviscid, incompressible and steady, the

flow field consists of the super-position of a radial sink flow and a potential vortex.\* By continuity the radial velocity at the exit radius  $r_e$  is then

$$u_e = u_o \frac{r_o}{r_e} \quad (6)$$

and the tangential velocity at  $r_e$  noting that for a potential vortex the circulation  $\Gamma = vr$  at any radius  $r$  is equal to  $v_o r_o$  may be derived as:

$$v_e = v_o \frac{r_o}{r_e} \quad (7)$$

The pressure drop across the chamber may be computed from the radial momentum equation as [43, 44]:

$$P_o - P_e = \int_{P_e}^{P_o} dP = \rho \int_{r_e}^{r_o} \frac{v^2}{r} dr - \int_{r_e}^{r_o} u \frac{du}{dr} dr \quad (8)$$

where when (6) and (7) are used:

$$P_o - P_e = \frac{1}{2} \rho [(u_e^2 + v_e^2) - (u_o^2 + v_o^2)] \quad (9)$$

#### Exit Region

If the flow through the exit orifice is assumed to be related to the pressure at  $r_e$  and the ambient pressure  $P_a$  by a quadratic relationship, then  $W_o$  the total flow is:

$$W_o = c_e A_e \sqrt{2\rho(P_e - P_a)} \quad (10)$$

\*This analysis assumes that the flow is uniform at any angular position in the chamber and assymetric effects due to inlet jet attachment are neglected.



where:

$A_e$  = total exit area

$c_e$  = exit area discharge coefficient

The triode relationship between nondimensional total flow  $\bar{W} = W/W_m$  and control flow  $\bar{W}_c = W_c/W_m$  may be derived by combining (1) to (10) to yield:

$$\bar{W}_o^2 = 1 - \gamma^2 \left[ \frac{c_e^2 A_e^2}{c_s^2 A_s^2} \left( \frac{r_o^2}{r_e^2} - 1 \right) \frac{\bar{W}_c^4}{\bar{W}_o^2} - \frac{c_e^2 A_e^2}{c_s^2 A_s^2} (2\bar{W}_o \bar{W}_c - \bar{W}_c^2) \right] \quad (11)$$

where the maximum flow  $W_m$  is:

$$W_m = \gamma c_e A_e \sqrt{2p(P_s - P_a)} \quad (12)$$

with:

$$\gamma = \frac{1}{\sqrt{1 + \frac{c_e^2 A_e^2}{c_s^2 A_s^2} + \frac{c_e^2 A_e^2}{4\pi r_e^2 h^2} \left(1 - \frac{r_e^2}{r_o^2}\right)}} \quad (13)$$

The dimensionless triode characteristic of (11) is a function of inlet and outlet area discharge coefficients and four geometric ratios:

- (a)  $A_s/A_e$ : supply to exit area ratio
- (b)  $h/r_e$ : chamber height to exit radius ratio
- (c)  $A_c/A_e$ : control to exit area ratio
- (d)  $r_e/r_o$ : the radius ratio

To achieve a maximum flow rate through the triode for a given supply pressure at  $W = 0$  and, in turn, a maximum TR and minimum  $P_c$ , both  $A_s/A_e$  and  $h/r$  should be made large as shown in (12) and (13). If  $A_s/A_e > 4.0$  and  $h/r > 2.0$  N where N is the number of outlets, the maximum flow is within 94% of its theoretical

maximum value, and the exit orifice becomes the primary restriction to flow through the triode for  $W = 0$ . If the conditions on  $A_s/A_e$  and  $h/r_e$  are met, the characteristic is simply:

$$\bar{W}_o = 0.707 \sqrt{1 \pm \sqrt{1 - \frac{\bar{W}_c}{G^4}}} \quad (14)$$

where

$$G = \frac{\frac{c_c}{2c_e} \left( \frac{r_e}{r_o} \right) \frac{A_c}{A_e}}{\sqrt{1 - \frac{r_e^2}{r_o^2}}} \quad (15)$$

The inviscid triode characteristic is illustrated in Fig. 4 for two values of  $G$ . As  $G$  or  $A_c/A_e$  and  $r_e/r_o$  increase, the amount of control flow required at each point on the characteristic is increased. Thus, the inviscid characteristic indicates that  $A_c/A_e$  and  $r_e/r_o$  should be minimized to reduce control flow requirements. Fig. 4 also shows the inviscid triode characteristic is multivalued for all values of  $W$ . A triode with such a characteristic would tend to oscillate between the two values of total flow which exist for a given value of control flow. In real triodes the effects of viscous losses in the inlet mixing region and main chamber modify the characteristics. As these losses increase, a triode characteristic passes from a multivalued characteristic to a more proportional characteristic, and generally both the cutoff control flow ratio and pressure ratio increase.

The ideal analysis may be used to estimate the high resistance flow direction loss coefficient of a diode. By combining (1)---(10) for the condition  $A_s = 0$  and  $h/r_e > 2$ , the following relationship may be derived.

$$\frac{P_c - P_a}{W_c^2 / (2\rho(C_e A_e)^2)} = 1 + \left( \frac{r_o^2}{r_e^2} - 1 \right) \left( \frac{c_e A_e}{c_c A_c} \right)^2 \quad (16)$$

If the discharge coefficients for flow back through the diode are represented as  $c_{ed}$  and  $c_{cd}$  for the exit and control areas, then the low resistance direction loss coefficient may be written as:

$$\frac{P_a - P_c}{W_c^2 / (2\rho(c_{ed}A_e)^2)} = 1 + \left( \frac{c_{ed}A_e}{c_{cd}A_c} \right)^2 \quad (17)$$

if the exit and control restrictions are the only significant resistances to flow. Thus, the ideal analysis indicates the diodicity is for

$c_e = c_{ed}$ :

$$D_1 = \frac{1 + \left( \frac{r_o}{r_e} - 1 \right) \left( \frac{c_e A_e}{c_{cd} A_c} \right)^2}{1 + \left( \frac{c_{ed} A_e}{c_{cd} A_c} \right)^2} \quad (18)$$

Equation (18) indicates that by increasing  $r_o/r$  the diodicity may be increased. While (18) provides an indication of the effects of geometry on  $D_1$ , it is noted in [18] that values of  $D_1$  predicted by an inviscid analysis may be greater than four times the experimental values obtained because of viscous losses in the diode flow chamber for flow in the high resistance direction.

### Viscous Model

To describe more accurately the characteristics of the vortex flow in triodes and diodes, viscous effects must be considered for each chamber region.

### Inlet region

In the inlet region, if the flow is considered incompressible, then the supply  $W_s$  and control  $W_c$  flows entering the region may be computed as given in (1) and (2), and if the flow is considered to be completely mixed and uniform, the radial velocity at the outer chamber radius  $r_o$  may be determined directly from continuity as given by (3) and the total flow  $W$  by (4). Conservation of angular momentum requires that the angular momentum leaving the mixing region,  $W v r_o$ , equal that entering the region  $W (W / \rho A_c) r$  minus the angular moment due to shear at the outer wall  $2\pi r_o^2 \tau$ , where  $\tau$  is the outer wall shear. By balancing the angular momentum and shear, the angular velocity at the outer wall may be written as:

$$v_o = \epsilon \frac{W_c^2}{\rho c A W_o} = \epsilon v_o^+ \quad (19)$$

where  $\epsilon$  is the jet recovery factor [43, 44] which incorporates the shear losses at the outer wall and  $v_o^+$  is the ideal tangential velocity in (5); thus, if  $\epsilon = 1.0$ , no losses occur, and the ideal angular velocity is achieved, while as increasing shear losses occur the value of  $\epsilon$  decreases.

Measurements [45] have indicated that even for chambers with only tangential jets, such as occur in diodes, the loss of momentum at the outer wall can be substantial with  $\epsilon$  approaching 0.5 for large values of the swirl parameter  $\lambda = v_o^+ / u_o$ . Theoretical values of  $\epsilon$  have been derived [44], assuming the Prandtl shear law used for turbulent flow over a flat plate in which the shear is a function of tangential velocity squared, a friction factor  $f_1$ , and a tangential Reynolds number to the 1/4 power. Theoretical data from [44] is presented in Fig. 5 for a given friction factor  $f_1$ , which indicates  $\epsilon$  is a strong function of ideal swirl  $\lambda^+ = v_o^+ / u_o$  and a weak function of Reynolds number  $R_o = u_o r_o \rho / \mu$ . For  $\lambda^+ \approx 0$ , the recovery factor  $\epsilon \approx 1.0$  and the ideal case is achieved. As  $\lambda^+$  increases and approaches 250,  $\epsilon$  approaches 0.8 and for larger swirl  $\lambda^+ \approx 700$ , the recovery factor  $\epsilon$  decreases to less than 0.7. As the strength of the vortex increases, the angular momentum loss increases.

#### Main chamber region

In the main chamber region the pressure drop generated by the vortex flow may be computed using (8). To determine the pressure drop  $P_o - P_i$ , the tangential and radial velocity distributions in the chamber are required. For the inviscid flow case, these distributions were shown to be the super-position of a sink and potential vortex. When viscous effects are considered, it has been shown both experimentally [26, 38] and analytically [35, 36, 37, 39, 40, 43 and 44] that the velocity distributions in a short vortex chamber are strongly influenced by the end wall shear. Fig. 6 illustrates conceptually the angular and radial velocity profiles occurring in a chamber for several values of swirl  $\lambda$ . These profiles have been drawn using the experimentally measured profiles in [26, 38] as a guide. At very low values of  $\lambda$ , flow proceeds from the outer periphery of the chamber to the inlet with radial flow existing at all axial points in the chamber. In this condition, the flow conditions are similar to the super-position of a sink and a potential vortex. At higher values of  $\lambda$ , as the

flow proceeds from the outer periphery, an increasing fraction of the flow is drawn into the end wall boundary layers. While near the chamber midplane, the inward pressure gradient force due to fluid tangential velocity is nearly balanced by the centrifugal force due to fluid velocity, in the end wall boundary layers the fluid tangential velocity is reduced by the shear stress and approaches zero; thus in the boundary layer the centrifugal force is reduced by the shear, while the pressure force persists resulting in an acceleration of the radial flow in the boundary layer. As shown in Fig. 6 at high values of  $\lambda$  all the radial flow through the chamber may occur in the end wall boundary layers, and the midplane radial velocity may be reduced to zero or even become negative [38]. When all the radial flow is drawn into the chamber end wall boundary layers, a potential vortex can no longer be supported in the chamber, and at the midplane, the circulation distribution decreases due to the strong end wall shear. Studies in [35, 36, 37, 43 and 45] have analyzed the circulation decay in a chamber due to end wall shear. In [43] the circulation distribution in a short chamber with incompressible flow is derived using a Prandtl shear law for the end walls and tangential and radial velocity profiles similar to those illustrated in Fig. 6. The circulation distribution derived in [43] is summarized in Fig. 7. The distribution is a function of only two parameters--the swirl  $\lambda$  and the modified boundary layer coefficient  $BLC^* = BLC\lambda$  where the boundary layer coefficient  $BLC$  is:

$$BLC = \frac{2r}{h} \frac{f}{\omega} \quad (20)$$

where

$$f = f_2 / \left( \frac{\rho u h}{2\mu} \right)^{1/4}$$

For small values of  $BLC^* < 0.25$ , the circulation distribution is constant and a potential vortex is formed. As  $BLC^*$  increases, due to increased swirl  $\lambda$ ,  $r/h$ , or friction factor  $f_2$ , the circulation distribution decays and a potential vortex is obtained only over a portion of the chamber. For  $BLC^* > 2.5$  essentially the entire chamber is influenced strongly by the shear and only over a small region near the outer edge is the circulation constant. Since the pressure drop across a chamber is a function of  $v^2/r$ , a decrease in tangential

velocity at small radii from that given by the potential vortex  $\Gamma = v r = \Gamma_0$  decreases the pressure drop across the chamber significantly from that predicted by an inviscid analysis.

The data in Fig. 7 indicates that the circulation distribution  $\Gamma$  is principally a function of  $BLC^*$  and only weakly depends independently upon  $\lambda$ . Thus the circulation and, in turn, the pressure distributions are principally a function of  $BLC^*$  which may be written in terms of triode quantities as:

$$BLC^* = 2f \frac{h}{r_0} \frac{v_0}{u_0} = \frac{4\pi f_2 \epsilon r_0^2 \bar{W}_c^2}{c_c A_c \bar{W}_c \bar{W}_0^{1/4} (0.5 R_w)^{1/4}} \quad (21)$$

In terms of triode parameters  $BLC^*$  depends strongly upon nondimensional total  $\bar{W}$  and control  $\bar{W}_0$  flows, chamber radius  $r_0$ , control port area  $A_c$ , inlet jet recovery factor  $\epsilon$  and the end wall friction coefficient  $f_2$ ; it depends weakly upon the maximum flow Reynolds number and is independent of chamber height. At a point on a vortex triode near the maximum flow condition  $\bar{W}_c \approx 0$ ,  $\bar{W}_0 \approx 1.0$ ,  $BLC^*$  is small, i.e.,  $BLC^* < 0.25$ , and the flow is nearly inviscid; thus, near the maximum flow conditions vortex triode characteristics are similar to the ideal characteristics as illustrated in Fig. 4. At a point near cutoff in a triode,  $\bar{W}_c \approx \bar{W} \approx 0.05 - 0.3$ , or in the high flow resistance condition of a diode  $BLC^*$  tends to be large, i.e.,  $BLC^*$  approaches 1.0, and the influence of viscous effects are of major importance. As the chamber radius ratio  $r_0$  increases or the control area  $A_c$  decreases, viscous effects become more important at corresponding larger values of total flow. Thus near cutoff viscous effects require more control flow to reduce the total flow to given value, and triode characteristics are modified significantly as shown in Fig. 4.

Using an analysis similar to that in [39, 43] or the analysis in [44], the radial and tangential velocity distribution resulting from the effects of end wall shear in the chamber may be determined, and, in turn, the pressure distribution computed directly from (8).

#### The exit region

Studies of the exit region in vortex chambers have been conducted in [39, 44]. Because the flow in the outlet may have substantial angular velocity, the axial velocity and pressure may

vary as a function of radius. As shown schematically in Fig. 8, at low tangential velocities the axial velocity  $w$  is nearly uniform, while at high tangential velocities,  $w$  may reach negative values at the centerline, and the flow may be drawn into the chamber through the outlet along the centerline.

The total exit flow may be determined from the axial velocity  $w$  distribution in the exit region as:

$$W_o = 2\pi \int_0^r w r dr \quad (22)$$

In [39, 44, and 46] methods for computing the axial velocity distribution in the exit are presented which include the effects of the tangential and radial velocities existing at the exit radius  $r_e$  on the axial velocity distribution.

#### Complete viscous models

Theoretical models which include the effects of the cylindrical wall shear in the inlet mixing region, the end wall shear on the tangential and radial velocities in the main chamber region and the influence of the axial velocity distribution in the exit region on the total flow described above have been formulated by Bichara and Orner [44], Levellen, Burns and Strickland [39] and Bauer [36]. While these analyses require estimates of the side and end wall friction coefficients and are restricted to symmetrical inlet geometries with parallel top and bottom plates, they have provided a good basis for understanding the primary effects of geometry and fluid properties on triode characteristics.

#### INFLUENCE OF GEOMETRY ON VORTEX TRIODE STATIC CHARACTERISTICS

The results of analytical [39, 44 and 46] and experimental [17, 25--31, 47--49] studies which describe the influence of geometry on triode and diode characteristics are summarized below for incompressible flow through amplifiers with parallel top and bottom plates. Data illustrating the influence of Reynolds number, supply to exit area ratio  $A/A_e$ , control to exit area ratio  $A_c/A_e$ , chamber radius ratio  $r/r_e$  and chamber height to radius ratio  $h/r_e$  are presented. These geometric quantities are the principal geometric factors influencing triode performance identified in both the ideal and viscous analytical studies.



Reynolds Number:  $R_w$

Analytical studies [39, 43 and 44] have indicated that triode characteristics are relatively insensitive to Reynolds number for sufficiently large values of  $R_w$ , since both the side and end wall shear laws are functions of Reynolds numbers to the one fourth power. Data in [28] has shown triode characteristics to be relatively insensitive to Reynolds number  $R_w = W / 2\pi r \mu$  for  $R_w > 750$  for tests made up to  $R_w < 3300$ . The insensitivity of triode characteristics over a wide range of  $R_w$  greater than 750, indicates that once a characteristic for a specific geometry is obtained for a given supply pressure, it may be scaled to yield characteristics at other supply pressures. The ability to scale characteristics greatly facilitates the design of systems utilizing vortex triodes [30]. However, for lower values of Reynolds number data in [28, 31 and 50] show that triode characteristics may be quite sensitive to Reynolds number. As pointed out in [31, 50] for triodes operated on hydraulic oil, the Reynolds number sensitivity may be of particular significance in hydraulic circuit applications.

Supply to Exit Area Ratio:  $A_s/A_e$

The supply area  $A_s$  has a negligible effect on amplifier characteristics if  $A_s/A_e > 3.0$  [30]. The supply port is effectively a series resistance between the supply pressure source and the chamber as described in [17]. At the cutoff point it has no effect on the flow and the pressure at  $r_0$  must reach  $P_s$ . At maximum flow, as  $A_s$  is decreased to values less than  $A_s/A_e \approx 3.0$ , TR decreases and  $P_{cc}$  increases; thus for triodes with maximum turndown ratios, values of  $A_s/A_e > 3.0$  are desired.

Control Area to Exit Ratio:  $A_c/A_e$

References [17, 27--30, 44 and 47--49] indicate that as the control port area is decreased, the control flow required to reduce the total flow to given level decreases while the control pressure increases. Thus, as  $A_c/A_e$  is decreased, both TR and  $P_{cc}$  increase. As  $A_c$  is decreased for a given control flow, the tangential control jet velocity is increased as shown in (19), and thus a stronger vortex is created for a given control flow.\*

\*As discussed below and shown in Fig. 6 for  $A_c/A_e < 0.1$ , values of TR may become relatively insensitive to  $A_c$  or decrease slightly as  $A_c$  decreases due to inlet mixing region losses.



Exit Area Ratio:  $r_e/r_o$

As shown analytically [44] and experimentally [29], the vortex chamber radius ratio  $r/r_o$  is the parameter which most strongly influences the shape of the triode characteristic and determines strongly whether a proportional or bistable characteristic is obtained. Data from [29] is presented in Fig. 9. As  $r/r_o$  is increased, the value of the nondimensional control flow at any nondimensional total flow is increased, and the turndown ratio increases. The characteristic for  $r/r_o = 0.089$  is proportional while the characteristics for  $r/r_o \geq 0.12$  are bistable. As  $r/r_o$  increases, viscous dissipation is reduced, and the characteristics become more nearly bistable.

Chamber Aspect Ratio:  $h/r_o$

The analysis in [43, 44] has shown for aspect ratios  $h/r_o$  varying from 0.2 to 0.8 that triode characteristics are relatively insensitive to aspect ratio. Data in [30] shows for  $0.14 < h/r_o < 0.64$  that experimental characteristics are relatively independent of chamber height. The range over which a triode characteristic is chamber height independent is limited by  $h/r_o$  or equivalently  $r/r_o$ . If  $h$  is so small that the curtain area  $2\pi hr_o$  is less than  $Nr_o^2$ , where  $N$  is the number of exits, the triode characteristic will depend more strongly on  $h$  since the chamber height will set the exit area. Data [31] for smaller values of  $h/r_o$  in which the curtain area is the controlling exit area indicates that TR increases as  $h/r_o$  increases until TR becomes relatively insensitive to  $h/r_o$  over a range of values of  $h/r_o$ .

Turndown Ratio and Cutoff Control Pressure Design Charts

The data described above has demonstrated that for

$$A_s/A_e > 3 \quad (23)$$

$$h/r_o > 2 \quad (24)$$

$$0.14 < h/r_o < 0.64 \quad (25)$$

$$750 < R_w < 3300 \quad (26)$$

triode characteristics are relatively insensitive to  $A_s$ ,  $h$ , and  $R_w$  and thus become a function of only

$$A_c/A_e \text{ and } r_e/r_o$$

Lawley and Price [29] have conducted experiments which extend the data in [27, 28] summarizing the influence of  $A_c/A_e$  and  $r_e/r_o$  on triode turndown ratio and cutoff control pressure ratio for single exit amplifiers satisfying (23) -- (26). The data presented in [29] is for an unsymmetrical single supply and control inlet geometry, while the data in [27, 28] are for multi-input port symmetric geometries. A summary of data from [29] is presented in Fig. 10. Lawley and Price indicate that for unsymmetrical configurations, the values of TR and  $P_{cc}$  may yield errors on the order of 20% when compared with symmetric geometries; however, the estimates obtained may yield a good first approximation for triode design.

The Figure shows that as  $r_e/r_o$  is decreased for a given  $A_c/A_e$  both  $W$  and  $P_{cc}$  increase. It also shows that as  $A_c/A_e$  is decreased for fixed  $r_e/r_o$ ,  $P_{cc}$  increases and TR first increases and then decreases. At small enough values of  $A_c/A_e$ , as  $A_e$  decreases, TR decreases somewhat since the decrease in jet recovery factor essentially counteracts any gain in tangential velocity.

The plot also indicates that as  $A_c/A_e$  and  $r_e/r_o$  are decreased, the characteristic tends to be proportional, while as  $A_c/A_e$  and  $r_e/r_o$  increase, a more nearly bistable characteristic is obtained. As shown by (19) and (21) as  $A_e$  and  $r_o$  are decreased both the viscous losses on the side and end walls increase and the characteristics tend to be proportional, while as  $A_c/A_e$  and  $r_e/r_o$  increase, a more nearly bistable characteristic is obtained. In [28] a systematic method for triode design is developed based on Fig. 10. This method has been implemented in a computer assisted design program described in [50].

#### Studies of Profiled Chambers and Alternate Exit Configurations

A number of variations in triode geometry have been employed in addition to the geometries described above. Syred and Royal [26] and Bell [51] have employed taper of the internal chamber end walls in triodes. They found that tapering the chamber with an increasing depth as flow moves to the exit increases the linearity of the triode characteristics and the turndown ratio. Syred and Royal [26] also show that outlet diffuser angles may significantly influence amplifier characteristics.

Mayer [17] and Taplin [52] have also conducted extensive studies of vortex triodes and have shown the effectiveness of using a vented outlet geometry employing a receiver tube to decouple the load from the chamber. Because a very low pressure may be established in a vortex core, it is possible to aspirate flow from the outlet tube into the vortex chamber; thus, the outlet tube may provide both positive and negative flows and pressures (relatively to atmospheric pressure). Additional work on the influence of receiver tube geometry on triode performance is discussed by McCloy and Stevenson [31].

Otsap [49] has also employed a vented amplifier configuration which is suitable for driving a ram-type load.

Work cited in [31, 39, 44 and 48] has shown that using two exit ports, one in each end wall, increases the triode turn-down ratio and increases the tendency for a bistable characteristic in comparison to an otherwise similar single exit triode.

#### INFLUENCE OF GEOMETRY ON DIODE CHARACTERISTICS

The influences of geometry on diode characteristics has been discussed in [13, 14, 18, 19 and 53]. Paul [18] has found for a fixed chamber radius diode that the diodicity increases as  $A/A_c$  increases for  $0.23 < A/A_c < 2$ , while Koerper [48] found that a two exit hold geometry is superior to a single exit geometry. The observation of Heim [13] that projecting the exit port pipe into the chamber so that the edge is at the chamber midplane increases diodicity has been confirmed by Baker [19]. It is also noted that triode turndown ratio results presented in Fig. 10 provide an initial method of estimating the influence of geometry on the resistance of diodes in the high flow resistance direction, thus as  $A/A_c$  and  $r/r_c$  are reduced the flow resistance in the high flow resistance direction increases.

#### TRIODE AND DIODE DYNAMIC CHARACTERISTICS

In [24, 54] Taplin has developed dynamic lumped parameter models to represent vortex triode dynamic behavior. In [24] a functional representation of the response, supported by experimental data, is described which indicates the small signal linear response of a triode may be characterized by a time delay  $T_D$  and a first order lag time constant  $T_L$  with the delay time equal to  $T_D = 0.25 T_f$

and the lag time equal to  $T_L = 0.25 T_f$  where  $T_f$  is the vortex chamber fill time.

$$T_f = \frac{\pi h(r_o^2 - r_e^2)}{\bar{Q}} \quad (27)$$

where  $\bar{Q}$  is the average volume flow rate through the triode.

Anderson [55] has developed a dynamic lumped parameter model similar to Taplin for small signal response of a triode, but in which model parameters are related directly to the flow field in the triode. This lumped parameter representation is summarized in Fig. 11 and includes the following parameters.

- (1) The linearized control, supply and exit port resistances,  $R_c, R_s, R_e$
- (2) An inlet mixing region described by linearization of the continuity (3) and angular moment equations (19):

$$\Delta u_o = K_u \Delta W_o \quad (28)$$

$$\Delta v_o = K_c \Delta W_c - K_o W_o \quad (29)$$

with

$$K_u = \frac{1}{2\pi r_o h \rho}$$

$$K_c = \frac{2\epsilon W_{co}}{c_c A_c \rho W_{oo}}$$

$$K_o = \frac{\epsilon W_{co}^2}{c_c A_c W_{oo}^2 \rho}$$

where  $W_{co}$  and  $W_{oo}$  represent operating point flows.

- (3) A main chamber region in which two effects are represented:

- (a) the time delay associated with the fluid transport
- (b) the viscous action between the end wall boundary layers and the main core.

These effects are represented as:

$$\Delta(p_o - p_e) = \frac{K_1 e^{-T_D s}}{1 + T_L s} \Delta v_o + K_2 \Delta u_o \quad (30)$$

where:

$$K_1 = \left. \frac{\partial P}{\partial v_o} \right|_o$$

$$K_2 = \left. \frac{\partial P}{\partial u_o} \right|_o$$

the quantities  $K_1$  and  $K_2$  are steady-state gains calculated from the distributed parameter response,  $s$  is the Laplace operator and  $e$  is exponential. The time constants  $T_D$  and  $T_L$  are determined by fitting (30) to the distributed parameter response developed in [55].  $T_D$  and  $T_L$  have been shown to be a function of the boundary layer coefficient BLC, the swirl  $\lambda$  and the chamber height ratio  $h/r$  as shown in Fig. 12. The Figure indicates that as  $\lambda$  increases for fixed geometry and fixed BLC,  $T_D/T_f$ , the delay time to fill time ratio decreases from about 0.3 to 0.1. The ratio is relatively insensitive to  $h/r$ , indicating the dimensional delay time  $T_D$  is almost proportional to chamber volume. The decrease in  $T_D/T_f$  as  $\lambda$  increases indicates that as the vortex strength in the chamber increases and more fluid is in the boundary layer, the delay time decreases in proportion to the fill time.

The lag time to fill time ratio  $T_L/T_f$  is influenced by  $h/r$ . As  $h/r$  increases  $T_L/T_f$  increases indicating the lag time increases faster than the chamber height. As the swirl increases and a stronger vortex is formed,  $T_L/T_f$  increases since the boundary layers play an increasingly important role. The range of  $T_L/T_f$  lies between 0.2 and 0.6 in the Figure.

Experimental data presented in [55] indicates that for low swirl conditions, i.e. for a triode operating near maximum flow, using\*

$$T_D/T_f \approx T_L/T_f \approx 0.25 \quad (31)$$

\*These are the values recommended by Taplin [24].

provides an approximate estimate for the triode response. As a triode operating point is changed and operation near cutoff is considered, the time constant values approach:

$$T_D/T_F \rightarrow 0.1 \quad (32)$$

$$T_L/T_f \rightarrow 0.5--0.6$$

Using the approximations of (31)--(32), a rough estimate of the range of response times occurring in a triode for small signal response may be obtained.

Experimental data for vortex triode response is presented in [24, 54] with direct comparisons of analysis and data presented in [55]. This data essentially verifies the delay-lag character of the response described.

The dynamic analysis presented in [24, 55] have been for small signal disturbances. Some data for estimating the response from full on to off has been described by Neve [56]. Data in [56] indicates for triodes with  $0.1 < h/r < 2$  that the on-to-off and off-to-on response times are similar and that the large scale switching response time may be represented approximately for  $0.1 < h/r_o < 2$  as:

$$\frac{T_r}{T_f} = 0.47 \left[ \frac{2r_o}{h} \right]^{1.32} \quad (34)$$

where  $T_r$  is the response time.

For triodes, analytical and experimental response data indicate that as the chamber volume is increased and as the average flow through the triode decreases, the response time for both small perturbation and large signals increases. Thus, to minimize the triode response time, the chamber height should be reduced to the minimum height permitted by static considerations.

Dynamic response data for vortex diodes is presented in [53]. Neve [56] has shown that the results in [53] correlate well with equation (34).

#### VORTEX DIODE AND TRIODE APPLICATIONS

Because among various types of pure fluid diodes, the vortex diode has been shown to have the highest ratio of forward to reverse

flow resistance, it has a strong potential for application in systems requiring no moving part diodes. Application of the diode in classical rectification circuits is discussed in [57] while further discussion of diode applications is contained in [13, 14, 18, 19 and 20]. The use of a vortex triode which is configured to act as a high gain active diode is discussed in [58].

The ability of the vortex triode to modulate the total flow from a load makes it attractive for applications requiring no moving part open center valves. The triode may be used in applications similar to classical open centered valves as described in [20, 30 and 57] and may directly replace classical two- and four-way valves in some applications. Hydraulic and pneumatic servovalves have been constructed using vortex triodes as described in [20, 23] while additional hydraulic system applications are described in [31, 50].

Studies describing the application of triodes to specific flow modulation and signal processing systems include [24] for aircraft flight control systems, [6, 24] for thrust vector control systems, [59] for aircraft fuel control and air conditioning systems and [52] for dynamic signal processing circuits. The use of triodes in constructing a digital to analog converter is described in [60] and as an adjustable pressure regulator in [61].

Discussion of the application of triodes to the control and metering of flows in large scale water distribution systems and river basins is summarized in [32, 62].

The construction of a direct electric to fluid transducer using a triode operating upon liquid and an electromagnetic field is described in [63].

## REFERENCES

1. Smith, J. L., Jr., "An Experimental Study of the Vortex in a Cyclone Separator," Trans. ASME, JOURNAL OF BASIC ENGINEERING, Vol. 84, 1962.
2. Kerrcbrock, J. L. and Meghreblian, R. V., "Vortex Containment for the Gaseous Fission Rocket," J. AEROSPACE SCIENCE, Vol. 28, 1961.
3. Ragsdale, R. G., "NASA Research on the Hydrodynamics of the Gaseous Vortex Reactor," Tech. Report NASA TN-D-288, 1960.
4. Hilsch, R., "The Use of the Expansion of Gases in a Centrifugal Field as a Cooling Process," Review of Scientific Instruments, Vol. 18, 1947.
5. Savino, J. M. and Ragsdale, R. G., "Some Temperature and Pressure Measurements in Confined Vortex Fields," ASME Paper No. 60-5A-4, 1960.
6. Gillespie, T. D. and Shearer, J. L., "The Control of Thrust and Flow Rate in Choked Nozzles by Vortex Generation," FLUIDICS QUARTERLY, Vol. 4, 1972.
7. Pengelley, C. D., "Thermal Phenomena in a Vortex," Symposium on the Vortex Tube as a True Free Air Thermometer, Armour Research Foundation, 1955.
8. Rodely, A. E., White, D. F. and Chanaud, R. C., "A Digital Flow Meter without Moving Parts," ASME Paper No. 65-WA-FM-6, 1965.
9. Kwok, C. K. and Nastou, D., "Investigation of a Vortex Flowmeter," Proceedings, Sixth Cranfield Fluidics Conference, 1974.
10. Sarpkaya, T., Pavlin, C. and Phasook, S., "A Theoretical and Experimental Investigation of a Confined Vortex Oscillator," Trans. ASME, J. OF BASIC ENGINEERING, Vol. 91, 1969.
11. Sarpkaya, T., Goto, J. M., Kirshner, J. M., "A Theoretical and Experimental Study of the Vortex Rate Gyro," Advances in Fluidics, ASME 1967.



12. Hayes, W. and Tucker, H. G., "Dynamic Range and Frequency Response of the Vortex Rate Sensor," Proceedings of the Fifth Cranfield Fluidics Conference, 1972.
13. Heim, R., "An Investigation of the Thoma Counterflow Brake," Transactions of the Munich Hydraulic Institute, 1929, ASME, Translation by M. P. O'Brien, 1935.
14. Zobel, R., "Experiments on a Hydraulic Reversing Elbow," Mitt. Hyd. Inst., Tech. Hochschule Munchen 8, 1, (Risley Translation No. 439).
15. Bowles, R. E. and Horton, B. M., "Fluid Amplifier," U. S. Patent 3,276,259, 1966.
16. Dexter, E. M., "No Moving Parts--A Feature of New Valves," JOURNAL, SOCIETY OF AUTOMOTIVE ENGINEERS, 1961.
17. Mayer, E. A., "Large Signal Vortex Valve Analysis," Advances in Fluidics, ASME, 1967.
18. Paul, F. W., "Survey of Steady-State Fluidic Diode Performance," ASME Paper No. 69-WA/FLCS-14, 1969.
19. Baker, P. J., "A Comparison of Fluid Diodes," Proceedings, Second Cranfield Fluidics Conference, 1967.
20. Foster, K. and Parker, G. A., Fluidics Components and Circuits, Wiley-Interscience, New York, 1970.
21. Kirshner, J. M., Fluid Amplifiers, McGraw-Hill Book Company, New York, 1966.
22. Rivard, J. G. and Walberer, J. C., "A Fluid State Vortex Hydraulic Servovalve," Paper presented at the 21st National Conference on Fluid Power, 1965.
23. Vos, C. E., "Design, Fabrication and Test of a Fluoric Servovalve," Tech. Report NASA CR-54783, 1965.
24. Taplin, L. B., "Small Signal Analysis of Vortex Amplifiers," AGARDograph 118, 1968.
25. Gebben, V. D., "Vortex Valve Performance Power Index," Advances in Fluidics, ASME, 1967.
26. Syred, N. and Royle, J. K., "Operating Characteristics of High Performance Vortex Amplifiers," FLUIDICS QUARTERLY, Vol. 4, 1972.

27. Chow, S. K., "An Experimental Study on the Characteristics of Vortex Valves," Proceedings of the IFAC Symposium on Fluidics, 1968.
28. Wormley, D. N. and Richardson, H. H., "A Design Basis for Vortex-type Amplifiers Operating in the Incompressible Flow Regime," Trans. ASME, JOURNAL OF BASIC ENGINEERING, Vol. 92, 1970.
29. Lawley, T. J. and Price, D. C., "Design of Vortex Fluid Amplifiers with Asymmetric Flow Fields," Trans. ASME, JOURNAL OF DYNAMIC SYSTEMS, MEASUREMENT AND CONTROL, Vol. 94, 1972.
30. Wormley, D. N. and Richardson, H. H., "Experimental Investigation and Design Basis for Vortex Amplifiers Operating in the Incompressible Flow Regime," Tech. Report No. DSR 70167-1, Dept. of Mechanical Engineering, Massachusetts Institute of Technology, 1968.
31. McCloy, D. and Stevenson, I. J., "Some Experiments with Oil Hydraulic Vortex Valves," Proceedings, Fifth Cranfield Fluidics Conference, 1972.
32. Brombach, H., "Vortex Devices in Hydraulic Engineering," Proceedings, Fifth Cranfield Fluidics Conference, 1972.
33. Al-Shamma, K. A., Royle, J. K., Boucher, R. F. and Asquith, R., "Axial Vortex and Coanda-Vortex Flow Controls," Proceedings, Fifth Cranfield Fluidics Conference, 1972.
34. Fitt, D. W., "A Vortex Valve and Ejector Combination for Improved Turn Down Ratios," Proceedings, Sixth Cranfield Fluidics Conference, 1974.
35. Rosenzweig, M. L., Lewellen, W. S. and Rose, D. H., "Confined Vortex Flows with Boundary Layer Interaction," AIAA JOURNAL, Vol. 2, 1964.
36. Ostrach, S. and Loper, D. E., "An Analysis of Confined Vortex Flows, AIAA Paper No. 66-88, 1966.
37. Kwok, C. C. K., "Vortex Flow in a Thin Cylindrical Chamber and its Application in Fluid Amplifier Technology," Report No. 66-8, Department of Mechanical Engineering, McGill University, 1966.

38. Savino, J. M. and Keshock, E. G., "Experimental Profiles of Velocity Components and Radial Pressure Distributions in a Vortex Contained in a Short Cylindrical Chamber," Technical Report No. NASA TN D-3072, 1965.
39. Lewellen, W. S., Burns, W. J. and Stirckland, H. J., "Transonic Swirling Flow," AIAA Paper No. 68-693, 1968.
40. Farris, G. J. et. al., "A Theoretical and Experimental Study of Confined Vortex Flow," ASME Paper No. 69 WA/APM-3, 1969.
41. Lawley, T. J., Lea, J. F. and Price, D. C., "Flow and Performance Characteristics for Non-Vented Vortex Amplifiers," ASME Paper No. 70-WA/FLCS-18, 1970.
42. King, W. S., "Momentum Integral Solutions for the Laminar Boundary Layer on a Finite Disk in a Rotating Flow," Aerospace Corp. Report No. ATN-63 (9227)-3, 1963.
43. Wormley, D. N., "An Analytical Model for the Incompressible Flow in Short Vortex Chambers," Trans. ASME, JOURNAL OF BASIC ENGINEERING, Vol. 91, 1964.
44. Bichara, R. T. and Orner, P. A., "Analysis and Modeling of the Vortex Amplifier," Trans. ASME, JOURNAL OF BASIC ENGINEERING, Vol. 91, 1969.
45. Kendall, J. M., Jr., "Experimental Study of a Compressible Viscous Vortex," Jet Propulsion Laboratory, Tech. Report No. 32-290, 1962.
46. Bauer, A. B., "Vortex Valve Operation in a Vacuum Environment," ASME Paper No. 63-FB-47, 1968.
47. Mayer, E. A., "Parametric Analysis of Vortex Amplifiers," Bendix Technical Journal, 1969.
48. Koerper, D. E., "Design of an Optimized Vortex Amplifier," Engineering Design Center Tech. Report No. 7-65-6, Case Institute of Technology, 1965.
49. Otsap, B. A., "The Vortex Pressure Amplifier Characteristics," Proceedings, IFAC Symposium on Fluidics, 1968.

50. **Skoog, A. I., "Oil Hydraulic Fluidic Amplifiers,"**  
**Proceedings, Fifth Cranfield Fluidics Conference, 1972.**
51. **Bell, A. C., "Optimization of a Vortex Valve," S.M.**  
**Thesis, Department of Mechanical Engineering, Massachusetts**  
**Institute of Technology, 1965.**
52. **Taplin, L. B., "Phenomenology of Vortex Flow and its**  
**Application to Signal Amplification," FLUIDICS**  
**QUARTERLY, Vol. 1, 1968.**
53. **Jacobs, B. E. A. and Baker, P. J., "The Steady-State**  
**and Transient Performance of Some Large-Scale Vortex**  
**Diodes," Proceedings, Fifth Cranfield Fluidics**  
**Conference, 1972.**
54. **Taplin, L. B. and Saleno, A. A., "Dynamic Equivalent**  
**Circuit for a Vortex Amplifier," Proceedings, Fourth**  
**Cranfield Fluidics Conference, 1970.**
55. **Anderson, W. W., "A Dynamic Model of Vortex-type Fluid**  
**Amplifiers," Ph.D. Thesis, Department of Mechanical**  
**Engineering, Massachusetts Institute of Technology,**  
**1971.**
56. **Neve, R. S., Ph.D. Thesis Investigation at the City**  
**University, London, England.**
57. **Tippetts, J. R., "General Design Methods to Circuits**  
**Associated with Regenerative Systems," Proceedings.**  
**Sixth Cranfield Fluidics Conference, 1974.**
58. **Syred, N. and Tippetts, J. R., "A High Gain Active**  
**Diode--the Reverse Flow Vortex Amplifier,"**  
**Proceedings, Sixth Cranfield Fluidics Conference,**  
**1974.**
59. **Taylor, A. F., "Vortex Devices in Aircraft Fluid Systems,"**  
**Proceedings, Fourth Cranfield Fluidics Conference,**  
**1970.**
60. **Vande Vegte, J., and Chowdhury, A. K., "A Vortex**  
**Amplifier Digital-to-Analog Converter," Proceedings,**  
**Fifth Cranfield Fluidics Conference, 1972.**

61. Mayer, E. A., "Adjustable Vortex Pressure Regulator," ASME Paper No. 70-FLCS-9, 1970.
62. Brombach, H., "Flow Control by Use of Digital and Analog Switched Vortex Amplifiers," Proceedings, Sixth Cranfield Fluidics Conference, 1974.
63. Shimada, K., "Static Characteristics of an Electromagnetically-Controlled Vortex-type Liquid Amplifier," Proceedings, Sixth Cranfield Fluidics Conference, 1974.

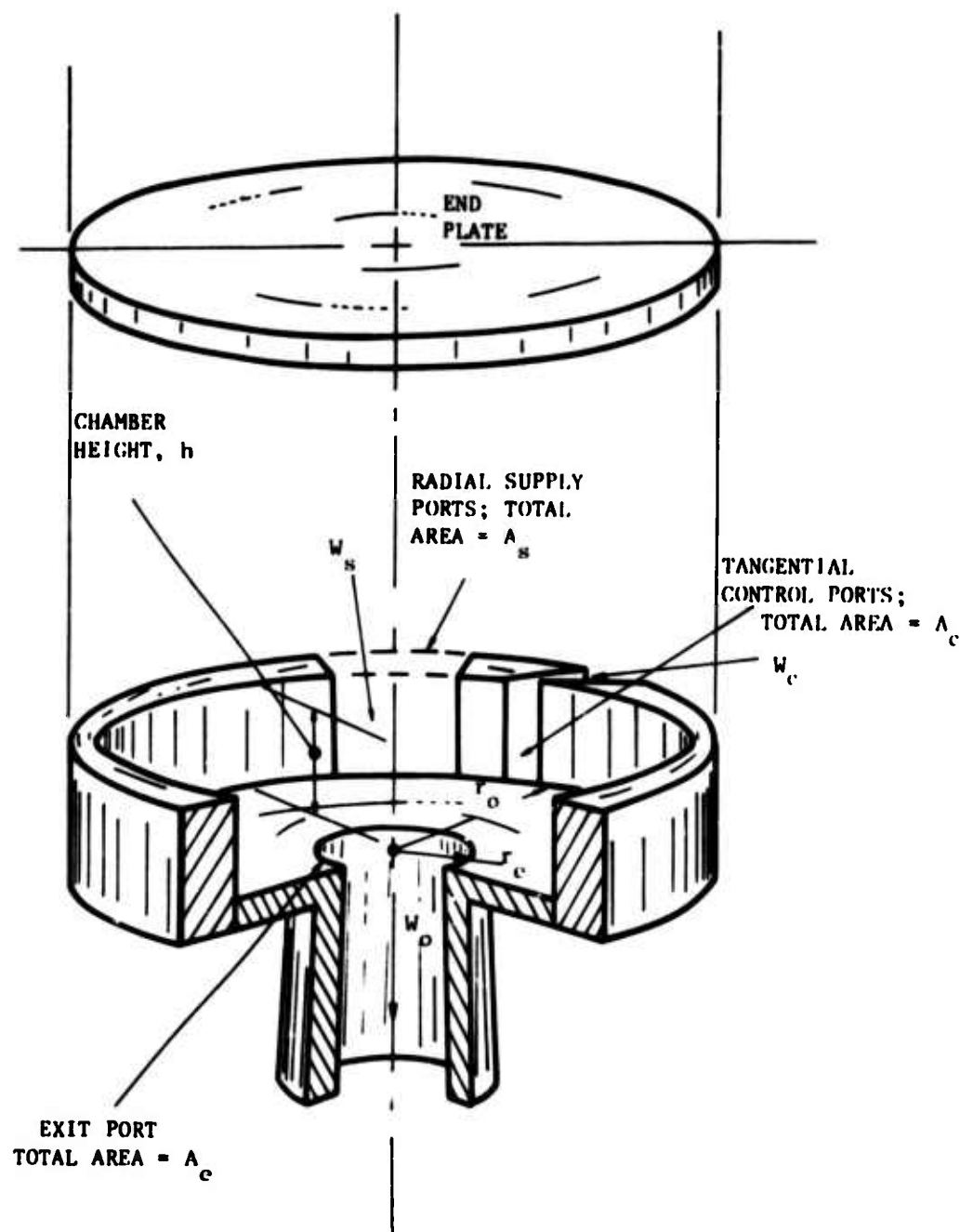
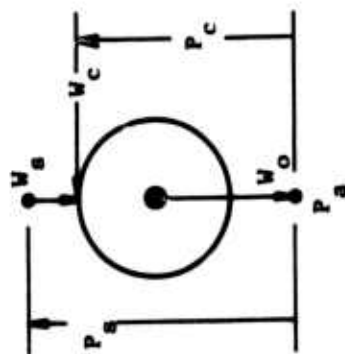


FIG. 1--Conceptual Diagram of a Vortex Triode Amplifier



CIRCUIT  
SYMBOL:

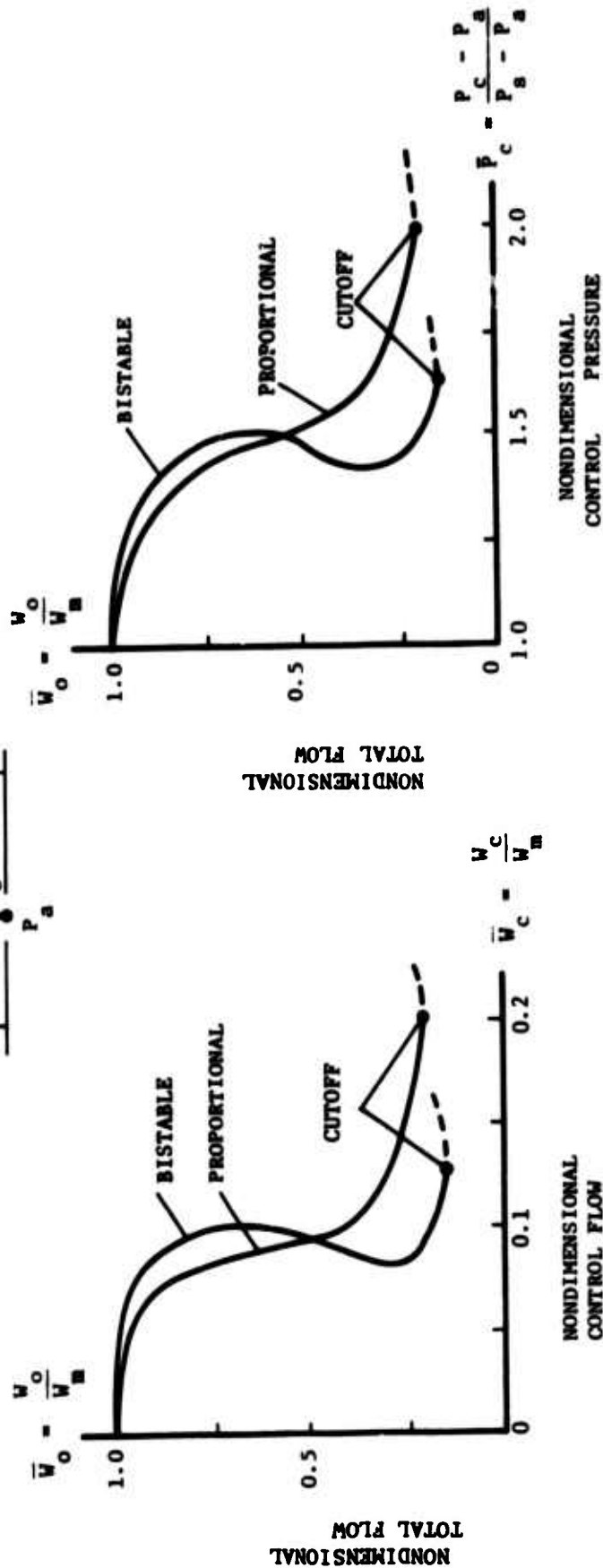
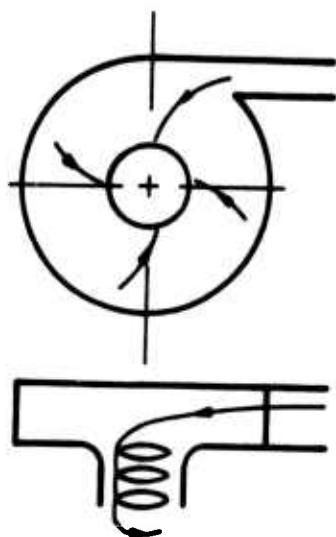
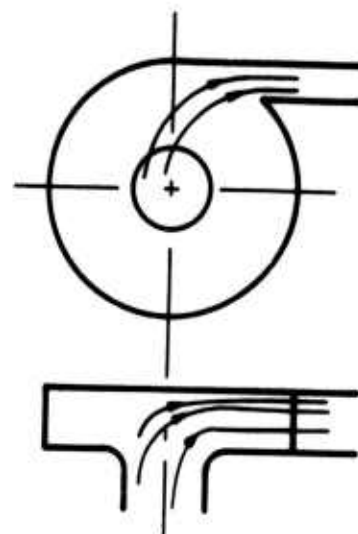


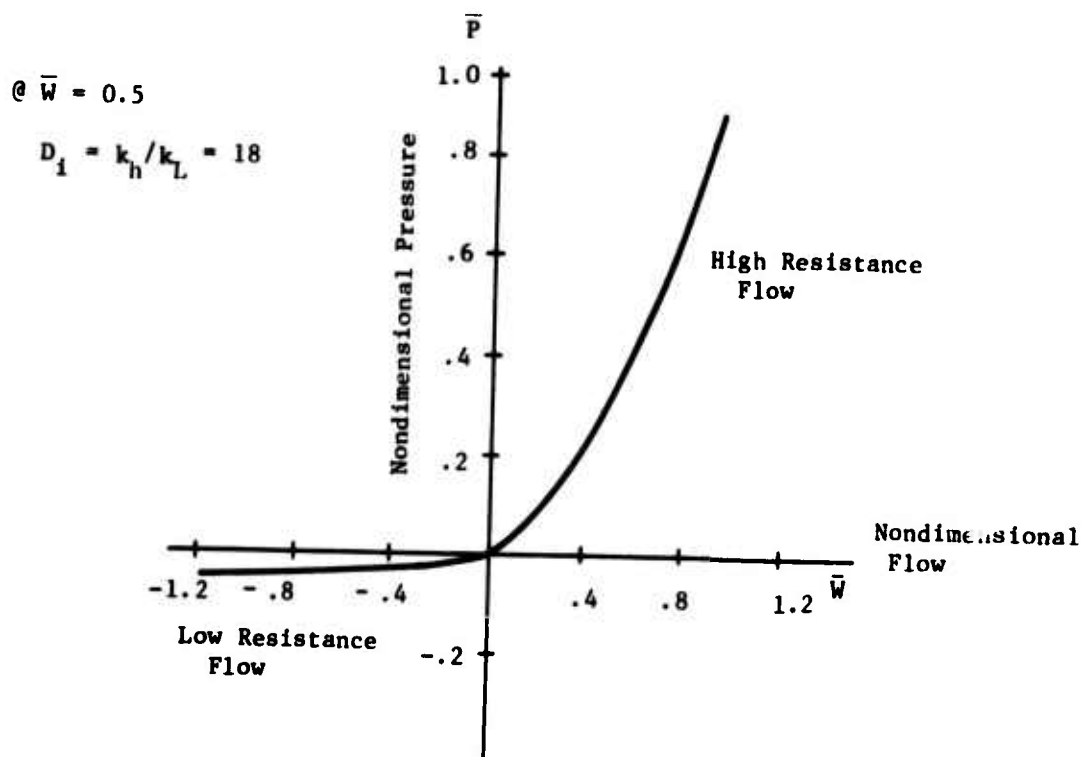
FIG. 2--Vortex Triode Transfer Characteristics at Constant Supply and Exhaust Pressure



High Resistance Flow Direction



Low Resistance Flow Direction



Nondimensional Characteristic of Vortex Diode Described in [18]

FIG. 3--Vortex Diode Configuration and Typical Characteristics



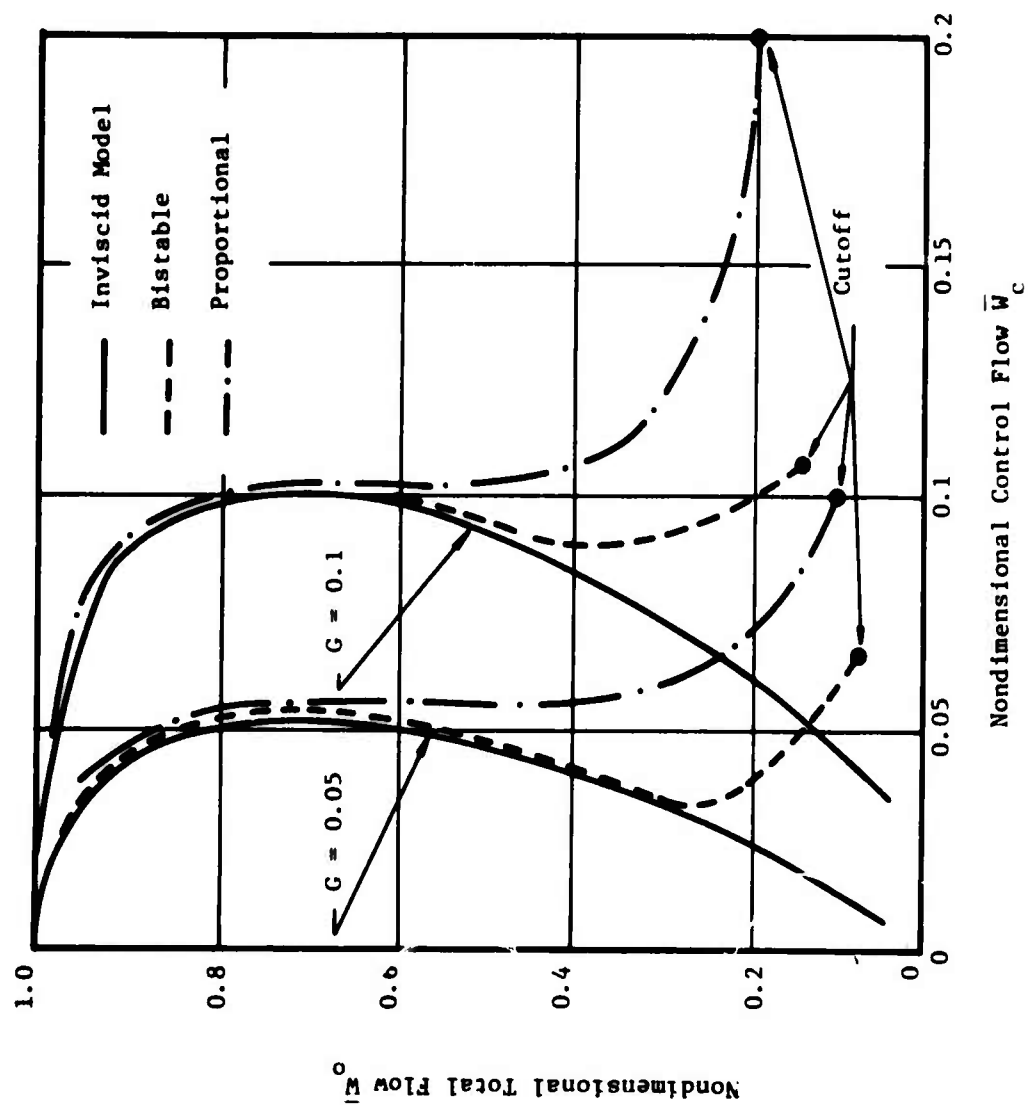


FIG. 4--Inviscid Model Triode Characteristics Compared with Typical Bistable and Proportional Prototype Triode Characteristics

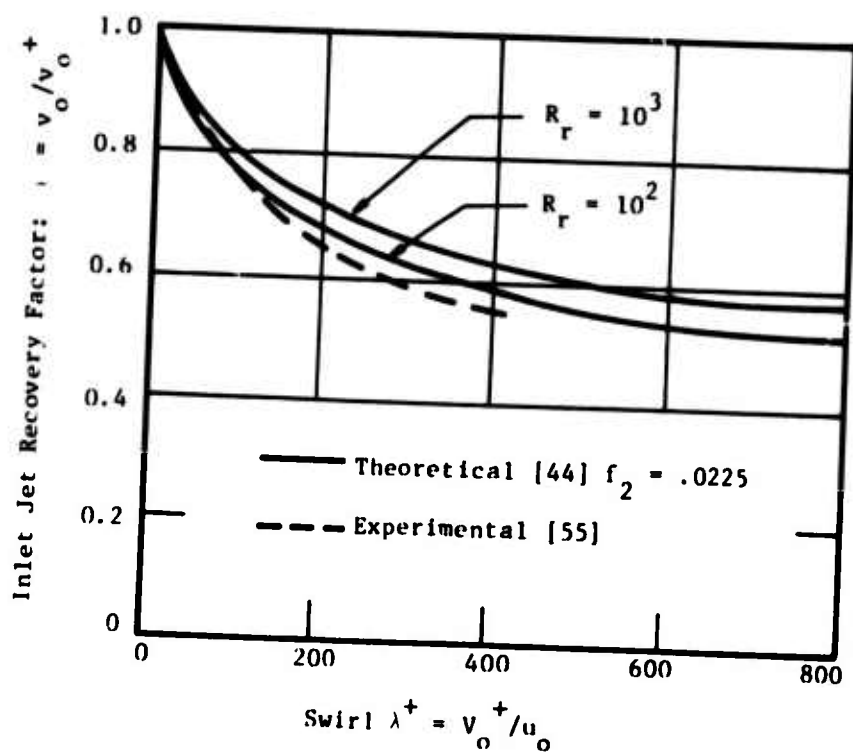


FIG. 5--Theoretical and Experimental Inlet Jet Angular Momentum Recovery Factor Versus Swirl

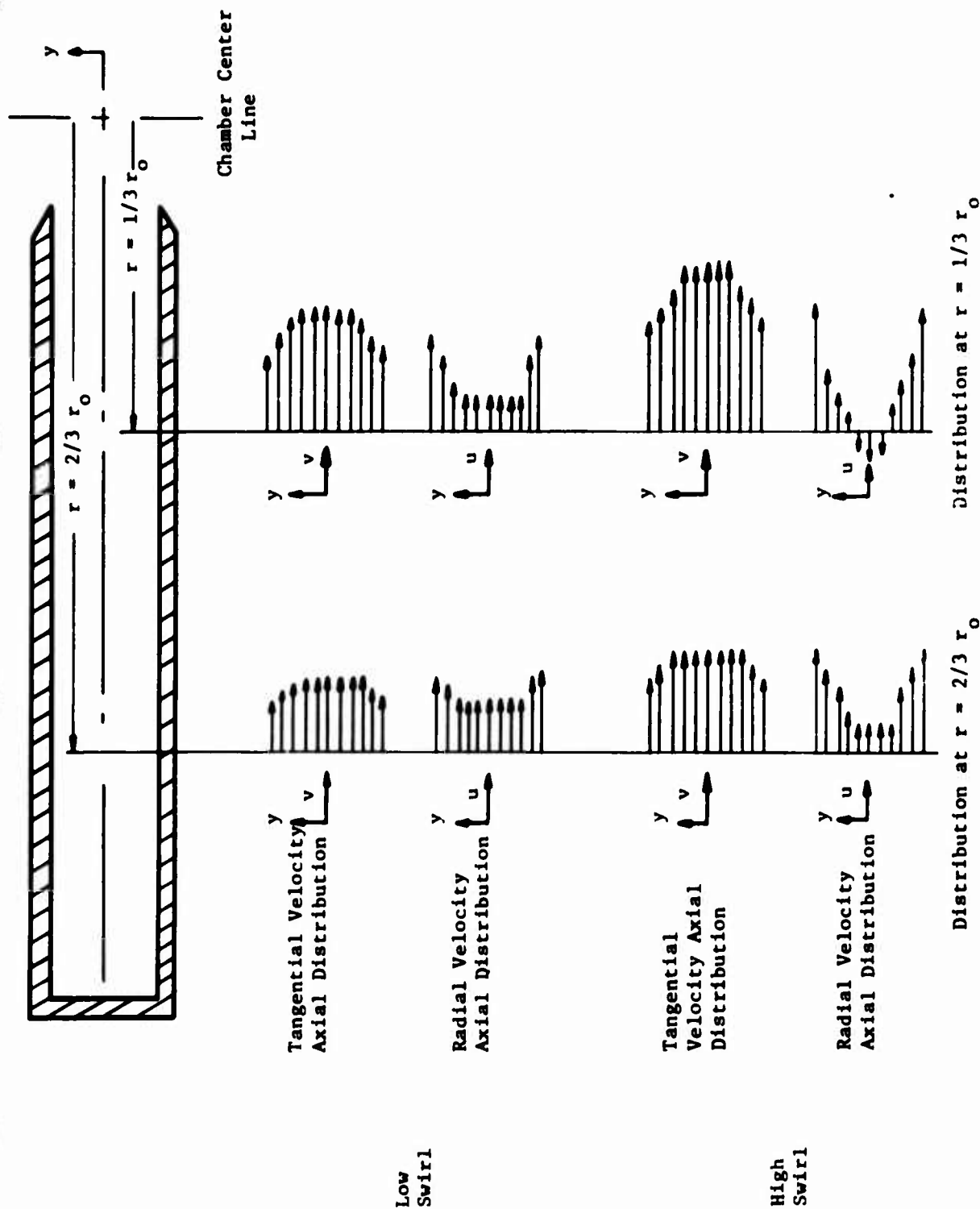


FIG. 6---Typical Tangential and Radial Velocity Profiles for Low and High Swirl Conditions in a Vortex Chamber

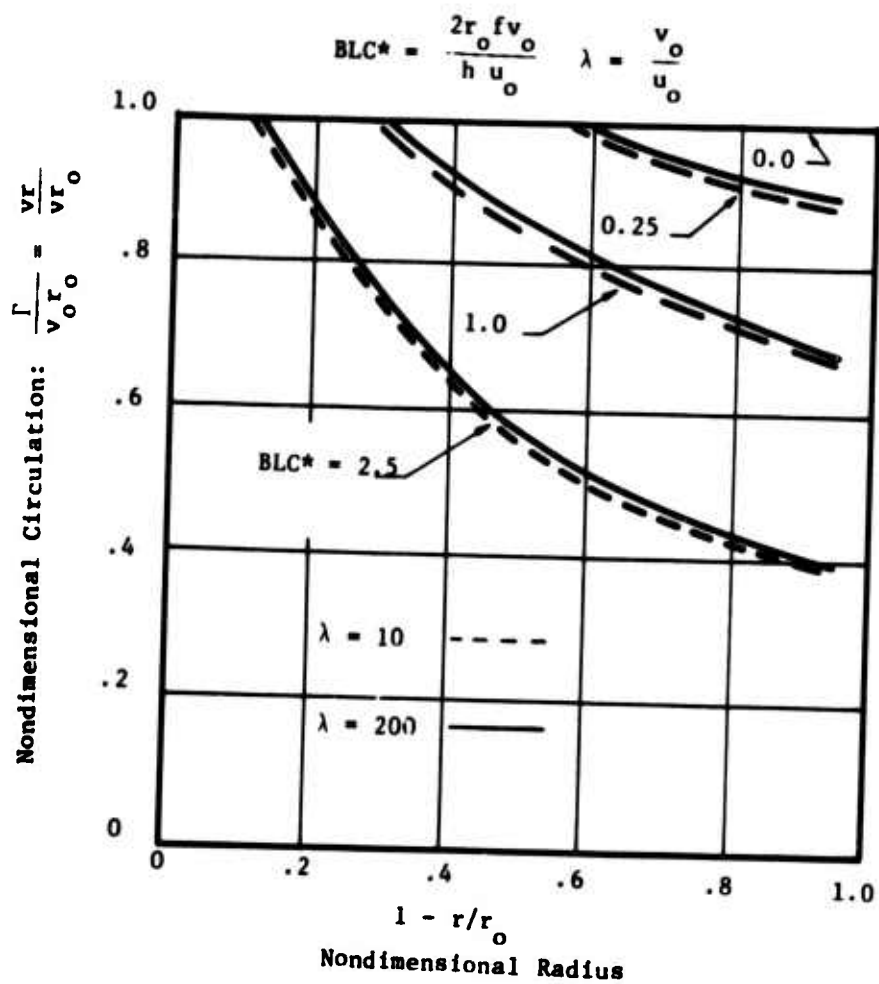


FIG. 7--Circulation Distribution in a Vortex Chamber as a Function of Radius for Selected Values of the Modified Boundary Layer Coefficient  $BLC^*$  and the Swirl  $\lambda$

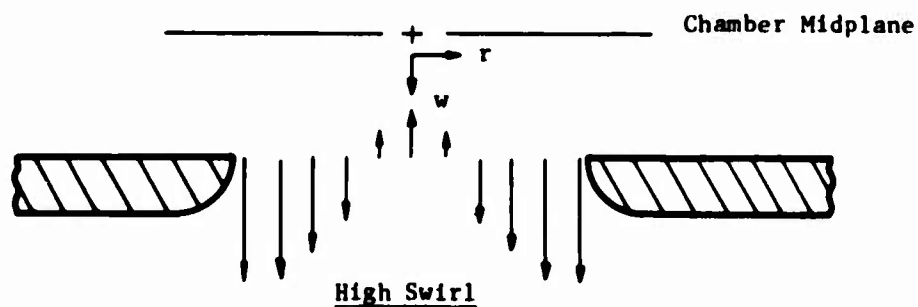
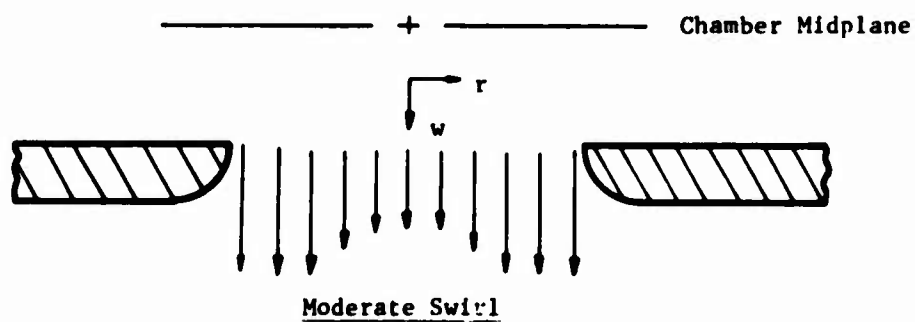
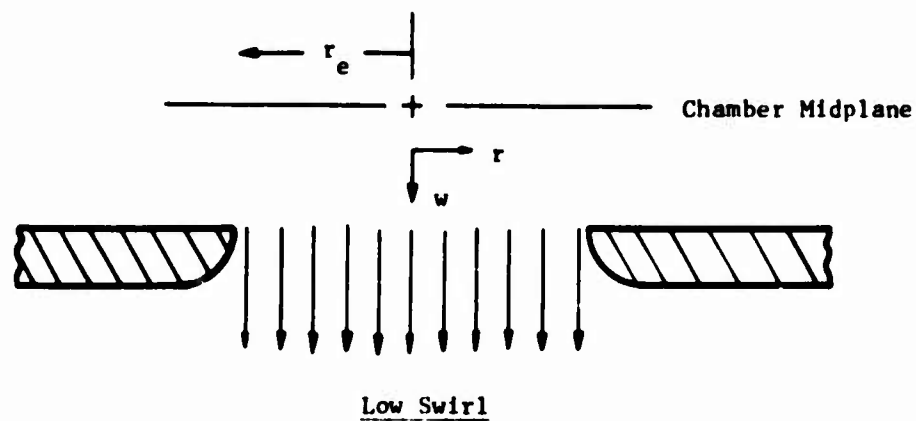


FIG. 8--Axial Velocity  $w$  Distribution in Vortex Chamber Exit for Selected Swirl Conditions as Illustrated in [44].

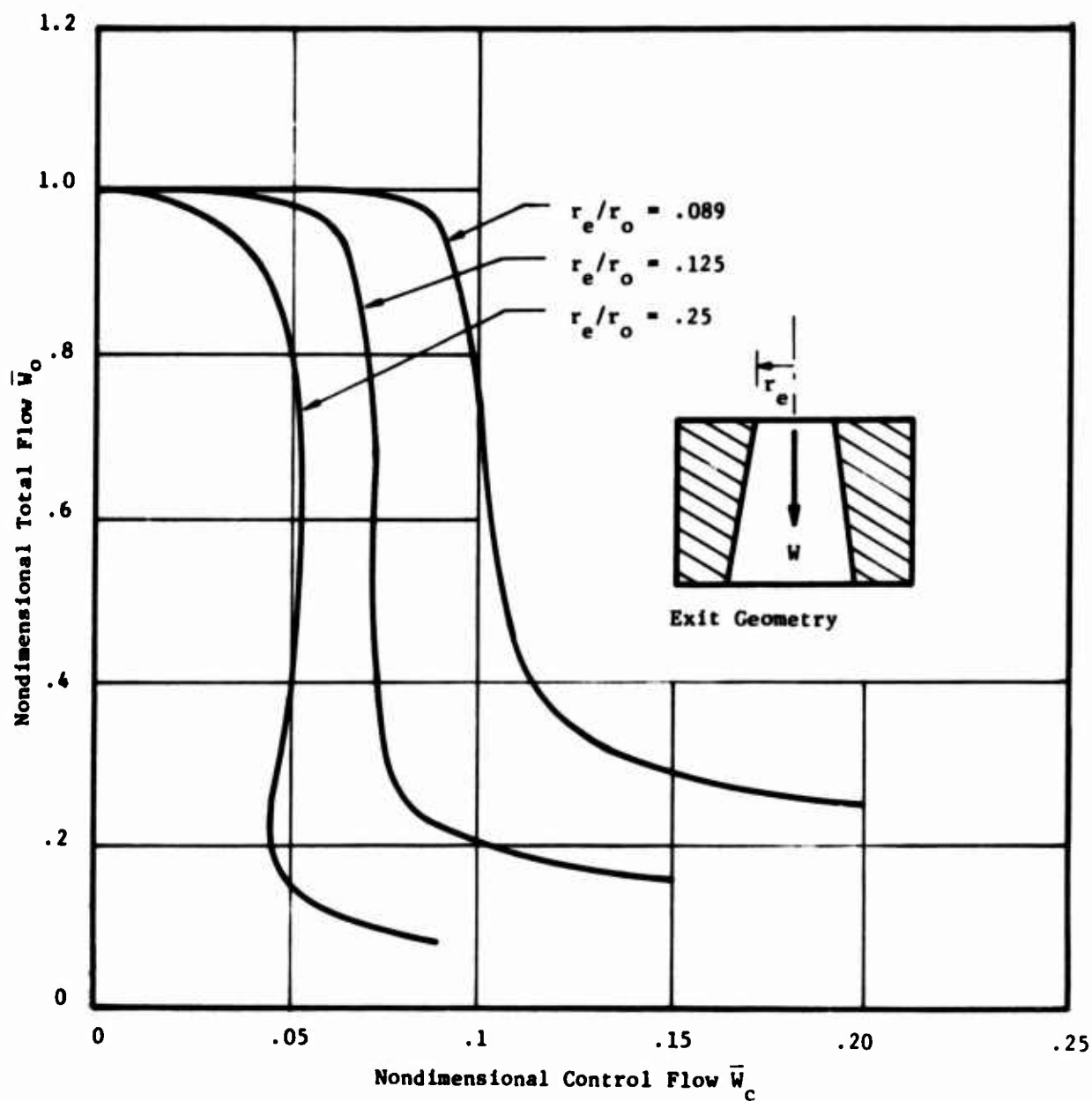


FIG. 9--Influence of Chamber Radius Ratio on Vortex Triode Transfer Characteristics--From Data in [28].

— Data from [28]  
 — Data from [29]  
 - - - Postulated in [29]

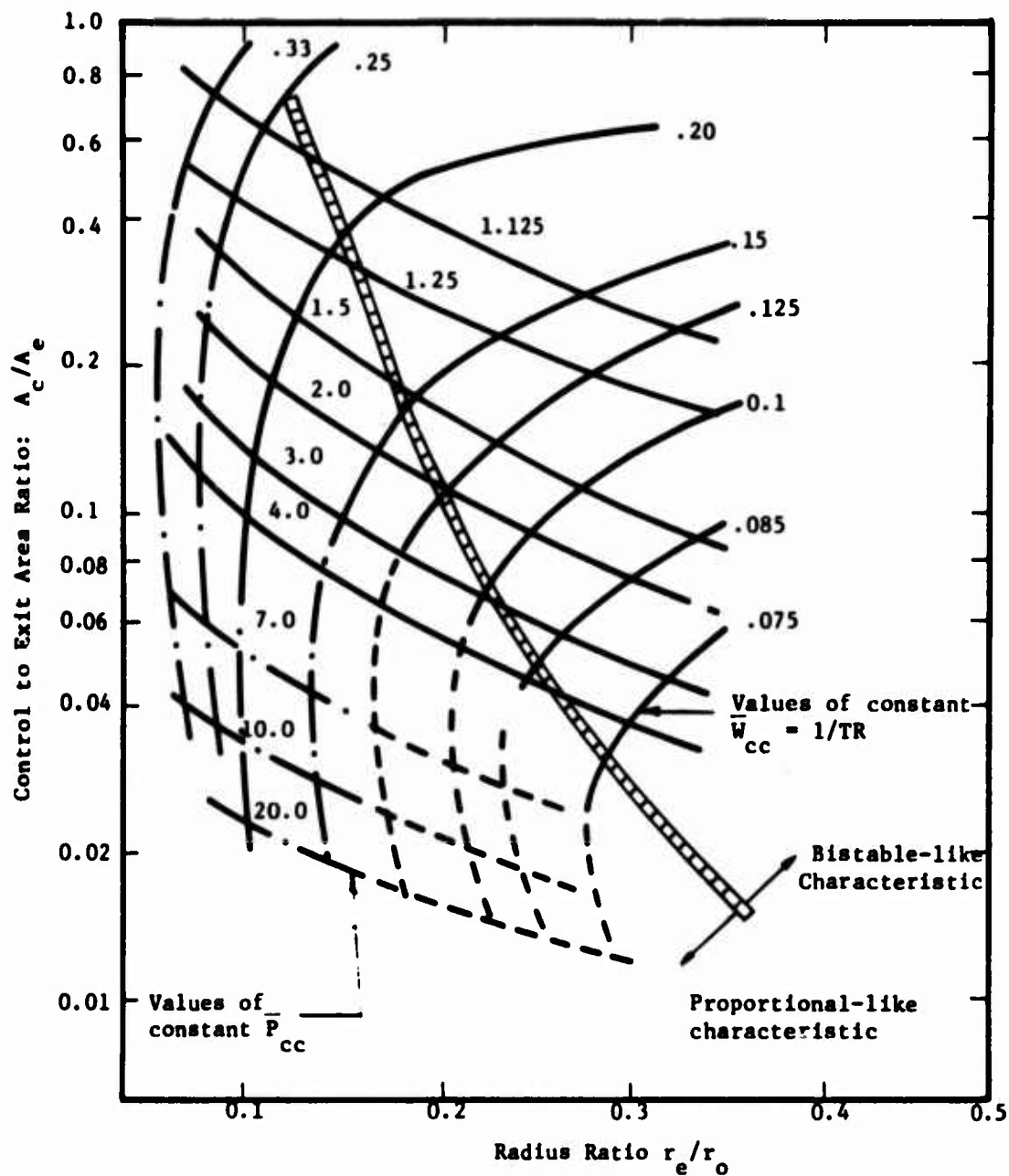


FIG. 10--Single Exit Vortex Triode Turndown Ratio and Cutoff Control Pressure Ratio Versus Radius Ratio and Control to Exit Area Ratio as Illustrated in [29].

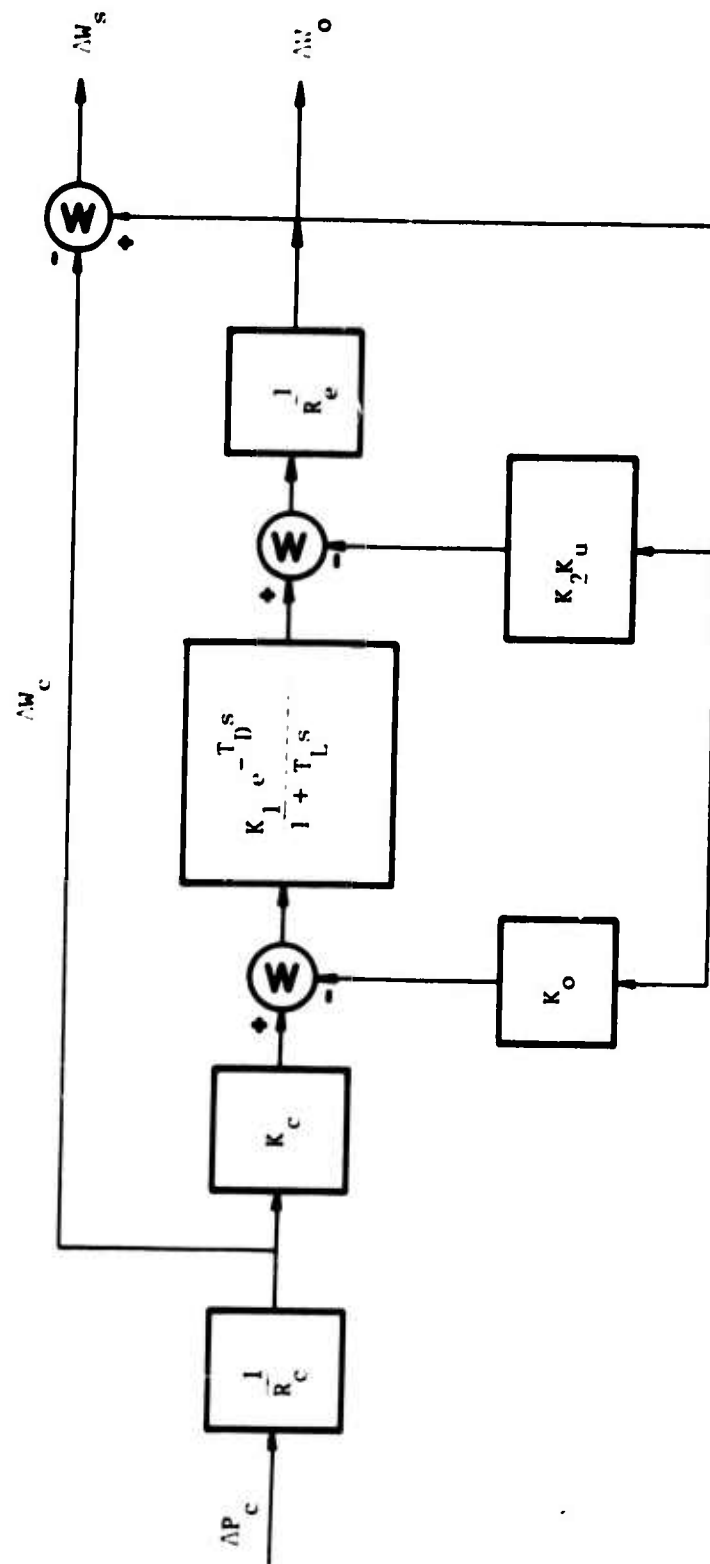


FIG. 11--Small Signal Perturbation Dynamic Model of Triode as Illustrated in [55].



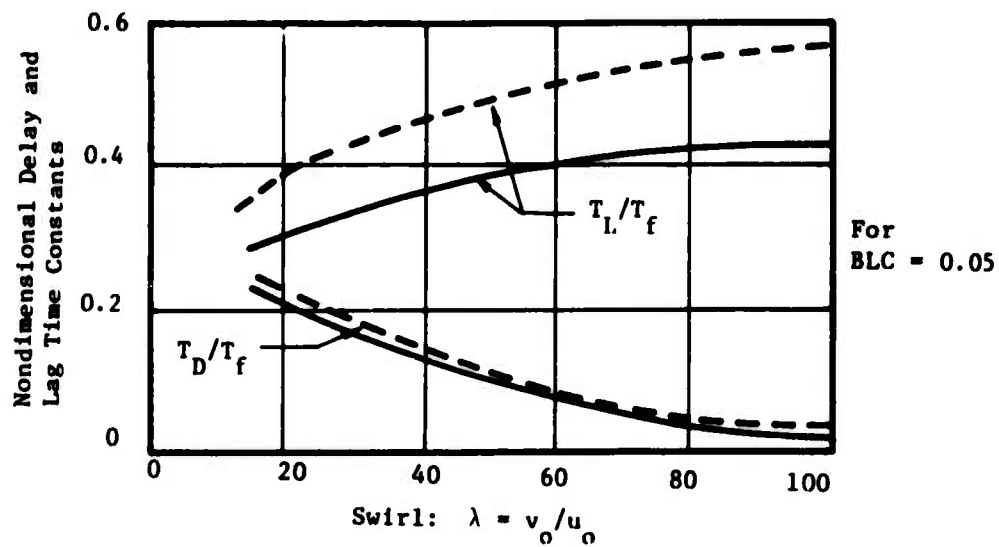
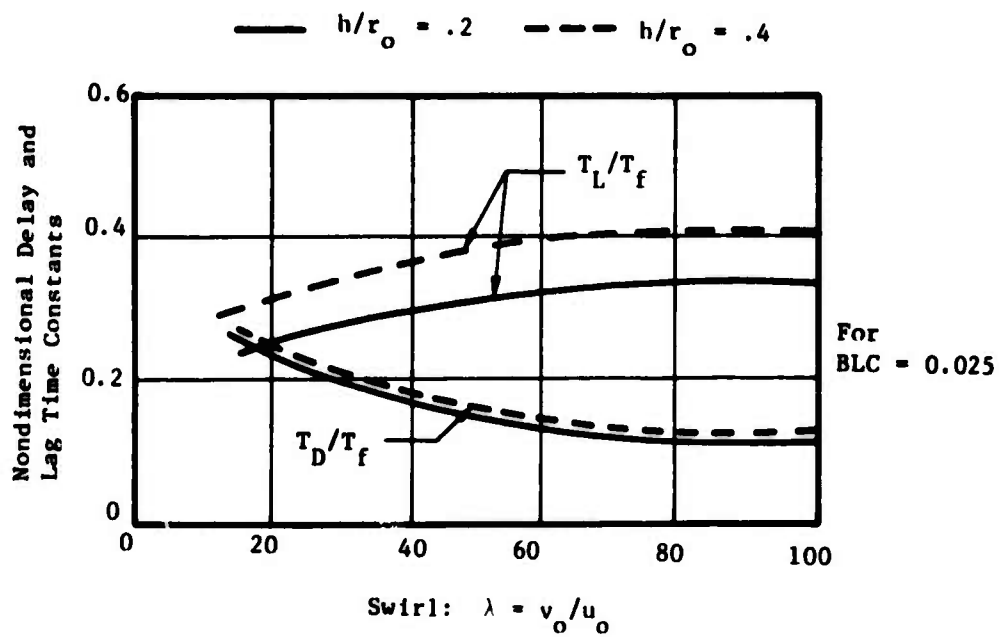


FIG. 12--Delay  $T_D$  and Lag  $T_L$  Time Constants as a Function of Swirl  $\lambda$  for a Triode as Illustrated in [55].

VORTEX DIODES

FOR PRESENTATION AT  
HARRY DIAMOND LABORATORY

1974

STATE-OF-THE-ART  
FLUIDICS SYMPOSIUM

S. S. FINEBLUM  
BELL LABORATORIES  
Whippany, New Jersey 07981

## VORTEX DIODES

### Abstract

The two elements of the vortex diode rectification ratio, the pressure drop in the "backward" or vortex path, and the "forward" path are separately studied. The effectiveness of the vortex as a means of generating pressure drop, is expressed as the ratio of vortex pressure drop to the inlet nozzle velocity head. This, in turn, is a function of the nondimensional vortex radius and "n", the vortex

exponent in the expression  $V = V_1 \left( \frac{r_1}{r} \right)^n$ . Maximum vortex n (where n = 1.0 only for a "free" vortex) was obtained by increasing the axial length-to-vortex diameter ratio to 0.35 or above. These results are consistent with other observations. The forward-flow pressure drop was minimized and the diode effectiveness or "diodicity" thereby improved, by means of avoiding both cavitation at the tangential nozzle and by minimizing drastic changes in fluid velocity. Design and development procedures are presented.

## SYMBOLS

A - Area  
a - Area  
C - A constant  
 $C_V$  - Pressure drop coefficient  
for a vortex  
E - Diode effectiveness,  
Rectification effec-  
tiveness,  $K_I/K_F$   
D - Vortex diameter  
 $D_O$  - Orifice diameter  
f - Friction factor  
F - Force  
G - Flow rate  
 $G_f$  - Flow gain  
K - Pressure drop coefficient  
L - Axial length

M - Mass  
N - Nozzle width  
n - General vortex  
exponent  
P - Pressure  
p - pressure  
Q - Dynamic pressure  
R - Ratio of inlet to  
outlet radii  
r - radius  
S - Distance  
v - Velocity  
V - Velocity  
W - Flow rate  
 $\rho$  - Density  
 $\omega$  - Rotational velocity

## Subscripts

F - Forward flow  
I - Inverse flow  
i - Inlet

N - Nozzle  
o - Central orifice  
O - Central orifice  
V - Vortex

## VORTEX DIODES

S. S. Fineblum

Bell Laboratories  
Whippany, New Jersey 07981

### INTRODUCTION

Fluid diodes were among the first fluidic devices. Various fluid diode inventions by Tesla [1], Kantrowitz [2], Wislicenus [3] (a vortex diode) and Putnam [4], as well as others, have been described previously.

P. J. Baker [5] presented a survey of early fluidic diodes and reported his own experimental work on the vortex and other diodes.

Basically, the fluidic diode is useful in lieu of the ordinary check-valve when special conditions exist. First, absolute shut-off in the inverse direction must not be a requirement because such diodes are inherently very leaky as check-valves. Secondly, elimination of the mechanical parts of the conventional check-valve may be required in a violent environment. In general, the fluid diode fills the need for a highly reliable, low-cost valve.

The fluid diodes has been limited, as Scudder [6] has noted, to applications where low values of the ratio of backward to forward resistance, or "diodicity" (approximately 5 achieved at Harry Diamond Laboratories by 1965) is satisfactory. A very simple two-way restrictor vortex diode for a heat pump (Figure 1), requiring a resistance ratio of only 1.90, was demonstrated in 1964 [7].

The purpose of the present work is to report a rational approach to inviscid (primarily incompressible) vortex diode design.

### INDEX OF EFFECTIVENESS

The vortex diode is effective because a pressure drop is developed by the centrifugal force of rotating fluid (note left-hand sectional view in Figure 1). This pressure drop is much greater than that generated by the flow through the central orifice, radially toward, and out through the

tangential nozzle. Therefore, the tangential inlet acts as the cathode, and the central orifice acts as the anode in obvious analogy to electronic diodes.

Diode effectiveness (diodicity) in a fluid diode,  $E$ , is the ratio of the inverse-flow to forward-flow pressure drop at equal flows.

$$E = \left[ \frac{\Delta P(\text{INVERSE})}{P(\text{FORWARD})} \right]_{\text{CONSTANT FLOW}}. \quad (1)$$

This resistance ratio or rectification ratio (or diodicity), is a criterion of effectiveness of fluidic diodes just as for diodes in general.

In many systems, the ratio of forward-flow to inverse-flow at equal pressure may be a more useful index. Since these vortex diodes operate in the turbulent region, the flow ratio is approximately the square-root of the resistance ratio at the same conditions.

The fundamental similarity between a vortex amplifier and a vortex diode is worth exploring. The overall flow gain of a vortex amplifier can be expressed as the ratio of the difference between unimpeded radial flow with zero signal and the minimum flow with maximum signal. When the main flow is completely shut off, the flow gain is

$$G_f = \frac{W_{\text{max}} - W_{\text{min}}}{W_{\text{signal}}} = \frac{W_{\text{max}-0}}{W_{\text{signal}}}. \quad (2)$$

Since the unrotated radial flow in either direction is through the vortex chamber, the maximum radial flow would be approximately equal to the unrotated forward flow through a vortex diode; and the signal flow at complete radial shut-off equals the tangential flow in the reverse direction. Thus, the fluid amplifier index, the flow gain, is comparable to a vortex diode index - the flow ratio. This similarity permits us to apply results obtained for one device to the other.

In constant pressure systems, obviously, the flow ratio will be preferred; while in constant flow systems, the resistance or rectification ratio will be more useful.

In general, the inverse path of a vortex diode includes an entrance, a nozzle, a vortex chamber, a central exit orifice (or one in each end) and finally an outlet tube at each exit. The forward flow path is identical, but in reversed direction. These series components all contribute to the total pressure drop, so that the resistance ratio and diode effectiveness,

$$E = \frac{\Delta P_I}{\Delta P_F} \frac{[\Delta P_e + \Delta P_N + \Delta P_{VC} + \Delta P_O + \Delta P_t]_I}{[\Delta P_t + \Delta P_O + \Delta P_{VC} + \Delta P_N + \Delta P_e]_F} \quad (3)$$

where I and F refer to inverse and forward flow; e, the diode entrance in the inverse path; N, the nozzle; VC, the vortex chamber; O, the outlet orifice; and t, the outlet tube. The greatest pressure drop is expected in the vortex chamber with vortex flow in the inverse-flow direction. If the main purpose of diode design is to obtain the greatest possible resistance, or rectification, ratio; then the primary target of design improvement is the maximum pressure drop due to the vortex flow in the inverse direction with minimum forward-flow pressure drop through the entire device.

#### THE VORTEX

Early practical interest in vortex devices was directed toward separators, atomizers, Ranque tubes and heat transfer enhancement devices. The literature on the vortex and its application is ample. Earlier bibliographies have been compiled by Mayer and Maker, and Erfurth [8,9]. Goto, Mayer and many others [8,10-15] present practical summaries of the vortex fluid dynamics.

In general, the tangential velocity in a vortex varies with the radius

$$v = v_1 \left( \frac{r_1}{r} \right)^n \quad (4)$$

where  $V_1$  and  $r_1$  are the velocity and radius at the inlet of the vortex, and  $n$  is the general vortex exponent. In a free vortex, angular momentum is preserved.

$$V_1 r_1 = V_2 r_2 = C \quad (5)$$

while angular velocity,  $\omega = V/r$  increases toward the center. Thus:

$$V_1 = V_2 \left( \frac{r_2}{r_1} \right)^n = V_2 \left( \frac{r_2}{r_1} \right) \quad (6)$$

where the vortex exponent,  $n$ , is unity for a free vortex.

The shear between circular layers of fluid and between the walls of the chamber and the fluid inhibits the increase in velocity with decreasing radius until the velocity is constant with radius. This portion of the vortex is said to enclose the "core" of the vortex. Here, where velocity is constant, the vortex exponent,  $n$ , is zero.

The radius at which the transition from a free vortex to a forced vortex occurs, the core radius, has been shown by Soo [16] to be proportional to the one fifth power of the kinematic viscosity. Thus, in viscous fluids, the forced vortex core would dominate the vortex chamber with little room for the free vortex to develop.

In the inner portion of the vortex, wherein the rotational velocity  $\omega$  is constant, the tangential velocity varies directly with the radius, and Equation (4) becomes

$$V_2 = V_1 \left( \frac{r_1}{r_2} \right)^{-1} \quad (7)$$

The forced vortex is realistic for viscous liquids [11] and also for the core of all vortices in general.



Actual flow within a vortex valve combines tangential flow and radial, centripetal flow. The radial flow toward the central orifice, has been shown by several researchers [11,17,18] to travel primarily within the boundary layer at the ends of the vortex chamber. This boundary layer increases in proportion to viscosity and surface roughness [19,20]. Kamel and Farag have shown in this regard, that the leakage through the boundary layer in the vortex chamber increases with viscosity [11] and surface roughness [21].

#### PRESSURE DROP GENERATED BY A VORTEX

The centrifugal pressure reaction to the rotary flow is simply the centrifugal force per unit area, (a),

$$dF = \frac{dMv^2}{r} = \frac{\rho a v^2 dr}{r} \quad (8)$$

$$dF = \rho v^2 \frac{dr}{r} \quad (9)$$

This equation was used by Mayer and Maker [8], as well as others, as the basis of a preliminary analysis of a vortex valve. Using the value of  $V$  from Equation (4), the pressure change can be expressed as,

$$dP = \rho V_N^2 \left( \frac{r_1}{r} \right)^{2n} \frac{dr}{r} \quad (10)$$

where  $V_N$  and  $r_1$  are the inlet velocity and radius.

Integration between radii produces the total pressure differential across vortex

$$\Delta P = \int_1^0 \rho V_N^2 r_1^{2n} r^{-2n-1} dr \quad (11)$$

$$\Delta P = \rho V_N^2 \left[ \frac{-r_1^{2n}}{r^{2n(2n)}} \right]_1^0 \quad (12)$$

$$\Delta P = \frac{\rho V_N^2}{2n} \left( 1 - \frac{r_1^{2n}}{r_0^{2n}} \right). \quad (13)$$

The coefficient of vortex pressure drop,  $K_V$  is defined simply as the ratio of vortex pressure drop to nozzle dynamic pressure,  $Q_N$ .

$$K_V = \frac{\Delta P_V}{Q_N} = \frac{\frac{1}{2} \rho \frac{V_N^2}{n} (1-R^{2n})}{\frac{1}{2} \rho V_N^2} \quad (14)$$

$$= \frac{1}{n} (1-R^{2n}) \quad (15)$$

where  $R$  here is the ratio of the outer to inner radius.

For the three special cases, free, constant velocity, and forced or solid-body vortex, the vortex pressure drop coefficient becomes

$$K_V = -(R^2 - 1) \quad n = 1, \text{ (Free)} \quad (16)$$

$$K_V = -(2 \log R) \quad n = 0, \text{ (V = C)} \quad (17)$$

and

$$K_v = -\left(1 - \frac{1}{R^2}\right) \quad n = -1, \text{ (Forced)} \quad (18)$$

### EXPERIMENTS

Vortex diodes were constructed as assemblies of cylindrical cut-outs of various dimensions, end plates (one transparent) with various outlets and with variations of tangential inlet nozzles. The pressure across the valves was varied, and flows and pressure drops across the vortex and the entire assembly were measured with flow directed in both directions - tangentially for "reverse," or "backward" high-resistance flow, and centrally for radial "forward" flow.

The vortex chambers used in our experiments (Figure 2) varied in diameter from 1.58 to 3.52 inches (4 to 8.95 cm) and in length from .188 to 1.0 inches (0.477 to 2.54 cm). The maximum available pressure and flow were 100 psi ( $6.895 \times 10^5$  N/m<sup>2</sup>) and 6 gpm ( $3.78 \times 10^{-5}$  m<sup>3</sup>/sec).

### TEST RESULTS AND ANALYSIS

Most of the experimental results and some of the analyses were reported earlier [12].

#### Vortex Pressure Drop Coefficient

The variation of the pressure drop coefficient K with the ratio of the outer-to-inner radius R in various vortex valves is shown in Figure 3. Lines of computed K versus R with constant values of n are plotted for comparison. The test results show that for most vortex chambers the effective vortex exponent is approximately constant. The vortex exponent n should be considered an effective n to express the fact that many modes of flow in the vortex chamber result in a specific pressure drop and that the resulting pressure drop coefficient is a function of R, the ratio of the outer and inner radii.

$$K_v = \frac{1}{n} (1 - R^{2n}) \quad (15)$$

Therefore,  $n$  is an average correlation quantity rather than a true vortex exponent indicating the exact mode of vortex flow.

#### Consequences of Axial Length-to-Diameter-Ratio

In general, very thin vortex chambers develop very weak vortex flow. The consequences of varying the axial length,  $L$ , to the vortex diameter,  $D$ , are somewhat as expected. For very thin diodes the boundary layer will completely fill the chamber. As the axial length between the circular endplates,  $L$ , increases, the available distance free of the boundary layers increases. Once this free distance is much greater than the boundary layer, further increase in  $L/D$  is not profitable.

The average vortex exponent,  $n$ , increases with  $L/D$  as seen in Figure 4, but becomes relatively insensitive to any increase above  $L/D = .35$ . All the points shown are results of our experiments except the one point shown at  $L/D = 0.8$ , which was reported by Holman and Moore. Kwok and Farag's work with a large vortex chamber [22] showed that the discharge coefficient decreased with increasing  $L/D$ . Expressed in the form of pressure drop coefficient  $K$  ( $K = 1/C_D^2$ ), this agreed with our tests and indicated an increase in pressure drop coefficient at constant radius ratio,  $R$ , with  $L/D$  at very low  $L/D$  and relative insensitivity to  $L/D$  at higher values. In addition, Tsai [14] found no significant improvement when he varied  $L/D$  from .5 to 1.6.

#### Vortex Chamber Outlet

The flow field in a vortex chamber is primarily "a strong two-dimensional vortex superimposed on a weak sink" [14]. Thus, it can be expected that the exact shape of the vortex chamber outlet is not important. This was verified by results of experiments with rounded and chamfered outlets, as shown in Figure 5 and by Kamel [11].

#### Vortex Generated Pressure Drop in Outlet Tube

In most cases, the pressure drop measured across the outlet tube was relatively insignificant and the vortex alone almost equaled the pressure drop across the entire diode assembly. However, at very high values of vortex radius ratio and vortex pressure drop coefficient, the pressure

drop through the outlet tube downstream of the vortex chamber is a major portion of the total. (For instance, the pressure drop across an entire valve (labeled EG in Figure 3), was much greater than that across the vortex chamber alone (shown as G). Thus, it became important to study the pressure drop of swirling flow through the outlet tube.

Pressure taps in the central outlet tube showed a value of pressure drop per inch that was about 12 times that of straight unswirled flow. T. J. Lawley and his associates [23] similarly showed that the pressure drop in a vortex chamber outlet tube increased with the strength of the vortex.

However, they, along with M. K. King and F. Kreith and their associates [24,25] also reported that both vortex strength and the tube pressure decayed most rapidly in the upstream portions of the tube. For instance, King reported that the vortex had lost 60% of its strength in the first 20 diameters of a tube which was 100 diameters long. Similarly, one tube with swirling flow lost about 75% of static pressure in the first 10 diameters of its length and the remaining 25% in the downstream 17 diameters. Thus, it is clear that the pressure drop in the tube immediately downstream of the vortex chamber contributes significantly to the vortex generated pressure drop.

For the three best vortex diodes, the ratio of the measured pressure drop across the total vortex assembly including the outlet tube to that of the vortex alone followed this equation:

$$\frac{\Sigma \Delta P}{\Delta P_V} = (.0143)R^{2.5}.$$

The addition of vortex generated pressure drop in the outlet tube to increase the reverse flow resistance is, however, of very limited use for diode design, as will be seen later.

#### Forward Flow

The temptation to concentrate on the vortex chamber of a vortex diode to the exclusion of other portions leads to disappointing results.

It is clear from Equation (6) that effective vortex diodes cannot be achieved unless excessive pressure drop is carefully avoided throughout the entire forward-flow path. The most serious head losses in forward-flow occur in the inlet tube and at the tangential nozzle.

#### Inlet Tube Losses

The usual Darcy-Weisbach Equation for pressure drop in a tube

$$\Delta P = f \frac{L}{D} \left( \frac{1}{2} \rho v^2 \right) \quad (19)$$

when expressed as a function of volumetric flow rate,  $G$  and tube diameter,  $D_0$  becomes

$$\Delta P = f \frac{L}{D} \left( \frac{1}{2} \rho \left( \frac{G}{\pi D_0^2 / 4} \right)^2 \right) \quad (20)$$

$$= f \frac{L \rho 8 G^2}{\pi^2 D_0^5} \quad (21)$$

Thus, the pressure drop increases with the reciprocal of the fifth power of the central orifice diameter. For any one vortex chamber,  $R$  was increased by decreasing the central outlet in the end plate. In Figure 6, we show the measured variation of total forward flow pressure drop coefficient as well as the computed change in the orifice related pressure drop coefficient. The starting point for the calculations was the measured total resistance to forward flow at  $R = 6.39$ . The assumed  $K$  factors were 1.5 and 0.9 for the inlet tube orifice and the nozzle, respectively, as estimated from handbook values for the tube, an expansion, and a  $90^\circ$  bend for the former and a  $75^\circ$  bend and a contraction for the latter. These estimates were, frankly, selected to be consistent with accepted values and to total a  $K$  of 2.4 which was determined experimentally. As the

radius ratio R is increased from 6.39 to 13.33 by decreasing the outlet radius by a factor of 2.086, the fifth power of that factor of radius change is 39.50. This factor times the inlet K factor 1.5, equals 57.9. This plus the K factor through the unchanged nozzle results in an estimated total found flow K factor of 58.8 at R = 13.3 as shown in Figure 6. The actual measured total K factor was approximately 61.

In an earlier section, it was shown that the vortex pressure drop coefficient increased with the radius ratio. However, if the increased radius ratio R is obtained with a small outlet orifice, the forward pressure loss through the inlet tube and orifice will be excessive as shown in Figure 6 and diode effectiveness will decrease rather than increase.

Going in the opposite direction, the inlet tube pressure drop will decrease with the radius ratio. At smaller radius ratios, the orifices are relatively larger. The pressure drop contribution from the tube itself decreases with the reciprocal of the fifth power of the inlet diameter.

The orifice losses, however,

$$\Delta P = K \left( \frac{1}{2} \rho V^2 \right) = K \frac{1}{2} \rho \left( \frac{Q}{\pi D_o^2 / 4} \right)^2 \quad (22)$$

will decrease with fourth power of the inlet diameter.

This is a practical insight for the extrapolation of losses with very short inlet tubes.

#### Pressure Drop Through the Tangential Nozzle

The pressure drop from the vortex chamber out through the tangential nozzle for typical nozzles is shown in Figure 7.

In one diode, the nozzle lip was given an .012 inch (.03 cm) radius which was about 25% of the nozzle width, N. The forward-flow K factor across the nozzle dropped from approximately 1.9 with a sharp nozzle lip to 1.0 with the rounded lip as shown in Figure 8. Note that the reverse flow vortex was not measurably influenced so the resistance ratio rose

from 4.8 for the sharp lip to 6.0 for the rounded one. The improvement is clearly shown in Figure 9.

It was observed that a cavitation bubble formed just downstream of the sharp lip in the nozzle as shown in Figure 10. Superficially, at least, it was reminiscent of the cavities reported by Eisenberg [26] in his early reports of the cavitation method of designing torpedoes. The generalization that the cavity boundary approximates the surfaces of constant pressure and minimum restriction was appropriate. By means of a magnifying glass, the contour of the cavity was carefully measured and used as a pattern for the nozzle. As a result, the forward-flow K factor across the nozzle dropped from 1.86 to .78 in one case and from 1.0 to 0.45 in another.

In the forward flow direction, the fluid contracts and turns as it enters the tangential nozzle. The dynamical equation for forward-flow,

$$\frac{1}{2} \frac{\partial(v^2)}{\partial S} - v \times (\text{CURL } v) = \frac{1}{\rho} \frac{\partial P}{\partial S} \quad (23)$$

reminds us that pressure gradient along the flow path is proportional to the sum of the convective linear acceleration and the rotary acceleration. If the nozzle is expanded, the contraction and the acceleration along the path from the chamber into the nozzle would be diminished. In addition, such an expanded nozzle would permit a lower velocity which would lower the value of the rotary term in Equation (23) above. Thus, increasing the area of the tangential nozzle can be expected to reduce both the convective acceleration and velocity and thereby to reduce the nozzle entrance pressure drop. The curl term can be reduced by adding a radius or a contour to the nozzle lip. As noted above, these expected improvements were realized.

#### Other Restrictions

Whenever restrictions or irregularities in the flow path were removed or ameliorated, the forward-flow pressure drop invariably decreased and, as a result, the rectification ratio proportionally improved.



### OPTIMIZATION

Diode performance, summarized in Table 1, is dependent primarily upon the strength of the vortex generated in the chamber and the lack of resistance in the forward flow path.

The geometric ratios that significantly influence diode performance are:

$$\left. \begin{array}{l} \text{Radius, } \frac{r_1}{r_0} \\ \text{Diameter, } \frac{D}{D_0} \end{array} \right\} = R$$

Length,  $L/D$

Nozzle-Outlet Area,  $A_N/A_0$

Nozzle,  $N/D$

Lip Radius,  $r_N/N$

### Axial-Length-Diameter-Ratio

As noted earlier, the effective vortex exponent,  $n$ , increased until  $L/D$  equaled 0.35. Above that point, no significant improvement occurred.

### Nozzle-Outlet Ratio

The nozzle and outlet area must be so balanced as to minimize total pressure drop across these restrictions. The optimum seems to be approximately 3.0.

### Nozzle

The nozzle width divided by vortex chamber diameter  $N/D$  is a measure of the ease of entry into the nozzle from the vortex chamber during forward-flow. This is, of course, limited by the requirement for a difference in radial dimension of the nozzle and the orifice required to generate a strong vortex. The optimum nozzle width seems to be about 0.2 times the vortex diameter.

In general, these ratios were selected somewhat arbitrarily in the area of very flat variations of performance.

These values can be used to compute an optimum radius ratio  $R$

$$R = \frac{r_1}{r_0} = \frac{D}{D_0} \quad (24)$$

The approximate optimums are

$$\frac{L}{D} = .35 \quad (25)$$

$$\frac{A_N}{A_0} = \frac{LN}{\pi D_0^2 \frac{r}{r_0}} = 3.0 \quad (26)$$

$$\frac{N}{D} = .2 \quad (27)$$

The central diameter,  $D_0$ , is the chamber diameter,  $D$ , divided by the radius ratio,  $R$ ,

$$D_0 = \frac{D}{R} \quad (28)$$

In addition

$$L = .35D \quad (29)$$

and

$$N = .2D \quad (30)$$

Substitution of these values, in the expression for the nozzle-outlet area ratio, Equation (26) yields;

$$\frac{A_N}{A_O} = \frac{(.35D)(.2D)}{\frac{\pi}{4} D^2/R^2} = 3.0 . \quad (31)$$

From this, the optimum radius ratio  $R$  is approximately 5.8. The estimated errors in the many measurements that were used were such, and the performance variation was so slight in the vicinity of the selected optimum, that this value can be considered only as a rough approximation. Baker [5] refers to Zobel's conclusion that the optimum radius ratio is closer to 8.

The interpolated diode effectiveness was computed from the results of the best diode and plotted in Figure 11. The measured optimum radius ratio is apparently between 5.6 and 6.2

The diode effectiveness can be expressed as;

$$E = \frac{R^{2n} - 1}{n} / K_N + C_O R^5 \quad (32)$$

$$= \frac{R^{2n} - 1}{n} / \left( \frac{K_N}{C_O R^5} + 1 \right) / C_O R^5 , \quad (33)$$

where  $K_N$  is the nozzle pressure coefficient and  $C_O$  is a constant that, multiplied by  $R^5$ , equals the central orifice and tube coefficient  $K_O$ .

It can be shown that the optimum rectification ratio occurs when the upstream and downstream forward flow resistances are approximately equal, i.e, when  $K_N/C_O R^5 \approx 1$ .

### Compressible Versus Incompressible Flow

Holman and Moore [13] and Tsai [14] report results with gasses which were consistent with the results obtained with water. However, at rather high gas velocities, Kendall [27] witnessed greatly different effects of the L/D ratio. At the very low velocities required for effective diode performance, findings with liquids apply to gasses and vapors as well.

### DESIGN PROCEDURE

A. If the required rectification ratio is 15 or less:

1. Select the radius ratio corresponding to desired rectification ratio from Figure 11.
2. Set L/D the axial length-to-diameter ratio between .35 and .45.
3. Select nozzle width N to be approximately .20 times chamber diameter and large enough to assure inverse flow velocity of 4 ft/sec (1.22 meters/sec) or less.
4. Design the nozzle with a radius of approximately 1.5 times the nozzle width, N.
5. Limit the central tube to a length of 10 diameters or less.
6. Avoid any restrictions, or discontinuities in the entire branch of the fluid circuit containing the diode.

Modifications in performance can be easily achieved. If the resultant rectification is too high, simply add resistance in series with tangential inlet in direct proportion to desired decrease. The total pressure drop in the inverse direction can be increased by a small percentage without greatly influencing the rectification ratio by increasing L/D<sub>0</sub> of central tube in proportion to required resistance. If the rectification is too low, continue to decrease the length-to-diameter ratio of the branch containing the diode and other hydraulic resistance both upstream and downstream.

B. If, however, a rectification much higher than 15 is required:

1. Design tangential inlet line and nozzle (cathode) with the least possible resistance at design forward flow (use radius or contour as necessary).
2. Select vortex chamber diameter which is four or five times optimized nozzle width.
3. Select central orifice size and shortest possible central tube to match K factor of optimized nozzle. Use fifth power relation for extrapolation of pressure drop factor with R.
4. Divide design forward flow K factor which is sum of minimized nozzle  $K_N$  and matched central orifice and tube  $K_O$  into inverse flow K factor for "G" diode from Figure 3 at R obtained from chamber and orifice selection steps 2 and 3 to predict diode effectiveness, E.

Example: If a clean low pressure-drop nozzle (cathode) branch has a forward-flow K of 0.4 and if the short central tube matches it at R = 6, the conservatively predicted vortex pressure drop coefficient from Figure 3 is 19, and the predicted rectification ratio is then  $19/(0.4+0.4) = 23.75$ .

Further improvement is possible only if the branch of the fluid circuit containing the diode can be improved for lower head losses.

One approach to such improvement is to have an enlarged central tube with a convergent nozzle to direct fluid in forward-flow into the central orifice. Similarly, a well designed diffuser would reduce the losses in a large low-loss forward-flow outlet.

From the above, it is clear that fluid diodes are very sensitive to installation. Identical diodes will perform differently in different fluid circuits.

Empirical pressure drop coefficients as listed in handbooks are sufficiently accurate to permit a practical design with minimum development effort.

The results achieved, if extrapolated for low-loss nozzles and improved associated tubing, suggest the routine attainment of rectification ratios of approximately 40. Baker [5], on the other hand, lists Zobel's attainment of a rectification ratio of 50 as well as still higher rectification ratios with other type of diodes.

#### Suggested Development

For further improvement one approach seems worthy of development. As noted earlier, Kamel and Farag [21] showed that the vortex strength and resultant vortex generated throttling increases as the end plates become smoother. Thus, super-smooth end plates as polished or as coated with a polymer can be expected to decrease the parasitic loss of vortex strength and consequent improvement to both the vortex and forward-flow, and, as a result, the diode effectiveness.

TABLE I  
SUMMARY OF DIODE CONFIGURATIONS

DIAM		LENGTH		E	An/Ao	L/D	R	N/D	R <sub>N/N</sub>
Inches	Cm	Inches	Cm						
3.25	8.26	.188	.478	1.2	.085	.0517	8.5	.010	0
1.575	4.00	.300	.762	1.5	.0714	.1905	4.028	.0178	0
2.00	5.08	.631	1.60	1.61	.0833	.315	5.15	.008	0
1.575	4.00	.300	.762	3.55	.3042	.1905	8.40	.0178	0
2.0	5.08	.631	1.60	3.6	.1961	.315	5.12	.016	1.2
1.575	4.00	.502	1.28	4.0	.200	.318	4.02	.029	0
2.0	5.08	.631	1.60	4.4	.1961	.315	5.12	.016	1.5
2.5	6.35	1.0	2.54	5.5	15.87	.40	13.3	.175	0
2.0	5.08	.631	1.60	5.9	.1652	.315	5.15	.016	1.2
1.575	4.00	.502	1.28	6.61	.200	.318	4.02	.029	1.008
1.575	4.00	.502	1.28	7.0	.2058	.322	4.02	.031	.24
1.575	4.00	.502	1.28	8.0	.9091	.318	8.4	.029	1.00
2.00	5.08	.631	1.60	8.6	.7143	.315	10.66	.016	1.5
[1] 2.00	5.08	.631	1.60	9.0	.7246	.315	10.66	.015	1.5
[2] 4.2	10.67	1.1	2.78	12.5	1.12	.216	4.02	.261	0
2.5	6.35	1.0	2.54	14.6	3.94	.400	6.4	.175	0

[1] Flow patn discontinuities removed upstream of nozzle  
[2] From Baker (5)

## REFERENCES

1. Tesla, N., "Valvular Conduit," U. S. Patent 1,329,559, 1920.
2. Wooten, F. O., "An Experimental Study of an Aerodynamical Rectifier," WADC TR 57-356, A.R.D.C. Wright Patterson Air Force Base, Ohio.
3. Wislicenus, G. F., "Flow Control Means for Pulse Jet Combustion Units," U. S. Patent 2,618,925, 1947.
4. Putnam, A. A., and Speich, C. F., "A Study of the Feasibility of a Resonant Combustor - Pump System to Pump Fresh Air," Battelle Memorial Institute, Columbus, Ohio, 1958.
5. Baker, P. J., "A Comparison of Fluid Diodes," Proceedings 2nd Cranfield Fluidics Conference, Cambridge, January 1967.
6. Scudder, K. R., "Vortex Devices," Fluid Amplifiers, Kirschner, ed., McGraw-Hill Book Company, New York, New York, 1966.
7. Fineblum, S. S., "Restrictor Means for Heat Pump System," U. S. Patent 3,404,542, October 1968.
8. Mayer, E. A., and Maker, P., "Control Characteristics of Vortex Valves," Proceedings - Fluid Amplification Symposium, Vol. II, Harry Diamond Laboratories, A.M.C. Washington 25, D. C., May 1964.
9. Erfurth, K., "Bibliography on Vortex Flow in Tubes," Aerospace-Research Laboratories, O.A.R. Wright-Patterson Air Force Base, Ohio, received February 1965.
10. Goto, J. M., "Elements of Vortex Motions," Chapter 10, Fluid Amplifiers, Edited by J. M. Kirschner, McGraw-Hill Book Company, New York, 1966.
11. Kamel, N. Y. M., "The Effect of Swirl on the Flow of Liquid Through Bottom Outlets," A.S.M.E. Winter Meeting 1964 - paper No. 64-WA/FE-37.
12. Fineblum, S. S., "Vortex Diode - A Beginning Analytical Approach," TP-3-65 RANCO Controls, Columbus, Ohio, July 1965.



13. Holman, J. P., and Moore, G. O., "An Experimental Study of Vortex Chamber Flow," Aeronautical Research Laboratory, WADC, TN 59-388 WADC, ARDC, Wright-Patterson Air Force Base, October, 1959.
14. Tsai, D. H., "Flow Field in a Swirl Chamber," J. Am. Inst. Aeronautics and Astronautics Vol. 2, No. 8: 1504-5 August 1964.
15. Savino, J. M., and Keshock, E. G., "Experimental Profiles of Velocity Components and Radial Pressure Distribution in a Vortex Contained in a Short Cylindrical Chamber," proceedings of Third Fluid Amplification Symposium, 1965, Harry Diamond Laboratories, AMC Washington D. C.
16. Soo, S. L., "Vortex Flow Adjacent to a Stationary Surface," Appl. Sci. Res. 28:20-26, July 1973.
17. Syred, N., and Royle, J. K., "Operating Characteristics of High Performance Vortex Amplifiers," Second IFAC Symposium on Fluidics, 1971, Prague.
18. Weber, H. E., "Boundary-Layer Inside Conical Surfaces Due to Swirl," J. Applied Mechanics, Vol. 23, 1956.
19. Wormley, D. N., "An Analytical Model for the Incompressible Flow in Short Vortex Chambers," Trans. ASME, J. Basic Engineering, June 1969, Page 264.
20. Tani, I., "Effect of Two-Dimensional and Isolated Roughness on Laminar Flow," Boundary Layer and Control Volume 2, Edited by G. V. Lachmann, Pergamon Press, New York, 1961.
21. Kamel, M. Y. M., and Farag, E. A., "The Swirling Flow of Liquids Through Vortex Chambers," ASME Paper 73-WA/FE-12, November 1973.
22. Kwok, C. K. and Farag, E. A., "Investigation of Swirling Flows of Liquids Through Rotating Vortex Chambers," ASME Paper No. 73-WA/Flcs-8, November 1974.
23. Lawley, T. J., Lea, J. F., and Price, D. C., "Flow and Performance Characteristics for Non-Vented Vortex Amplifiers," ASME Winter Annual Meeting, 1970, ASME Paper 70-WA/Flcs-18.

24. King, M. K., Rothfus, R. R., and Kermode, R. I., "Static Pressure and Velocity Profiles in Swirling Incompressible Tube Flow," AIChE Journal, Vol. 15, No. 6: 837-842, November 1969.
25. Kreith, F., and Sonju, O. K., "The Decay of a Turbulent Swirl in a Pipe," J. Fluid Mech., Vol. 22, Part 2: 257-271, 1965.
26. Eisenberg, P., "A Cavitation Method for Development of Forms Having Specified Critical Cavitation Numbers," The David W. Taylor Model Basin Report C-14, September 1947.
27. Kendall, J. M. Jr., "Experimental Study of a Compressible Viscous Vortex," TR 32-290 J.P.L., C.I.T. Pasadena, California.

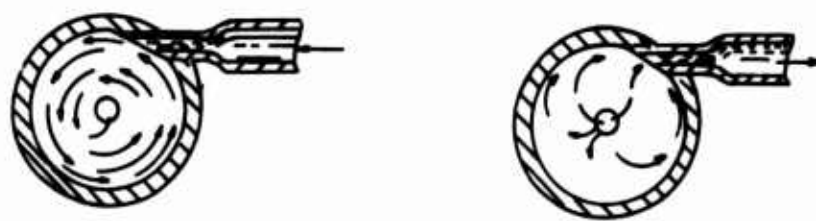
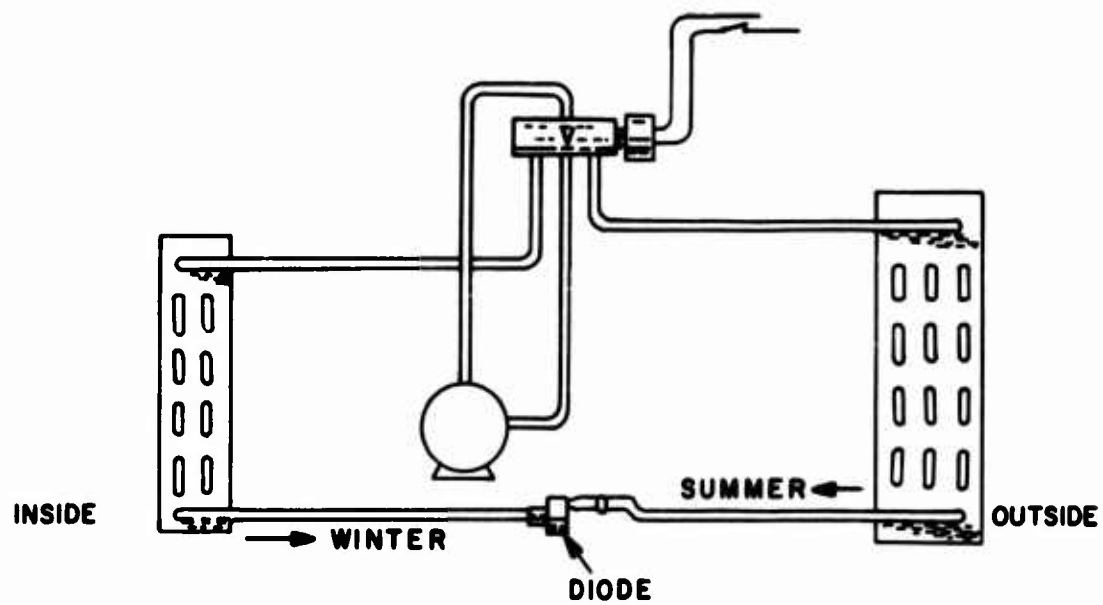


FIGURE 1 - VORTEX DIODE RESTRICTOR FOR HEAT PUMP SYSTEM

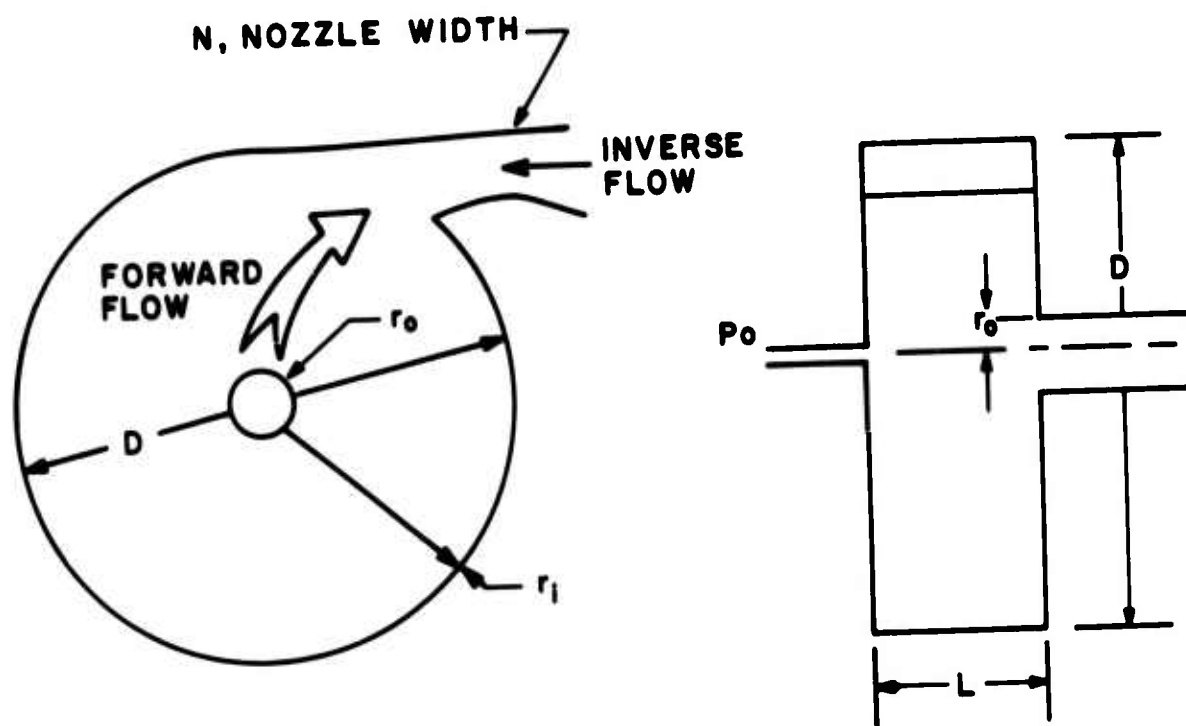


FIGURE 2 - VORTEX DIODE GEOMETRY

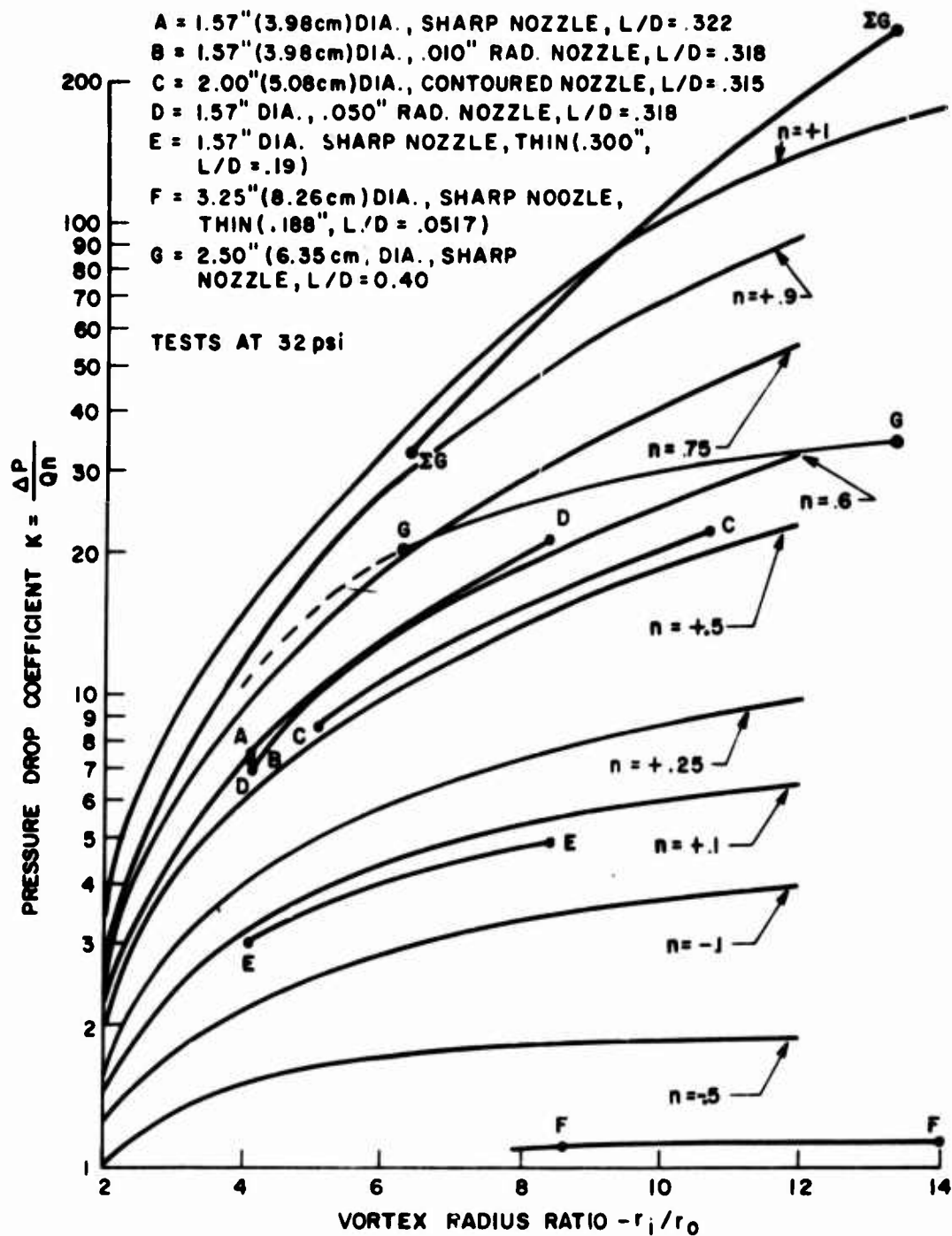


FIGURE 3 - TEST RESULTS: - TOTAL PRESSURE DROP COEFFICIENT ACROSS DIODE VERSUS RADIUS RATIO

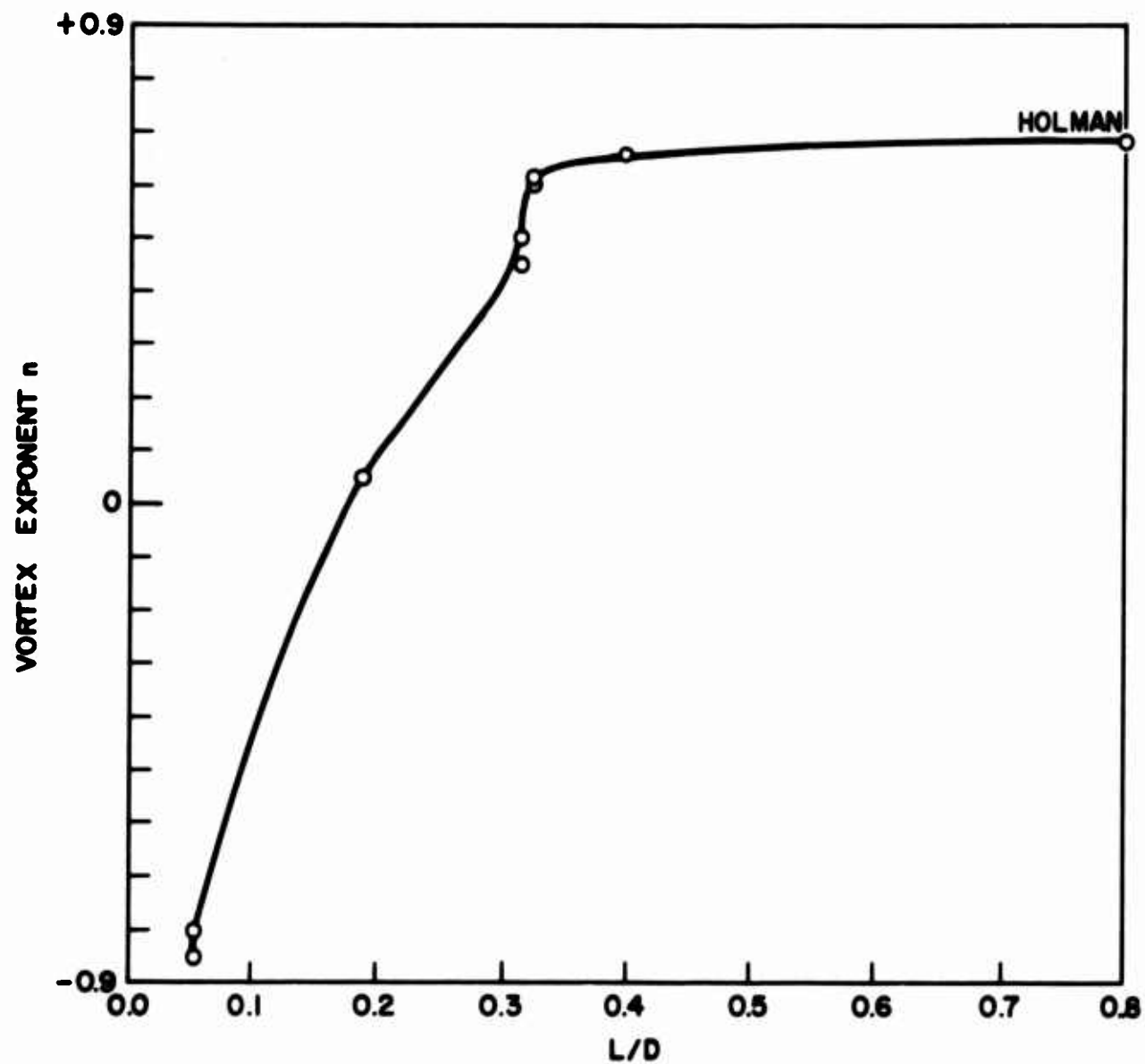


FIGURE 4 - VARIATION OF VORTEX EXPONENT,  $n$  WITH RATIO OF VORTEX AXIAL LENGTH TO DIAMETER

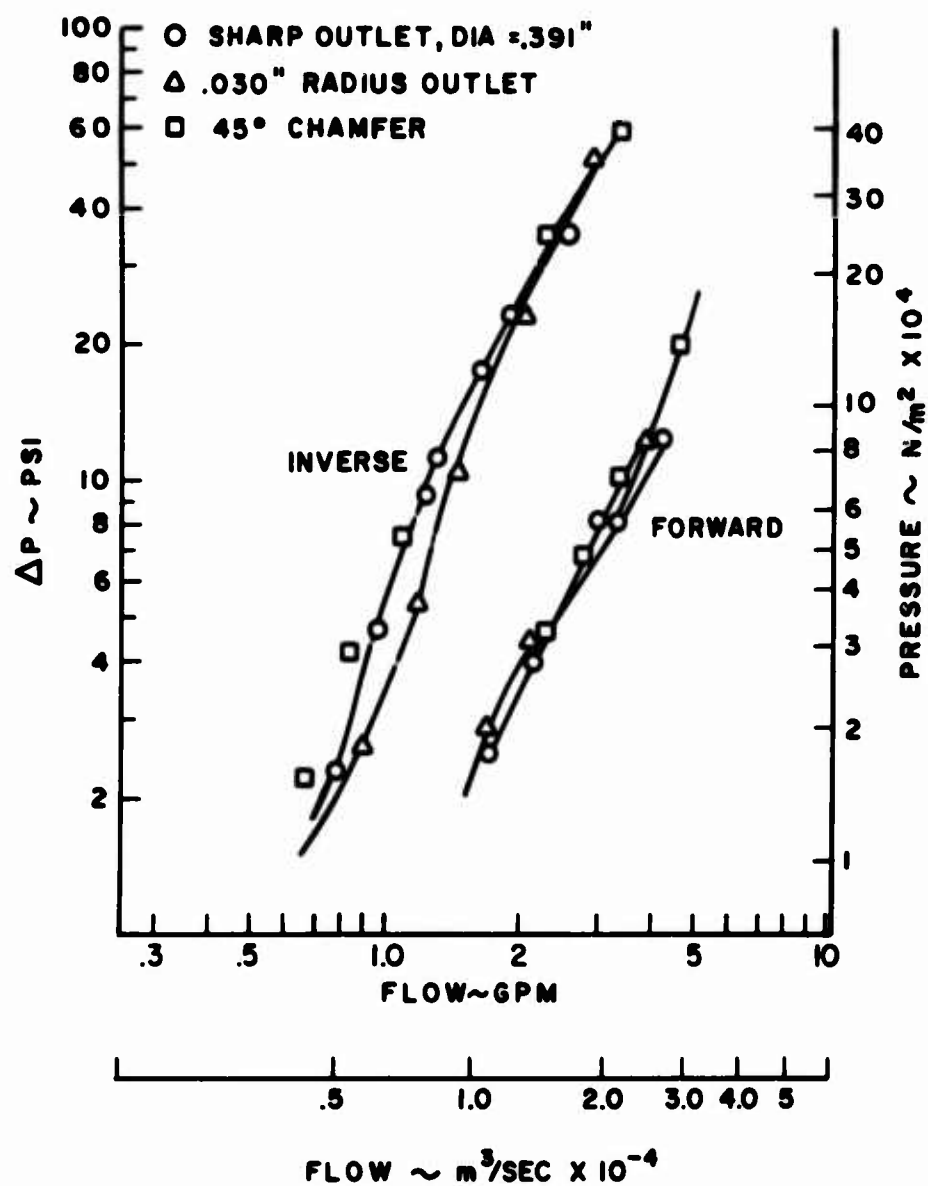


FIGURE 5 - LACK OF EFFECT OF OUTLET CONFIRURATION UPON VORTEX FLOW

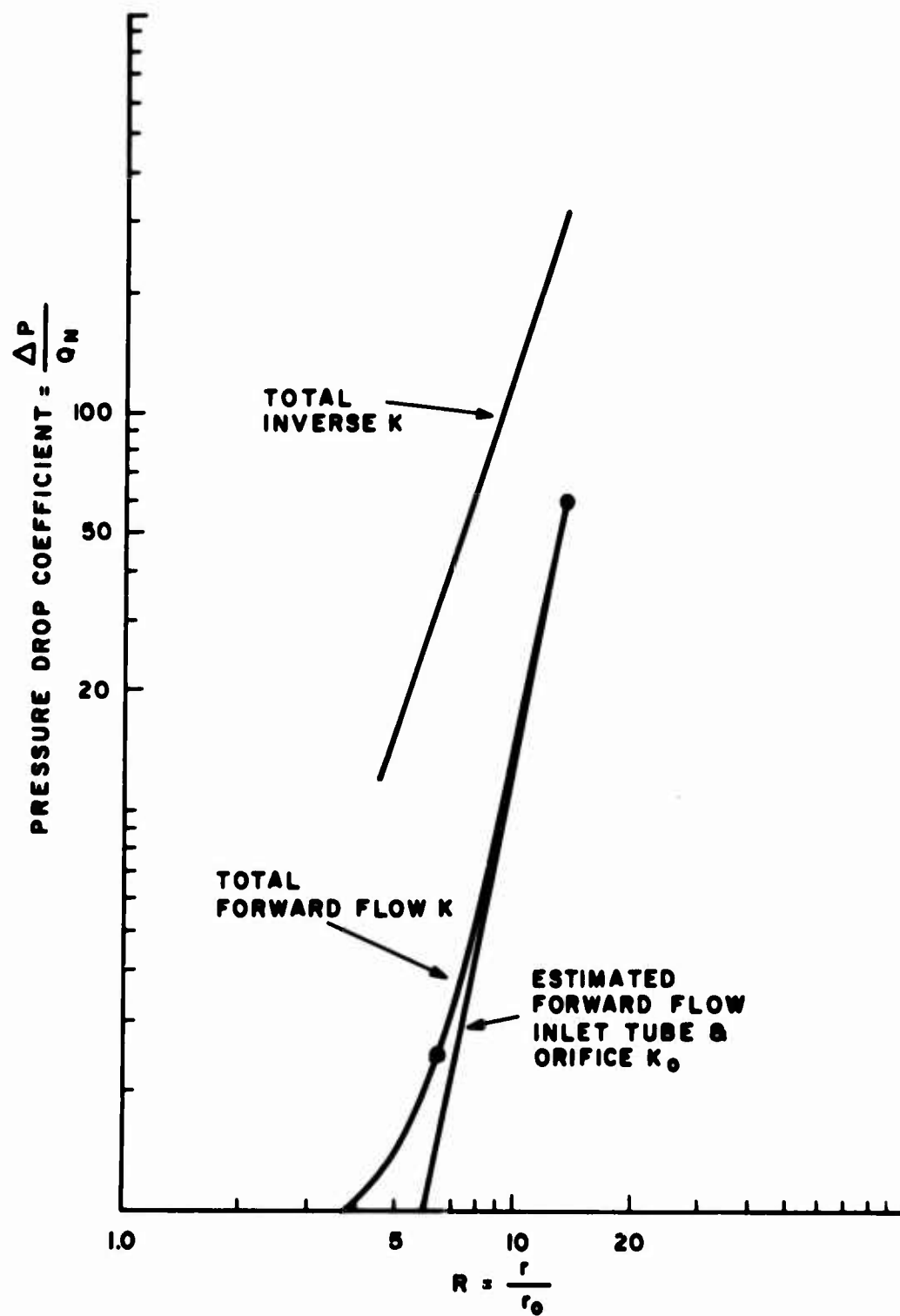


FIGURE 6 - INVERSE & FORWARD FLOW PRESSURE DROP COEFFICIENTS  
AS FUNCTION OF RADIUS RATIO, R FOR VALVE "G" L/D = .400



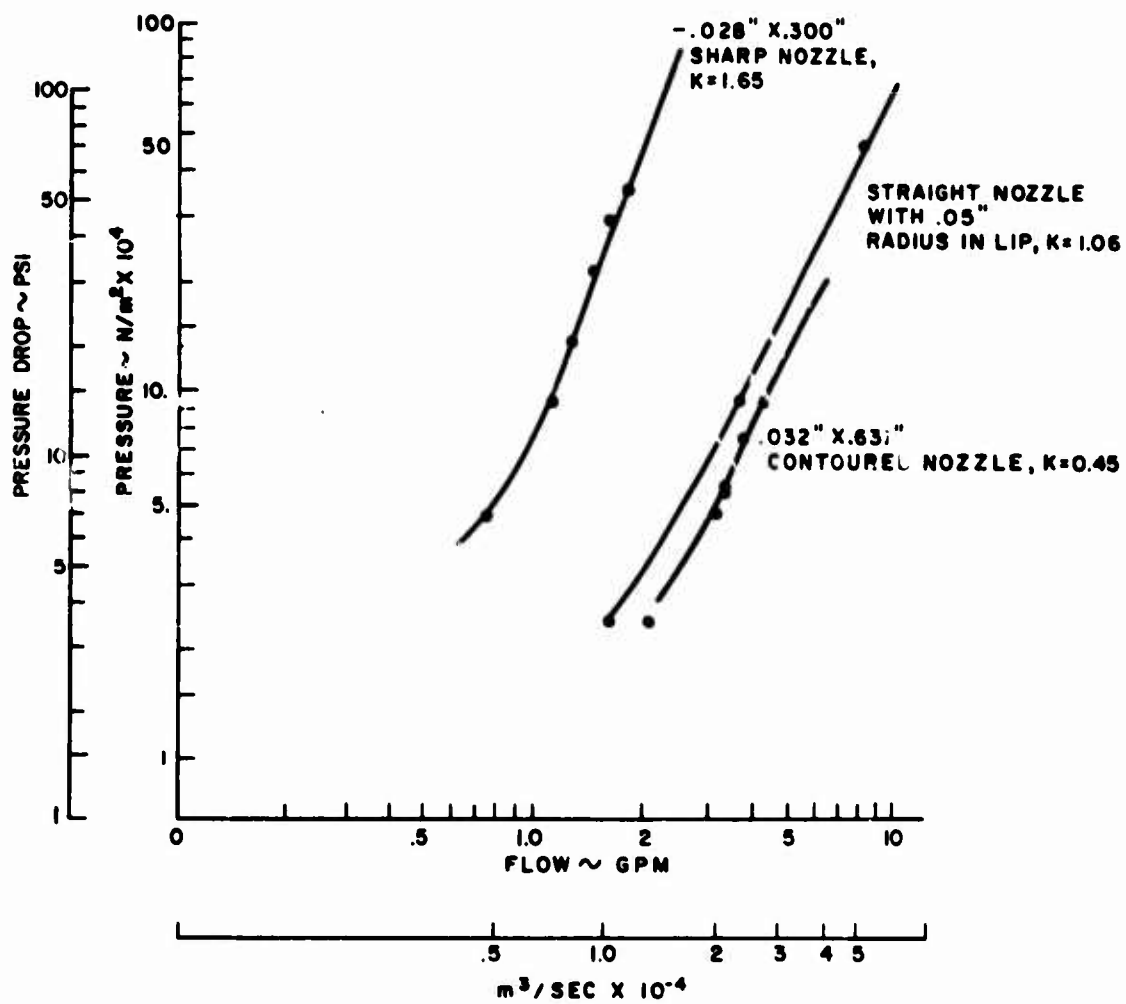


FIGURE 7 - PRESSURE DROP ACROSS TYPICAL NOZZLES IN FORWARD FLOW

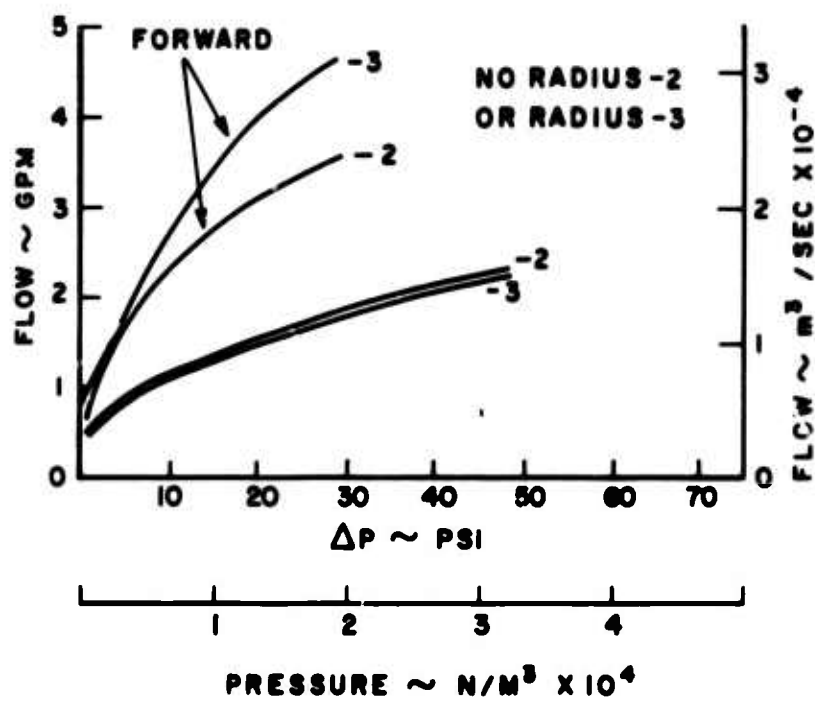


FIGURE 8 - DIODE FLOW WITH & WITHOUT RADIUS ON NOZZLE LIP

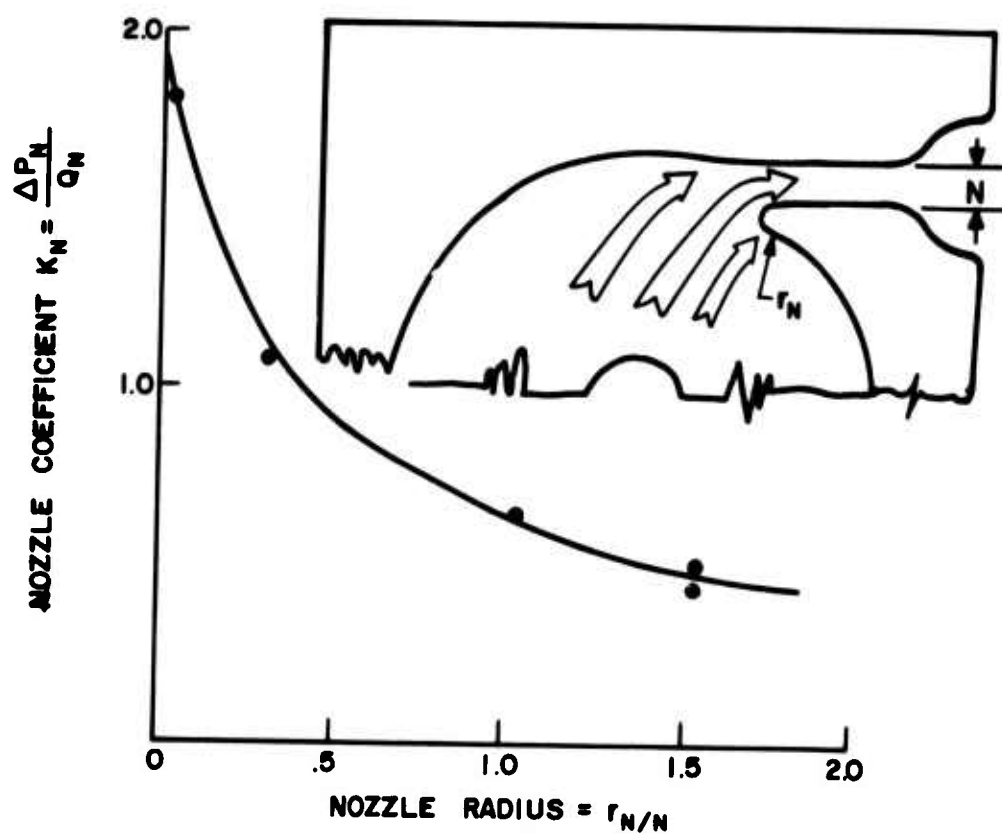


FIGURE 9 - VARIATION OF NOZZLE PRESSURE DROP COEFFICIENT  
WITH NOZZLE ENTRANCE RADIUS

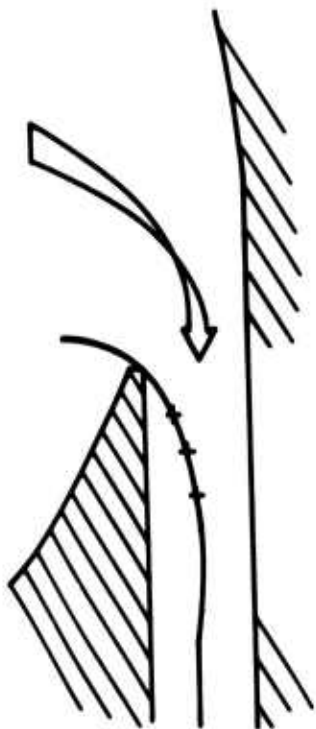


FIGURE 10 - CAVITATION BUBBLE PAST LIP IN FORWARD FLOW

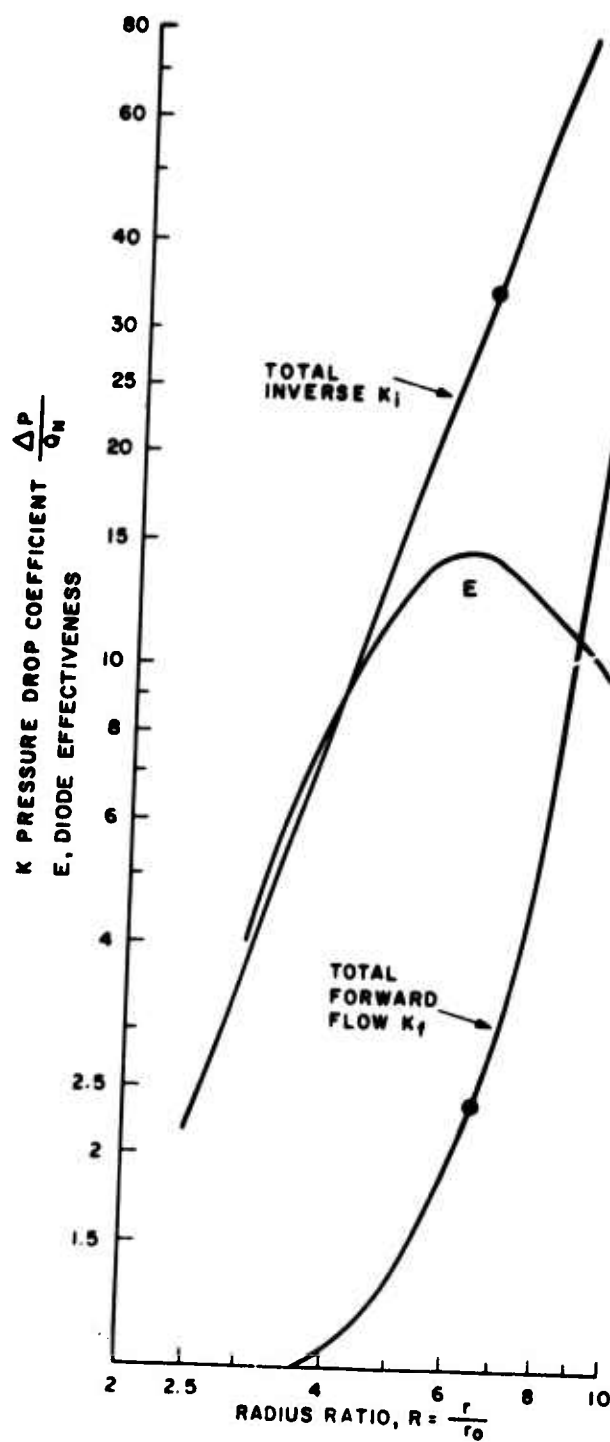


FIGURE 11 - OPTIMIZATION OF DIODE EFFECTIVENESS  
"G" VALVE  $L/D = .40$   $N/D = .175$

THE TURBULENCE AMPLIFIER

Adam C. Bell  
Associate Professor  
Department of Mechanical Engineering  
State University of New York at Buffalo

## THE TURBULENCE AMPLIFIER

### INTRODUCTION TO THE TURBULENCE AMPLIFIER

In 1962, early in the brief history of fluidics, Raymond Auger introduced the Turbulence Amplifier or T/A [1,2]. The T/A is unique among fluidic devices in that its operation hinges on the transition from laminar to turbulent flow in a jet. Its operation depends on two related factors: the ease with which a control jet can switch a laminar jet to turbulence; and the very large difference in pressure recovery for the same supply conditions that a receiver in a laminar or turbulent jet will experience.

Laminar jets at Reynold's numbers greater than 11 [3] are quasi-stable. A submerged laminar jet in the absence of any external disturbance contains the seeds of its own destruction; although it may remain laminar for from 15 to 100 nozzle diameters (depending on  $Re$ ), it will eventually become spontaneously turbulent in as little as one diameter. This is illustrated in Figure 1. Because of this quasi-stability, disturbances to the jet are rapidly amplified and the transition then moves rapidly upstream in the jet to a point near the disturbance. Thus a control jet near the jet emitter can control the position of the jet transition. If a receiver aligned with the emitter, as shown in Figure 2, is placed so that the undisturbed laminar jet will reach it, then control action will determine whether the receiver sees a laminar jet or one that has been turbulent from a point just past the control.

Laminar jets at source Reynolds numbers of much greater than 60 [4,5] spread much more slowly than turbulent jets of the same source conditions. Laminar jets exchange momentum with their surroundings in shear only and loose kinetic energy and central stagnation pressure gradually. Turbulent jets, on the other hand, redistribute their momentum rapidly and dissipate energy quickly through turbulent mixing processes. A central receiver in a laminar jet can capture a large fraction of the jet's initial momentum with excellent pressure recovery, while a receiver placed in an induced turbulent jet that has dissipated and exhausted its stagnation pressure will exhibit low pressure recovery.

The most graphic demonstration of these principles is provided by a stationary cigarette in still air. A long laminar tendril of smoke arises from it that could easily be captured by a drinking straw. The slightest puff of air, or even a loud snap of the fingers, however, will break the jet up into turbulence near its source and very little smoke would then be captured by the straw.

If we call the laminar or high recovery state ON and the control generated turbulent or low recovery state OFF, we have a logical NOT. Clearly, since multiple inputs are possible, and as many as eight are practical with equal effectiveness, the turbulence amplifier is a logical NOR element. If any (or several) of its inputs are ON the output is OFF. A logical NOR is primitive: that is, it forms a basis for a complete logic system. All of the other required logic functions can be synthesized by combining NOR's.

These combinations can obviously be assembled of individual elements or can be incorporated into a single element.

As one of the earliest NOR elements to be commercially available, the T/A has enjoyed considerably success, stemming very largely from the ease with which individual gates can be interconnected into a large switching circuit without the loading and crosstalk difficulties so common to fluidics. Indeed, it is the absence of interaction between individual controls, between the output and the controls and between controls and supply that accounts for the widespread use of T/A's in this country, throughout the Common Market, and in Eastern Europe.

Consider Figure 2 again. This is a typical T/A geometry with the shroud omitted, and with only one control shown. In a 3-dimensional (cylindrical) geometry, other controls would be arranged radially around the same spot on the main jet for equal effectiveness. In a planar geometry (not really 2-dimensional) other controls would be arranged in two fan-like arrays in the plane of the element on each side of the main jet. The fans would be centered on the same spot on the jet and control jet angles from  $45^\circ$  to  $135^\circ$  from the main jet are effective. One of the outstanding features of the T/A is that the controls are not additive; control action (jet switching) is obtained only if one of the controls exceeds the switching threshold without regard to the state of the others; whether they are at zero flow or near the threshold flow. Jet deflection devices sum momenta usually; the T/A does not.

The emitter or supply tube is shown long and of uniform bore in Figure 2. It is now universally recognized that the most satisfactory laminar jets are produced from initially parabolic emitter profiles. At the Reynolds numbers typical of T/A operation, between 500 and 2,000, full parabolic development requires approximately 60 diameters of emitter length; more is a waste of supply pressure; less produces shorter, nervous jets. The receiver or collector is accurately aligned with the emitter and in normal practice has the same section dimensions as the emitter. The emitter-receiver gap is a design trade-off. A large gap requires smaller control signals for switching but reduced ON recovery. A short gap improves ON recovery, but reduces the difference between ON and OFF which may result in cascading problems. Normally the receiver is made as short as is possible to reduce the element output impedance.

Although not shown in Figure 2, a turbulence amplifier must have a shroud whose function, in addition to providing the structure that aligns the nozzles, is to protect the very sensitive laminar jet from ambient noise (sound) and from air currents. This shroud must be symmetrically placed around the jet for equal control effectiveness, and of sufficiently large internal dimensions that a turbulent jet cannot become self-exciting. In cylindrical geometries, the shroud diameter is usually greater than 10 jet diameters. In planar geometries, the shroud interior is usually of rectangular section with the short dimension more than 6 jet widths. The shroud must also be very generously vented so that its interior will remain at ambient pressure for any jet state and load return through the receiver.



The large shroud vents required are responsible for the lack of interaction and interconnection difficulties that characterize the T/A. With the exception of the receiver, all of the tubes (of ducts in a planar version) that form the T/A supply and controls remain at atmospheric pressure at their internal ends irrespective of the state of the amplifier. Under normal operating situations, backflow in the receiver is not sensed at either the emitter or the controls, and for small backflows or any outflow up to the zero load flow, the receiver appears to be connected to a plenum maintained at the jet centerline stagnation pressure, either ON pressure or OFF pressure. Unless the backflow is large or the shroud vents are too small, a backflow (from a diaphragm interface device for example) will not switch the jet, although it might switch others whose controls were attached to the same T/A. Unfortunately, there is a trade-off in vent sizing. The larger they are, the more sound sensitive the element will be. Shrouding, as might be expected, has no effect on the mechanical vibration sensitivity of turbulence amplifiers although this is rarely reported to be a problem.

Auger summarized these characteristics very nicely in the following lists of advantages and disadvantages paraphrased from Reference [6].

#### Advantages

1. Performance as a NOR gate, enabling it to be the only element needed to build circuits which perform all conventional logic operations.
2. Ease of interconnection without any need for biasing, bleeding or impedance matching.
3. Relatively high fan-out (ability of one output to drive multiple inputs). Eight easily attained.
4. Multiple inputs (up to eight commercially available) fully isolated from each other, the supply line and the output load.
5. High resistance to contamination by oil or water vapor in the supply line.
6. Insensitivity to input signals below its threshold. (See Figure 3). This means both low level noise immunity and nonadditive controls. Switching occurs only if one or more inputs exceed the threshold.

#### Disadvantages

1. Sensitivity to both ambient sound and vibration at frequencies not uncommon in industrial environments.
2. Supply pressure regulation is required because the permissible Reynolds number range for good operation is relatively narrow.
3. Maximum output pressure attainable is less than 0.5 psi. More typical outputs are in the 1.0 to 10.0 in. H<sub>2</sub>O range.
4. Extremely noisy operation between the ON and OFF states virtually precludes T/A operation as a proportional amplifier.

5. Undisturbed laminar length of a submerged laminar jet is as yet unpredictable. A weakness in design as only guidelines exist.

6. Relatively slow dynamic response.

#### STATIC PERFORMANCE OF THE T/A

##### The Essential Characteristics

Historically, the static characteristics of turbulence amplifiers have been only partially presented, usually as output pressure versus control pressure for constant or fixed values of supply pressure and zero output flow, and output pressure versus supply pressure, with no control or output flow [1,2,5-11]. While such presentations proved suitable and useful in circuit applications, they obscure internal relationships in the amplifier because the characteristics of the tubes or duct flows and the jets mechanics are not separated. Verhelst [12], however, has devised a complete and comprehensive presentation of T/A characteristics now almost universally used in the literature on T/A's. The Verhelst Diagram is more useful to the designer than others, because it separates tube characteristics from jet effects and readily displays the figures of merit of the element. It displays on one plot the five essential characteristics of the turbulence amplifier:

1.  $P_s - Q_s$ ; supply pressure-supply flow
2.  $P_c - Q_c$ ; control pressure-control flow
3.  $P_o - Q_o$ ; output pressure-output flow
4.  $P_o - Q_s$ ; output pressure-supply flow
5.  $P_o - Q_c$ ; output pressure-control flow

The first three of these are tube or duct self-impedance curves and the last two are the transfer characteristics from the controls and supply to the output. Obviously, the old presentations can be easily obtained by combining the fifth with the second and the fourth with the first. The third relationship, if given at all in early papers, was usually incorporated as a parameter in a series of  $P_o - P_c$  curves with multiples of one control as a load. Such a family can be obtained easily by combining characteristics 2 through 5 appropriately. It should be clear that reversing these procedures is nearly impossible. Figure 3 shows a typical Verhelst Diagram. The arrows summarize the effects of geometry to illustrate the ease with which geometries can be compared on this presentation.

The figures of merit for the turbulence amplifier, all easily obtained from a Verhelst Diagram, are as follows:

1. Fanout: a digital specification for gain, fanout is the interger number of similar amplifiers that may be turned OFF by the output of one that is ON.

2. Cascadability: a determination that the OFF output of an amplifier is not sufficient to trigger a single cascaded amplifier which should remain ON. The output impedance of the driving amplifier is usually neglected in this determination to make it conservative.

3. Power Consumption: computed from the operating point  $P_s$ ,  $Q_s$  values. Usually expressed in watts. Frequently around 1.

4. Flow Ratio: the maximum available output flow compared to supply flow.

5. Pressure Ratio: the maximum output pressure compared to supply pressure.

### The Parameters of Design

Since the Verhelst Presentation is not readily generalized, alternative presentations of the parameter groups are required and a rational procedure for developing a dimensioned set of characteristics from them must be developed. The geometry of the turbulence amplifier is most readily characterized with respect to the emitter diameter. Of the remaining eight dimensions necessary to specify the geometry, four are of major importance to the amplifier performance. From Figure 2 these are given in non-dimensional form:

$$L = l/d$$

the emitter length, which exerts an important influence on the initial jet velocity profile, emitter pressure-flow relationships, and jet stability.

$$G = g/d$$

the emitter-receiver gap, which determines jet attenuation and maximum supply conditions.

$$L_o = l_o/d_o$$

the receiver length, determines output impedance.

$$L_c = l_c/d_c$$

control length; determines the control pressure-flow relationships.

Somewhat less flexible are:

$$d_o/d$$

receiver to emitter diameter ratio. Almost always one, for the simple reason that one works well.

$$b/d$$

control set back; a weak optimum in control effectiveness exists for  $b/d = 2$ .

$$a/d$$

control offset; again a weak optimum for  $a/d = 2$ .

$d_c/d$

control size; influences the control pressure-flow relationships very strongly. It can be chosen by impedance matching.

The fluid properties also influence performance. The fundamental parameter characterizing the flow is Reynolds Number based on the emitter diameter and mean velocity. Unfortunately, turbulence amplifier interactions are too complex to be described entirely by this simple parameter and two modified forms are required: for tube flows, which are basically developing flows,  $Re/L$  is used as it incorporates tube length into the parameter. For jet pressure recovery, another modified Reynolds number coalesces the data:  $Re/KG$ , which incorporates both gap,  $G$ , and a dimensionless constant associated with the jet origin as a function of emitter conditions,  $K$ .

Pressures are most conveniently non-dimensionalized with respect to a dynamic pressure, which is flow related. Rather than the traditional  $1/2\rho U^2$  based on average velocity commonly used in pressure drop calculations, the dynamic pressure based on the emergent jet centerline velocity effectively accounts for differences in emitter mouth velocity profiles which can occur at the same average flow with different emitter lengths. This choice also plays an important role in the receiver pressure recovery model employed, in which only centerline velocity attenuation in the jet is considered.

Finally, the jet model suggested for design requires two integral properties of the emitter exit velocity profile; a momentum factor,  $\beta$ , relating nozzle exit jet momentum to the momentum based on average velocity, and a centerline velocity factor,  $\lambda$ , relating true centerline velocity to average velocity. With this basic set of parameters, a set of design charts can be developed to completely specify open amplifier static performance.

For planar geometries, the same basic set of parameters hold after appropriate modification for duct geometry. As most planar designs have low aspect ratios, often one (square ducts), they are not really two-dimensional. A hydraulic diameter is then more appropriate than slot width for a linear dimension. As these differ only by a multiplied constant, design charts can obviously be derived for either or be easily converted from one to the other.

#### Analysis for Jet and Tube Flows

In the analytical development that follows, the major emphasis is placed on a calculation of the characteristics of round jets and tubes in an open (unshrouded) amplifier because these results are based on the author's own work [4,14,15]. These results are not directly applicable to planar geometries which are probably more useful commercially, but with only minor modifications, these analyses could all be converted to low aspect ratio planar types with generous shrouds. The salient feature of this presentation is the approach; the pursuit of the five basic characteristics just outlined. We will see that some features of T/A performance cannot be approached analytically but must be empirically determined. No studies comparable to

those reported in References [4,14,15] have been reported for planar T/A's. Such studies are required before a comprehensive design procedure for planar T/A's can be drawn up.

The free jet profiles of laminar jets were originally characterized by Schlichting [16] and Bickley [17] for jets issuing from point and line sources. Andrade and Tsien [18] then showed, in an elegant series of experiments, that the Schlichting jet profile matched those in real round jets from finite sources with initially uniform velocity profiles, if the Schlichting jet was assumed to issue from a virtual origin at  $x_0/d = Re/25$  inside the emitting orifice. They extended their work to initially parabolic exit plane profiles by suggesting that the location of the virtual origin might be obtained by equating the kinetic energies calculated for the initial parabolic profile and the similarity profile. This results in a virtual origin at  $x_0/d = Re/20$ , but they did not confirm this. The author [4,14] suggested an alternative calculation based on matching centerline velocities in the parabolic profile and Schlichting profile for which  $x_0/d = Re/16$ . This was not directly confirmed by centerline velocity measurements, but it led to accurate predictions of recovered pressure in the jet, and has the additional advantage of not requiring integration of the jet profile. Beatty and Markland [19] and later, McIlhagger and Markland [11] developed useful jet matching schemes based on streamline matching, i.e., by insisting that the Schlichting jet radial velocity be zero at the edge of the tube exit. For a parabolic tube profile this leads to a virtual origin given by:  $x_0/d = Re/16$ . It should be clear that none of these methods will predict the velocity profile in the developing region of the jet. Du Plessis, Wang and Tsang [6], however, made accurate predictions of the developing profile in a round laminar jet with an initially parabolic profile by solving the appropriate boundary layer equations numerically. They confirmed their results experimentally and found that  $x_0/d = Re/18$  was the best virtual origin location. Their boundary layer solutions are not tabulated or expressed in closed form, however. The author and H. W. Chang [20] have also confirmed that for parabolic emitter profiles,  $x_0/d = Re/18$  gives a best match. These experiments were conducted in a large tank with a one inch diameter emitter. Velocity profiles were accurately measured by hot film anemometry in a working fluid of 99% distilled water and 1% Union Carbide Polyox WSF N-3000 resin which had a viscosity of 21.2 centipoise at 71.5°F. Figure 4 shows a typical array of developing profiles in an undisturbed jet for which  $Re/L = 5.75$ . The salient features to note, typical of all of the profiles measured in this research, are the small "humps" in the profile at the radius of the nozzle. These humps are thought to be due to the velocity profile discontinuity between the parabolic profiles inside the jet emitting nozzle and the entrained flow boundary layer on the outside of the nozzle at its edge. This ring discontinuity persisted to the jet transition. Previous investigators of axisymmetric jet profiles have not shown this detail, probably because they took discrete point measurements and missed it, or because their probe size, compared to the jet diameter, limited their resolution. Close examination of Andrade and Tsien's [3] or du Plessis' [6] data reveal some suggestive points in their profiles, however. The size of these humps also varies with nozzle geometry, being

very large for a blunt thick-walled nozzle. The humps in the data given in this paper are for the nozzle shown in Figure 5.

Before proceeding to jets from undeveloped emitter profiles, it is appropriate to discuss the fully developed jet profile and the transition region in which the jet profile changes from the emitter induced initial profile to a Schlichting developed jet profile. In the developed region, laminar jets are affinely similar. Schlichting's well known solution for the velocity profile can be expressed in dimensionless form as:

$$\frac{u}{u_{cl}} = \frac{1}{(1 + \frac{1}{4} \xi^2)^2} \quad (1)$$

where  $u$  is velocity,  $u_{cl}$  is centerline velocity and  $\xi$  is a dimensionless coordinate given by:

$$\xi = \frac{1}{4} \sqrt{\frac{3J}{\pi\rho}} \cdot \frac{y}{v(x + x_0)} \quad (2)$$

in which  $J$  is the jet momentum,  $\rho$  is the fluid density,  $v$  is the fluid kinematic viscosity,  $y$  is the radial coordinate,  $x$  the axial coordinate measured from the emitter mouth, and  $x_0$  is the distance within the emitter at which the virtual point source origin of the jet appears to be.

For values of  $x/d < 10$ , the jet profile is not fully developed and will not scale on  $u/u_{cl}$  vs  $\xi$  coordinates. Figure 6 and 7 show this. As the jet is symmetric, only half of the profiles are plotted with the underdeveloped profiles on the right and the fully developed profiles on the left. The slight scatter of data in the region  $1 < \xi < 2$  is due to the hump in the profile, which does not occur at a fixed value of  $\xi$ . The underdeveloped profiles do not scale because they are in transition from a parabolic start at the emitter mouth, i.e.:

$$\frac{u}{u_{cl}} = 1 - \left(\frac{2y}{d}\right)^2 \quad (3)$$

which is not similar to equation 1. It is useful, however, to recast equation 3 in terms of  $\xi$ . Equation 3 can be rewritten, with  $x = 0$  at the emitter mouth and with the momentum of the parabolic profile expressed in terms of Reynolds number:

$$\xi = \frac{Re \cdot y}{4x_0} \quad (4)$$

But  $x_0 = Re d/18$  so that  $\xi = 9y/2d$  for a parabolic profile. Then the term  $2y/d$  in equation 3 can be expressed as  $4\xi/9$ , and equation 3 can be expressed approximately as:

$$\frac{u}{u_{cl}} = 1 - \frac{1}{4} \xi^2 \quad (5)$$

This can be re-expressed in the form of equation 1 as follows:

$$\frac{u}{u_{cl}} = \left(1 - \frac{1}{4} \xi^2\right) \left(1 + \frac{1}{4} \xi^2\right)^2 \frac{1}{\left(1 + \frac{1}{4} \xi^2\right)^2}$$

or

$$\frac{u}{u_{cl}} = \left(1 + \frac{1}{4} \xi^2 \left[1 - \frac{1}{4} \xi^2 - \frac{1}{16} \xi^4\right]\right) \frac{1}{\left(1 + \frac{1}{4} \xi^2\right)^2} \quad (6)$$

in which the term in braces can be viewed as a profile correction factor for the similarity profile,  $F(\xi)$ . However, equation 6 becomes infinite as  $\xi \rightarrow \infty$ , and because of this and because an approximation was included in equation 5 for convenience, a denominator term is required in the correction factor and adjustable constants are required. Starting with equation 6, the following approximation was developed.

$$F(\xi) = 1 + \frac{ab}{4} (\xi^2) \left[ \frac{1 - \frac{c}{4} \xi^2 - \frac{1}{16} \xi^4}{1 + \frac{b}{64} \xi^2} \right] \quad (7)$$

where, by trial and error, the constants are determined as:

$$a = 1 - x/10d$$

$$b = 1.1026 \quad (8)$$

$$c = 1.2150$$

Equation 7 is similar to a correction factor developed by Sato [21] for Bickley's plane jet [2], except that Sato's expression contains a constant which is a function of  $Re$ . Equation 7 is applied to Schlichting's profile in Figure 8, for four values of  $x/d$ . Superposition of these curves on either Figure 6 or 7 will show the excellent agreement obtained in predicting the developing profiles.



To determine the magnitude of the velocity profile at any station in the jet the centerline velocity is required as a function of  $x$ , measured from the emitter mouth outward. This can be calculated (following Schlichting [16]) in terms of Reynolds number, gap and virtual origin location as:

$$u_{cl} = \frac{3\beta Re^2 v}{32(x + x_o)} \quad (9)$$

where the factor  $\beta$  is the momentum ratio, expressing the ratio of emitter mouth jet momentum to the momentum based on average velocity. Thus:

$$\text{Jet Momentum} = 4\rho Q_s^2 \beta / \pi d^2. \quad (10)$$

For a uniform emitter profile  $\beta = 1$ ; for a parabolic profile  $\beta = 4/3$ .  $x_o$ , the position of the virtual origin is given for a parabolic profile as  $x_o/d = Re/18$  and thus:

$$u_{cl} = \frac{Re^2 d v}{8(\frac{x}{d} + \frac{Re}{18})} \quad (\text{Parabolic emitter profile}) \quad (11)$$

#### The Laminar Turbulent Jet Transition

The location of the free transition in the jet determines the maximum Reynolds number for a given gap at which the laminar portion of the jet will reach the receiver, and therefore determines the maximum recovered pressure for that gap. Even though a portion of the jet may remain laminar for an increase in Reynolds number, the output pressure will fall as the transition moves inward in the gap, and a turbulent jet reaches the receiver. The position of the transition is also very sensitive to the ambient conditions and emitter geometry. Figure 9 illustrates typical output pressure-supply flow behavior with the maximum on the curve corresponding to the jet flow at which the laminar-turbulent interface has just reached the receiver mouth [4]. The location of this transition as a function of main jet Reynolds number is the weakest link in the design of T/A's. No analytical prediction of free laminar length is presently possible. Figure 10 is a composite plot summarizing the literature on laminar to turbulent transition, and illustrates the very broad range of possibilities. (Data from an additional reference, McKenzie and Wall [27], are not shown because both the very low Reynold's numbers and transition lengths place this data in the lower left of the figure 10 below all other data.) The effect of tube length on free transition length is not clear. The author [4,15] contends that increasing emitter length increases jet transition length weakly, while Marsters [26], for example, maintains that for fully developed emitter profiles at least, emitter length has no effect. It is clear that shrouding effects transition length in a substantial way, but no systematic studies have been



done to date. Figure 11 is a suggested design limit for free transition length of round laminar jets from emitter profiles at or near full development. It is taken from Marsters, Reference [26] and represents a reasonable summary of pertinent data. Reference [38] presents some planar data.

Ambient sound has a very strong effect on unshrouded laminar jet length. When the frequency of incident sound falls within the range of frequencies that the jet can amplify, the jet transition length is significantly shortened. Efforts at predicting the stability of laminar flows were for many years entirely unsuccessful. It has been only in more recent times that Prandtl, Tollmein and others have had success with predictions of conditions of neutral stability in parallel flows near surfaces, using the method of small disturbances. This method, stated briefly, is to postulate the form of the disturbance as a function of space and time, substitute this into the Navier-Stokes equations and obtain a fourth-order differential equation: the stability equation or Orr-Sommerfeld equation. The four particular solutions of this equation are exceedingly difficult to obtain. Two can be found from the frictionless case and the remaining two are usually not found at all, or are found from a subsidiary equation obtained with the first two by considering only the most important viscous term. From these solutions a curve of neutral stability is obtained, C-shaped in the wave number - Reynolds number plot. (Wave number gives radians of wave per unit length.) This is the locus of disturbances that will neither grow nor decay, and the minimum Reynolds number corresponds to the point at which no wavelength will grow. It must be understood that the point of instability is not the point of transition. Amplification of disturbances begins at the point of instability and continues downstream inducing transition, and the distance downstream obviously depends on both the initial disturbance amplitude and on the degree of amplification.

This approach has been proven satisfactory for bounded parallel flows, where good agreement is obtained for critical Reynolds number and neutral stability but the transition cannot be predicted. The step from bounded parallel flows to free flows (jets) has been made with great difficulty. Curle [28] and Tatsume and Kakutani [44] applied the Orr-Sommerfeld Equation to a Pseudo-laminar or non-spreading parallel two-dimensional jet with moderate success. At high Reynolds number, where laminar jet flow is nearly parallel, Sato [21] found that the region of transition from slit profile to similarity profile corresponded to the region of interest. His modifications were an improvement, however. Chanaud and Powell [29] measured curves of neutral stability for a sound excited jet and found them to be amplitude sensitive; the larger the disturbance, the lower the critical Reynolds number and the larger the span of frequencies to which the jet was sensitive.

In 1962 Batchelor and Gill [30] were able to solve the inviscid stability equations for an axisymmetric parallel jet. They were able to show that a point of inflection in the velocity profile was a necessary condition for growth of disturbances. Such a point always exists for a square profile at the nozzle where there is a very sharp inflection, and in typical bell shaped velocity profiles found in the developed jet. It is particularly

pronounced in velocity profiles with a ring "hump." They found that the wave speed of disturbances is either the velocity at the inflection or the centerline velocity depending on the disturbance. Near the jet orifice, axisymmetric disturbances (vortex rings) are possible and travel with the centerline velocity of the jet, otherwise, in the fully developed jet, only sinuous disturbances will grow and travel at the inflection velocity. This is discussed later.

From this brief review of some of the pertinent literature we may form the following expectations:

a) The C-shaped neutral stability curve, typical of analyses in which viscosity is included, suggests that there will exist a minimum Reynolds number for an absolutely stable jet above which the laminar jet exists in a state of transition. Viilu [3] has confirmed this. In a series of careful experiments he found the critical Reynolds number for the axisymmetric case to be  $11.2 \pm 0.7$ . Above this Reynolds number, the C curve is double valued, unstable on the inside, suggesting that there will always be a range of frequencies to which the jet will be sensitive.

We might expect that outside this frequency range, noise would have little or no effect.

b) We would expect the frequency range of sensitivity to be a weak function of intensity of the sound.

c) We would expect that the jet stability would be sensitive to the exit profile for two reasons: First, that square profiles have high shear rates at they leave the nozzle and are prone to vortex formation, and second, underdeveloped profiles have higher turbulence levels that have not damped out in the emitting tube.

d) We would expect that disturbances introduced near the jet origin would have more influence than those introduced downstream both because the jet is more sensitive there and because they will have more time to grow.

Sound sensitivity measurements for open, round laminar jets were made by the author [4] by radiating a jet with sound from an 8 inch speaker one foot from the jet and perpendicular to it. Reflections were prevented by absorption and the sound amplitude was held constant at approximately 70 db. The jet sensitivity was recorded only at  $P_o$  max, at incipient transition, and this is the worst case condition. Figure 12 shows a typical frequency sweep versus output pressure plot. As expected, there is a lower and upper bound on sensitive frequencies at least in the range of 0 to 20 KCPS. For Figure 12 no frequency below 2150 or above 10,000 cps influenced the jet. This method of measuring jet response to sound is quite sensitive and is pertinent to turbulence amplifier technology, but limits the range of Reynold's numbers tested to those for incipient transition in jets at gaps between 15 and 50;  $1200 < Re < 2700$  in this particular study. Figure 13 is a compilation of all this data for various emitters. The solid bars between points indicate that the points and all frequencies in between were sensitive,

the broken lines over several points indicate sensitivity (complete transition) at the points with partial or no sensitivity in between. Although scattered, the data seem to indicate a very definite upper and lower limit of sensitivity. Sato, Reference [21] did a series of experiments with a high Reynold's number two-dimensional jet, measuring the frequencies amplified in the jet when it was excited by sound and found the Strouhal number to be independent of Reynold's number. His Strouhal number was defined as the frequency occurring in the jet, non-dimensionalized with jet width and centerline velocity. For an axisymmetric jet the jet width,  $b \sim x$  and the centerline velocity,  $U_{cl} \sim 1/x$  so  $b/U_{cl}$  is constant and may be computed at the nozzle. In the literature on stability it is usually only the upper limit that is detected. Figure 13 also shows a definite lower limit but it increases with Reynold's number; that is, the frequency range decreases with Re, contrary to expectation. This is an artifact of the experimental procedure, because as Reynold's number increases, the free transition moves in towards the emitter and the gap at which the measurement is must be decreased, i.e., the geometry is not constant. At the high end of the scale of Figure 13 the gap is 10 diameters while at the low end, the gap is 50 diameters. Since

$$\frac{1}{STR} = \frac{\text{velocity}}{\text{frequency} \cdot \text{diameter}} = \frac{\text{wavelength}}{\text{diameter}},$$

the wavelength in jet diameters can be computed along the lower boundary and varied from 18 diameters at  $Re = 1500$  to 2.5 diameters at  $Re = 2700$ . The gaps at these Reynold's numbers are varying from 50 to 13 for this data in such a way that along the lower boundary of Figure 13, the gap is only 3-4 times the disturbance wavelength which increases with Re. The behavior of the lower limit may therefore be due only to insufficient time for growth of disturbances whose wavelengths are longer than  $1/3$  to  $1/4$  of the gap. The broken line through the lower limit is the curve of transition gap times Strouhal Number = 3.5; the line on which transition occurs in  $3-1/2$  wavelengths of the disturbance.

It should be mentioned that enclosing the jet in a shroud will introduce new strong frequencies to the spectrum; the resonances of the shroud chamber itself. For typical geometries, however, tube resonances are not a factor as simple calculations show that these frequencies are generally too high.

Recall Batchelor and Gill's [30] prediction of jet instability by vortex ring growth and the importance the assigned to the inflection point of the velocity profile. Re-examine Figure 4 and notice the "humps" in the velocity profile. Figure 14 is a turbulence intensity profile in the same jet as measured by Chang [20]. The two curves shown are normalized differently; with respect to centerline and local velocity. In either case, notice the peaks that occur just inside the humps in the velocity profile in the region of "super-inflection" where the velocity gradient actually reverses. This "hump" appears to play a role in the control-induced transition as well.

Figures 15, 16 and 17 are a series of velocity profiles of the same main jet with increasing control flow. The figures are x-y recordings of velocity versus position taken in slow constant velocity traverses. Incipient turbulence shows up as chart painting so that the figures speak quite eloquently for themselves and for the importance of the vortex generated hump at the velocity profile inflection point. Figure 18 shows corresponding turbulence intensities.

#### Recovered Pressure in the Jet

Until recently, blocked load pressure recovery has usually been calculated, with very little experimental justification, by integrating free jet total pressure over the receiver mouth area, (e.g., [31-34]), at an axial location in the free jet corresponding to the receiver position. Experiments have shown this value to be too low, often by a factor of two or more, presumably because of secondary flows in the receiver mouth. Because stagnation pressures are higher near the center of the receiver than near the edge, some spill flow is to be expected and the centerline total pressure should predominate. Reid [35] first proposed utilizing centerline stagnation pressure in pressure recovery calculations and verified that this was accurate within 6% for turbulent jets with emitter-receiver gaps of less than 10 diameters. Blocked load pressure recovery for an aligned receiver is then given by the expression:

$$P_o = \frac{1}{2} \rho u(0)^2 \quad (12)$$

at the axial location of the receiver, rather than by a complex integral.

The author [4,14,15] confirmed this approach for laminar jets at gaps of up to 30 diameters, and the same approach has been suggested and used successfully by Jansen and Winnikow [36] and by McIlhagger and Markland [11] for long laminar jets in turbulence amplifier geometries. Generally speaking, the centerline velocity pressure is very slightly higher than the actual recovered pressure as evidenced by a slight decrease in recovered pressure with increasing receiver diameter. Careful studies of laminar jet-receiver interactions similar to those of Reid [35] for a turbulent jet have not been done.

With the centerline stagnation point of view, the matching of tube and jet properties necessary to establish the location of the virtual origin,  $x_o$  when the emitter flow is not fully parabolic, can also be based on centerline velocity so that centerline stagnation pressure at the tube exit is matched to centerline stagnation pressure in the Schlichting jet. Recovered pressure in the receiver is then given simply in terms of the attenuation of centerline stagnation pressure in the jet over the emitter-receiver gap,  $G$ . Returning to equation (9) with  $x = 0$ , (13) is obtained:

$$u(0) = \frac{3\beta \nu Re^2}{32 x_o} \quad (13)$$

and the corresponding tube exit centerline velocity is given by (14)

$$u(0) = \frac{Q}{A} \lambda_o = \frac{4Q}{\pi d^2} \lambda_o = \frac{v Re \lambda_o}{d} \quad (14)$$

where  $\lambda_o$  is the centerline velocity factor relating the true centerline velocity at the emitter exit plane to the average velocity. Equating these yields

$$\frac{x_o}{d} = \frac{Re}{32 \lambda_o / 3\beta}, \quad \frac{x_o}{d} = \frac{Re}{K}, \quad K = \frac{32 \lambda_o}{3\beta} \quad (15)$$

(Similar calculations are made for flow, energy and spread angle and are compared in Reference [4]. The values of K obtained are different for each. For streamline matching,  $K = 32/\sqrt{3\beta}$ .) No current matching technique gives the experimental value of  $K = 18$  for a fully developed parabolic emitter profile.

The centerline stagnation pressure at the emitter mouth,  $P_{CL}$ , is given by  $1/2 \rho U(0)^2$  there, or from (14)

$$P_{CL} = \frac{1}{2} \rho \left( \frac{v Re \lambda_o}{d} \right)^2 \quad (16)$$

From equations (9) and (12), with  $x = g$ ,  $P_o$  becomes:

$$\begin{aligned} P_o &= \frac{1}{2} \rho \left[ \frac{3\beta v Re^2 / 32}{g/d + x_o/d} \right] \\ &= \frac{1}{2} \rho \left[ \frac{3\beta v Re^2 / 32}{G + Re/K} \right] \end{aligned} \quad (17)$$

Forming the ratio of 16 and 17 yields an expression for the recovered receiver pressure in terms of the centerline stagnation pressure at the emitter mouth.

$$\frac{P_o}{P_{CL}} = \left( \frac{3\beta Re}{32 \lambda_o} \right)^2 \bigg/ \left( G + \frac{Re}{K} \right)^2 \quad (18)$$

The numerator term is immediately recognized as  $Re/K$  ( $K$  as given by equation (15)), so the pressure ratio may be simplified to read:

$$\frac{P_o}{P_{CL}} = \frac{1}{\left(\frac{KG}{Re} + 1\right)^2} \quad (19)$$

A similar expression may be derived for the turbulent jet arising from control action. For the induced turbulent jet, the region of interest lies well outside the region of the development of the velocity and turbulence intensity profile. Deflections of the main jet by control jet momentum may be shown to be negligible and asymmetries in the velocity profile are diffused quickly. Boyd and Barbin [37] reported uniform turbulence intensity profiles at 12.8 diameters and full velocity profile development by 16 diameters in jets disturbed by a control at two diameters. Large scale studies, conducted by Chang [20], confirm these measurements. Normal emitter-receiver gaps exceed 15 diameters. For these reasons, the simple Goertler [16] jet model, modified for a finite source, was used to describe the "off" jet. This model is identical to the Schlichting laminar jet model with a simple substitution of the eddy viscosity  $\epsilon_o$  for the laminar kinematic viscosity,  $\nu$ . As a consequence of Prandtl's mixing length hypothesis, the eddy viscosity is constant throughout a given jet and is a function only of the jet momentum and fluid density. Reichardt [16] deduced the relationship as

$$\epsilon_o = 0.0161 \sqrt{M/\rho} \quad (20)$$

The spread angle in jets, defined by the locus of points where the radial velocity is zero in a Schlichting model is given by  $\arccot(\gamma/2)$  where  $\gamma$  is given by the following:

$$\gamma = [3M/16\pi\rho\nu^2] \quad (21)$$

In a turbulent Goertler jet  $\nu$  is replaced by  $\epsilon_o$ , and with equation 20 becomes  $\gamma = 15.2$ . Thus the spread angle is constant in a turbulent jet while laminar jets get narrower with increasing  $Re$ . Laminar and turbulent jets have the same spread angle at  $Re = 60.7$ .

Applying the centerline velocity matching scheme used for laminar jets the virtual origin is found:

$$\frac{x_o}{d} = \frac{7.664 \sqrt{\beta}}{\lambda_o} \quad (22)$$

which has a numerical value of 4.42 for a fully parabolic emitter profile, and of 7.66 for a square profile. Since the control is actually two diameters downstream of the emitter mouth and the location of the transition to turbulence after the control is uncertain, it may be reasonably assumed that



the virtual origin of the turbulent jet is at the emitter mouth.

In the induced turbulent jet, the emitter outlet profile is not affected so that the turbulent pressure recovery can be normalized with respect to equation (16) as before by normalizing the turbulent centerline velocity at the receiver location with respect to the laminar emitter outlet centerline velocity.

$$u(0) = \frac{2\epsilon_o \gamma^2 \text{ TURB}}{x} \quad (23)$$

and

$$\frac{u(0)}{U_{CL}} = \frac{2\epsilon_o \gamma^2 \text{ TURB}}{G_o \text{ Re } v} \quad (24)$$

but

$$\frac{\epsilon_o}{v} = 0.0139 \sqrt{\beta} \text{ Re} \quad (25)$$

and after some manipulation:

$$\frac{P_o}{P_{CL}} = \frac{41.0 \beta}{G_o^2 \lambda_o^2} \quad (26)$$

This is not a simple function of Reynolds number. Emitter performance, however, will be shown to be a function of  $\text{Re}/L$  only so that  $\beta$  and  $\lambda_o$  are both functions of that parameter as well. Rearranging:

$$\frac{G_o^2 P_o}{41.0 P_{CL}} = \frac{\beta}{\lambda_o^2} = f(\text{Re}/L) \quad (27)$$

a more useful form. One difficulty, however, is that  $\beta/\lambda_o^2$  approaches  $(4/3)(4) = 1/3$  as  $\text{Re}/L$  approaches zero, so that  $P_o/P_{CL}$  does not go to zero but approaches  $41/3G_o^2$ . This is of no consequence in design, however, because amplifier operation at low Reynolds numbers is unsatisfactory.

The approach just outlined is not the only satisfactory approach. Bendor [5] suggests using laminar theory with  $\text{Re} = 60.7$  to predict turbulent jet profiles in his momentum based development. Returning to equation 17 in which  $x_o/d = 0$  and  $\text{Re} = 60.8$ , we can follow the same development to arrive at equation 28 below:

$$\frac{P_o}{P_{CL}} = \frac{32.5 \beta^2}{\lambda_o^2 G^2} \quad (28)$$

or in the form of equation 27:

$$\frac{G^2 P_o}{41 P_{CL}} = \frac{.792 \beta^2}{\lambda_o^2} \quad (29)$$

This differs from equation 27 by a factor of .792  $\beta$ , a maximum difference of only 5% decreasing to 3% at  $Re/L = 30$ . In view of the extreme noise of the OFF jet, the simplest calculation still reasonable is that

$$\frac{P_o}{P_{CL}} = \frac{14}{G^2} \quad (30)$$

A completely different but apparently accurate approach to predicting laminar pressure recovery was taken by Jansen and Winnikow [36], who developed an empirical expression for output pressure in terms of jet exit average stagnation pressure.

$$\frac{P_o - P_\infty}{\frac{1}{2} \rho U^2} = 3.68 (1 - e^{-0.002 Re}) - 0.0425 G \quad (31)$$

This expression successfully predicts pressure recovery in their experiments (using very long emitters) in the ranges  $12 < G < 40$  and  $1000 < Re < 2300$ . No attempt has been made to compare equation 31 to other laminar jet recovery data.

As a final comment in this section, it should be mentioned that McIlhagger and Markland [11] present a method for computing  $P_o/P_s$  as a function of  $Re$  very similar to the one outlined in this paper, but unfortunately restrict their results to  $P_o/P_s$  which combines emitter and jet performance. Their model, however, is directed at planar amplifiers and represents a good first step in the analysis of those geometries.

#### The Tube Characteristics

Three of the five basic characteristics specifying the static performance of a given turbulence amplifier are just tube or duct characteristics. Both the emitter and controls are typically fed from a large passage or plenum at essentially constant pressure and exhaust to ambient. The receiver sees an ON or OFF jet as its source, and a load impedance determines its output conditions. The flow in all of these is a developing flow in which an initially uniform velocity profile at the tube or duct inlet progressively approaches a parabolic profile as it moves downstream. The literature on such flows is abundant and is extensively reviewed for flow in round tubes



in Reference [4]. No closed form solutions are available for either round tubes or rectangular ducts. Convenient numerical solutions are available, however, due to Hornbeck [39] for round passages, and due to Han [40] for rectangular ducts. The development that follows is for round tubes following References [4,14,15]. It should be clear that similar developments can be generated for rectangular ducts as well, but this is not done here.

Table 1 shows Hornbeck's results in modified form [14]. By interpolating in the table, the centerline velocity, momentum factor and pressure drop are easily obtained for any  $Re/L$ . The tabulated pressure drop is the drop in static pressure from tube mouth to exit. Added to this must be the Bernoulli drop from plenum to tube mouth,  $\rho u^2/2$ , plus any entrance losses that will occur if the tube entrance is not a smooth bell-mouth. For the tests reported in [14], the tubes were interfaced with a plenum at a  $60^\circ$  semi-apex angle conical borda inlet made by chamfering the inside edge of the tube mouth with a drill and inserting it 10d into the plenum. For these entrance conditions the total entrance pressure drop was found to be

$1.3 \left( \frac{\rho u^2}{2} \right)$ , corresponding to a discharge coefficient for an equivalent beveled orifice plate of  $C_D = 0.88$ , well within the range of values usually assumed. Chang [20] found the factor 1.3 too large and used 1.0 with good results.

The centerline stagnation pressure is calculated from Table 1 by adding 1.3 or another factor appropriate to the geometry to the value in the pressure drop column and dividing this by the square of the  $\lambda_0 = \lambda(R=0)$  entry corresponding to it. Since the tube exit pressure is ambient, the resulting number is  $P_s/P_{cl}$ .  $\beta$  is calculated by numerically integrating the tabulated velocity profile. Figure 19 is a plot of  $\lambda_0$ ,  $\beta$ ,  $K$  and  $\beta/\lambda_0^2$  as functions of  $Re/L$ . Note that for  $Re/L < 15$  the fully developed values may be used without error and Chang's profile correction is valid.

In the case of the receiver, the input is not a plenum but the jet, and the receiver output pressure-flow relationship will depend on how the jet approximates a plenum. Generally, the approximation would be a poor one because under some circumstances receiver flow can exceed jet flow (as it does in a jet pump). In a turbulence or flow mode amplifier, however, the gap is typically 20 to 30 diameters and the receiver is very nearly the same size as the emitter. Under these conditions the jet profile is quite flat and many diameters wider than the receiver, so that jet pumping is not possible. A reasonable working assumption under these circumstances is, therefore, that the jet will not contribute to the output impedance of the amplifier. The jet stagnation pressure is assumed to remain constant independent of receiver flow. In other words, a blocked receiver sees jet stagnation pressure as static pressure, but as flow increases in the receiver, the static component falls and the dynamic components of pressure rises. As full jet flow is accepted at the receiver, the jet velocity profile is disturbed only by the thin walls of the receiver. Assuming an entrance loss of the same value as experienced by the emitter and controls, the pressure-flow relationship is found from Table 1 by adding 1.3 to the  $P/\frac{1}{2} \rho U^2$  entries in

Re/L	R = r/(d/2)	DIMENSIONLESS AXIAL VELOCITY $U(R)/(4Q/\pi d^2) = \lambda$										DIMENSIONLESS PRESSURE $\frac{\Delta P}{\frac{1}{2}\rho U^2}$	
		0	0.1	0.2	0.3	0.4	0.5	0.6	0.7	0.8	0.9	1	
	1.0000	1.0000	1.0000	1.0000	1.0000	1.0000	1.0000	1.0000	1.0000	1.0000	1.0000	0	0
2000	1.1503	1.1503	1.1503	1.1503	1.1503	1.1503	1.1503	1.1502	1.1485	1.1293	0.9434	0	0.3220
800	1.2269	1.2269	1.2269	1.2269	1.2268	1.2268	1.2264	1.2230	1.2016	1.0950	0.6893	0	0.5034
400	1.3126	1.3126	1.3125	1.3124	1.3115	1.3068	1.3068	1.2867	1.2144	1.0098	0.5908	0	0.7204
267	1.3782	1.3781	1.3779	1.3770	1.3733	1.3596	1.3596	1.3160	1.2006	0.9511	0.5417	0	0.8960
200	1.4332	1.4331	1.4324	1.4299	1.4214	1.3959	1.3959	1.3292	1.1814	0.9107	0.5102	0	1.0506
133	1.5239	1.5232	1.5204	1.5120	1.4902	1.4395	1.4395	1.3308	1.1476	0.8585	0.4720	0	1.3212
100	1.5977	1.5960	1.5893	1.5727	1.5358	1.4623	1.4623	1.3308	1.1218	0.8261	0.4496	0	1.5610
80	1.6595	1.6562	1.6448	1.6188	1.5675	1.4751	1.4751	1.3245	1.1023	0.8040	0.4346	0	1.7822
57.1	1.7555	1.7488	1.7269	1.6831	1.6073	1.4874	1.4874	1.3125	1.0757	0.7756	0.4159	0	2.1900
44.4	1.8240	1.8142	1.7829	1.7244	1.6306	1.4927	1.4927	1.3034	1.0588	0.7584	0.4047	0	2.5692
33.3	1.8920	1.8785	1.8366	1.7626	1.6509	1.4962	1.4962	1.2943	1.0433	0.7429	0.3947	0	3.1064
25	1.9431	1.9266	1.8763	1.7901	1.6650	1.4981	1.4981	1.2875	1.0321	0.7319	0.3677	0	3.7894
20	1.9698	1.9517	1.8969	1.8042	1.6721	1.4990	1.4990	1.2840	1.0264	0.7263	0.3840	0	4.4520
16	1.9863	1.9672	1.9095	1.8128	1.6764	1.4996	1.4996	1.2818	1.0229	0.7229	0.3818	0	5.2688
0	2.0000	1.9800	1.9200	1.8200	1.6800	1.5000	1.5000	1.2800	1.0200	0.7200	0.3800	0	5.2688

- Notes:
1. Dimensionless Pressure does not include entrance Bernoulli drop or losses.
  2.  $\Delta P/P_{cl} = \Delta P / \frac{1}{2} \rho U^2 \lambda_0^2$
  3. Converted from Hornbeck's Table.

the last column, taking  $P$  as  $P_{c1} - P_o$  and iterating to find a receiver flow that generates corresponding values of  $Re/L_o$  and  $P/\frac{1}{2} \rho U^2$  in the table. The procedure is outlined more clearly in the design section of this paper to follow.

#### Confirmation of Tube and Jet Analysis

An experimental investigation was conducted [4] to confirm the analyses presented so far. The working fluid for all of the tests conducted was air, and the limits of basic parameter variation consistent with turbulence amplifier operation were set as shown in Table 2.

Table 2: Experimental Limits

Reynolds Number	Performance poor, recovered pressures excessively low	$< 500 < Re < 3000 <$	Premature laminar to turbulent transition in the emitter or jet.
Emitter Diameter	Alignment problems critical for discrete tubes. Photo-etching techniques required	$< 0.0262 < d < 0.1093 <$	Velocities and recovered pressure excessively low at reasonable Reynolds number.
Emitter Length, L	Small diameters difficult to mount and handle, jet stability degraded	$< 25 < L < 100 <$	No improvement in amplifier performance but increasing supply pressure.
Emitter-Receiver Gaps, G	Insufficient space for turbulent jet development	$< 10 < G < 60 <$	Alignment problems critical, jet velocities very low to reach receiver.

Within these limits, a very large number of measurements were made across the range of geometries and fluid conditions. In all cases, the amplifiers were constructed of commercial hypodermic needle tubing aligned in a special three-axis traversing fixture. Details of the apparatus and experimental procedures are available in Reference [4]. While not all of the geometries considered can be classified as "useful," the intent of the investigation was to encompass as broad a variation as was practicable.

#### Experimental Results

Figure 20 is a comparison of the emitter performance,  $P_{c1}/P_s$  vs.  $Re/L$ ,

as predicted from Table 1 and as measured for five tube diameters and four tube lengths,  $L$ . Although data is given over the range  $5 < Re/L < 80$ , most amplifiers operate in the range  $10 < Re/L < 40$ . The agreement shown is quite good.

Figure 21 presents jet performance data in the form of centerline stagnation pressure ratio,  $P_o/P_{cl}$ , as a function of modified Reynolds number,  $Re/KG$ . The solid line is a plot of equation 18. The chain-dotted line is fitted to data for  $L = 50$  and is in reasonable agreement with the theory. The dashed line, however, is for  $L = 25$  and diverges significantly from the theory, presumably because  $K$  does not completely compensate for the profile obtained from so short a tube. Notice also that the data appear too low near  $Re/KG = 0$ . In this region Reynolds number is low and the gap is large so that alignment becomes critical because of the very low velocities in the jet. Any misalignment, in any direction, will always produce low results since the centerline is a maximum value.

The ratio of output pressure to supply pressure is a frequently quoted figure of merit for fluidic devices.  $P_o/P_s$  is the product  $(P_{cl}/P_s)(P_o/P_{cl})$ . It would be expected that:

$$\frac{P_o}{P_s} = f(Re, L, G)$$

but the relation for  $P_{cl}/P_s$  is tabulated, rather than in closed form which hinders the analytical selection of an appropriate parameter. Despite this fact, a reasonable correlation can be obtained by plotting  $P_o/P_s$  vs.

$Re/KGL$  within the range of  $Re$ ,  $L$  and  $G$  normally encountered in turbulence amplifier operation. Figure 22 presents this plot. The two solid lines shown are the calculated values of  $P_o/P_s$  assuming that  $G$  is the largest possible valve at the given Reynolds number for  $L = 50$  and 100. The largest possible  $G$  is that for which the natural or free transition occurs just past the receiver.

Figure 23 presents the data for the "OFF" or turbulent jet recovery compared to the prediction of equation 27. The choice of the turbulent recovered pressure is somewhat arbitrary because of the long tail on the  $P_o - Q_c$  characteristic at increasing control flows. The data in Figure 23 is taken at  $Q_c = 3Q_{cl}$ , a fixed location in the characteristic. (Refer to Figure 26 for the location of  $3Q_{cl}$ ). Because the turbulent jet at large gaps is very unsteady and noisy, and the recovered pressure is low as well, the data scatter quite badly but at least justify the analytical approach.

Figure 24 compares observed blocked receiver pressure with a value calculated from the observed output flow when output pressure is held at zero (ambient). When the receiver is the same diameter as the emitter, agreement is excellent, and departs less than 10% for larger and smaller receivers. The receiver performance is self similar for a given receiver

length,  $L_o$ , when normalized with respect to  $P_o(\text{MAX})$  and  $Q_o(\text{MAX})$  as shown in Figure 25. That data is shown for  $L_o = 25$ , and the points shown cover the entire range of Reynolds numbers for the main jet. For increasing values of  $L_o$ , the curve shown approaches a straight line; for smaller values the curvature increases toward an inverted parabola centered on  $P_o/P_o^* = 1$ .

#### Control Effectiveness

Of all the phenomena associated with the turbulence or flow-mode amplifier, the induction of turbulence by a transverse impinging jet is the most difficult and mysterious to understand and measure. Figure 26 explains the nomenclature used in discussing the output pressure-control flow ( $P_o - Q_c$ ) characteristic associated with this behavior. Although shown as a smooth curve in the figure, the plunge from  $P_{on}$  to  $P_{off}$  in the characteristic is very noisy and the region between  $Q_{c1}$  and  $Q_{c3}$  is not particularly repeatable. For these reasons, the data presented here must be considered typical rather than absolute. A complete discussion of the experimental procedure is given in Reference [4]. Only general observations are given here covering the location of the controls with respect to the main jet, and variations in performance as a function of amplifier geometry and main jet conditions.

Some insight into the physics of this control induced transition is found in Figures 15, 16 and 17 with the discussion on laminar turbulent transition.

The position of the control jets with respect to the main jet centerline and emitter mouth is the only geometric absolute in turbulence amplifier design, because an easily found optimum exists from which there is no point in variation. This position is perpendicular to the main jet with the control nozzle centerline approximately two diameters downstream of the emitter mouth (offset), and the control mouth set back from the main jet centerline approximately two diameters. These are shown in Figure 2 as "a" and "b" respectively. They are explained as follows: with a setback (b) of less than two main jet diameters, the control interferes with the entrainment of the main jet which then becomes less stable and prone to turbulent bursts. As setback is increased the control effectiveness decreases slightly, with  $Q_{c1}$  and  $Q_{c2}$  shifting slowly to the right. Two diameters represents a good compromise in the tradeoff between control effectiveness and interference. With an offset (a) of less than two diameters the emitter interferes with the control jet and control is erratic. The output pressure frequently increases before reaching the upper knee because control flow is entrained instead of disturbing the main jet (see Figure 16). As offset is increased, control effectiveness increases to a maximum at  $a = 1.5$  to  $2d$ , depending slightly on control diameter, and decreases thereafter as the  $P_o - Q_c$  characteristic flattens. This loss of control may be due to the decreasing portion of the gap in which the turbulent jet is spreading.

Additional experiments indicated that the angle between the control axis and the main jet axis could lie between  $45^\circ$  and  $135^\circ$  with very little change in control effectiveness as long as the centerline intersection remained approximately two diameters downstream and the edge of the control tube did not interfere with the main jet.

The remaining degree of freedom in control location is position out of plane: i.e., the perpendicular distance between the control centerline and the emitter-receiver centerline. Figure 27 shows a typical traverse of the main jet with a control jet in which the control flow was held constant at the  $Q_{c2}$  determined when the centerlines intersected. The surprising conclusion to be drawn from this and other results like it is that the vertical position of the control is very flexible: the centerline of the control jet may intersect the main jet anywhere, even tangentially.

#### Supply Conditions

The empirical results presented in this section and those following and the conclusions drawn for variations in amplifier geometry and supply conditions are all with the control at the optimum position, with centerlines perpendicular and intersecting. The data shown are for a particular geometry but they are typical of many such tests.

Recall that the free transition position is a strong function of emitter Reynolds number and possibly a weak function of emitter length. Figures 28 and 29 indicate that this is not so for induced transition. The upper knee control flow,  $Q_{c1}$ , is constant, Figure 28 and for three emitter lengths, traces of the  $P_o - Q_c$  characteristic cannot be distinguished, Figure 29. It can be concluded that control performance is independent of the main jet  $Re/L$ .

#### Control Diameter and Emitter-Receiver Gap

As might be expected, control gain decreases with decreasing gap, probably because of decreasing space available for the development of turbulence (analogous to sound tests Figure 13). Tests run at constant output pressure (decreasing  $Re/L$  with gap) and with constant main jet  $Re/L$  (increasing  $P_o$  with decreasing gap) both indicate an increase of  $Q_{c1}$  and  $Q_{c2}$  with decrease of gap. At gaps less than 15, performance is entirely unsatisfactory because the "OFF" pressure is high and very noisy. As gap exceeds 20 diameters the  $P_o - Q_s$  characteristics tend to converge somewhat; i.e., further increase in gaps does not bring a commensurate increase in control effectiveness. Control effectiveness varies more uniformly with changes in control diameter. Figure 30 illustrates the form of variation. A very large number of these curves was run to obtain sufficient data for determining the  $P_o - Q_c$  characteristic.

As illustrated by Figure 31, where two control jets acting simultaneously are compared to individual controls acting singly, although the individual controls taken one at a time act very nearly equally, the



parallel (same side) controls acting simultaneously require very nearly twice the total flow to reach  $Q_{c1}$  and the opposed controls require slightly more than twice the single tube flow at  $Q_{c1}$ . Although not shown here, controls at some angle between  $0^\circ$  and  $180^\circ$  apart around a plane perpendicular to the main jet at  $a = b = 2$  require intermediate values of total flow at  $Q_{c1}$ . The conclusion to be drawn is that two controls in concert are not twice as effective as one, but each require very nearly the same flow as they would one at a time to induce turbulence. This explains the independence and lack of interaction of T/A controls outlined in the introduction.

#### Data for Construction of $P_o - Q_c$ Characteristic

We have already developed methods for computing the "ON" received pressure and the "OFF" recovered pressure and know that  $P_{on}$  occurs with  $Q_c$  near zero and  $P_{off}$  is defined at  $Q_c = 3Q_{c1}$  (refer to Figure 26). It remains to find  $Q_{c1}$  and  $Q_{c2}$ , the control flow at the knees of the  $P_o - Q_c$  characteristic. Unfortunately, scaling laws are not available for these conditions.  $Q_{c1}$  can be defined as the intersection of the "ON" pressure and the line through the rise of the characteristic and, for optimal control location, is a function of control diameter and gap only. Figure 32 is a plot of these data. Although very scattered, the data suggest a straight line relationship between  $Q_{c1}$  and control diameter with approximately uniform spacing between lines of differing gap. The line shown for  $G = 50$  is estimated. Close examination of the data reveals no systematic dependence between emitter diameter and  $Q_{c1}$ .  $Q_{c1}$ , therefore, appears to be independent of  $Re/L$ , and of its factors ( $\rho$ ,  $U$ ,  $d$ ,  $\nu$ ,  $L$ ) taken individually, although viscosity was not varied.

To determine  $Q_{c2}$  as outlined in Reference [15] (see Table 2, that reference), where  $Q_{c2}$  is taken as the intercept of the extended characteristic plunge with the abscissa of the  $P_o - Q_c$  plot, the simple relationship  $Q_{c2} = 4/3 Q_{c1}$  holds well. The  $P_o - Q_c$  characteristic for air in small diameter tubes can thus be predicted by calculating  $P_{on}$  and  $P_{off}$  and joining them by a line from  $(P_{on}, Q_{c1})$  to  $(P_o = 0, 4/3 Q_{c1})$ . The corners should then be rounded as shown in Figure 26.

#### Static Design Procedure

The analytical and empirical results presented so far are sufficient to completely specify turbulence amplifier static performance, at least within the experimental bounds considered earlier, for control diameters in the range:  $0.027 < d_c < 0.063$  inches. Within those bounds the designer can construct all or part of a set of characteristics depending on his requirements. (Because of the large number of parameters involved, procedures for design depend on the initial choice of known and on how many of the remain-

ing dependent variables are required.) The following procedures illustrate what can be done. No matter what is specified, however, the designer will almost always have to determine a flow given a pressure drop. The turbulence or flow-mode amplifier is primarily flow dependent, and iteration is required to determine a  $Q$  given  $P$ . The following procedure may be thought of as a subroutine:

A) Flow Determination given Pressure Drop for a Tube

1. Start with  $P$ ,  $d$  and  $l$  for the tube
2. Estimate  $Q$  from  $Q = \pi d^4 P / 128 \mu l$
3. Calculate  $Re/L = 4Q / \pi l \nu$
4. Enter figure (20), find  $P_{CL} / P$  (Entrance loss = 1.3)
5. Enter figure (19), find  $\lambda_o$  or use 2 for  $Re/L < 15$
6. Calculate  $P_{CL} = 0.5 \rho (4 \lambda_o Q / d^2)^2$
7. Calculate  $P_1 = \text{Step 6} / \text{Step 4}$
8. Compare  $P_1$  to the initial  $P$ , step 1.
9. Iterate as necessary by guessing a new value of  $Q$  and returning to step 3. This converges very quickly because step 2 is a good estimate.

Suppose the designer specifies  $P_g$  and  $d$  but is flexible about  $l$  and  $G$ . He will have to choose one or the other to get started and will have to guess at values of  $l_o$  and  $d_c$  as well. If the designer specifies  $l$ , then the procedure is as follows:

- A) 1. Using procedure A, determine  $Re$
2. Enter figure (11), with  $Re$ , find  $G_{max}$
3. Choose  $G < G_{max}$
4. Enter figure (19), find  $K$ , or use 18
5. Enter figure (21), with  $Re/KG$ , find  $P_o / P_{CL}$
6. Using Step 6 in A, calculate  $P_o$  from Step 5 here
7. Enter figure (19), find  $\beta / \lambda_o^2$ , or use eqn. (30)
8. Enter figure (23), find  $P_{off}$ , skip if using (30)
9. Enter figure (32), with  $d_c$ , find  $Q_{c1}$
10. Calculate  $Q_{c2} = 1.33 Q_{c1}$ ,  $Q_c(\text{TURB}) = 3Q_{c1}$
11. Following figure (26), construct  $P_o - Q_c$
12. Guess  $Q_o(\text{max}) = \pi d_o^4 P_o / 128 \mu l_o$ , with  $l_o$  decided
13. Enter A to determine  $P_o$ , checking against true value
14. Sketch  $P_o - Q_c$
15. Using A from Step 2, find  $P_{c1}$  and  $P_{c3}$  using  $Q_{c1}$  and  $3Q_{c1}$  as entries:
16. Check that  $P_{c1} > P_{off}$ , otherwise two amplifiers cannot be cascaded



17. Enter  $P_o - Q_c$  sketch with  $P_{c3}$ , find  $Q_{03}$ , truncate  $Q_{03}/3Q_{c1}$ , to nearest integer, the fanout.

If  $P_o$  is specified instead of  $P_s$ , then with  $G$ ,  $l$ ,  $d_c$  and  $d_s$ :

1. Enter figure (22), with a guess for  $P_o/P_s$
2. Find  $Re/KGL$ , compute  $Re/KL$
3. Enter figure (19), and guessing  $K$  iterate within the figure to find  $Re/L$  and  $K$  satisfying step 2.
4. Enter figure (21) with  $Re/KG$ , find  $P_o/P_{CL}$
5. Compute  $P_{CL}$
6. Enter figure (20), find  $P_{CL}/P_s$ , then  $P_s$
7. Calculate  $Q_s$  from  $Re$
8. Check on figure (11) that  $G < G_{max}$
9. Continue to determine other parameters as before

If, in any of these procedures, the original design objectives are not met, experience is the best indicator of what variables to alter. The most convenient variable to change is  $P_s$  because although it changes output pressure level, it does not alter  $Q_{c1}$  or  $Q_{c2}$ .  $P_{off}$  increases slightly with increasing supply pressure but this does not necessarily decrease fanout because the  $P_o - Q_s$  curve is also shifted. Frequently, but not for all geometries, there is a best supply pressure for maximizing fanout. Drazan [10] presents a method of choosing control geometry to maximize fanout by impedance matching, but it is predicated on the assumption, not proven, that maximum control power will give best switching.

#### A Design Example

GIVEN:

$$\begin{aligned} d &= 0.0476 \text{ in} \\ d_o &= 0.0476 \text{ in} \\ d_c &= 0.0205 \text{ in} \\ G &= 30 \\ L &= 75 \\ L_o &= 25 \end{aligned}$$

FIND THE CHARACTERISTICS.  $L_c$  would normally be included, but the  $P_c - Q_c$  curve is omitted from this example because the experimental apparatus used [4] demanded  $L_c > 100$  and this is not representative.

With increments of  $Q_s$ , Table 4 is easily calculated, and the  $P_o - Q_s$  curves are plotted in Figure 33.

Table 4

$Q_s$	Re	Re/L	$\lambda_o$	K	$P_{cl}$	$\frac{P_{CL}}{P_s}$	$P_s$	$\frac{Re}{KG}$	$\frac{P_o}{P_{cl}}$	$P_o$
400	490	6.5	2.00	15.95	0.325	0.32	1.01	0.88	0.21	0.07
600	735	9.8	2.00	15.90	0.731	0.44	1.66	1.32	0.31	0.23
800	980	13.0	1.99	15.85	1.287	0.53	2.43	1.76	0.40	0.52
1000	1225	16.3	1.99	15.80	2.011	0.61	3.30	2.21	0.47	0.95
1200	1470	19.6	1.97	15.79	2.838	0.66	4.30	2.66	0.53	1.49
1400	1715	22.9	1.96	15.70	3.824	0.72	5.31	3.12	0.57	2.18
1600	1960	26.1	1.94	15.60	4.894	0.76	6.44	3.59	0.62	3.01
1800	2200	29.3	1.92	15.50	6.066	0.79	7.68	4.00	0.64	3.88
2000	2450	32.6	1.90	15.40	7.334	0.81	9.05	4.50	0.67	----

For  $G = 30$ :  $Re(max) = 2250$ ,  $Q_s(max) = 1835$  cc/min

The solid points shown are data taken for this geometry. If a supply pressure,  $P_s$  is chosen,  $P_o$  and  $Q_s$  are immediately established. In Figure 33,  $P_s = 5$  ins.  $H_2O$ , so that  $Q_s = 1350$  cc/min and  $P_o = 2$  ins.  $H_2O$ .  $Q_o(Max)$  is not calculated by trial and error:

	<u>Try 1</u>	<u>Try 2</u>	<u>Try 3</u>
Guess $Q_o(max)$	= 1100 cc/min	1000 cc/min	1050
Then Re	= 1350	1225	
Re/ $L_o$	= 54, $\lambda_o = 1.77$	49, $\lambda_o = 1.80$	
$P_{CL}$	= 1.92	1.63	
$P_s/P_{CL}$	= 0.88	0.875	
$P_s$	= 2.18 ins. $H_2O$	1.86 ins. $H_2O$	2.0
Result	too high	too low	OK

$Q_{cl}$  is determined from Figure 32:  $Q_{cl} = 35$  cc/min  
 $Q_{c2} = 46.7$  and  $Q_{c3} = 105$  cc/min

$Q_o = 1350 \text{ cc/min}; Re/L = 22, \lambda_o \text{ (Fig. 19)} = 1.96$

$P_{CL} = 3.56$  and since  $G^2 = 900$ ;

$P_o(\text{TURB}) = P_{off} = .0552.$

The  $P_o - Q_c$  curve is constructed from this data using Figure 26 as a guide.

#### Dynamics of the Turbulence Amplifier

The relative uncertainty of turbulence amplifier dynamics has long been its principal weakness. "The unequal, erratic and relatively slow dynamic switching response characteristic of particular turbulence amplifier geometries frequently offsets their advantages of low power consumption, input feedback isolation load impedance matching capabilities and high power gain in digital control system implementation" [41]. Their relative slowness arises because of the low jet velocities required for laminar operation (by Reynolds number limitations), so that the only cure is in decreasing size. It has long been known that turbulence amplifier "switch on" times are much longer than "switch off" times, and it is the relatively erratic "switch on" time that creates major problems in parallel coupled switching circuits.

Although almost every researcher of T/A characteristics has measured response time and noted the discrepancy between ON and OFF times, only two careful experimental studies of T/A dynamics have been found in current literature. These two are independent of each other [41,42] and form the basis for the following discussion.

Abramovich and Solan [42] conducted a careful study in both liquids and air of the dynamics of the centerline velocity of laminar jets whose sources were suddenly switched on or off. They identified two characteristic times for each case; a pure delay followed by a rise or decay time of velocity in the jet. Their entire presentation is in the form of empirical equations based on three non-dimensional variables as follows:

A non-dimensional velocity,

$$U^* = \frac{Ud}{2\nu Re} \quad (32)$$

A non-dimensional distance,

$$X^* = \frac{X}{D\sqrt{Re}} \quad (33)$$

These were empirically related for steady unshrouded round jets,  $200 < Re < 500$ , for the centerline velocity in the jet as:

$$U_{CL}^*(x) \sim \frac{1}{ax^* + b} \quad (34)$$

$a = 1.13$ ,  $b = 0.89$ . From this relationship, a non-dimensional time is obtained.

$$t = \int \frac{dx}{U} = \frac{D^2}{2\nu\sqrt{Re}} \left\{ \frac{ax^{*2}}{2} + bx^* \right\}$$

or

$$t^* = \frac{2\nu\sqrt{Re}}{D^2} \quad t = \left\{ \frac{ax^{*2}}{2} + bx^* \right\} \quad (35)$$

which is the time required for a fluid particle to traverse the jet.

It is instructive to consider the relationship between the theory presented earlier in this paper and equation 34. For a parabolic emitter profile  $U_{CL}(0) = 2U_{AVE}$  so that  $Re = U_{CL} d/2\nu$ . Thus,  $U_{CL}^*(x)$  from equation 32 is

$$U_{CL}^*(x) = \frac{U_{CL}(x)d}{2\nu Re} = \frac{U_{CL}(x)}{U_{CL}(0)} \quad (36)$$

and, from 32, 33, 34 and 36

$$U_{CL}(x) = \frac{2\nu Re}{d} \frac{d\sqrt{Re}}{ax + bd\sqrt{Re}}. \quad (37)$$

Recall equation 11. For both 11 and 37 to be true,

$$\frac{Re^2 \nu}{8(x + x_0)} = \frac{2\nu Re^2}{ax\sqrt{Re} + b Re d}$$

from which, substituting for  $x_0 = Re d/18$ ,

$$\begin{array}{cc} 16x + .89 Re d = 1.13\sqrt{Re} x + .89 Re d & (38) \\ \text{(THEORY)} & \text{(ABRAMOVICH \& SOLAN)} \end{array}$$

This is true only at  $Re = 200$ , the lower limit of these experiments.

The dynamic results presented in reference [42] can be summarized as follows. The switch ON time for a step change in the source of a jet was so erratic that the rise times of the jet velocity could not be accurately determined. The two times for which good correlations were found were the delay time,  $t_D$  and the time to 70% of the full ON pressure  $t_{70\%}$ . Three values of each are given: minimum, mean and maximum all of the same form:

	c	d	e	f	
$t_d^* = cx^{*2} + dx^*$	minimum 1.17	1.13	1.4	1.3	
	mean 1.58	1.48	1.85	1.6	(39)
$t_{70\%}^* = ex^{*2} + fx^*$	maximum 1.67	2	2.4	1.95	

The switch OFF time can be characterized as the sum of a delay and a first order lag.

$$t_D^* = .764x^* + .6x^{*2} \quad (40)$$

$$\tau^* = 1.2x^* + .6x^{*2}$$

For  $t^* < t_D^*$ , the jet velocity is given by equation 34. After  $t_D^*$  has passed,

$$U_{CL}^*(x) = \frac{1}{1.13x^* + .89} \exp \frac{-t^*}{1.2x^* + .6x^{*2}} \quad (41)$$

#### Switching Time Calculations

To calculate the time to switch a T/A OFF, the times for two jet events must be considered. First the control jet must come ON and propagate to the main jet. Unless the control setback,  $b$ , is very small, this is given by equation 39. Second, the main jet must turn OFF and decay at the receiver, as determined by equation 40. The rate of change of output pressure,  $P_O/P_{CL}$  can be computed from equation 41 squared for a blocked load and with only a knowledge of the load and output impedance of the amplifier otherwise. To calculate switch ON time, the time for control jet fadeout must be added to the time for re-establishment of main jet flow. Again, the control dynamics are likely to be negligible and equation 39 will probably determine the range of turn ON times to sufficient accuracy.

These results for ON time are for unshrouded amplifier, it should be recalled. Clearly, a shroud will interact with the dynamics of the jet by helping to hold it off. Hayes [41] has shown in a series of experiments in air, that shroud diameter has little effect on switch OFF times but has very significant effects on switch ON dynamics. The delay time increases with decreasing shroud size except for uselessly short gaps, but the velocity buildup dynamics decreases with shroud size. The erratic behavior of T/A's during turn ON can be reduced only by shortening the gap, although its spread decreases with decreasing cavity dimensions. There are still insufficient data, however, to draw firm conclusions on shrouded amplifier performance, and the rather large number of variables makes it doubtful that empirical designs can be entirely replaced by theory.

### Suggested Avenues of Future Research

First and foremost among the requirements for pencil and paper design of T/A's is an analytical understanding or at least a normalized empirical characterization of the effects of shrouding and vent geometry on T/A performance. The rather large number of variables makes this task seem forbidding at present.

Next, the planar geometries must be characterized more completely along the lines presented in this paper so that planar design procedures can evolve.

Finally, work on integrated design must progress. The problem a designer of T/A's faces is to optimize the figures of merit of an amplifier within a specified performance range of supply pressure, size, required output pressure for interface device operation and speed of response. Clearly, not all of the figures of merit may be simultaneously required by a given element and there is a natural tendency on the part of T/A logic circuit designers to standardize, to design one element that suits all of the requirements of a given circuit. From one point of view, this is like designing a computer from standard logic gates, but from another viewpoint worth considering, it is like designing a complex circuit using only one transistor type. There is a sensible compromise: to design logic modules analogous to integrated circuits to be used as building blocks, but within these to design the individual T/A's to best meet the circuit requirements of their modules. This will inevitably require some standardization of supply pressures, and selection of output ON and OFF levels guaranteed to interface any block to any other. This is not a new concept, certainly, and in fact Siwoff et al. [43] in the fifth Cranfield Conference presented designs of turbulence amplifier logic blocks intended for more general purpose use than as individual elements. Not all inputs or outputs are externally available to the user but are internally connected. The large electronic logic companies now manufacture an incredible variety of large scale integrated circuits; how did they decide what packages to offer? The answer is in standardization of supply and logic levels and in grouping by common functions like counters, memory, shift registers, gate arrays (two, four and eight in a package) and external drivers. Turbulence amplifiers, and particularly planar T/A's are very well suited to integration because they are building blocks from which all other logic functions can be synthesized and because they are easily and reliably interconnected. This must be the direction of the future.

## References

1. R.N. Auger, "Turbulence Amplifier Design and Application," Proc. Fluid Ampl. Symp., Vol. 1, p. 357, Harry Diamond Labs, Washington, D.C., Oct. 1962.
2. R.N. Auger, "A New "Solid State" Pneumatic Amplifier for Logic Systems," Automatic Control, Dec. 1962, p. 28.
3. A. Villu, "An Experimental Determination of the Minimum Reynolds Number for Instability in a Free Jet," J. Appl. Mech., Vol. 29, Trans. ASME, Series E, Vol. 84, Sept. 62, pp. 506-508.
4. A.C. Bell, "An Analytical and Experimental Investigation of the Turbulence Amplifier," ScD Thesis, Mechanical Engineering Dept. M.I.T., 1969.
5. E. Bendor, "The Performance of Fluidic Flow Mode Amplifiers," Fluidics Quarterly, Vol. 4, No. 3, p. 13, 1972.
6. R.N. Auger, "The Turbulence Amplifier After Four Production Years," Fluidics, Fluid Amplifier Associates, Boston, Mass., 1965.
7. R.N. Auger, "How to Use Turbulence Amplifiers for Control Logic," Control Eng., June 1964, p. 89.
8. R.N. Auger, "The Turbulence Amplifier in Control Systems," Proc. Fluid Ampl. Symp., Vol. 2, p. 361, Harry Diamond Labs, Washington, D.C., May 1964.
9. E.E. Metzger and C.G. Lomas, "Turbulence Amplifier for Integrated Two Dimensional Fabrication," Proc. Fluid Ampl. Symp. Vol. 2, p. 363, Harry Diamond Labs, Washington, D.C., Oct., 1965.
10. R.A. Oels, R.F. Boucher and E. Markland, "Experiments on Turbulence Amplifiers," Proc. 1st Int. Conf. on Fluid Logic and Ampl. D3-33, BHRA Cranfield, England, Jan. 1967.
11. R. McIlhagger and E. Markland, "Experiments on Turbulence Amplifiers," Fluidics Quarterly, Vol. 4, No. 1, p. 74, 1972.
12. H.A.M. Verhelst, "On the Design, Characteristics and Construction of Turbulence Amplifiers," Proc. 2nd Int. Conf. on Fluid Logic and Ampl., F2-9, BHRA, Cranfield, England, Jan. 1967.
13. P. Drazan, "Optimal Design of the Control Jet of a Fluid Amplifier," Proc. 2nd Int. Conf. on Fluid Logic and Ampl., BHRA, Cranfield, England, Jan. 1967.
14. A.C. Bell, "An Analytical and Empirical Basis for the Design of Turbulence Amplifiers, Part I, Analysis and Experimental Confirmation," J. Dyn. Sys., Meas. and Cont., ASME Trans. Series G., Vol. 95, No. 2, p. 133-140.

15. A.C. Bell, "An Analytical and Empirical Basis for the Design of Turbulence Amplifiers Part II, Empirical Relationships and Design Procedure," J. Dyn. Sys., Meas. and Contr., ASME Trans., Series G., Vol. 95, No. 2, p. 141-147.
16. H. Schlichting, Boundary Layer Theory, McGraw-Hill, New York, 1955.
17. W. Bickley, "The Plane Jet," Philosophical Magazine, Vol. 7, 1937, p. 156.
18. E.N. da C. Andrade and L.C. Tsien, "The Velocity Distribution in a Liquid-into-Liquid Jet," Proc. Phys. Soc., Vol. 49, 1937, p. 381-391.
19. E.K. Beatty and E. Markland, "Feasibility Study of Laminar Jet Deflection Fluidic Elements," 3rd Cranfield Fluidics Con , H1-1, BHRA, Cranfield, England, 1968.
20. H.W. Chang, "An Analytical and Experimental Investigation of a Large Scale Turbulence Amplifier, M.S. Thesis, Dept. of Mech. Eng., SUNY at Buffalo, 1972.
21. H. Sato, "Stability and Transition of a Two Dimensional Jet," J. Fl. Mech., Vol. 7, Pt. 1, pp. 53-80.
22. A.J. Reynolds, "Observations of a Liquid into Liquid Jet," J. Fl. Mech., Vol. 4, Pt. 4, pp. 552-556, 1962.
23. K.J. McNaughton and C.G. Sinclair, "Submerged Jets in Short Cylindrical Flow Vessels," J. Fl. Mech., Vol. 25, Pt. 2, pp. 367-376, 1966.
24. R.F. Osborn, "A Theoretical and Experimental Investigation of a Liquid Type Turbulence Amplifier," M.S. Thesis, Dept. of Mech. Eng. Oklahoma State Univ., 1965.
25. J.E. Snyder, "Laminar-Turbulent Transition of Submerged Liquid Jets," B.S. Thesis, Dept. of Mech. Eng., M.I.T., 1967.
26. G.F. Marsters, "Some Observations on the Transition to Turbulence in Small Unconfined Free Jets," Fluidics Quarterly, Vol. 3, No. 3, p. 20, 1971.
27. C.P. McKenzie and D.B. Wall, "Transition from Laminar to Turbulence in Submerged and Bounded Jets," Fluidics Quarterly, Vol. 1, No. 1, pp. 38-47, 1967.
28. N. Curle, Proc. Royal Soc., A, Vol. 238, p. 265, 1957.
29. R.C. Chanaud and A. Powell, "Experiments Concerning the Sound Sensitive Jet," J. Acous. Soc. Amer., Vol. 34, p. 907, 1962.
30. G.K. Batchelor and A.E. Gill, "Analysis of the Stability of Axisymmetric Jets," J. Fl. Mech., Vol. 14, Pt. 4, pp. 529-551, 1962.



31. A.K. Simson, "A Theoretical Study of the Design Parameters of Subsonic Pressure Controlled Fluid Jet Amplifiers," Ph.D. Thesis, Dept. of Mech. Eng., M.I.T., 1963.
32. L.A. Zalmonzon and A.I. Semikova, "Investigation of the Characteristics of Pneumatic Jet Elements," Automation and Remote Control, Vol. 20, No. 4, pp. 431-448, 1959.
33. R.J. Reilly and P.A. Moynihan, "Notes on Proportional Fluid Amplifier," Symp. on Fluid Jet Control Devices, ASME, 1961.
34. S.J. Peperone, S. Katz, and J.M. Goto, "Gain Analysis of the Proportional Fluid Amplifier," Proc. of the Fluid Ampl. Symp., Vol. I, Diamond Ordnance Fuse Labs, 1962.
35. K.N. Reid, "Static and Dynamic Interaction of a Fluid Jet and a Receiver Diffuser," ScD Thesis, Dept. of Mech. Eng., MIT, 1964.
36. T.J. Jansen and S. Winnikow, "Pressure Recovery Characteristics of a Laminar Axisymmetric Free Jet," Fluidics Quarterly, Vol. 3, No. 1, p. 16, 1971.
37. M.A. Boyd and A.R. Barbin, "Effects of Transverse Secondary Flow on the Laminar-Turbulent Transition of a Free Axisymmetric Jet," Advances in Fluidics, ed. F.T. Brown, ASME, 1967.
38. P. Drazen and K. Foster, "A Note on the Stability of a Bounded Laminar Jet," 4th Cranfield Fluidics Conf., Vol. 2, Pp. 4-41, BHRA, Cranfield England, 1970.
39. R.W. Hornbeck, "Laminar Flow in the Entrance Region of a Pipe," Applied Science Research Series A13, pp. 224-232, 1962.
40. L.S. Han, "Hydrodynamic Entrance Length for Incompressible Flow in Rectangular Ducts, J. Appl. Mech., ASME Trans., Series E, Vol. 27, p. 403, 1960.
41. W.F. Hayes, "The Dynamic Response of Fluidic Turbulent Amplifiers," Proc. of 4th Cranfield Conf., Vol. 1, A1-1 BHRA, Cranfield, England, 1970.
42. S. Abramovich and A. Seban, "Turn-ON and Turn-OFF Times for a Laminar Jet," J. Dyn. Sys., Meas., and Contr., ASME Trans., Series G, Vol. 95, No. 2, pp. 155-160, 1973.
43. F. Siwoff, N. Nikolov, G. Rashev, Tch. Christov and D. Dochev, "Fluidic Universal Logical Block for Machine Control," Proc. 5th Cranfield Conf. Vol. 2, F4-45, BHRA Cranfield, England, 1972.
44. T. Tatsume and T. Kakutani, "The Stability of a Two Dimensional Laminar Jet," Jour. Fluid Mech., Vol. 7, Part 1, pp. 53-80.

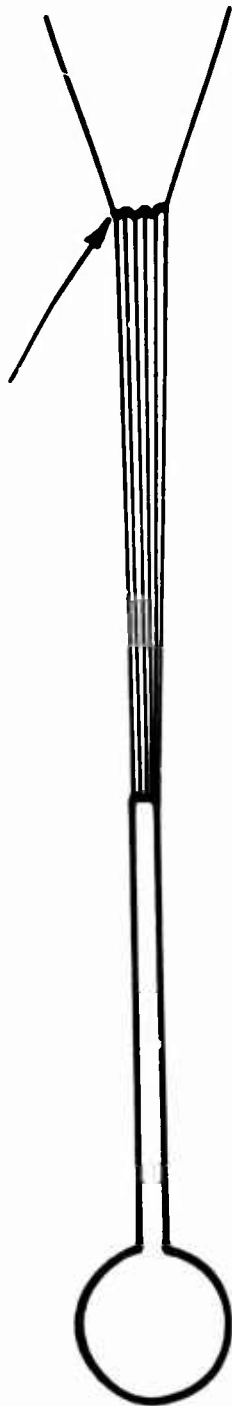


FIGURE 1 TRANSITION TO TURBULENCE

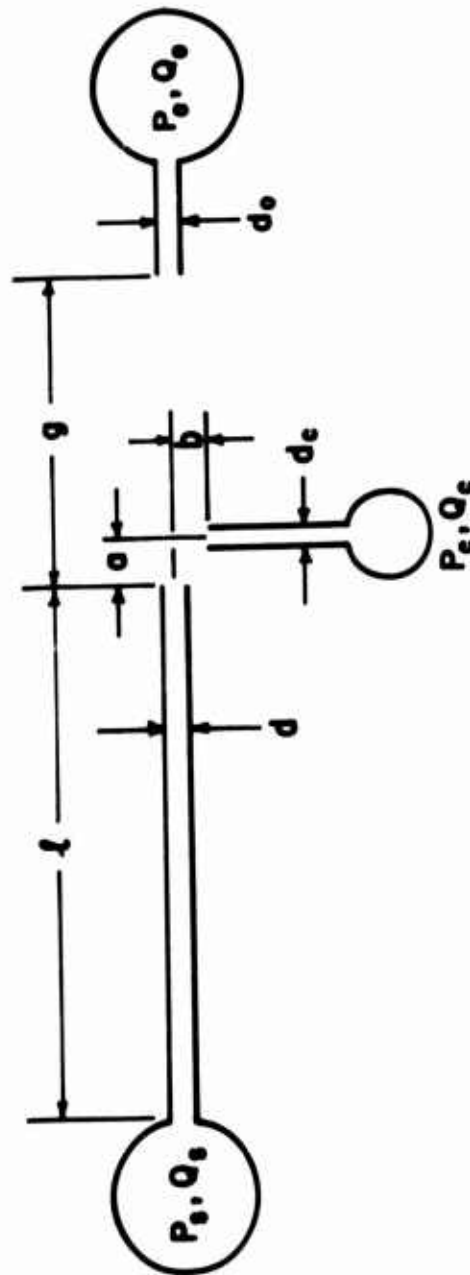
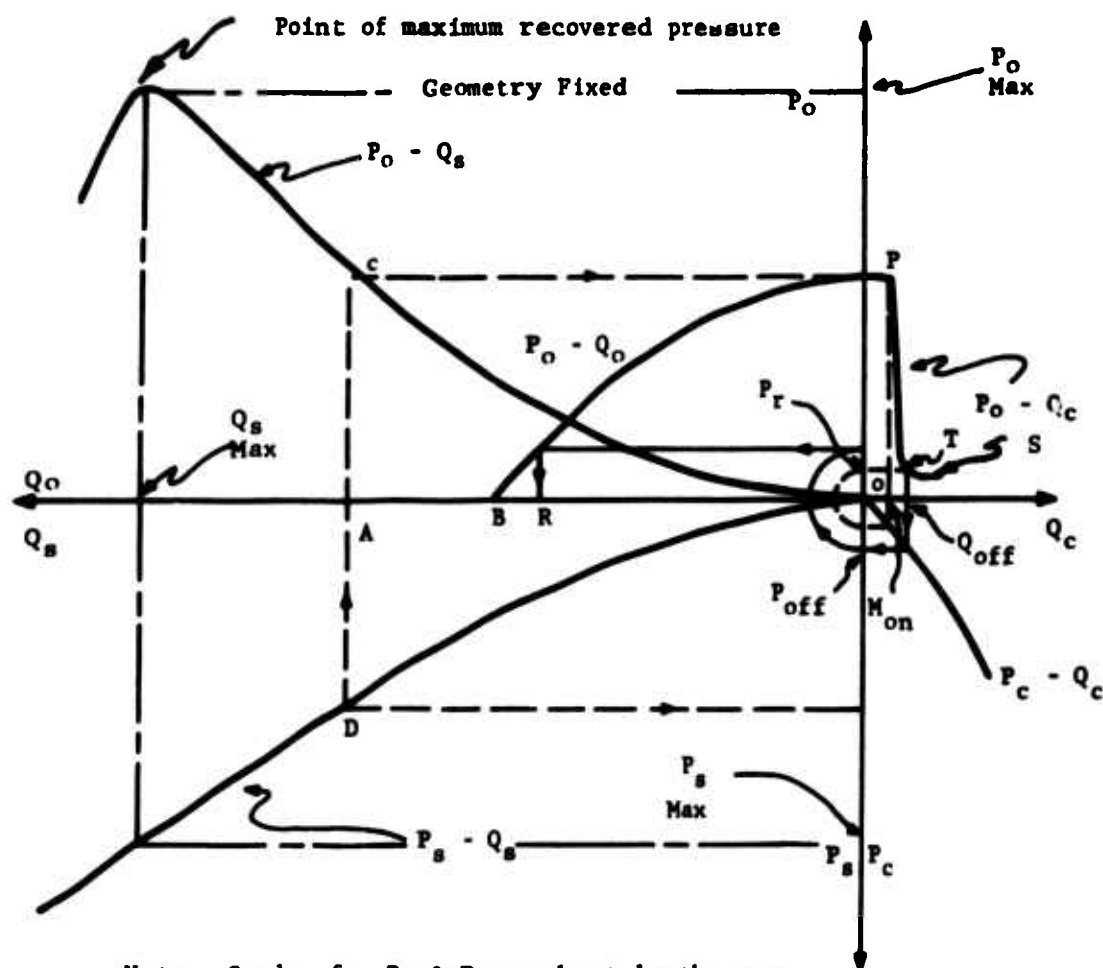


FIGURE 2 GEOMETRY AND NOMENCLATURE



Note: Scales for  $P_s$  &  $P_c$  need not be the same, but  $Q_0$  must match  $Q_s$  and  $P_c$  must match  $P_0$  scales.

FIGURE 3 VERHELST DIAGRAM

$$\frac{U}{U_0} = 1.0$$

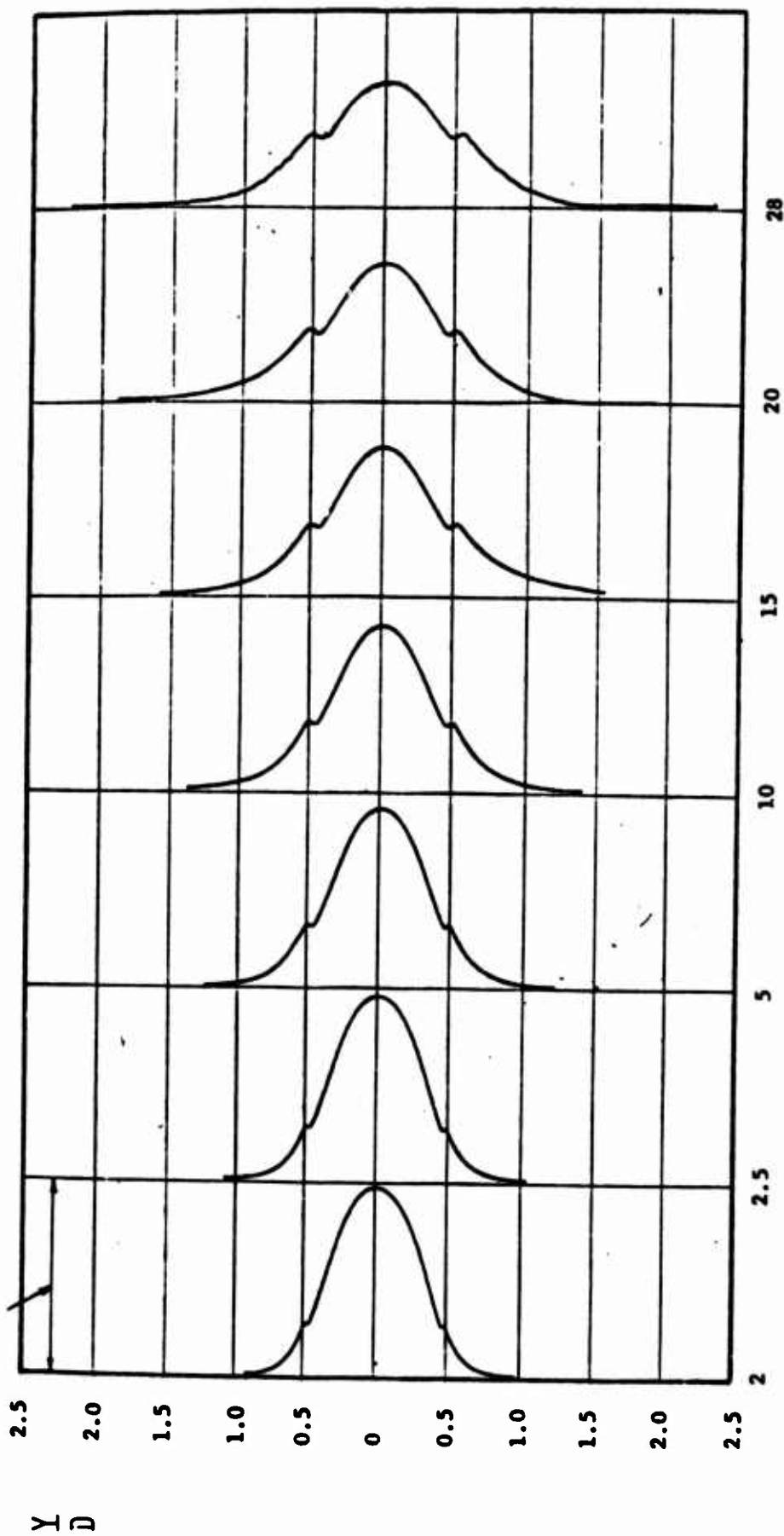


FIGURE 4 VELOCITY DISTRIBUTIONS IN THE UNDISTURBED JET

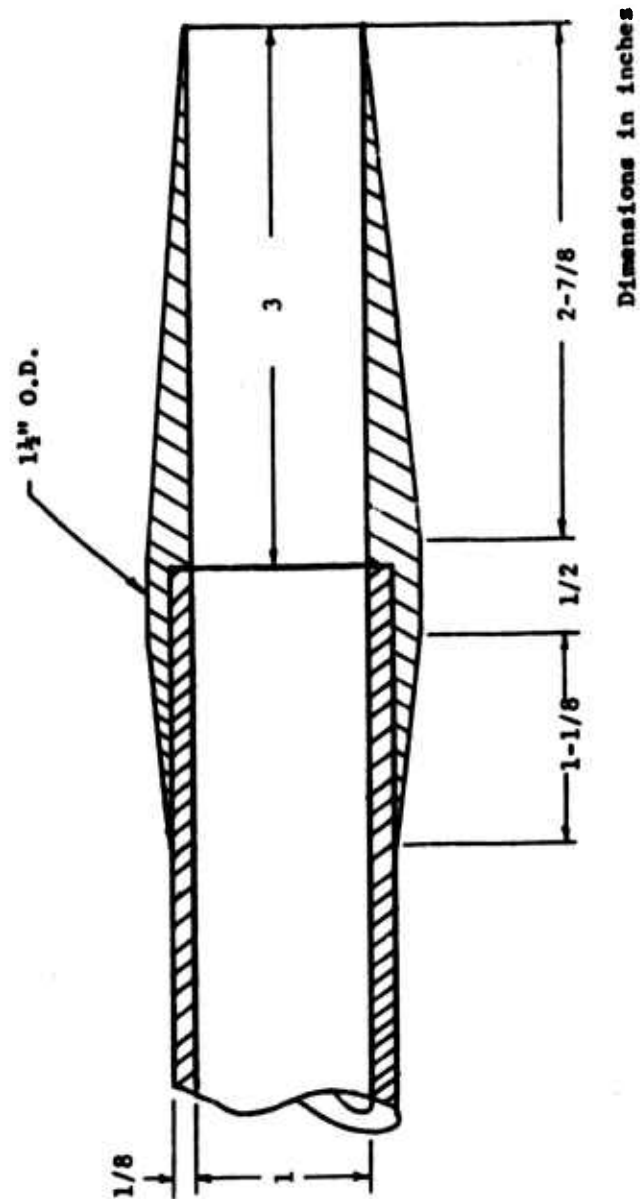


FIGURE 5 EMITTER TIP

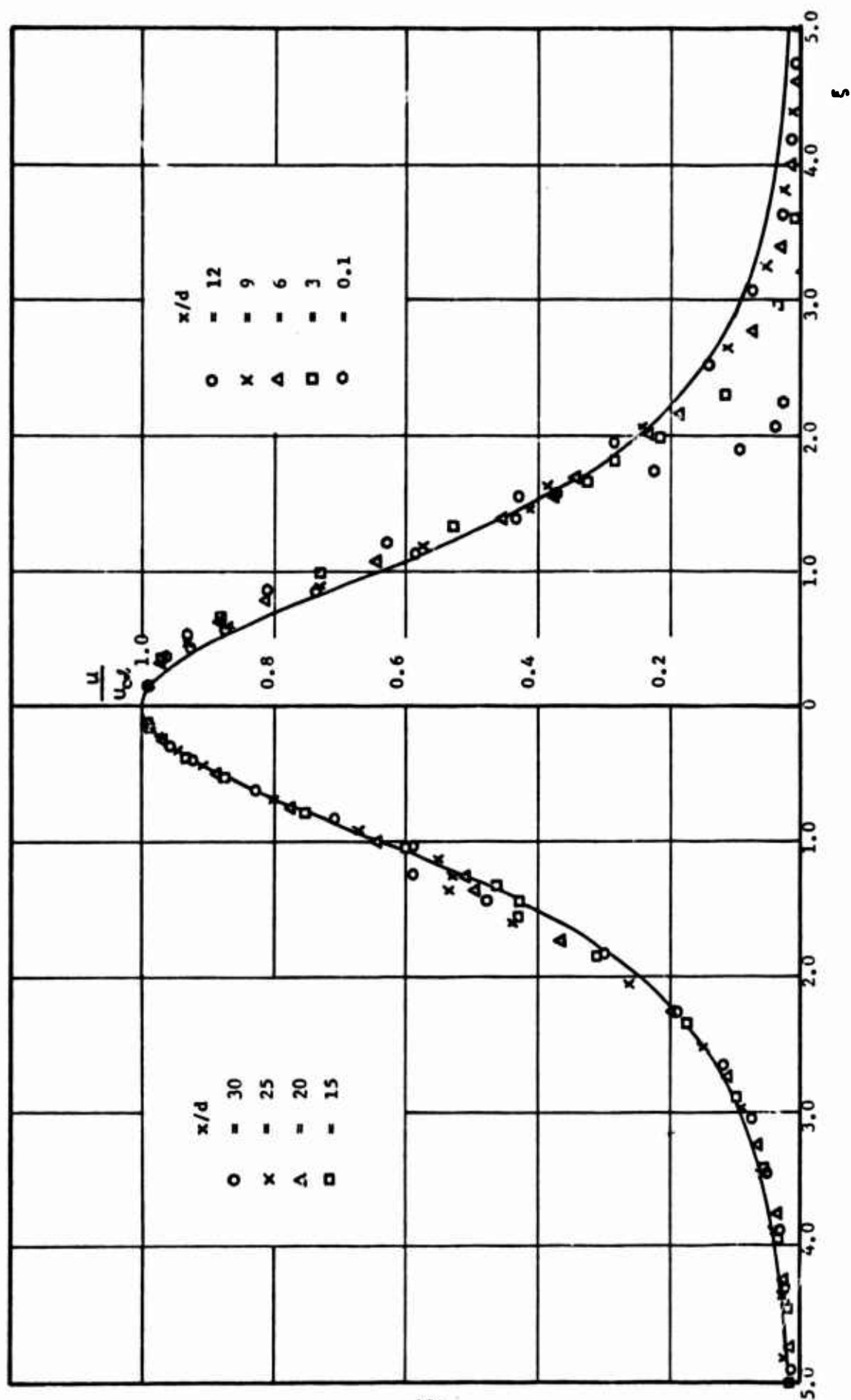


FIGURE 6 VELOCITY DISTRIBUTION IN AXISYMMETRIC LAMINAR JET,  $Re/L = 5.75$

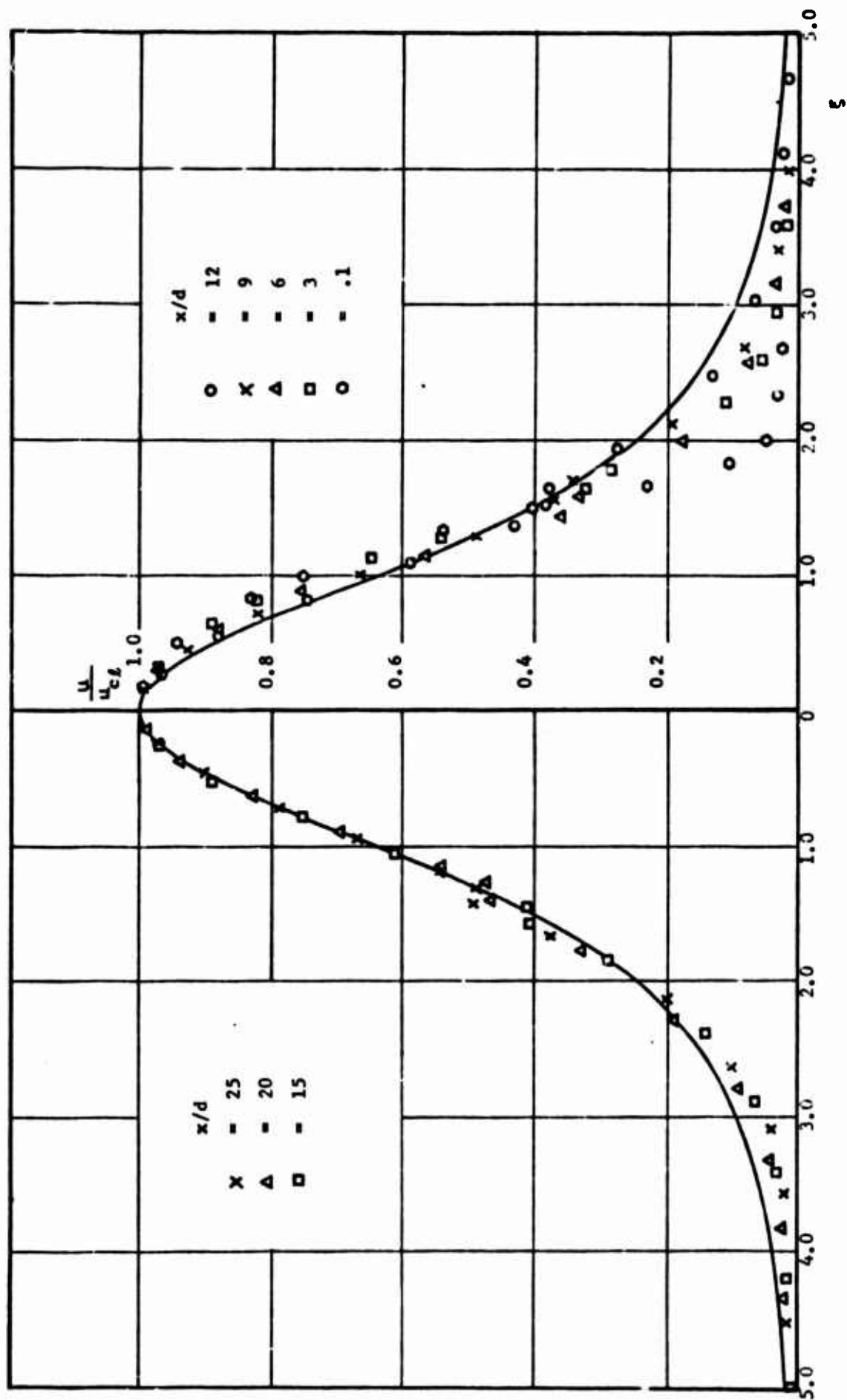


FIGURE 7 VELOCITY DISTRIBUTION IN AXISYMMETRIC LAMINAR JET,  
 $Re/L = 8.05$

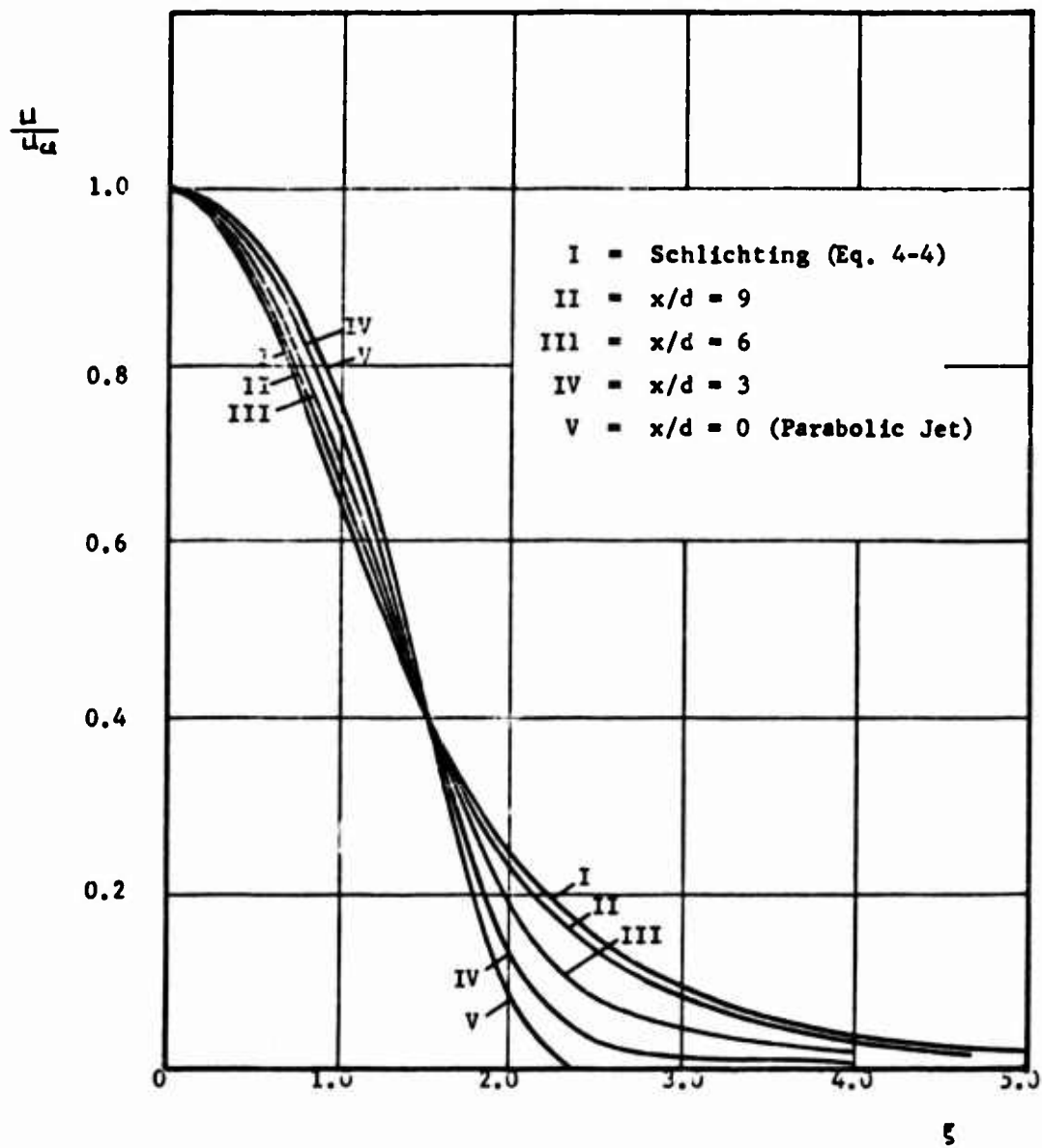


FIGURE 8 MODIFIED VELOCITY DISTRIBUTION  
IN THE ZONE OF FLOW DEVELOPMENT



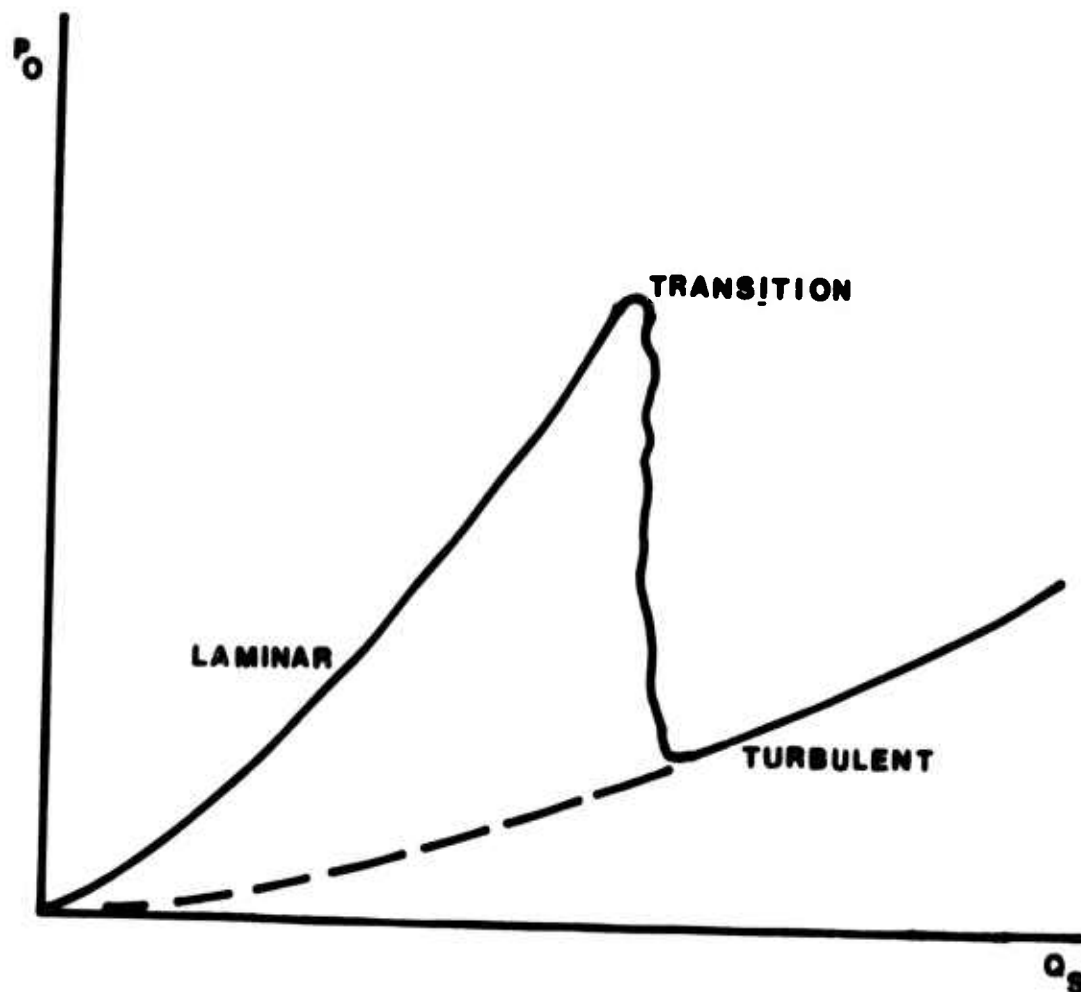


FIGURE 9 LAMINAR TO TURBULENT TRANSITION

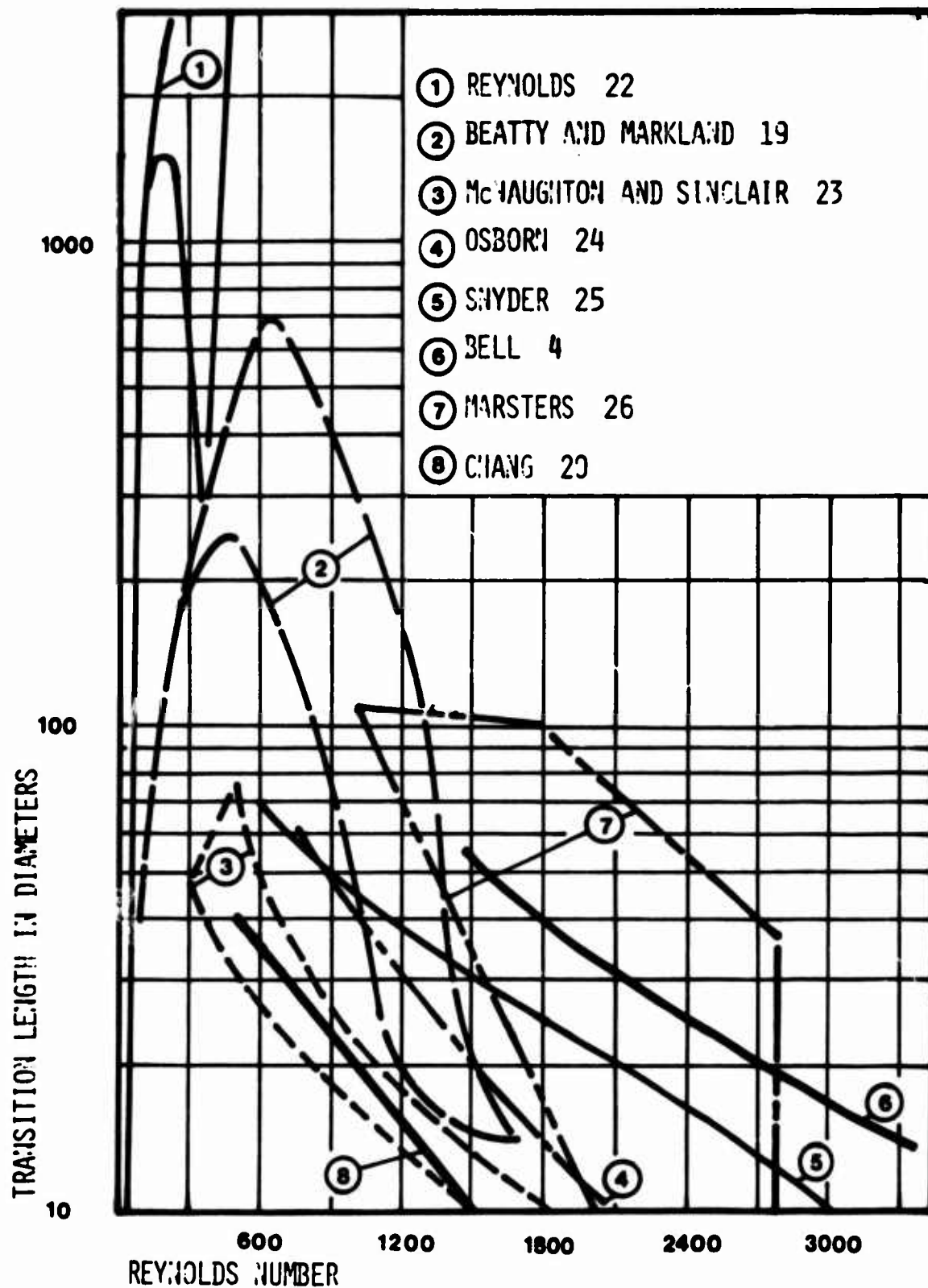


FIGURE 10 SUMMARY OF LAMINAR TO TURBULENT TRANSITION DATA

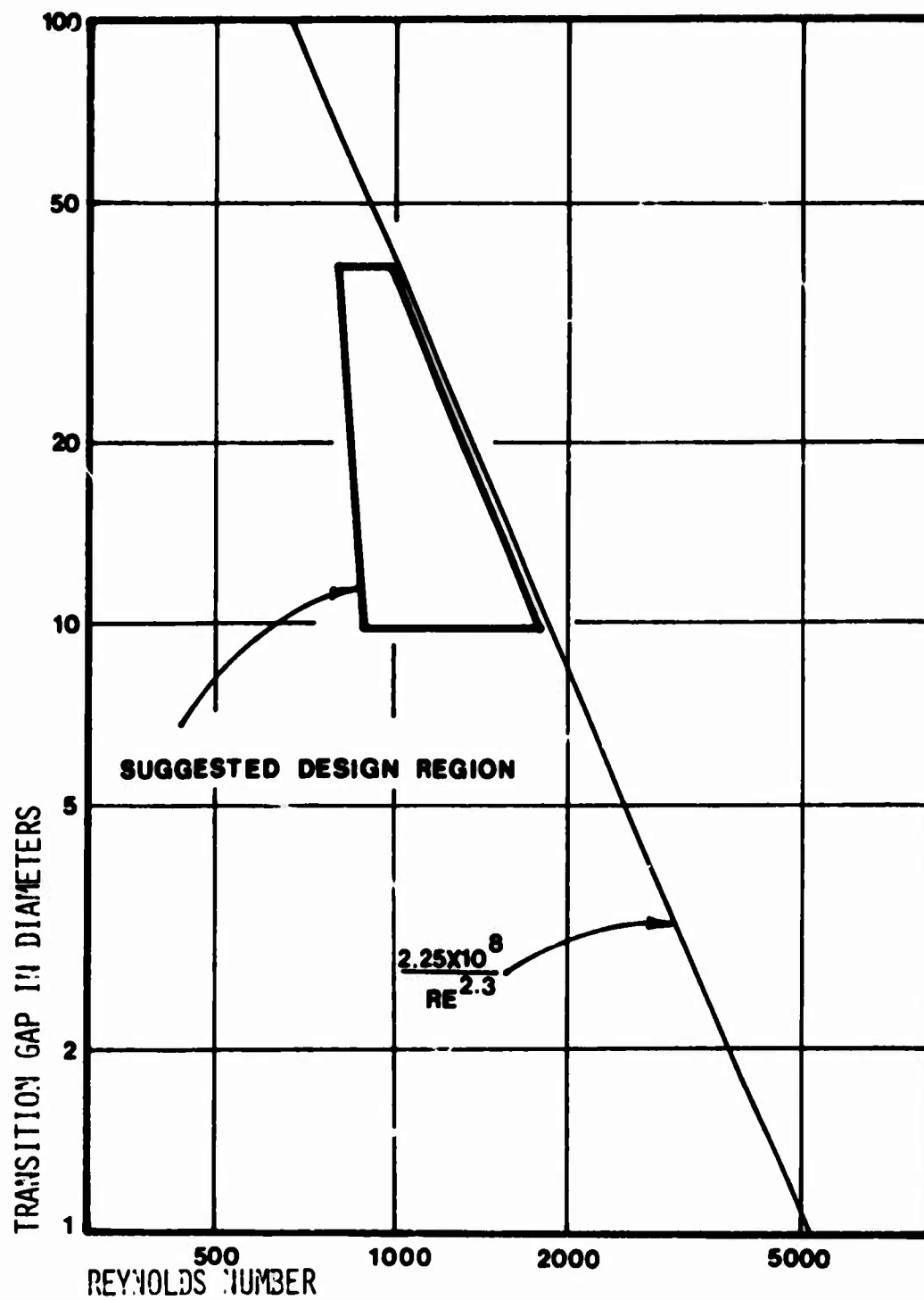
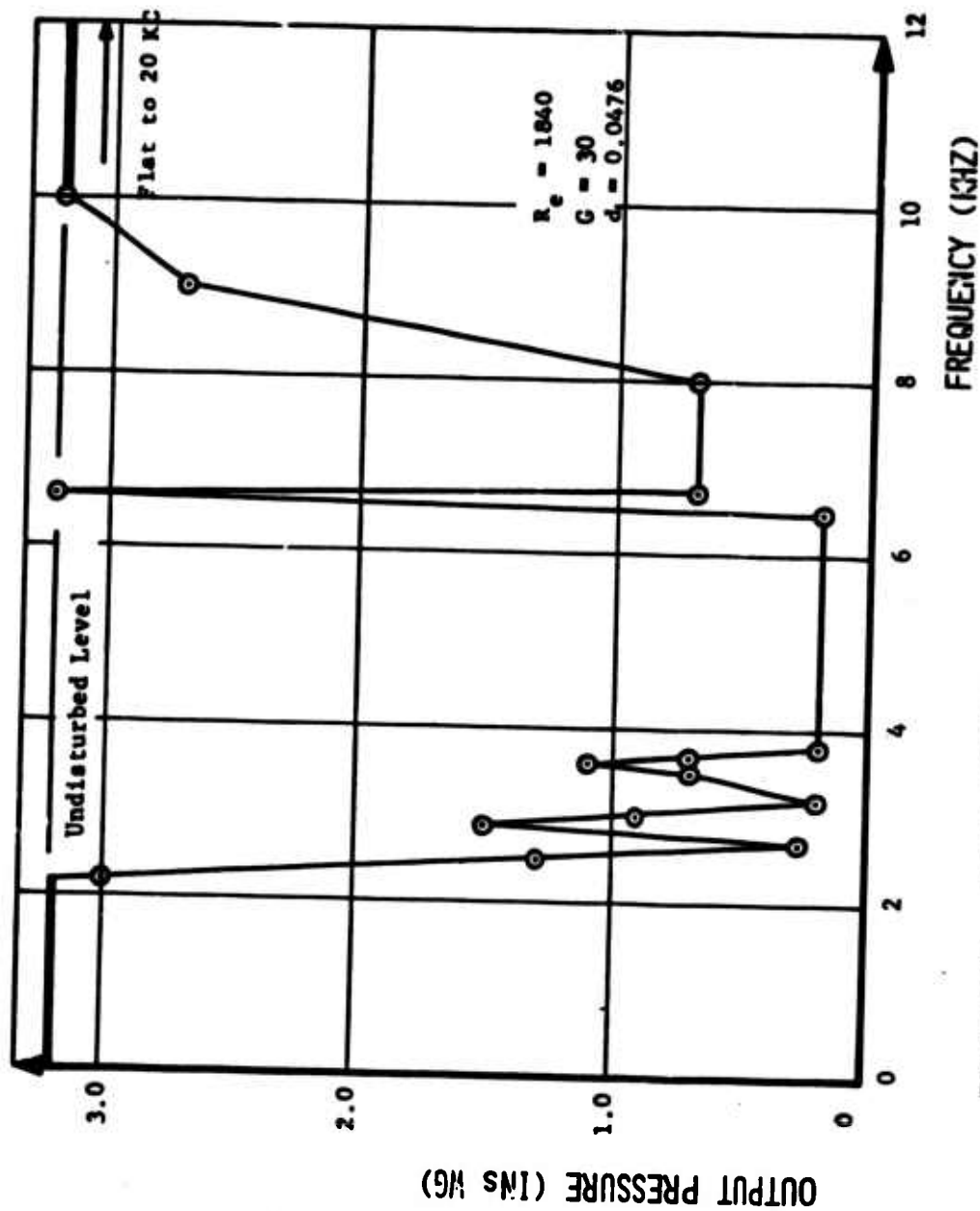


FIGURE 11 FREE TRANSITION LIMITS



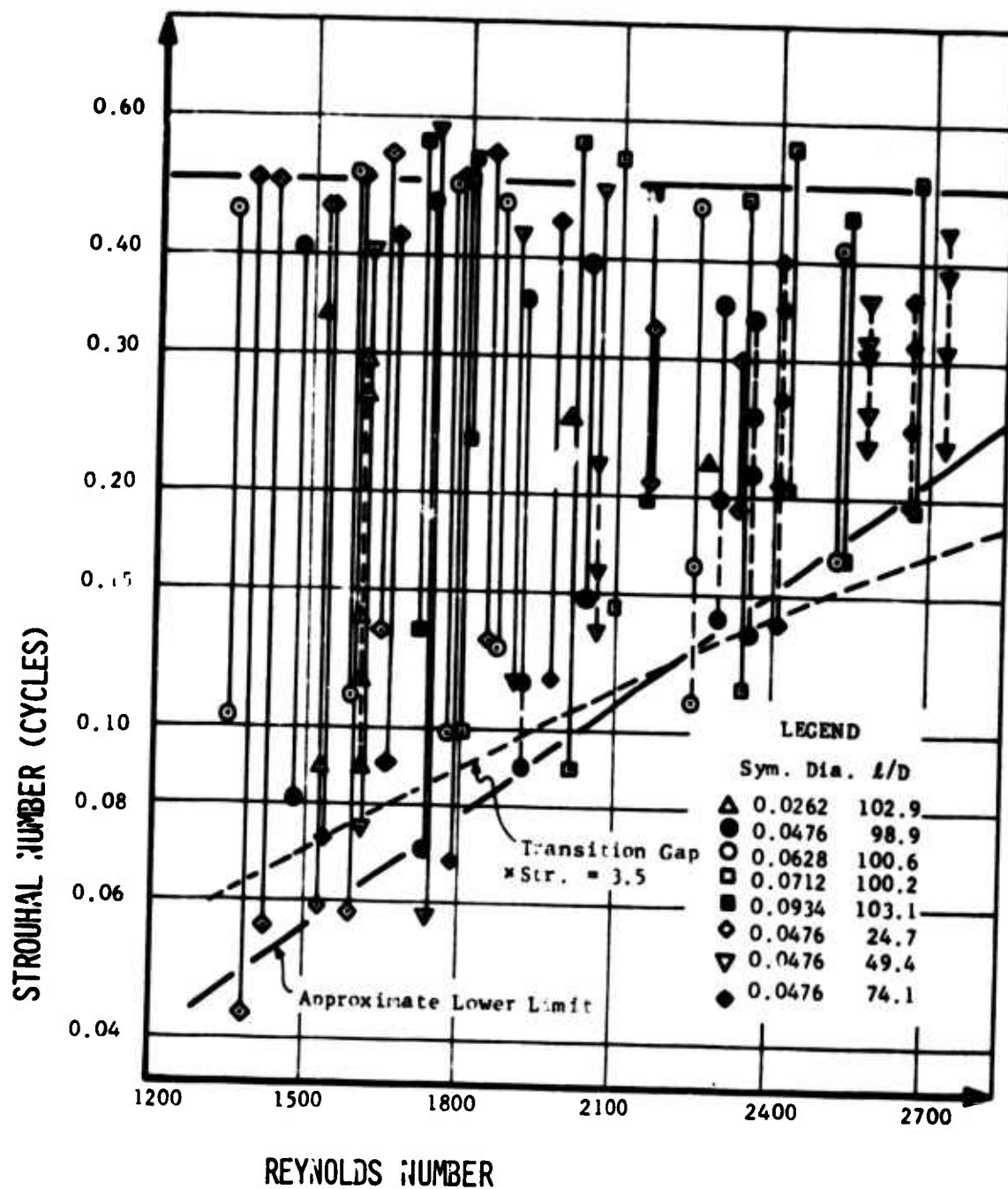


FIGURE 13 STROUHAL NUMBER FOR SOUND EXCITED JETS.  
OF VARYING REYNOLDS NUMBER AND GAPS

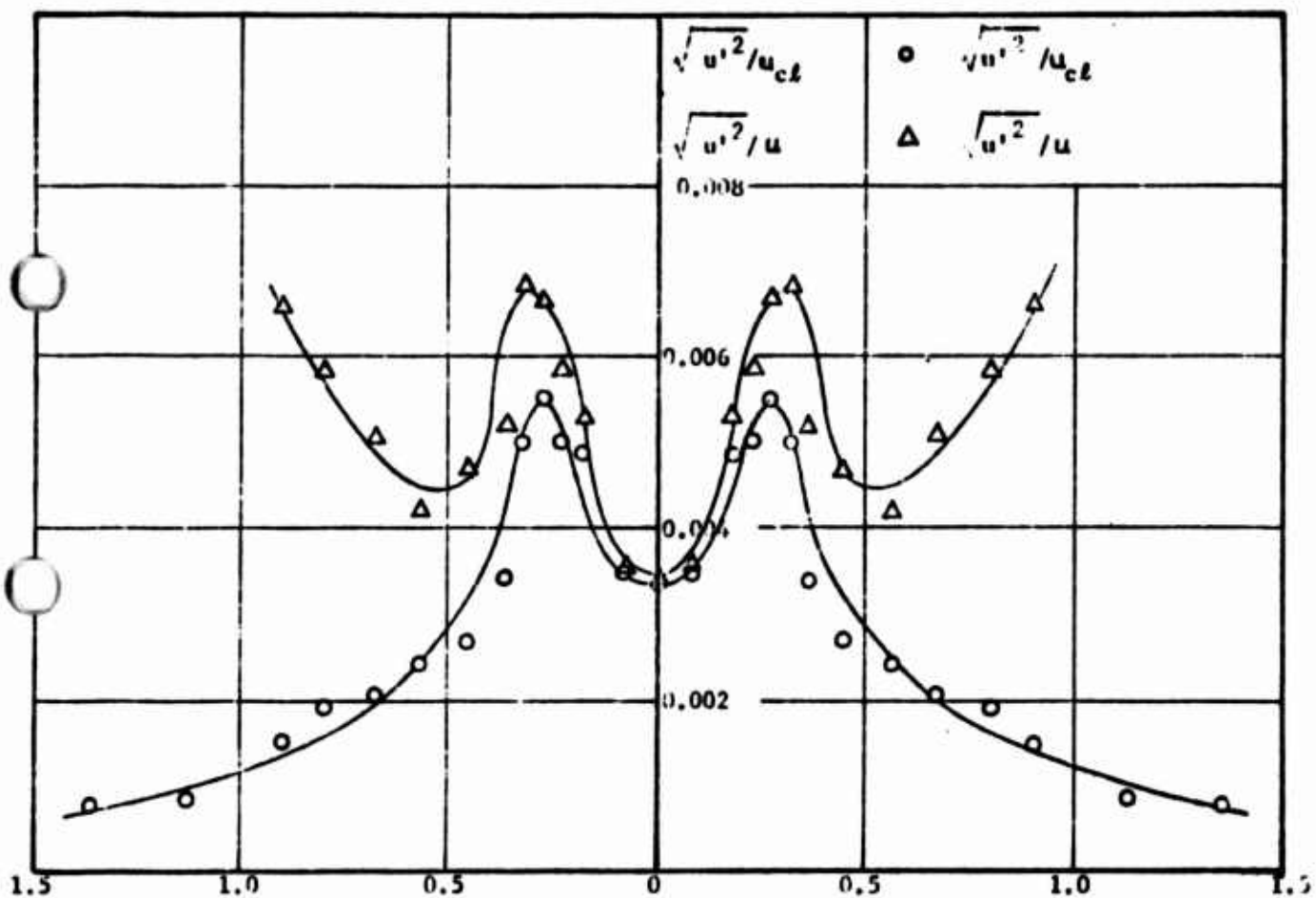


FIGURE 14 DISTRIBUTION OF INTENSITY OF U-FLUCTUATIONS,  
 $x/d = 25$ ,  $Re = 507.7$

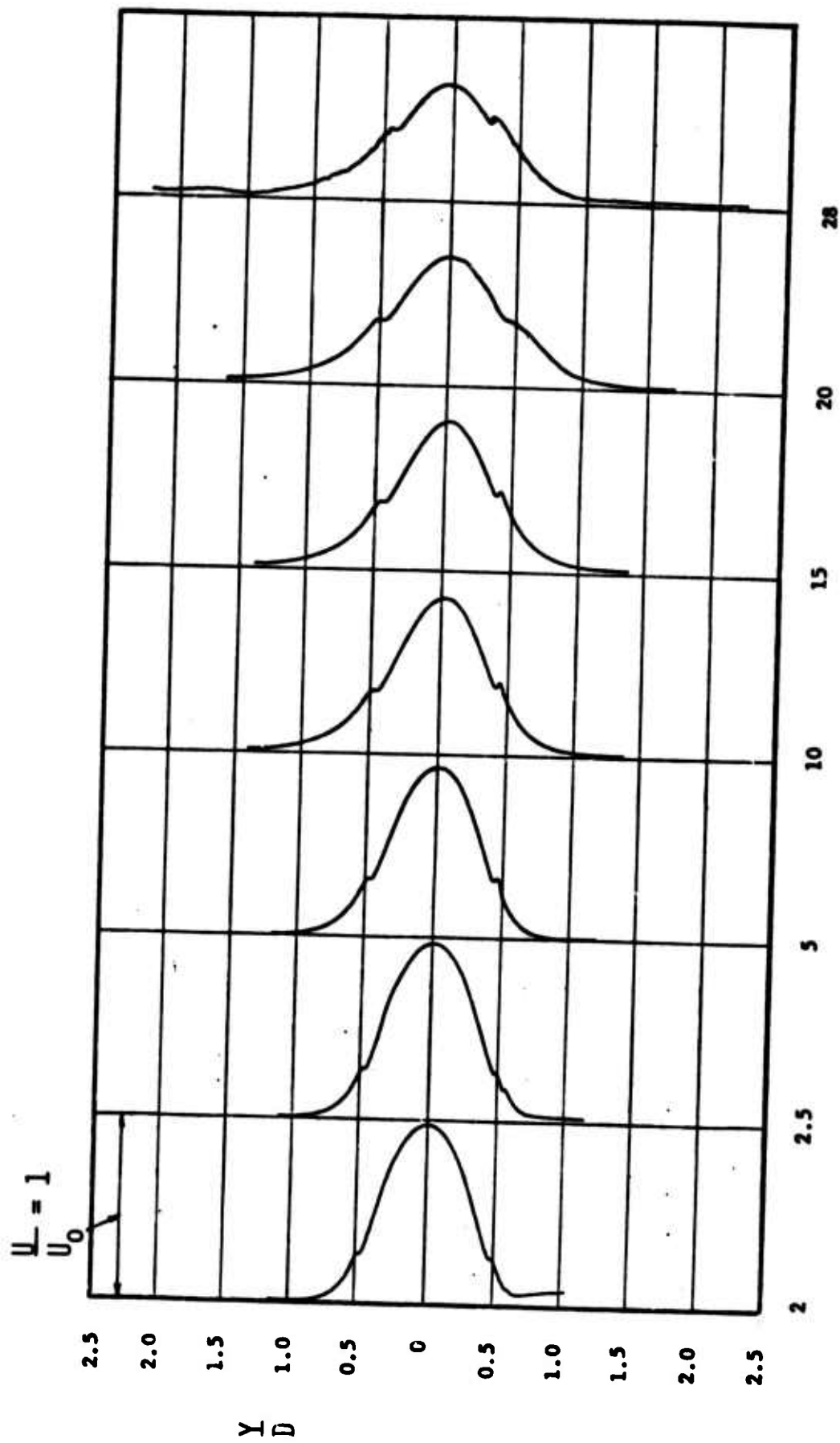


FIGURE 15 VELOCITY PROFILES WITH CONTROL FLOW,  $Q_c = 26 \text{ IN}^3/\text{MIN}$

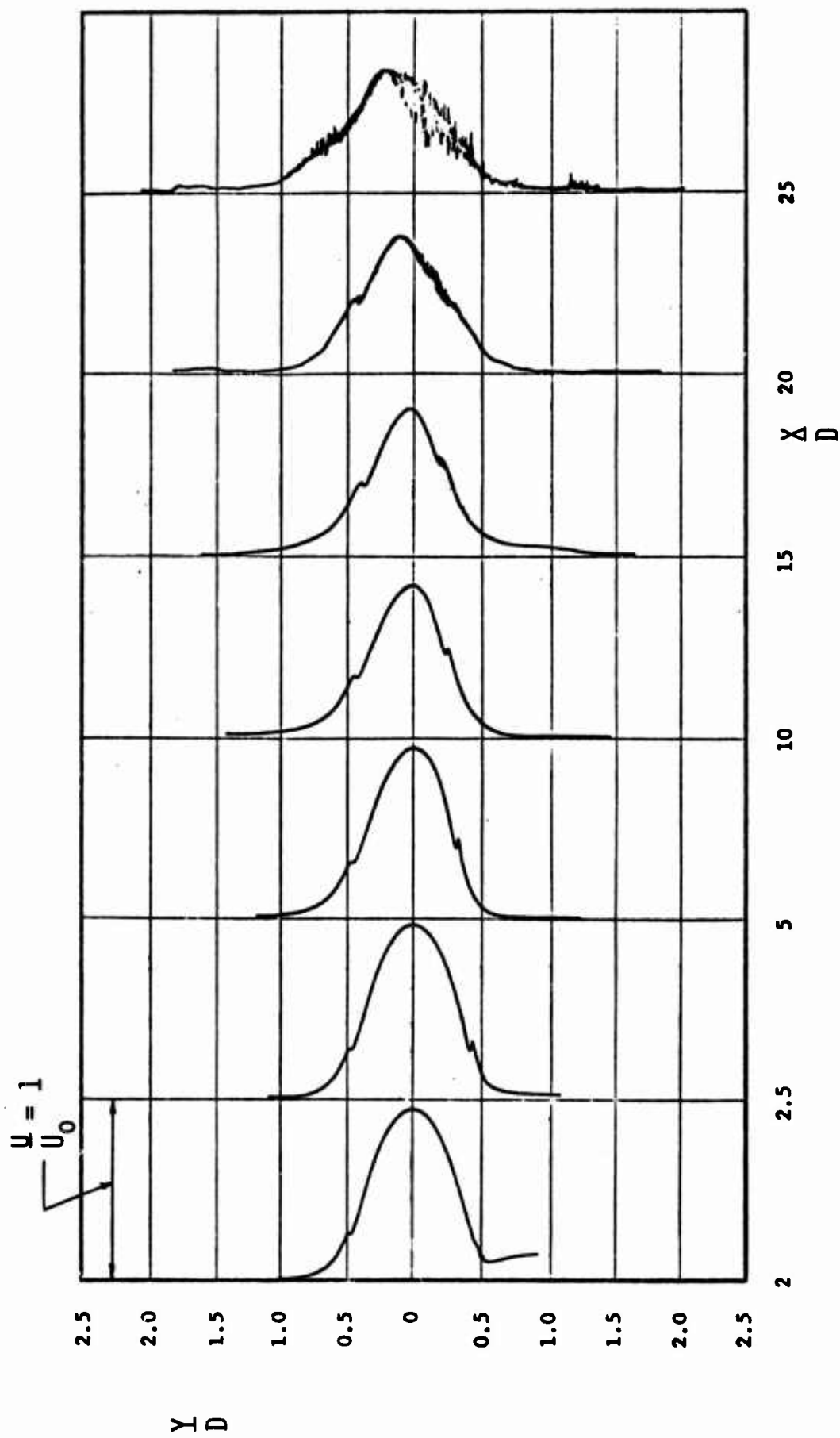


FIGURE 16 VELOCITY PROFILES WITH CONTROL FLOW,  $Q_c = 44 \text{ IN}^3/\text{MIN}$



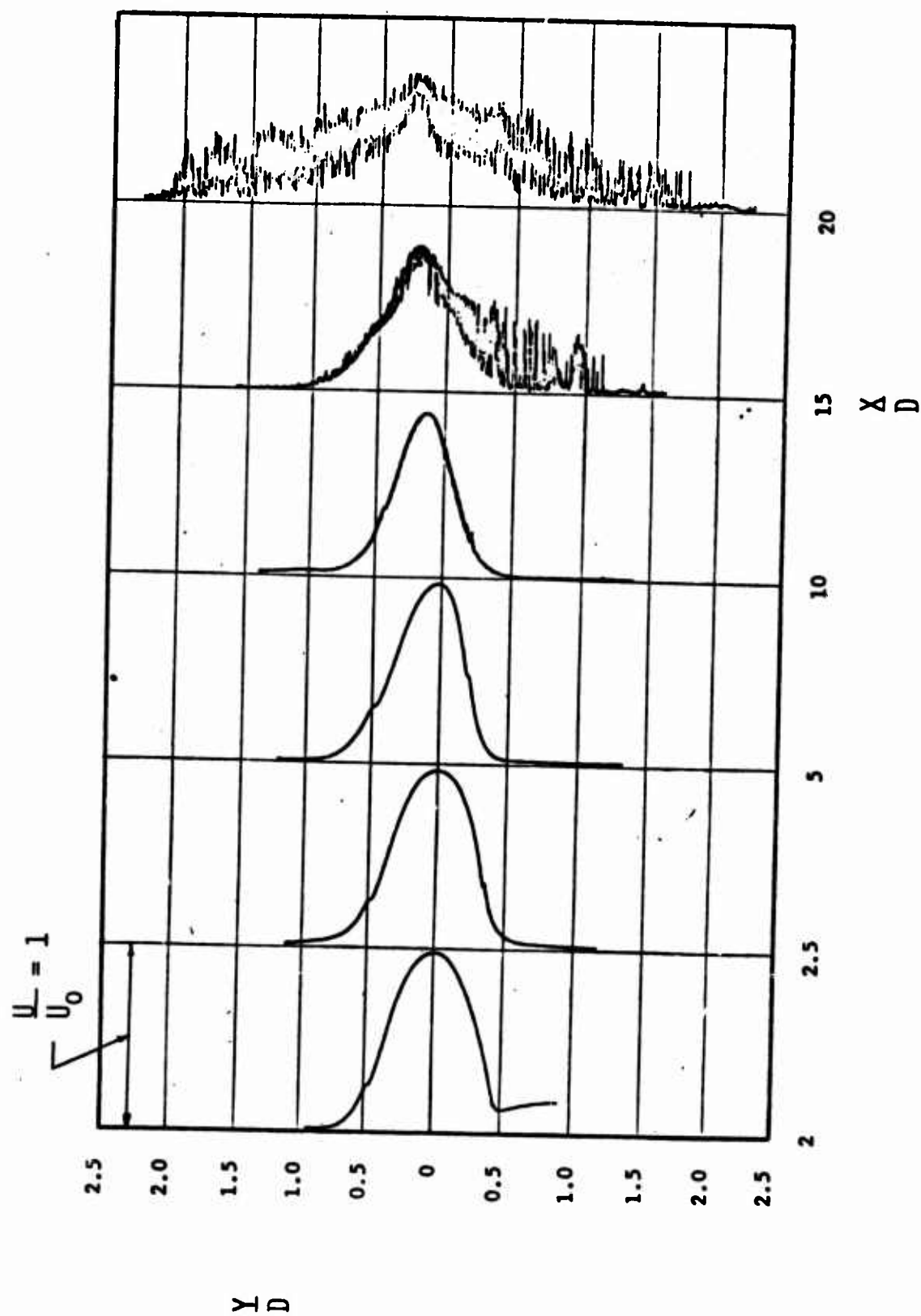


FIGURE 17 VELOCITY PROFILES WITH CONTROL FLOW,  $Q_c = 60 \text{ IN}^3/\text{MIN}$

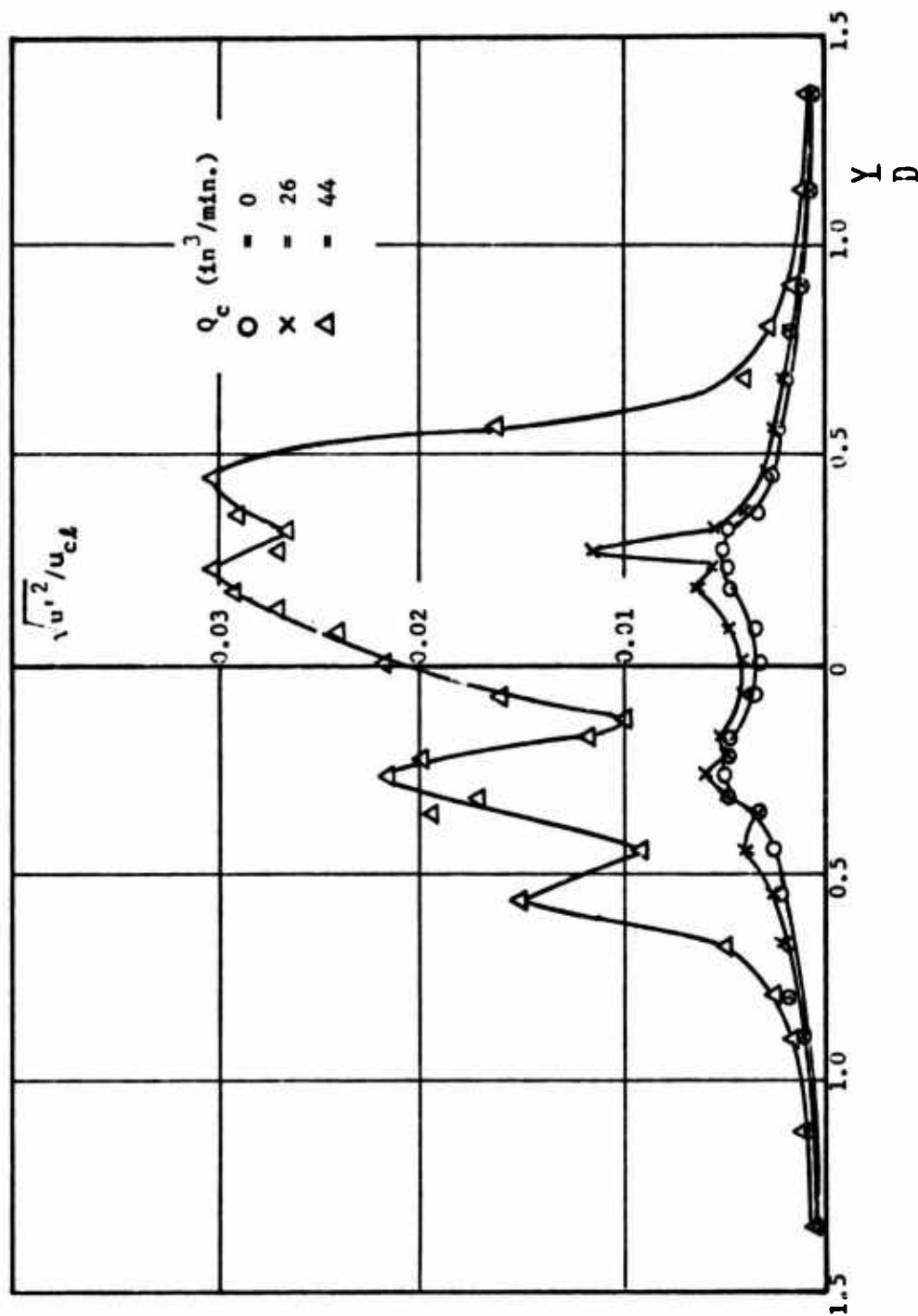


FIGURE 18 EFFECTS OF CONTROL FLOW ON VELOCITY FLUCTUATIONS  $x_0/D = 25$ ,  $Re = 507.7$

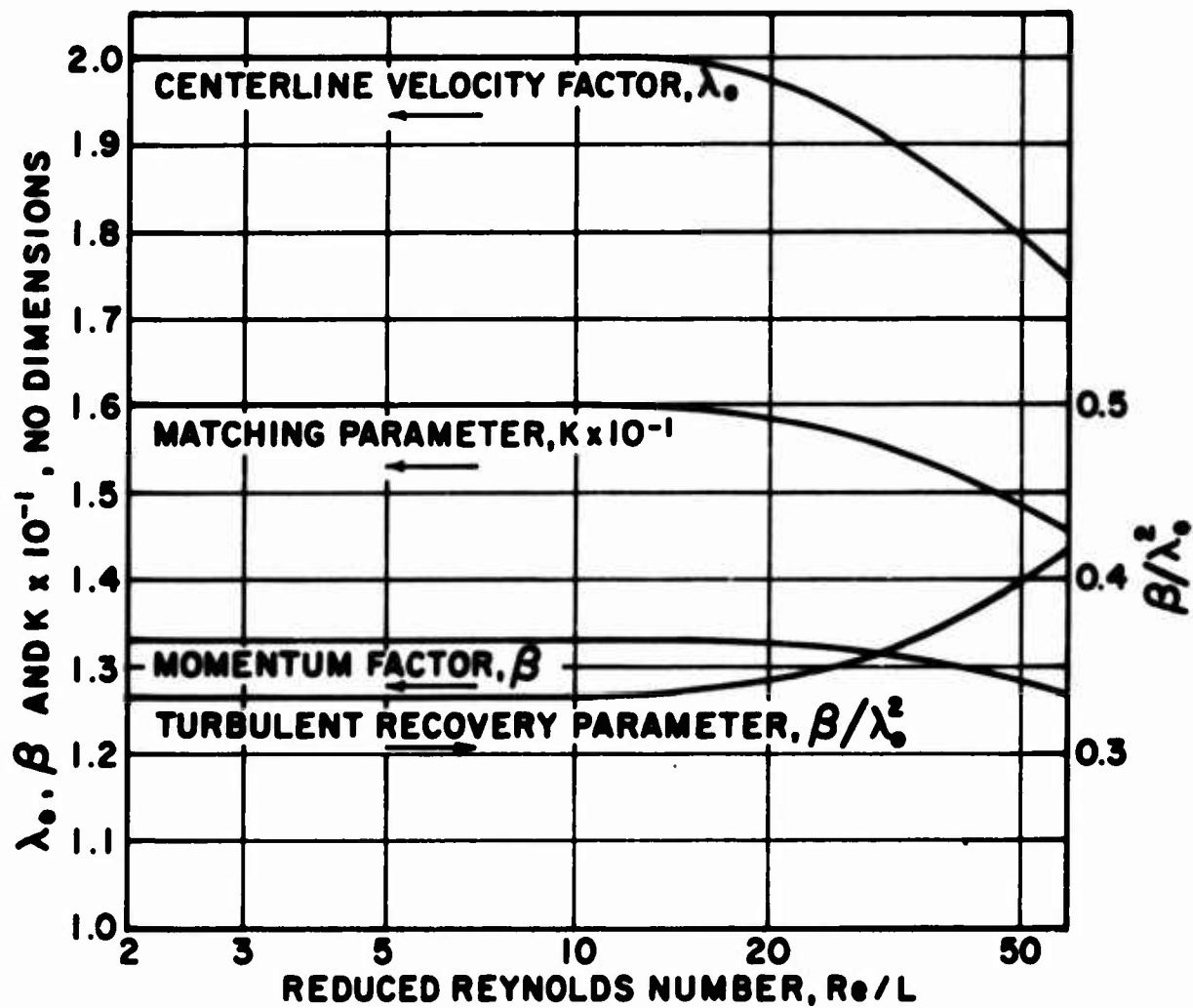


FIGURE 19 JET PROPERTIES

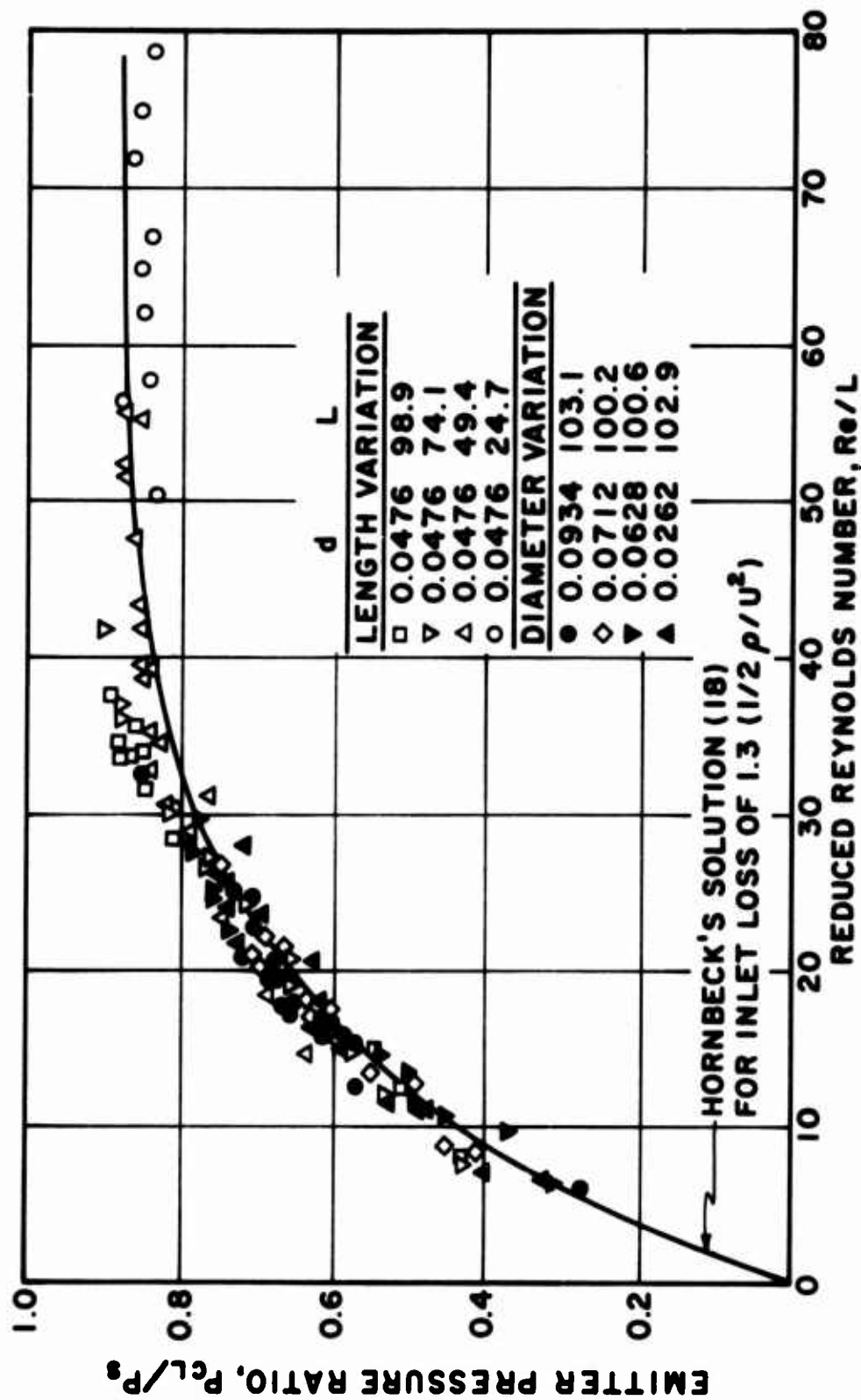


FIGURE 20 EMITTER PERFORMANCE

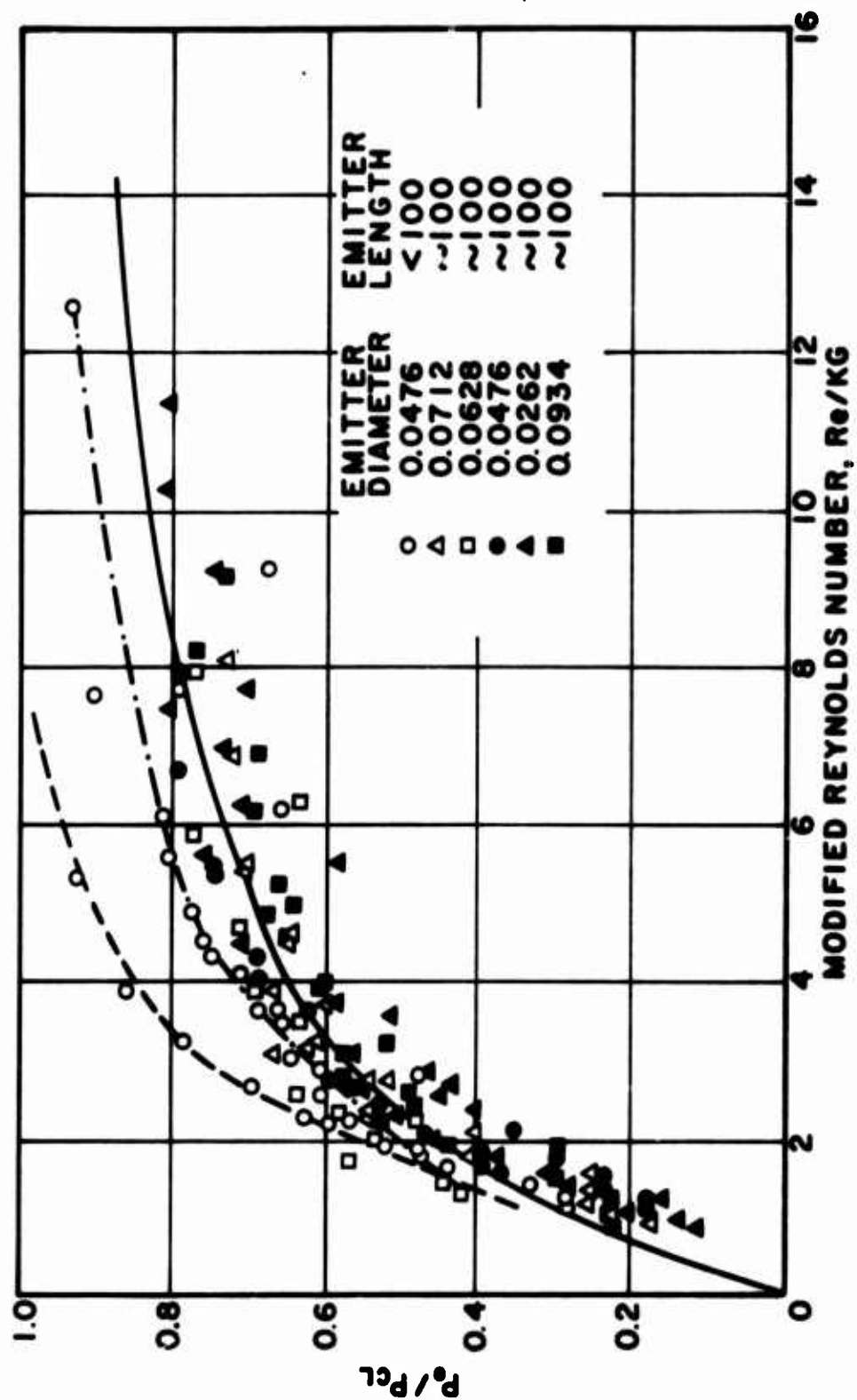


FIGURE 21 LAMINAR PRESSURE RECOVERY

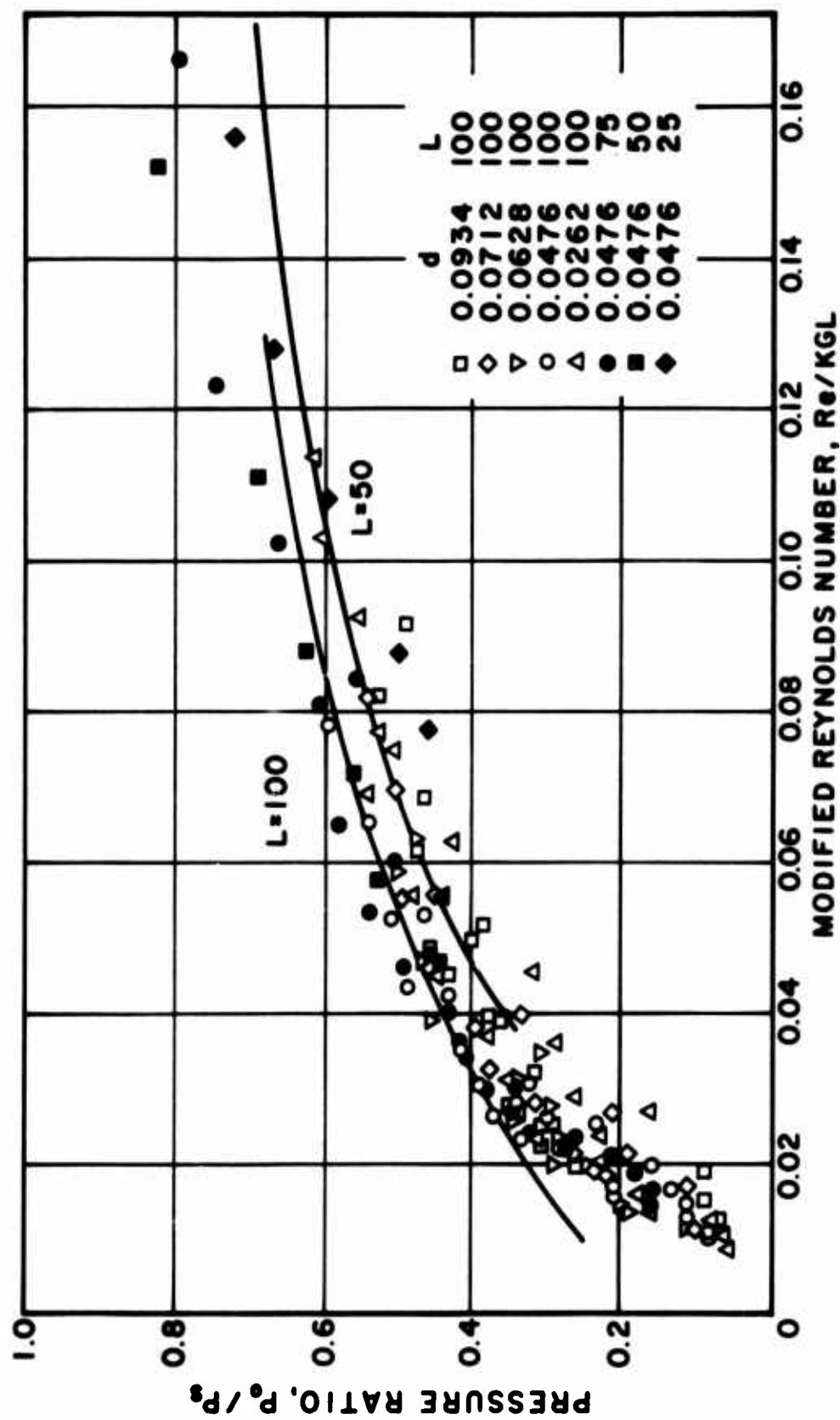


FIGURE 22 T/A PRESSURE RATIO

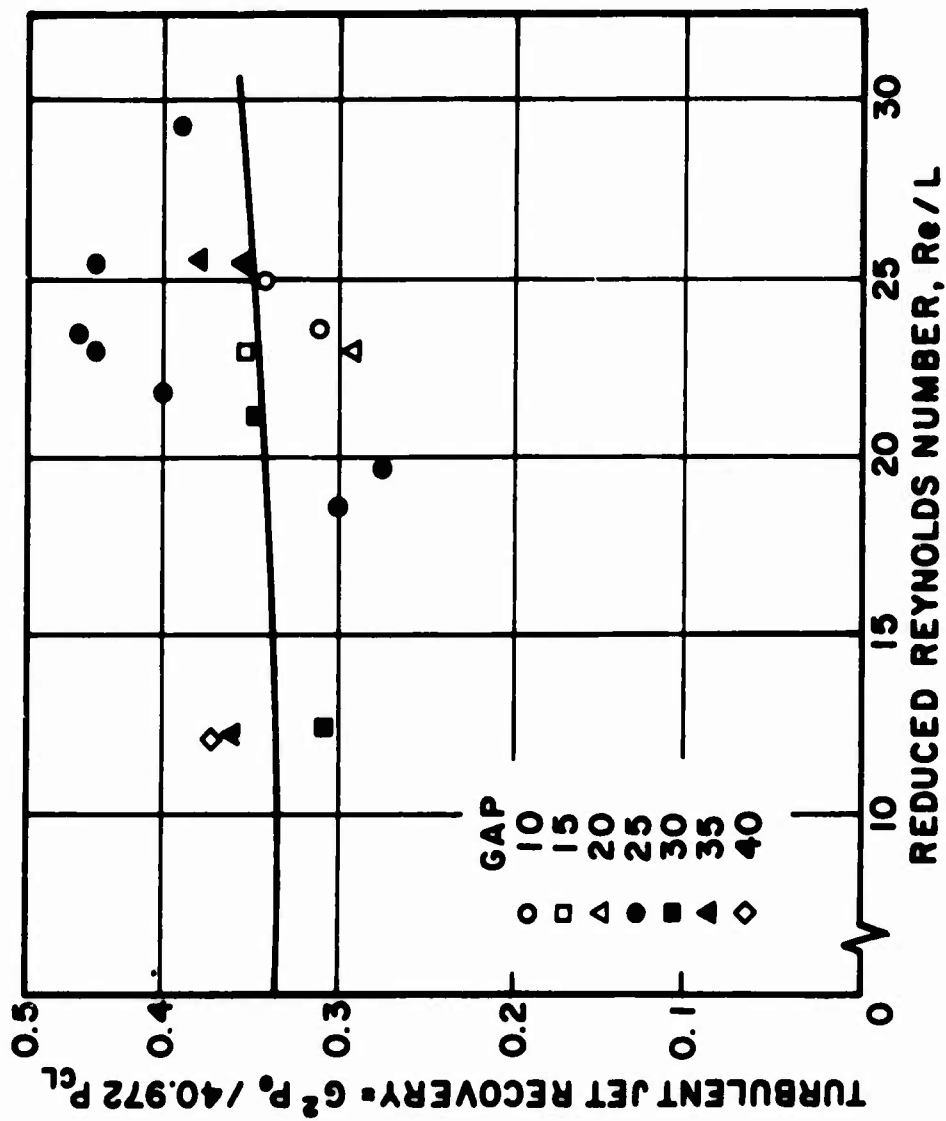


FIGURE 23 TURBULENT PRESSURE RECOVERY

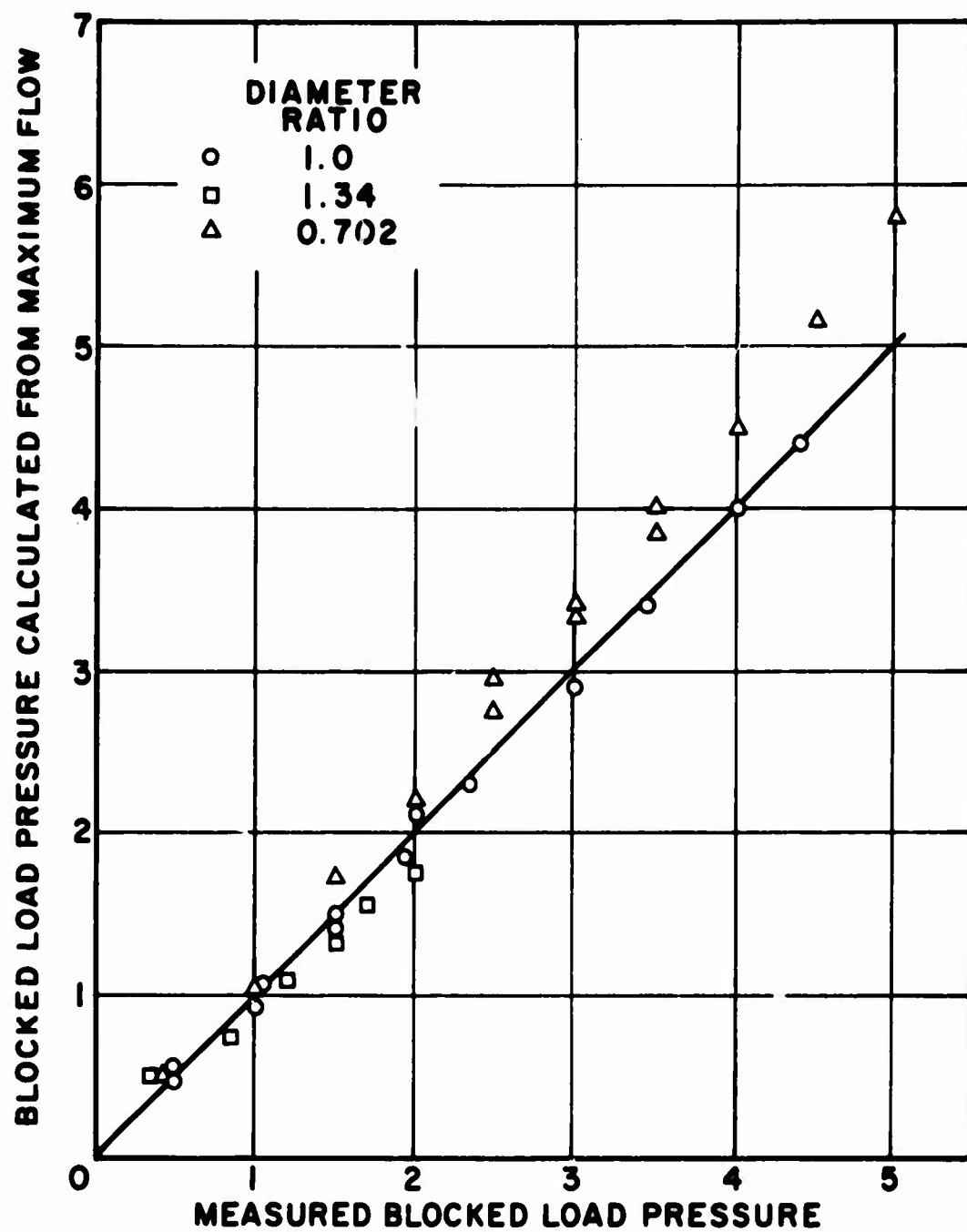


FIGURE 24 CONFIRMATION OF  
OUTPUT CALCULATIONS



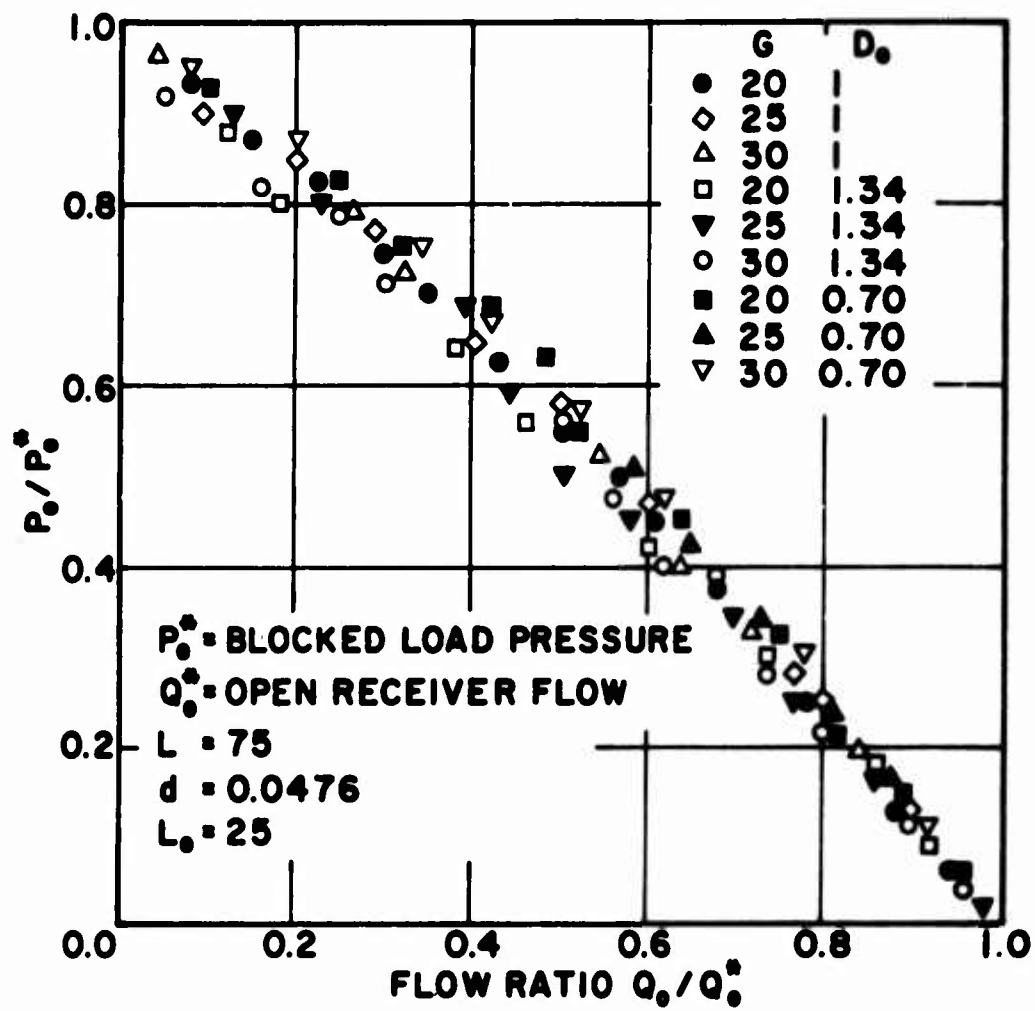


FIGURE 25 NORMALIZED OUTPUT PERFORMANCE

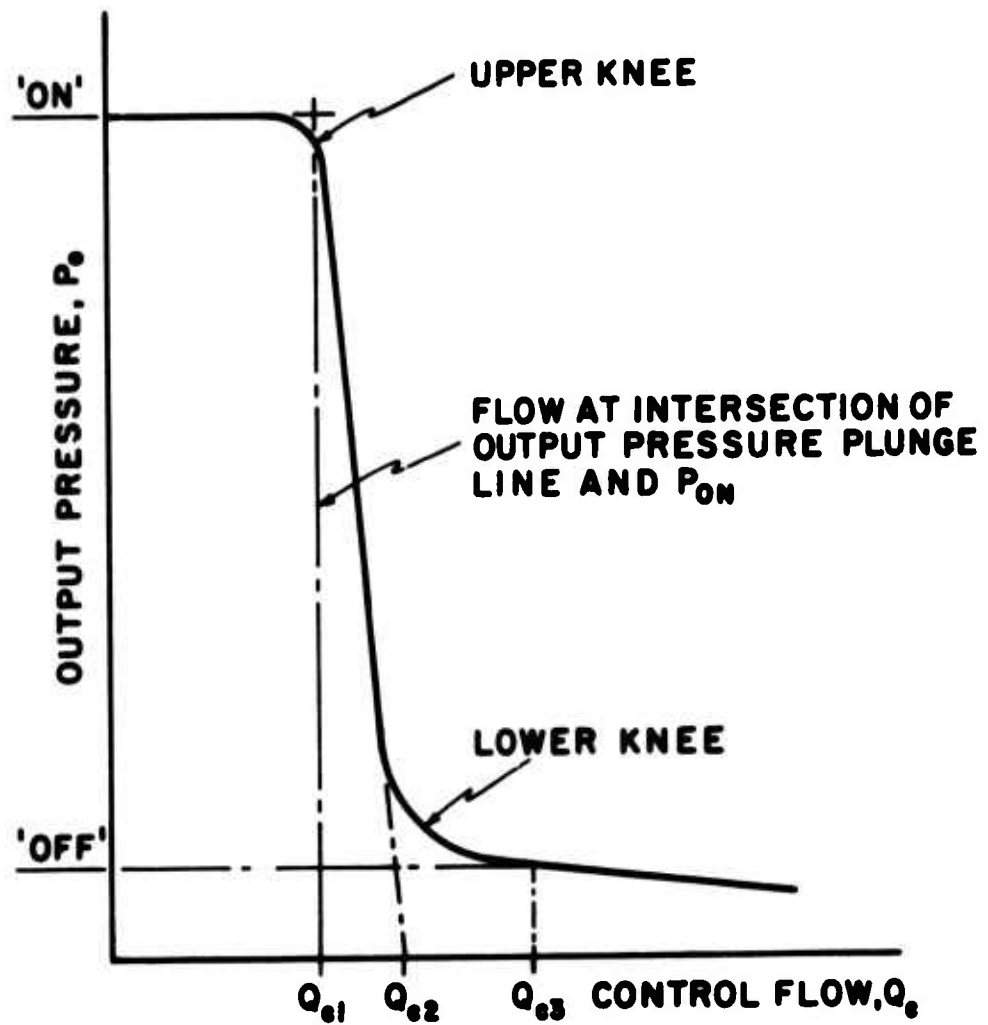


FIGURE 26 NOMENCLATURE FOR  $P_o - Q_c$  CURVES

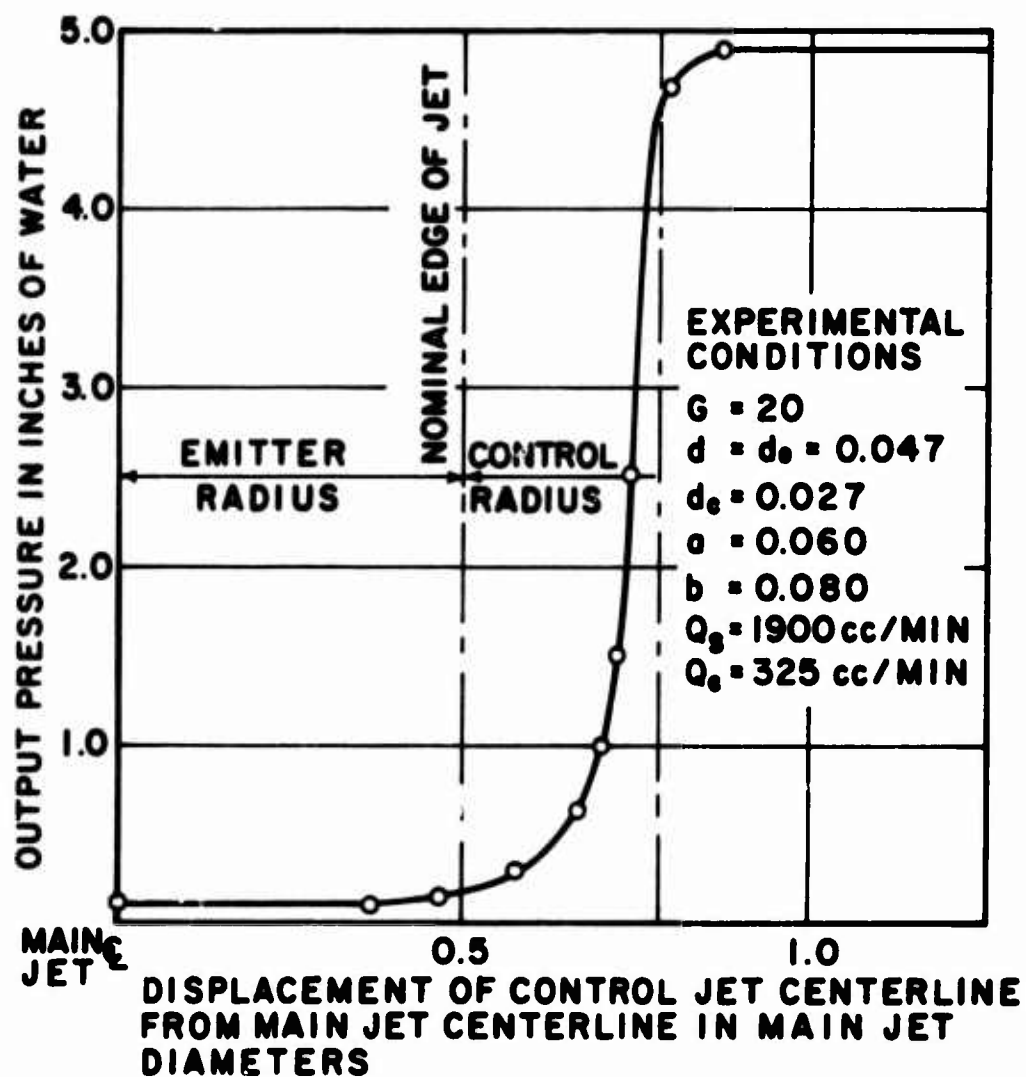


FIGURE 27 CONTROL JET TRAVERSE OF MAIN JET

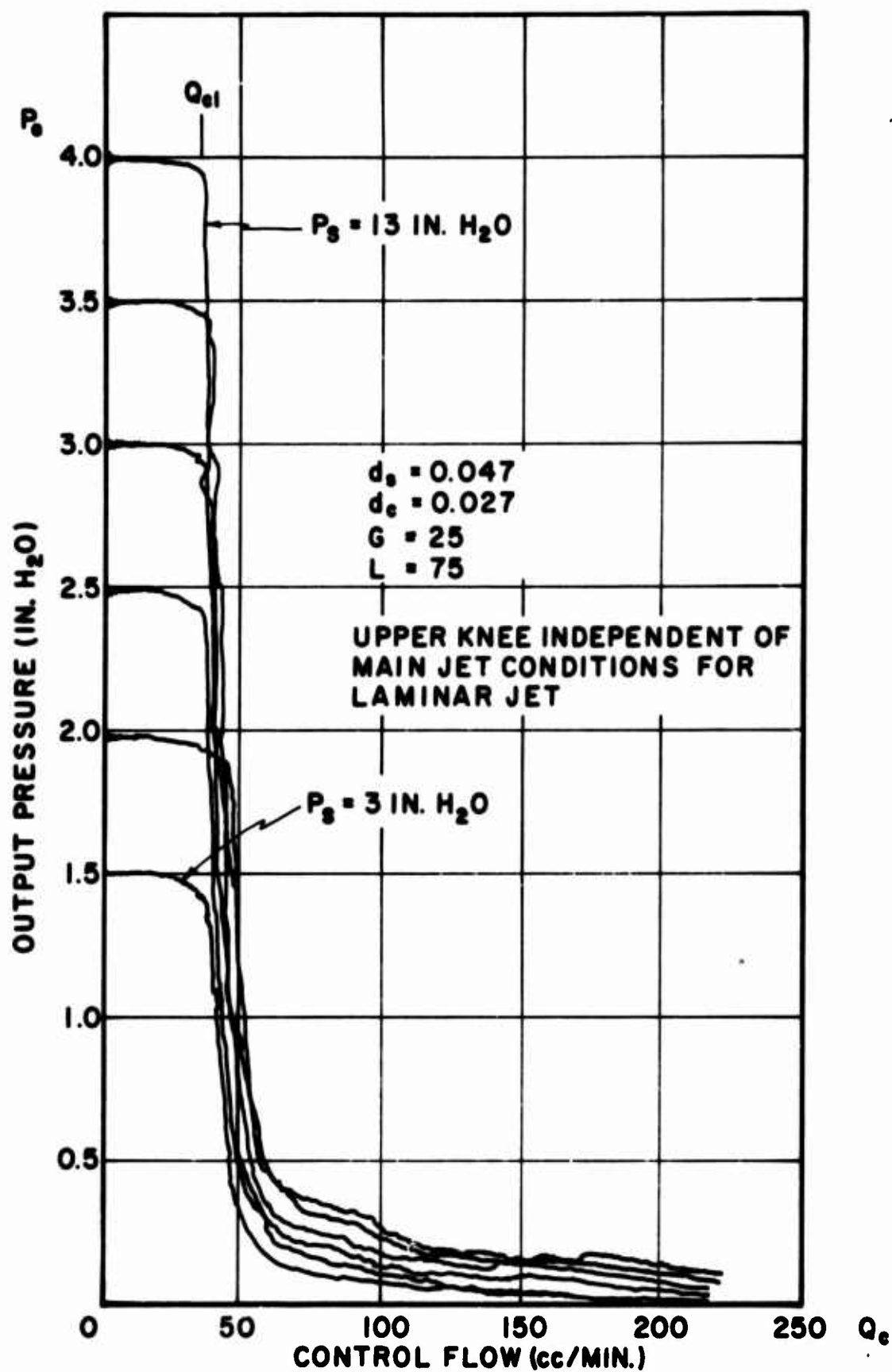


FIGURE 28 CONTROL CHARACTERISTICS WITH VARIABLE SUPPLY

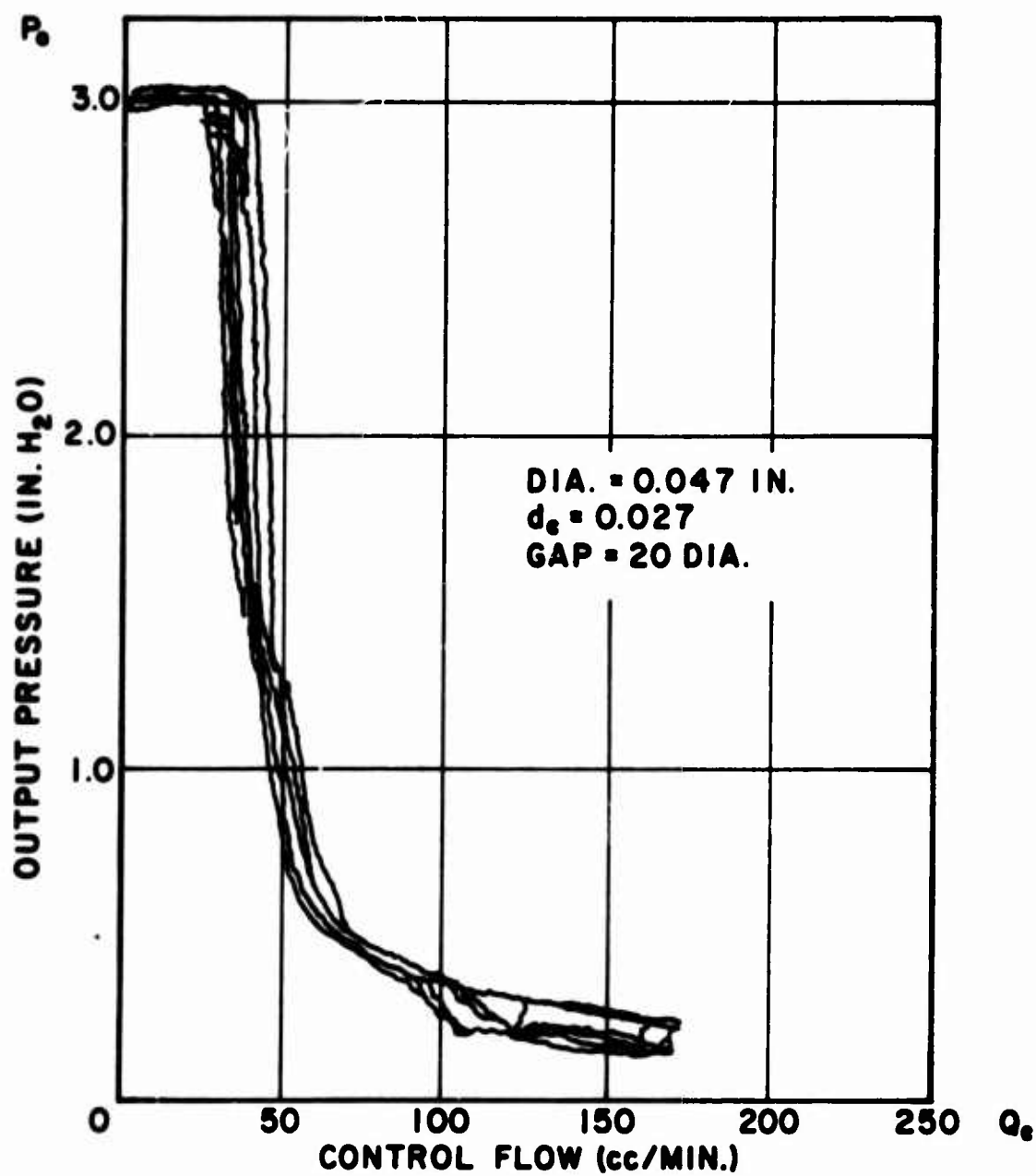


FIGURE 29 CONTROL CHARACTERISTICS WITH VARYING  $L$

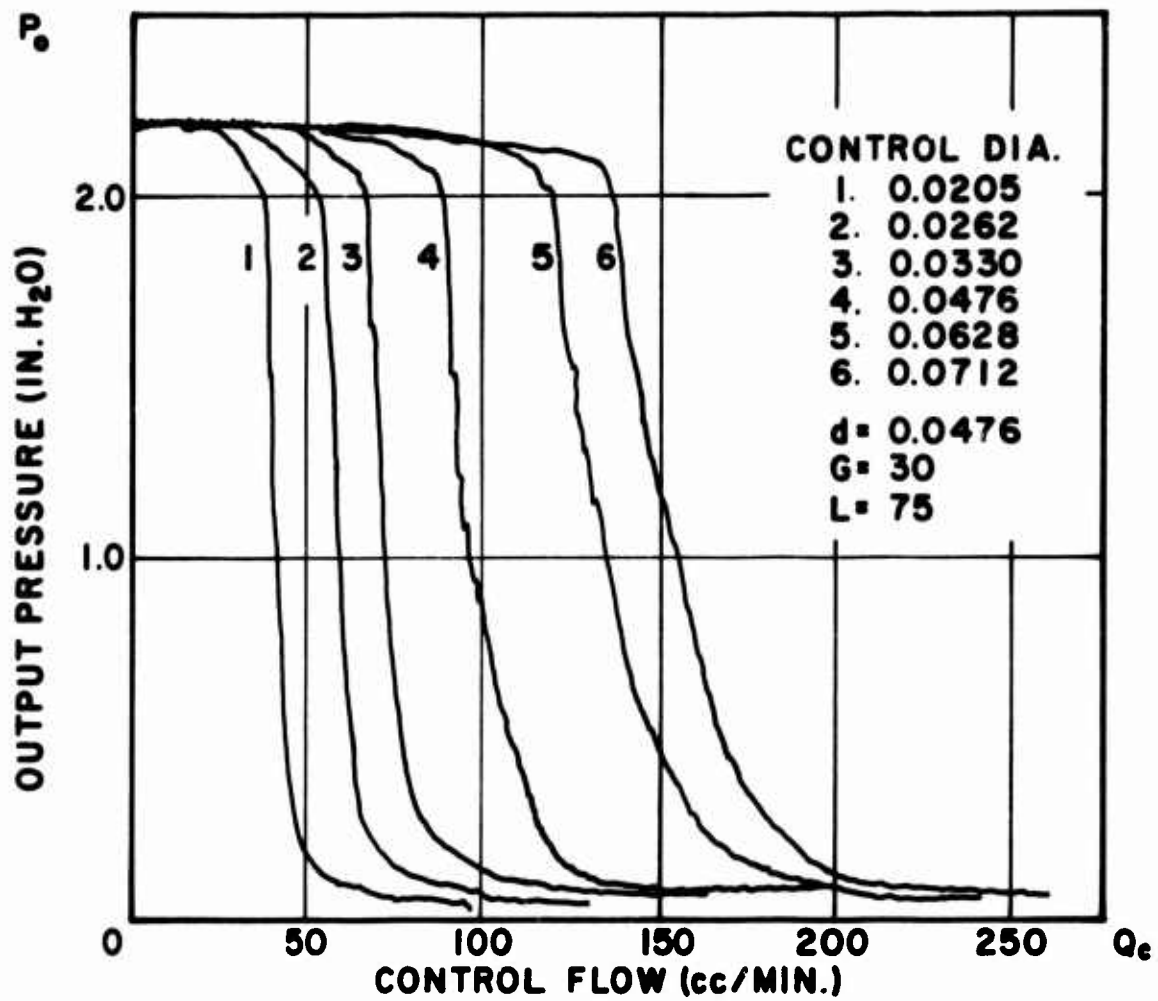


FIGURE 30 CONTROL CHARACTERISTICS  
WITH VARYING  $D_c$

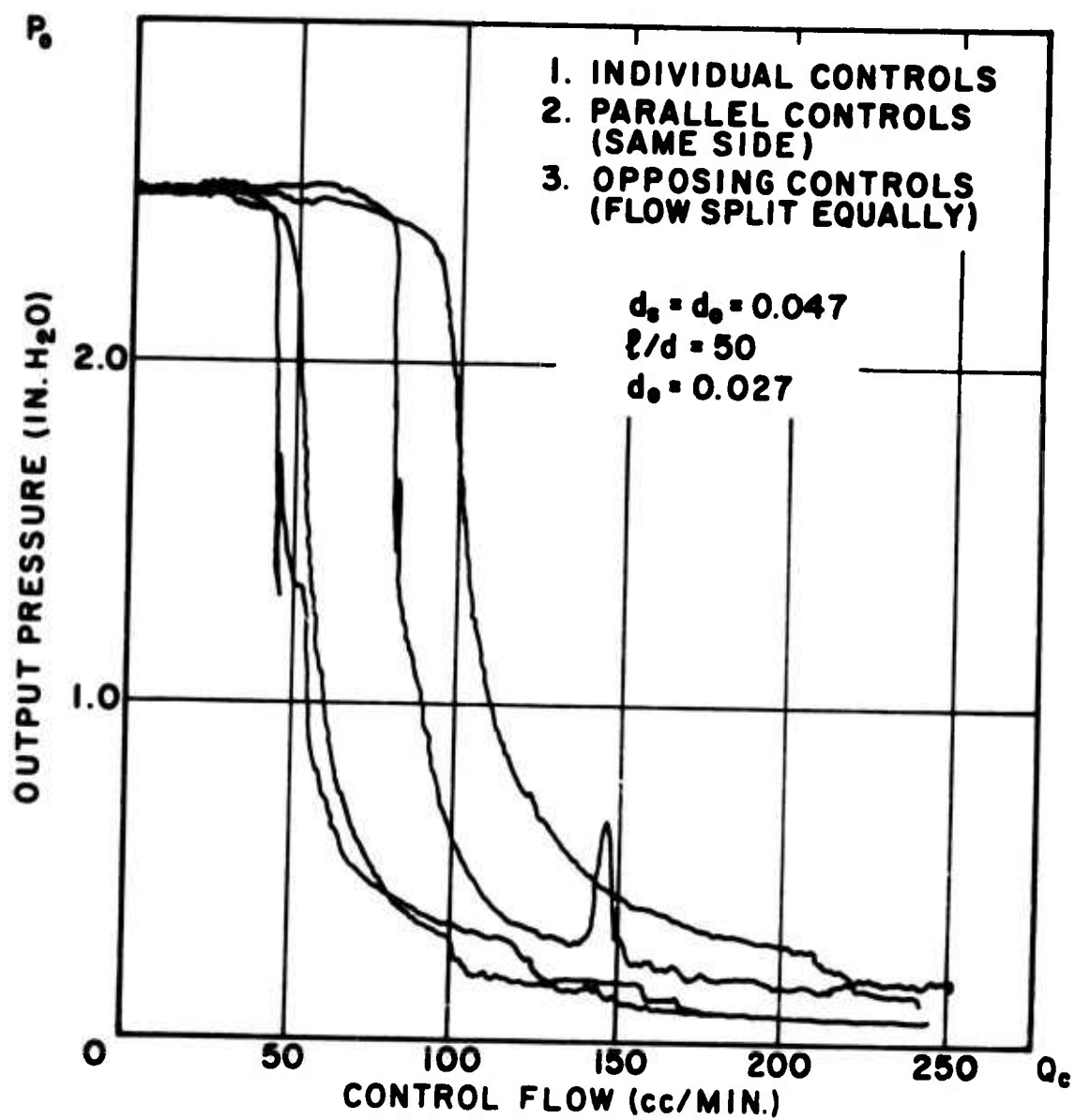


FIGURE 31 EFFECT OF MULTIPLE CONTROLS

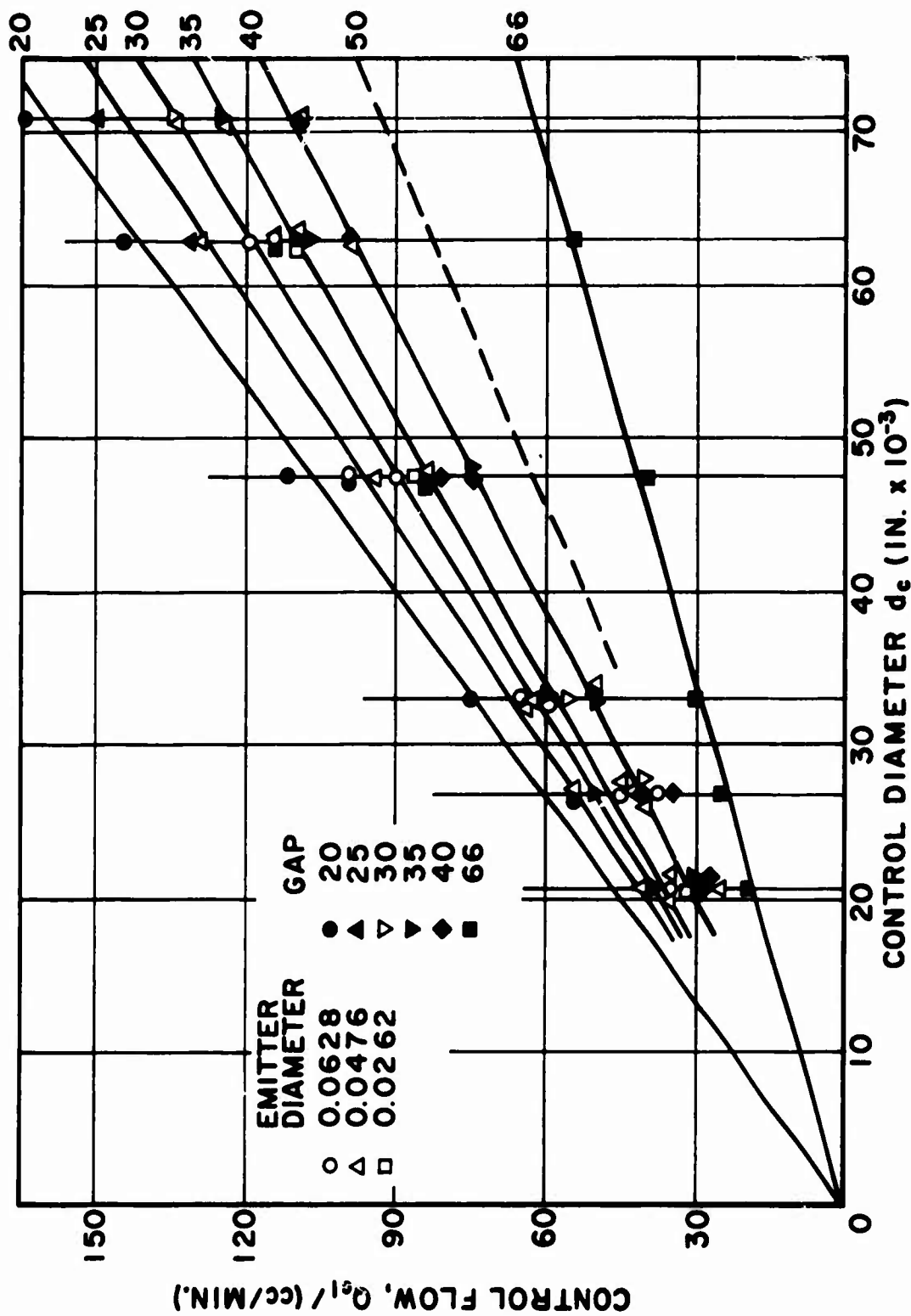


FIGURE 32 SUMMARY OF CONTROL EFFECTS



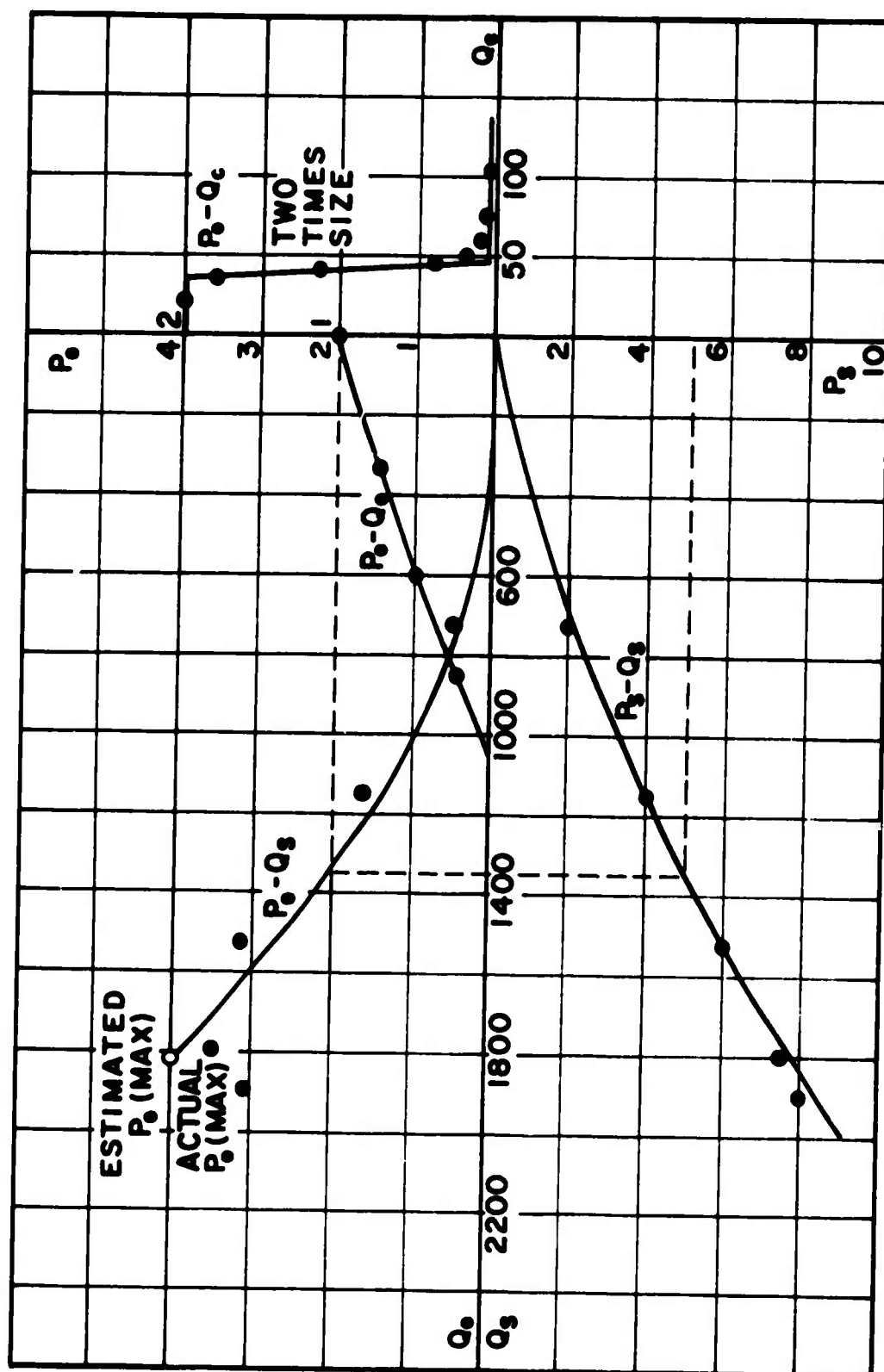


FIGURE 33 STATIC DESIGN EXAMPLE

**ANALYTIC DESIGN OF LAMINAR  
PROPORTIONAL AMPLIFIERS**

by

**FRANCIS M. MANION  
TADEUSZ M. DRZEWIECKI**

**Harry Diamond Laboratories  
Washington, D.C. 20438**

## CONTENTS

	Page
ABSTRACT .....	151
NOMENCLATURE .....	152
LIST OF FIGURES .....	154
1. INTRODUCTION .....	156
2. MODELING OF A LAMINAR PROPORTIONAL AMPLIFIER .....	158
2.1 A General LPA Geometry .....	158
2.2 General Assumptions .....	160
2.3 Supply Characteristic .....	162
2.4 Input Characteristic .....	164
2.4.1 Control Channel Resistance .....	166
2.4.2 Jet Edge to Downstream Control Edge Resistance ...	166
2.5 Analysis of Amplifier Jet Deflection Gain and Dynamics ..	174
2.5.1 Jet Deflection Gain .....	174
2.5.2 Frequency Response Estimate .....	181
2.5.3 Input Impedance .....	185
2.5.4 Centered Jet Impedance .....	185
2.5.5 Deflected Jet Impedance .....	186
2.5.6 Bias Sensitivity .....	187
2.6 Operating Reynolds Number Range .....	188
2.7 Output Characteristics .....	193
2.8 Transfer or Gain Characteristics .....	198
2.9 Miscellaneous Analytical Results .....	200
2.9.1 Geometric Configuration Sensitivity .....	200
2.9.2 Contamination Sensitivity .....	203
3. EXPERIMENTAL RESULTS .....	204
3.1 Input Characteristic Parameters .....	204
3.2 Output Characteristics .....	213
3.3 Gain Characteristics .....	215
3.3.1 Gain versus Reynolds Number .....	215
3.3.2 Gain versus Control Bias Pressure .....	218
3.3.3 Gain versus Input Frequency (Bode Diagram) .....	218
4. DESIGN EXAMPLE OF MULTIPLE ELEMENT STAGING .....	221
5. DISCUSSION .....	227
6. SUMMARY AND CONCLUSIONS .....	229
7. LITERATURE CITED .....	231

## ABSTRACT

This paper discusses the analytic design of laminar proportional amplifiers. Starting with a historical review of analog fluidic devices, the text shows the advantages of and rationale for using laminar devices. Among some of the more desirable features of laminar devices are the improvements obtained in gain, dynamic range and signal-to-noise ratio, not to mention the ease of scaling. A general geometric configuration for laminar proportional (analog) amplifiers is presented that considers control and output-port width, splitter-to-nozzle distance, splitter thickness, aspect ratio, and spacing between downstream edges of the control ports normalized to the supply nozzle width as the parameters of concern in design. The approach geometry, such as the supply, control, output and vent lines are treated in terms of known viscous impedance variables. Expressions are derived for each in turn, but are treated separately since their values attenuate the response derived from the general parameters and may be chosen independently. Staging techniques are presented also. Experimental data reported previously for typical element designs indicate that single-stage blocked pressure gain of over 25 and dynamic range of 4000:1 is obtainable, verifying the theoretical calculations. Other experimental data for air, oil, water, large and small scale devices for input, output and supply characteristics, dynamic response and internal flow parameters are similarly close, within a few percent, of the expected analytical predictions. Design examples of multiple-stage amplifiers are presented, along with measured characteristics that compare favorably to the design specifications.

In addition, laminar proportional amplifiers (LPA's) are shown to form the basis for many important sensors and devices used in control circuits such as rate sensors, linear accelerometers, digital switches and gas-liquid interface amplifiers. A working knowledge of the design and operating principles of the LPA suffices to design devices for both static and dynamic specifications.

# NOMENCLATURE

- a - speed of sound, m/s
  - $a_1$  - net entrainment coefficient, dimensionless
  - A - channel cross-sectional area,  $m^2$
  - b - width dimension, m
  - B - width dimension normalized by  $b_s$ , dimensionless
  - $c_d$  - discharge coefficient -  $Q_a/Q_{1d}$ , dimensionless
  - $c_\theta$  - momentum flux discharge coefficient,  $J_a/J_{1d}$ , dimensionless
  - C - fluid capacitance,  $kg/m^4s^2$
  - f - frequency, Hz
  - F - normalized frequency
  - $G_p$  - blocked pressure gain
  - h - height, m
  - J - momentum flux,  $kg\ m/s^2$
  - $k_j$  - jet deflection coefficient, dimensionless
  - K - constant
  - L - fluid inertance,  $kg/m^4$
  - $N_M$  - Mach number,  $u_{max}/a$ , dimensionless
  - $N_R$  - Reynolds number,  $b_s \sqrt{2(P_s - P_v)/\rho} / \nu$ , dimensionless
  - $N_R'$  - modified Reynolds number,  $N_R / (X_{eff} (1 + 1/\sigma)^2)$ , dimensionless
  - $N_{Rh}$  - Reynolds number based on height =  $\sigma N_R$ , dimensionless
  - P - pressure, Pa
  - Q - flow,  $m^3/s$
  - r - radius of curvature, m
  - R - fluid resistance,  $kg/m^4s$
  - s - distance, m
  - S - normalized distance by  $b_s$
  - T - temperature,  $^{\circ}C$
  - u - downstream direction velocity, m/s
  - U - free stream velocity, m/s
  - V - volume,  $m^3$
  - x - length, m
  - X - length normalized by  $b_s$
  - y - lateral distance, m
  - Y - admittance,  $1/Z$ ,  $m^4s/kg$
  - z - height coordinate dimension, m
  - Z - complex impedance,  $kg/m^4s$
- 
- $\beta$  - jet deflection angle, rad
  - $\delta$  - jet deflection, m
  - $\delta^*$  - displacement thickness, m
  - $\theta$  - momentum thickness, m
  - $\theta_s$  - separation angle, rad

- $\mu$  - fluid, dynamic viscosity,  $\text{kg}/(\text{ms})$
- $\nu$  - fluid, kinematic viscosity,  $\text{m}^2/\text{s}$
- $\xi$  - damping coefficient, dimensionless
- $\rho$  - fluid density,  $\text{kg}/\text{m}^3$
- $\sigma$  - aspect ratio,  $h/b_s$ , dimensionless
- $\tau$  - wall skin friction,  $\text{kg}/(\text{ms}^2)$
- $\omega$  - frequency,  $\text{rad}/\text{s}$

#### Subscripts

- a - actual
- $b_s$  - supply nozzle width
- $b_w$  - bandwidth
- B - bias
- c - control
- d - deflection
- dyn - dynamic
- D - downstream
- e - entrained
- eff - effective
- h - height
- i - integer index, or input
- id - ideal
- j - jet or jet edge
- $\ell$  - linear
- max - maximum
- min - minimum
- n - natural
- o - output
- oc - output channel
- Q - flow
- s - supply
- SB - spill back
- sp - splitter
- t - amplifier throat
- th - supply nozzle throat
- tr - transition
- v - vent
- vo - virtual origin
- w - wall
  
- 1 - refers to lateral nozzle walls, or first
- 2 - refers to plane nozzle walls, or second
- +

#### Superscripts

- ' - "prime" indicates a perturbation quantity
- - "bar" indicates average quantity

## FIGURES

Figure no.	page no.
1. Schematic of a laminar proportional amplifier (LPA) .....	159
2. An LPA flow field .....	161
3. Discharge coefficient versus modified Reynolds number ...	163
4. Static equivalent circuit for LPA input .....	164
5. Control volume for LPA input .....	165
6. Jet flow past downstream edge of control channel .....	168
7. Definition of jet virtual origin and linear jet spread ..	171
8. Comparison of experimentally determined location of jet entrainment streamline with theory .....	173
9. Dynamic equivalent circuit for LPA input .....	175
10. Jet deflection gain versus control bias pressure .....	182
11. Jet deflection gain versus frequency, showing bias effects .....	184
12. Jet deflection admittance versus control bias pressure ..	189
13. Jet deflection admittance versus control bias pressure showing effects of non-centered jet .....	190
14. Location of downstream point where downstream effects are first felt .....	192
15. Flow in the vicinity of the leading edge of a splitter ..	196
16. Sketch of a rounded supply nozzle exit .....	202
17. Separation angle versus Reynolds number for flow past a cylinder .....	203
18. Planviews of LPA's with long approach geometry .....	205
19. Comparison of theoretical and experimental jet centered input characteristics, $\sigma = 0.5$ , Silicone oil model, $b_s = 10$ mm .....	209
20. Comparison of theoretical and experimental, jet centered and jet deflection, input characteristics, $\sigma = 1.0, 1.4$ , MIL-H-5606B red oil, $b_s = 2.54$ mm .....	210

	page no.
21. Comparison of theoretical and experimental dynamic input impedance for an LPA, $\sigma = 1.2$ , $b_s = 0.51$ mm, air ...	212
22. Comparison of theoretical and experimental, centered jet, output characteristics, $\sigma = 0.75, 0.5$ , $b_s = 0.5$ , air .....	214
23. Comparison of theoretical and experimental values for gain versus Reynolds number, $\sigma = 0.8, 1.2, 1.6$ , $b_s = 0.5$ mm, air .....	216
24. Comparison of theoretical and experimental values for gain versus Reynolds number, $\sigma = 0.5$ , $b_s = 10$ mm, silicone oil .....	217
25. Comparison of theoretical and experimental values for gain versus control bias pressure, $\sigma = 0.8, 1.2$ , $b_s = 0.5$ mm, air .....	219
26. Comparison of theoretical and experimental values for gain versus frequency (Bode Diagram), $\sigma = 2.0$ , $b_s = 0.5$ mm, red oil .....	220
27. Measured interstage gain characteristics in a gain block .	227



## 1. INTRODUCTION

Flueric proportional amplification was a major goal of the inventors of fluidics, Horton, Bowles and Warren. Early work centered on high-energy turbulent streams deflected by the momentum of a turbulent control stream. The work of Peperone, Katz and Goto<sup>1\*</sup> in 1962 provided a basis for most of the analytical work in momentum interaction devices. In essence, the deflection of the turbulent jet was made proportional to the ratio of control-to-supply momentum flux and the pressure recovered at ports downstream was proportional to the integrated total pressure impinging on the receivers, which is a function of the jet lateral position. Hence, gain could be related to the ratio of recovered pressure-to-deflection, times the ratio of deflection-to-control pressure. Devices of this nature had pressure gains rarely exceeding ten and more commonly about four or five<sup>1-4</sup>. Even now, commercially available momentum-exchange turbulent amplifiers have pressure gain of the order of only six to ten<sup>5</sup>.

Soon after the news release in 1960 on fluid amplification, work started on devices called impact modulators. These devices provide amplification by essentially modulating the back pressure or spill-back pressure of two axially impinging axisymmetric jets. These devices operate in the turbulent flow regime, but since they do not fall into the class of beam deflection amplifiers, they are not considered here in any detail. The pressure gain of such devices is generally higher than for momentum-exchange turbulent amplifiers; however, they generally suffer from poor signal-to-noise ratios due to the inherent instability of axially stagnating turbulent flows, and hence are generally used as logic devices<sup>6</sup> where their outputs are driven from saturation to saturation.

The increase of beam-deflection amplifier pressure gain was sought after from the beginning. In 1962, Manion<sup>7</sup> reported the augmentation of jet deflection by a pressure field in addition to momentum when a special interaction region geometry is considered. By providing a setback wall with a control nozzle some distance downstream, whose axis is perpendicular to the supply jet, a pocket of fluid is formed when both supply and control jets are on. When the control flow enters into this region in excess of the demanded entrainment flow of the supply jet, this region is pressurized and the opposite side pressure is reduced so the pressure field forces, in addition to the momentum forces, help to deflect the jet. The pressure field in effect acts over the entire jet length from exit to the control port. Analytic studies of this effect are included in references 7 and 8. Pressure fields also may have an adverse effect on gain if they act in a manner opposing the control signals. Manion<sup>9</sup> has shown that a pressure field in a vented region, caused by the spill-back flow from receivers, is detrimental to gain. Here the pressure acts on the whole jet field to oppose the jet deflection. The possibility of using pressure fields to deflect jets has several promising advantages. One of these advantages is that if the pressure can be applied over a sufficiently large area of the supply jet, the pressure difference required to cause a unit jet deflection can be quite a bit less than that required

\*Superscripts indicate reference numbers in section 7.

to deflect a jet by momentum, hence the pressure gain is increased. Initial design work and analysis<sup>10-13</sup> was crude but did indicate that the reasoning was correct, and that some gain improvement was likely when using pressure field devices. The first practical useage of a pressure field amplifier was reported by F. T. Brown et al<sup>10</sup>. Others worked on the problem later<sup>11,12</sup>, culminating with the work of Griffin and Gebben<sup>14</sup>. Brown et al used a turbulent jet and built such an amplifier with relatively good gain. Griffin and Gebben<sup>14</sup> used a pressure field and geometry to obtain a flat saturation characteristic by limiting the excursion of the jet deflection to the downstream position of the control channels. This device, however, did not exhibit the improved pressure gain one would have expected, but did indeed have a flat saturation.

As time progressed and system requirements were of more concern to the fluidic designer, emphasis was placed on increased dynamic range (signal-to-noise ratios), bandwidth and stability, in addition to high gain. The major sources of noise in fluid amplifiers are flow turbulence and internal resonances. Turbulence can be reduced and virtually eliminated by operating in the laminar flow regime. Several researchers<sup>5,15,16</sup> have shown that proportional amplifiers can operate with gain in the laminar flow regime. Hellbaum of NASA Langley, as reported by Manion and Mon<sup>15</sup> utilized the Griffin<sup>11</sup> amplifier in the laminar regime and got good gain. Mon<sup>16</sup> indicates that with the pressure controlled device he used, blocked pressure gains of 26 were readily attainable, and gains of over 20 were attained with a dynamic range of 2000 at a bandwidth of 20 Hz. Manion and Mon<sup>15</sup> indicate that they were able to obtain experimental bandwidths of over 600 Hz for moderately large elements ( $b_s = 0.5$  mm).

Diminishing their size would result in an increase in bandwidth commensurate to the inverse ratio of size. The work of Manion and Mon<sup>15</sup> also indicates that pressure-field jet deflection is more suited to laminar jets than turbulent jets, as opposed to momentum deflection. Since a laminar jet is sensitive to disturbances, it tends to break up more readily when a high-velocity stream is impinged on it, while a large, low-velocity pressure field does not disturb the flow. On the other hand, a turbulent device with a pressure field has a very high entrainment rate that is tied closely to large turbulent eddies on the sides. These eddies may interact with a large control and induce spurious pressure fluctuations, resulting in random deflections of the jet--producing an additionally noisy output on an amplifier. A turbulent jet is not as greatly disturbed as a laminar jet by control momentum, since it is already turbulent.

Additional advantages of laminar jet devices are: increased pressure recovery due to low entrainment--hence higher possible gain, and the ability to scale in any Newtonian fluid, since the devices follow the well-behaved laws of Reynolds number scaling<sup>17</sup>. Other advantages will become apparent when it is shown that laminar-proportional amplifiers form the basis for many other devices, such as: angular rate sensors, linear accelerometers, digital logic gates and gas-to-liquid interface amplifiers.

This paper provides the reader with a general analysis for laminar jet proportional amplifiers to include expressions for the supply, input, output, transfer and dynamic response characteristics in terms of six basic geometric parameters. A basic model for staging the amplifiers will be expanded upon, and a practical design example suitable for use with an amplifier gain block will be presented. In addition, a simple two-dimensional laminar jet flow-field analysis will be presented to familiarize the reader with flows in the interaction, vent and splitter regions.

With an understanding of the nature of the flows in a typical amplifier, fabrication process problems can also be understood. Design compromises due to poor fabrication techniques, process deficiencies such as etching or stamping, and lamination techniques will be discussed.

With a background on the nature of the flow field, some typical problems rising from element contamination by dry and wet contaminants and typical solutions will be discussed.

Experimental verification in all phases will be presented and the analysis will be shown to be within engineering accuracy ( $\pm 10\%$ ) for most cases.

General "trouble-shooting" guides will also be presented to help the designer decide what problem he may have, what might be causing them, and possible solutions regarding a single-stage amplifier design.

The paper concludes with a general statement of the laminar proportional amplifier analysis as it relates to other laminar jet devices to include angular rate sensors, linear accelerometers, digital logic gates and gas-to-liquid interface amplifiers.

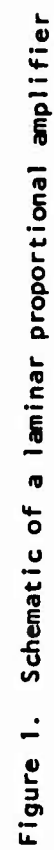
## 2. MODELING OF A LAMINAR PROPORTIONAL AMPLIFIER

This section is devoted solely to the mathematical and physical modeling of a laminar proportional amplifier. The first part presents a general geometric configuration that will cover most cases. The second part covers the assumptions and the type of modeling employed. The latter part presents models and general expressions for the important characteristics of laminar proportional amplifiers.

For the sake of simplicity, the laminar proportional amplifier will be referred to as an LPA.

### 2.1 A General LPA Geometry

In any type of beam-deflection amplifier there are at least three normalized geometric parameters that are basic: (fig. 1) control port width,



$B_c$ ; <sup>+</sup> output port width,  $B_o$ ; and supply nozzle-to-splitter distance,  $X_{sp}$ . LPA's that normally operate by pressure field deflection have in addition three other basic parameters:<sup>15</sup> aspect ratio, (nozzle height-to-width ratio  $\sigma$ ); lateral spacing between the downstream edges of the controls,  $B_c$ ; and splitter thickness,  $B_{sp}$ . There are other parameters that may affect an LPA's performance--these are called approach geometry parameters. Such parameters are supply, control, and outlet lengths or shapes. Since these parameters tend to attenuate the performance derived from the basic parameters and can be chosen at will (for example, passages may be chosen to fit a particular packaging configuration) they are treated separately. Figure 1 shows a schematic of an LPA. The dashed outline denotes the region of the basic parameters, while everything outside the outline is a part of the approach geometry. Figure 1 shows, in addition, a vent vane dividing the vented region into two vents on each side of the LPA. This vane eliminates swirling vent flows in the control region caused by spillover from the outlets. It provides a virtually true ground at the downstream edge of the controls, and acts to help decouple the outputs from the inputs. Such a device has been shown to be virtually load insensitive.<sup>15</sup> Photographs of the flow, visualized by Spyropoulos,<sup>17</sup> indicate that the flow field upstream of the vanes is virtually unaffected by downstream conditions.

Figure 2 is a photograph of a typical LPA flow field. Shown in detail are the jet-edge and the splitter flow patterns when the output port is blocked.

## 2.2 General Assumptions

Several basic assumptions to simplify the analysis are listed below:

- (1). The flow is incompressible, i.e.  $\Delta\rho/\rho = \frac{1}{2} N_M^2 < 0.1$  less than 10 percent density variation in field. (This need not be a limiting assumption if a suitable relation between static pressure and density can be found. The addition of compressibility adds to the complexity of the problem, but not to the basic principle of operation).
- (2). The laminar jet, emanating from the supply nozzle, has its momentum-flux and entrainment characteristics calculable from two-dimensional laminar jet theory. (The velocity distribution is not so described due to a mixing or potential core region).
- (3). The flow field can be treated as the summation of various two-dimensional flow fields. For example, the top- and bottom-plate boundary layers can be calculated from simple two-dimensional momentum-integral relations independent of the rest of the geometry.

<sup>+</sup>Distances are normalized by dividing by the power jet nozzle width,  $b_s$

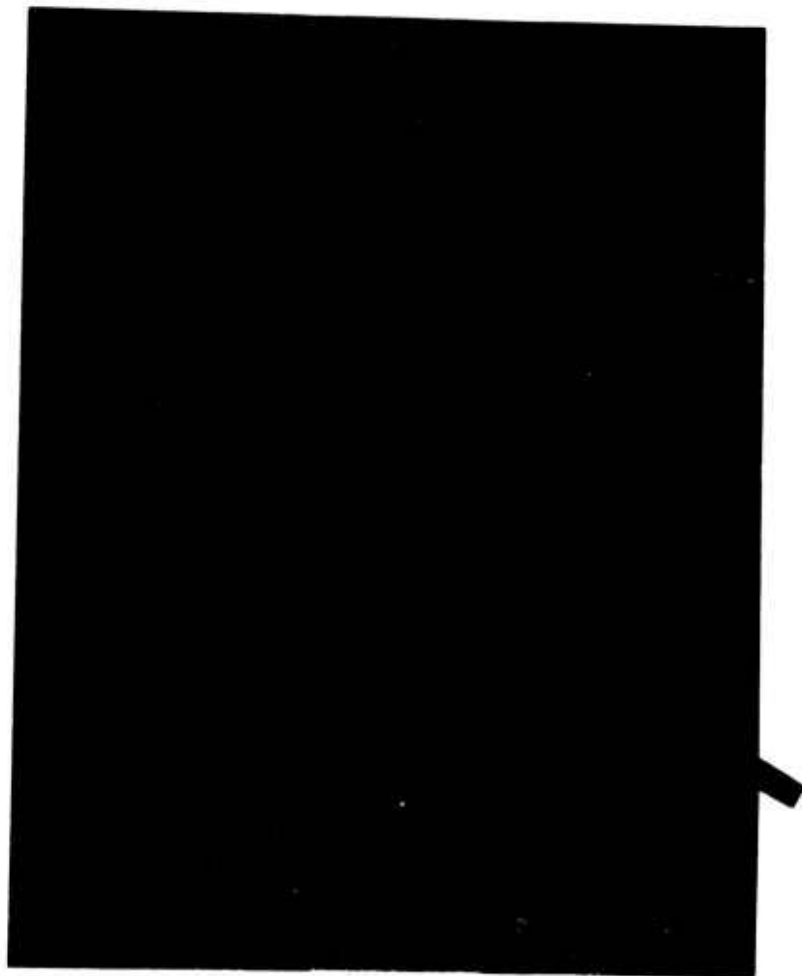


Figure 2. Photograph of an LPA flow field

- (4). The dynamic response of the approach geometry channels (e.g. control channel) can be approximated by simple lumped-parameter relations.
- (5). The impedance to flow offered by the jet edge-control edge spacing is purely resistive, with no frequency dependency.

### 2.3 Supply Characteristic

The supply characteristic of an LPA is the relation between the supply volumetric flow rate and the supply stagnation pressure. This relation is important because it is used to define the supply operating point resistance  $R_s$ , to which all other impedances are referenced. The supply dc impedance is defined as the ratio of the pressure difference across the supply nozzle to the supply volumetric flow,  $Q_s$ ; where the exit static pressure is taken as the vent pressure  $P_v$  for reference. The supply operating point resistance is therefore referenced to a zero-bias condition.

$$R_s \equiv (P_s - P_v)/Q_s \quad (1)$$

The volumetric flow exhausting from a nozzle is related to the square root of the pressure difference, the nozzle area  $b_s h$  and a discharge coefficient  $c_d$  by Bernoulli's equation, which can be written for a nozzle as:<sup>18,19</sup>

$$Q_s = c_d b_s h \sqrt{2(P_s - P_v)/\rho} \quad (2)$$

where  $\rho$  is the fluid density,  $b_s$  is the supply nozzle width, and  $h$  is the supply nozzle height. The discharge coefficient has been found to be uniquely related to a modified Reynolds number,<sup>19</sup>  $N_R'$  such that

$$c_d = f(N_R') \quad (3)$$

for

$$N_R' \equiv (b_s/\nu) \sqrt{2(P_s - P_v)/\rho} / [X_{eff} (1 + 1/\sigma)^2] \quad (4)$$

where

- $\nu$  - fluid kinematic viscosity.
- $X_{eff}$  - effective length of a straight duct having the same resistance as the supply nozzle and can be approximated for most smooth nozzles<sup>20</sup> as  $X_{eff} = X_{th} + 1$ .
- $X_{th}$  - normalized length of nozzle-throat straight section.
- $\sigma$  - nozzle aspect ratio,  $h/b_s$

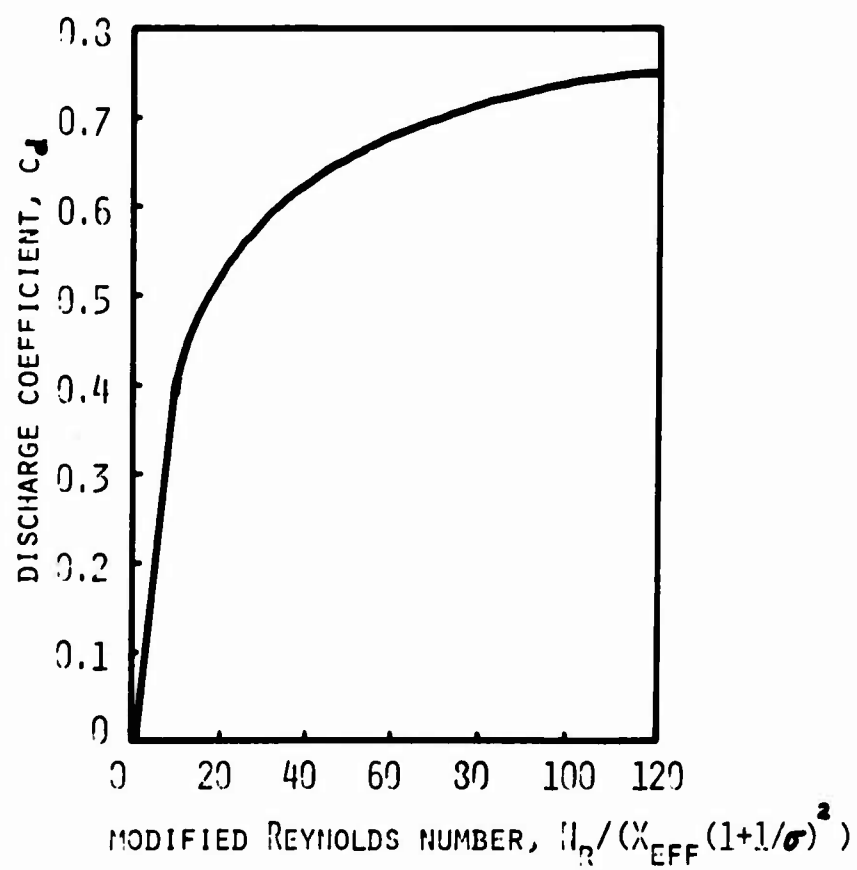


Figure 3. Discharge coefficient versus modified Reynolds number



The relationship indicated in equation 3 is presented graphically in reference 19, and is reproduced here as figure 3, since it is essential for the LPA design. In equation 4 the numerator is simply the Reynolds number, based on nozzle width and Bernoulli velocity,  $N_R = (b_s/v) \sqrt{2(P_s - P_v)/\rho}$ .

Substituting equation 2 into equation 1, the final expression for supply dc impedance becomes simply

$$R_s = \sqrt{\rho (P_s - P_v)/2} / (c_d b_s h) \quad (5)$$

#### 2.4 Input Characteristic

The input characteristic is defined as the relationship between control volumetric flow,  $Q_c$ , and control stagnation pressure,  $P_c$ . For dc conditions, Manion and Mon<sup>15</sup> describe the input impedance as being an equivalent series circuit to ground composed of the viscous resistance of the control channel,  $R_c$ , and the resistance of the space between the jet and the downstream control edge (fig. 2),  $R_v$  with entrained flow removed at the  $P_j$  node. This is shown schematically in figure 4 and physically in figure 5.

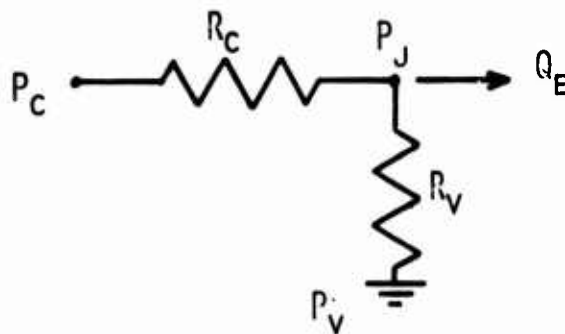


Figure 4. Static equivalent circuit of LPA control

The evaluation of  $P_j$  and  $R_v$  is based on some simple fluid relations; for that reason, the equivalent circuit of figure 4 can be shown in terms of a control volume in figure 5.  $Q_e$  is the flow entrained by the jet, the vent resistance  $R_v$  is  $(P_j - P_v)/Q_v$ , and the control channel resistance  $R_c$  is  $(P_c - P_j)/Q_c$ .

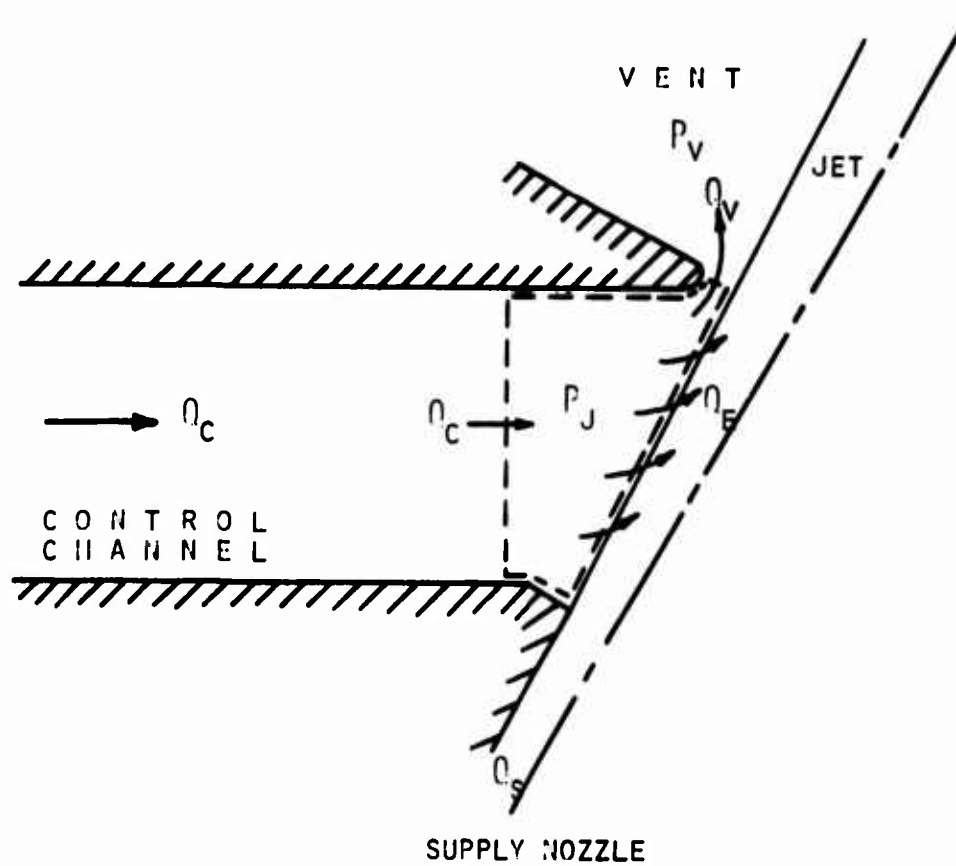


Figure 5. Control volume for LPA control

### 2.4.1 Control Channel Resistance

The resistance of the control channel is attributed simply to the viscous losses associated with flow in a rectangular channel--the entrance-length losses plus the fully developed losses. Drzewiecki<sup>19</sup> has shown that the losses in a rectangular channel of moderate aspect ratio can be represented by the following expression

$$R_c = \frac{12 \mu X_c}{(b_c h_c)^2} [\sigma_c (1 + 1/\sigma_c^2) + K] + 0.475 \rho Q_c / (b_c h_c)^2 \quad (6)$$

where

- $\mu$  - fluid dynamic viscosity
- $X_c$  - control channel length
- $\sigma_c$  - control channel aspect ratio
- $K$  - empirical fitting constant<sup>19</sup>

$$1 \leq \sigma_c \leq 2, 0.35 \leq K \leq .5; \sigma_c \geq 2, K = 0.5$$

Normalized to supply dc impedance, equation 6 becomes

$$R_c/R_s = \frac{24 X_c c_d}{B_c^2 \sigma N_R} \left[ \frac{\sigma}{B_c} \left( 1 + \left( \frac{B_c}{\sigma} \right)^2 \right) + K \right] + \frac{0.95 c_d^2}{B_c^2} \frac{Q_c}{Q_s} \quad (7)$$

As an acceptable engineering approximation for the dc impedance of long channels with a non uniform cross-sectional area (as, for example, in the device of fig. 1) the average width is used in the linear (first) term and the minimum width is used in the non-linear (second) term. Thus equation 7 may be written as

$$R_c/R_s = \frac{24 X_c c_d}{B_c^2 \sigma N_R} \left[ \frac{\sigma}{\bar{B}_c} \left( 1 + \left( \frac{\bar{B}_c}{\sigma} \right)^2 \right) + K \right] + \frac{0.95 c_d^2}{B_{cmin}^2} \frac{Q_c}{Q_s} \quad (8)$$

where capitalized dimensions have been normalized by the supply nozzle width,  $b_s$ , and now:

$$1 \leq \frac{\sigma}{\bar{B}_c} \leq 2, 0.35 \leq K \leq 0.5; \frac{\sigma}{\bar{B}_c} > 2, K = 0.5.$$

### 2.4.2 Jet edge to Downstream Control-Edge Resistance (Resistance to Vent)

The dc impedance of the space between the jet and the downstream

edge of the control channel, shown in figures 2 and 5, is determined from a relatively simple fluid mechanics relation. As stated in the assumptions, the two-dimensional laminar jet equations do not describe the velocity profiles near a nozzle exit. This is due to the presence of a development section and because the slit is not infinitesimal and the exit velocity is not therefore infinite. Instead it has been found that the midplane velocity distribution can be reasonably well described by fitting a bell-shaped hyperbolic-secant-squared distribution, whose integrated flow per unit depth is equal to the per-unit-depth flow plus entrained flow of the midplane. In explanation, consider that the entrained flow is known, the supply flow is known, and the nozzle exit-velocity distribution is known. The exit-velocity distribution at the midplane will then develop into a jet shape. Hence, the per-unit-depth flow at the midplane is greater than the average flow over the depth. If one considers that the nozzle discharge coefficient  $c_d$  is a product of two terms, one of which is the effect of the side walls and the other the bounding planes,<sup>18,19</sup> then

$$c_d = [1 - 2\delta_1^*/b_s][1 - 2\delta_2^*/(b_s \sigma)] = c_{db_s} \cdot c_{dh} \quad (9)$$

where  $\delta_i^*$  are the exit displacement thickness, and  $c_{db_s}$  and  $c_{dh}$  are the coefficients for the width and height respectively. Under most circumstances the displacement thicknesses are very close in value. Hence, for  $\delta_1^* = \delta_2^*$ :

$$c_{db_s} = (1 - \sigma)/2 + \sqrt{(\sigma + 1)^2/4 - \sigma(1 - c_d)} \quad (10)$$

A jet velocity distribution,  $u = u_{\max} \operatorname{sech}^2 K_1 y/b$  has a flow associated with it of

$$b_s \int_0^\infty u d(y/b_s) = \frac{u_{\max} b_s}{K_1} \tanh K_1 y/b \Big|_0^\infty = \frac{u_{\max} b_s}{K_1}$$

This flow must be equal to the midplane flow which is the entrained flow,  $Q_e$  plus half the midplane per unit height supply flow,

$$c_{db_s} b_s \sqrt{2(P_s - P_v)/\rho} = c_{db_s} b_s u_{\max}$$

$$\frac{u_{\max} b_s}{K_1} = Q_e + c_{db_s} b_s u_{\max}/2 \quad (11)$$

or

$$K_1 = 1/(c_d Q_e/Q_s + c_{db_s}/2) \quad (12)$$

Hence, the velocity distribution at some distance downstream from the nozzle exit is

$$u/u_{\max} = \text{sech}^2 \frac{y/b_s}{(c_d Q_e/Q_s + c_{db_s}/2)} \quad (13)$$

Using the assumption of a laminar two-dimensional jet, the entrained flow  $Q_e$  is shown to be

$$\frac{Q_e}{Q_s} = \frac{1.651}{c_d} (0.021 c_d c_\theta + \frac{c_\theta B_c}{N_R})^{1/3} - \frac{1}{2} \quad (14)$$

To determine the impedance such a profile has to flow, imagine that this flow flows past the downstream edge of the control channel as in figure 6.

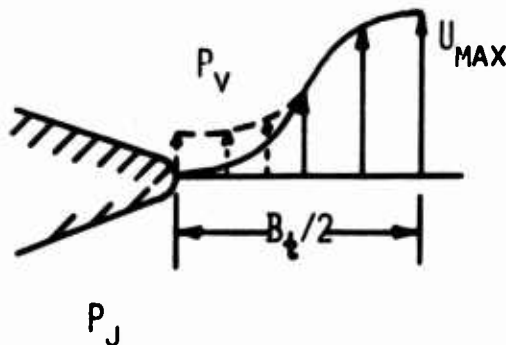


Figure 6. Jet flow past downstream edge of control

If a pressure  $P_j$  is imposed upstream of the edge relative to a vent pressure  $P_v$ , then the velocity profile will change as shown by the dashed outline in figure 6. The additional flow can be determined by noting that adding the static pressure  $P_j$  to the local dynamic head of the profile  $\frac{1}{2} \rho u^2$  results in the new local velocity that will be the square root of the sum or

$$u/u_{\max}|_{P_j = P_v} = \sqrt{(u/u_{\max}|_{P_j = P_v})^2 + P_j/P_s} \quad (15)$$

or simply

$$u/u_{\max}|_{P_j \neq P_v} = [\operatorname{sech}^4 K_1 (y/b_s) + P_j/P_s]^{1/2} \quad (16)$$

The additional flow is just the difference of the integrals of the profile from the point where the total head was equal to the applied pressure  $P_j$  with and without  $P_j$

$$y_o/b_s = [\operatorname{sech}^{-1} [(P_j/P_s)^{1/4}]]/K_1 \quad (17)$$

and

$$Q_v = c_{dh} u_{\max} b_s \int_{y_o/b_s}^{B_t/2} [u/u_{\max}|_{P_j > P_v} - u/u_{\max}|_{P_j = P_v}] d(y/b_s) \quad (18)$$

where  $c_{dh}$  is used to decrease the flow due to the presence of the bounding surfaces. Normalizing with the supply flow  $Q_s = c_d b_s \sqrt{2(P_s - P_v)}/\mu = c_d b_s u_{\max}$  results in

$$Q_v/Q_s = \frac{c_{dh}}{c_d} \int_{y_o/b_s}^{B_t/2} \{[\operatorname{sech}^4 K_1 (y/b_s) + P_j/P_s]^{1/2} - \operatorname{sech}^2 K_1 y/b_s\} d(y/b_s) \quad (19)$$

Note that  $c_d/c_{dh} = c_{db_s}$ . The impedance then is the ratio of the applied static pressure  $(P_j - P_v)$  to  $Q_v$  or normalized

$$R_v/R_s = \frac{c_{db_s} P_j/P_s}{B_t/2} \int_{y_o/b_s} \{[\operatorname{sech}^4 K_1 (y/b_s) + P_j/P_s]^{1/2} - \operatorname{sech}^2 K_1 (y/b_s)\} d(y/b_s) \quad (20)$$

For aspect ratios from 0.5 to 2.0 and  $B_t = 2.0$ , for  $N_R$  from 250 to 2000 and for  $P_j > .02 P_s$ ,  $K_1$  varies from 2.0 to 2.175 and the term

$$\frac{R_v/R_s}{C_{db_s}} = \text{const} = 1.1 \quad (21)$$

This explains why several investigators<sup>15-17</sup> have found the jet-centered impedance to be quite linear, since the viscous contribution  $R_c/R_s$  is mostly linear and the clearance impedance  $R_v/R_s$  is linear.

This model can be justified by seeing what happens physically as a pressure is applied simultaneously to both sides of a jet. Flow starts to enter the vent and increases with increasing pressure. If one thought of the jet as a semi-rigid or compliant body, one would expect it to be squeezed down as the pressure increases, thus "opening" up the space between the jet and the control edge, allowing more flow to pass. If the space were considered an orifice, the resistance would increase with increasing  $P_j$  and decrease with increasing spacing. The net effect would be a cancellation of sorts. Experience indicates that the impedance is quite constant so that cancellation is complete. As suggested above, the impedance is a constant at a given Reynolds number and decreases slightly with decreasing Reynolds number. This is expected, since the jet flow is "softer" at the lower Reynolds numbers so it is easier to "push" flow through to the vent.

In a somewhat simple approach to defining a jet edge, the location of the jet entrainment streamline can be determined fairly readily. The value of this becomes apparent when later determining the lower limits of the amplifier operation.

The distance from the control edge to the jet edge is hard to define since the flow is three-dimensional and one does not expect to have the same width near the bounding surfaces as at the midplane. However, based on the assumption that the jet spreads linearly, the following arguments can be made: Consider that the virtual origin of a laminar jet can be defined by equating the flow in the two-dimensional jet (Schlichting,<sup>21</sup> eq. 9.62, p. 168) to the efflux from the nozzle from equation 2.<sup>22,23</sup> The virtual origin is the apex of the diverging boundary of the jet as shown in figure 7; hence, from geometric relations the distance from this jet edge and the downstream control edge  $B_v$  can be calculated.

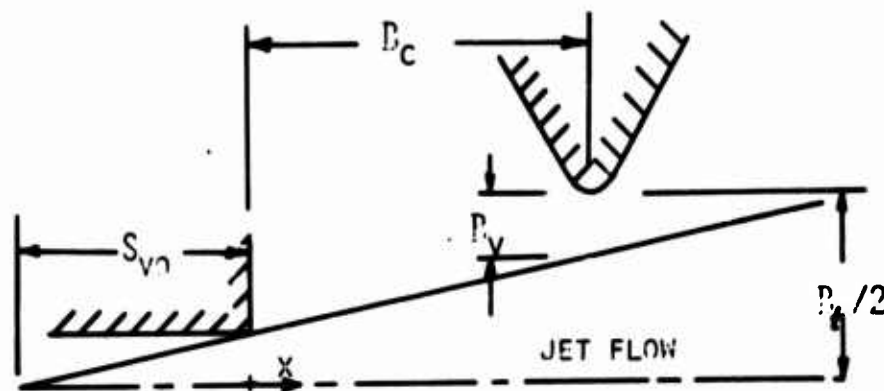


Figure 7. Definition of two-dimensional jet virtual origin

The expression for virtual origin distance,  $S_{vo}$  is

$$S_{vo} = 0.0278 \frac{c_d^3}{c_\theta} N_R \quad (22)$$

where  $c_\theta$  is the momentum-flux discharge coefficient. Therefore, the expression for the spacing between the jet entrainment streamline and the downstream control edge  $B_v$  is

$$B_v = \frac{1}{2} [B_t - 1 - B_c / (0.0278 c_d^3 N_R / c_\theta)] \quad (23)$$

The relationship for  $c_\theta$  is found to be such that  $c_\theta \sim c_d^2$ . Since  $c_d$  is a function only of  $N_R'$  then  $c_\theta$  must also be only a function of  $N_R'$ ; hence, a determination of  $c_\theta$  vs  $c_d$  at one value of aspect ratio can be related to all aspect ratios through  $N_R'$ , the modified Reynolds number. For large  $N_R'$ , the expression for  $c_\theta$  can be obtained from boundary layer considerations. Assuming as before that the boundary layers are roughly



equal on all sides and that  $\delta^*/\theta = 2.554$  then<sup>++</sup>

$$c_\theta = (1 - 2.783 \delta^*/b_s)(1 - 2.783 \delta^*/b_s \sigma) \quad (24)$$

where

$$\delta^*/b_s = \frac{\sigma + 1}{4 \sigma^2} - \sqrt{\frac{(\sigma + 1)^2}{16 \sigma^4} - (1 - c_d) \frac{\sigma}{4}} \quad (24a)$$

If the flow is completely fully developed through the nozzle (e.g.  $l_R$  is low) then, by assuming parabolic vertical and horizontal velocity profiles, the momentum flux discharge coefficient is

$$c_\theta = 1.15 c_d^2 \quad (25)$$

As a rule of thumb even for the most efficient nozzles, laminar amplifiers rarely operate with  $c_d > 0.75$ , hence a comparison of equations 24 and 25

at  $\sigma = 1$  reveals only a small discrepancy over the range  $0 \leq c_d \leq 0.75$ .

Since equation 24 is probably valid at the high end and equation 25 at the low end, an average value curve can be struck. Hence

$$c_\theta = 1.32 c_d^2 \quad (26)$$

Equation 26 satisfies the condition that  $c_\theta \rightarrow 0$  as  $c_d \rightarrow 0$  as expected.

Equation 23 for the jet-control edge space thus becomes

$$B_v = \frac{1}{2} [B_t - 1 - B_c / (0.021 c_d N_R)] \quad (27)$$

The validity of equation 27 is demonstrated by agreement with the experimental data of Spyropoulos<sup>17</sup>. In figure 8 data is shown for the space between the jet edge dye stream shown in reference 17 as a function of flow Reynolds number,  $N_{R0} = c_d N_R$ . The theory agrees very well over the entire range, even at low  $N_R$  if that data is corrected to a linear spread value.

<sup>++</sup> In the same way the discharge coefficient is defined, momentum-flux discharge coefficient,  $c_\theta$  is defined by reducing the nozzle dimensions by the sum of the displacement  $\delta^*$  and momentum thickness  $\theta$ ,<sup>18</sup> so that

$$c_\theta = (1 - 2(\delta_1^* + \theta_1)/b)(1 - 2(\delta_2^* + \theta_2)/h)$$

where subscripts 1 and 2 refer to boundary layers on the side and plane walls.

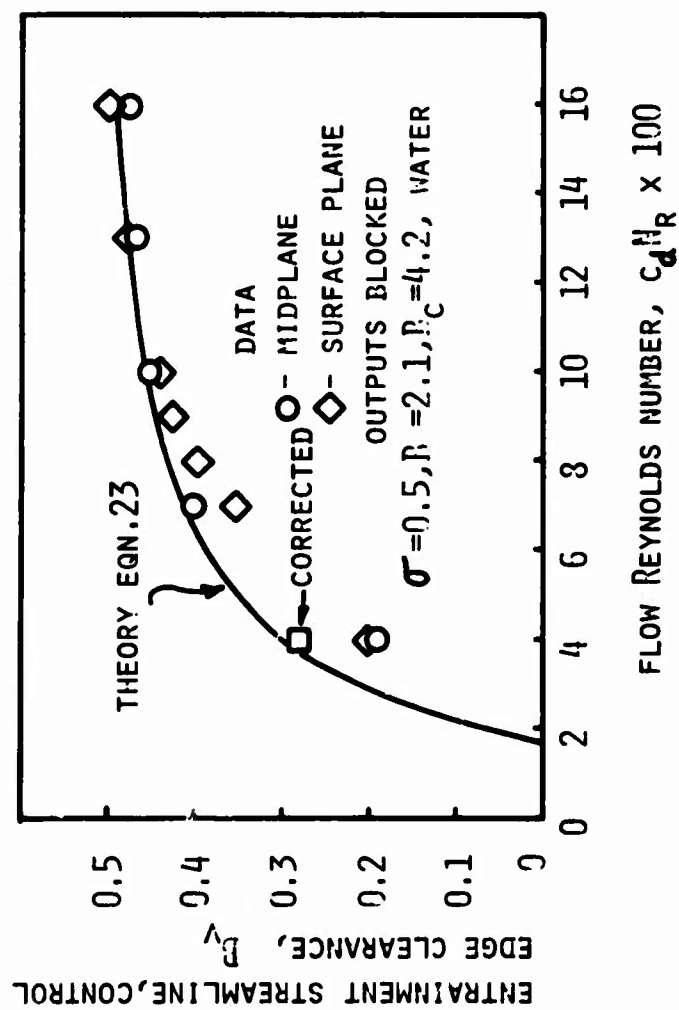


Figure 8. Comparison of experimentally determined location of jet entrainment streamline with theory

## 2.5 Analysis of Amplifier Jet Deflection Gain and Dynamics

The analysis presented in this section is based on a control volume model of the amplifier input flow field shown in figure 2 and is limited to a small-signal analysis that uses small perturbations in order to linearize the flow equations.

The control volume model is actually a one-dimensional model of the flow field and can be shown schematically as an equivalent electrical circuit (fig. 9). Since this is a one-dimensional linearized model of a complex flow field, it can only be used for small-signal analysis. In this model the electrical current analog is volume flow rate and the voltage analog is pressure.

In the analysis, input flows, entrainment flows and the flows through the downstream vent passage are included, along with the apparent jet capacitance due to the volume swept out as the jet is laterally deflected. This jet capacitance is shown in figure 9 in parallel with a leaking resistance due to flow through the jet surface boundary layers. This leaking resistance can be neglected since it is usually much larger than the resistance to the downstream control vent.

In calculation of the dynamic frequency response, Manion and Mon<sup>15</sup> have shown that the inertia of the fluid in the downstream control vent passage can be neglected if the bandwidth calculation extends only to the initial break frequency. Experiments have confirmed that the input control inertia coupled with the jet displacement capacitance does predict the break frequency quite accurately (section 3). The actual break frequency depends on the bias pressure and this will be shown in the calculation of the amplifier frequency response.

The analysis first calculates the jet's pressure gain by calculating the deflection of the jet with control pressure signal; then the bias sensitivity is determined from this model. The underdamped or overdamped response depends on bias level and an example calculation of this effect is given. The analysis is then used to determine the input characteristic impedance for the centered jet and for the deflecting jet stream, with some sample calculations and test data. From these analyses, the amplifier's gain sensitivity to bias level, its frequency response (bandwidth and damping) and its deflection input impedance can be estimated.

### 2.5.1 Jet Deflection Gain

Manion and Mon show that the jet deflection gain depends on the quotient  $\delta/\Delta P_c$  -- the deflection of the jet at the downstream edge of the control nozzle divided by difference between the pressures of each input control port. The pressure gain is given<sup>15</sup> as

$$\frac{\Delta P_o}{\Delta P_c} = \frac{\Delta P_o}{\Delta y_o} \frac{\Delta y_o}{\Delta P_c}$$

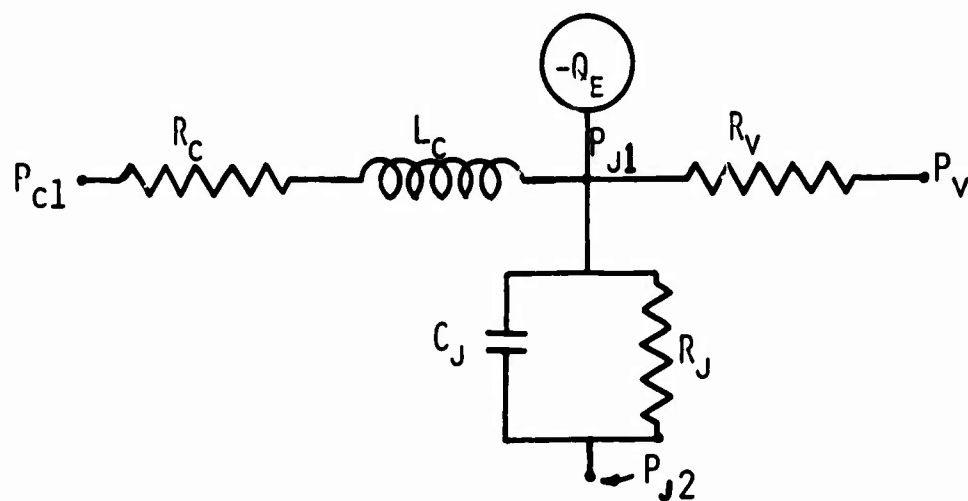


Figure 9. Dynamic equivalent circuit for LPA input

where

- $\Delta P_o$  - difference in amplifier output pressure
- $\Delta P_c$  - difference in amplifier input control port pressure
- $\Delta y_o$  - jet deflection at receiver entrance

The jet's deflection  $\Delta y_o$  is also given as

$$\Delta y_o = (2 X_{sp}/B_c - 1)\delta$$

where

- $X_{sp}$  - total length separating supply nozzle and receiver entrance
- $B_c$  - total length of control nozzle measured along the supply jet's axis
- $\delta$  - deflection of the jet at downstream edge of control nozzle.

The analysis that follows will be a refined analysis to determine the amplifier response. In this section, all quantities are normalized.

Using figure 9, the summation of flow equation is written to determine the ratio of the jet deflection to input signal pressure. This summation is given in flows that are normalized by the actual supply flow in equation 28:

$$\frac{P_{c1} - P_{j1}}{Z_c} - Q_e - \frac{\delta}{c_d} \sqrt{P_{j1} - P_v} \operatorname{sgn}(P_{j1} - P_v) - \frac{P_{j1} - P_v}{R_v} = \gamma_j (P_{j1} - P_{j2}) \quad (28)$$

where  $P_c$  is the control pressure,  $P_j$  is the jet edge pressure and  $P_v$  are the vent pressure normalized by  $P_s$  supply pressure.

$\frac{P_{c1} - P_{j1}}{Z_c}$  - is the input flow, and  $Z_c$  is the input channel impedance normalized by  $R_s$ .

$Q_e$  - net entrainment flow due to fluid shear and spillback.

$\delta \sqrt{P_{j1} - P_v} \operatorname{sgn}(P_{j1} - P_v)$  - flow through the downstream control volume vent due to displaced supply-jet stream and the pressure difference

$\frac{(P_{j1} - P_v)}{R_v}$  - flow through the downstream control volume vent due to pressure difference

$Y_j (P_{j1} - P_{j2})$  - flow due to jet capacitative admittance, where  $Y_j = C_j (j\omega)$  and  $C_j = B_c^3 / (12 c_\theta)$ , or the volume swept by jet lateral displacement due to the pressure difference that deflects the jet stream.

$$Z_c = R_c + j\omega L_c, L_c = 2 c_d^2 X_c / B_c \text{ (normalized by } R_s)$$

For the jet centered, this equation applies to each control volume--one on each side of the jet stream--and  $\delta$  is zero.

Perturbing equation 28 with respect to  $\delta'$ , we obtain equation 29, where primed quantities are small perturbations; (note,  $P_{j1} = P_{j1} + P_j'$ ,  $P_{j2} = P_{j2} - P_j'$ ) and terms with  $\delta'^2$  are neglected.

$$\begin{aligned} \frac{1}{Z_c} \left( \frac{P_{c1}'}{\delta'} - \frac{P_{j1}'}{\delta'} \right) - \frac{Q_{e1}'}{\delta'} - \frac{1}{R_v} \frac{P_{j1}'}{\delta'} - \frac{\sqrt{(P_j - P_v)} \operatorname{sign}(P_j - P_v)}{c_d} \\ - \frac{\delta}{2 c_d \sqrt{|P_j - P_v|}} \operatorname{sign}(P_j - P_v) = 2 Y_j P_j' / \delta' \end{aligned} \quad (29)$$

The jet deflection,  $\delta'$  is proportional to the difference in control volume pressure therefore

$$\delta' = 2 k_j P_j' \quad (30)$$

where  $k_j = B_c^2 / 4 c_\theta$

$c_\theta$  - is the momentum flux discharge coefficient.

This deflection equation assumes that the change in  $P_j$  with time is small when compared to the jet stream's transport time between the control volumes.

$$\frac{\Delta P_c}{\delta} = \left\{ \frac{k_j}{[1 + a_1 k_j Z_c + Y_j Z_c + Z_c/R_v + \frac{2k_j Z_c (P_j - P_v)}{c_d \sqrt{|P_j - P_v|}} + \frac{\delta Z_c \operatorname{sgn}(P_j - P_v)}{2 c_d \sqrt{|P_j - P_v|}}]} \right\}^{-1} \quad (31)$$

for  $P_j - P_v \neq 0$ .

For zero frequency and small deflections  $Z_c = R_c + jL_c \omega + R_c$  and  $Y_j = 0$

$$\delta|_{\omega=0} = \frac{k_j P_c'}{1 + a_1 k_j R_c + R_c/R_v + \frac{2k_j R_c (P_j - P_v)}{c_d \sqrt{|P_j - P_v|}} + \frac{\delta R_c \operatorname{sgn}(P_j - P_v)}{2 c_d \sqrt{|P_j - P_v|}}} \quad (32)$$

As equation 32 indicates, the amplifier's jet deflection gain is jet bias-pressure ( $P_j - P_v$ ) sensitive, and this sensitivity depends on one term for a centered jet,  $\delta = 0$ . This term is the product of the deflection scale factor,  $k_j$  and  $R_c (P_j - P_v)/\sqrt{|P_j - P_v|}$ .

For negative bias pressure ( $P_j - P_v$ ) this term tends to cause instability, whereas the vent clearance term  $R_c/R_v$  stabilizes the jet's lateral position. As this clearance term is increased by increasing  $B_t$ , the bias sensitivity is reduced and the jet's position is more stable for negative jet edge pressures. However, larger vent width results in larger non-deflecting power drain.

Bias can be adjusted by choice of either  $P_j$  or  $P_v$ .

The coefficient  $a_1$  defines the rate of change of the difference in net entrained flow on either side of the jet as it is being deflected. The net entrained flow is simply the flow that is required by the jet to satisfy entrainment over that which is spilled back by the control edges. Therefore

$$a_1 = \frac{\partial \Delta Q_{enet}}{\partial \delta} = \frac{\partial (\Delta Q_e - \Delta Q_{SB})}{\partial \delta} = \frac{\partial \Delta Q_e}{\partial \delta} - \frac{\partial \Delta Q_{SB}}{\partial \delta} \quad (33)$$

The change in entrained flow with deflection is negligible as can be determined from the two-dimensional jet equations. (Reference 24 gives a complete analysis to show that entrainment differences are negligible)

$$a_1 \text{ is therefore } -\partial \Delta Q_{SB} / \partial \delta = \left. \frac{\partial Q_{SB}}{\partial \delta} \right|_{+\delta} - \left. \frac{\partial Q_{SB}}{\partial \delta} \right|_{-\delta} = 2 \frac{\partial Q_{SB}}{\partial \delta}$$

The velocity profile in the midplane has been found, as in equation 13 to be

$$u/u_{max} = \text{sech}^2 K_1 (y/b_s)$$

and as in the previous section the flow in the profile between any two points for  $P_j = P_v$  is:

$$Q/Q_s = \frac{1}{c_{db_s}} \int_{y_1/b_s}^{y_2/b_s} \text{sech}^2 K_1 (y/b_s) d(y/b) = \frac{1}{c_{db_s} K_1} (\tanh K_1 y_2/b_s - \tanh K_1 y_1/b_s)$$

The flow spilled back is the flow in the profile from  $B_t/2$  to  $\infty$ , hence

$$Q_{SB}/Q_s = \frac{1}{c_{db_s} K_1} [1 - \tanh (K_1 B_t/2)] \quad (34)$$

and as a function of a jet deflected through  $\pm \delta$ ,

$$Q_{SB}(\delta)/Q_s = \frac{1}{c_{db_s}} [1 - \tanh K_1 (B_t/2 \pm \delta)] \quad (35)$$

The derivative of this relationship is simply

$$\frac{\partial Q_{SB}}{\partial \delta} = - \frac{1}{c_{db_s}} \text{sech}^2 K_1 (B_t/2 \pm \delta) \quad (36)$$

Evaluated for the centered jet condition  $\delta = 0$  equation 36 becomes



$$\left. \frac{\partial Q_{SB}}{\partial \delta} \right|_{\delta=0} = - \frac{\text{sech}^2 (K_1 B_t/2)}{c_{db_s}} \quad (37)$$

and

$$a_1 = - 2 \left. \frac{\partial Q_{SB}}{\partial \delta} \right|_{\delta=0} = 2 [\text{sech}^2 (K_1 B_t/2)] / c_{db_s} \quad (38)$$

for

$$K_1 = 1 / (c_d Q_e / Q_s + c_{db_s} / 2)$$

and

$$c_{db_s} = (1 - \sigma) / 2 + \sqrt{(\sigma + 1)^2 / 4 - \sigma (1 - c_d)}$$

A typical value for  $a_1$  for  $K_1 = 2.175$ ,  $c_{db_s} = 0.89$  ( $N_R = 2000$ ,  $\sigma = 0.5$ ,  $c_d = 0.7$ ), and  $B_t/2 = 1.0$  results in  $a_1 = 0.1135$ .

To relate the jet deflection-gain bias sensitivity to the input-control port pressure, flow equation 28 is used. Solving equation 28 for  $P_c$  in terms of  $P_j$ , equation 39 can be obtained for zero frequency.

$$P_c = P_j + R_c \left[ Q_e + \frac{P_j - P_v}{R_v} \right] \quad (39)$$

or simply  $P_c = P_j + R_c Q_c$

where  $R_c = R_{cl} + K_c |Q_c|$ , a linear and a nonlinear part

and  $Q_c = Q_e + (P_j - P_v) / R_v$

The jet edge pressure  $P_j$  can be readily expressed in terms of  $P_c$ ,

$$P_j = P_c \left( \frac{R_v}{R_v + R_c} \right) - \left( \frac{R_v R_c}{R_v + R_c} \right) Q_e + \frac{R_c}{R_v + R_c} P_v \quad (40)$$

or

$$P_j = P_c \left( \frac{R_v}{R_v + R_c} \right) - \left( \frac{R_v R_c}{R_v + R_c} \right) Q_e \text{ for } P_v = 0 \text{ (Gage).}$$

Equation 40 can be used with equation 32 for  $R_v = 1$ ,  $R_c = R_{cl} + K_c |Q_c|$   
 (from measurement  $R_c = 0.1312 \frac{P_s}{Q_s}$ ) and the entrainment flow,  $Q_c = 0.04 Q_s$ .

Using the above equations, the total amplifier pressure-gain .  
 ( $\delta = 0$ ) is

$$\frac{\Delta P_o}{\Delta P_c} = \frac{\Delta P_o}{\Delta y_o} \cdot \left( \frac{X_{sp}}{B_c} - 1 \right) \cdot$$

$$k_j / \{ [1 + Z_c [a_1 k_j + 2Y_j + 1/R_v + (2k_j(P_j - P_v) + \delta \text{sgn}(P_j - P_v)) / (c_d \sqrt{P_j - P_v})]] \}$$

(41)

Assuming that  $\frac{\Delta P_o}{\Delta y_o} = 1$  equation (41) is shown plotted in fig. 10 for

$R_v = \frac{P_s}{Q_s}$ ,  $k_j = 6.18$ ,  $a_1 = 0.0668$  and  $P_v = 0$ , as a function of  $P_c$ .

### 2.5.2 Frequency Response Estimate

To estimate the frequency response of the jet deflection amplifier it is assumed that the primary low frequency terms result from the input impedance and the dynamics of the jet pressure field. This is certainly true for low pressure amplifiers such as the first stage of a multistage gain block. If the flows are all divided by the actual supply flow, the pressures by supply jet pressure, and time by the quotient of the supply nozzle width to the average supply jet velocity, then the governing equations are normalized and become more manageable from a numerical standpoint.  $Z_c$  is taken as  $R_c + j\omega L_c$  and  $Y_j = j\omega C_j$  where  $L_c$  is the control line inertance and  $C_j = B_c^3 / 12 C_\theta$ . As noted earlier, the impedance between the control volume and vent is assumed to be resistive in the frequency range of this amplifier configuration.

Equation 31 is used to estimate the frequency response by evaluating the denominator of this jet deflection equation. From equation 41 for  $\delta = 0$

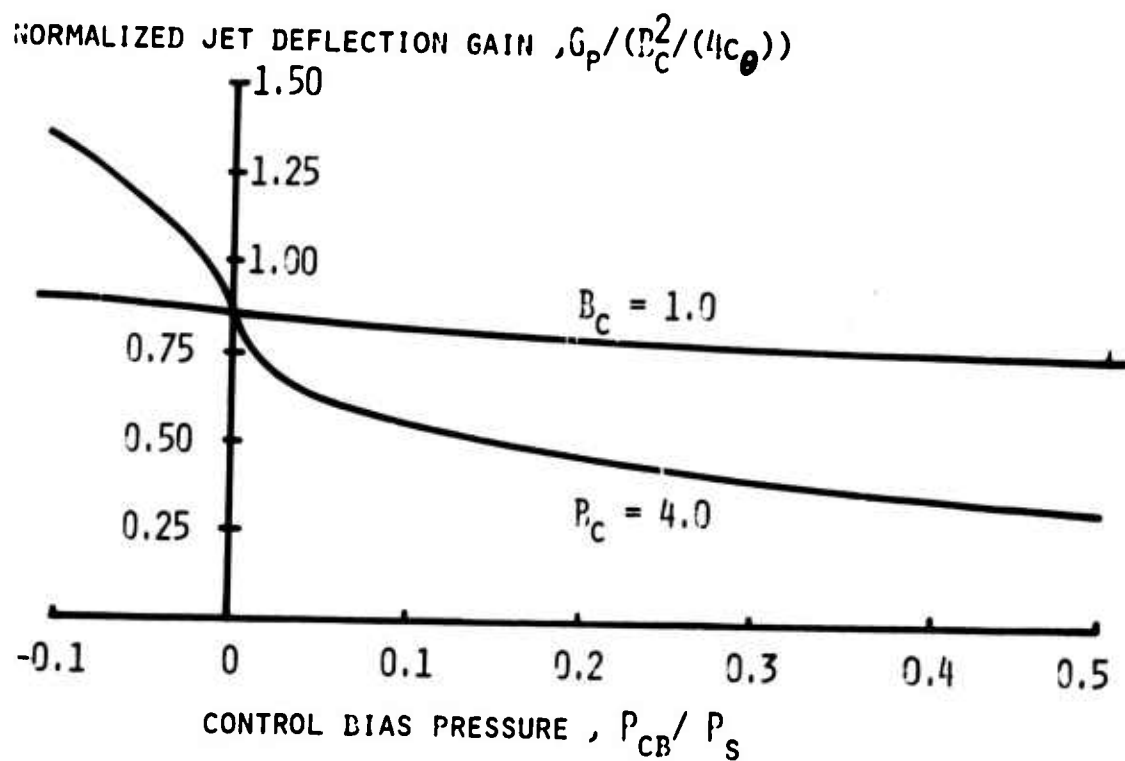


Figure 10. Jet deflection gain versus control bias pressure

$$\frac{\Delta P_o}{P_c} = \frac{\Delta P_o}{\Delta y_o} \cdot \left( \frac{2 X_{sp}}{B_c} - 1 \right) \left( \frac{k_j}{A_2 j \omega^2 + A_1 j \omega + A_o} \right), \quad (42)$$

where

$$A_o = 1 + a_1 k_j R_c + R_c/R_v + 2 k_j R_c (P_j - P_v)/(\sqrt{|P_j - P_v|})$$

$$A_1 = a_1 k_1 L_c + L_c/R_v + 2 k_j L_c (P_j - P_v)/(\sqrt{|P_j - P_v|})$$

$$A_2 = 2 L_c C_j$$

The response characteristic is normalized in the same way as in reference 15 so that

$$f_{bw} = \frac{k_1}{2\pi} \frac{c_d U_s}{b_s} \quad \text{where } F = f/(c_d V_s/b_s)$$

where

$$k_1^2 = \frac{1}{2 L_c C_j} \left[ 1 + a_1 k_j R_c + (R_c/R_v) + 2 \frac{k_j R_c}{c_d} \frac{(P_j - P_v)}{\sqrt{|P_j - P_v|}} \right]$$

$U_s$  - supply velocity,  $\sqrt{2(P_s - P_v)/\rho}$

$c_d$  - discharge coefficient

$f_{bw}$  - corner frequency in Hz.

A few sample calculations show that for negative and even some positive bias the jet deflection response is underdamped. As the bias is made positive the response becomes more damped, and the resonant frequency increases. However, in an overdamped 2nd-order system the phase lag is actually increased at low frequency over the undamped system.

Calculating the estimated response for the amplifier at 10% control bias and at zero control bias using equation 42 with  $c_0 = 0.64$ ,  $a_1 = 0.0668$ ,  $R_v = 1$  and  $Q_e = 0.04$  for  $P_c = 0.10$  and  $P_j = +0.0773$  the denominator of equation 42 can be factored to  $(s + .032)(s + .265)$ . The lowest normalized frequency is  $\omega_{bw} = .032$  or  $F_{bw} = \frac{\omega_{bw}}{2\pi} = .0050$ . For  $P_c = 0.0$  and  $P_j = -0.006$  the denominator is  $(s^2 + 2\xi\omega_n s + \omega_n^2)$  where  $\omega_n = 0.0738$ ,  $F = 0.0117$  and the damping ratio,  $\xi = 0.185$ . These two responses are shown plotted in figure 11. At a value of jet edge pressure  $P_j = -.00746$ , ( $P_c = -.00175$ ) the jet will oscillate since  $A_1 = 0$ . In designs where  $R_c$  is larger,  $P_j$  can be more negative before zero damping is encountered.

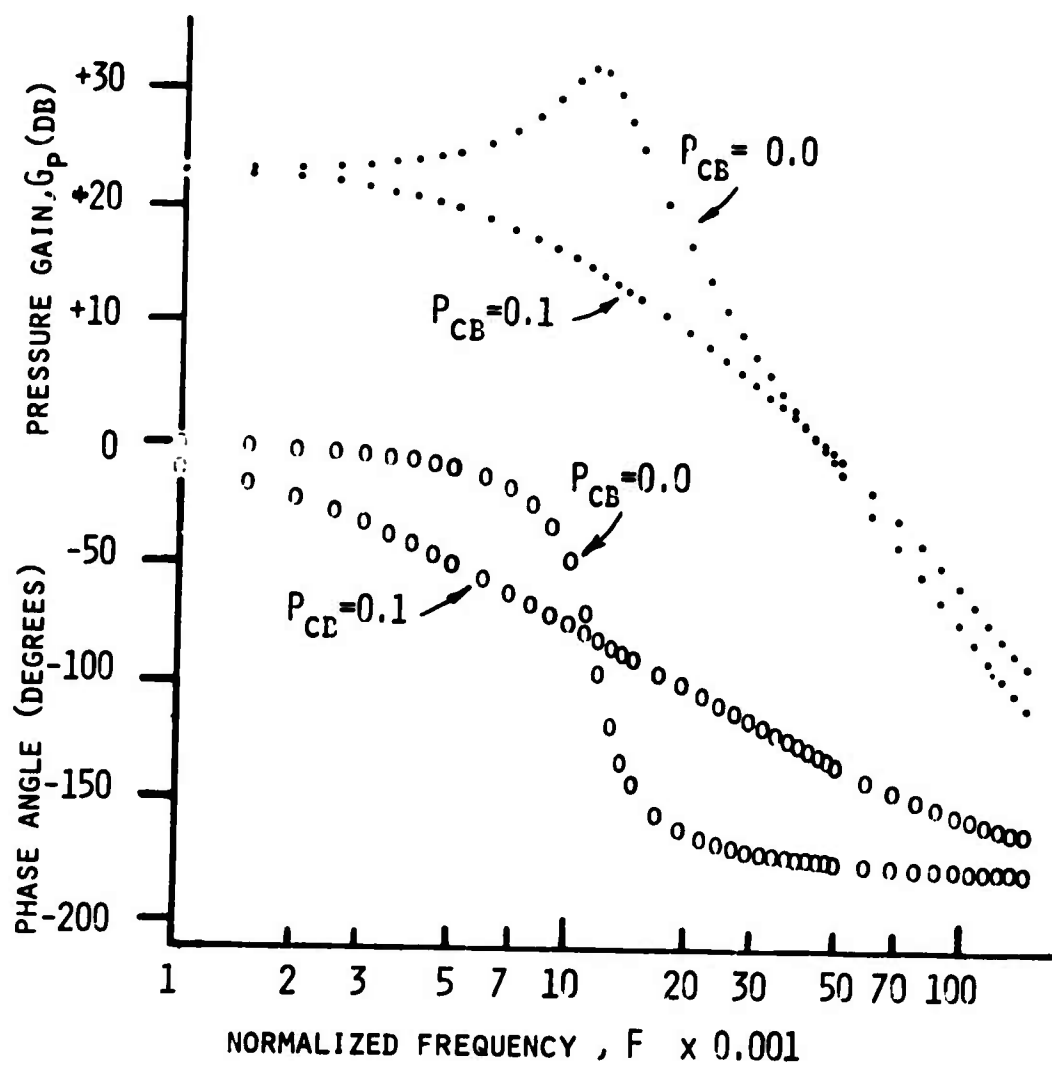


Figure 11. Jet deflection gain versus frequency, showing bias effects

The important point of this section is to show the dependence of frequency response characteristic on bias level for this amplifier.

### 2.5.3 Input Impedance

The input impedance of the amplifier is very important in design and staging of amplifier cascades. This jet deflection amplifier has two impedances that are important, the centered jet impedance and the deflection impedance. The centered jet impedance can be easily calculated by computing the pressure flow characteristic for a non deflecting centered jet as in section 2.4. Using a given bias level on this centered jet input characteristic the deflection impedance for small signals ( $\Delta P_j$  small compared to  $P_j$  level) or small deflections can be computed. This deflection impedance depends on the bias pressure and varies as the operating point is changed.

### 2.5.4 Centered Jet Impedance

The pressure flow relationship for the centered jet can be determined by first calculating the flow as a function of the control volume, jet edge pressure and then computing the input control pressure using the jet edge pressure, the flow and input resistance.

The relationship is given in equation 39 as

$$P_c = P_j + R_c Q_c \quad (39)$$

where

$$R_c = R_{c\ell} + K_c |Q_c|$$

and

$$Q_c = Q_e + \frac{P_j - P_v}{R_v}$$

Expanding equation 39, the centered jet resistance can be evaluated from the pressure flow equation as

$$P_c = P_j + R_{c\ell} \left( Q_e + \frac{P_j - P_v}{R_v} \right) + K_c \left[ \left( Q_e + \frac{P_j - P_v}{R_v} \right) \times \left( Q_e + \frac{P_j - P_v}{R_v} \right) \right] \quad (43)$$

$$P_c/Q_c = [1 + R_c/R_v] [Q_e/P_c + 1/R_v] \quad (43a)$$

For non-zero frequencies, substitute  $Z_c$  for  $R_c$  since  $P_c = P_j + R_c Q_c + L_c \dot{Q}_c = P_j + Z_c Q_c$ .

### 2.5.5 Deflected Jet Impedance

Equation 32 relates  $\delta$ , the control volume jet deflection, to the difference in input port pressure (for small signals). To determine an impedance, the relationship between the difference in input flows and

$\delta$  is required. The impedance is  $\frac{\Delta P_c}{\Delta Q_c} = \frac{\Delta P_c}{\delta T} \times \frac{\delta}{\Delta Q_c}$  and can be calculated

if  $\frac{\delta}{\Delta Q_c}$  can be determined since  $\frac{\Delta P_c}{\delta T}$  is given in equation 32 or equation 30.

The relationship between jet deflection and flow signal is obtained in the same way equations 30 and 32 were obtained. In equation

28,  $\frac{P_c - P_j}{Z_c}$  is the input flow; therefore, using equation 28 but writing

$Q_c$  instead of  $\frac{P_c - P_j}{Z_c}$  equation 28 becomes

$$Q_c - Q_e - (P_j - P_v)/R_v - \frac{\delta}{c_d} \sqrt{|P_j - P_v|} \operatorname{sgn}(P_j - P_v) = Y_j P_{j1} - P_{j2} \quad (44)$$

Developing this equation in the same manner as before by perturbation, the following equation 45 is obtained

$$\frac{\delta'}{\Delta Q_c} = \frac{1}{a_1 + 2Y_j + 1/R_v + \frac{2(P_j - P_v)}{c_d \sqrt{|P_j - P_v|}} + \frac{\delta k_j \operatorname{sgn}(P_j - P_v)}{c_d \sqrt{|P_j - P_v|}}} \quad (45)$$

The product of this equation and equation 31 gives the desired impedance relationship.

$$\frac{\Delta P_c}{\Delta Q_c} = \frac{Z_c \left[ 1 + a_1 k_j Z_c + \frac{Z_c}{R_v} + \gamma_j Z_c + \frac{2 k_j Z_c (P_j - P_v)}{c_d \sqrt{P_{j1} - P_v}} + \frac{\delta Z_c \operatorname{sgn}(P_j - P_v)}{c_d 2 \sqrt{P_j - P_v}} \right]}{\left[ a_1 k_j Z_c + \frac{Z_c}{R_v} + \gamma_j Z_c + \frac{2 k_j Z_c (P_j - P_v)}{c_d \sqrt{P_j - P_v}} + \frac{\delta Z_c (\operatorname{sgn}(P_j - P_v))}{2 c_d \sqrt{P_j - P_v}} \right]} = Z_i \quad (46)$$

For zero frequency and a centered jet the deflection resistance is

$$R_i = \frac{\Delta P_c}{\Delta Q_c} = R_c \left\{ \frac{1 + a_1 k_j R_c + \frac{R_c}{R_v} + \frac{2 k_j R_c (P_j - P_v)}{c_d \sqrt{P_j - P_v}}}{a_1 k_j R_c + \frac{R_c}{R_v} + \frac{2 k_j R_c (P_j - P_v)}{c_d \sqrt{P_j - P_v}}} \right\} \quad (47)$$

### 2.5.6 Bias Sensitivity

The bias sensitivity of the LPA is the result of the deflection impedance of the jet. Equations 31 and 32 illustrate this effect

in the resistances  $\frac{1}{2 k_j \sqrt{P_j - P_v}}$  and  $\frac{2 \sqrt{P_j - P_v}}{\delta}$ . As these resistances

change, the ratio of  $P_j$  to  $P_c$  changes and the gain changes since  $P_c \cdot (P_{j1} - P_{j2}) / P_c \cdot k_j = \delta$ . In the deflection equation these terms are multiplied by the inlet line impedance so if  $Z_c$  approaches zero the bias sensitivity approaches zero. This is a trivial solution to the problem since it implies a zero deflection impedance. In equation 32, note that at large values of  $P_j - P_v$  or at large deflections the deflection impedance approaches  $Z_c$  -- somewhat obvious since this is the minimum impedance of the inlet to vent.

For a centered jet, the deflection scale factor  $k_j$  is the primary parameter that determines the bias sensitivity. This is shown in the above equations, especially if the denominator of equation 46



is rearranged in the form  $1 + \frac{2 k_j Z_c \sqrt{(P_j - P_v)/c_d}}{1 + a_1 k_j Z_c + Z_c/R_v}$ . The jet deflection constant  $k_j$  depends on  $B_c^2$  and inversely on  $c_\theta$ . As the discharge coefficient is increased the bias sensitivity is decreased. More significant is the reduction of bias sensitivity as  $B_c$  is decreased.

The tradeoff between bias sensitivity, deflection gain and deflection impedance is that a reduction of deflection gain is required in order to reduce bias sensitivity and to increase the deflection impedance. This can be done by a reduction of  $B_c$ . As an example, amplifiers with  $B_c = 4$  and  $B_c = 1$  have been designed and built. For  $B_c = 4$ ,  $k_j$  is 6.18 (if  $c_\theta = 0.64$ ) and for  $B_c = 1$ ,  $k_j$  is 0.39. This is a factor of 16; but since the scale factor is less, approximately three times the control pressure is needed to fully deflect the jet to saturation. Since pressure level affects bias as a square root, the bias reduction is actually  $\frac{16}{\sqrt{3.2}} \approx 9$ . However, when an element is built with  $B_c = 1$ ,  $R_c$  is somewhat larger due to the convergence of the control structure. As a result, a reduction of about 8 in bias sensitivity was expected. Data confirmed that this reduction in bias sensitivity is about what was measured. The effect of bias on the reciprocal of the deflection resistance, for  $B_c = 4$  and  $B_c = 1$  is shown in figure 12. The value approaches a constant at large  $P_{c0}$ .

In staging it is important to note that the driving point impedance is the output impedance of the driving stage plus the inlet line impedance of the driven stage. If an amplifier is driven from a high impedance source it will appear very bias sensitive; whereas, if the amplifier is driven from a low impedance source the bias effect will be minimized. The latter is usually the case where pressure gain devices are cascaded.

The saturation point of the transfer characteristic can be estimated by evaluating equation 46 at various values of  $\delta$  to determine where the term that contains  $\delta$  becomes significant in the deflection gain equation. Figure 13 shows a sample calculation for both positive and negative jet displacement,  $\delta$ . As can be seen the jet deflection impedance decreases when  $\delta > 0$  and increases when  $\delta < 0$ . This means that the deflection characteristics ( $Q_c$  vs  $P_c$ ) will increase in slope above the jet centered case and decrease below. Data will be shown in section 3.

## 2.6 Operating Reynolds Number Range

The information on the control edge clearance can be used to determine the lower limit of amplifier operation. The amplifiers

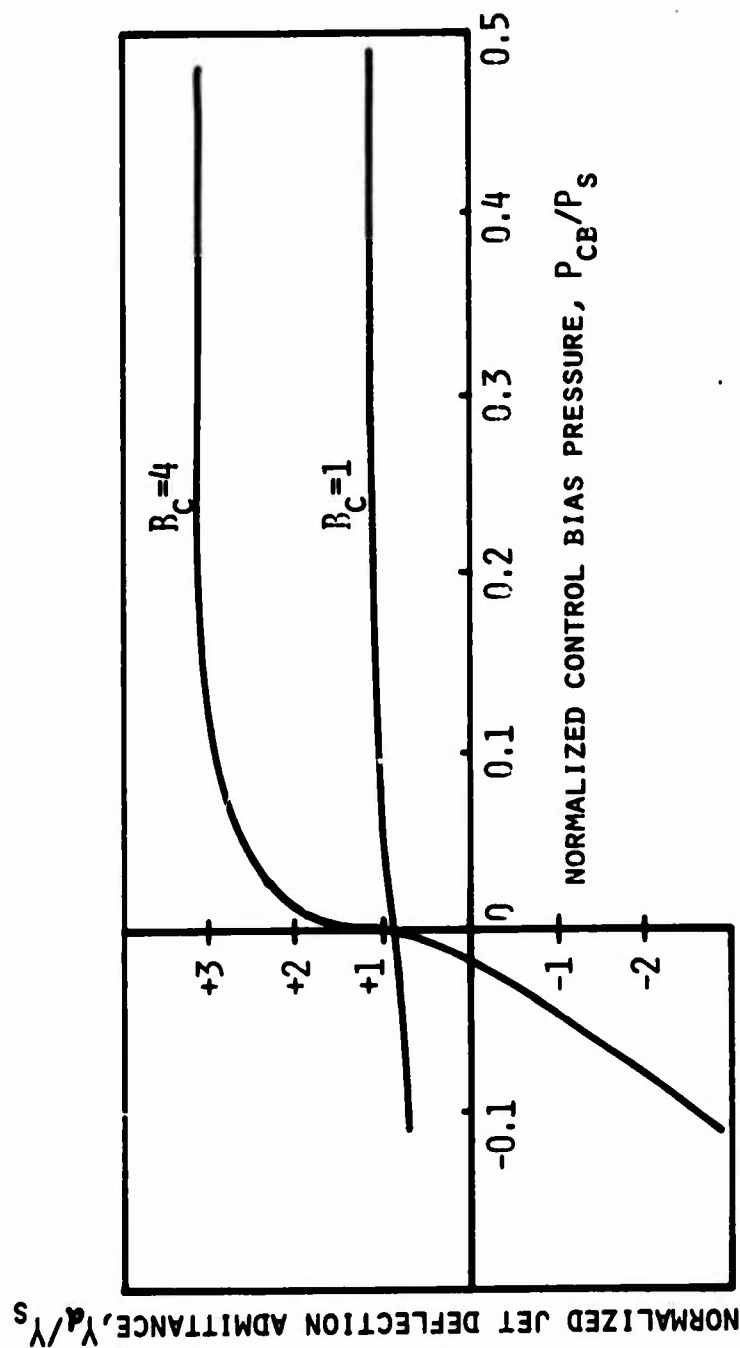


Figure 12. Jet deflection admittance versus control bias pressure

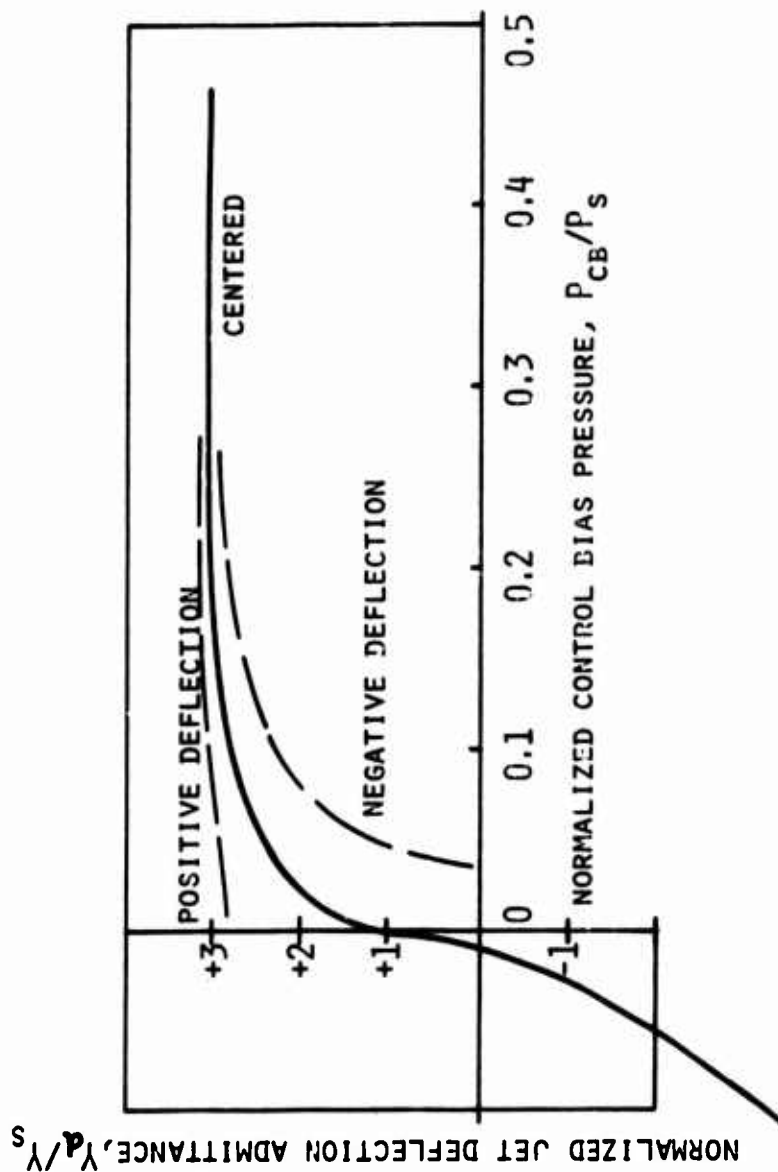


Figure 13. Jet deflection admittance versus control bias pressure showing effects of non-centered jet

normally do not operate properly in the range where downstream effects are felt within the interaction (control) region. The lower limit of operating Reynolds number can thus be defined. Spyropoulos<sup>17</sup> data and other (unreported) data can be used to plot the downstream location where spread is no longer linear,  $X_D$ , (i.e. downstream effects are felt) as a function of flow Reynolds number. The data are shown in figure 14. The two curves presented show that the effects of blocked outputs are felt more than of open outputs. If one models the blocked output condition as a inviscid jet impinging on a flat plate (e.g. flow can only go laterally through the downstream vents) then the location of the point of stream divergence is 2.2 nozzle widths from the plate (splitter). If the open output flow can be modeled as an inviscid uniform flow impinging on a cylinder whose diameter equals the splitter thickness, then the flow will start to diverge at a distance equal to ten times the cylinder radius, so for  $B_{sp} = 0.25$  the distance from the splitter will be  $1.25 b_s$ . If the splitter is  $8 b_s$  downstream, then for the blocked case and high Reynolds number one expects that downstream effects will be felt only up to  $5.8 b_s$  from the nozzle and  $6.75 b_s$  for open outputs. Notice that in figure 14 the measured data is indeed asymptotic to the inviscid solutions. From the data for the worst case, (output blocked) the effects of blockage are felt within the control region ( $X_D < 4$ ) at a flow Reynolds number,  $c_d N_R$  of about 500. This figure then may be used as a guide for determining the lower limit for other configurations by extrapolation. For example if  $B_c = 1.0$  then the lower limit might be about  $c_d N_R = 200$ . From equation 18 the point where there is no clearance can be used if it results in a higher  $c_d N_R$  than the data of figure 14, since the device ceases to function if there is no clearance, because the jet cannot deflect.

The upper limit of Reynolds number is defined by a function of the point of transition-to-turbulence. Drzewiecki<sup>20</sup> has indicated that the Reynolds number for the establishment of fully established turbulence can be determined by noting that the modified Reynolds number  $N_R' = 1000$ . It appears reasonable to assume that the laminar flow limit should perhaps occur at some constant value of  $N_R'$ . The data of Spyropoulos<sup>17</sup> on the flow field and that of Manion and Mon<sup>15</sup> and Mon<sup>16</sup> on gain indicate that the flow becomes noisy or the gain becomes constant at  $N_R' = 100$ . Kelley and Boothe's<sup>5</sup> data, which has been plotted against modified Reynolds number by Drzewiecki<sup>20</sup>, shows that gain becomes constant at  $N_R'' = N_R / (1 + 1/\sigma)^2 = 300$ . For an effective nozzle straight section of roughly  $3.0 b_s$ , this too reduces to  $N_R' = 100$ .

The location of the point of transition in a bounded jet, of  $\sigma = 1$ , can be determined from the equation given by Drzewiecki,<sup>25</sup> which is

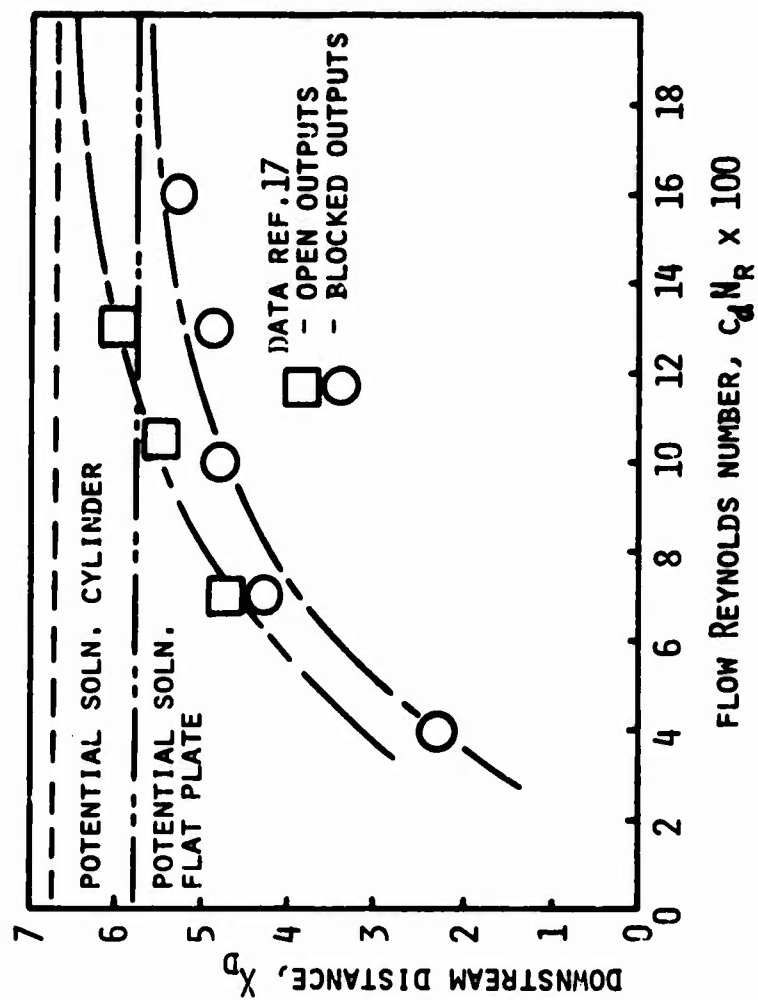


Figure 14. Location of downstream point where downstream effects are first felt

$$N_R (x_{tr}/b_s)^{1/2} c_d^2 = 7000$$

for his bounding-plate size (length  $75 b_s$ , width  $150 b_s$ ). This results in  $N_R' = 193$  for transition to occur for  $c_d = 0.8$  at  $X_{sp} = 8$ . It is reasonable to assume that the same kind of dependence on  $X_{sp}$  exists for fluid amplifiers especially the LPA. Since the data quoted above for LPA's used splitter locations all roughly the same (8-10), it was not surprising that  $N_R'$  was relatively constant.  $N_{R_{tr}}'$  will decrease with increasing  $X_{sp}$ , hence the operating range will be decreased. There is in addition some reason to believe that transition will occur when the edge-tone frequency produced by the jet impinging on the splitter equals the most sensitive frequency of the jet. However, since little or no work has been done in this area for low-aspect-ratio bounded jets, no solutions are presently forthcoming.

The conclusions that can therefore be drawn are that the lower limit of operating Reynolds number is determined by the point where downstream effects are felt in the interaction region and the upper limit by transition where  $N_R' = 100$ . It can be noted here that at least for the case of  $B_c = 4.0$  the lower limit of Reynolds number also corresponds to the point where the amplifier gain is one-half the maximum.

## 2.7 Output Characteristics

The output characteristic of a proportional amplifier is the volumetric output flow versus the output pressure at a given jet position. This characteristic is a measure of the output impedance. Output impedance is dependent on the resistance of the output channel. In most instances the representation for the resistance of the output channel  $R_{oc}$  can be looked upon as a linear term plus an orifice (nonlinear) term,

$$R_{oc} = R_{ol} + K_2 Q_o \quad (48)$$

and in general is computed in the same way as the viscous control impedance in equation 8, with  $B_o$  being the channel width and  $X_o$  the channel length, except that when  $Q_o$  vs  $P_o$  is desired it must be noted that the driving pressure difference for the flow is the difference between the average total pressure  $P_+$  impinging at the receivers and that at the port.

$$\frac{P_+ (Q_o) - P_o}{Q_o} = R_{oc} \quad (49)$$

The average total pressure when  $Q_o = 0$  at the receivers  $P_+$  ( $Q_o = 0$ ) is, in effect, the blocked recovered pressure and is different from the supply total pressure to the supply nozzle due to three dissipative or viscous loss mechanisms: 1) the loss in the supply nozzle; 2) the loss due to the top and bottom plates; and 3) the loss due to boundary layer growth on the splitter.

Working backwards, the blocked pressure recovery at the output is simply the force, divided by the area, required to divert the momentum flux entering the receiver  $J_o$ , since the spill flow leaves at right angles to the jet stream. (fig. 2) With the jet centered, each receiver "sees" half the jet momentum flux  $J_o$  at that point so that the pressure recovered  $P_+$  is

$$P_+|_{Q_o=0} = \frac{J_o}{2b_o h} \quad (50)$$

The momentum flux at the receiver can be written as the ideal momentum flux supplied,  $J_{s,id} = 2P_s b_s h = \rho V_s^2 b_s h$  multiplied by three coefficients, each less than one

$$J_o = \frac{J_s}{J_{s,id}} \times \frac{J_{sp}}{J_s} \times \frac{J_o}{J_{sp}} \times J_{s,id}$$

$$J_o = 2c_{\theta} c_{\theta, X_{sp}} c_{\theta, B_{sp}} P_s b_s h \quad (51)$$

The loss in the supply nozzle is given by  $c_o$  from equation 25, while the plate and splitter losses are in  $c_{\theta, X_{sp}}$  and  $c_{\theta, B_{sp}}$  respectively, to

be determined here. There is yet another mechanism that occurs at low Reynolds numbers by which the momentum flux is decreased when the jet spreads so far that the receiver is unable to capture it all. This occurs also at large jet deflections, but since most of the analysis is for jet centered and small signals this is not discussed here.

The loss in momentum flux due to friction on the bounding surfaces may be estimated simply by assuming that a velocity distribution exists in the vertical direction that is invariant with downstream distance. Further, if one assumes--for the sake of argument--that this distribution is parabolic, then the loss in momentum in the downstream direction can be estimated by equating the shear forces to change in momentum flux. Thus the velocity distribution is

$$\frac{u(z)}{U_{max}} = 1 - \left(\frac{z}{h/2}\right)^2 \quad (52)$$

where

- $u$  - downstream component of velocity
- $z$  - vertical (normal-to-plane bounding surfaces) coordinate
- $U_{\max}$  - maximum velocity of the profile.

For moderate aspect ratios  $0.3 \leq \sigma \leq 3$ , and fully developed flow  $U_{\max} \approx 2 \bar{u}$ , (ref. 25), and  $\bar{u}$ , the average velocity is just  $c_d U_s = c_d \sqrt{2(P_s - P_v)/\rho}$ . For  $c_d \geq 0.5$   $U_{\max} = U_s/c_d = \sqrt{2(P_s - P_v)/\rho}$ . From equation 52 the local wall shear stress  $\tau_w$  is simply

$$\tau_w = \mu \frac{\partial u}{\partial z} = \mu U_{\max} \left( -\frac{8z}{h^2} \right) \Big|_{h/2} = -\frac{4 U_{\max} \mu}{h} \quad (53)$$

For  $c_d < 0.5$ , normalizing by  $P_s = \frac{1}{2} \rho U_s^2$

$$\frac{\tau_w}{P_s} = -\frac{16 c_d}{\sigma N_R} \quad (54a)$$

For  $c_d \geq 0.5$

$$\frac{\tau_w}{P_s} = -\frac{8}{\sigma N_R} \quad (54b)$$

The net force exerted by the stream on the plane surfaces per unit width is simply  $2\tau_w x_{sp}$ , which by Newton's 2nd Law must equal the difference in momentum flux per unit width  $(J_s - J_{sp})/b_s$ , therefore

$$\frac{J_s - J_{sp}}{b_s} = \begin{cases} 32 c_d P_s x_{sp}/\sigma N_R ; c_d < 0.5 \\ 16 P_s x_{sp}/\sigma N_R ; c_d \geq 0.5 \end{cases} \quad (55)$$

Since  $J_{sp}/J_s = 1 - (J_s - J_{sp})/J_s$  then

$$\frac{J_{sp}}{J_s} = c_{\theta x_{sp}} = \begin{cases} 1 - 16 c_d x_{sp}/(\sigma^2 N_R c_{\theta}) ; c_d < 0.5 \\ 1 - 8 x_{sp}/(\sigma^2 N_R c_{\theta}) ; c_d \geq 0.5 \end{cases} \quad (56)$$

where  $x_{sp} = x_{sp}/b_s$  (note: capitalized dimensions are normalized by  $b_s$ ).

The loss in momentum due to boundary layer on a finite width,



circular cylindrical leading edge of a splitter may be visualized by figure 15.

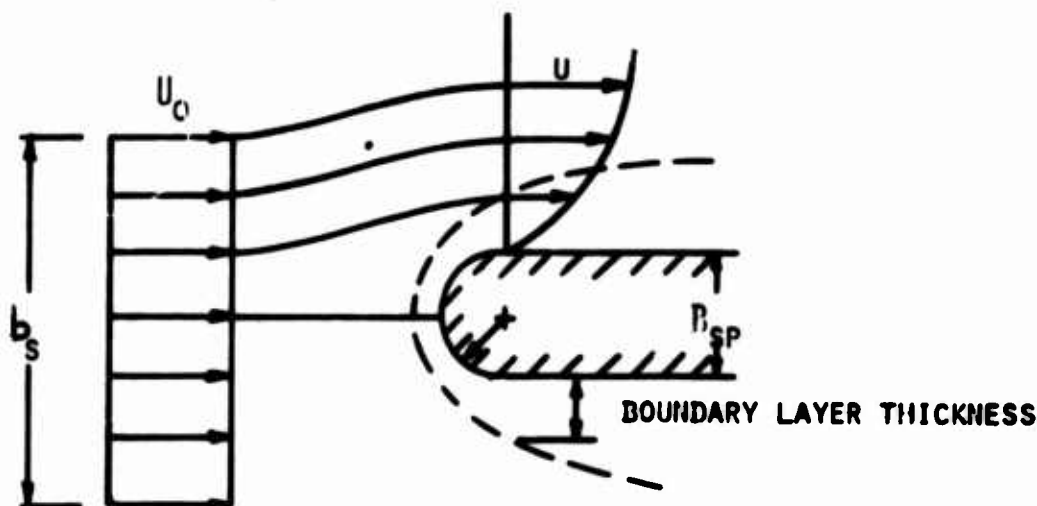


Figure 15. Flow in the vicinity of the leading edge of a splitter.

The flow up to the end of the curvature is merely that due to the impingement of a uniform stream on a circular cylinder whose solution is presented in Schlichting (p. 252).<sup>21</sup> The solutions for the momentum and displacement thickness,  $\theta$  and  $\delta^*$ , at the top of a cylinder are

$$(2\theta/r) \sqrt{U_0 r/\nu} = 0.6 \text{ and } (\delta^*/r) \sqrt{U_0 r/\nu} = 0.8 \quad (57)$$

where  $r/b_s = B_{sp}/2$  and  $U_0$  is the average velocity of the jet impinging. These values are probably not low even though they are ideally for high  $N_R$ . The data of Dimopoulos and Hanratty<sup>26</sup> and that of others indicates that the high Reynolds number solutions are almost valid to as low a Reynolds number,  $N_R(r/b_s)$  as 100, so for splitter thickness,  $B_{sp}$  of 0.25 ( $r/b_s = 0.125$ ) the analytical expressions for  $\theta$  and  $\delta^*$  are valid for  $N_R > 800$  and for  $B_{sp} = 0.5$ ,  $N_R > 400$ . Since in most cases this covers the greater part of the operating range, only equation 57 will be considered.

The ratio of the momentum flux at the top of the cylinder  $J_0$  to that impinging  $J_{sp}$  is

$$\frac{J_0}{J_{sp}} = \frac{\rho U_0^2 h [b_s/2 - (\delta^* + \theta)]}{\rho U_0^2 h (b_s/2)} = 1 - \frac{\delta^* + \theta}{(b_s/2)} \quad (58)$$

From equations 57, and noting that  $U_o = c_d \sqrt{2(P_s - P_v)/\rho}$  and  $r/b_s = B_{sp}/2$

$$\frac{J_o}{J_{sp}} = 1 - \frac{1.1 B_{sp}}{\sqrt{c_d N_R} (B_{sp}/2)} \quad (59)$$

The recovered pressure, equation 50, therefore becomes

$$P_t = \frac{c_\theta \left\{ \frac{1 - 16 c_d X_{sp}/\sigma^2 N_R c_\theta}{1 - 8 X_{sp}/(\sigma^2 N_R c_\theta)} \right\} \left[ 1 - \frac{1.1 B_{sp}}{\sqrt{c_d N_R} (B_{sp}/2)} \right] P_s}{B_o} \quad (60)$$

For very high Reynolds numbers this would become

$$\frac{P_t}{P_s} = c_d^2/B_o; N_R \gg 100 \quad (61)$$

( $c_\theta \rightarrow 1$ ,  $N_R \rightarrow \infty$  therefore, since  $c_\theta \propto c_d^2$  for  $N_R \rightarrow \infty$   $c_\theta \rightarrow c_d^2$ )

The average total pressure when the output pressure is zero, or full output flow, is simply the average dynamic pressure of the jet. The average dynamic head is simply one-half the velocity squared, multiplied by density and the ratio of the jet half-width to the receiver width:

$$P_{dyn} = \frac{1}{2} \rho U_o^2 \left( \frac{\frac{1}{2} b_s}{b_o} \right)$$

and normalized by  $P_s = 1/2 \rho U_s^2$  this becomes

$$P_{dyn}/P_s = \frac{U_o^2}{U_s^2} \frac{1}{2B_o}$$

The ratio  $U_o^2/U_s^2$  is simply the net momentum discharge coefficient  $c_\theta c_{\theta x_{sp}} c_{\theta B_{sp}}$ . The above expression then is simply one-half the blocked pressure  $P_+|_{Q_o=0}$ . Assuming that the driving pressure varies

quadratically with flow so that

$$\frac{P_+}{P_s} = \frac{P_+|_{Q_o=0}}{P_s} - \frac{P_+/P_s|_{Q_o=0}}{2(Q_o/Q_s)^2|_{P_o=0}} (Q_o/Q_s)^2$$

then the expression for the output characteristic is simply

$$P_o/P_s = (P_+/P_s)|_{Q_o=0} - \left[ \frac{2(R_{oc}/R_s|_{P_o=0})^2}{(P_+/P_s)|_{Q_o=0}} \frac{Q_o}{Q_s} + \frac{R_{oc}}{R_s} \right] Q_o/Q_s \quad (62)$$

The complete expression for the output characteristic can be obtained from the above equations where  $P_+$  is obtained from equation 60,  $R_{oc}$  from equation 49 and  $R_s$  from equation 5. The expression for the output impedance  $R_o = \partial P_o / \partial Q_o$  can be obtained from equation 62.

## 2.8 Transfer or Gain Characteristic

In section 2.5 the jet deflection gain was discussed and, for the sake of simplicity, the term  $\Delta P_o / \Delta y_o$  was assumed constant. Recall now the expression for blocked pressure gain

$$G_p = \frac{\Delta P_o}{\Delta P_c} = \frac{\Delta P_o/P_s}{\Delta y_o/b_s} \frac{\Delta y_o/b_s}{\Delta P_c/P_s} \quad (63)$$

where  $\Delta P_o$  is the difference in recovery at zero flow between two receivers when the jet is deflected some  $\Delta y_o$ .

Recalling now that the expression for recovered pressure was obtained by considering the momentum flux to the receiver, then for the case when the jet is deflected  $\Delta y_o$

$$\frac{\rho U_o^2 b_s h}{2} + \rho U_o^2 \Delta y_o h = P_{+1} b_o h$$

$$\frac{\rho U_o^2 b_s h}{2} - \rho U_o^2 \Delta y_o h = P_{+2} b_o h$$

where  $P_{+1}$  and  $P_{+2}$  are the total pressure impinging on receivers 1 and 2.

Taking the difference and noting that  $\rho U_o^2 b_s h = c_\theta c_{\theta x_{sp}} c_{\theta B_{sp}} J_{s,id}$  where  $P_s = J_{s,id} / 2b_s h$  and  $P_{t1} = P_{t2} = \Delta P_o$  then

$$\Delta P_o / P_s = 4 c_\theta c_{\theta x_{sp}} c_{\theta B_{sp}} (\Delta y_o / b_s) / B_o \quad (64)$$

Therefore the first term in equation 63 is

$$\frac{\Delta P_o / P_s}{\Delta y_o / b_s} = \frac{4 c_\theta c_{\theta x_{sp}} c_{\theta B_{sp}}}{B_o} \quad (65)$$

Combining equation 65 with the jet-deflection gain term  $(\Delta y_o / b_s) / (\Delta P_c / P_s)$  from equation 41 results in the complete equation for pressure gain to include Reynolds number effects, bias effects and dynamic effects

$$G_p = \frac{\Delta P_o}{\Delta P_c} = \frac{c_{\theta x_{sp}} c_{\theta B_{sp}}}{B_o} \left( \frac{2X_{sp}}{B_c} - 1 \right) \frac{B_c^2}{\left[ 1 + a_1 k_j Z_c + 2Y_j Z_c + \frac{\delta Z_c \operatorname{sgn}(P_j - P_v)}{2c_d \sqrt{P_j - P_v}} + \frac{Z_c}{R_v} + \frac{2k_j Z_c (P_j - P_v)}{c_d \sqrt{P_j - P_v}} \right]} \quad (66)$$

where  $P_j$  is given by equation 40,  $k_j = B_c^2 / 4c_\theta$ , and  $Z_c$  is given by

$$Z_c = \frac{R_c}{R_s} + \frac{j\omega L_c}{R_s} \quad (67)$$

The relationship without dynamic terms reduces to a simpler formulation as in equation 68.

$$G_p = \left[ 1 - \frac{8 X_{sp}}{c_\theta N_R \sigma^2} \right] \left[ 1 - \frac{1.1 B_{sp}}{\sqrt{c_d} N_R (B_{sp}/2)} \right] \left[ \frac{B_c^2}{B_o} \right] \left[ 2 \frac{X_{sp}}{B_c} - 1 \right] \times \left[ 1 / \left[ 1 + \frac{a_1 B_c^2 R_c}{4 c_\theta R_s} + \frac{R_c / R_s}{(R_v / R_s)} + \frac{B_c^2 (R_c / R_s) (P_j - P_v)}{2 c_\theta c_d \sqrt{P_j - P_v}} \right] \right] \quad (68)$$

Equations 1 - 68 constitute a set with which the operating characteristics of an LPA can be computed.

Staging of the amplifiers can be achieved analytically by using the method outlined by Mon.<sup>16</sup>

## 2.9 Miscellaneous Analytical Results

In addition, there are other considerations that can be made regarding the operation of LPA's that result from geometric irregularities or anomalies due to either fabrication problems or contamination. Section 2.9.1 deals with a quasi-sensitivity analysis to provide a trouble shooting guide and section 2.9.2 suggests problems that might arise due to contamination and what can be done to alleviate the problems.

### 2.9.1 Geometric Configuration Sensitivity

There are five geometric anomalies considered in this section. The first three are merely a perturbation of some basic dimension; for example, a nominal dimension is over or undersized. The latter two are anomalies in shape.

The first, though not necessarily most important anomaly is the error in splitter width,  $B_{sp}$ . If  $B_{sp}$  is larger than specified, by equation 68 one sees that the gain goes down and by equation 60 the pressure recovery goes down.  $X_{sp}$  may decrease slightly however, which may counteract the decrease.

The second anomaly is the error in distance between the downstream edges of the controls,  $B_t$ . If  $B_t$  is oversized, the jet clearance increases, the net input impedance decreases, gain decreases, and bias sensitivity decreases because  $P_j$ , which is proportional to  $R_v$ , approaches  $P_v$ . In addition, if this clearance is not symmetrical it will cause a null output signal since the side with the smaller clearance will be drawing a vacuum relative to the wider side, due to different values of  $R_v$  for jet centered; thus a pressure differential will exist across the jet.

The third anomaly is splitter misalignment. This will cause a null signal on the outputs proportional to the offset--as if it were simply a jet deflection. Using equation 64, the null signal can be computed or the misalignment can be computed if one is sure that no other mechanism is affecting null.

The next two are shape anomalies. If the leading edge of the splitter is supposed to be circular but is flattened on one side or asymmetrical, this too will cause a null shift on the output.

The last case is of some interest because it delves into an almost completely theoretical discussion with little experimental evidence to prove the theory, but with some data to indicate that the anomaly is the problem. When considering extremely low threshold problems of jet deflection, as in a laminar jet angular rate sensor, there is a null shift that varies with Reynolds number. In light of the above discussion it is not surprising, but consider another possible cause of null shifting. If the exit corners of the supply nozzle are manufactured so that two different radii exist, will this not tend to steer the jet? Consider the following sketch of the exit of a supply nozzle. (fig. 16)

The deflection angle  $\beta$  as a rough first-guess might be just the arc tangent of the ratio of the difference of the radii to the nozzle width. This assumes that the jet separates at the beginning of the radius. A second, more satisfying guess would be that the deflection is related to the angle between separation points  $S$  on the respective radii. (fig. 16) It is reasonable to consider that the location of this separation will vary with Reynolds number.<sup>26</sup> Assuming that the radii are not very different so that the separation angle is roughly the same for both sides, then from geometry the deflection angle is

$$\beta = \frac{(r_2 - r_1)(\sin \theta_s - 1)/b_s}{1 + (r_1 + r_2)(1 - \cos \theta_s)/b_s} \quad (69)$$

Note that for  $\theta_s = 0$ ,  $\beta = (r_2 - r_1)/b_s$  as expected. The relation between separation angle and Reynolds number, for lack of anything better, is assumed to be the same as for separation from a cylinder as given empirically by Dimopoulos et al.<sup>26</sup> Using their data and equation 69 will result in a relation between jet deflection angle as a function of Reynolds number. Dimopoulos<sup>26</sup> data are reproduced here in figure 17 with Reynolds number based on radius,  $r \sqrt{2(P_s - P_v)/\rho} / \nu$ .

In general, based on the above reasoning, the results indicate that the spurious deflection angle  $\beta$  increases with difference in radii, and also increases with increasing Reynolds number. The rate of change of angle with Reynolds number  $d\beta/dN_R$  decreases with  $N_R$  and may approach zero at high enough values. An interesting point occurs, in that for constant difference in radii but difference average value of radii at high Reynolds number  $d\beta/dN_R$  may be considerably lower for the higher average radii. This is important when one considers the temperature dependence of null shifts. If  $d\beta/dN_R = 0$ , there will be no shift of the output with change in temperature.

This last section is open to debate and certainly there is much room for the study of such an effect.

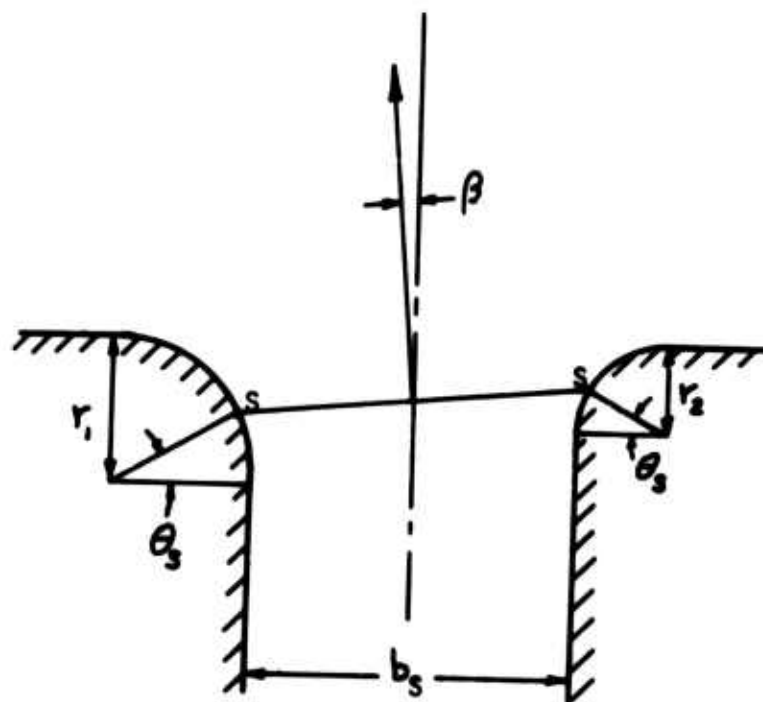


Figure 16. Sketch of a rounded supply nozzle exit

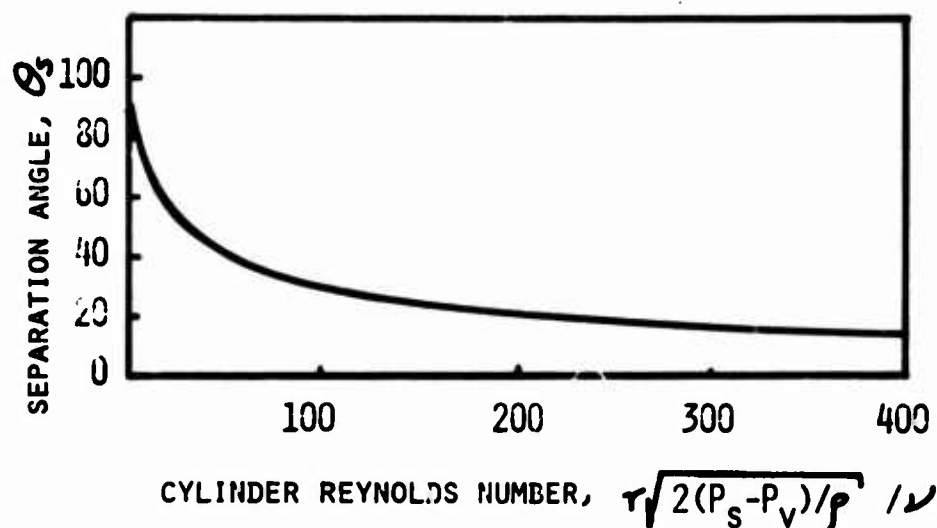


Figure 17. Separation angle for flow past a cylinder versus Reynolds number

#### 2.9.2 Contamination Sensitivity

The sensitivity of proportional amplifiers to contamination buildups is considered from an experimental point of view by Comparin et al.<sup>27</sup> They indicate three main problem or buildup areas: the supply plenum, the control edges, and the near output region (splitter and receivers).

The supply plenum buildup stems from flow impingement on the back plane from a fitting, when flow is brought in normal to the plane of the amplifier. Immediate results are an increase in supply impedance, so for constant supply pressure the pressure recovery falls, the gain falls and supply flow falls. This blockage condition may be alleviated to some degree by providing a recess in the impinging plane for the contaminant to build up in. Appropriate design of such a recess can indefinitely extend the plenum life.

The buildup on the upstream face of the downstream wall of the control port causes an increase in control impedance, hence a decrease in gain. Uneven accumulations will cause null shifts. This buildup can be reduced by designing that part of the approach geometry with a low grazing angle so the flow will exert more shear on that section.

The buildup on the leading edge of the splitter and in the receivers blocks the outputs and makes the splitter effectively thicker.



As was noted in the previous section, 2.9.1, a thicker splitter results in lowered gain. Again, uneven depositions can cause null shifts. This appears to be the main cause of contamination failure of LPA's, and not much appears possible to be done about it. This condition limits the eventual reliability of the device. It should be noted that mean-time-to-failure (MTTF), under normal conditions, for these devices is probably several years and with nominal servicing, indefinite.

Operation of devices under constant flow conditions will virtually assure that the same jet issues from the nozzle--even though the supply pressure may change; thus, the dynamics should be relatively unchanged. Of course all quantities relative to  $P_s$  will change.

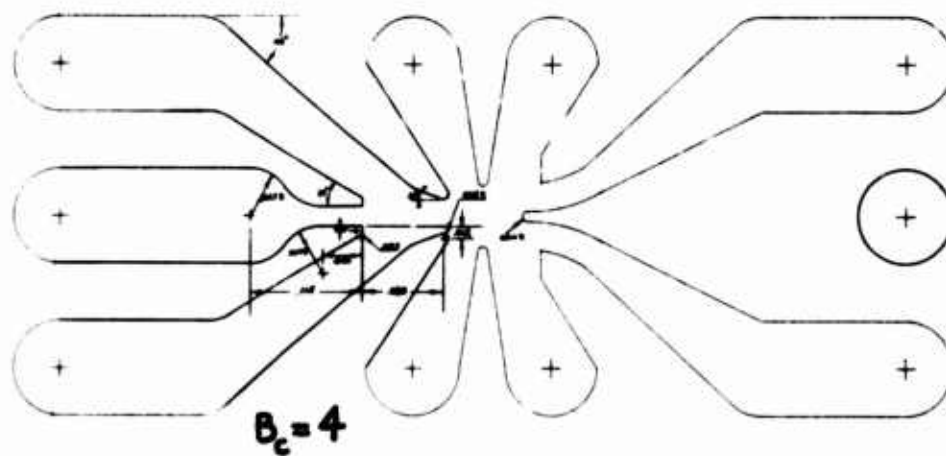
### 3. EXPERIMENTAL RESULTS

To present as much experimental data as possible showing the validity of the equations derived in the preceding sections, the data will be presented in three general sections, each dealing with a specific characteristic of the amplifiers. The three sections will consider the input characteristics, output characteristics, and gain (as a function of Reynolds number, as a function of control bias pressure ( $P_{CB} = [(P_{c1} - P_v) + (P_{c2} - P_v)]/2$  for  $P_v = 0$ ), and as a function of frequency).

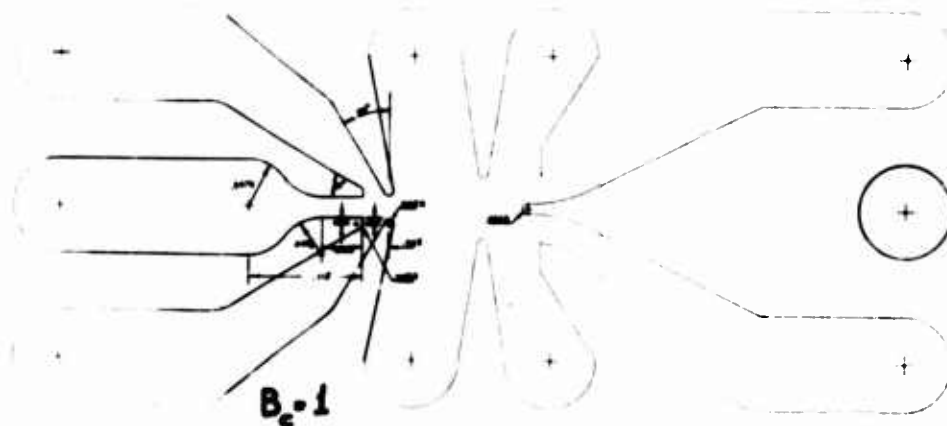
Inasmuch as the field of laminar amplification is relatively new, there is not much data on variations of geometry--certainly not as much as desired. The geometric variations are basically limited to aspect ratios  $\sigma$ , from 0.25 to about 4, control widths  $B_c$  of 1.0 and 4.0, although careful measurements of some devices has shown that  $B_c = 1.1$  and 4.2, so that four widths are actually available. The downstream control edge spacing  $B_t$  has been nominally held to one value, but it too has some small variation. The approach geometrics are two - short controls and outputs from Manion and Mon,<sup>15</sup> Mon,<sup>16</sup> and Spyropoulos,<sup>17</sup> and long controls and outputs (fig. 18). The splitter thickness  $B_{sp}$  has been varied from  $0.25 b_s$  to  $0.5 b_s$ . Data will not be presented on the supply characteristic or, in other words  $c_d$ , since the validity of the expressions has been well established.<sup>18,19</sup>

#### 3.1 Input Characteristic Parameters

The input characteristic is the most important part of the LPA. It determines the input impedance, the bias sensitivity, the gain and the dynamics of the system. This section will present data, to be compared with theory, on the relation for the viscous losses in the control channel, the actual relationship of  $Q_c$  vs  $P_c$ , and qualitative dynamic impedance measurements of the input.<sup>28</sup>



(a)



(b)

Figure 18. Planviews of LPA's with long approach geometry

An important part of the input impedance is the viscous loss in the approach control channel. Although the theoretically computed value was used in computing a satisfactory input characteristic, it is of interest to see if this component part is valid alone. To this end, a static tap was located at the exit of the control channel in four amplifiers and the differential pressure and through flow were monitored to obtain  $\Delta P_c / Q_c = R_c$ . The data was normalized to the supply impedance  $R_s$ . Equation 8 was used to compute the theoretical results. A comparison of data and theory is shown in table 1, where the coefficients of the equation  $R_c / R_s = A + B (Q_c / Q_s)$  are listed.

Figure 18 shows the planview of the amplifiers used in collecting the data of table 1. The set of data for  $B_c = 3$  was obtained on the  $B_c = 1$  amplifier with the static tap located about  $3b_s$  in from the exit, hence  $X_c = 16$  and  $B_{cmin} = 3$ . The agreement is quite satisfactory for the constant coefficient in all but one case. No immediate answers for the discrepancy are presented. The theory's results are low for the nonlinear term for all but the narrow control devices. The explanation is simply that the experimental data was obtained by measuring the control pressure upstream of a fitting normal to the planview. In such an event, added impedance, which is a function of flow, will be noticed due to flow making the turn. In the narrow width case ( $B_c = 1.0$ ), the orifice effect of the narrow width is considerably more than the turning effect.

The measured input characteristic can be presented in two ways. A base curve of flow entering equally through both control ports versus applied pressure will give the characteristic for a centered jet. Stopping at some value of control pressure establishes a level of control bias. If now the pressure in the controls is changed differentially (one goes up as much as the other goes down), the jet will move and a different control flow will ensue. This will be called the deflection impedance characteristic, and the former, the centered jet impedance characteristic. The other way of measuring an input characteristic is to hold one control at a constant pressure and increase the flow on the other side. This curve then is a variable bias curve. In applications where differential signals are not encountered this may be the more important curve. The centered jet impedance curve is obtained from equation 43 and the deflection impedance is given by equation 44. The constant control pressure impedance characteristic can be obtained from equation 44 by varying the bias. For a device with  $\sigma = 0.5$ ,  $B_c = 4$ ,  $X_{sp} = 8$ ,  $B_o = 1.5$ ,  $\bar{B}_c = 3$ ,  $B_{cmin} = 2$ ,  $X_c = 19$  at a typical operating Reynolds number,  $N_R = 2000$  and  $c_d = 0.7$ ,  $R_c|_{Q=0}$  calculates to be 0.236 from equation 8. The jet spacing impedance as shown previously is  $R_v = 1$ ,  $B_t = 2$  and the

Table 1. Experimental and Theoretical Viscous Input Impedance  
Correlation  $R_c/R_s = A + B (Q_c/Q_s)$  (eq. 8)

Supply Conditions		$P_s = 1.0 \text{ mm Hg}; N_R = 508$ $\sigma=1.6 \quad c_{d_s}=0.68 \quad b_s=0.508\text{mm}$			$P_s = 7.0 \text{ mm Hg}; N_R = 1344$ $\sigma=0.8 \quad c_{d_s}=0.7175 \quad b_s=0.508\text{mm}$		
Dimensions		$B_c=4$	$B_c=3$	$B_c=1$	$B_c=4$	$B_c=3$	$B_c=1$
		$X_c=19$	$X_c=16$	$X_c=19$	$X_c=19$	$X_c=16$	$X_c=19$
		$\bar{B}_c=3$	$\bar{B}_c=3.2$	$\bar{B}_c=2.5$	$\bar{B}_c=3$	$\bar{B}_c=3.2$	$\bar{B}_c=2.5$
		$B_{c_{min}}=2$	$B_{c_{min}}=3$	$B_{c_{min}}=1.6$	$B_{c_{min}}=2$	$B_{c_{min}}=3$	$B_{c_{min}}=1.6$
A	EXP	0.13419	0.101	0.157	0.1312	0.124	0.094
	THEOR	0.1230	0.094	0.165	0.1527	0.192	0.118
B	EXP	0.1953	0.159	0.337	0.1956	0.1866	0.3162
	THEOR	0.1098	0.05	0.304	0.1222	0.054	0.3396

entrained flow  $Q_e$  from equation 14 is  $Q_e = 0.021$ . The equation describing the relationship between input pressure  $P_c$  and input flow  $Q_c$  is

$$\frac{P_c}{P_s} = \frac{Q_c}{Q_s} (1.236 + .22 \frac{Q_c}{Q_s}) - 0.021 \quad (70)$$

The equation is shown plotted in figure 19 as compared with experimental data collected on a large-scale model operated with 50 cs silicone oil at 25°C, where  $b_s = 10$  mm, and  $\sigma = 0.5$  much as described by Spyropoulos.<sup>17</sup>

The agreement is excellent, well within experimental or engineering accuracy.

Further experimental data has become available through the efforts of Smith and Shearer at Pennsylvania State University.<sup>29</sup> Using an early design LPA as described by Manion and Mon,<sup>15</sup> they made input characteristic measurements with MIL-H-5606 B red oil and a large nozzle width,  $b_s = 2.54$  mm. They took data at various aspect ratios and various but quite high Reynolds numbers. Typical results are shown in figure 20 for  $\sigma = 1.0$  and 1.4 with the theoretical input characteristics (both jet centered and push-pull jet deflection) shown as the solid lines. Again, agreement between data and theory is quite satisfactory. The jet centered experimental data appears to have slightly more curvature than the theory, which is, for all intents and purposes, a straight line. This probably can be accounted for by variations in the jet edge impedance, which does vary a few percent over the bias range, since as bias increases, the Reynolds number effectively decreases and so does  $c_{d_{b_s}}$ ; therefore,  $R_v/R_s$  decreases slightly.

The dynamics of the input of the amplifier have been assumed to be represented by a lumped parameter circuit that considers the control channel as inductive and resistive, the impedance of the jet edge - control edge  $R_v$  purely resistive and the motion of the jet provides

a compliance (capacitance) to ground when the jet is deflecting. Toda and Katz<sup>28</sup> have developed a unique system for measuring impedance--both real and imaginary parts--for an arbitrary load, by using measured values of pressure amplitude and phase on a half-bridge circuit in conjunction with a known impedance. Using this device they have measured the dynamic input impedance of an LPA described in figure 18a. The data is presented in figure 21. The upper portion shows the resistive (real) part of the impedance as a function of frequency and the lower portion shows the dynamic (imaginary) part of the impedance. The theoretical curves shown are a constant value of deflection impedance of 0.4 (for  $R_s = 10^5$  kPa/m<sup>3</sup>/s) as determined for 5% bias from equation 47 (see also figure 12). The imaginary part should be calculated from equation

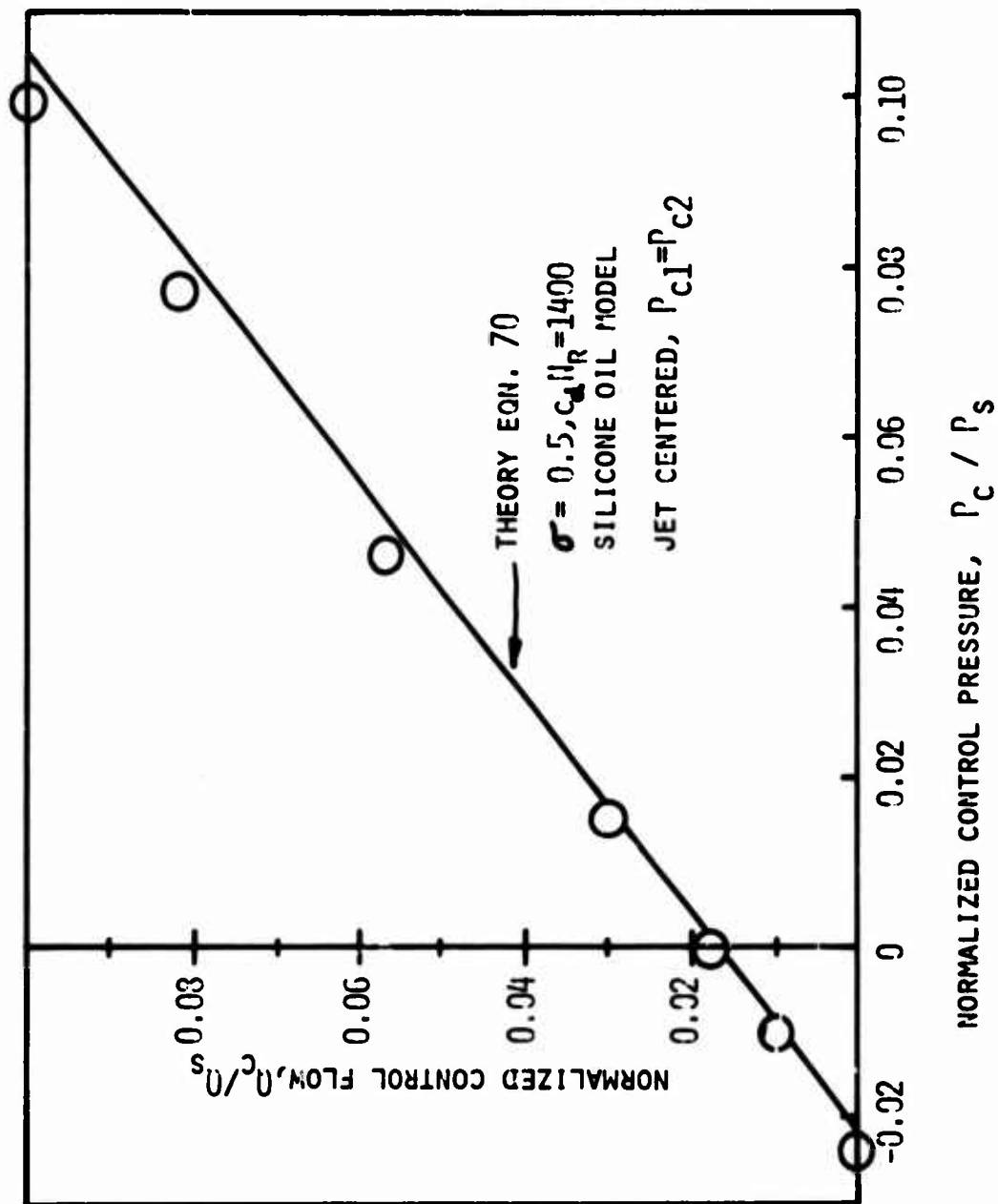


Figure 19. Comparison of theoretical and experimental jet centered input characteristics,  $\sigma = 0.5$ , silicone oil model,  $b_s = 10 \text{ mm}$

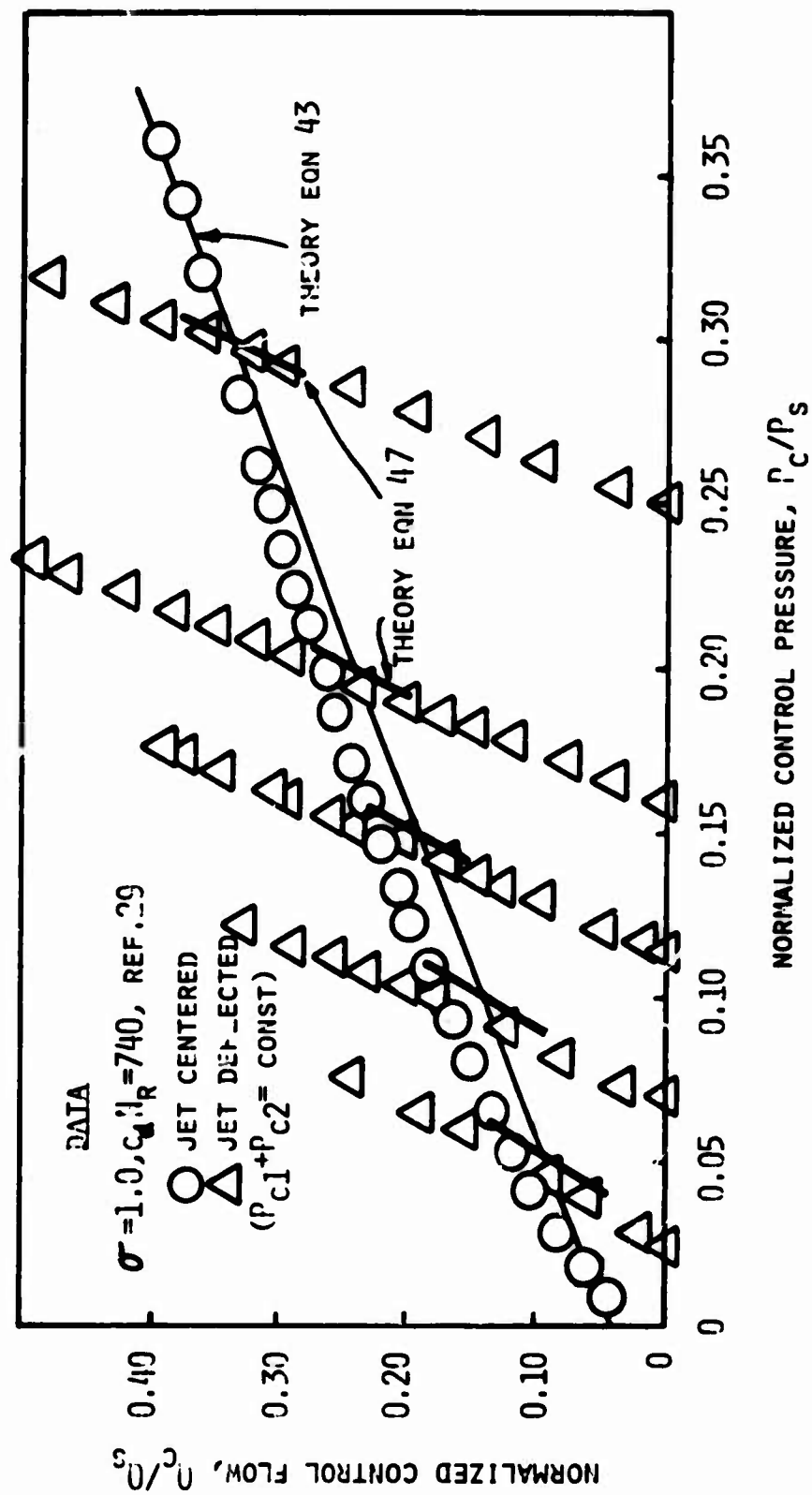


Figure 20. Comparison of theoretical and experimental, jet centered and jet deflected, input characteristics,  $\sigma = 1.0$ , H-56068 red oil,  $b_s = 2.54$  mm

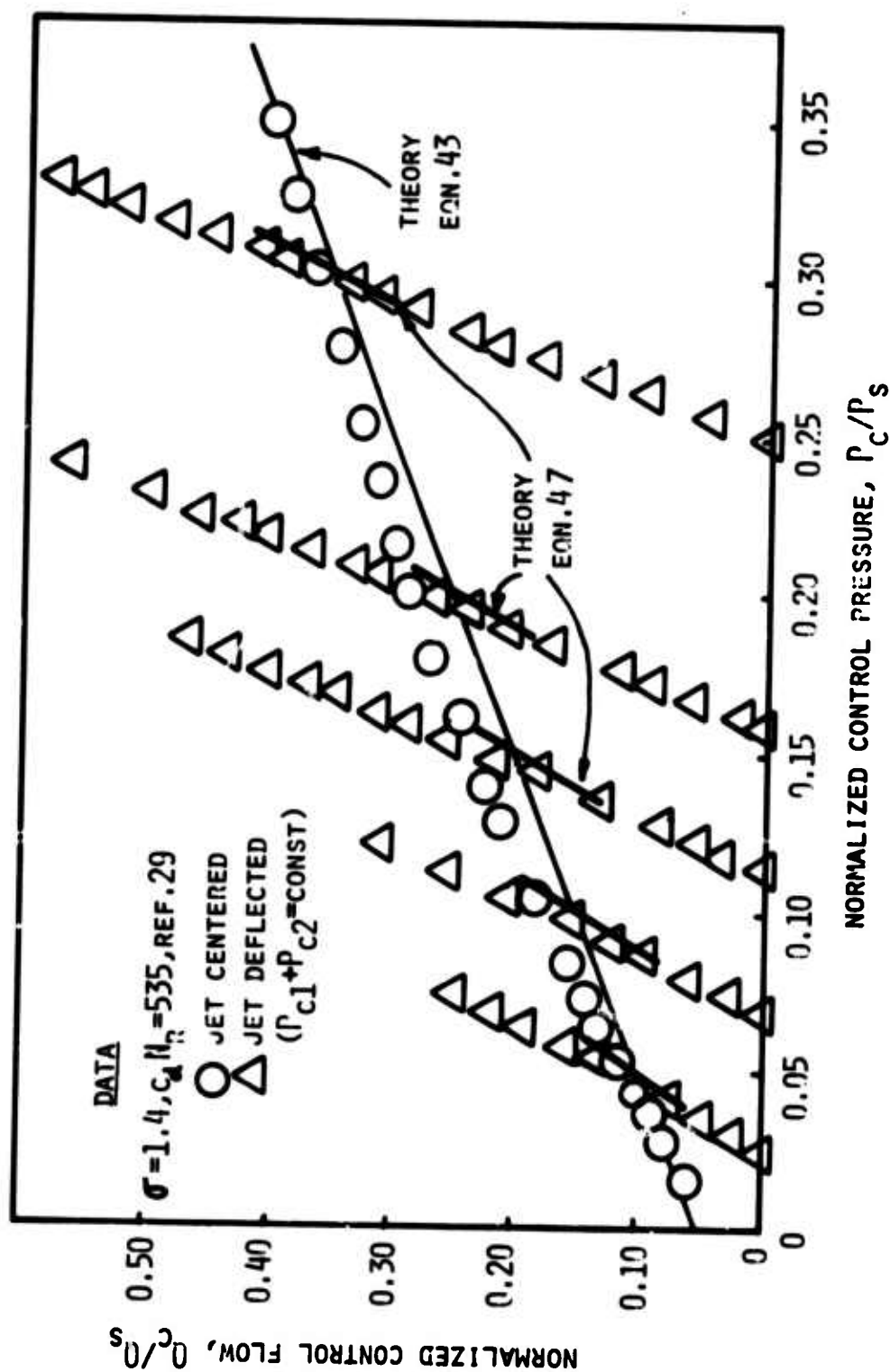


Figure 20b. Comparison of theoretical and experimental, jet centered and jet deflection, input characteristics,  $\sigma = 1.4$ , MIL-H-56068 red oil,  $b_s = 2.54 \text{ mm}$



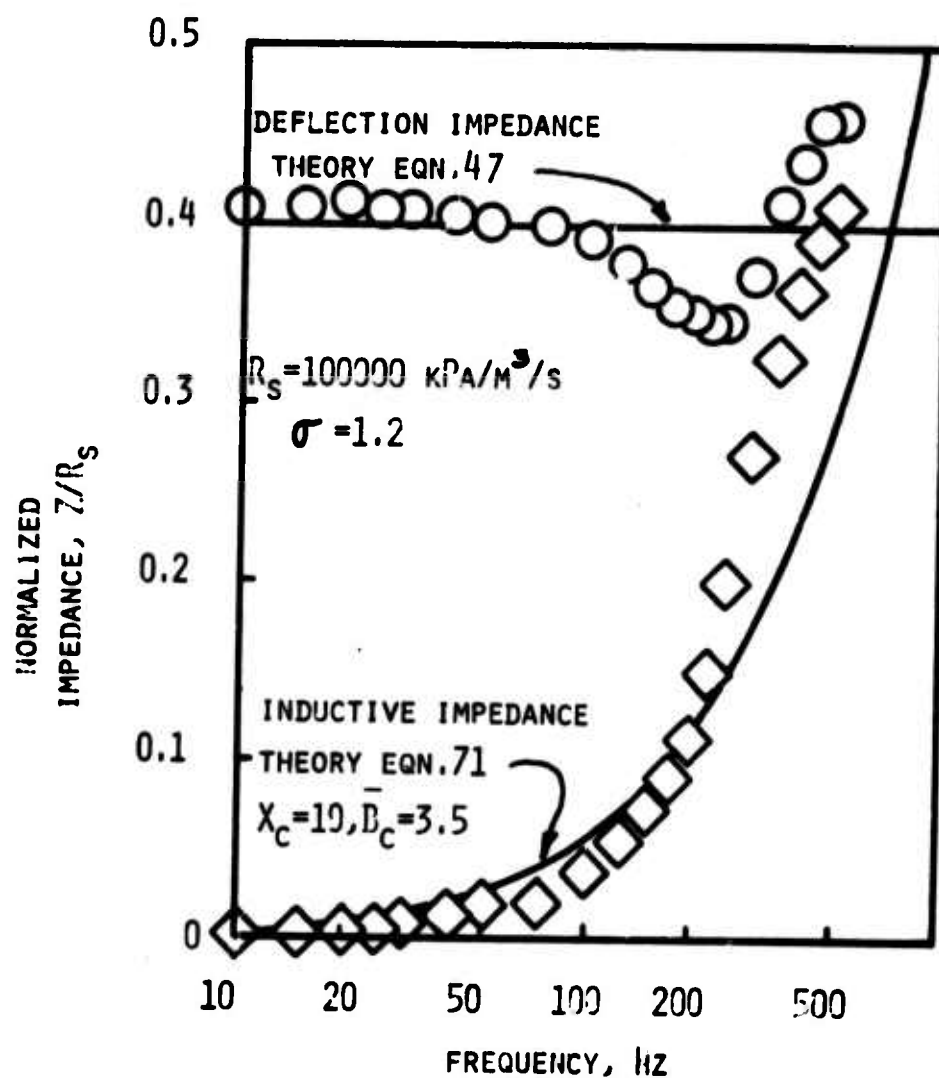


Figure 21. Comparison of theoretical and experimental dynamic input impedance for an LPA,  $\sigma = 1.2$ ,  $b_s = 0.51 \text{ mm}$ , air

46, but for simplicity an approximate fit can be obtained by just considering the inductive impedance of the channel.

$$\text{Inductive Impedance} = [2 \pi \rho X_c / (\bar{B}_c \sigma b_s)] \cdot f. \quad (71)$$

The agreement is satisfactory and especially good up to 100 Hz. The decrease in the resistance is accounted for physically by the compliant nature of the impedance between the jet and the control edge  $R_v$ . This "resistor" is obviously not a fixed value and, as the nature of the jet velocity profile changes, so does the value of  $R_v$ . It is conceivable that as frequency increases, and the jet swings back and forth, the flow may have to be integrated to a streamline closer to the center, but as the frequency increases even more, the effective spacing may approach the RMS value of the deflection, or less than at DC, hence a higher impedance. Further study is definitely called for; however, for engineering purposes up to the bandwidth of the amplifier, the simple lumped parameter approximations are certainly valid.

### 3.2 Output Characteristics

Typical output characteristics have been obtained on the device shown in figure 1 for  $\sigma = 0.75$  and  $0.5$  at  $\sigma N_R = 1250$ . The amplifier output dimensions are such that the average width is  $\bar{B}_o = 3.155$  and the minimum width is  $B_{omin} = 1.4$ . The length of the outputs is  $X_o = 20$ . Substituting these values into equation 62 results in two equations for the two output characteristics. For  $\sigma = 0.75$

$$\frac{P_o}{P_s} = 2.2855 - 0.348 \left( \frac{Q_o}{Q_s} \right)^2 - (0.1187 + 0.186 \frac{Q_o}{Q_s}) \frac{Q_o}{Q_s} \quad (72)$$

and for  $\sigma = 0.5$

$$\frac{P_o}{P_s} = 0.265 - 0.51 \left( \frac{Q_o}{Q_s} \right)^2 - (0.167 + 0.186 \frac{Q_o}{Q_s}) \frac{Q_o}{Q_s} \quad (73)$$

These two equations are shown plotted and compared to data in figure 22. The agreement again is acceptable. The higher aspect ratio gives a higher pressure and flow recovery, as might be expected. The fact that the theory has slightly more curvature indicates that the chosen distribution for the driving pressure should be more constant as it approaches the pressure for full flow.

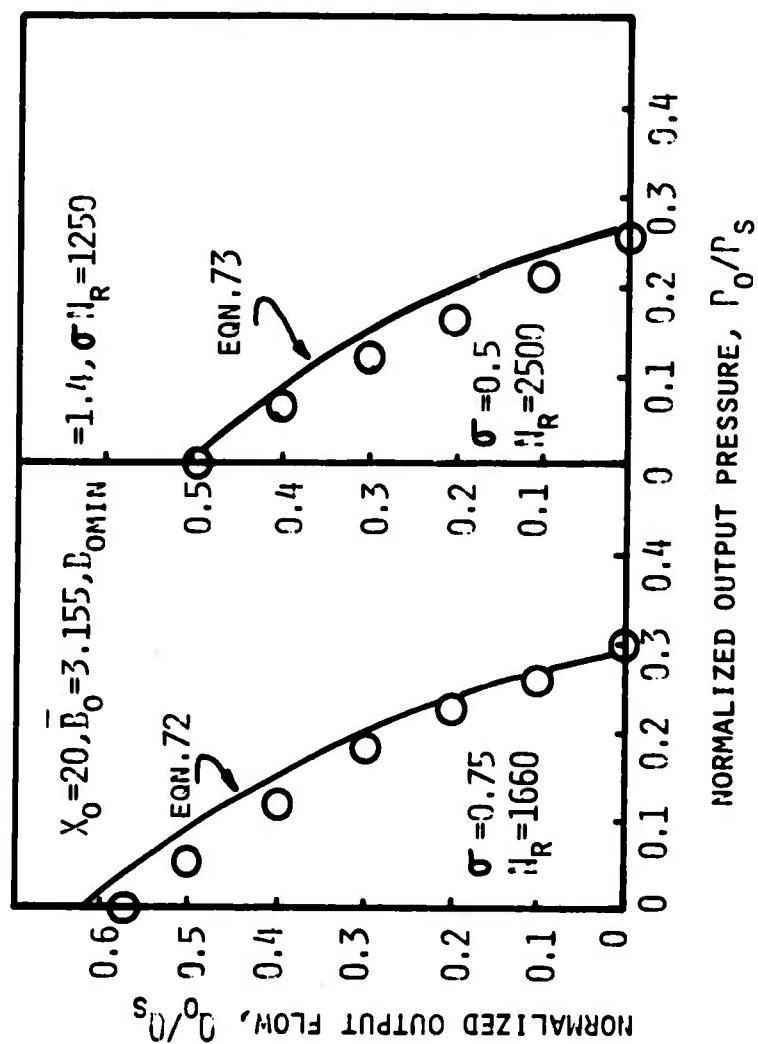


Figure 22. Comparison of theoretical and experimental centered jet, output characteristics,  $\sigma = 0.75, 0.5$ ,  $b_s = 0.5$  mm, air

### 3.3 Gain Characteristics

This section would be of most interest to a systems designer. Here the relationships between gain and three important parameters, Reynolds Number, bias, and frequency, are discussed.

#### 3.3.1 Gain versus Reynolds number

Limited data are available for gain as a function of Reynolds number. The data of Mon<sup>16</sup> for three aspect ratios, ( $\sigma = 0.8, 1.2, 1.6$ ) and some data obtained on a large-scale silicone oil model are readily available.

For Mon's<sup>16</sup> data, a lower discharge coefficient is used than that shown in figure 3 since the nozzle on his device was not smooth. In general, his values of  $c_d$  are roughly between 82% and 90% of those given in figure 3, in the range of interest. The critical dimensions are shown in figure 23, as is the theoretical curve in comparison with the data. The theoretical curve shown is an average for the three aspect ratios, but it should be noted that there is very little variation when  $G_p$  is plotted as a function of the Modified Reynolds number  $N_R$  to eliminate the dependency on aspect ratio. The calculations have been made assuming that  $P_j = P_v$ . The theoretical curve determined by equation 68 is in good agreement with the data.

Data collected on a large-scale silicone oil model described in section 3.1 is shown in comparison with theory in figure 24. Here bias pressure is slightly above zero, resulting  $P_{CB} \approx 0.0028 P_s$ . The aspect ratio was 0.5. The tests were conducted under three different conditions to vary the Reynolds number. Two tests were conducted at constant temperature ( $T_s = 25^\circ\text{C}$  and  $T_s = 50^\circ\text{C}$ ) where the supply pressure  $P_s$  was varied, and one test was conducted by holding the pressure constant ( $P_s = 21 \text{ kPa}$ ) and varying the temperature (hence the viscosity). The supply nozzle of this device was smooth, so the discharge coefficient distribution from figure 3 is valid. The effective length of the nozzle was 3.0. Since the aspect ratio and nozzle shape are the same for the experiments, the data is presented against only Reynolds number  $N_R$ . Under most circumstances, with the three different tests there would be a discrepancy due only to the fact that the bias pressure might vary. In this case only slight variation might be expected. The pertinent amplifier dimensions are given in figure 24. The agreement between data and theory is good.

The theoretical relation for pressure gain may be used to determine the pressure gains at some operating point, by using the output characteristic relation. For pressure gains at a given output

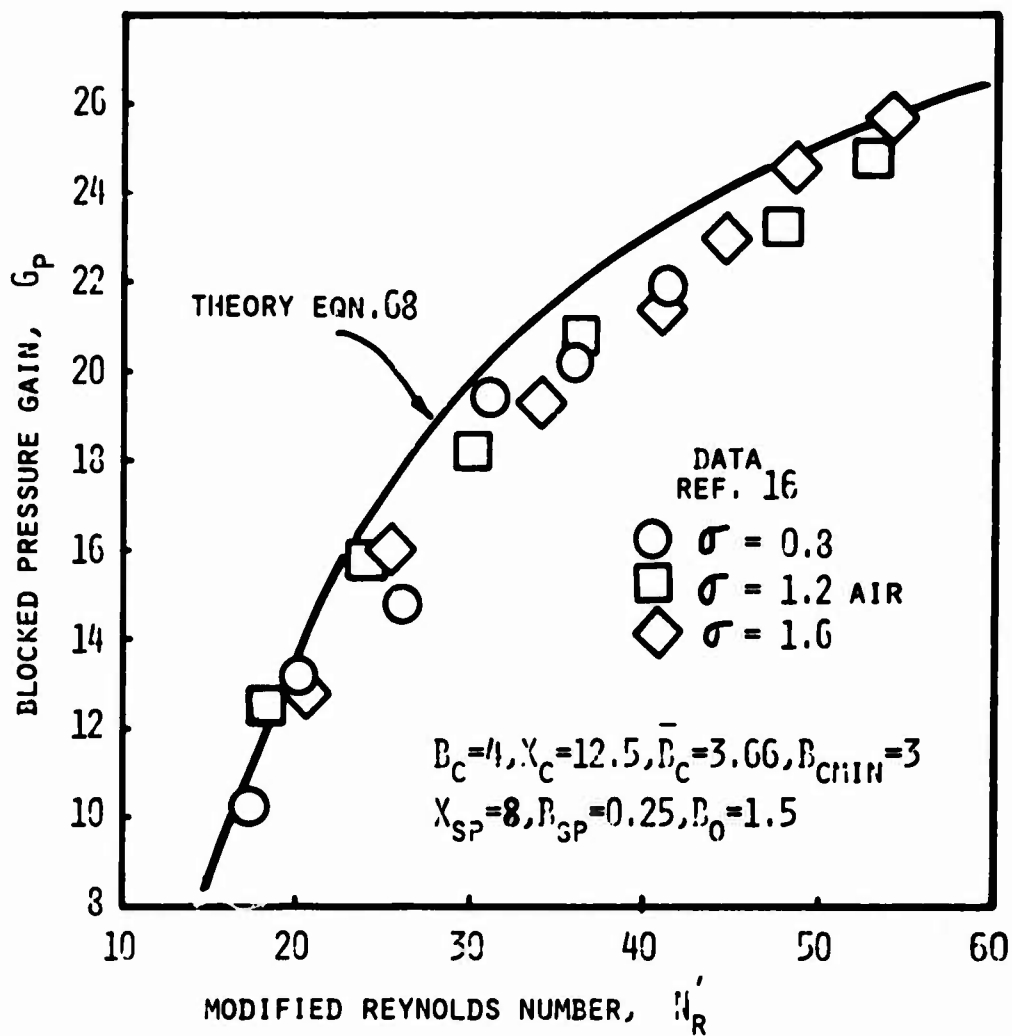


Figure 23. Comparison of theoretical and experimental values for gain versus Reynolds number,  $\sigma = 0.8, 1.2, 1.6$ ,  $b_s = 0.5$  mm, air

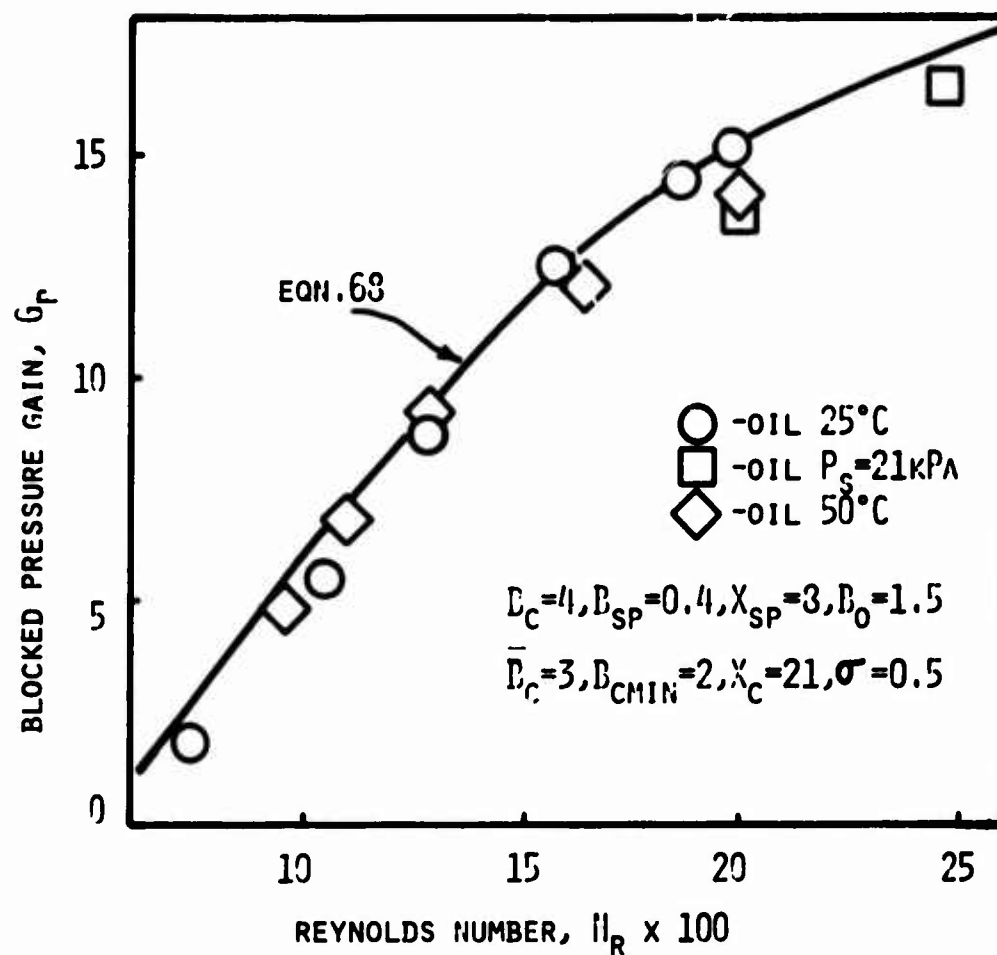


Figure 24. Comparison of theoretical and experimental values for gain versus Reynolds number,  $\sigma = 0.5$ ,  $b_s = 10 \text{ mm}$ , silicone oil

flow, the gain is the blocked gain reduced by the ratio of the driven deflection resistance to the sum of the driven deflection resistance and the driving output resistance ( $R_o = \partial P_o / \partial Q_o$ ).

### 3.3.2 Gain versus Control Bias Pressure

Again the data of Mon<sup>16</sup> is used to illustrate the validity of the theoretical expressions obtained for gain. For his geometry the gain decreases with control bias pressure,  $[(P_{c1} - P_v) + (P_{c2} - P_v)]/2$ , at  $P_{c1} = P_{c2}$  for  $P_v = 0$ , as shown by the data in figure 25. Equation 68 is evaluated for  $\sigma = 0.8$  and  $\sigma N_R = 1000$ , by assuming that  $P_c = P_j$ . For low values of entrained flow this relationship is almost exact. The theoretical expression, as derived from equation 68, is in good agreement with the data for low values of bias pressure and is slightly high for the high bias. This may be accounted for by the fact that the experiment was run at a constant supply pressure, but as the bias increases the net differential pressure across the supply nozzle decreases, effectively decreasing the Reynolds number and the discharge coefficient. These lower values of  $c_d$  and  $N_R$  make themselves manifest on all terms of the expression for gain,  $G_p$ , in that they all decrease, hence the theory would be lower if the decreased  $N_R$  were taken into account. It is however sufficiently close to the data to assume constant  $N_R$ . If very high bias were to be considered then the appropriate changes would have to be incorporated.

### 3.3.3 Gain versus Input frequency (Bode Diagram)

As discussed in section 2.5, the frequency dependence of the gain is determined by the jet deflection response. In such a manner then, equation 66 is used, where it is noted that the only frequency dependent term is the same term that determines bias sensitivity shown in section 3.3.2, except that now there are complex terms in the input impedance and a complex term due to the jet compliance. The validity of the complex form of the input impedance has already been established in section 3.1, so that agreement of theory and data at this point would be a direct verification of the validity of the concept of the jet compliant frequency dependent impedance  $Z_j$ .

Work done at the Massachusetts Institute of Technology<sup>30</sup> has resulted in some dynamic gain data on amplifiers using MIL H 5606B red oil as the working medium. The data was collected on a device where  $B_{sp} = 0.5$ ,  $B_c = 4$ ,  $\bar{B}_c = 3.5$ ,  $B_{cmin} = 3.0$ ,  $X_c = 19.0$ ,  $X_{sp} = 8.0$ , and  $\sigma = 2$  for a 5% control bias with a supply nozzle the same as used by Mon.<sup>16</sup>

Figure 26 shows this data compared with the results from equation 66. The agreement is good over the operating range. This is one point of verification for the dynamic model.

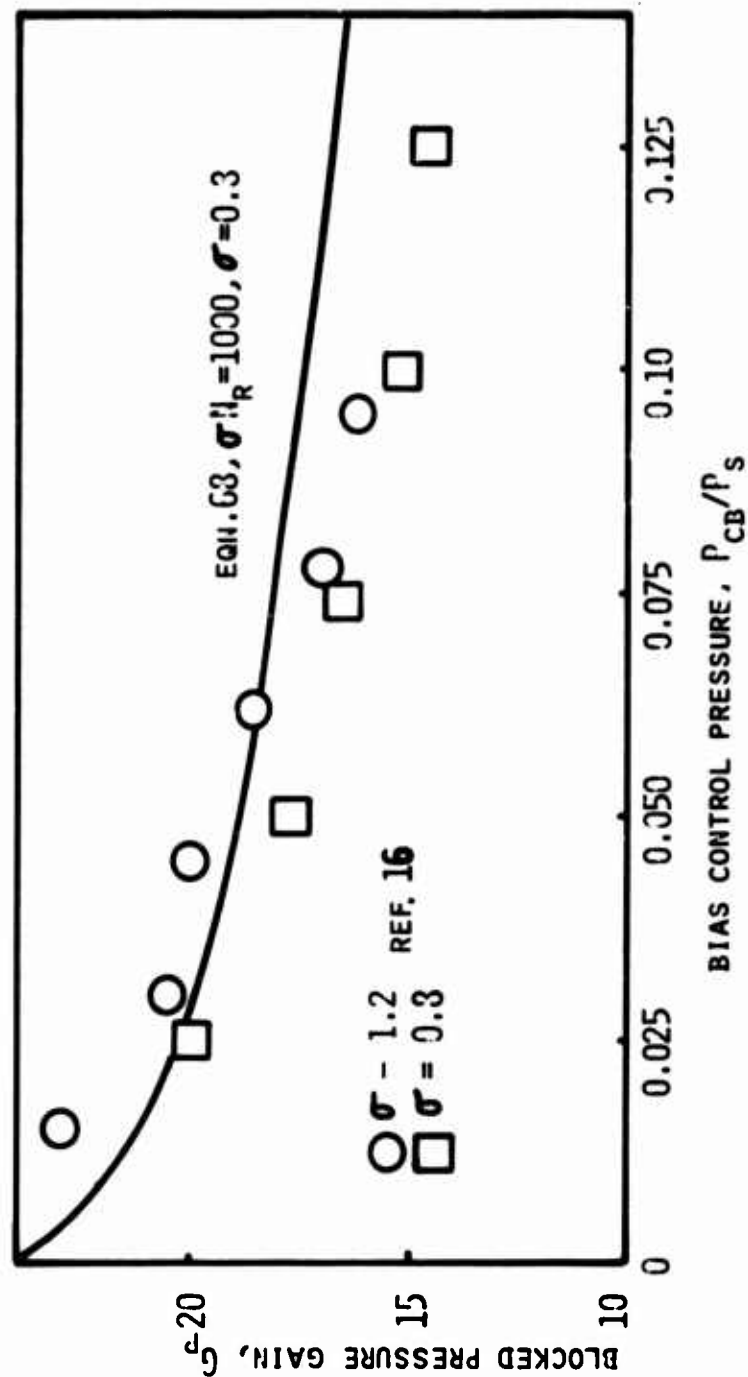


Figure 25. Comparison of theoretical and experimental values for gain versus control bias pressure,  $\sigma = 0.8, 1.2, b_s = 0.5$  mm, air



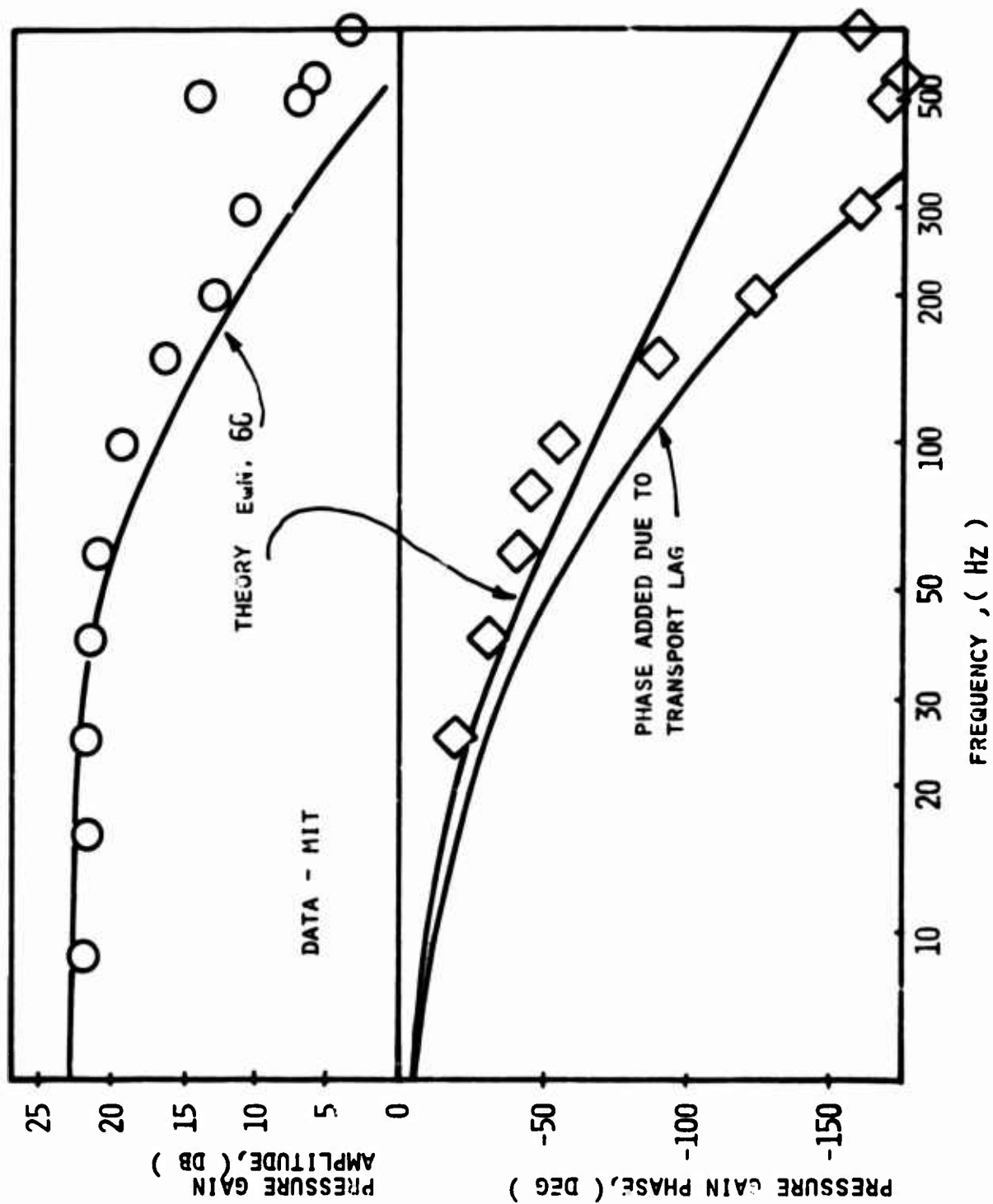


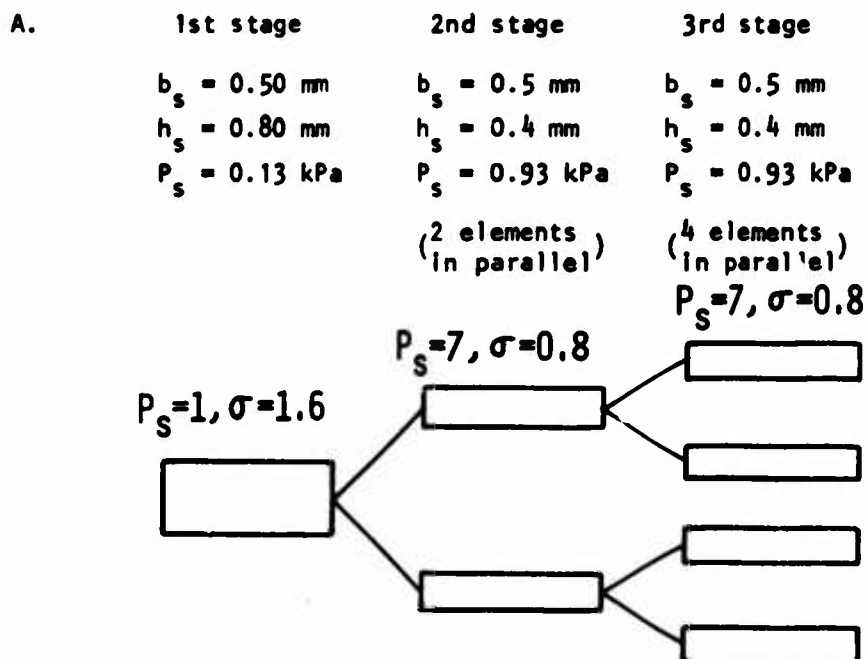
Figure 26. Comparison of theoretical and experimental values for gain versus frequency (Bode Diagram),  $\sigma = 2.0$ ,  $b_s = 0.5$  mm, red oil

The transport time of the flow to the receivers adds phase lag to the response. This has been added and is the lower analytical curve in figure 26. The measurement of phase is at best approximate when considering the low frequencies encountered, and the added or parasitic dynamics of instrumentation have an effect on phase shift. In light of this uncertainty, the agreement is fair-to-good. The damping coefficient for this case is  $\xi = 1.7$ , indicating the response should be well over-damped, as can be seen.

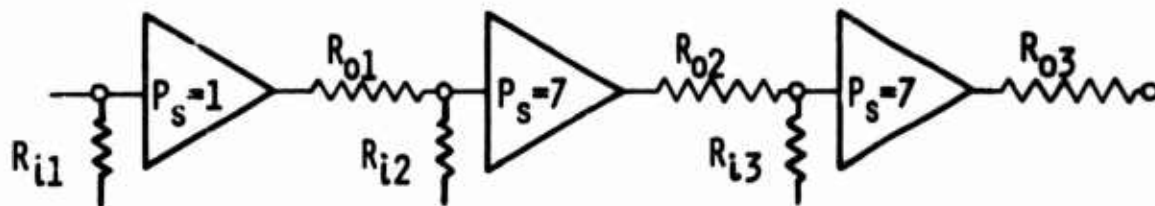
#### 4. DESIGN EXAMPLE OF MULTIPLE-ELEMENT STAGING

In references 15 and 16 the staging of the single amplifiers to form a multistage cascade without a reduction of the amplifier's dynamic range is discussed. This concept assures that in all stages the jets are deflected through the same angle. Further work is ongoing in multistage cascades that will formally outline the staging principles with regard to impedance match, jet deflection and bias effects on the inter-stage performance. The results of this work are not available for this report, but some test data on staging cascades is available and will be described. The fact that simple circuit analogs can be used to predict multistage amplifier performance to a reasonable degree of accuracy is significant. Examples are given to illustrate the straightforwardness of the staging method.

In the first example, HDL amplifier model 2-2B of figure 1 was multistaged in three separate configurations. These configurations are discussed below.



modeling as shown below referencing the supply pressures to the supply of the first stage.



If these models are operated at the same Reynolds number,  $N_{Rh} = \sigma N_R$  (based on height) the normalizing resistances  $\frac{P_s}{Q_s}$  essentially scale as their supply pressures. This can be shown by noting  $\frac{P_s}{Q_s} = \frac{P_s}{b_s h_s v_s c_d} = \frac{P_s}{N_{Rh} b_s v c_d}$ . This assumes that  $N_{Rh} c_d$  is the same for all stages.  $c_d N_{Rh}$  is, of course, the Reynolds number based on flow and element depth. Making this simplifying assumption, the gains can be estimated.

From section 2.5, the input resistance of this amplifier when the jet is being deflected is about  $0.3 \frac{P_s}{Q_s}$ . The supply impedance  $\frac{P_s}{Q_s}$  of the first stage is taken as the normalizing resistance for each stage. The output resistance for each stage is approximately  $0.5 \frac{P_s}{Q_s}$ . Therefore we can write

$$\begin{aligned} R_{i1} &= 0.3 \\ R_{o1} &= 0.5 \\ R_{i2} &= \frac{7}{2} \times 0.3 \quad (\text{two stages}) \\ R_{o2} &= \frac{7}{2} \times 0.5 \quad (\text{two stages}) \\ R_{i3} &= \frac{7}{4} \times 0.3 \quad (\text{four stages}) \\ R_{o3} &= \frac{7}{4} \times 0.5 \quad (\text{four stages}) \end{aligned}$$

The bias effect can be estimated from equation 52. From this equation the gain can be written as

$$G_p = \frac{G_p|_{P_j=0}}{1 + K_3 \sqrt{P_j}} \quad \text{assume for higher bias } P_j = P_c.$$

where  $K_3 = \frac{2 k_j R_c / c_d}{1 + a_1 k_j R_c + \frac{c}{R_v}} = 2.20$  for this amplifier,  $a_1 = 0.12$ ,  
 $k_j = 6.18$  and  $R_c = 1.2$ .

The model 2-2B has a  $G_p = 16$ , at zero bias.

To estimate the bias pressure, the output blocked-area pressure recovery in each channel for a centered set is assumed to be  $0.25 P_s$ . This varies with Reynolds number but for simplicity a constant value is assumed.

Calculating the bias effect of the first stage where  $2\% P_s$  was the bias pressure level

$$1 + K_3 \sqrt{P_c} = 1 + 2.20 \sqrt{0.02} = 1.31.$$

For the first to second stage,

$$1 + K_3 \sqrt{P_c} = 1 + 2.20 \sqrt{\left(\frac{0.25}{7}\right) (0.875)} = 1.39$$

where 0.87 is the ratio of centered jet resistance to the total resistance between stages

and  $\frac{0.25}{7}$  is the pressure normalized to the second-stage supply.

For the second to third stage,

$$1 + K_3 \sqrt{P_c} = 1 + 2.20 \sqrt{(0.25) (0.5)} = 1.78$$

where (0.5) is the ratio of the centered jet resistance to the total resistance between stages and the supply pressures of the second and third stages are the same. The total gain of the cascade can now be calculated. Total cascade gain for blocked-area 3rd stage.

$$G_p = \frac{G_{p1}}{1 + K_3 \sqrt{P_{c1}}} \cdot \frac{R_{12}}{R_{01} + R_{12}} \cdot \frac{G_{p2}}{1 + K_3 \sqrt{P_{c2}}} \cdot \frac{R_{13}}{R_{02} + R_{13}} \cdot \frac{G_{p3}}{1 + K_3 \sqrt{P_{c3}}}$$

$$G_p = \frac{16}{1 + 0.31} \cdot (0.636) \cdot \frac{16}{1 + 0.37} \cdot (0.23) \cdot \frac{16}{1 + 0.78}$$

$$G_p = 185 \quad (\text{values of 175 to 180 have been measured}).$$

where  $G_{p1,2,3}$  are the zero bias blocked-output pressure gains of each stage.

B. A similar example, with only two parallel third stages being driven.

The resistance values are the same except that

$$R_{13} = \frac{7}{2} \times 0.3$$

$$R_{03} = \frac{7}{2} \times 0.3$$

and the bias effect of the second to third stages changes

$$1 + K_3 \sqrt{P_{c3}} = 1 + 2.2 \sqrt{0.25 (0.667)} = 1.89$$

where 0.667 is the ratio of centered jet resistance to total resistance between stages

and the total cascade gain is

$$G_p = \frac{16}{1 + 0.31} (0.636) \frac{16}{1 + 0.39} (0.374) \frac{16}{1 + .89}$$

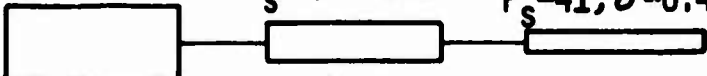
$$G_p = 283 \quad (\text{Actual measured value is 260}).$$

The elimination of two of the parallel third stages improves the resistance ratio between the second and third stages, but it also increases the third stage bias pressure.

C. A third example is a multistage cascade with single second and third amplifiers. This is shown schematically as

$b_s = 0.5 \text{ mm}$	$0.5 \text{ mm}$	$0.5 \text{ mm}$
$h_s = 0.8 \text{ mm}$	$0.4 \text{ mm}$	$0.2 \text{ mm}$
$P_s = 0.13 \text{ kPa}$	$0.93 \text{ kPa}$	$5.67 \text{ kPa}$

$P_s = 1, \sigma = 1.6$      $P_s = 7, \sigma = 0.8$      $P_s = 41, \sigma = 0.4$



The first stage bias is the same as previous examples, though the resistances are significantly different.

In normalized form, referenced to  $\frac{P_s}{Q_s}$  of first stage the resistors are

$$R_{i1} = 0.3, R_{o1} = 0.5, R_{i2} = 7 \times 0.3 = 2.1, R_{o2} = 7 \times 0.5 = 3.5,$$

$$R_{i3} = 41 \times 0.3 = 12.3, R_{o3} = 41 \times 0.5 = 20.5.$$

The resistance ratios are  $\frac{R_{i2}}{R_{i2} + R_{o1}} = \frac{2.1}{2.1 + 0.5} = 0.807, \frac{R_{i3}}{R_{o2} + R_{i3}} =$

$$\frac{12.3}{3.5 + 12.3} = 0.778.$$

The second-stage bias effect is

$$1 + K_3 \sqrt{P_{c2}} = 1 + 2.2 \sqrt{\frac{0.25}{7} (0.933)} = 1.4$$

where 0.933 is the ratio of the centered jet resistance to the total resistance between stages

and the third stage bias effect is

$$1 + K_3 \sqrt{P_{c3}} = 1 + 2.2 \sqrt{(0.25) \left(\frac{7}{41}\right) (0.92)} = 1.43$$

where 0.92 is the ratio of jet centered resistance to total resistance between stages.

The total cascade gain is

$$G_p = \left(\frac{16}{1 + .31}\right) (0.807) \left(\frac{16}{1 + .4}\right) (0.778) \left(\frac{16}{1 + .43}\right) = 980$$

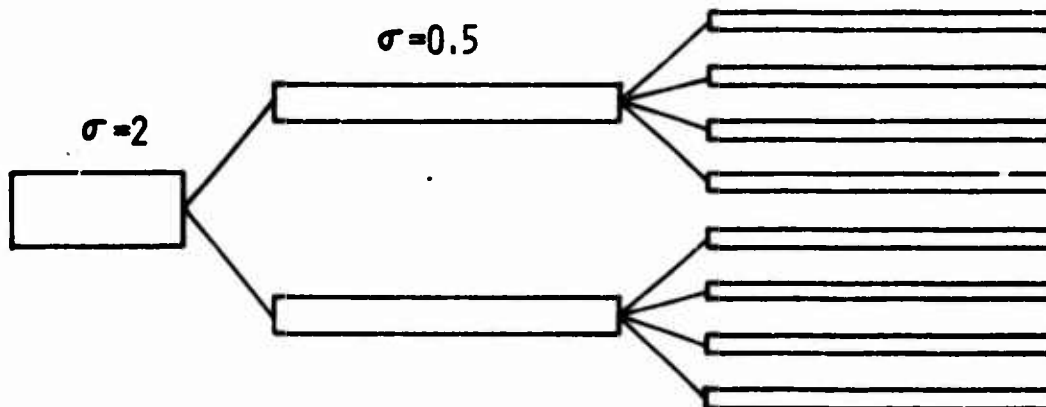
$$G_p = 980.7 \text{ (Actual measured value for such a cascade is 910)}$$

This last assembly over-predicts the actual measured gain but the measurement of this gain may be off by 10

All of the above estimates assumed K was constant, centered jet pressure recovery was constant and that resistances scaled as the supply pressure. This last assumption is clearly in error for the shallow third stage; nevertheless, the cascade gain is estimated within 10.

Additional examples are results obtained by D. N. Wormley<sup>30</sup> at MIT testing multistage amplifier cascades (of the same design) in hydraulic oil. Wormley's example is

$P_{s1} = 110 \text{ kPa}$	$P_{s2} = 660 \text{ kPa}$	$P_{s3} = 3960 \text{ kPa}$
$b_{s1} = 0.5 \text{ mm}$	$b_{s2} = 1.0 \text{ mm}$	$b_{s3} = 1.0 \text{ mm}$
$h_1 = 1 \text{ mm}$	$h_2 = 0.5 \text{ mm}$	$h_3 = 0.25 \text{ mm}$
$R_{i1} = 0.3$	$R_{i2} = 0.3(6)(.5)(.5)$	$R_{i3} = 0.3(36/6)(2/8)$
$R_{o1} = 0.5$	$R_{o2} = 0.5(6)(.5)(.5)$	$R_{o3} = 0.5(36/6)(2/8)$
		$\sigma = 0.25$



He reports a pressure gain of 375 whereas, if the Reynolds number, discharge coefficients and centered-jet pressure recovery are assumed constant for all stages, the gain is calculated at 406. The first stage bias effect is  $1 + 2.2 \sqrt{P_c} = 1 + 0.490$  for  $P_{c1} = 0.05$

and for the second stage  $1 + 2.2 \sqrt{\frac{(0.25)(1)}{6}} (0.75) = 1 + 0.39$   
 where  $0.75 = \Delta P_c / \Delta Q_c|_{1, \delta=0} / (\Delta P_c / \Delta Q_c|_{2, \delta=0} + R_{o1})$ .

(MIT reports  $P_{c2} = 0.024$  and the calculation estimates  $P_{c2} = 0.03$ ).  
 The third stage bias effect is

$$1 + 2.2 \sqrt{\frac{0.25}{36} \times 6} (0.75) = 1 + 0.39$$

where 0.75 is the ratio of jet centered resistance to total resistance between stages.

The gain is then

$$G_p = \left(\frac{16}{1.49}\right) (.64) \left(\frac{16}{1.39}\right) (.446) \left(\frac{16}{1.39}\right) = 406$$

The inaccuracy is only 8% even though the assumptions in discharge coefficient, Reynolds number and pressure recovery that were assumed cannot be assumed if more accuracy is desired.

Another example of an earlier HDL design model<sup>16</sup> 2-1, used an amplifier with a thin splitter and less inlet-line loss ( $R_c$  depends on the inlet line length) and gave a measured pressure gain of about 3000, whereas it was calculated to be 2800 assuming  $G_p$  was 20 per stage. This staging arrangement is the same as the example in part C above. The deflection characteristics of this example are shown in figure 27 as differential output pressure vs differential control pressure as measured between stages. From this figure it can be seen that the last stage is into saturation well before the output of the first reaches its saturation. This indicates that these elements have not been properly staged for maximum dynamic range and as a result the dynamic range has been reduced.

By paralleling individual amplifier laminates, the amplifier can be designed to operate at a design pressure with a lower output impedance. A multisection amplifier is still one amplifier whose design is specified by the pressure range, the impedance needed and the working fluid. This can be illustrated by considering a high pressure stage designed to have the same impedance as a low pressure stage. Since the input resistance is approximately  $0.3 P_s / Q_s$  and if each section has the same flow (same Reynolds number based on depth), and if  $P_s$  is increased by a factor of ten, then ten parallel sections are required. Note that each amplifier section is about  $\sqrt{10}$  the depth of the low pressure stage if the operating Reynolds based on unit depth is maintained. As a result the higher pressure stage is 3 to 4 times as tall as the low pressure stage but it handles 10 times the flow at 10 times the pressure.

## 5. DISCUSSION

The information presented here attempts to quantify some particularly complicated flow problems in laminar jet deflection amplifiers. It has been the intent of the authors to present the material in as concise a form as possible, without sacrificing any intuitive or physical reasoning.



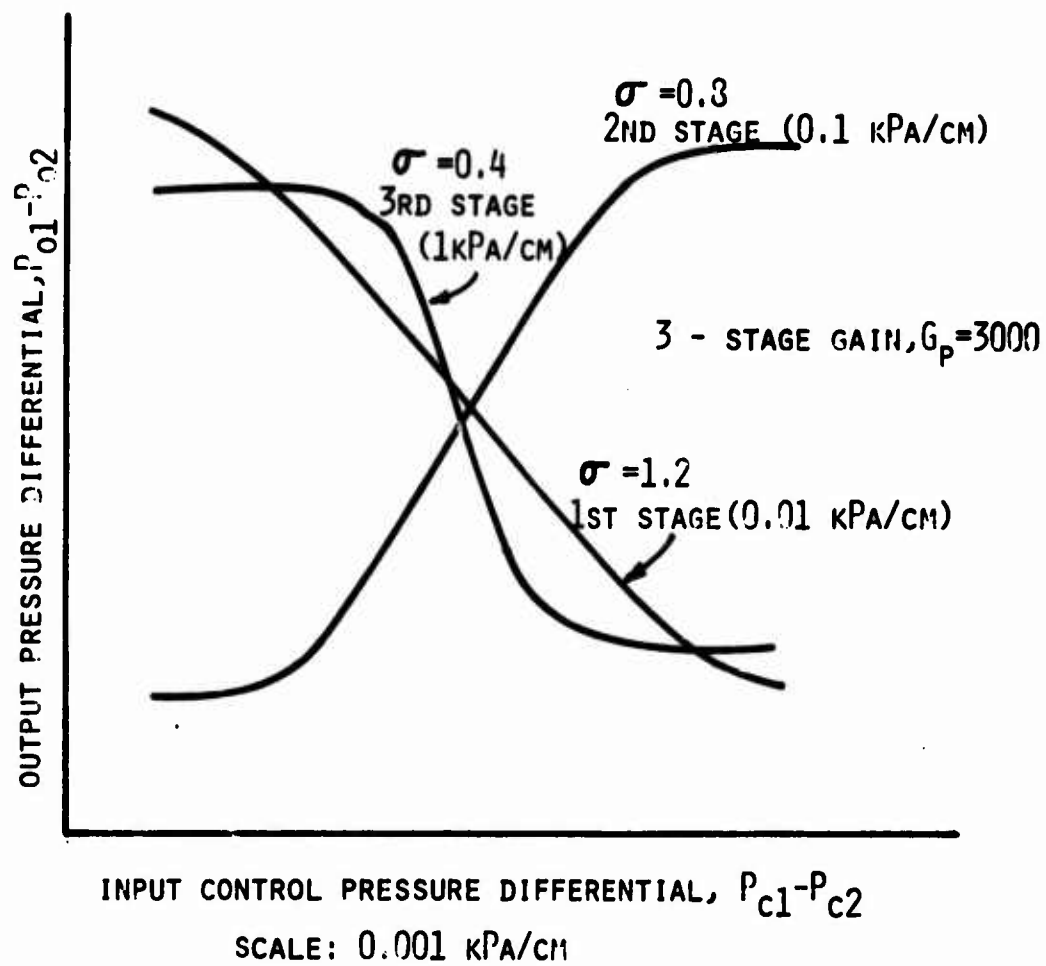


Figure 27. Measured interstage gain characteristics in a gain block

Certainly the fluid mechanics can be improved upon, but from an engineering standpoint the accuracy obtained from this model is well within accepted standard engineering practice.

On the whole, laminar jet deflection can be utilized in a number of different amplifiers and sensors. The basic calculations for gain, response and resistances presented here can be used to estimate the response of these other devices. For example, a laminar flip-flop has been reported<sup>31</sup> where internal feedback in the form of a regulated vent pressure is used to drive the LPA into saturation so that only the saturation states are stable. Another device that operates on the pressure field principle is a gas-liquid interface amplifier as reported by Woods.<sup>32</sup> This amplifier may actually often be used in the transition or even turbulent regime for more output power; however, its basic dynamics and response can be estimated if surface tension effects are included using the results presented.

Two sensors also utilize the basic principles of laminar jet deflection. The Laminar [Jet] Angular Rate Sensor (LARS)<sup>33</sup> is basically a laminar jet, impinging on receivers, that is deflected by the Coriolis acceleration due to a rotation of the geometry. The jet deflection, dynamic response and threshold can be estimated using the analysis presented here. Yet another sensor is a Laminar Jet Linear Accelerometer that utilizes an LPA with a gaseous medium. The gas exiting from the supply nozzle is at a slightly higher pressure than the surrounding fluid, hence its density is slightly higher. If a high acceleration is imposed transverse to the jet, then the jet may be deflected in proportion to the acceleration and the density difference. For a given density difference, output is linearly proportional to acceleration. The threshold of such a device is greater than 20-g. Again--since this is basically an LPA--all the analysis herein pertains.

## 6. SUMMARY AND CONCLUSIONS

This report presents an analysis for the flow parameters and the operating characteristics of laminar jet deflection devices. The feasibility of the assumptions and method has been established by good agreement between theory and experimental data. Basically, the method of solution used has been a combination of lumped-equivalent circuits, control volume and superposed integral techniques. The resistances of the channels have been determined based on their analytically determined viscous losses using integral methods. The jet deflection has been determined from a control volume approach, and the dynamic response of the inputs and the gain have used lumped parameter equivalent circuit techniques.

The analysis has shown that the gain of an LPA is a complex function of Reynolds number where for a particular planview the aspect ratio can be eliminated by dividing  $N_R$  by the quantity  $(1 + 1/\sigma)^2$ . The maximum gain of a device is determined by the geometry and the bias.

The dynamic range of such a device is limited only by the flow noise in the source and any noise generated inside the amplifier. If the flow field is truly laminar and the source is noiseless, then the dynamic range should be limited only by thermal noise within the bandwidth of the device. Edgetones and resonances out of the bandwidth will not affect the dynamic range. Observed values of dynamic range have been of the order of 5000, using air as the working medium. The limiting factor was ambient room noise. Operating in hydraulic oil offers more isolation from outside perturbations and, consequently, the promise of even higher dynamic range.

The fact that the flow is laminar offers, in addition, the great advantage of the ability to scale. Accurate large-scale modeling<sup>17</sup> allows a great deal of flexibility in testing and evaluating new designs. An accurate model may be simply machined and the performance readily determined. In addition, since the analysis scales, larger amplifiers as well as miniature amplifiers are related simply through Reynolds number.<sup>20</sup>

In conclusion, a design analysis for laminar proportional amplifiers is now available for the engineer, who can now design--completely on paper--specialized amplifiers, gain blocks and cascades, and incorporate the results in control systems, since the amplifiers can be looked at only in terms of input and output impedances and gain.

The authors recommend that more basic research is needed to determine with greater precision the vent impedance  $R_v$  and the pressure recovery, to include the losses due to the plates, splitter and deflections. The area of null shifts due to fabrication anomalies and the steering effect of nozzle exit radii should be further investigated. The form of the equations presented here should be sufficient to suggest other areas of research.

7. LITERATURE CITED

- (1) Peperone, S., Katz, S. and Goto, J., "Fluid Amplification 4. Gain Analysis of the Proportional Fluid Amplifier," Harry Diamond Labs, Wash., DC, October 1962, AD-296513.
- (2) Katz, S., Ch. 13, Fluid Amplifiers, J. M. Kirshner editor, McGraw-Hill, New York, 1966.
- (3) Van Tilburg, R., Bellman, R., and Cochran, W., "Fluidics 21. Optical Fabrication of Fluid Amplifiers and Circuits," Harry Diamond Labs, May 1966, AD 636842.
- (4) Weinger, S., "Effect of Aspect Ratio on Noise in Proportional Amplifiers," Advances in Fluidics ed F. T. Brown, ASME, 1967.
- (5) Kelley, L., and Boothe, W., "Hydraulic Fluidics," Trans. ASME, Journal of Dyn. Syst., Meas. and Control, June 1973.
- (6) Drzewiecki, T. M., "Test Report on Fluidic Logic Devices," HDL-TR-1601, Harry Diamond Labs, Wash., DC, July 1972.
- (7) Manion, F. M., "Jet Interaction in a Defined Region," M.Sc. Thesis, The Catholic University of America, 1962.
- (8) Foss, J. F., and Kleis, S. J., "The Defined Region Geometry for High-Gain Proportional Fluid Amplifiers," Progress Report No. 1, Contract DAAG-39-68-C-0034, Michigan State University, Jan., 1970.
- (9) Manion, F. M., "Proportional Amplifier Simulation," Advances in Fluidics, ed. F. T. Brown, ASME, 1967.
- (10) Brown, F. T., and Simpson, A. K., "Research in Pressure Controlled Jet Amplifiers," AD-605860, 1963.
- (11) Gurski, R. J., "Static and Dynamic Modelling of a Pressure Controlled Subsonic Fluid Jet Modulator," Sc.D. Thesis, MIT, May 1965.
- (12) Shearer, J. L., and Stiffler, A. K., "Fluid Amplifier Pressure Sensor Research," Penn. St. Syst. and Controls Lab, Report #2, Oct 1965.
- (13) Drzewiecki, T. M., "Analytical and Experimental Investigation of Pressure Field Amplifiers," Proc. HDL Student Trainee Technical Symposium, Part I, Graduate, Harry Diamond Labs, Wash., DC, 1967.
- (14) Griffin, W. S. and Gebben, V. D., "A Proportional Fluid Jet Amplifier with Flat Saturation Characteristics and its Application to a Gain Block," NASA TM X-1915, Nov., 1969.

- (15) Manion, F. M. and Mon, G., "Fluerics 33. Design and Staging of Laminar Proportional Amplifiers," HDL TR-1608, Harry Diamond Labs, Wash., DC, Sept. 1972.
- (16) Mon, G., "Laminar Proportional Amplifier," Proc. 6th Cranfield Fluidics Conference, Cambridge, England, March, 1974.
- (17) Spyropoulos, C. E., "Large Scale Modeling of Laminar Fluoric Devices," HDL TM-73-28, Harry Diamond Labs, Wash., DC, Aug. 1973.
- (18) Drzewiecki, T. M., "Planar Nozzle Discharge Coefficients," Proc. 13th Midwestern Mechanics Conference, Developments on Mechanics vol. 7, Aug. 1973.
- (19) Drzewiecki, T. M., "Fluerics 37. A General Planar Nozzle Discharge Coefficient Representation," HDL-TM-74-5, Harry Diamond Labs, Wash., DC, 1974.
- (20) Drzewiecki, T. M., "A Fluid Amplifier Reynolds Number," Proc. HDL Fluidics State-of-the-Art Symposium, Adelphi, MD, 30 Sep - 3 Oct 1974.
- (21) Schlichting, H., Boundary Layer Theory, 4th edition, McGraw-Hill, N.Y., 1960.
- (22) Bourque, C. and Newman, B. G., "Reattachment of a Two-Dimensional, Incompressible Jet to an Adjacent Flat Plate," Aero. Quart, Vol. XI, Aug. 1960.
- (23) Goto, J. M., and Drzewiecki, T. M., "Fluerics 32. An Analytical Model for the Response of Fluoric Wall Attachment Amplifiers," HDL-TR-1598, Harry Diamond Labs, Wash., DC, June 1972.
- (24) Williams, J. C., III, Cheng, E. H., and Kim, K. H., "Curvature Effects in the Laminar and Turbulent Freejet Boundary," AIAA Journal, V. 9, no. 4, April 1971.
- (25) Drzewiecki, T. M., "The Interpretation of Surface Static Pressure Distributions in Fluid Amplifier Applications," HDL-TR-1627, Harry Diamond Labs, Wash., DC, July 1973.
- (26) Dimopoulos, H. G. and Hanratty, T. J., "Wall Shear Stress Distribution for Flow Around a Circular Cylinder,  $60 < Re \text{ (sic)} < 340$ " Dept. of Chemistry and Chemical Eng., U. of Illinois, Urbana, ILL., Oct 1967 (AD 662015).
- (27) Comparin, R. A., Moses, H. L. and Rowell, E. F., "Contamination Effects in a Laminar Proportional Amplifier," Proc. HDL Fluidics State-of-the-Art Symposium, Adelphi, MD, 30 Sep - 3 Oct, 1974.

- (28) Toda, K. and Katz, S., "Fluidic Impedance Measurement with a Half Bridge Circuit," Proc. HDL Fluidics State-of-the-Art Symp., Adelphi, MD, 1974.
- (29) Smith, G. V., and Shearer, J. L., "Static Characteristics of Laminar Proportional Amplifiers," Progress Report Contract DAAG-39-73-C-0213, Penn St. Univ., April, 1974.
- (30) Wormley, D., Personal Communication, MIT contract DAAG-39-73-C-0223, Jan 1974.
- (31) Drzewiecki, T. M., and Manion, F. M., "The Laminar Flip-Flop," Proc. HDL Fluidics State-of-the-Art Symposium, Adelphi, MD 30 Sep - 3 Oct 1974.
- (32) Woods, R. L., "A Gas-to-Liquid Interface Amplifier," Trans. of ASME, J. Dyn. Syst. Meas. and Control, June, 1973.
- (33) Young, R., "Development of a Laminar Angular Rate Sensor (LARS)," Proc. HDL Fluidics State-of-the-Art Symp., Adelphi, MD, 30 Sep - 3 Oct 1974.

**EXPERIMENTAL DESIGN OF LAMINAR PROPORTIONAL AMPLIFIERS**

**R. F. Hellbaum**

**NASA Langley Research Center  
Hampton, Virginia**

**Presented at the Fluidics State-of-the-Art Symposium**

**Adelphi, Maryland  
September 30-October 3, 1974**

**Preceding page blank**

## EXPERIMENTAL DESIGN OF LAMINAR PROPORTIONAL AMPLIFIERS

R. F. Hellbaum  
NASA Langley Research Center  
Hampton, Virginia

### SUMMARY

An experimental program was initiated at Langley Research Center to study the effects of various parameters on the design of laminar proportional beam deflection amplifiers. Matching and staging of amplifiers to obtain high-pressure gain was also studied. Dynamic effects were not included. Variable parameters were aspect ratio, setback, control length, receiver distance, receiver width, width of center vent, and bias pressure levels. Usable pressure gains from 4 to 19 per stage can now be achieved, and five amplifiers have been staged together to yield pressure gains up to 2,000,000.

### INTRODUCTION

Early models of fluid amplifiers were operated on turbulent flow which produced excessive noise levels and low gain. Background information on the prior development and design of jet deflection proportional amplifiers is detailed by Kirshner and Manion (Ref. 1). This also provides an excellent source bibliography. A pressure field proportional amplifier which was developed by Griffin and Gebben (Ref. 2) was modified to be useful with laminar flow. Because of the success of this program, an experimental effort was initiated to show how various parameters affect the design of fluid amplifiers and to show how to match and stage the amplifiers to obtain high-pressure gain. The scope of this work includes design and staging of beam-deflection proportional amplifiers operated in the laminar mode. Dynamic effects are not included; however, they are treated by Manion and Mon (Ref. 3) which also includes important staging concepts. Harry Diamond Laboratories provided the use of their facilities for testing the water models. Significant improvements have been made in both hardware and analytical procedures. To date, five amplifiers have been staged together to yield pressure gains up to 2,000,000, and usable pressure gains from 4 to 19 per stage can now be achieved. By operation in the laminar flow region, noise level and power consumption have both been reduced.

### SYMBOLS

$B_c$  Control length (normalized to  $b_s$ )

$B_{cv}$  Width of center vent (normalized by  $b_s$ )

L-9714



$B_r$	Receiver width (normalized to $b_s$ )
$B_{sb}$	Setback (normalized to $b_s$ )
$b_m$	Maneuvering distance, m
$b_s$	Supply duct width, m
$b_t$	Width of throat between control ducts, m
$d$	Distance swept by supply jet at receiver, m
$G_p$	Gain, pressure
$h_s$	Supply duct depth
$L_r$	Receiver distance (normalized to $b_s$ )
$N_R$	Reynolds number (based on height)
$P_B$	Bias pressure (% of $P_s$ )
$P_c$	Control pressure, $N/m^2$
$P_{cd}$	Control differential pressure, $N/m^2$
$P_o$	Output pressure, $N/m^2$
$P_{od}$	Output differential pressure, $N/m^2$
$P_s$	Supply pressure, $N/m^2$
$P_v$	Vent chamber pressure, $N/m^2$
$Q_c$	Control flow, $m^3/s$
$Q_o$	Output flow, $m^3/s$
$Q_s$	Supply flow, $m^3/s$
$V_s$	Average supply velocity at the exit throat, m/s
$\Delta p_o$	Change in output pressure, $N/m^2$
$\theta$	Supply jet deflection angle, radians
$\nu$	Kinematic viscosity, $m^2/s$
$\sigma$	Aspect ratio

## TEST AND APPARATUS

Two types of tests were conducted. Water models provided flow visualization and qualitative information, and pneumatic models provided quantitative data. The variable parameters were aspect ratio, setback, control length, receiver distance, receiver width, and width of the center vent. The water models were eight times larger than the pneumatic models, which had a supply throat width of 1 mm. Twenty-five water models were machined in plexiglass on a line-tracing milling machine. The line drawings were generated by computer.

For the water model tests, cover and baseplates provided a collection manifold for the vents, water connections, dye trace inputs, and air bubble bleeds. The amplifier layer was sandwiched between the cover and baseplates and secured with large clamps (Fig. 1). Water from a large settling (deaeration) tank was pumped up to a constant head supply tank. The water then flowed through the test model to a constant head sink tank. Three rotometers were between the supply tank and test model to monitor supply and control flow. Provisions were made to permit dye trace tagging of individual streamlines in the supply flow (Fig. 2) in addition to coloring the entire supply duct flow. To obtain neutral buoyancy in the water, alcohol was added to the food coloring used as the dyeing agent. The use of the large water models has proven to be an excellent method of visualizing many of the complex flow phenomena found in amplifiers. However, many of the planned parametric variations do not exhibit noticeable changes in flow patterns; for example, small changes in gain cannot be easily distinguished.

The pneumatic models were machined on a pantograph using the water models as templates. The test instrumentation consisted of capacitance pressure transducers, laminar flow tubes, a signal generator, and an X-Y plotter. A test cover block was clamped to the model as shown in Figure 3. Supply, input, and output flows were monitored. Supply and input pressures were measured relative to vent pressure, and output and vent pressures were measured relative to ambient room pressure. Differential input and output pressures were plotted on the X-Y plotter as a measure of gain.

In setting up the tests, output flow was adjusted to approximately that required by a succeeding stage operating at a reduced aspect ratio and at zero bias. The signal generator was used to adjust the input pressures (with vent opened to ambient) to simulate a previous stage of greater aspect ratio. The vent chamber pressure was then adjusted to set the bias level back to zero. Gain was plotted by changing the differential pressure signal from the signal generator. The signal generator was then adjusted to a new bias and gain was replotted. Data were collected for bias levels of 0,  $\pm 5\%$ , and  $\pm 10\%$  of supply pressure.

## RESULTS

### Reynolds Number

As used in this text, Reynolds number is based on the supply duct depth  $h$  (Ref. 3) as shown in Equation (1).

$$N_R = \frac{V_s h_s}{\nu} \quad (1)$$

since supply flow is expressed as

$$Q_s = b_s h_s V_s \quad (2)$$

which can be rewritten as

$$V_s h_s = \frac{Q_s}{b_s} \quad (3)$$

substituting Equation (3) into Equation (1) gives

$$N_R = \frac{Q_s}{b_s \nu} \quad (4)$$

which is a more convenient form to use for calculation. A typical plot of gain versus Reynolds number is shown in Figure 4. From this curve it can be seen that gain does not increase substantially for  $N_R$  greater than 800. Since noise increases as Reynolds number increases, the dynamic range will decrease for Reynolds numbers larger than 800.

### Aspect Ratio

The aspect ratio of the amplifier is the supply duct depth divided by the width of the supply duct. If amplifiers, having the same silhouette but varying in depth are operated at the same  $N_R$ , they will exhibit many of the same properties, such as gain, supply flow, and effects due to bias normalized to supply pressure. The main differences are operating pressures. For example, an amplifier with a 1-mm by 1.5-mm-high supply duct ( $\sigma = 1.5$ ) might operate at a supply pressure of 133 N/m<sup>2</sup>, while one with a 1-mm by 0.3-mm-high supply duct ( $\sigma = 0.3$ ) might operate at a supply pressure 50 times higher.

### Bias Level

Bias ( $P_B$ ), as used in this paper, is defined as the average pressure level of the control ducts relative to the vent pressure. Bias pressure affects the

gain, stability, and noise level of an amplifier. The graph of gain versus bias (Fig. 5) shows that a higher bias yields reduced gain. Low bias yields reduced stability. Gain usually increases until an unstable condition exists but may reach a maximum and then decrease before going unstable. As stability is reduced, the noise level is increased.

#### Vent Pressure

The vent pressure is the pressure in the vent chamber which collects all the flow to and from the vents of the amplifier and is connected to the low-pressure return line through a restrictor. The restrictor is used to set the vent pressure level. By reducing the flow through the restrictor, the vent pressure is increased. If the vent pressure is increased, the bias is decreased which increases the gain. It has been found that changing the gain in this way is very useful when adjusting the gain of each stage in multiple amplifier chains.

#### Setback

Setback ( $B_{sb}$ ) is the distance between the downstream edge of the control duct and an ideal nonexpanded supply stream divided by supply duct width ( $b_s$ ) (Fig. 6). It can be calculated using Equation (5).

$$B_{sb} = \frac{b_t - b_s}{2b_s} \quad (5)$$

It would be meaningful to use a maneuvering distance which is the real clearance distance between the downstream edge of the control duct and a real supply stream (Fig. 7). Since maneuvering distance is difficult to calculate because the real supply stream width is not always easily obtained, setback is usually used for making comparisons.

Setback affects bias and saturation characteristics, gain, and input impedance. As setback is reduced (i.e., from 5/8 to 0), the gain increases (this is more noticeable for higher bias levels) (Fig. 8) and input impedance for bias flow (Fig. 9) increases. The input impedance for signal flow (i.e., bias equals a constant) increases only slightly for  $P_{cd} = 0$ . Since setback affects the saturation characteristics, the design choice depends on the particular application. If the application allows an amplifier to saturate, it is usually desirable for the output to remain at or close to its maximum value (Fig. 10(a)). This type of saturation characteristic is obtained at higher values of setback, that is, 5/8 to 1. As setback is decreased, the saturation characteristic deteriorates (Fig. 10(b)). In the extreme saturation characteristics shown in Figure 10(c), the output reverses itself at saturation, which might well be catastrophic to many control systems. This deterioration of the saturation characteristic usually occurs at low bias levels with a negative flow in one of the control ducts. The supply flow is deflected off the downstream edge of the control duct (Fig. 11). Figure 12 shows that greater

deflection by reduced setback provides greater reversed output. This process of deflecting the jet off the control duct edge tends to introduce secondary flows (Fig. 13), and disperses the jet which reduces the differential recovery pressure. Notice how the left tagged streamline separates to flow above and below the supply stream much like classical corner flow. A boundary-layer leak flow across the supply stream from the high-pressure side to the low-pressure control is also shown by the dark, heavily dyed control flow. Both the reverse deflection and the dispersion of the supply jet adversely affect the saturation characteristics.

#### Control Length

The width of the control duct at the supply stream is called the control length  $B_c$  (Fig. 6). Changing the control length from 1.25 to 5.25 results in an increase in the gain as shown in Figure 14. Increasing the control length increases the area over which the control pressure acts, producing greater deflection force.

It should be noted that increasing the control length decreases the maneuvering distance which adversely affects the saturation characteristic. More maneuvering distance is required for jet deflection if larger control lengths are desired. Increased maneuvering distance is achieved by increasing setback which, in turn, decreases gain and input impedance.

#### Receiver Distance

Receiver distance  $L_r$  (Fig. 6) is the distance from the supply duct outlet to the receiver. There are two major opposing factors in choosing receiver distance. The first consideration involves the deflection of the jet by an angle  $\theta$  (Fig. 15). The sweep distance is increased by increasing  $L_r$  which also acts to increase the gain. The opposing factor is the degeneration of the velocity profile as the supply jet proceeds downstream.

As the jet proceeds downstream, it loses peak velocity and spreads. The lower, wider pressure profile must sweep farther to create the same change in output pressure as seen in Figure 16. Optimum gain occurred at a receiver distance of approximately nine times the supply width,  $b_s$ , (Fig. 17).

#### Receiver Width

The choice of receiver width  $B_r$  (Fig. 6) involves several trade offs. The pressure at the receiver will be an average of the pressure profile imposed upon it by the supply jet. To achieve optimum results, the steepest portion of the pressure profile should be utilized (Fig. 18), which implies that the  $B_r$  should be small. This is substantiated by the data shown in Figure 19. One restraining factor is the amount of flow required. If more flow is required to drive a low impedance device, wider output will lower the output impedance of the amplifier. Another restraining factor is the

practical problem of fabricating narrower channels. This may involve a trade off in cost or contamination reliability.

#### Center Vent Width

The data in Figure 20 show that the narrower center vents  $B_{cv}$  (Fig. 6) produced higher gains. Extrapolation of the curve in Figure 20 seems to imply that the highest gain is achieved with no center vent. This has not been shown to be true. Amplifiers with no center vent are discussed in Reference 3. The center vent configuration was chosen because lower average recovery pressure levels can be obtained in the receivers. Since the bias level of an amplifier is affected by the output of the preceding amplifier, it is advantageous to reduce the average pressure received. This can be accomplished by use of a center vent which removes a portion of the midstream flow. The overriding factor in choosing a  $B_{cv} = 0.75$  for the working silhouette was the minimum channel dimension required for fabrication and reliability.

#### Supply Conditioning

A short supply duct is efficient from the standpoint of power and material (fabrication cost). However, the longer and more elaborate supply duct used in these experiments provides a quieting or settling and straightening effect which helps reduce downstream velocity profile degradation at the expense of a small power loss.

#### Tolerances

Ideally, the gain curve should pass through zero. Even more important, the output should not change even though the bias level is changed and the vent chamber pressure is varied. The change in output pressure with change in bias pressure is a measure of the common mode rejection. Vent pressure affects bias and may affect differential output pressure, so another type of common mode rejection is the change in output pressure with change in vent pressure.

These two types of common mode rejection become very important when staging amplifiers to achieve high gain, since small disturbances may feed back through the vent lines to the primary stages and be amplified through the entire gain block, resulting in catastrophic oscillation.

The kind of tolerance which should be placed on common mode rejection is dependent on many things, such as noise from the power source, other noise sources, and total gain required from staged amplifiers. The first amplifier must have higher specified tolerances than the second, because the noise or noise signal deviation generated in the first stage is amplified by all the rest of the amplifiers. For example, if two stages each generate one unit of noise, and each stage has a gain of 10, the output of the second stage would have 11 units of noise, 10 from the first stage and one from the second stage.

## MULTISTAGE MATCHING OF AMPLIFIERS FOR PRESSURE GAIN

In designing a multistage amplifier, the type of gain desired, that is, pressure, flow, or power is the first consideration. To achieve pressure gain, a low supply pressure is used for the first stage. Supply pressure is progressively increased at each stage by holding the silhouette and  $N_R$  constant and reducing the aspect ratio of each stage. Using this concept, the supply flow remains nearly constant between stages. The reduced heights cause each stage to operate into the higher impedance of the next stage. Nominal supply pressures for five stages might be 133 N/m<sup>2</sup>, 500 N/m<sup>2</sup>, 1000 N/m<sup>2</sup>, 2000 N/m<sup>2</sup>, and 6000 N/m<sup>2</sup>, respectively, for stages having aspect ratios of 1.5, 0.75, 0.5, 0.375, and 0.3, and a supply duct width of 1 mm. Figure 21 shows a cast block in which five amplifiers are internally connected, including supply and vent manifold. This amplifier chain has a pressure gain of 100,000. The gain is controlled by adjusting the vent chamber pressures so that bias pressures are all near zero for higher gain. Other amplifier types might require a different bias level for high gain due to input channel resistance and onset of instabilities. Higher bias yields greater stability and lower gains.

## CONCLUDING REMARKS

It was found that there is a Reynolds number which provides maximum gain and dynamic range in laminar proportional amplifiers. If the Reynolds number is kept constant, the aspect ratio can be changed to obtain different supply pressure. Gain was found to be a function of bias level and could be adjusted by changing the vent pressure level. Increasing setback reduces gain and impedance to control bias flow while improving saturation characteristics. Added control length increased gain but saturation characteristics were adversely affected. The optimum receiver length was found to be approximately nine times the throat width. Gain also increased when the center vent width decreased. Decreasing the receiver width improved gain for the load impedances tested. When staging amplifiers for high-pressure gain, common mode rejection became an important factor. Also important for obtaining high gain from multistage amplifiers is the capability of adjusting vent chamber pressure.



#### REFERENCES

1. Kirshner, Joseph M.; and Manion, Francis M.: The Jet-Deflection Proportional Amplifier. 70-Flcs-17, ASME Fluidics Conference, Atlanta, Georgia, June 22-23, 1970.
2. Griffin, William S.; and Gebben, Vernon D.: A Proportional Fluid Jet Amplifier With Flat Saturation and Its Application to Gain Blocks. NASA TM X-1915, 1969.
3. Manion, Francis M.; and Mon, George: Fluorics: 33. Design and Staging of Laminar Proportional Amplifiers. Harry Diamond Laboratories, HDL-TR-1608, 1972.



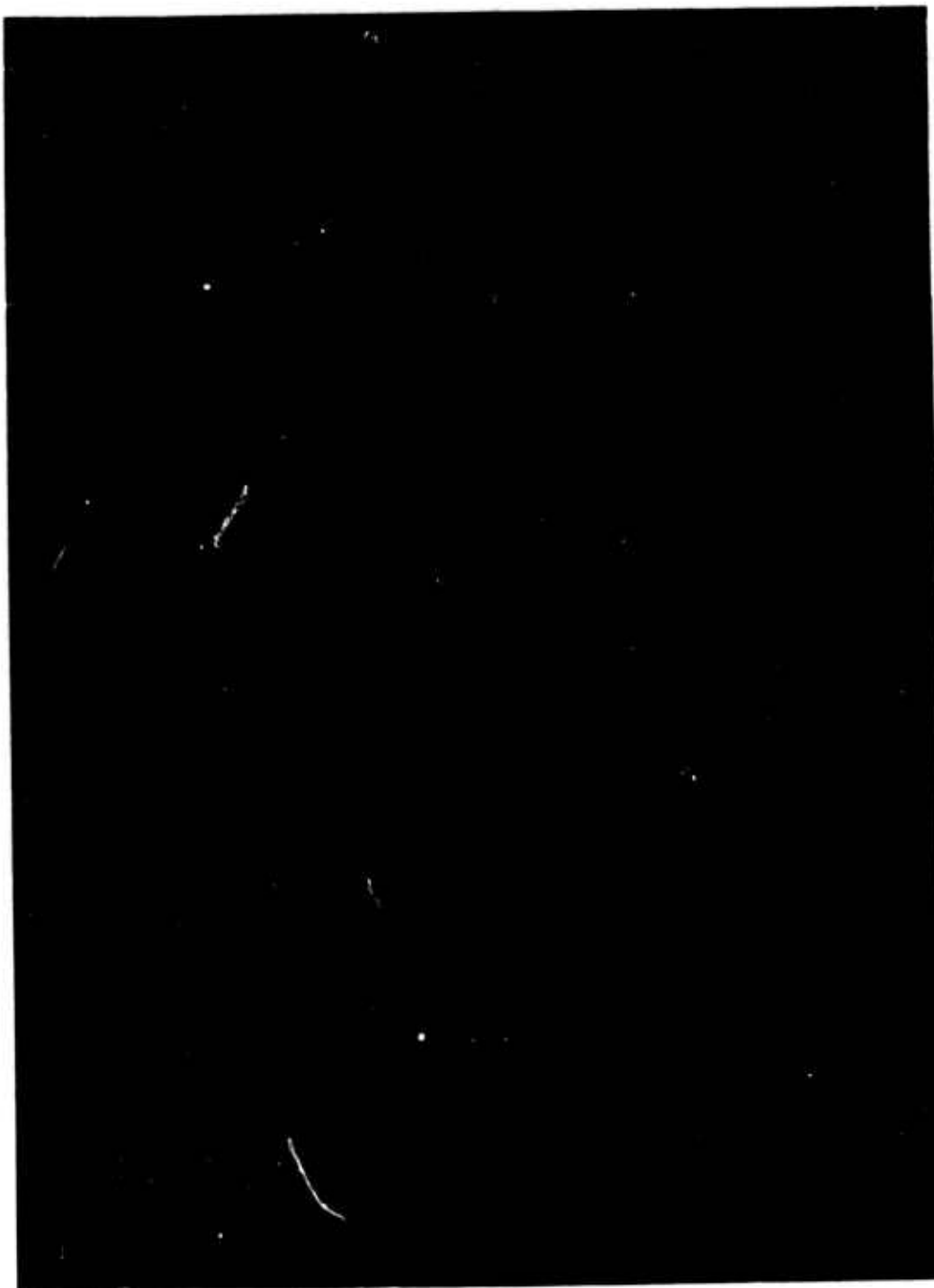


Figure 1. Two water model layers, one of which is assembled between the cover and base plates and secured with clamps.



Figure 2. Water model showing tagged streamlines in supply flow.

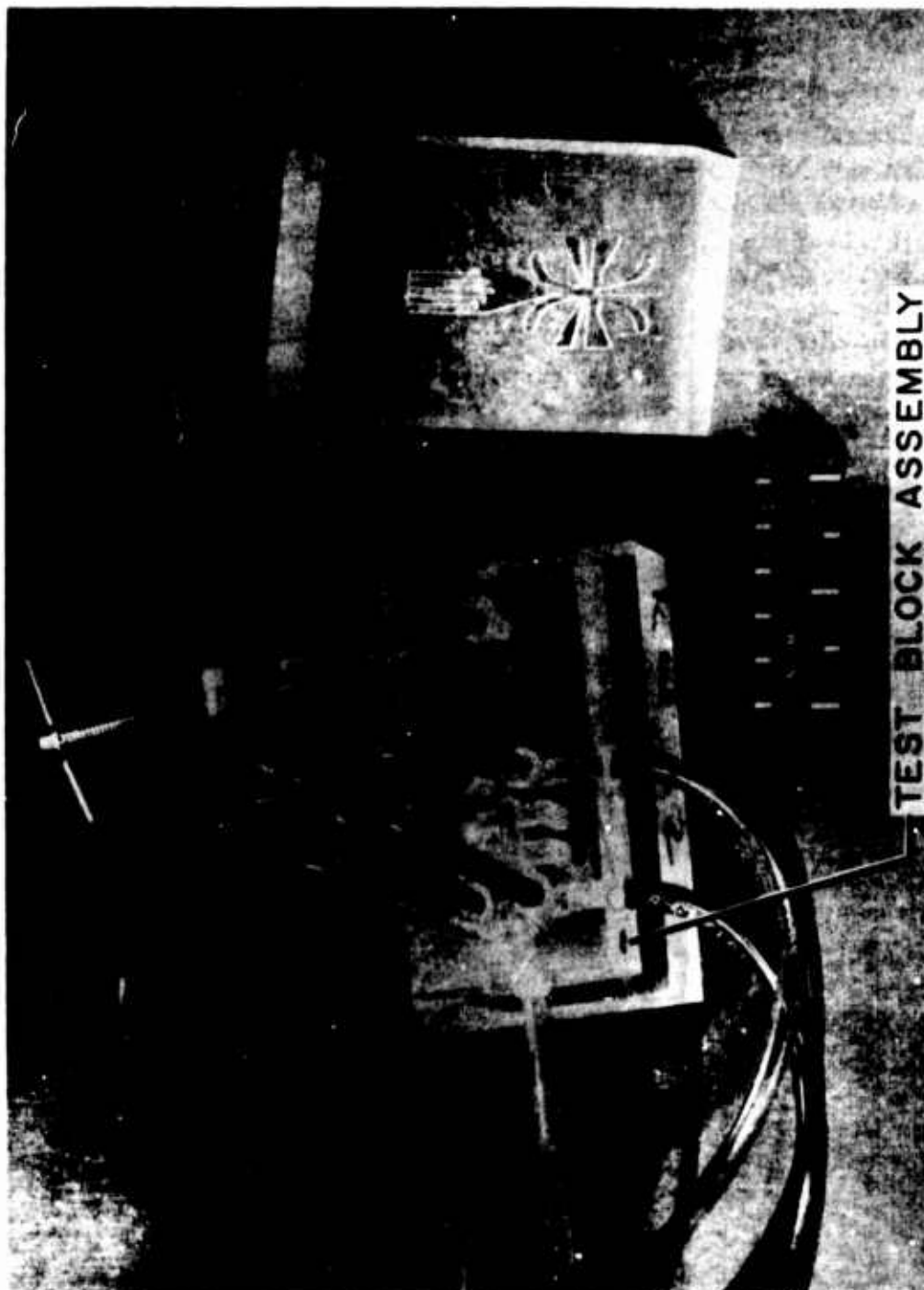


Figure 3. Two pneumatic models, one of which is assembled with the test cover block.

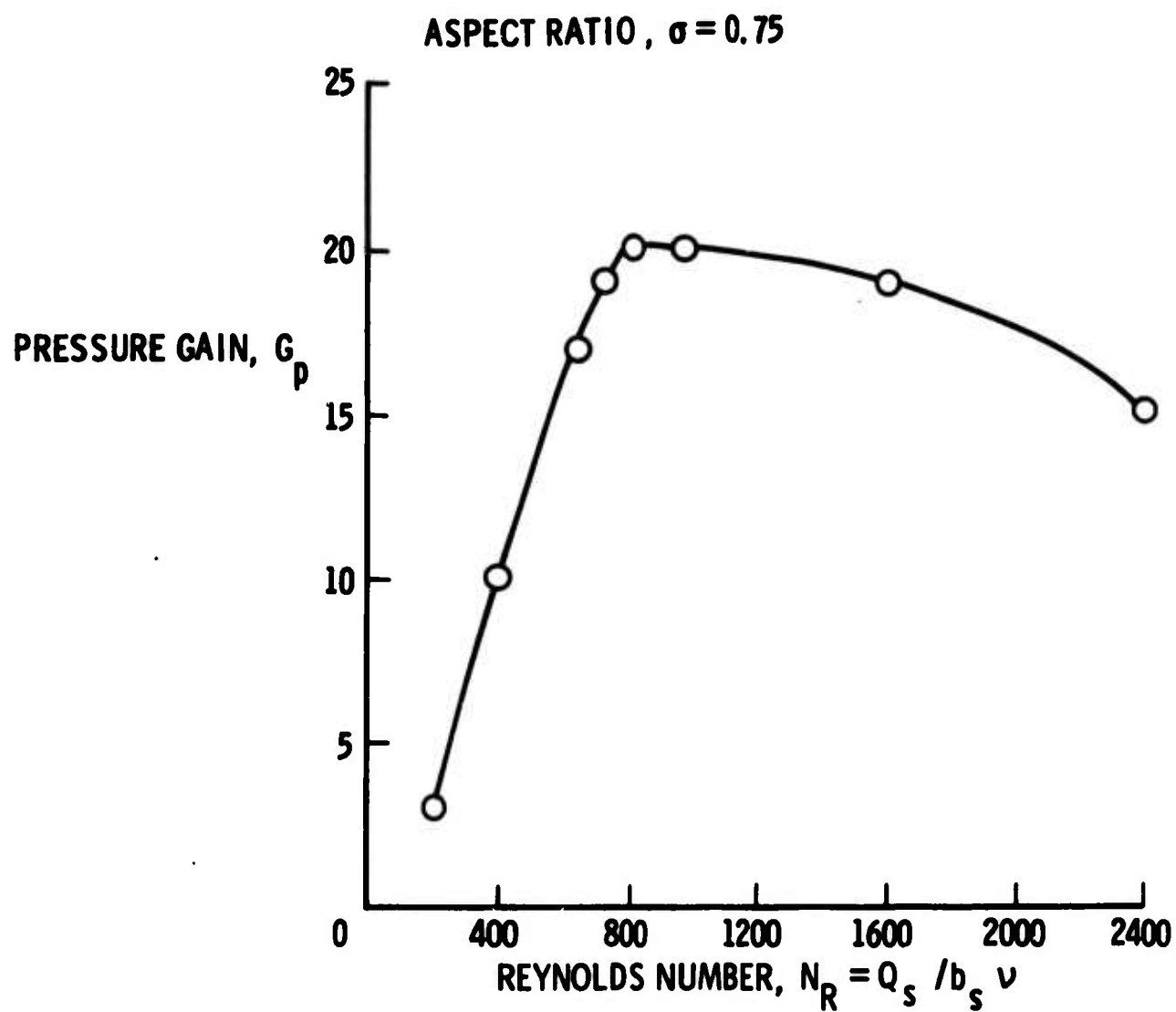


Figure 4. A plot of gain versus Reynolds number shows that the rapid increase of gain with  $N_R$  ceases for  $N_R$  greater than 800. Aspect ratio,  $\sigma = 0.75$ .

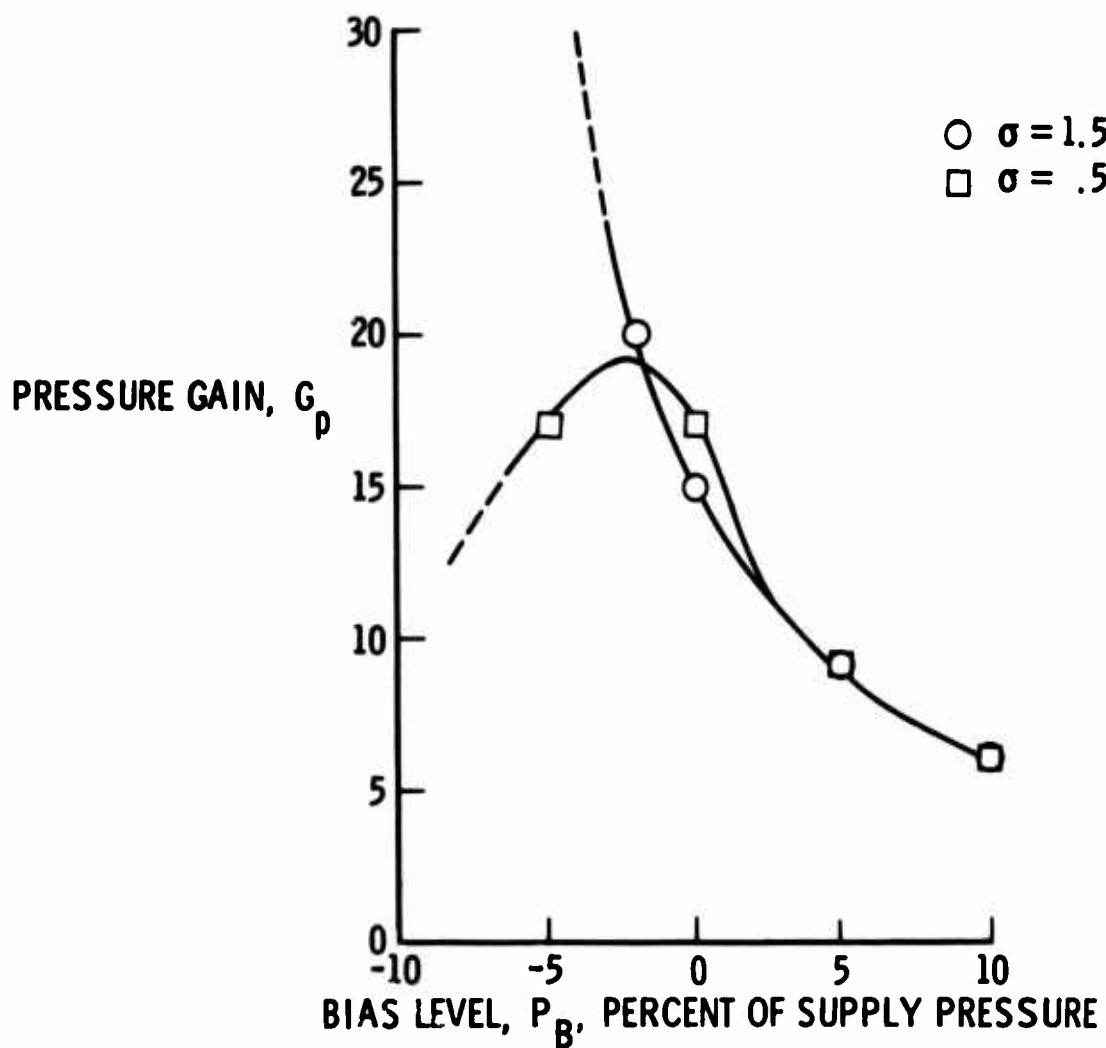


Figure 5. Higher bias levels yield reduced gain. Gain usually increases until an unstable condition exists but may reach a maximum and then decrease before going unstable.

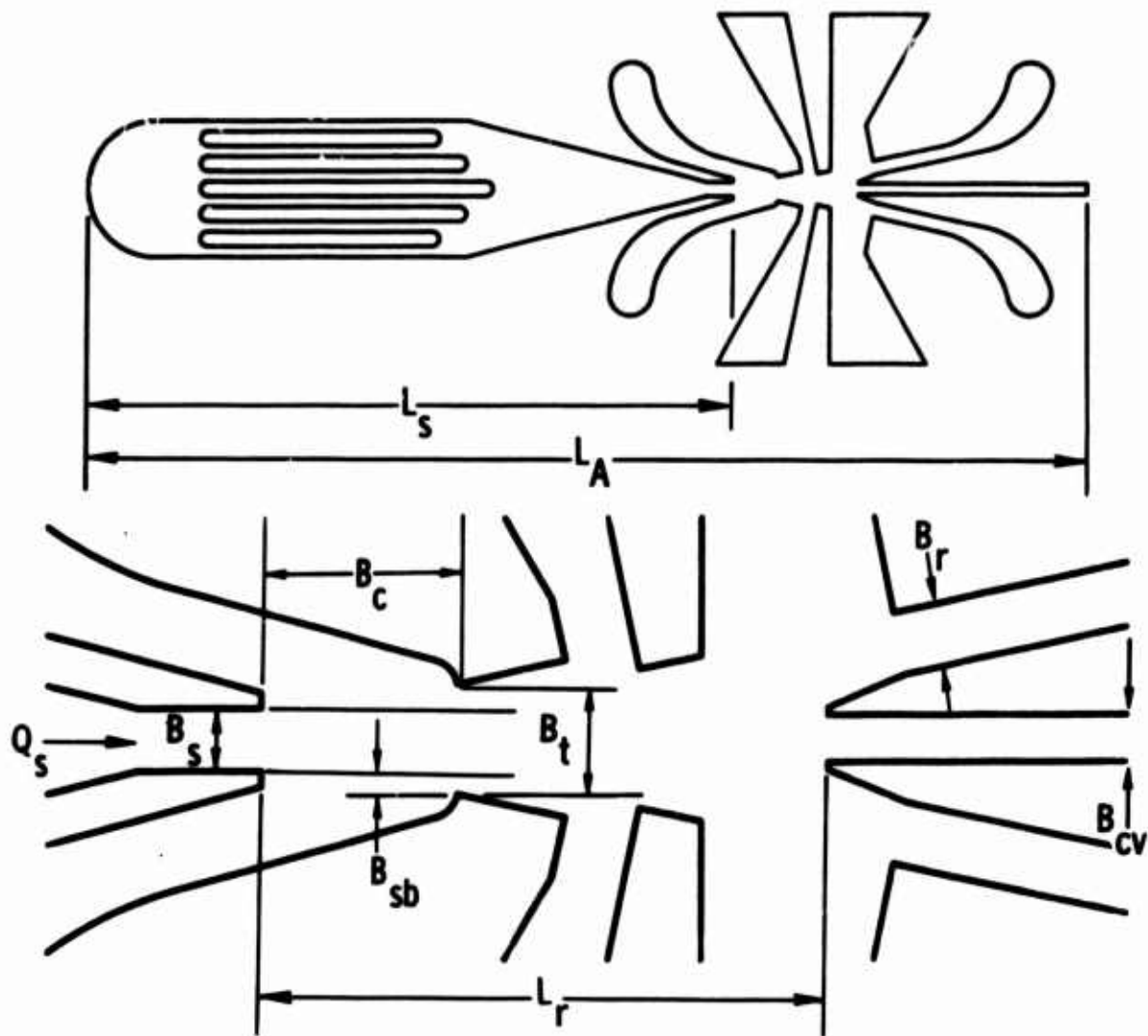


Figure 6. Amplifier silhouette dimensions.



between the downstream edge of the control duct and a real supply stream.

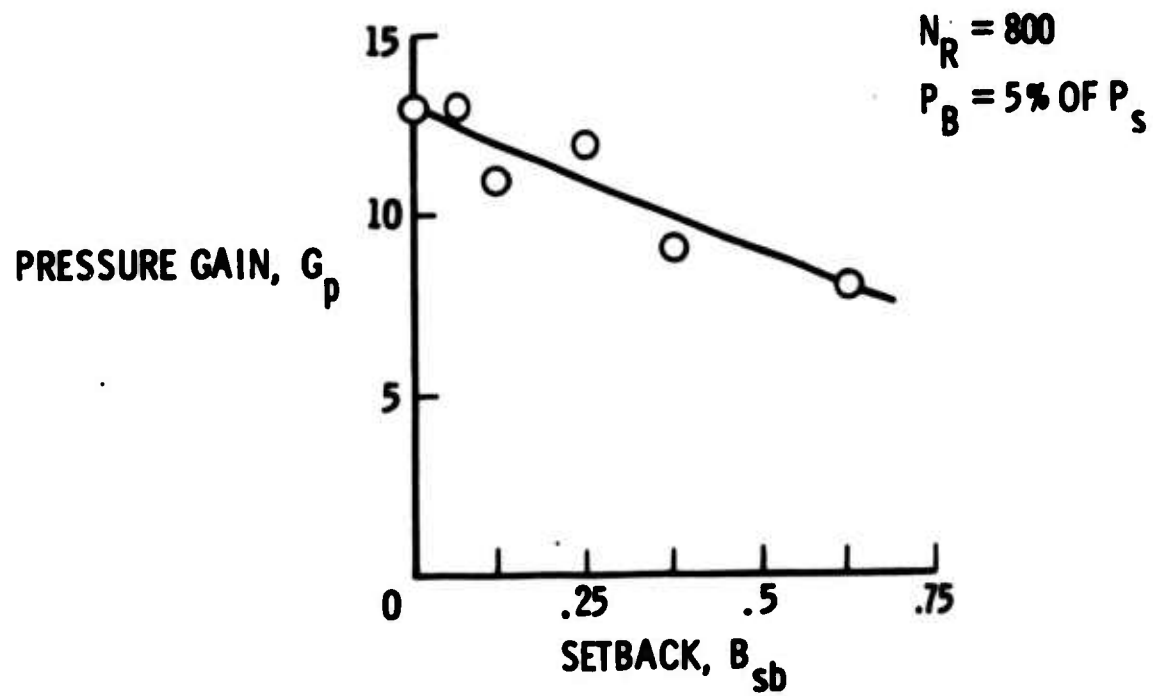


Figure 8. Gain is reduced as setback is increased.



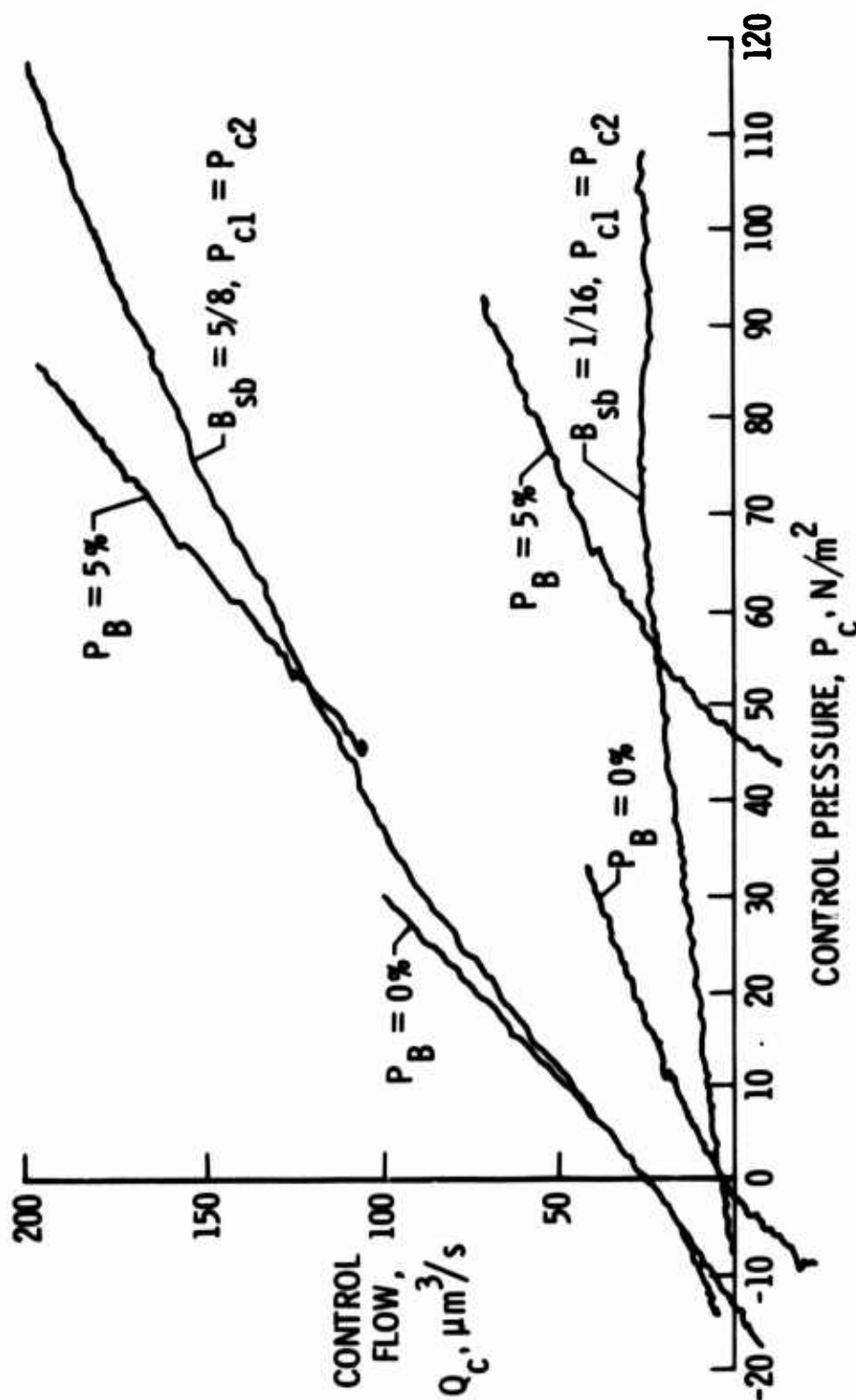


Figure 9. Input impedance to control bias flow (i.e., jet does not deflect) is decreased as setback is increased, but impedance to control signal (i.e., jet deflects) is not changed substantially.

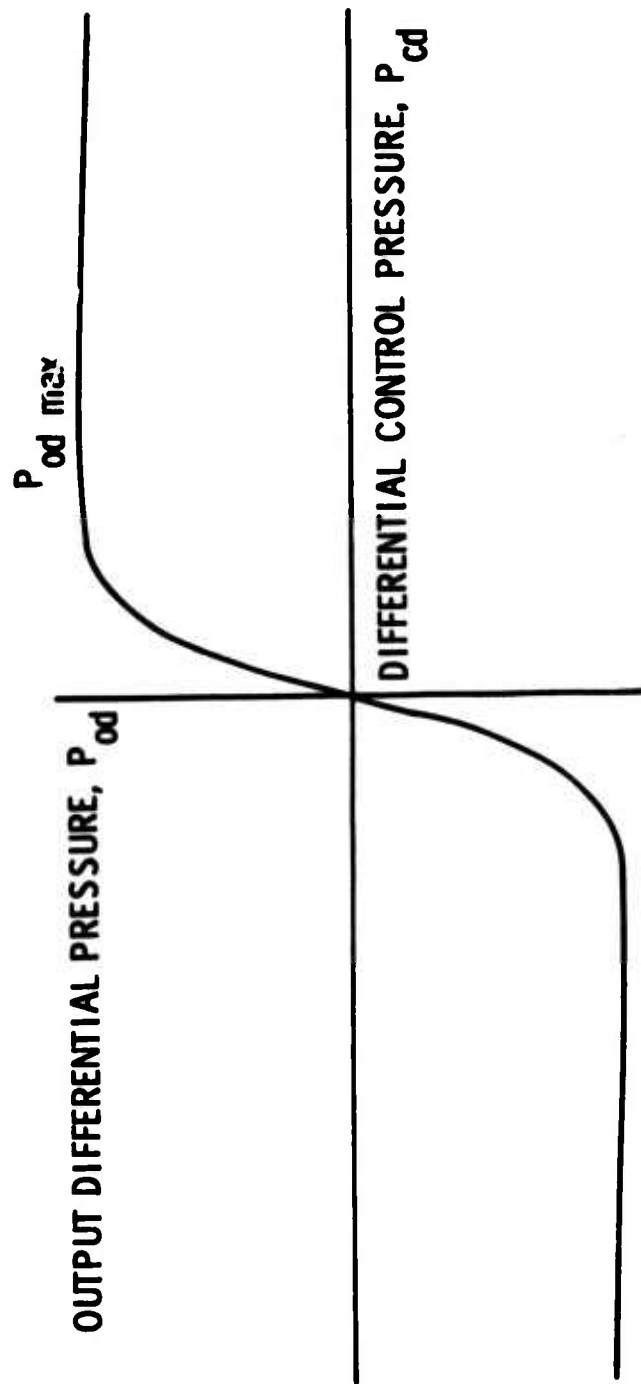
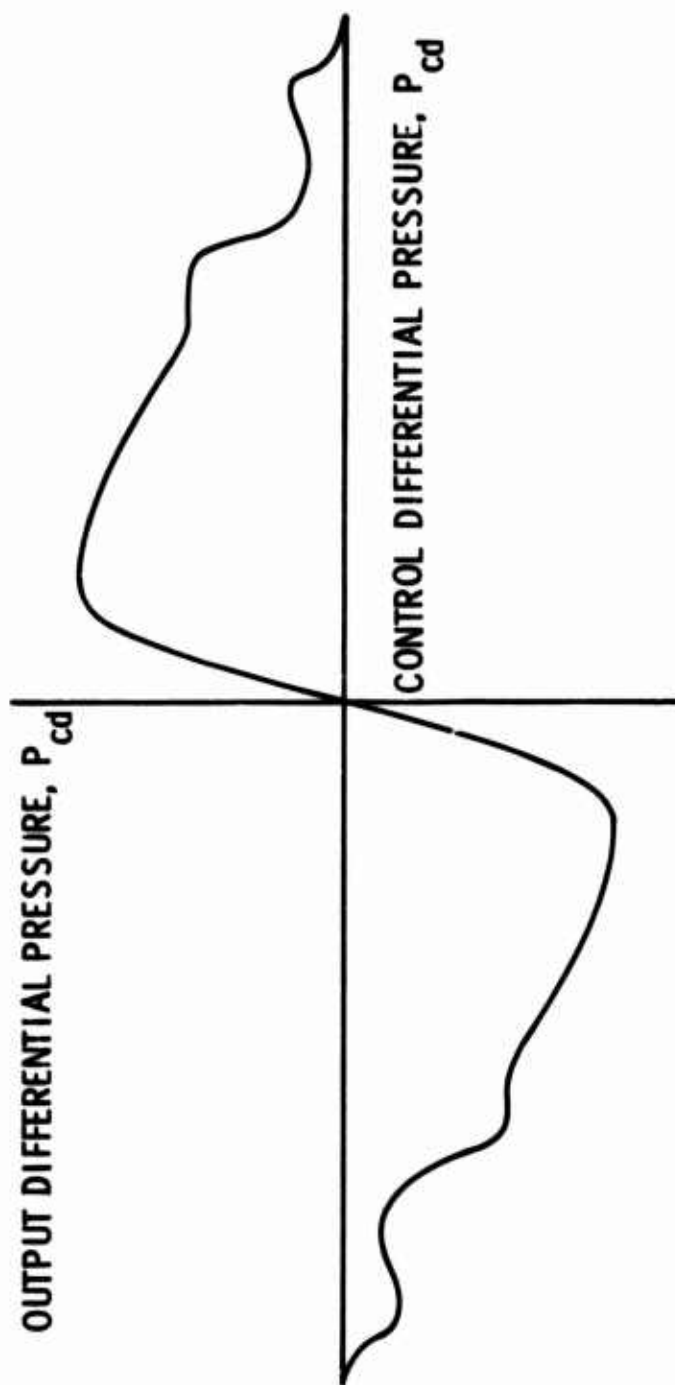
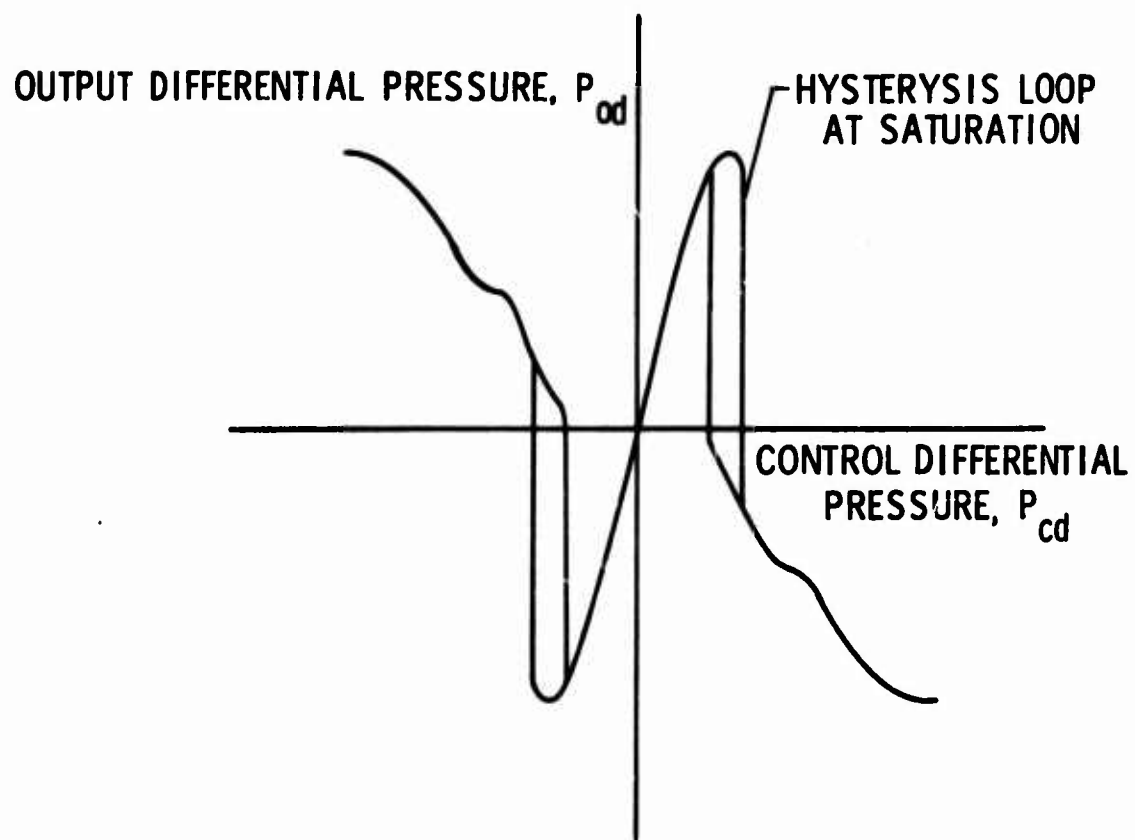


Figure 10. Pressure gain curve.  
(a) Output should remain high after saturation.



(b) Output, after saturation, is reduced as a result of decreased setback.



- (c) Output reversed itself after saturation as a result of setback being too small.

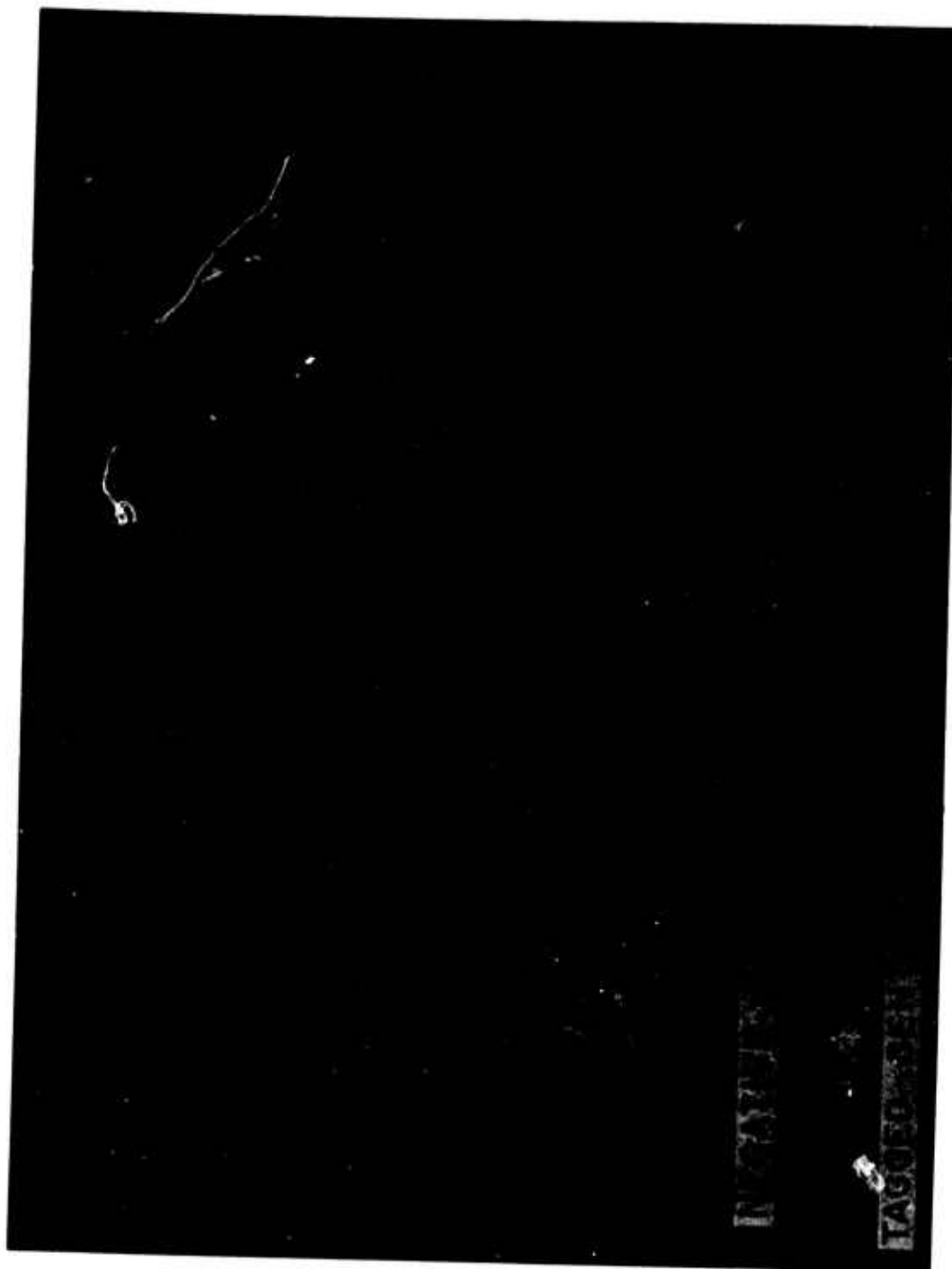


Figure 11. The supply is deflected off the edge of the control duct, reducing the output after saturation.



Figure 12. Supply stream has reversed outputs after saturation because the setback is too small. Both control ducts have negative flow. The tagged streamlines on both sides are caught in the negative control flows.

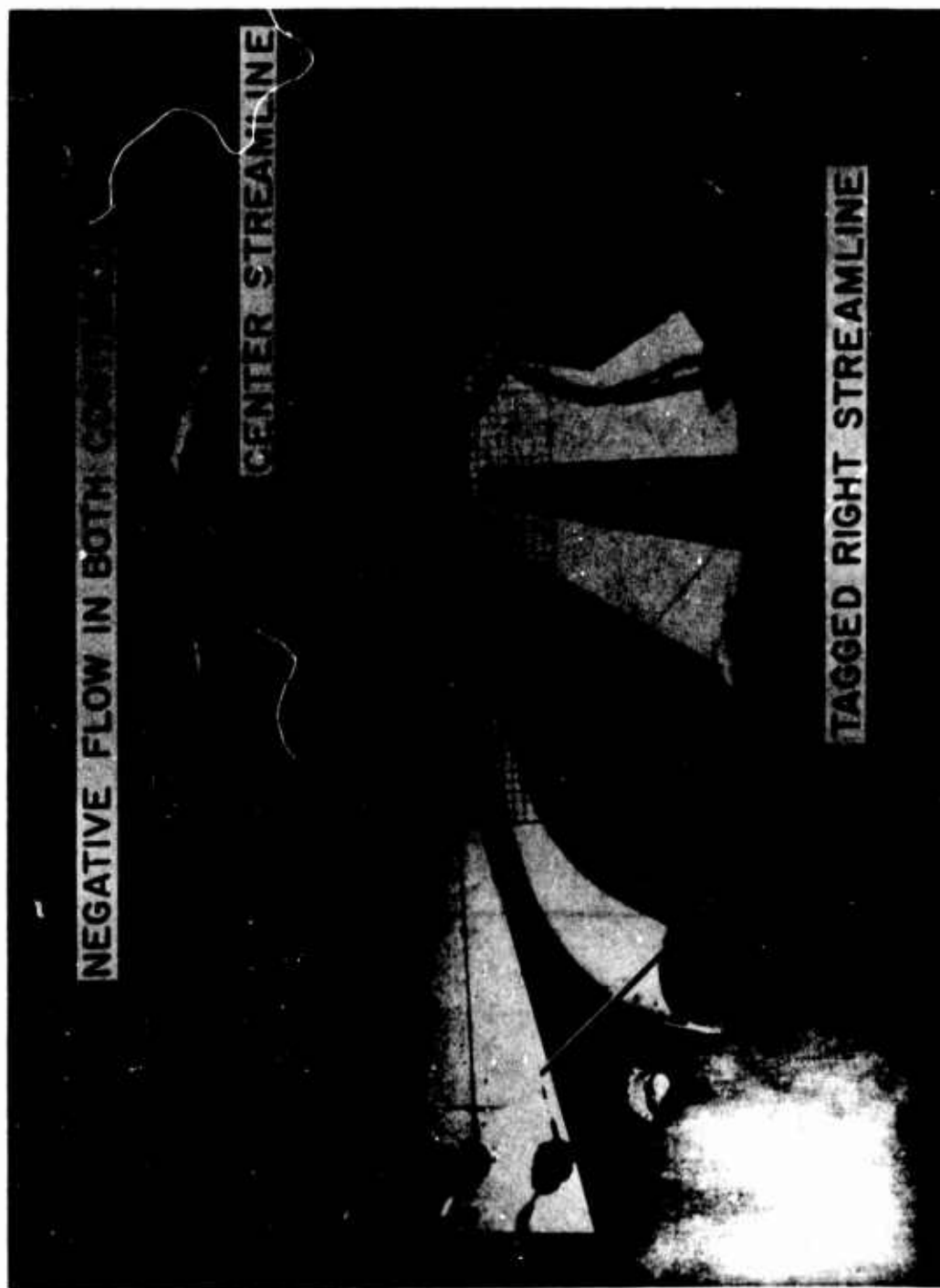


Figure 13. Angle shot of corner deflection. Deflecting the jet off the control duct edge tends to introduce secondary flows and disperse the jet. Notice how the left tagged streamline separates to flow above and below the main stream - much like classical corner flow. A boundary-layer leak flow across the supply stream from the high side to the low side control is also shown by the dark heavily dyed control flow.

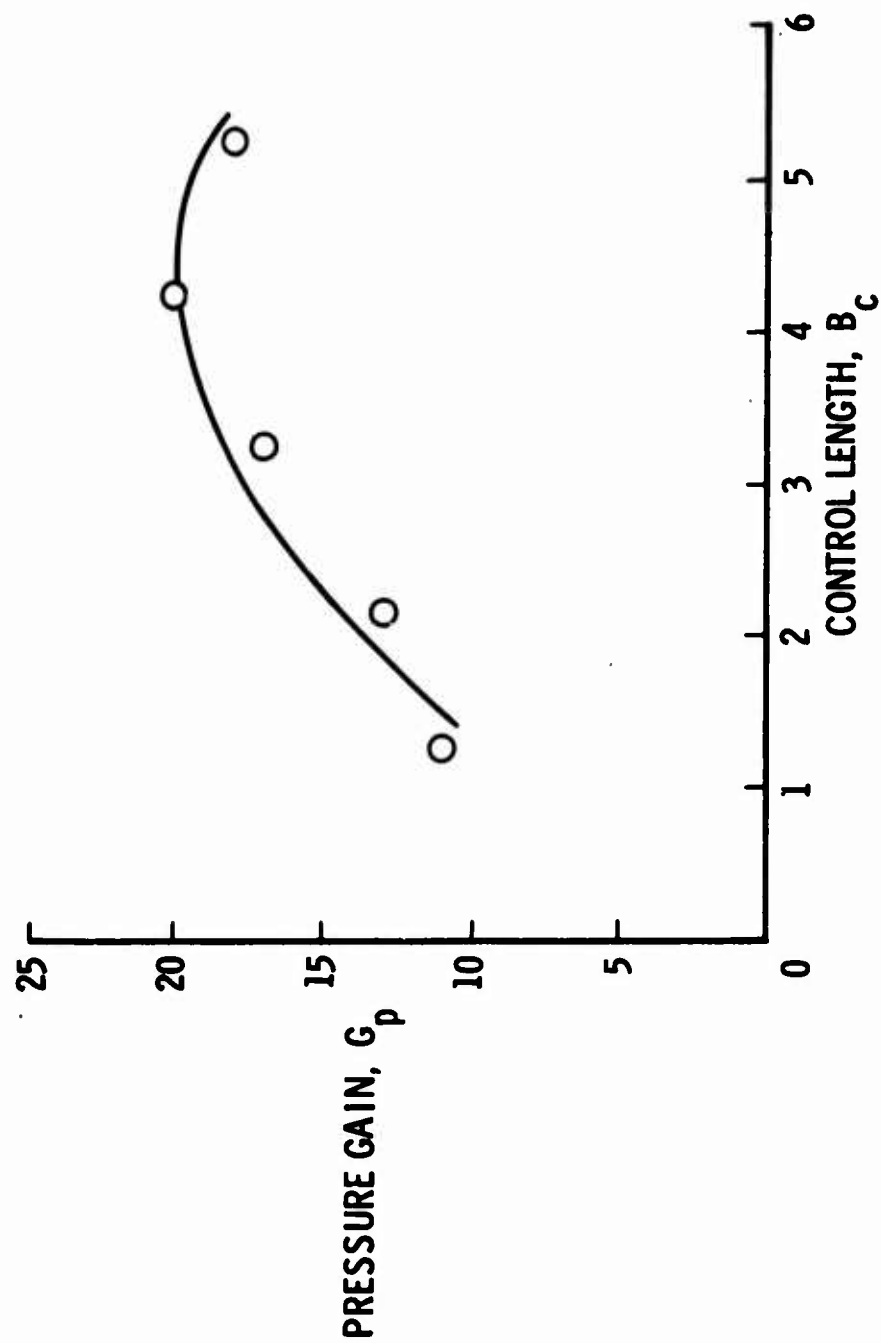


Figure 14. Increasing the control length tends to increase gain.



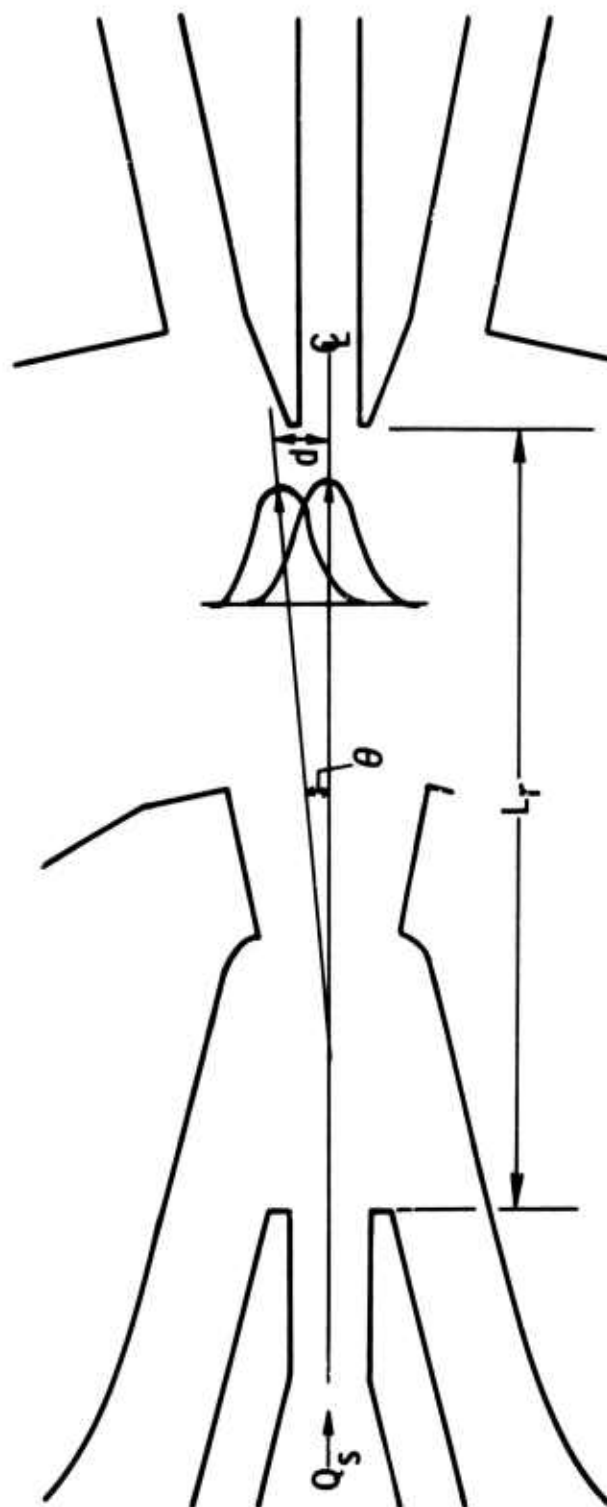


Figure 15. A supply stream deflected by angle  $\theta$  sweeps out greater distances as  $L_r$  is increased.

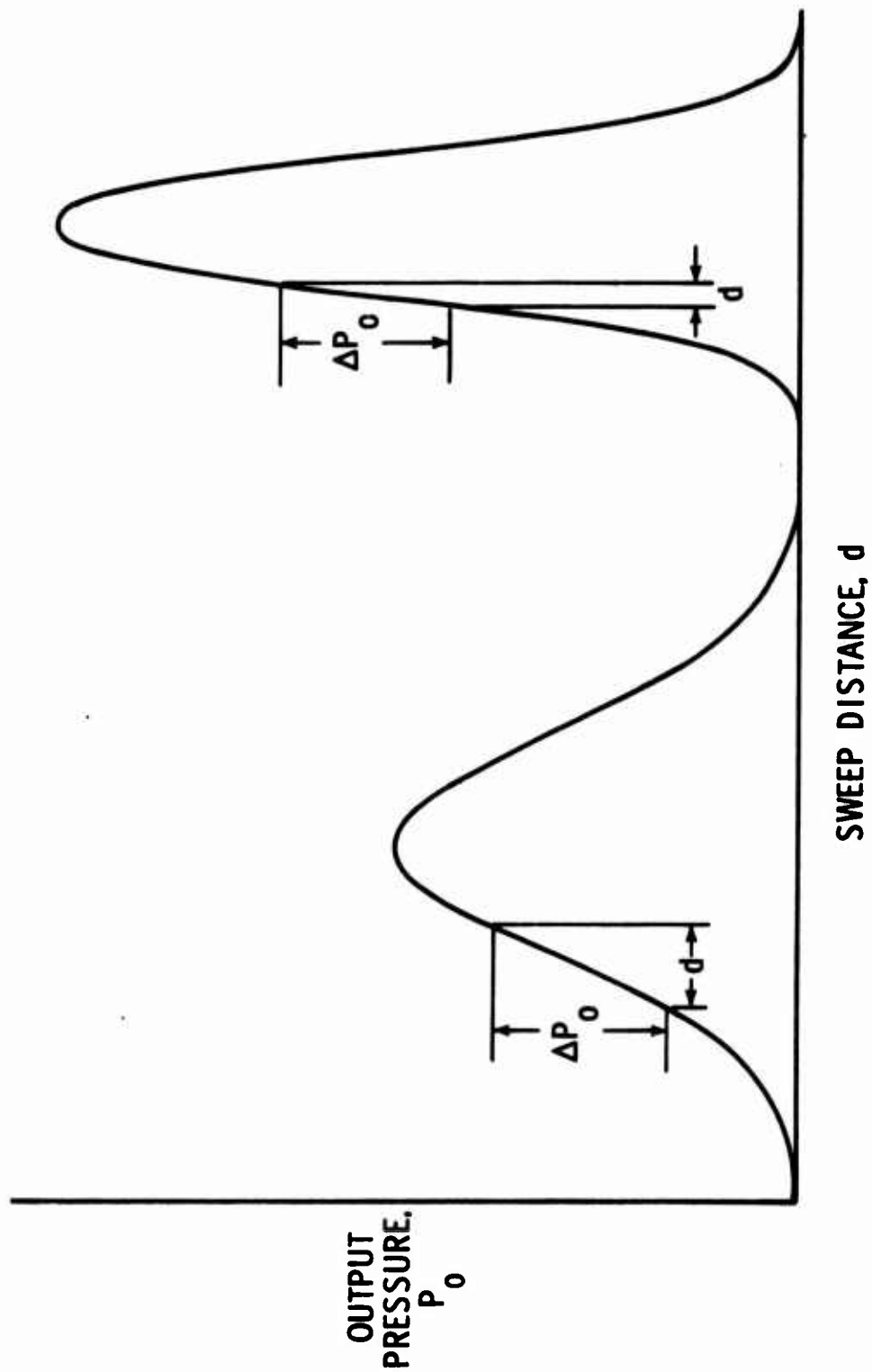


Figure 16. Wider pressure profiles require greater sweep distances to obtain equal change in output pressures.

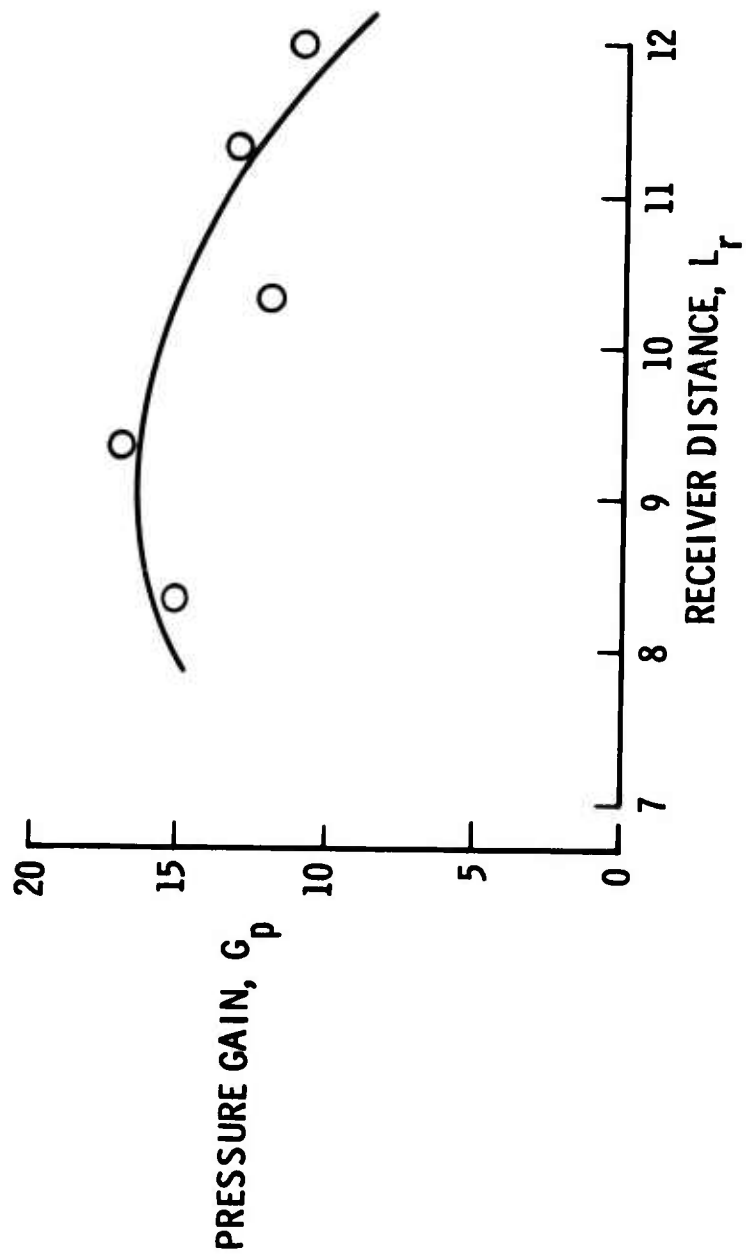


Figure 17. Optimum gain occurs with receiver length around 9.3.

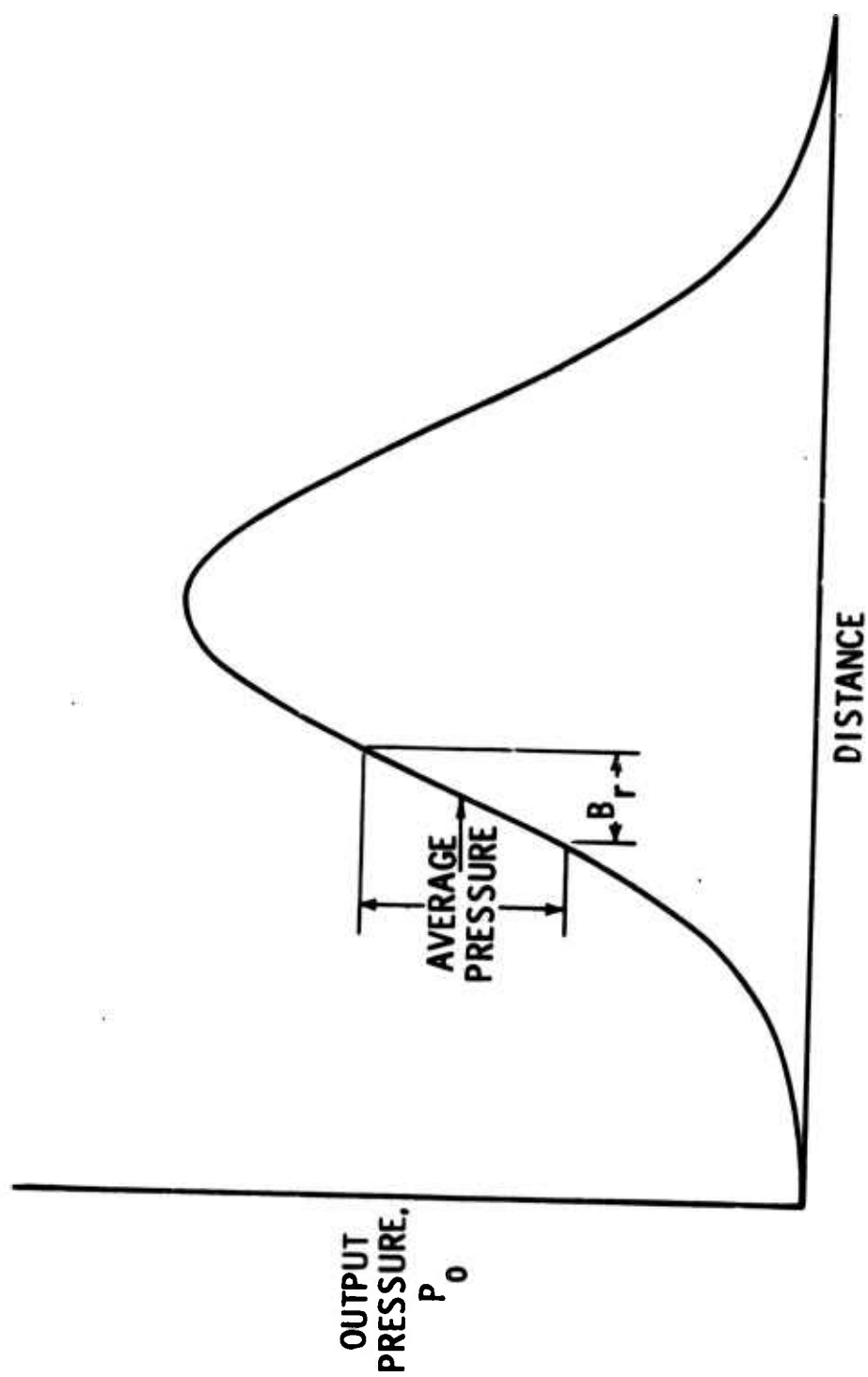


Figure 18. Average pressure should be taken from the steepest portion of the pressure distribution.

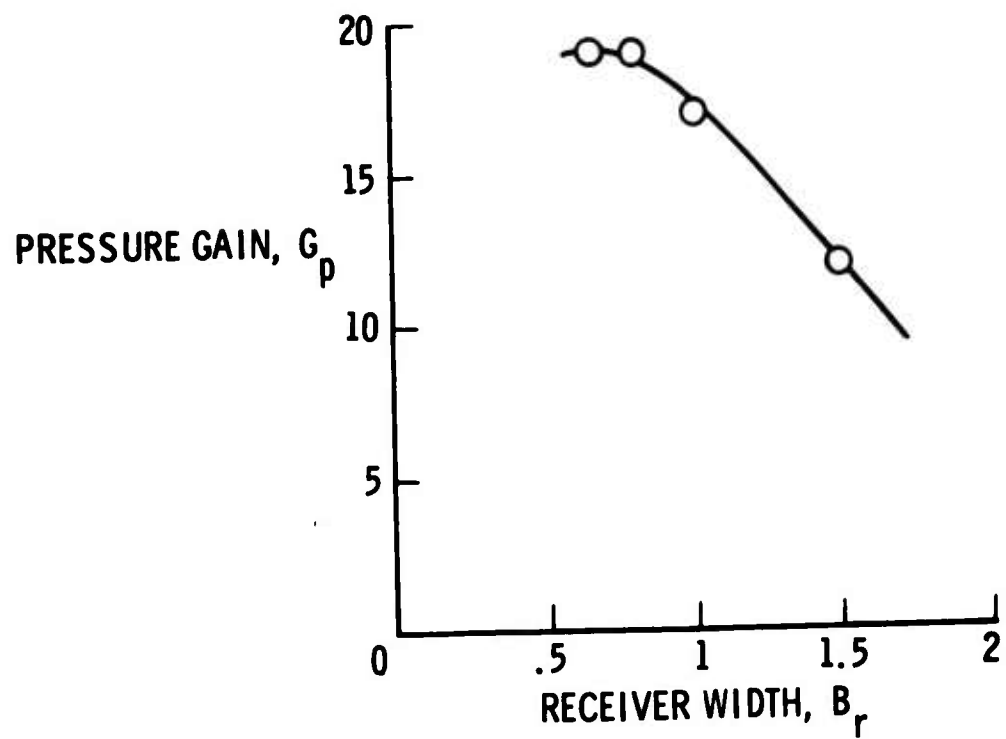


Figure 19. Maximum gain is obtained from narrower receivers.

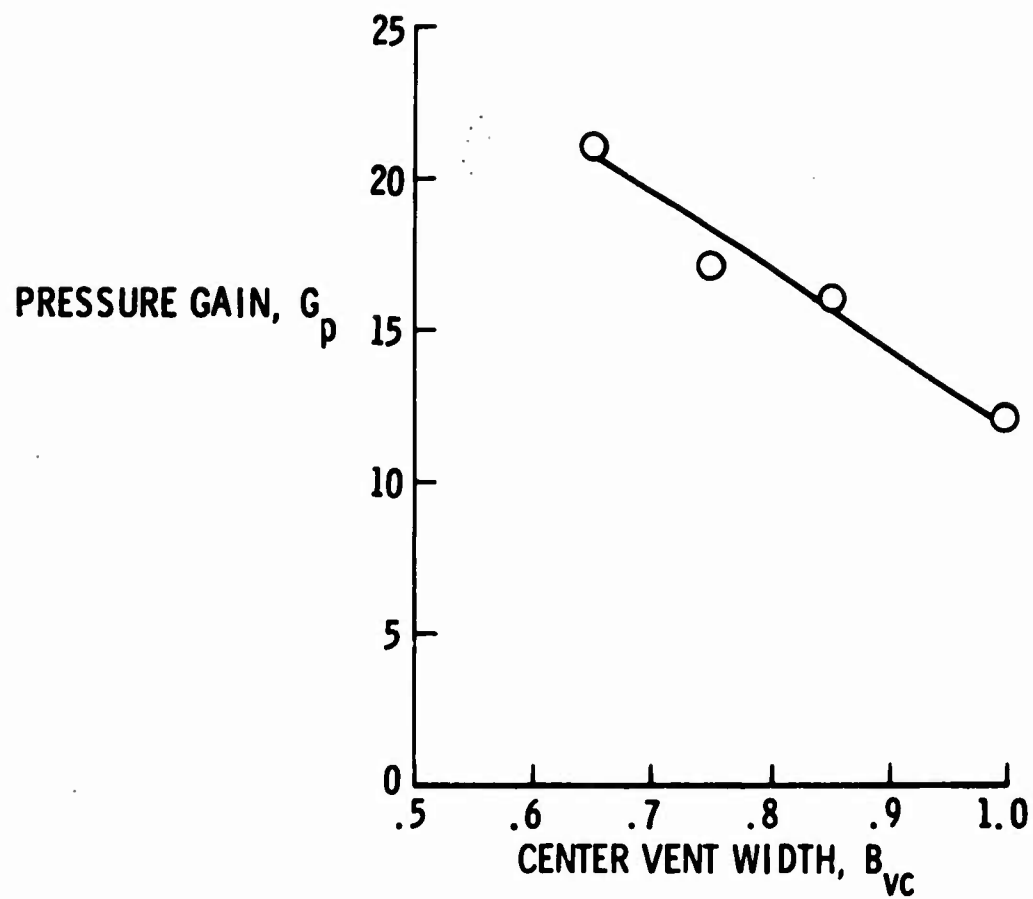


Figure 20. Narrower center vent widths  $B_{cv}$  produce higher gains.



Figure 21. Five amplifiers internally connected with supply and vent ducts have a pressure gain of 100,000.

**JET DEFLECTION PROPORTIONAL AMPLIFIER**

by

**A. J. Healey**

**Associate Professor of Mechanical Engineering**

**University of Texas**

**Austin, Texas**

**Abstract**

Some consideration is given to the underlying phenomena involved in the operation of the jet deflection proportional amplifier. Models for jet flow, jet deflection, output signal recovery and amplifier response are discussed.

The paper summarizes previous research which contributes to our current understanding of device performance.



## GENERAL CONSIDERATIONS

One of the most significant of fluidic devices, the proportional beam deflection fluid amplifier is the cornerstone of analog fluidic systems. It is the fundamental active element in operational amplifier circuits, system compensation networks, and amplitude and frequency modulation sensing systems [1,2,3].

After fifteen years of active work, however, we still know surprisingly little (of a quantitative nature) about the steady state and dynamic performance of these devices. It is the aim of this paper to describe some of the flow processes involved and to describe models for predicting operating performance.

The basic operation is conceptually simple. A main stream in the form of a power jet impinges on output holes called receivers. The energy recovered in the output holes is then modulated by lateral control action at the base of the power jet. Figure 1 shows a typical outline of a beam deflection amplifier. The large open areas between control and receiver passages can be either opened to ambient or closed. Open side areas (vented amplifiers) are employed when loads are such that high blockage of the receivers occur. The side vents provide a means of escape for the power jet fluid. Non-vented or (enclosed side areas) amplifiers are useful in application where no spill of the power jet fluid can be allowed. These amplifiers can only operate with low resistive loads so that receiver passages are not significantly blocked.

Performance considerations for amplifiers are linearity of the input-output characteristic, high input impedance, low output impedance, as well as high gain, range and signal/noise ratio.

Conflicting requirements are thus imposed in establishing geometric design. Increasing control passage width increases the angular deflection gain but reduces input impedance. Increasing distance between control passages and output receivers increases the lateral deflection gain of the power jet but beyond a given distance reduces overall gain because of shear losses and loss of jet kinetic energy. Widening receiver passages and separating their centerline respectively reduces output impedance and affects linearity of the input-output characteristic. Widening receiver passage width also reduces the amplifier range.

For very low power jet Reynolds Numbers 200 to 800, laminar flow is achieved over most of the internal field and signal noise is low, but boundary layers are relatively thick and the loss of gain has to be compensated by

increased deflection gain. This is accomplished by increased width of control passages [4]. At high power jet speeds, the turbulence in the flow field gives rise to signal noise.

### APPROACHES TO ANALYSIS

There are two approaches to the analysis of fluid amplifier performance. Both have the goal of indicating geometrical design effects on performance characterisation.

The first, based on control volume analyses employing assumptions as to unknown velocity profiles and pressure distributions, has had some reasonable but limited success.

The second, based on field solutions of continuity and momentum equations by finite difference methods has had little success to date because of stability and convergence problems in the algorithms used for numerical computation. Problems are also encountered with uncertainty of boundary conditions and high cost of computer simulation.

#### Part I - Processes Relevant to Operational Characteristics

Earlier approaches to the analysis of amplifiers were based on control volume methods and our discussion here will begin in a similar way.

Inherent in the control volume analytical procedure is a set of assumptions about profiles and pressure distributions within the device acting over the assumed control surfaces. The operation of proportional amplifiers hinges on jet formation, development, deflection by transverse pressure and momentum forces and energy recovery in output passages with impinging jet flows. These topics are treated separately in this section of the paper and separately used to indicate effects of internal flow characteristics on performance.

#### Development of Jet Flows

We are dealing here generally with three dimensional, laminar and turbulent jets issuing from rectangular cross section nozzles. While the development characteristics of those jets is not completely understood a good deal of work in recent years had led to a partial understanding.

## 2-Dimensional Jets

The development of a 2-dimensional turbulent jet from an infinitely thin slot was treated by Gortler [cf Schlichting] [5] using a similarity solution and showed that jet centerline velocity decayed with downstream distance to the negative half power. Expressions were given for the mean velocity profile

$$u = \frac{\sqrt{3}}{2} \sqrt{\frac{J\sigma}{\rho x}} (1 - \tanh^2 \eta)$$

$$v = \sqrt{\frac{3}{4}} \sqrt{\frac{J}{\rho x \sigma}} \{2\eta (1 - \tanh^2 \eta) - \tanh \eta\}$$

where  $\eta = \sigma y / x$  and  $\sigma$  is a free constant called the spread parameter.  $J = 4\rho U_s^2 s / 3\sigma$  and is the constant momentum flux in the jet. To overcome the difficulty introduced by the finite width nozzle in using these expressions, downstream distance  $x$  is usually assumed to be the distance downstream from the finite width power nozzle plus an appropriate constant  $s_1$  evaluated by equating momentum flux in the jet at the nozzle exit plane with the value of  $J(s_1)$ .

The volume flow in the jet  $Q(x)$  increases with  $\sqrt{x}$  and the entrainment flow rate  $dQ/dx$  is thus proportional to  $x^{-1/2}$ . Various other results have been obtained for a jet issuing into a region where pressure gradients were essentially zero (Reichart, Miller and Cummings, Albertson) [6,7,8]. These show that the development is divided into a core region of flow where a substantial amount of the flow is unaffected by the shearing at the edges, and a fully developed zone (Fig. 2). The core region extends some four to six jet nozzle widths downstream while in the fully developed zone, the streamwise velocity profile reaches similarity. Since the centerline velocity decays, similarity implies that the jet width increases. While kinetic energy flux in the jet is lost, momentum flux is essentially preserved.

Albertson [8] gives Gaussian normal distribution expressions for the forward velocity in the jet in the two regions (a) the zone of flow establishment and (b) zone of established flow.

(a) with reference to Fig. 2

$$\frac{u}{u_0} = e^{-k^2} ; \quad k = \frac{(y + \sqrt{\pi} C_1 x/2 - B_0/2)}{2(C_1 x)^2}$$

$$C_1 = \frac{1}{\sqrt{\pi}} \left( \frac{B_0}{x_0} \right) \quad \frac{Q}{Q_0} = 1 + \sqrt{\pi} (\sqrt{2} - 1) C_1 x/B_0$$

$$(b) \frac{u}{u_0} = \sqrt{\frac{B_0}{\sqrt{\pi} C_1 x}} e^{-\lambda^2} \quad \lambda = \left( \frac{1}{\sqrt{2} C_1} \right) (y/x) \quad \frac{Q}{Q_0} = \sqrt{\frac{2\sqrt{\pi} C_1}{B_0} x}$$

#### Effects of Bounding Cover Plates

The three dimensionality of power jets was studied by Foss and Jones [9] and by Holdman and Foss [10] for aspect ratios of 6:1 and 4:1 and found to induce a narrower jet at the mid-plane than for the 2-dimensional case with higher centerline velocity even though the nondimensional velocity profile agreed well with the Gaussian error function as shown in Figures 3 and 4.

The profile development is also affected by upstream turbulence. Gray and Shearer [11] show that although non-dimensionalised profiles were not significantly affected, centerline velocity decay in a 4:1 aspect ratio jet decays more rapidly as upstream turbulence intensity is increased (see Figure 5).

With 1:1 aspect ratio, Healey and Reynolds [12] show that more rapid decay of the jet centerline velocity occurs than for the 6:1 aspect ratio of Foss and Jones and, although turbulence levels may have been different it seems that the 1:1 aspect ratio case more nearly approaches the two dimensional case of Albertson.

#### Effect of Jet Curvature

The growth rate of curved jets is important as it relates to deflected power jets. Curved wall jets have been studied experimentally by Fekete [13] and Giles et. al. [14]. The results of Fekete for circular wall jets and Giles for spiral wall jets indicate that curvature significantly influences growth and entrainment and that convex curvature provides increased entrainment over the plane wall jet while concave curvature produces the opposite effect. Entrainment rates may be as high as 4 times that of the plane jet case for large convex curvature.

### Jet Deflection

The deflection of a jet flow occurs as a result of lateral pressure and momentum forces. In earlier days distinctions were made between pressure controlled and momentum controlled amplifiers. In reality both static pressure and momentum effects are always present in varying degrees. With wide control passages (large  $s$ ), the effect of pressure forces dominates, for large offsets (large  $d$ ) compared to the control passage width, momentum forces dominate.

Early work by Dexter [15] assumed that two uniform streams impinged and combined to form a Gaussian velocity profile and applied continuity and momentum to estimate jet deflection angles. Moynahan and Reilly [16] assumed no mixing to take place and used that model to predict angular deflection. Douglas and Neve [17] obtained good predictions by combining the two results in appropriate regions for a momentum dominated device. Douglas and Neve assumed that the deflection angle of the power jet was related through the equation

$$\tan = \frac{M_c}{M_p} \cdot C$$

$C$ , an empirical constant, was found to be 1.6. The assumed Gaussian velocity profile was found to establish itself within four nozzle widths downstream. Sarpkaya [18] showed that a free streamline potential flow model adequately described the deflection characteristics for a device with a setback equal to the control passage width (Fig. 7). For a dominantly pressure controlled amplifier Simson [19] used a constant entrainment and an atmospheric flow model together with a pressure deflection model to predict jet deflection and control port characteristics. No data, however, were presented to verify the work. Foss [20] showed that a simple control volume model was adequate to calculate power jet deflection. The development of the jet after deflection is usually assumed to continue as for a two dimensional jet with a Gaussian velocity profile.

Referring to Figure 8 and assuming that an ideal mixing occurs between lateral control flow and that the venting region is at constant ambient pressure a simple control volume model yields the basic influence of the design parameters such as control passage width  $d$  and control passage knife edge offset  $s$ .

Application of transverse and longitudinal momentum neglecting shearing stresses and assuming uniform velocity profiles at the control inputs gives,

$$\tan\theta = \frac{[P_{c12} + \frac{\rho(Q_{c1}^2 - Q_{c2}^2)}{(dh)^2}]}{\frac{\rho Q_s^2}{[(bh)(dh)]} + (\frac{b}{d}) \bar{P}_c} \quad (1)$$

$$Q_{c1} = K_q h(s + y_1) \sqrt{P_{c1}} + Q_e \quad (2)$$

$$Q_{c2} = K_q h(s - y_1) \sqrt{P_{c2}} + Q_e \quad (3)$$

and  $y_1 \approx d \sin\theta$  is the deflection of the jet at the control passage knife edge.

Assuming  $P_s$  is the supply stagnation pressure and employing a Bernovilli relationship for  $Q_s$  in terms of  $P_s$  and  $\bar{P}_c$ ,

$$\tan\theta = \left[ -\frac{d^*}{2 - \bar{P}_c^*} \right] P_{c12} + \frac{(1 - \bar{P}_c^*)}{d^* (2 - \bar{P}_c^*)} (Q_{c1}^{*2} - Q_{c2}^{*2}) \quad (4)$$

Pressure Con-      Momentum Control Term  
trol Term

in which starred variables are normalised with respect to  $P_s$ ,  $Q_s$ , and  $b$  for pressures, flows and lengths respectively.

Equation (4) illustrates that the deflection gain of a pressure controlled amplifier is influenced strongly by the control passage width ratio ( $d/b$ ). Also since the input flow conductance (equation 2) increases as setback increases, it is apparent that increasing  $s$  will increase  $Q_{c1}$ ,  $Q_{c2}$  for given pressures thereby increasing the momentum terms in the deflection equation 4.

A similar approach to the deflection of a momentum controlled deflection process is by Foss [20] who studied the case of a setback with stand off controls. The analysis was based on momentum interaction including the pressure force terms and showed as in Figure 9 that an increase in deflection gain was achieved by the pressure terms. Figure 9 compares his analysis with the momentum terms alone ( $\tan\alpha = mfr$ ) and includes experimental data. The absiscor is the ratio of lateral to longitudinal momentum fluxes.  $Q_e$  is the entrained flow in the power jet obtained by integrating the power jet velocity profile across its width at the section corresponding to the end of the control port and subtracting the jet flow at the power nozzle exit plane.

### Input Pressure-Flow Characteristics

Typical input characteristics are illustrated by the form of equation (2). Normalising yields

$$Q_{c1}^* = \beta (s^* + y_1^*) \sqrt{P_{c1}^*} + Q_e^* ; \quad \beta = \frac{K_{ghb} \sqrt{P_s}}{Q_s} \quad (5)$$

In equation (5),  $(s^* + y_1^*)$  refers to the flow area between the control passage knife edge and the "edge" of the power jet where  $s^*$  is the normalised setback of the knife edge and  $y_1^*$  is the lateral movement of the jet centerline at the plane of the control port edge.  $\beta$  is a normalised orifice conductance.

Since  $y_1^*$  is determined by the deflection of the jet, and arises from imbalance of control effort, equation (5) indicates that control flow in one port is a function, generally of pressures in both control ports. Only in large setback amplifier designs ( $s^* \gg y^*$ ) can the two control ports be effectively decoupled.

To examine the form of the input impedance characteristic we may take the case of an amplifier which is dominantly pressure controlled. Here the flow terms in equation (4) are negligible compared to the pressure terms so that

$$\tan \theta \approx \frac{d^*}{[2 - \bar{P}_c^*]} \Delta P_{c12}^*$$

Approximating for the sake of clarity here,

$$Q_{c1}^* \approx Q_e^* + \beta s^* \sqrt{P_{c1}^*} + \frac{\beta d^{*2}}{[2 - \bar{P}_c^*]} (P_{c1}^* - P_{c2}^*) \quad (6)$$

For constant  $P_{c2}^*$  the input pressure-flow characteristics take on an almost linear relationship.

Typical results for an amplifier with  $s^* = 0.125$  and  $d^* = 1.0$  are shown in Figure 10.

### Input Impedance

The local slope of these curves represents the linearised steady state input admittance. For small signal variations, with the amplifier of Shipp [31], from which Figure 10 is taken, gives

$$P_{c1}^* \approx 3Q_{c1}^*$$



The input admittance of (0.3) is typical of this type of device. With Push-Pull operation such that  $\bar{P}_c$  is constant the apparent slope in Figure 10 is less. In this case Push-Pull operation leads to

$$P_{cl}^* \approx 2.2Q_{cl}^*$$

### Jet Transport in Vent Regions

The usual assumptions regarding the development of the resultant power jet as it emerges from the control port edges are that its centerline follows a straight line trajectory and that the profile develops as for a free jet to a Gaussian normal form. The straight line trajectory is used to project the offset of the jet centerline with respect to the centerline of the receiver system as in Simson [19].

While this may seem a reasonable approach at first sight, this will only be the case if the jet issues into a venting region free of static pressure gradients. Unfortunately, the presence of top and bottom cover plates bounding the spillover of unwanted flow in the jet causes pressure gradients which react laterally on the main power jet.

While a complete discussion of this phenomenon is not appropriate at this point in the paper Figure 11 illustrates the physical process involved.

The flow in the power jet not accepted by the receivers is spilled into the venting region. This flow occurs in jet form and entrains flows  $Q_{e1}$  and  $Q_{e2}$ . Spillover flow  $Q_{s1}$  is greater than  $Q_{s2}$  thus  $Q_{e1} > Q_{e2}$  and with bounded top bottom covers  $P_{v1} < P_{v2}$ . It is apparent that any bounding of the venting region will create additional deflection of the power jet through restriction of entrainment.

This phenomenon has been utilised by Griffin [21] in an attempt to increase the deflection gain of an amplifier. Short walls are introduced as in Figure 12 to deflect the power jet through restriction of entrainment. Naturally, these walls are not long enough for a complete jet attachment to occur.

The total effect of vents is complex and we can divide the discussion into (a) perfectly vented and (b) imperfectly vented amplifiers. Perfect venting refers to the absence of coupling between loading and deflections of the power jet in the venting region. The latter case (b) will be discussed later in the paper and, for now, consider that a linear projection from the control passages will project the point of impact of the jet centerline on the receiver.



### Output Characteristics

The calculation of output pressure and flow with a jet impinging on a receiver system is usually accomplished by the assumption of a known jet velocity profile with centerline offset by some distance. The offset distance is the linear projection of the jet centerline found using the deflection angle at the exit from the control passages. Early work by Reid, Zalmonson, Rupert, Olson and others [22,23,24,25] was concerned with single receivers with no offset. In modelling the case of a deflected jet, Simson [19] integrated impinging portions of the power jet total pressure profile for computing blocked pressure recovery. This method underpredicts the pressure recovery with deflected power jets. The subsequent development here will be devoted to some recent work dealing with characteristics of first single but later, multiple receiver configurations.

### Characteristics of Single Receivers

Knopp [26] studied the pressure and flow recovery as well as the spillover flow characteristics in a single receiver. The problem is illustrated in Figure 13.

The static pressure at the end of a parallel wall receiver with sharp leading edges and the volume flow recovery depends primarily on deflection of the power jet centerline from the centerline of the receiver, the blockage at the end of the receiver and the velocity profile of the impinging jet.

The profile is usually assumed to be Gaussian as for a corresponding free power jet. Thus for given jet deflection, varying the receiver blockage will yield the output characteristic relating recovered static pressure to volume flow. A typical output characteristic is shown in Figure 14 taken from [27].

Knopp [26] showed that none of the previous analyses were adequate for predicting the output pressure-flow characteristics of the receiver. Discrepancies were particularly large when the power jet was offset from the receiver centerline. He proposed a model based on the cowl streamline concept with continuity and energy equations applied to the control volume within the streamlines as in Figure 13. The calculation procedure is to solve the three equations

$$\begin{aligned}
\text{Continuity} \quad Q_r^* &= \int_{y_1^*}^{y_2^*} U^* dy^* & U^* &= e^{-ky^{*2}} \\
\text{Energy} \quad P_r^* &= \frac{\int_{y_1^*}^{y_2^*} U^{*3} dy^*}{Q_r^*} - \left( \frac{Q_r^*}{d^*} \right)^2 & (7) \\
\text{Load} \quad P_r^* &= f(Q_r^*)
\end{aligned}$$

These three equations are written in terms of the four unknowns  $P_r^*$ ,  $Q_r^*$ ,  $y_1^*$ , and  $y_2^*$  and a fourth equation relating  $y_1^*$  to  $\delta^*$  (the jet deflection) is needed.

For jet deflections greater than half receiver width so that the jet centerline is outside the projection of the receiver tips, a high energy streamline model [27] was found to predict the recovery reasonable well. The high energy model fixes  $y_1^*$  at the projection of the receiver tip toward which the jet is deflected. The centered streamline model referred to in Figure 14 locates  $y_1^*$  and  $y_2^*$  equidistant about the centerline of the jet.

It was shown in [26] that averaging of the total pressure profile impinging on the receiver area--the approach used in [19] grossly underpredicts the recovery at large deflection.

As part of the study [26], the characteristics of the spillover flow from the single receiver were obtained. Using hot wire anemometers, experimental profiles were obtained for flow behavior in the spillover region. Knopp's receiver was sharp-edged and the spillover flow was found to occur either as a wall jet or as a separated jet. Generally, with high blockage and an offset condition, the flow configuration shown in Figure 15 is obtained.

The rebound angle  $\beta$  is dependent on receiver width, blockage, and power jet offset. Angles of  $\beta$  greater than  $90^\circ$  are possible and indeed likely when the receiver width is comparable to the jet width. As receiver loading is increased,  $\beta$  reaches a value at which a jump occurs as in Figure 16, [28]. This sudden increase is caused by a detachment from the outside wall of the receiver. Figure 16 shows that only with extremely narrow receivers can this jump be avoided.

A simple momentum model was insufficient to predict the rebound angle with the offset jet case.

More detailed studies would be needed to further investigate these rebound angles. With high blockage the spillover jet flow may interfere with power jet flow as illustrated in Figure 17--a case to be avoided because of the formation of the closed circulation region C and feedback of spillover flow into the main power jet flows. This is one cause of low frequency pulsation in fluidic devices.

Using the measured velocity profiles the values of spillover flow into the side regions were found and are shown below in Figure 18 [28]. Clearly more flow is spilled on the side toward which the receiver is deflected. The degree of spillover is conveniently expressed in terms of the linear relation between

$$(Q_{v_1}^* - Q_{v_2}^*)$$

and the normalised jet offset. The constant of proportionality varies with receiver configuration from and just over 1.0 but is largely independent of loading. For the single receiver, of width  $d^* = 1.0$ , the differential spillover constant was 0.8 while with  $d^* = .5$ , the constant increases to approximately 1.2. The sum of the two spillover flows is larger than unity because the normalising flow is the power jet nozzle exit flow whereas the total flow in the jet at the plane of the receivers is larger because of entrainment.

Further experiments in [26] showed that velocity decay and entrainment rates in the spillover jet flows were both larger than those expected with free jets of corresponding mass flows.

#### Characteristics of Multiple Receiver Systems

Experiments by Reynolds [12] with twin receivers and a center dump have shown the effect of some geometric parameters on the receiver characteristics.

The configuration is shown in Figure 19. Figure shows the typical result for static pressure recovery versus power jet deflection from the centerline of the receiver system. Although the figure is involved, it does show the general effect of increasing receiver blockage. The blockage area ratio has been kept the same for both receivers (symmetrical loading) and a detailed study of Figure 20 shows an interesting phenomenon. First, the increase in blockage ratio results in a general increase in both output pressures. This is expected. Secondly, however, unexpectedly, the

differential pressure recovery reaches a maximum at about 70% blockage. Higher blockage reduces the deflection to differential pressure gain. It is apparent from Figure 20 that blockage greater than 70% causes a relatively larger increase in the lower of the two output pressures than the higher resulting in a net reduction in differential pressure gain. It is due to coupling between receivers in the flow field in the near vicinity of the receivers. The same phenomenon does not show up in the flow gain characteristic of Figure 21 because of the lower pressures found with high flow rates.

Changes in  $\epsilon$  were found to have little effect on the recovery characteristics. Changes in  $\alpha$  from  $0^\circ$  to  $30^\circ$  were also found to produce little effect on the recovery characteristic (Fig. 22) although angles greater than  $30^\circ$  lead to unstable flow fields at high blockage. This is interesting and suggests that angles of  $30^\circ$  and less are required for blocked load stability. This may be physically attributed to the proximity of the upper vent wall which acts as a guide to the spillover jet flow and the attendant interaction with the main power jet is through entrainment only.

The effect of the center dump is interesting and significant. Figure 23 shows for the same receiver configuration that the center dump improves the linearity of the differential pressure recovery characteristic but this is at the expense of differential pressure gain. Further, an increase in gain is obtained by blocking the center dump. This increase comes entirely from reductions in recovered pressure in the receiver away from which the power jet is deflected. This result is unexpected since first thoughts would treat the center dump as a device to decouple the two receivers. Apparently, blocking the center dump produces a lower recovery in the low pressure receiver which is not easy to explain.

#### Calculation of Output Pressure and Flow in Multiple Receiver Systems

Because of some unexplained phenomena observed experimentally, a generalised solution to the calculation of recovery characteristics for a given receiver configuration and an impinging power jet profile is not possible at this time. But, for a basically representative geometry with  $e^*=0$ ,  $d^*=1$ ,  $e^*=.75$ ,  $\alpha^*=15^\circ$ , some insight can be gained using control volumes and dividing streamline concepts. In Figure 24, assuming increased flow within the control volumes, continuity and energy flux equations yield a set of nine equations in ten unknowns. The final equation is given by an empirical relationship between the location of the "lead streamline" as defined by Craig [29] and the power jet deflection.

Given a velocity profile according to the Reichardt solution given by Miller and Commings [7],

$$U/U_c = e^{-\frac{\pi}{8}\eta^2} \quad ; \quad \eta = y/b'$$

where  $b'$  is one half of the jet momentum thickness.  $b'$  is established according to the well known spreading characteristics of the free jet. The profile is taken to be that found in the free jet at the location of the receivers. In terms of the assumed given velocity profile, continuity and energy equations yield,

$$Q_i = \int_{y_i}^{y_{i+1}} \int_0^h U(y,z) dz dy \quad (8)$$

$y = 1 \rightarrow 3$

$$Q_1 = Q_{02}; \quad Q_2 = Q_{cd}; \quad Q_3 = Q_{01}$$

for the flows in the receivers and center dump,

and

$$\int_{y_i}^{y_{i+1}} \int_0^h \rho U^3(y,z) dz dy = \int_{A_i} \left( \rho \frac{Q_i^2}{A_i^2} + P_i \right) U dA \quad (9)$$

$i = 1 \rightarrow 3$

$$Q_i = f_i(P_i) \quad (10)$$

$i = 1 \rightarrow 3$

for recovery pressures and load equations respectively.

Equations (8) through (10) form a set of nine basic equations in ten unknowns,  $P_i$ ,  $Q_i$ ,  $y_i$ ,  $i \rightarrow 3$ , and  $y_4$ .

A consistent set of equations could possibly be formulated using the momentum equation for each control volume in the set, but this procedure introduces unknown pressure distributions around the control volumes. The effect of pressure gradients across the control volumes is to move the effective locations of the streamlines  $y_1$  to  $y_4$ . The approach here is to seek a tenth empirical relation for  $y_2$  as a function primarily of the jet offset  $\delta$  in order to render a solution.

Craig [29] found that when the jet was centered, symmetry introduced the relationship

$$y_2 = -y_3 = \bar{y} \quad (11)$$

for the tenth equation. This value of  $y_2$  is found essentially by solving the equations in the set (8) through (10) corresponding to the center dump.  $P_2$  at the outlet of the center dump is assumed zero and with an inviscid flow model  $y$  becomes the simple projection of the edges of the center dump into the undeflected jet profile. With a deflected jet,  $\delta$ ,

$$y_3 = \bar{y} - K\delta \quad (12)$$

was found to be an apparent relationship which fitted the data of Reynolds [30].

$K$  was found to vary with receiver loading from 0 to 0.6 and represents the effect that with open receivers the streamlines project essentially straight into the impinging jet, while at higher blockage, they tend to emanate in the high velocity portions of the jet following the jet centerline as it is deflected.

Figure 25 shows a comparison of predicted and measured jet profiles for various deflections while Figures 26 and 27 show a comparison for two blockages of measured and predicted pressure and flow recovery characteristics as a function of jet deflection. In each case the receivers were located ten nozzle widths downstream from the power jet nozzle exit. Figure 28 shows the comparison of the model given by equation (8), (9), (10) and (11) for the centered jet output characteristic as blockage is varied. Figure 29 shows experimental data for center dump flow indicating that it is largely independent of receiver loading.

Experimentally obtained data for jet spillover characteristics are given in Figures 30 and 31. As with the case of a single receiver the differential spillover flow characteristic is not a strong function of loading at small deflections and is mostly dependent on deflection.

These flows were obtained by integration of measured midplane velocity profiles and are roughly characterised by

$$Q_{v12}^* = K(\delta/b) \quad ; \quad K = 0.3.$$

This value of  $K$  is considerably less than that obtained from a single sharp edged receiver ( $K \approx 0.85 \rightarrow 1.0$ ) which is to be expected in view of the blunt nature of the receiver system.

### Effects of Side Vent Length

Earlier, it was pointed out that resistance to flow in the side vent areas creates subambient back pressure gradients which act to increase the power jet deflection over that obtained by a straight line projection control passage. This effect should increase with vent length as the restriction of externally entrained air increases. The basic cause of this effect lies in the fact that entrained flow is proportional to spillover jet flow which is proportional to deflection. For any restriction of entrained flow, the pressure difference on the sides of the power jet is thus proportional to deflection in a direction acting to increase deflection beyond the straight line projection.

Shipp [31] experimentally investigated this effect with a 0.1" square nozzle amplifier. His amplifier is shown in Figure 32. In Figure 33 the effect of vent length on the blocked load pressure gain is shown to improve the gain up to a point. With a parallel wall vent, the width of the vent jet (it flows along the upper vent wall) becomes comparable to the passage width at  $L_v^* = 20$  and begins to interfere with aspirated flow into the vent (Figure 34). At this point increasing vent length has no further influence on amplifier gain.

Vent length has no effect on the input characteristics of the amplifier and a slight effect on the output characteristics caused by the increased deflection gain of the power jet.

### Dynamic Response of Proportional Amplifiers

The dynamic response of proportional amplifiers varies with nominal size, loading and geometric configuration of the device, as well as fluid properties and supply pressure. Because of the generally non-linear behavior of large signal response, dynamic performance is usually specified in terms of the small signal linearised frequency response. Typical bandwidths of a 0.020" nozzle width amplifier operating at 1.0 psig supply pressure are 1,000 HZ (based on 3 db change in gain). While amplitude may not decay, the typical low frequency behavior is governed by an accumulation of phase shift corresponding to passage lags and jet transport delay. This feature is limiting in the case of cascaded amplifier circuits such as those used for operational amplifiers and leads to the need for stability compensation.



For a single receiver device used for rectification [3], the typical frequency response is shown in Figure 35 for two reduced nozzle aspect ratios. The resonance occurring between 1,000 HZ and 1,400 HZ results from an interaction between the inertance of the fluid in the side vents and the lateral bending capacitance of the jet [32,33]. Higher passage resonances do occur if excited [34]. Complete linearised transfer functions were determined by Humphrey and Brown for a 0.056" nozzle width amplifier resulting in a control to output admittance (output flow/control pressure) response as shown in Figure 36 in which the vent-jet dynamics are separated from the higher passage dynamics.

Since the low frequency behavior of the device is dominated by side vent effects it is convenient here to divide the discussion into two parts, (a) perfectly vented amplifiers and (b) vent effects.

#### Perfectly Vented Devices

In this context, a perfectly vented device is one in which the side areas are completely open to the ambient. This is good for increasing bandwidth but bad for the sensitivity to external disturbances. In this case, the control and output passages are coupled only in the forward direction.

Control passages, jet transport and output passage dynamics are cascaded as illustrated by the circuit model in Figure 37 for a largely pressure controlled amplifier.

The parameters  $I_i$  and  $C_i$  are given by

$$\rho \frac{L_i}{A_i} ; \frac{A_i L_i}{n \bar{P}_i} ;$$

where subscript  $i$  relates to either the control or the output passage.  $L$  and  $A$  are lengths and sectional areas,  $\bar{P}$  is the nominal absolute fluid pressure in the passage.  $n$  is a polytropic index for the fluid. A detailed discussion of lumped fluid elements is given in [36].  $R_c$  and  $R_o$  are the local slopes of the input and output pressure-flow characteristics of the device taken about the linearisation operating point.  $\tau$  is the delay corresponding to jet travel time at the jet centerline velocity for the distance between the control and the receiver passages and  $G$  is the pressure gain of the amplifier at the operating point. Good correlation may be obtained with this model provided the power jet is not enclosed by venting regions.



### Effects of Vents on Amplifier Response

A complete analysis of an amplifier with enclosed vents implies that the effect of control flows and output flows on vent flows, and the subsequent reaction of vent back pressures on the power jet be considered. Work done in this area is described by Healey [32], Manion [37] and Brown and Humphrey [33].

In [32], an amplifier transfer function of the form

$$\frac{\Delta P_O(s)}{\Delta P_C} = \frac{Ge^{-\tau s}}{(1 + \tau_1 s)(1 + 2\zeta_V(s/\omega_V) + (s/\omega_V)^2)}$$

was derived for blocked load pressure gain where the second order term in the denominator resulted from the interaction of a lumped inertance-resistance model for the side vent and a capacitance for the side vent and a capacitance for the lateral bending of the power jet. In terms of the device geometry, it was shown that

$$\frac{\omega_V l}{U} = \sqrt{\frac{3}{L_V^*}} \quad (13)$$

and

$$\zeta_V \approx \frac{\sqrt{3}}{24} \sqrt{L_V^*}$$

$\tau$  was the jet transport delay and  $\tau_1$  was the (I/R) time constant of the passage (passage capacitance was neglected in that work as water was used as the fluid).

While the analysis provided reasonable agreement with experimental data it did not satisfactorily include the effects of jet transport delay and the coupling effects between output flows and vent flows obtained for non-blocked receivers. Brown and Humphrey [33] neglected jet transport delay but modelled the side vents in terms of a single inertance-resistance lumped model and included the receiver output flow. The amplifier was described by a set of six state equations giving rise to a sixth order model--two orders each for control, vent and output passages. The model required the assumption of a value for the spillover constant relating spillover flow to power jet deflection, which was found by fitting the model simulation with data. For details of the equations of the model, the reader is referred to [33]. Good correlation was obtained once a value for spillover constant was found (Figure 38).

### Effects of Vent Length on Jet-Vent Interactions

Using a 0.1" square nozzle amplifier already shown in Figure 32, Shipp [31] experimentally determined the pressure gain by measurement of control differential pressure at the edges of the power jet and output differential pressure at the mouths of the receivers. This effectively eliminated both control and output passage dynamics from the experiment and the frequency response obtained for blocked receivers is shown in Figures 39, 40 and 41 for three lengths of side vent. The trends indicate that the low frequency resonance is accompanied by two higher frequency resonances. The low frequency behavior is controlled by both the power jet velocity and the side vent length while the high frequency peaks are independent of vent length. Power jet velocity effects collapse through the use of the Strouhal number  $\omega l/U$ , where  $\omega$  is radian frequency,  $l$  is the distance between control passage and receiver tips and  $U$  is the power jet nozzle exit velocity.

The experimental data for this device confirm qualitatively the trend expected by the analysis of [32]. The two high frequency peaks are associated with higher modes of jet dynamic behavior. In the experiments of Shipp the actual frequencies were well below passage resonance frequencies and the general existence of higher jet modes can be shown with a simple jet bending model [38] and [39]. However, while the presence of these higher modes can be shown, precise agreement of frequencies with experimental data has not been obtained so far.

While the higher modes of resonance are interesting, the bandwidth of the device is still limited by the low frequency jet-vent coupling and equation (13) still remains the simplest way of obtaining a first estimate of bandwidth.

### Part II - Field Solution Approach

Because of the lack of generality of approaches using control volumes or dividing streamline methods, a better method is sought to model relevant internal flow behaviors and to predict geometric effects. The field simulation model utilizes a finite difference scheme to solve the Navier-Stokes equations with appropriate boundary conditions. At the outset, this approach is restricted to 2 dimensional application because of the size of the problem. Additionally, work to date has suppressed the deflection of the power jet in favor of modelling the venting and receiver reactions. Further, initial studies have begun with non-vented devices for simplicity.

The model thus assumes a laminar jet flow with an initially parabolic velocity distribution issuing into a cavity zone and impinging on two receivers. Figure 42 shows the geometry and the Reynolds Number Range is 10 to 1,000. This is consistent with the range of Reynolds number in the work underway at Harry Diamond Laboratories in the development of low noise laminar amplifiers.

#### Development of the Equations of the Model

The analysis considers the flow to be modelled by two-dimensional laminar incompressible flow. The equations of momentum and continuity are combined into the vorticity transport equation and stream function equation in which the velocities are given by the derivatives of the stream function [40,41]. The governing equations are

$$\frac{\partial \zeta}{\partial t} = -u \frac{\partial \zeta}{\partial x} - v \frac{\partial \zeta}{\partial y} + \frac{1}{Re} \left( \frac{\partial^2 \zeta}{\partial x^2} + \frac{\partial^2 \zeta}{\partial y^2} \right) \quad (14)$$

$$\frac{\partial^2 \psi}{\partial x^2} + \frac{\partial^2 \psi}{\partial y^2} = \zeta \quad (15)$$

where

$$\zeta = \frac{\partial u}{\partial y} - \frac{\partial v}{\partial x} \quad (16)$$

$$u = \frac{\partial \psi}{\partial y}, \quad v = -\frac{\partial \psi}{\partial x} \quad (17)$$

All quantities are nondimensionalized using the supply port width and the average input velocity. Although the vorticity equation is an unsteady equation, the desired steady state solution will be obtained by allowing the unsteady problem to develop from some assumed initial state to its steady solution.

The governing equation for vorticity is solved using an alternating direction implicit (ADI) method. The method is based on the work of Peaceman and Rachford [42] and such methods are widely used for solution of viscous flow problems [41,43,44]. A major reason for the use of ADI methods is that the splitting of directions produces systems of equations with tridiagonal coefficient matrices, for which solutions can be obtained very efficiently. Another reason for its use is its excellent stability characteristics. Compared to explicit methods ADI methods allow much larger computational time steps and thus use less computer time to reach a steady state solution.

Problems with stability at higher Reynolds numbers led to the use of several differencing schemes on the nonlinear terms of the vorticity equation. In particular, second order accurate centered differencing was tried and abandoned in favor of the more stable, first order accurate, upwind differencing. This proved to have convergence problems at regions where velocity reversals occurred and was replaced by second upwind differencing [41,45]. After the above changes were made, other causes of instability were discovered and remedied. As will be discussed later it may be possible and desirable to try the second order accurate centered differencing again.

It should be noted that second upwind differencing is used only on the advection terms of (14). Centered differencing is retained on the diffusion terms.

Using the ADI method and the above differencing, the resulting difference equations are:

X-sweep:

$$\begin{aligned} \frac{\zeta_{ij}^{n+1/2} - \zeta_{ij}^n}{\Delta t/2} = & - \frac{[u_R \zeta_{RX} - u_L \zeta_{LX}]^{n+1/2}}{\Delta x} \\ & - \frac{[v_R \zeta_{RY} - v_L \zeta_{LY}]^n}{\Delta y} \\ & + \frac{1}{Re \Delta x^2} [\zeta_{i+1,j} + \zeta_{i-1,j} - 2\zeta_{ij}]^{n+1/2} \\ & + \frac{1}{Re \Delta y^2} [\zeta_{i,j+1} + \zeta_{i,j-1} - 2\zeta_{ij}]^n \end{aligned} \quad (18a)$$

Y-sweep:

$$\begin{aligned} \frac{\zeta_{ij}^{n+1} - \zeta_{ij}^{n+1/2}}{\Delta t/2} = & - \frac{[u_R \zeta_{RX} - u_L \zeta_{LX}]^{n+1/2}}{\Delta x} \\ & - \frac{[v_R \zeta_{RY} - v_L \zeta_{LY}]^{n+1}}{\Delta y} \end{aligned}$$

$$\begin{aligned}
& + \frac{1}{\text{Re}\Delta x^2} [\zeta_{i+1,j} + \zeta_{i-1,j} - 2\zeta_{i,j}]^{n+1/2} \\
& + \frac{1}{\text{Re}\Delta y^2} [\zeta_{i,j+1} + \zeta_{i,j-1} - 2\zeta_{i,j}]^{n+1} \quad (18b)
\end{aligned}$$

where

$$\begin{aligned}
u_R &= \frac{1}{2}(u_{i+1,j} + u_{i,j}) & v_R &= \frac{1}{2}(v_{i,j+1} + v_{i,j}) \\
u_L &= \frac{1}{2}(u_{i-1,j} + u_{i,j}) & v_L &= \frac{1}{2}(v_{i,j} + v_{i,j-1})
\end{aligned}$$

and

$$\begin{aligned}
\zeta_{RX} &= \zeta_{i,j} & u_R &> 0 & \zeta_{RY} &= \zeta_{i,j} & v_R &> 0 \\
\zeta_{RX} &= \zeta_{i+1,j} & u_R &< 0 & \zeta_{RY} &= \zeta_{i,j+1} & v_R &< 0 \\
\zeta_{LX} &= \zeta_{i-1,j} & u_L &> 0 & \zeta_{LY} &= \zeta_{i,j-1} & v_L &> 0 \\
\zeta_{LX} &= \zeta_{i,j} & u_L &< 0 & \zeta_{LY} &= \zeta_{i,j} & v_L &< 0
\end{aligned}$$

and

$$\zeta_{i,j} = \zeta(i\Delta x, j\Delta y)$$

$n$  is the time step index.

The elliptic equation governing the stream function is solved using successive overrelaxation, SOR [41]. Centered differencing is used on both second derivatives. After rearrangement and introduction of the overrelaxation factor  $\omega$ , (15) can be written as

$$\begin{aligned}
\psi_{i,j}^{k+1} &= \psi_{i,j}^k + \frac{\omega}{2(1+\beta^2)} [\psi_{i+1,j}^k + \psi_{i-1,j}^{k+1} \\
& + \beta^2 \psi_{i,j+1}^k + \beta^2 \psi_{i,j-1}^{k+1} - \Delta x^2 \zeta_{i,j}^{n+1} \\
& - 2(1+\beta^2) \psi_{i,j}^k] \quad (19)
\end{aligned}$$

where

$$\beta = \Delta x / \Delta y ,$$

k = iteration index

Due to the coupling between the stream function and vorticity equations (18a), (18b), and (19) must be solved simultaneously. Basically the solution procedure is the following:

- (1) Assume some initial distribution of  $\zeta$  and  $\psi$  for the mesh. For most cases the results of previous calculations at a different Reynolds number are available to be used as initial conditions.
- (2) Using ADI, solve for  $\zeta^{n+1}$ .
- (3) Using SOR, solve for  $\psi^{n+1}$ .
- (4) Update the time step index n and repeat (2)-(4) until steady state is reached; i.e., the changes in  $\zeta_{ij}$  are less than some specified  $\epsilon$ .

The error criterion  $\epsilon$  will be discussed more fully later.

Boundary conditions for the governing difference equations are of primary interest in this analysis. In order to simplify the boundary conditions for this preliminary study, the general beam deflection amplifier geometry has been modified. As shown in Figure 42, the amplifier under consideration is nonvented, has two output receivers with no center dump, has no control ports and has one supply or inlet port. The boundary conditions for this geometry can be divided into inlet, outlet, and solid wall conditions.

At the solid walls a no slip condition is assumed. Setting u and v to zero in (7), the no slip assumption implies a constant  $\psi$  on each wall. It is assumed that the left wall of the amplifier has  $\psi = 0$ , where the reference value 0 was arbitrarily chosen. As noted earlier the flow variables are nondimensionalized with respect to the average inflow velocity and the supply port width. Due to this choice of nondimensionalizing variables, the right wall has  $\psi = -1.0$ . It is assumed that both receivers see the same output impedance; i.e., the loading on the amplifier is symmetric. Then, since the jet is assumed undeflected, the flows through the receivers will be equal in magnitude. Therefore, between the receivers the wall value of  $\psi$  is  $\psi = -.500$ .

The no-slip condition allows the determination of boundary values of  $\zeta$  using a Taylor series expansion of  $\psi$  at a wall node [41]. For vertical, or horizontal, walls

$$\psi_{w+\Delta\eta} = \psi_w + \frac{\partial\psi}{\partial\eta} \Big|_w \Delta\eta + \frac{1}{2} \frac{\partial^2\psi}{\partial\eta^2} \Delta\eta^2 + O(\Delta\eta^3) \quad (20)$$

where  $w$  signifies a wall node and  $\Delta\eta$  is the grid spacing normal to the wall. The no-slip assumption makes the first derivative of  $\psi$  equal to zero (see equation (17)). Since  $\psi$  is constant on a wall the second derivative is the vorticity (see equation (15)). Substituting into (20) and rearranging gives

$$\zeta_w = \frac{2(\psi_{w+\Delta\eta} - \psi_w)}{\Delta\eta^2} + O(\Delta\eta) \quad (21)$$

The values of  $\zeta$  on the walls of the receivers can be similarly derived except that two series expansions are required. For example, consider the left wall of the left receiver. About a point  $i, j$  on the wall

$$\begin{aligned} \psi_{i+1,j} &= \psi_{i,j} + \frac{\partial\psi}{\partial x} \Big|_{i,j} \Delta x \\ &+ \frac{1}{2} \Delta x^2 \frac{\partial^2\psi}{\partial x^2} \Big|_{i,j} + O(\Delta x^3) \end{aligned} \quad (22)$$

and

$$\begin{aligned} \psi_{i,j+1} &= \psi_{i,j} + \frac{\partial\psi}{\partial y} \Big|_{i,j} \Delta y \\ &+ \frac{1}{2} (\Delta y)^2 \frac{\partial^2\psi}{\partial y^2} \Big|_{i,j} + O(\Delta y^3) \end{aligned} \quad (23)$$

Again the first derivatives are zero at the wall. The second derivatives can be rewritten as

$$\frac{\partial^2\psi}{\partial x^2} = -\frac{\partial v}{\partial x} \quad ; \quad \frac{\partial^2\psi}{\partial y^2} = \frac{\partial u}{\partial y} \quad (24)$$

Multiplying (23) by  $\beta$ , adding (23) to (22), and rearranging using (24) and (16) gives

$$\zeta_{i,j} = \frac{2}{\Delta x^2} [\psi_{i+1,j} + \beta^2 \psi_{i,j+1} - \psi_{i,j}(1+\beta^2)] + 0(\Delta x, \Delta y) \quad (25)$$

Similar expressions hold for  $\zeta$  at all solid walls in the receiver regions.

At both inflow and outflow a parabolic velocity profile is presently being assumed. At outflow this assumption is being implemented with boundary conditions of the form [41,p.154]

$$\frac{\partial \zeta}{\partial x} = 0 \quad (\text{axial gradient} = 0) \quad (26)$$

and

$$\psi = f(\eta) \quad (27)$$

where  $\eta$  is a transverse distance coordinate and the functional  $f$  is determined from the assumed parabolic profile.

At inflow the gradient condition on  $\zeta$  has produced convergence problems for higher Reynolds numbers. In its place the condition used is:

$$\zeta = g(\eta) \quad (28)$$

where  $g$  is determined from the assumed parabolic shape.

As mentioned earlier, the boundary conditions on outflow are interpreted to mean that both receivers see the same output impedance. With these boundary conditions the model has no way to input unsymmetrical loading. This will have to be added in the future.

Special care is given to the values of vorticity at the sharp corners in the amplifier geometry. At those six corners which are concave there is no problem, since these points never enter into the calculations. However, at the convex corners of the receiver inlets the proper value of  $\zeta$  to use is in question. Following Roach's recommendations [41,pp.169-171] the procedure being used is to allow  $\zeta_w$  to be discontinuous at these points. If the value of  $\zeta$  is needed for calculations dealing with mesh points inside the receivers,  $\zeta_w$  is defined as in equation (25). If the flow outside the receiver in the main amplifier cavity region is being considered,  $\zeta_w$  is defined as in (21).

At the receiver outlets one corner point enters the calculations. However, its value is defined by considering



the point to have an extension of the wall beyond it. Thus  $\zeta_w$  at this point is evaluated as in (25).

At the corners of the amplifier inlet the choice is not so clear.  $\zeta_w$  could either be defined as in (21) or as in (28). It seems most consistent with the handling of the receivers to define  $\zeta_w$  by (21). However, this choice is still under consideration.

Using an implicit method on the vorticity equation can produce a problem with the boundary conditions. The solution for the  $n+1$  time step requires boundary values which are not available [41,p.93], since they also need to be at the  $n+1$  level. Further, using lagged boundary conditions, i.e., using boundary conditions based on information at the  $n$  time level, has been shown to be numerically destabilizing [41,p.94]. The method chosen to resolve this problem is to (1) extrapolate from  $\zeta_w^{n-1}$  and  $\zeta_w^n$  to  $\zeta_w^{n+1}$  and (2) then iterate on the time step solution until the wall vorticities at the  $n+1$  level change less than some specified amount. This procedure is suggested by Roache and is similar to that used by Briley [43].

It is also possible with the above iteration scheme to set a variable time step based on the numbers of iterations for convergence of the previous time step [43]. This allows the solution to use a time step which is in a sense numerically optimal. This technique was tried with success on some cases. However, its general applicability is still to be determined for this problem.

The overall solution is assumed converged when the normalized, relative change in vorticity over a time step is less than some  $\epsilon$  for each point in the mesh. That is, the solution is converged when for all points

$$\zeta^{n+1} - \zeta^n < \left[ \frac{1}{NP} \sum_{i=1}^{I_{\max}} \sum_{j=1}^{I_{\max}} |\zeta_{i,j}| \right] \times \left[ \frac{\Delta t}{\Delta t_{\text{ref}}} \right] \times \epsilon \quad (29)$$

where

NP = number of points in the flow field

$\Delta t$  = time step

$\Delta t_{\text{ref}}$  = reference time step

At present an  $\epsilon$  of 0.001 is being used.

Solutions to the governing equations have been obtained for Reynolds numbers from 1 to 1,000 with an undeflected inlet jet, i.e.,  $\theta=0$ . These solutions have been generated

using two mesh spacings. The coarser of the two grids puts three points across the inlet and produces a 21 by 29 array of nodes on the amplifier geometry. The finer grid puts five points across the inlet and produces a 41 by 57 array of nodes.

### Results

Some typical results are shown in Figures 43, 44, and 45. Initially a grid size 21x29 was tried with large truncation errors and the results shown are for a 41x57 grid. The three figures denote the influence of Reynolds Number on the flow characteristics for the case where the power jet is centered. Results so far are encouraging and the method is being further explored. The computer plots in Figures 43 through 45 clearly show the vortices in the vent region. The results are obtained by solution of the time dependent equations. This means that if suitable initial conditions can be chosen, amplifier dynamic response can be computed. Simulation costs are not low, however, and are dependent on convergence criteria used. For example, a typical run with a very stringent error criterion ( $\epsilon = .001$  as defined by equation (29)) computer time on a CDC 6600 takes about 2,000 seconds. At \$26.00 per hour this costs in the neighborhood of \$15.00 per run.

### SUMMARY AND CONCLUSIONS

This paper has aimed at exposing the reader to some of the theoretical ideas and models used in the past and currently for predicting performance of jet deflection fluid amplifiers. Much remains to be done. Control volumes and dividing streamline methods are simple and easy to use but suffer from lack of general applicability. Field simulation methods are definitely a practical proposition and, while computationally more expensive, do offer greater detail and precision in the solutions.

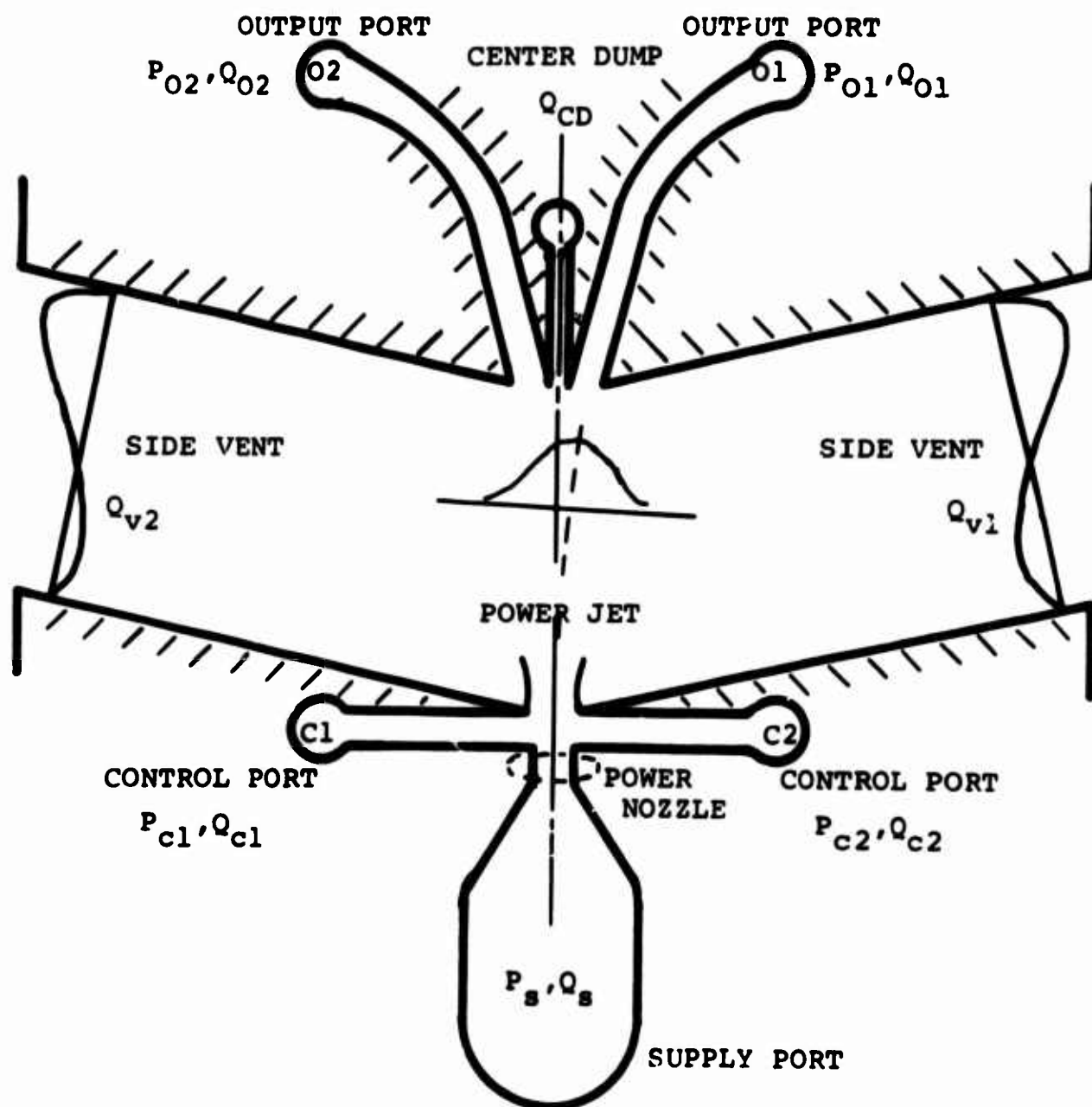
## REFERENCES

1. Urbanosky, T. F., "Flueric Operational Amplifier Survey," SAE Paper No. 670707 Presented at 1967 Aerospace Systems Conference, Los Angeles, June 27, 1967.
2. Rose, R. K. and Phipps, W. L., "Fluidic Control of a J79 Turbojet Engine," ASME Paper No. 67WA-FE-33 Presented at 1967 Winter Annual Meeting.
3. Kelley, L. R., "A Fluidic Temperature Control Using Frequency Modulation and Phase Discrimination" Trans. ASME Journal of Basic Engineering, Vol. 89, No. 2, pp. 341-348, 1967.
4. Mon, G., "Laminar Proportional Amplifier," Proceedings of the 6th Cranfield Conference on Fluidics, Stockholm, Sweden, March 1974.
5. Schlichting, H., "Boundary Layer Theory," Published by McGraw-Hill, p. 498.
6. Reichardt, H., GesetzmaBigkeiten der freien Turbulenz V.D.I.-Forschungsheft 414, (1942).
7. Miller, D. R. and Comings, E. W., "Static Pressure Distribution in the Free Turbulent Jet," Journal of Fluidic Mechanics, Vol. 3, Part I, pp.1-16, October 1957.
8. Albertson, M. L., Dai, Y. B., Jensen, R. A., and Rouse, H., "Diffusion of Submerged Jets," Trans. A.S.C.E., Vol. 115, 1950, pp. 639-664.
9. Foss, J. E., and Jones, J. B., "Secondary Flow Effects in a Bounded Rectangular Jet," Journal of Basic Engineering, Vol. 90, No. 2, June 1968, pp. 241-248.
10. Holdman, J. D. and Foss, J. F., "The Initiation, Development and Decay of the Secondary Flow in a Bounded Jet," ASME Paper 73-WA/FLCS-7 Presented at ASME Winter Annual Meeting Detroit, November 1973.
11. Gray, R. W. and Shearer, J. L., "Effects of Upstream Disturbances in the Spreading of Large Fluid Amplifier Jets," Journal of Dynamic Systems, Measurement and Control, Vol. 93, No. 1, March 1971, pp. 53-60.
12. Healey, A. J. and Reynolds, W. J., "Static Output Characteristics of a Beam Deflection Fluid Amplifier," Technical Report U.S. Army Research Office, Durham, December 1972.

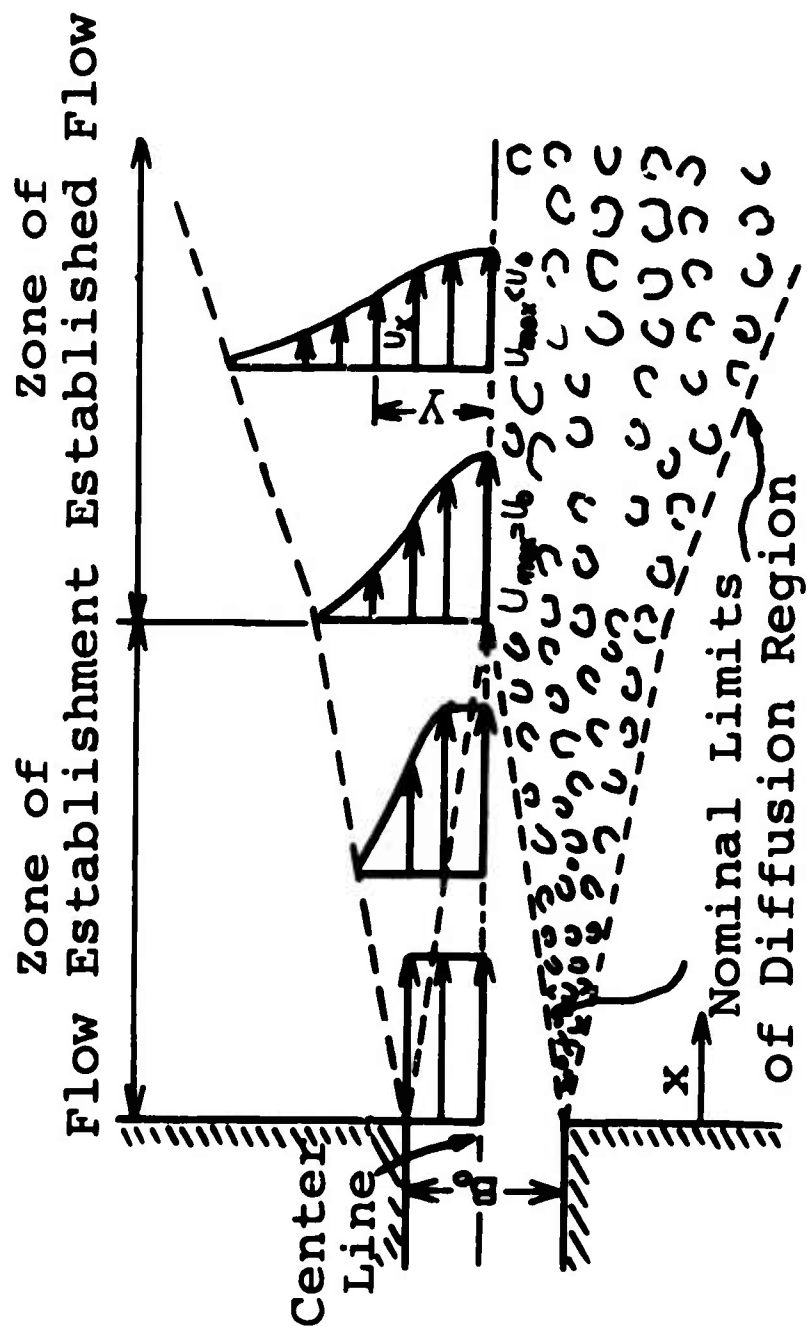
13. Fekete, G. I., "Coanda Flow of a 2-Dimensional Wall Jet on the Outside of a Circular Cylinder," McGill University M.E. Department Report 63-11, 1963.
14. Giles, J. A., Hayes, A. P., and Sayer, R. A., "Turbulent Wall Jets on Logarithmic Spiral Surfaces," Aeronautical Quarterly, Vol. 18, August 1966, pp. 201-215.
15. Dexter, E. M., "An Analog Pure Fluid Amplifier," Symposium on Fluid Jet Control Devices, ASME, November 28, 1962, pp. 41-49.
16. Moynihan, F. A. and Reilly, R. J., "Deflection and Relative Flow of Three Interacting Jets," Proceedings of Symposium on Fluid Amplification 1., 1964, pp. 123-146 (Rep. No. AD 601 499).
17. Douglas, J. F. and Neve, R. S., "Investigation into the Behavior of a Jet Interaction Proportional Amplifier," Paper C3 pp. C3-29 to C3-50, Proceedings of 2nd Cranfield Conference on Fluidics, B.H.R.A. Cranfield, January 1967.
18. Sarpkaya, T., Weeks, S. B., and Hiriart, G. L., "A Theoretical and Experimental Investigation of the Interaction of Jets in Beam Deflection Type Fluidic Elements," Proceedings of 4th Cranfield Fluidics Conference, 1970, pp. B3-33 to B3-46.
19. Simson, A. K., "Gain Characteristics of Subsonic Pressure Controlled Proportional Fluid Jet Amplifiers," Trans. ASME Journal of Basic Engineering, Vol. 88, No. 2, June 1966, pp. 295-305.
20. Foss, J. F., "Flow Characteristics of the Defined Region Geometry for High Gain Proportional Amplifiers," Advances in Fluidics, Published by ASME, 1967, pp. 45-61.
21. Griffin, W., "A Fluid Jet Amplifier with Flat Saturation Characteristics," Trans. ASME Journal of Basic Engineering, V. 91, No. 4, pp. 734-739, 1969.
22. Reid, K. N., "An Experimental Study of the Static Interaction of an Axi-symmetric Fluid Jet and a Single Receiver-Diffuser," Proceedings of the Fluid Amplification Symposium, Harry Diamond Laboratories, Washington D.C., Vol. 4, 1965.
23. Zalmanson, L. A. and Semikova, A. I., "Investigation of the Characteristics of Pneumatic Jet Elements," Proceedings of the First I.F.A.C. Congress, Moscow, Vol. 3, pp. 218-225, 1960.

24. Rupert, J. G., "Analysis of the Pressure Flow Characteristics of a Submerged Jet-Receiver-Diffuser-Load System," Proceedings of the National Conference on Fluid Power, Vol. 21, pp. 102-112, October 1967.
25. Olson, R. E., "Analytical Techniques for Predicting the Characteristics of Jet Flows in Fluidic Devices," Fluidics Quarterly, Vol. 1, part I, pp. 85-100.
26. Knopp, A. A., "A Study of Receiver Pressure-Flow and Vent Flow Characteristics of a Fluidic Rectifier," M.S. Thesis, The Pennsylvania State University, June 1971.
27. Healey, A. J., "Pressure and Flow Recovery Characteristics of a Single Fluid Amplifier Receiver with Offset Bounded Jets," Trans. ASME Journal of Dynamic Systems, Measurement and Control, Vol. 95, No. 2, pp. 191-193, 1973.
28. Healey, A. J., "An Experimental Study of Spillover Flow from a Single Fluid Amplifier Receiver," ASME Paper No. 73 WA-FLCS-6 Presented at 1973 Winter Annual Meeting, Detroit, November 1973.
29. Craig, S., "An Analytical-Empirical Approach to Signal Recovery in Fluid Amplifier Receivers," M.S. Thesis, The University of Texas, Austin, 1973.
30. Reynolds, W. J., "Static Output Characteristics of a Beam Deflection Fluid Amplifier," M.S. Thesis, The University of Texas, Austin, 1972.
31. Healey, A. J. and Shipp, E. M., "Vent Length Effects on a Proportional Amplifier," Technical Report - U.S. Army Research Office, Durham, North Carolina, September, 1973.
32. Healey, A. J., "Vent Effects on the Response of a Proportional Amplifier," Trans. ASME Journal of Basic Engineering, Vol. 90, No. 1, March 1968, pp. 90-96.
33. Brown, F. T. and Humphrey, R. A., "Dynamics of a Proportional Fluid Amplifier - Part 2," Trans. ASME Journal of Basic Engineering, Vol. 92, No. 2, 1970, pp. 312-321.
34. Humphrey, R. A. and Brown, F. T., "Dynamics of a Proportional Fluid Amplifier - Part 1," Trans. ASME Journal of Basic Engineering, Vol. 92, No. 2, 1970, pp. 303-312.

35. Belsterling, C. A. and Tsui, K., "Analysing Proportional Amplifier Circuits," Control Engineering, Vol. 12, No. 8, August 1965, pp. 87-92.
36. Shearer, J. L., Murphy, A. T., and Richardson, H. H., "Introduction to System Dynamics," Addison Weseley.
37. Manion, F. M. "Dynamic Analysis of Flueric Proportional Amplifiers," ASME Paper No. 68-FE-49, Presented at 1968 Fluidics Engineering Division Conference, 1968.
38. Healey, A. J., "Dynamics of Proportional Amplifiers," Proceedings of Symposium on Fluidics and Related Internal Flows, The Pennsylvania State University, University Park, Pennsylvania, 1968.
39. Kirshner, J. M., "Jet Dynamics and Its application to the Beam-Deflection Amplifier," HDL-TR-1630, U.S. Harry Diamond Laboratories, July 1973.
40. Schlichting, Hermann, Boundary-Layer Theory, McGraw-Hill, Inc., New York, 1968, pp. 68-69.
41. Roache, Patrick J., Computational Fluid Dynamics, Hermosa Publishers, Albuquerque, New Mexico, 1972.
42. Peaceman, D. W., and Rachford, H. H., Jr., "The Numerical Solution of Parabolic and Elliptic Differential Equations," J. Soc. Indust. Applied Mathematics, Vol. 3, No. 1, March 1955, pp. 28-41.
43. Briley, W. R., "A Numerical Study of Laminar Separation Bubbles using the Navier-Stokes Equations," Report J110614-1, United Aircraft Research Laboratories, East Hartford, Connecticut, 1970.
44. Pearson, Carl E., "A Computational Method for Viscous Flow Problems," J. Fluid Mechanics, Vol. 21, Part 4, 1965, pp. 611-622.
45. Runchal, A. K., and Wolfshtein, M., "Numerical Integration Procedure for the Steady State Navier-Stokes Equations," Journal of Mechanical Engineering Science, Vol. 11, No. 5, 1969, pp. 445-453.

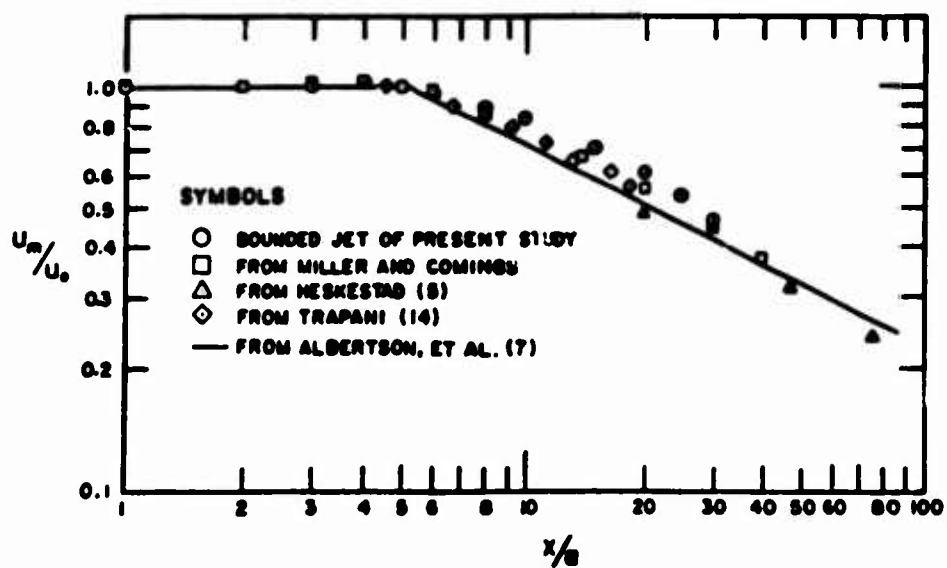
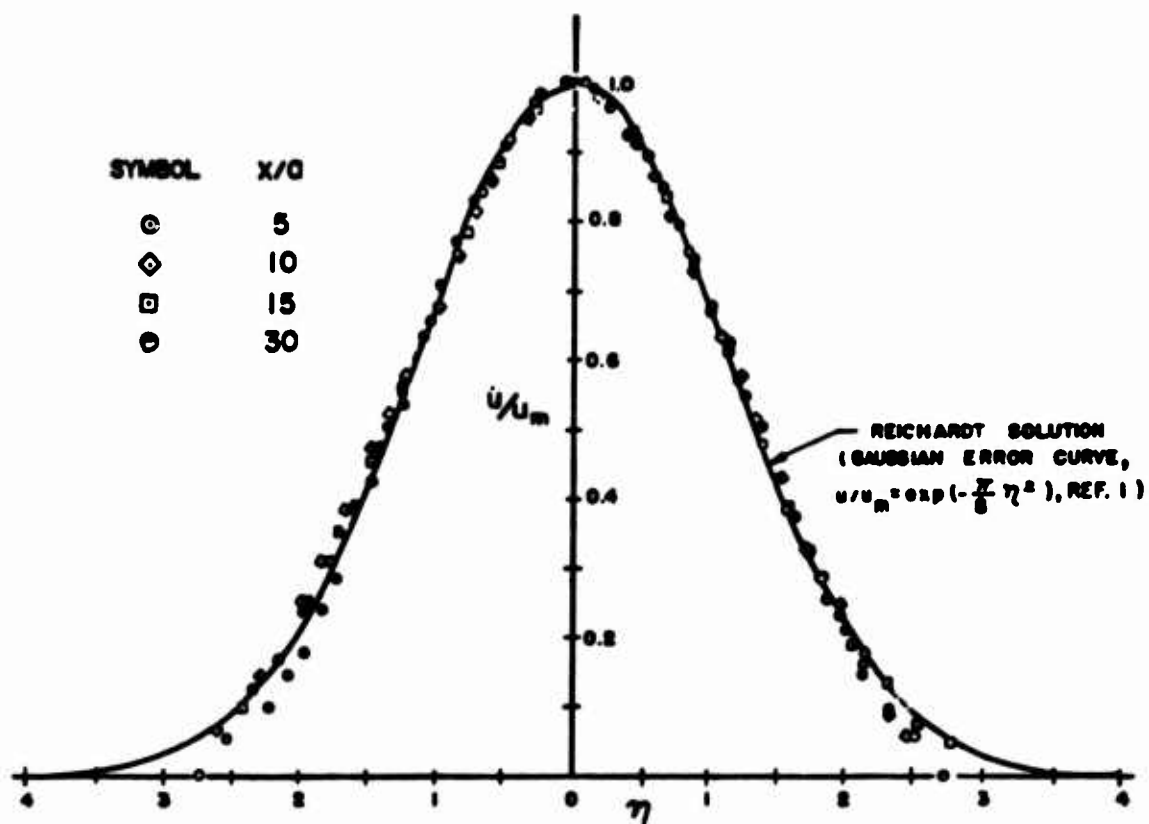


1. Schematic of a Vented Jet Deflection Amplifier.

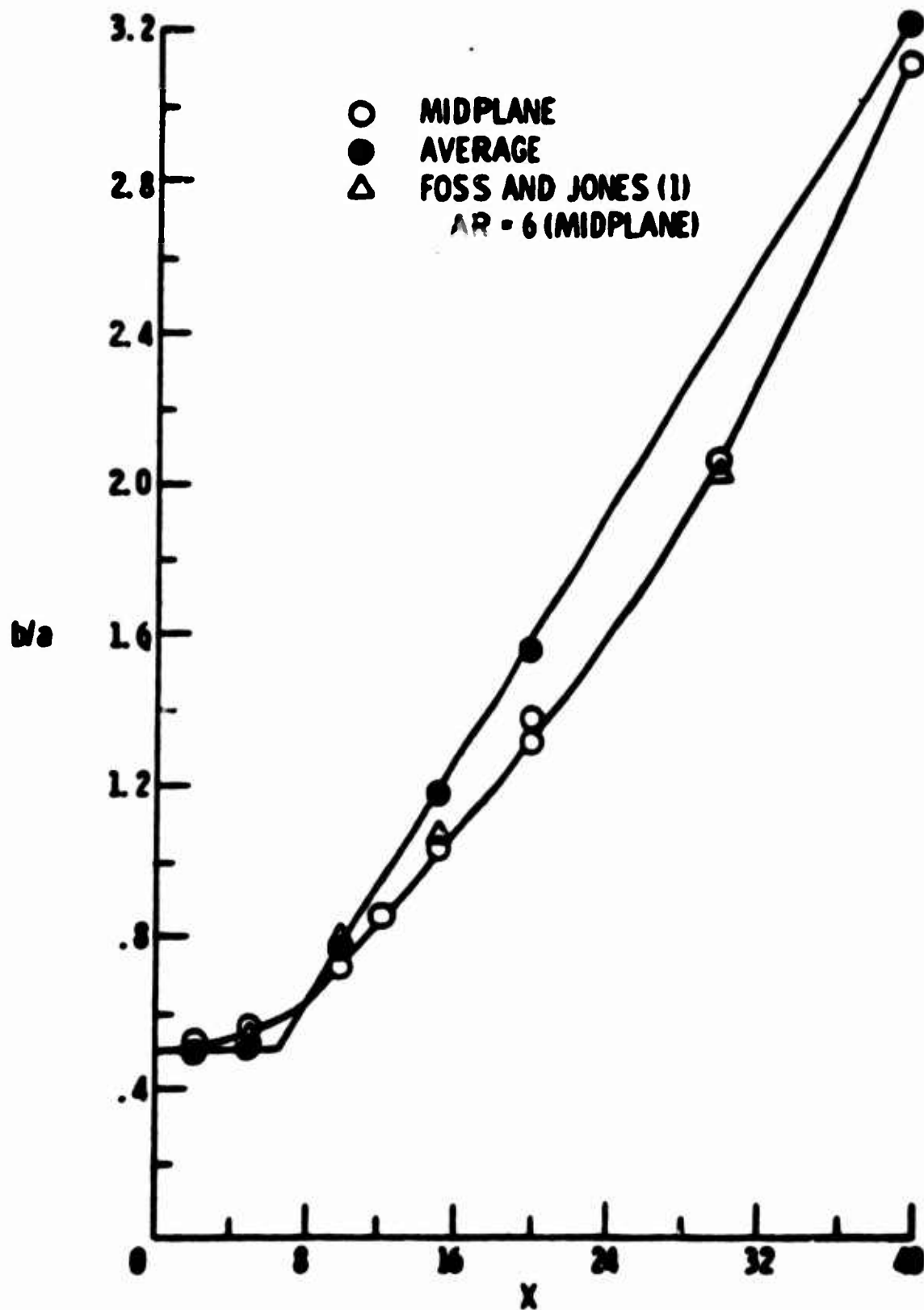


2. Jet Representation.

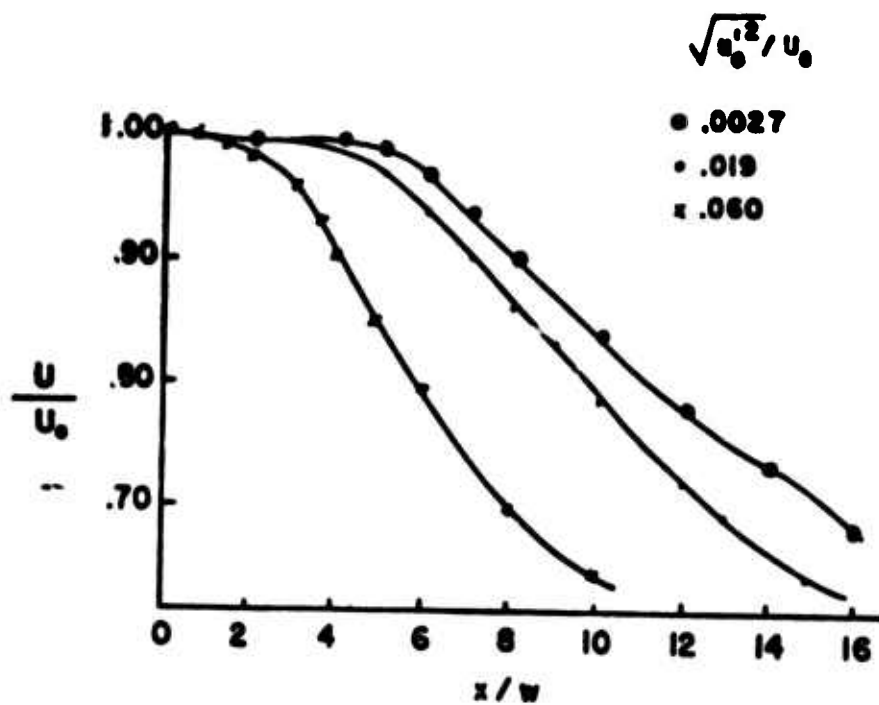




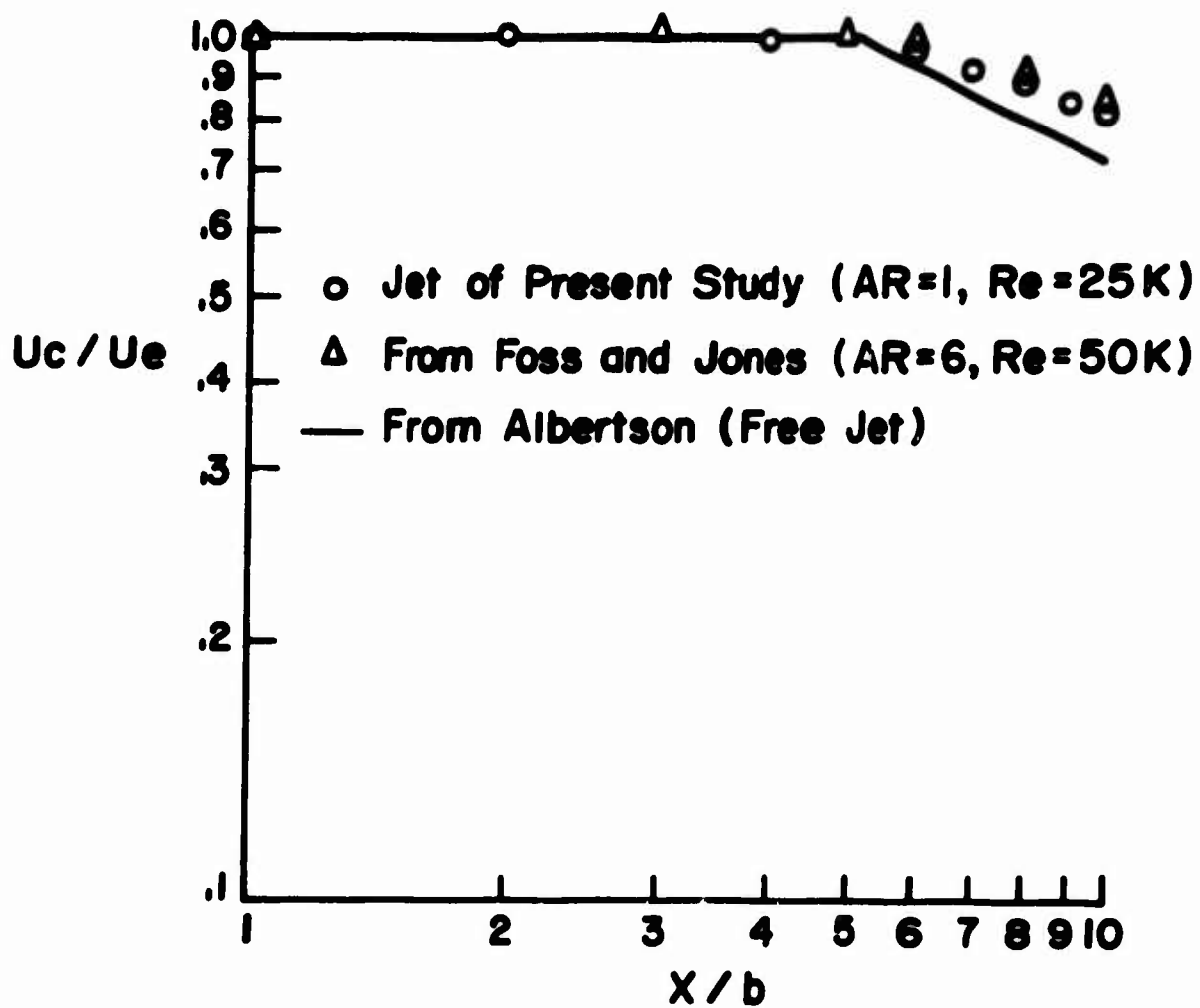
3. Velocity Distribution and Centerline Velocity Decay in a Bounded Jet [9]. (Aspect Ratio G:1).



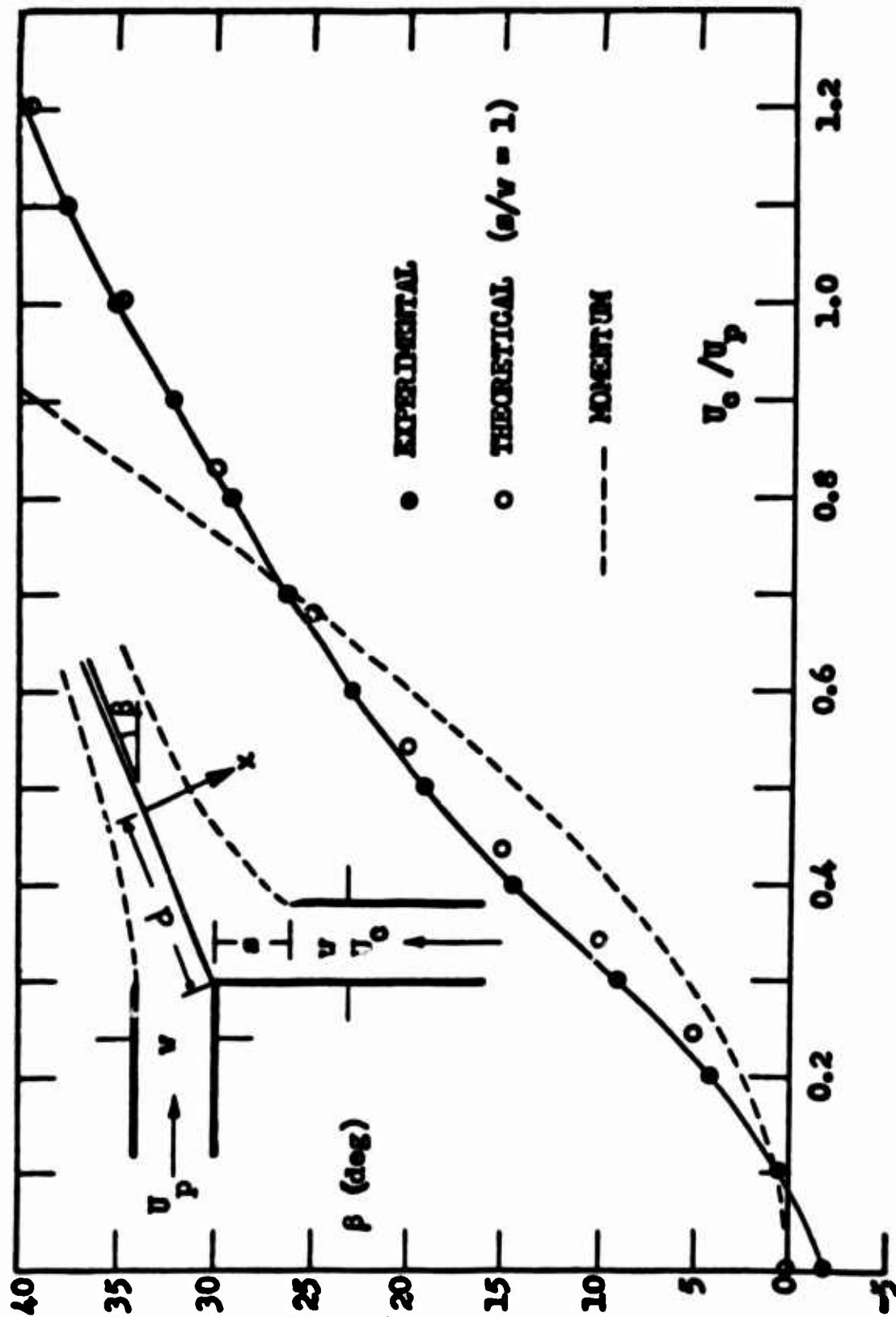
4. Midplane and Average Momentum Flux Thickness versus Downstream Distance, Aspect Ratio 4:1 [10].



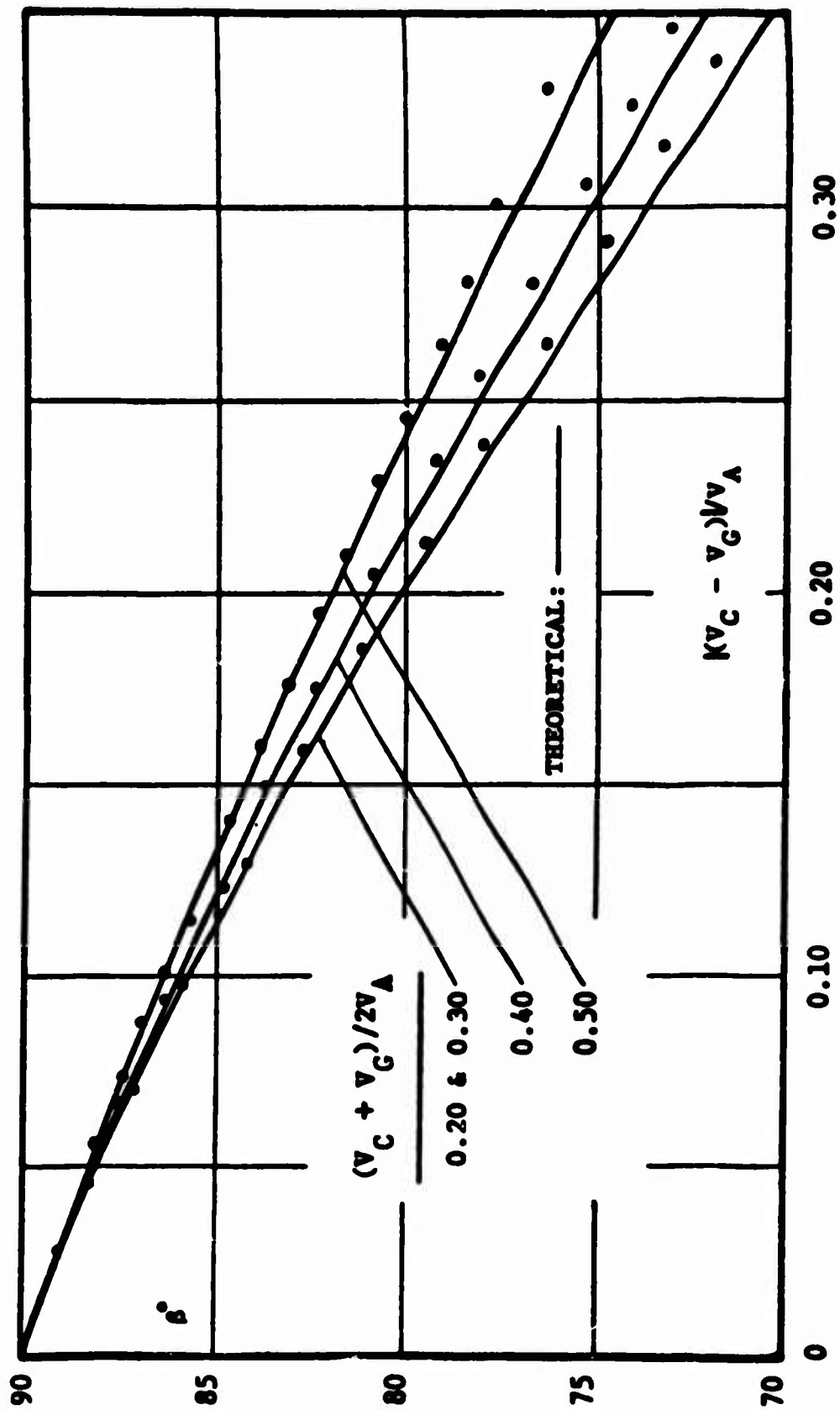
5. Effect of Nozzle Exit Turbulence on Centerline Velocity Decay from [11].



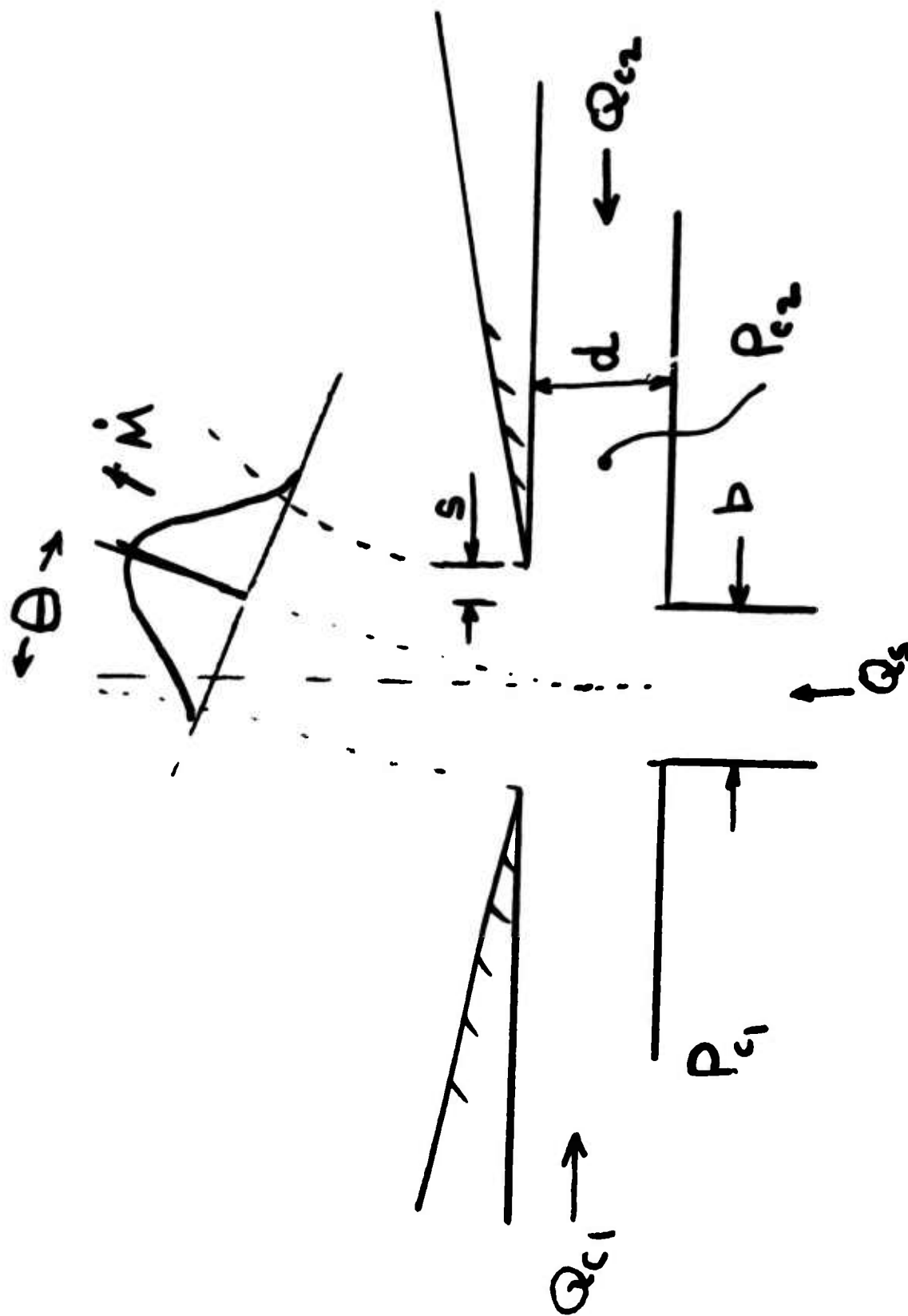
6. Centerline Velocity Decay in a 1:1 Aspect Ratio Turbulent Jet from [12].



7. (a) Deflection of Power Jet as a Function of  $U_c/U_p$ .  
Taken from [18].



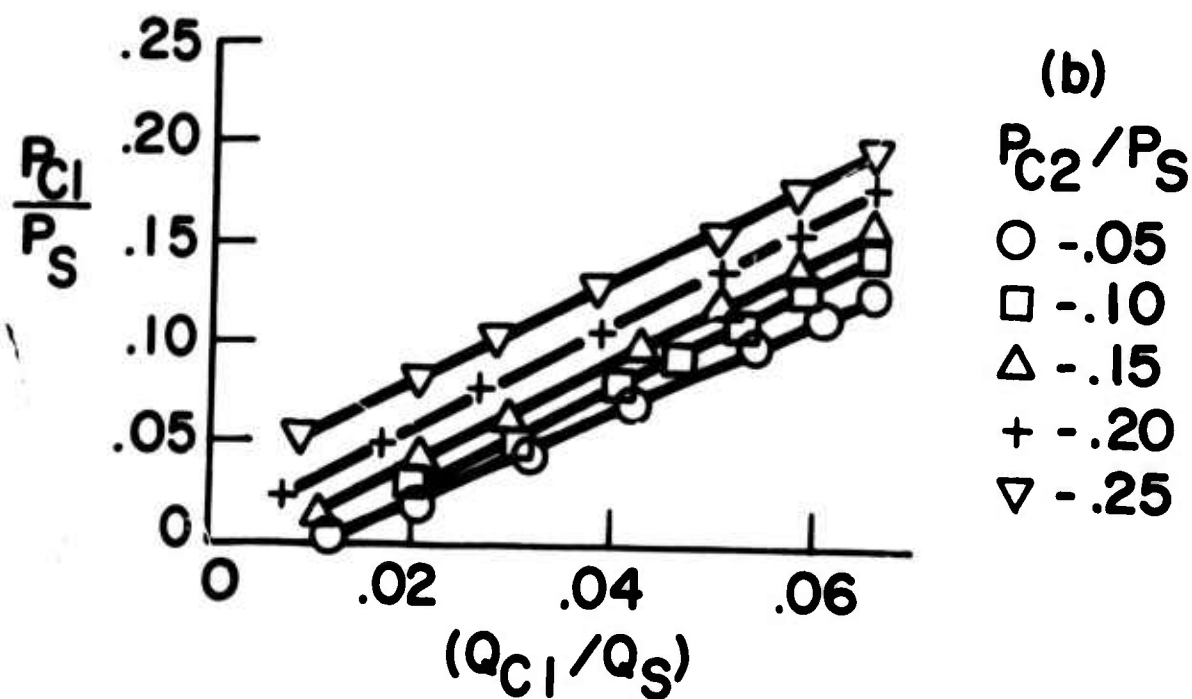
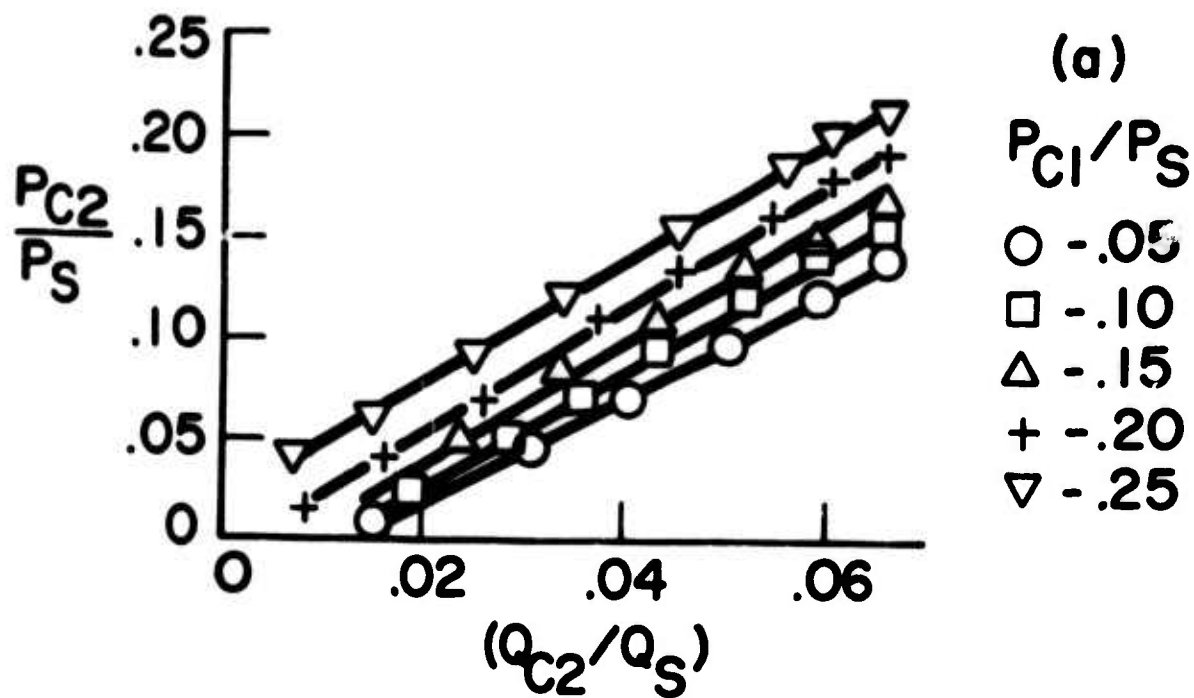
7. (b) Deflection in a two-sided Symmetrical Device [18].



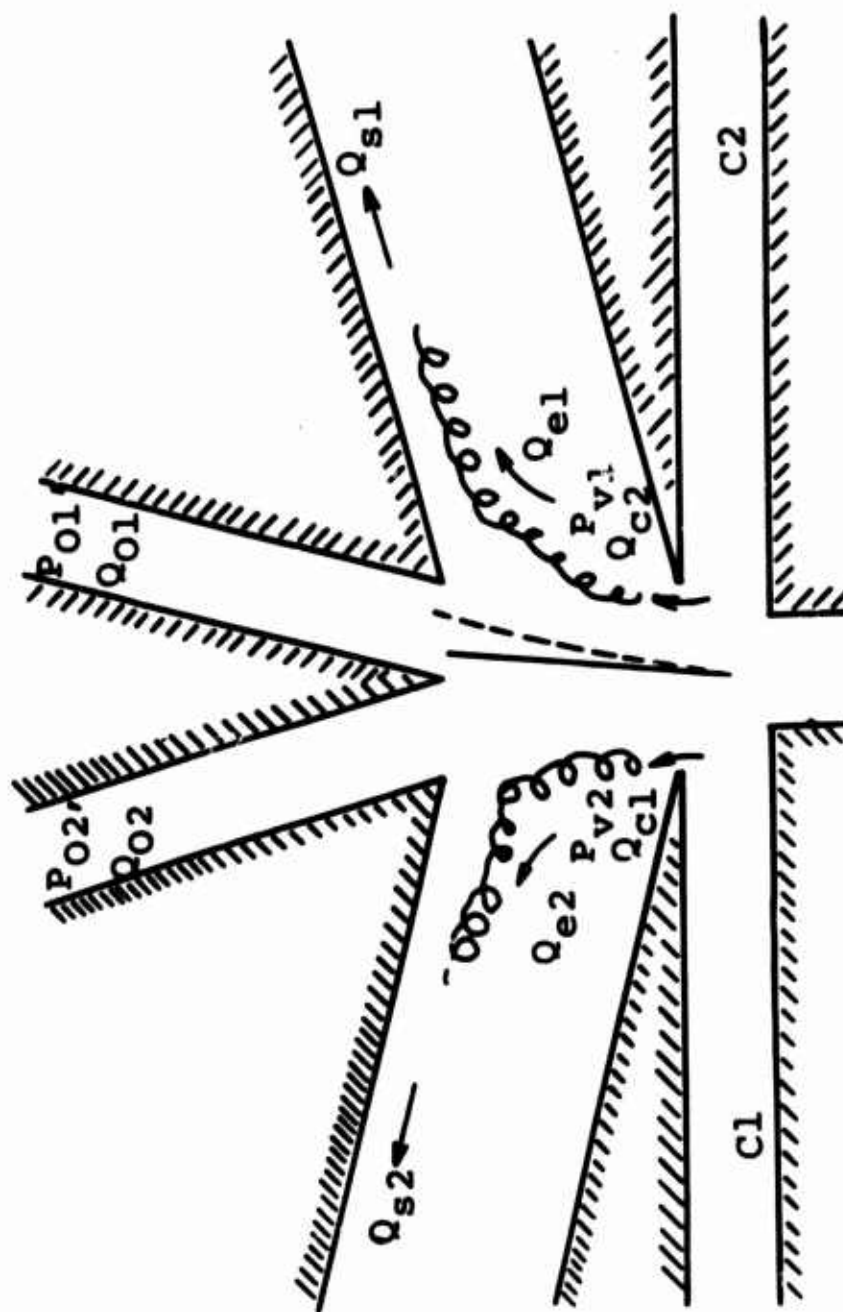
8. Diagram showing Control Interaction Region for a Dominantly Pressure Controlled Amplifier.





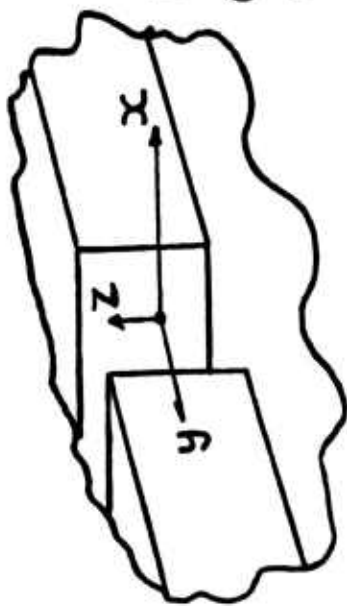


10. Control Pressure versus Control Flow for an Amplifier with  $s^* = 0.125$ ,  $d^* = 1.0$ , [21].

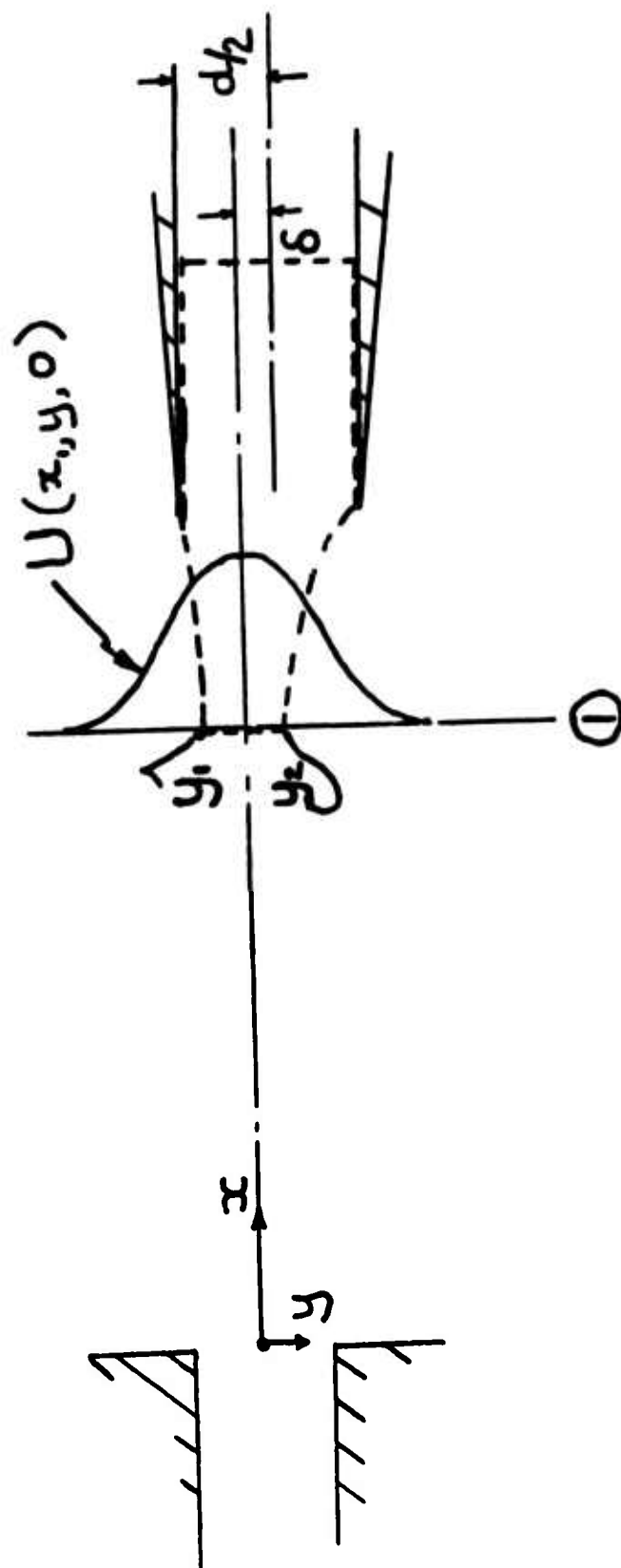


11. Schematic of Flow inside a Fluid Amplifier Showing interaction of Vent Flow with Power Jet Through Entrainment.





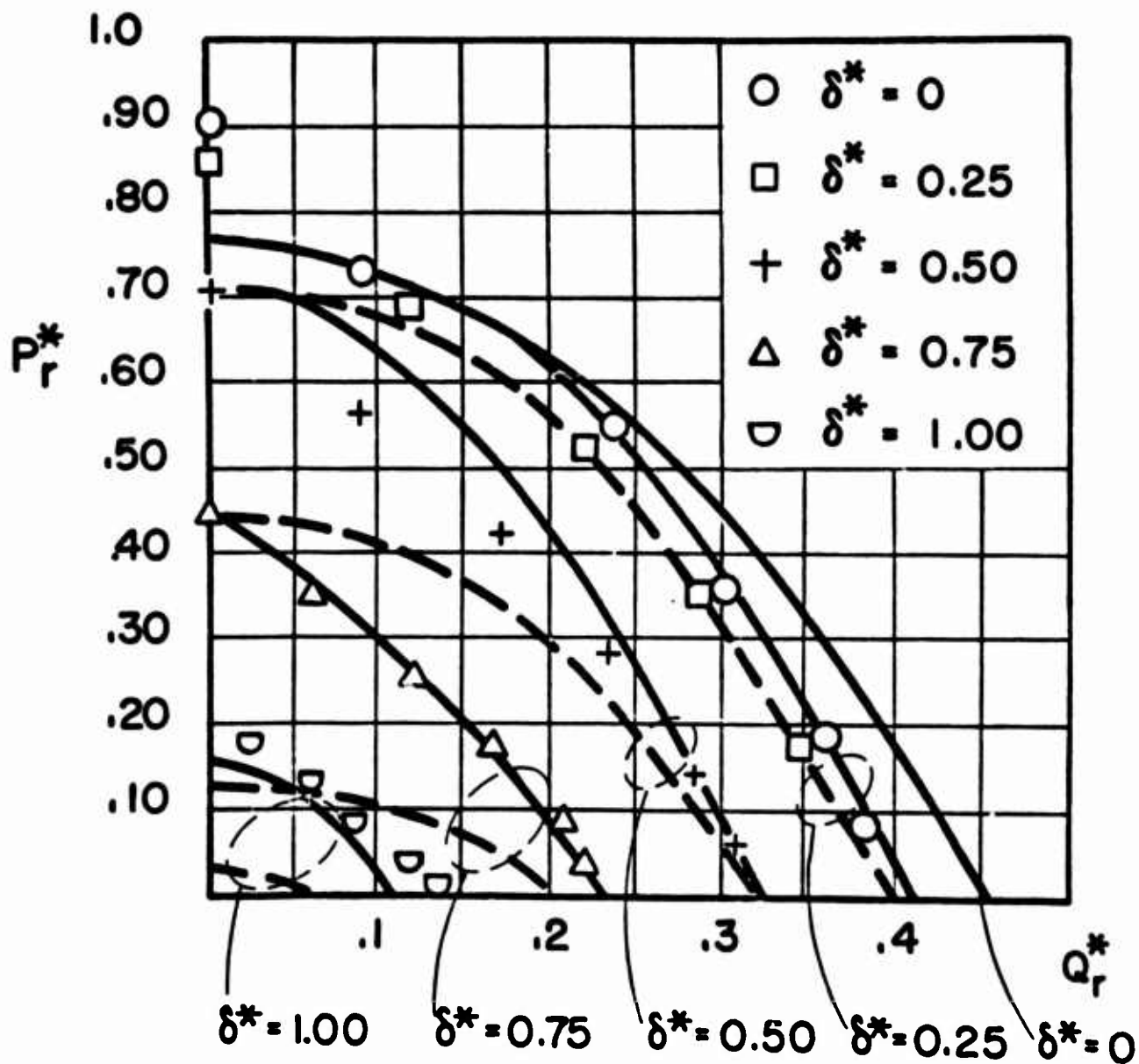
INSERT SHOWS  
COORDINATE SYSTEM  
USED



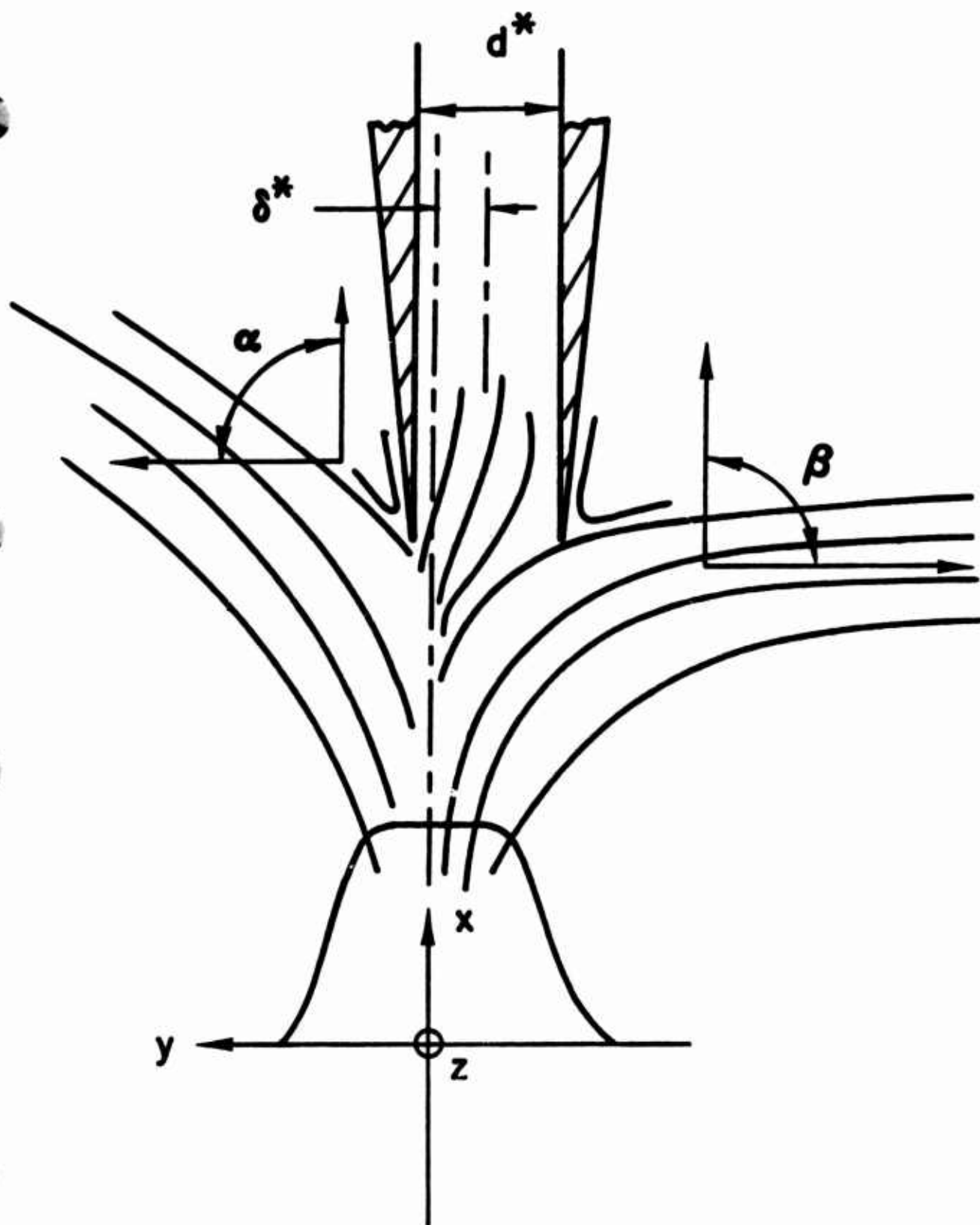
13. Schematic Diagram of Flow on a Single Receiver as in a Fluidic Rectifier from [27].

—— HIGH ENERGY MODEL  
 --- CENTERED STREAMLINE MODEL

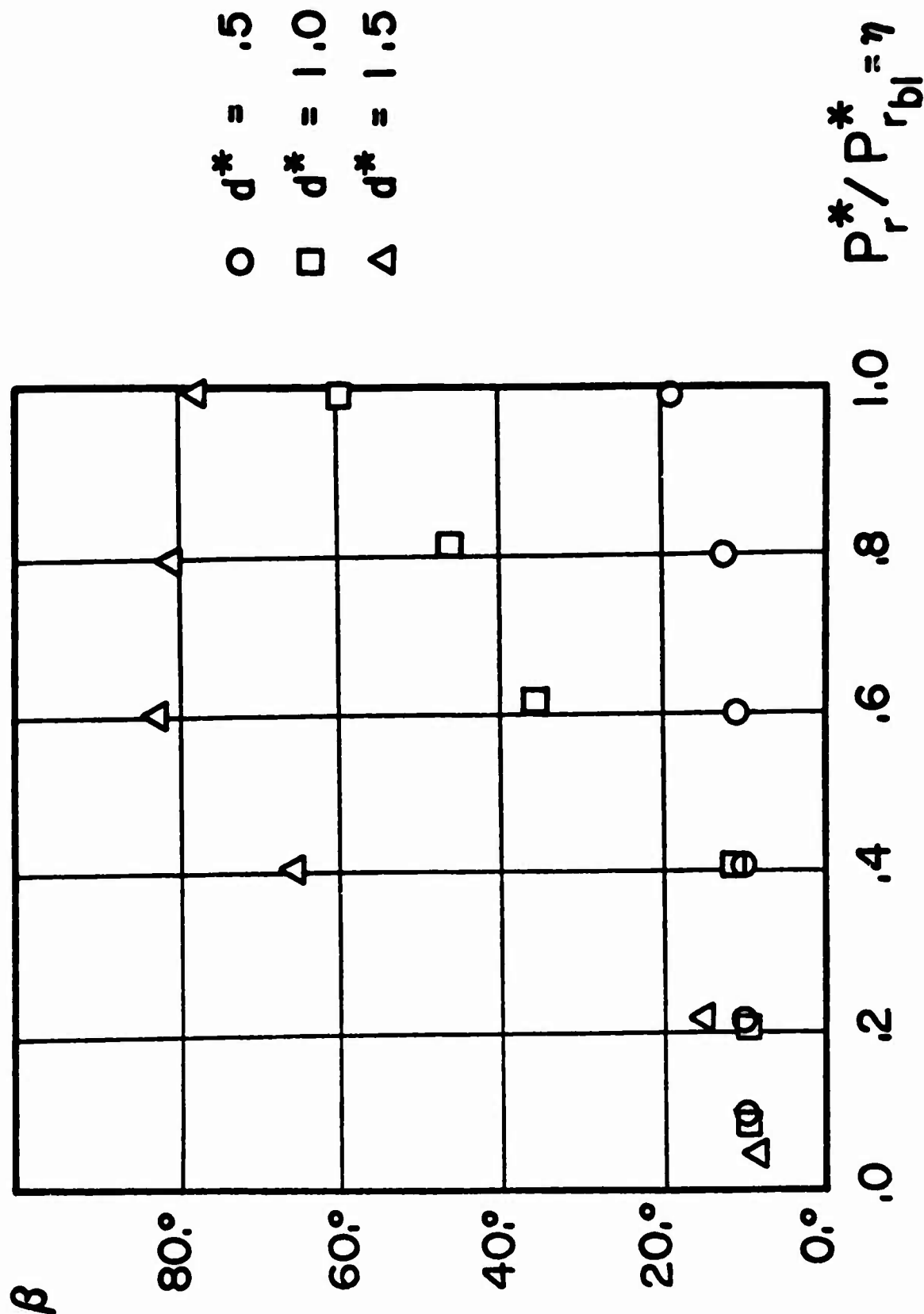
$$d^* = 0.5$$



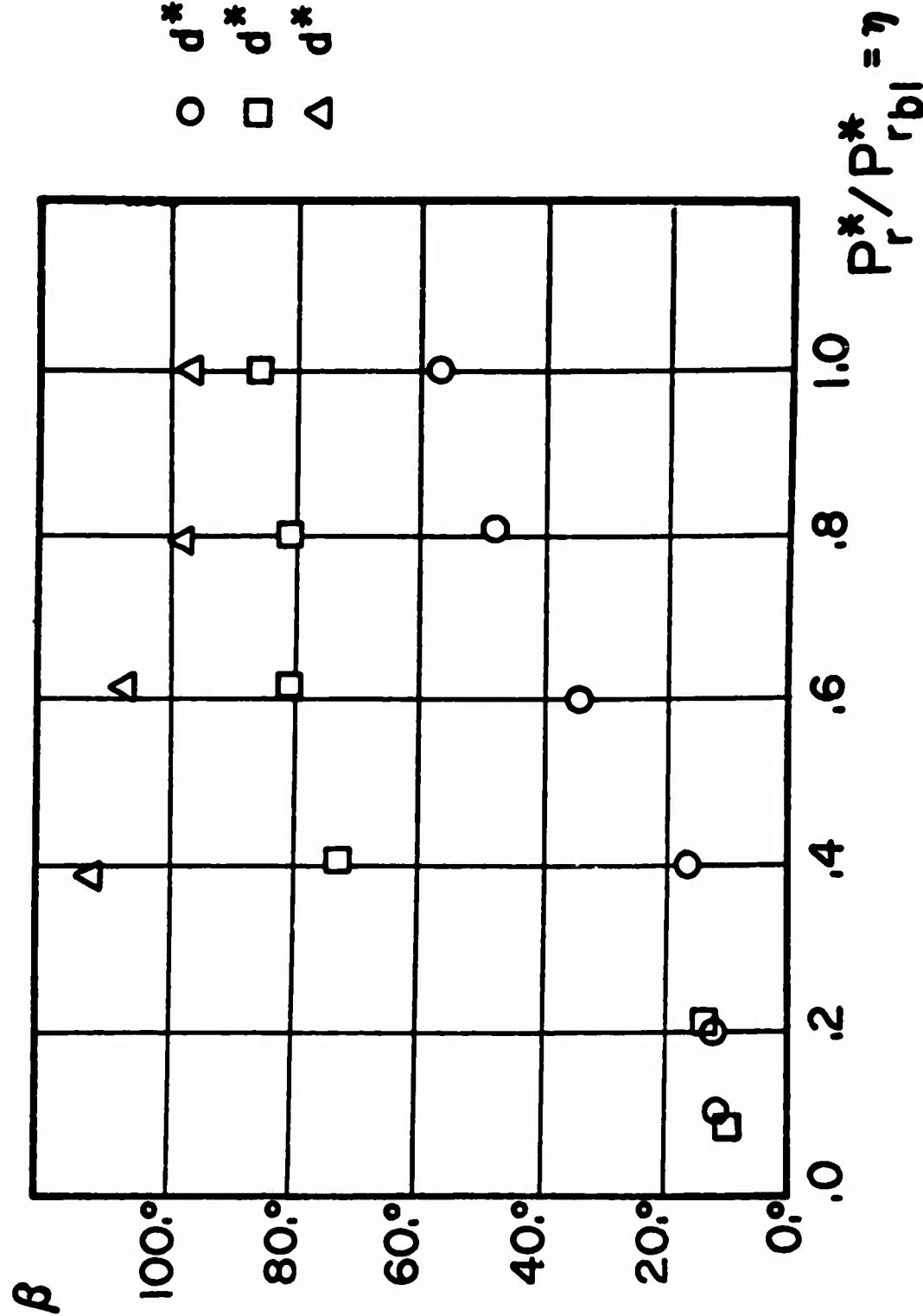
14. Output Characteristics of a 0.5 Nozzle Width Receiver, 6 Nozzle Widths Downstream from the Nozzle Exit.



15. Flow Pattern Showing Spillover Jets for a Single Fluid Amplifier Receiver [28].

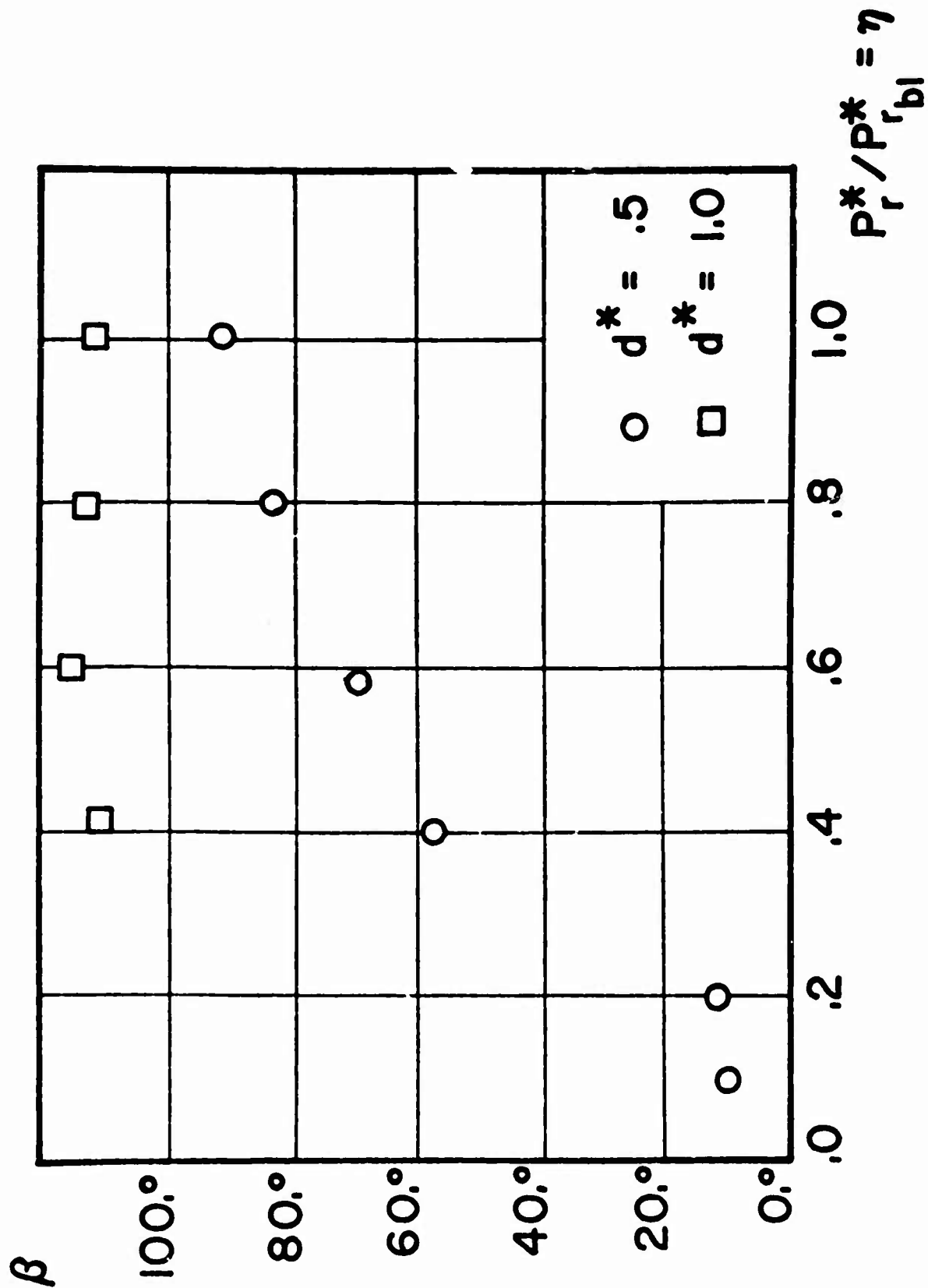


16. Plots of angle  $\beta$  as a function of Receiver Loading for various Receiver Widths and Jet Deflections [28]  
 (a)  $\delta^* = 0.25$

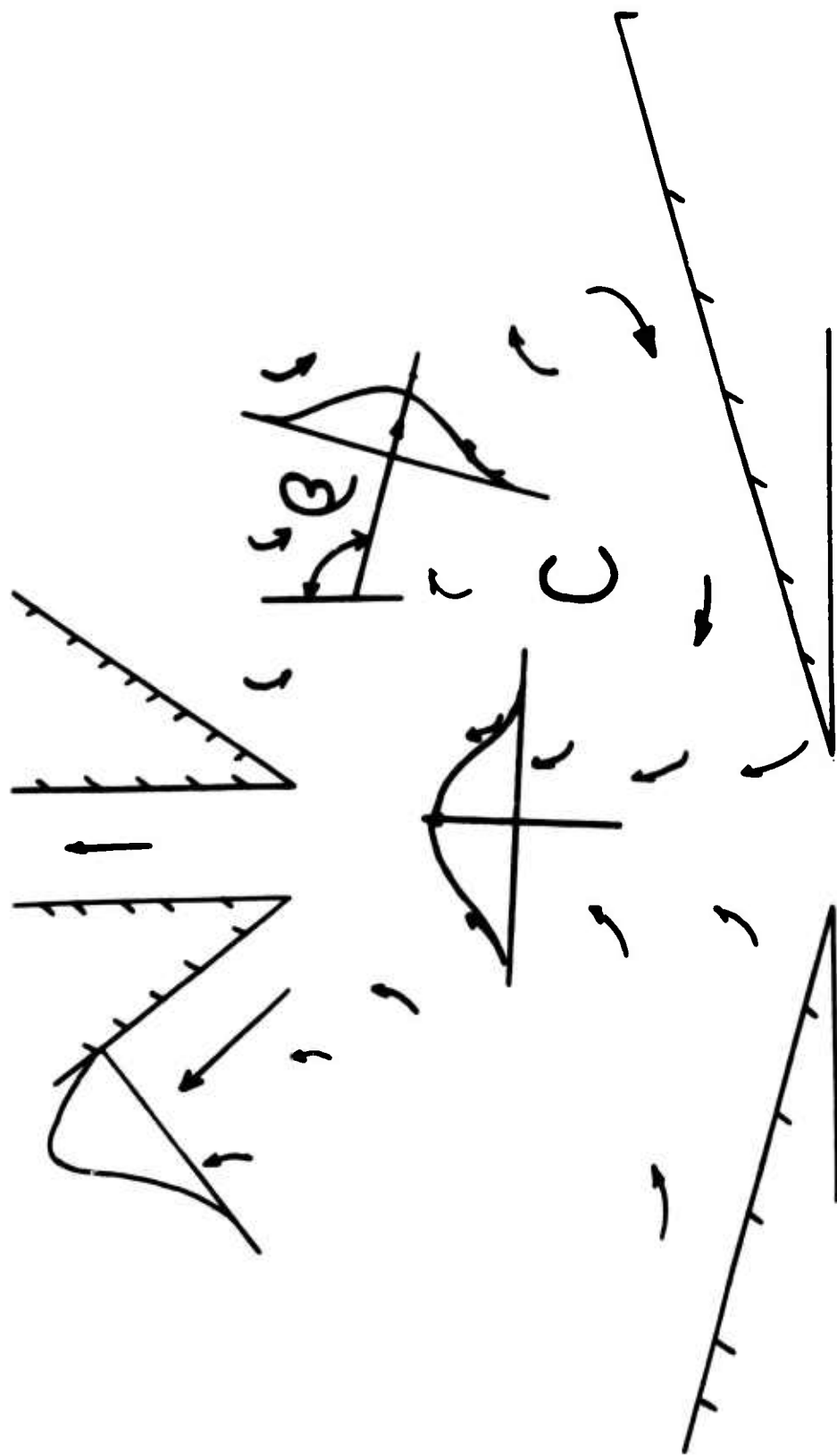


16. Plots of angle  $\beta$  as a function of Receiver Loading for various Receiver Widths and Jet Deflections [28]  
(b)  $\delta^* = 0.50$

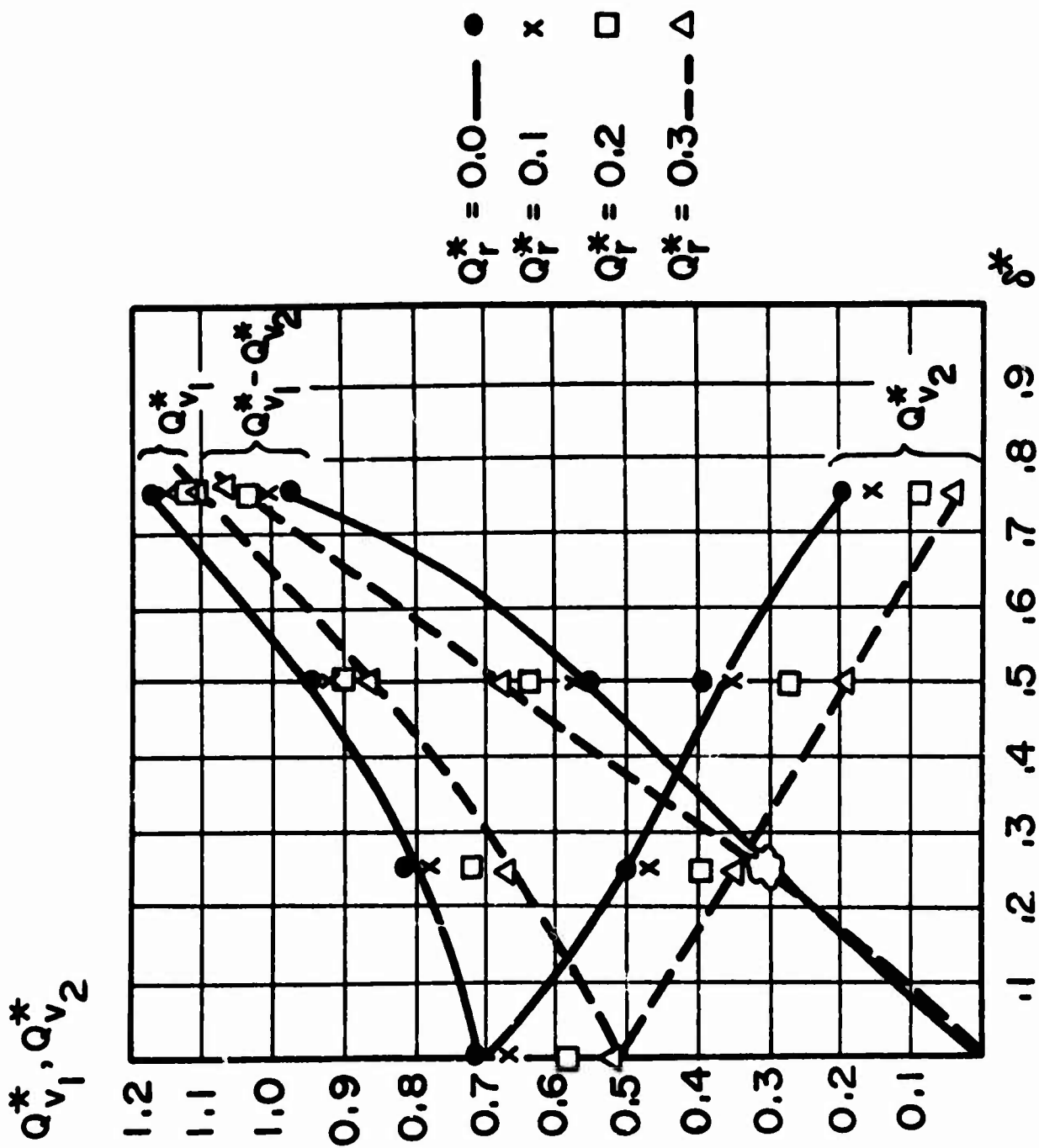




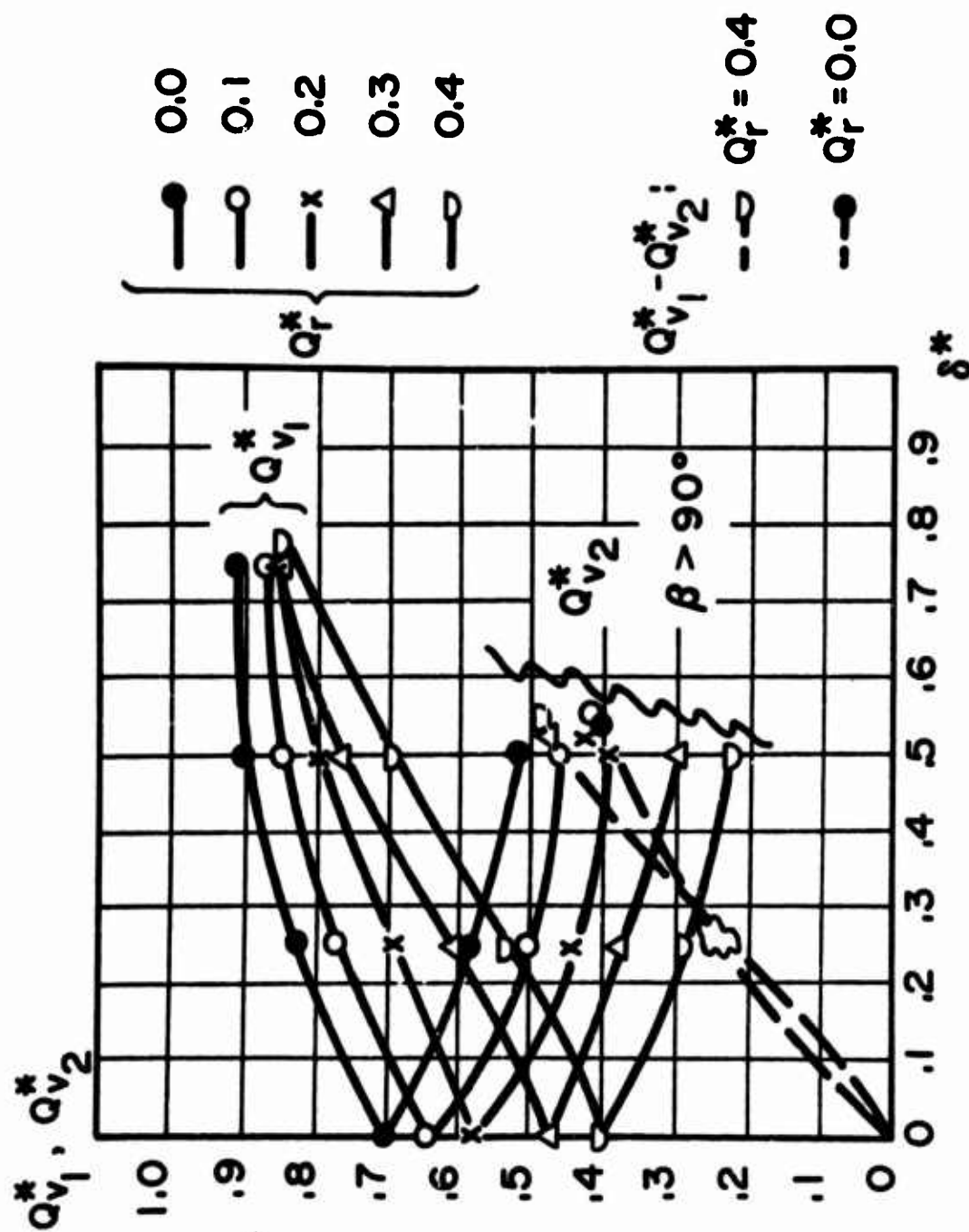
16. Plots of angle  $\beta$  as a function of Receiver Loading for various Receiver Widths and Jet Deflections [28]  
 (c)  $\delta^* = 0.75$ .



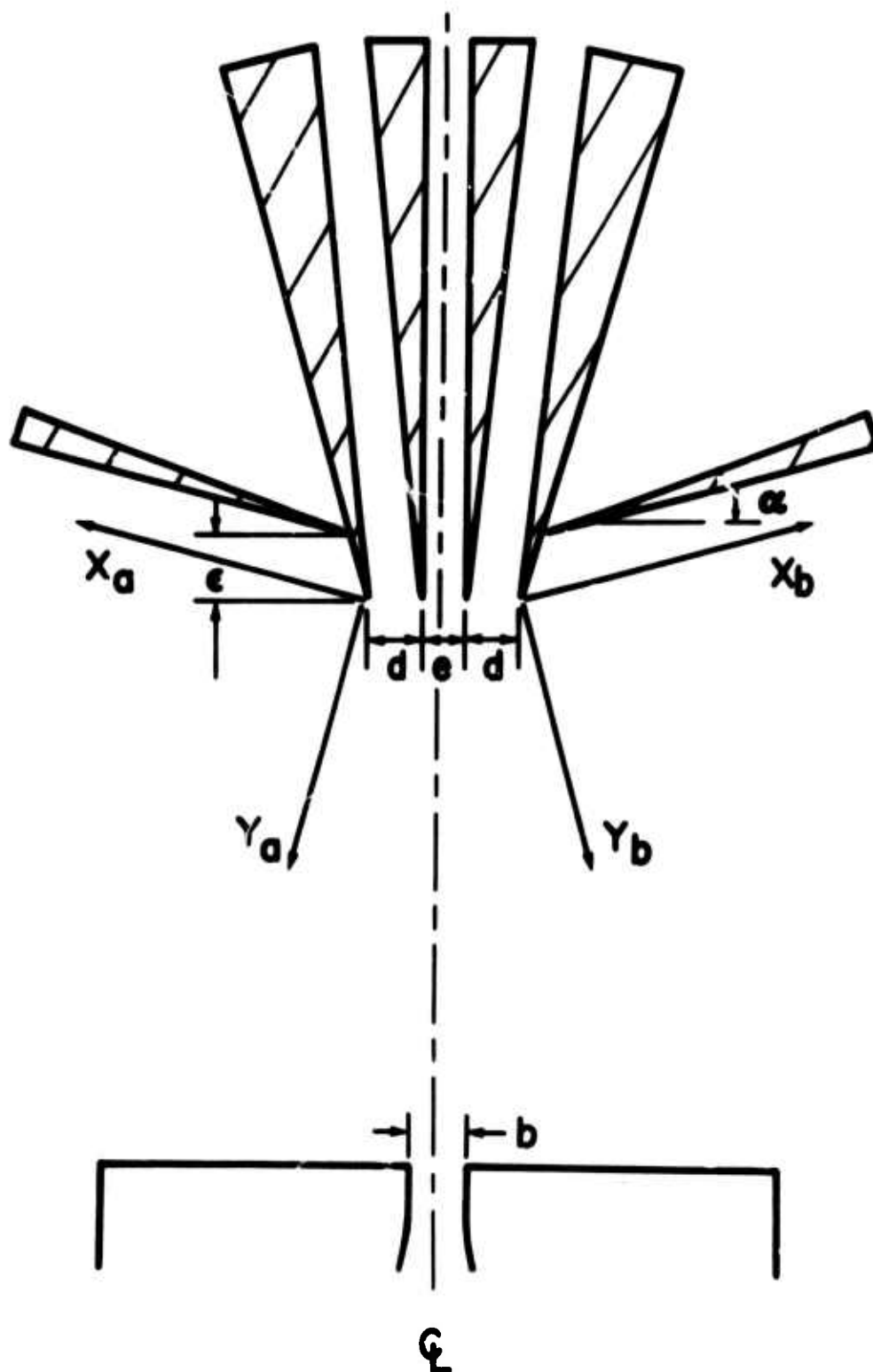
17. Interaction of Spillover Jets with Power Jet with Unstable Jet Vent System.



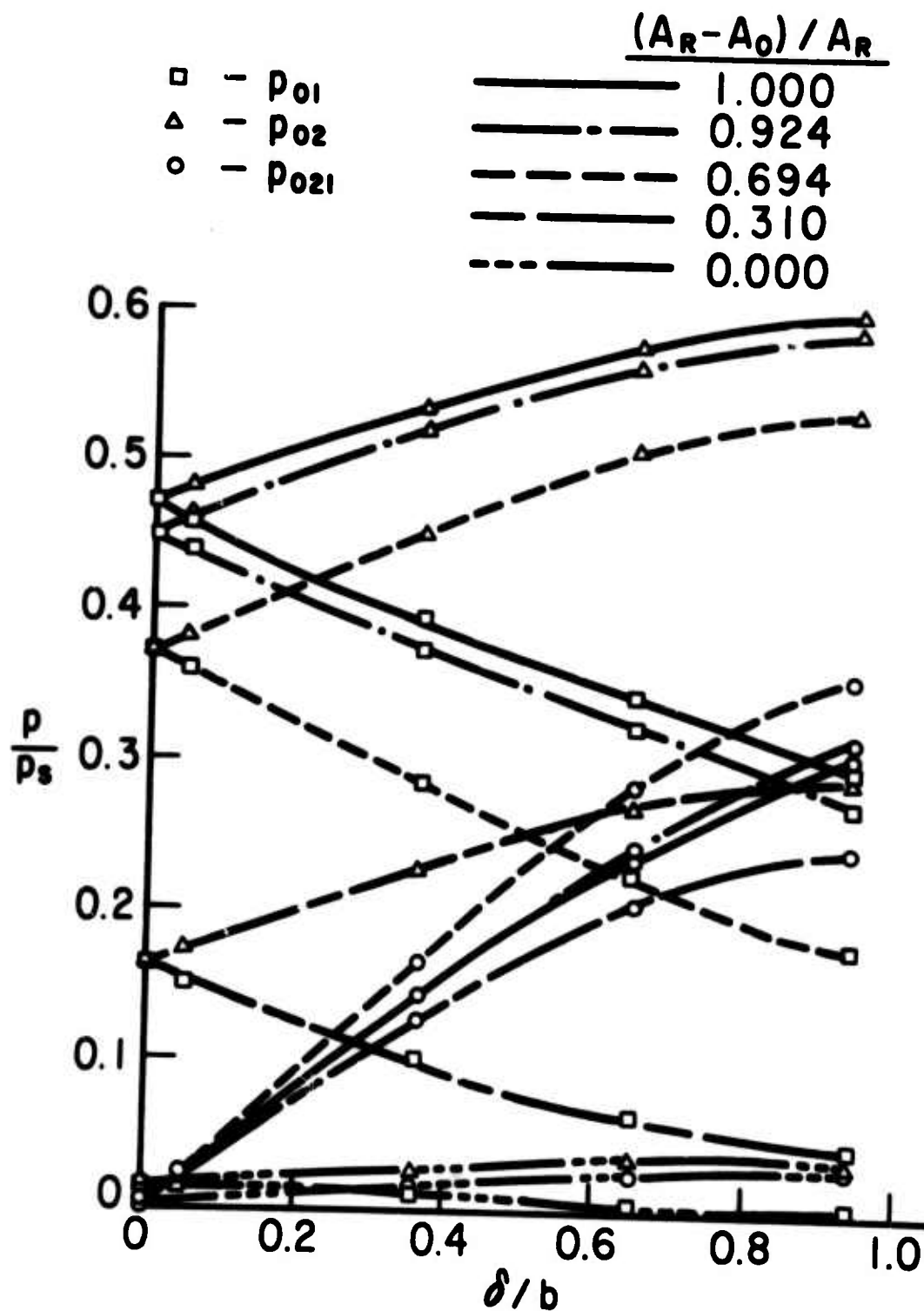
18. (a) Differential Spillover Flow Characteristics.



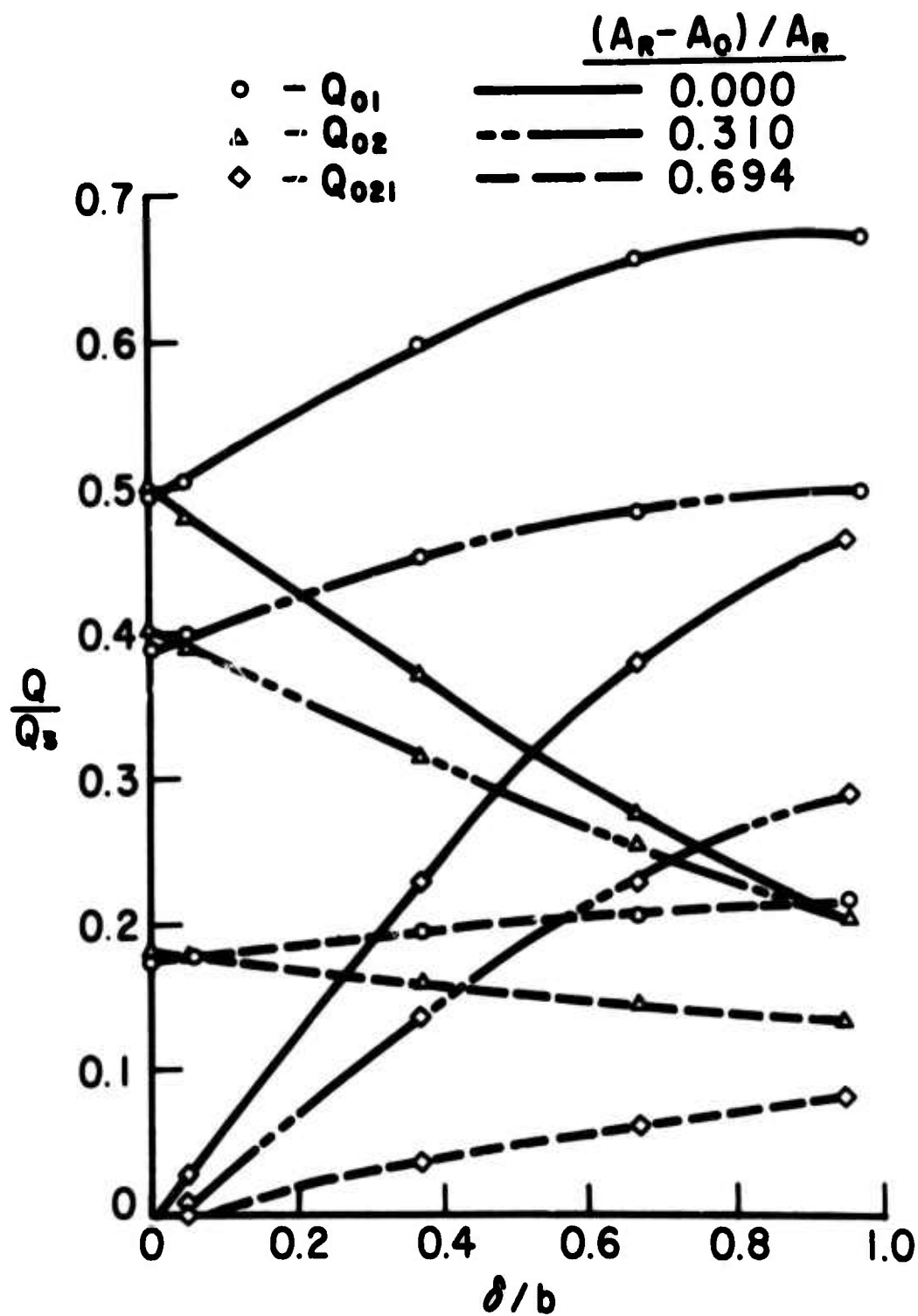
18. (b) Differential Spillover Flow Characteristics.



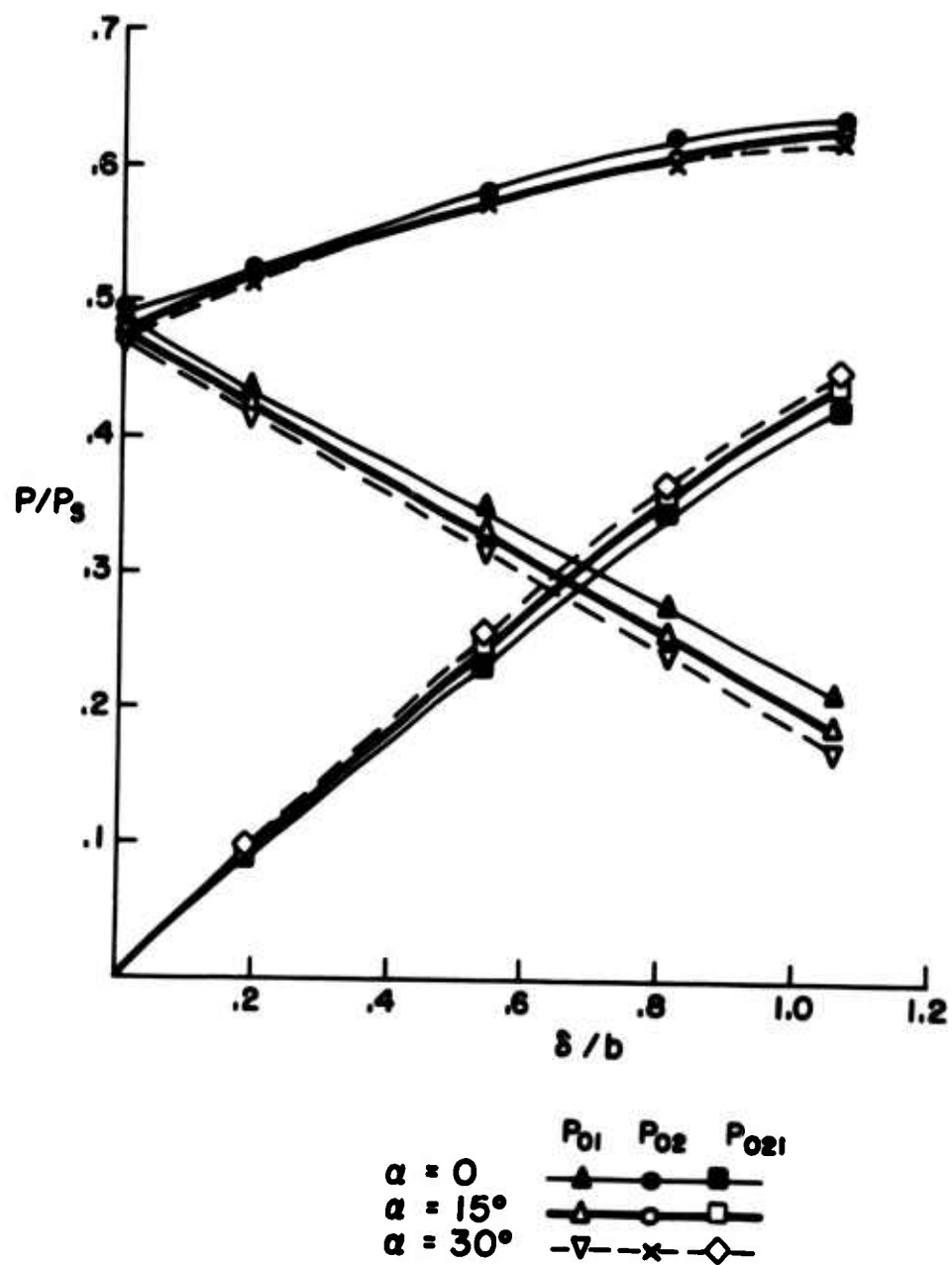
19. Multiple Receiver System with Center Dump [12].



20. Pressure Recovery versus Jet Deflection for the System in Figure 19 with  $d^*=1.0$ ,  $e^*=0.75$ ,  $\epsilon^*=0$ ,  $\alpha=15^\circ$ .

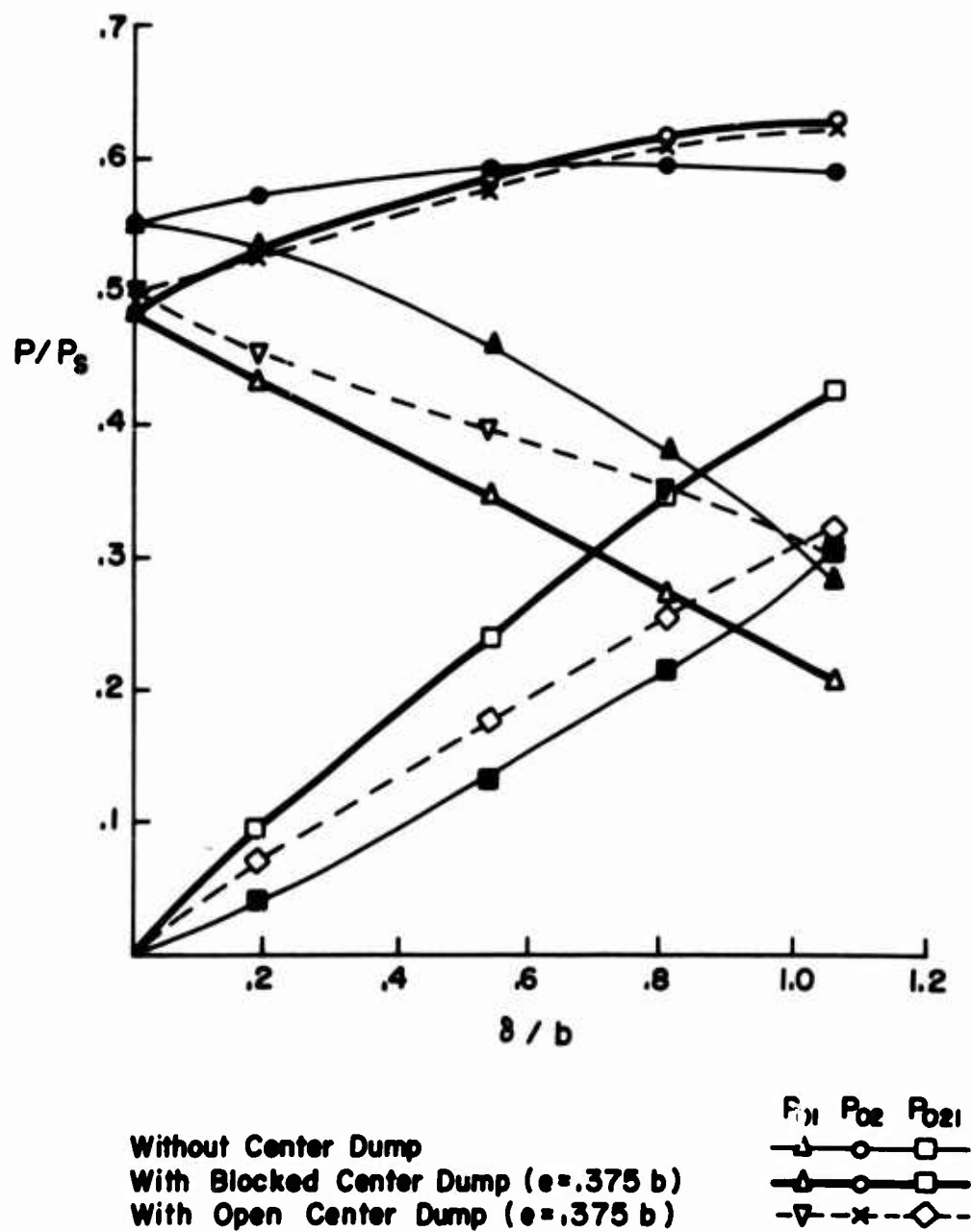


21 Flow Recovery versus Jet Deflection for the Same Configuration as in Figure 20.

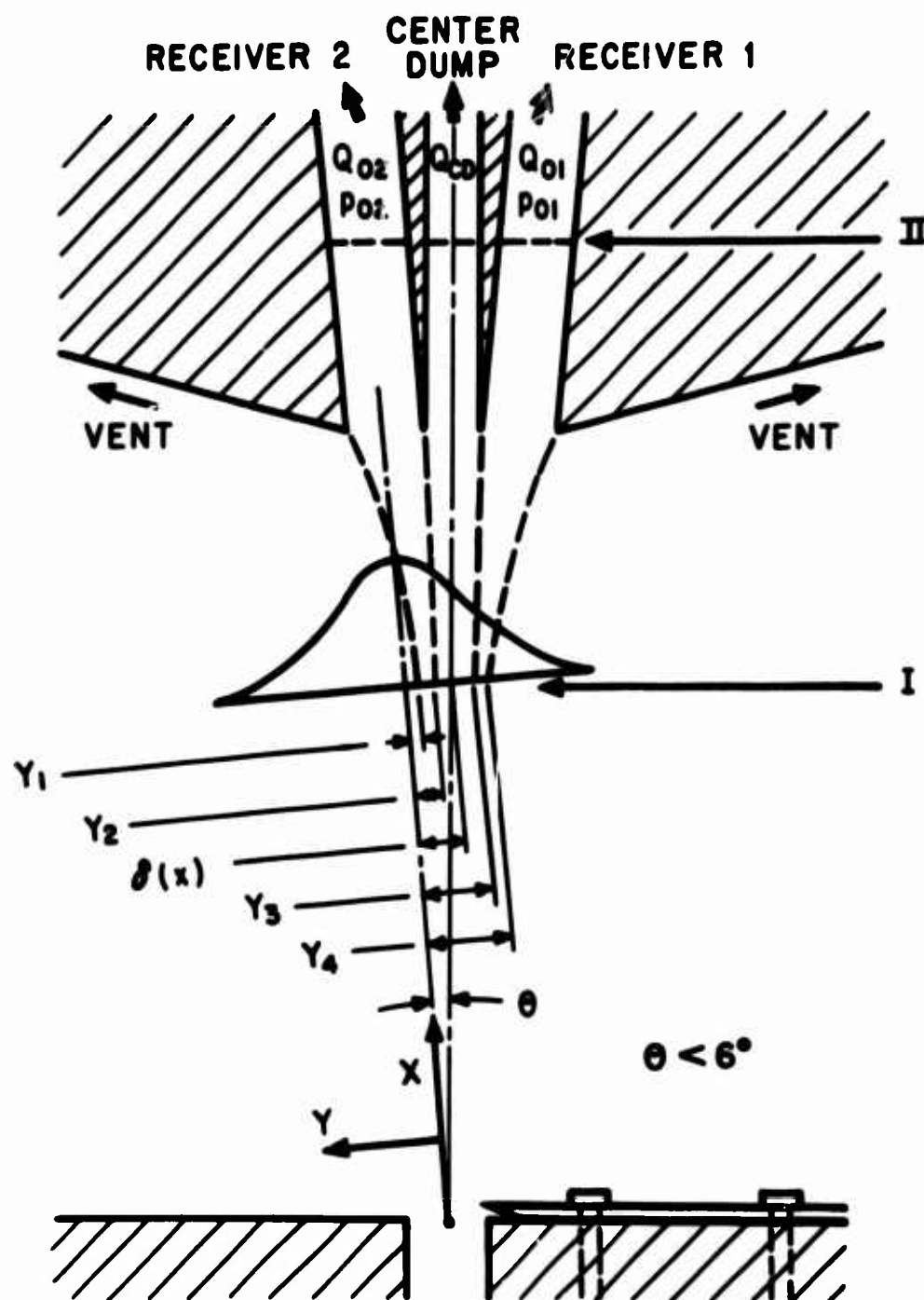


22. Effect of  $\alpha$  on Blocked Load Pressure Recovery with Blocked Center Dump and  $\epsilon^* = 0$ ;  $e^* = 0.75$ ;  $d^* = 1.0$ .

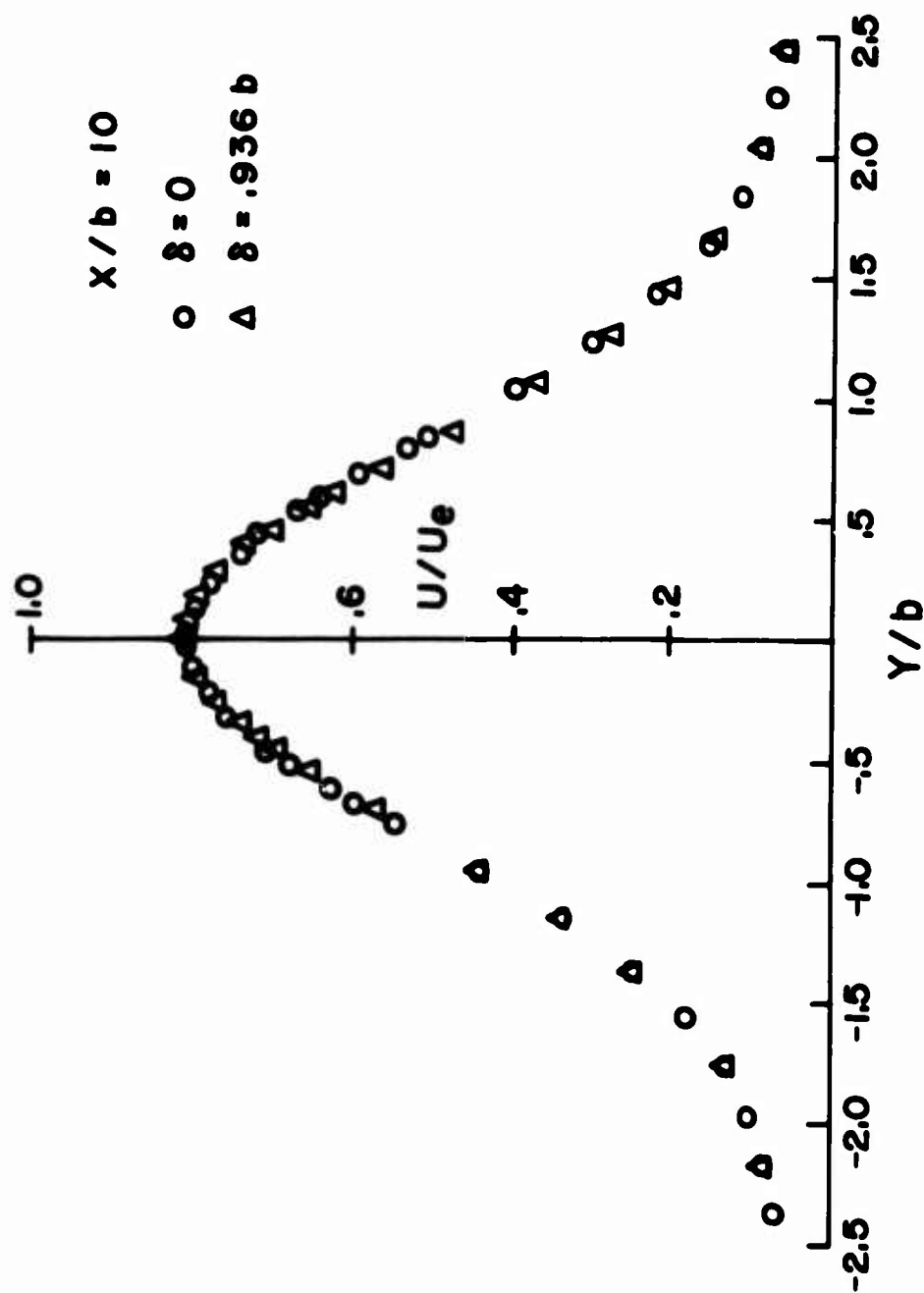




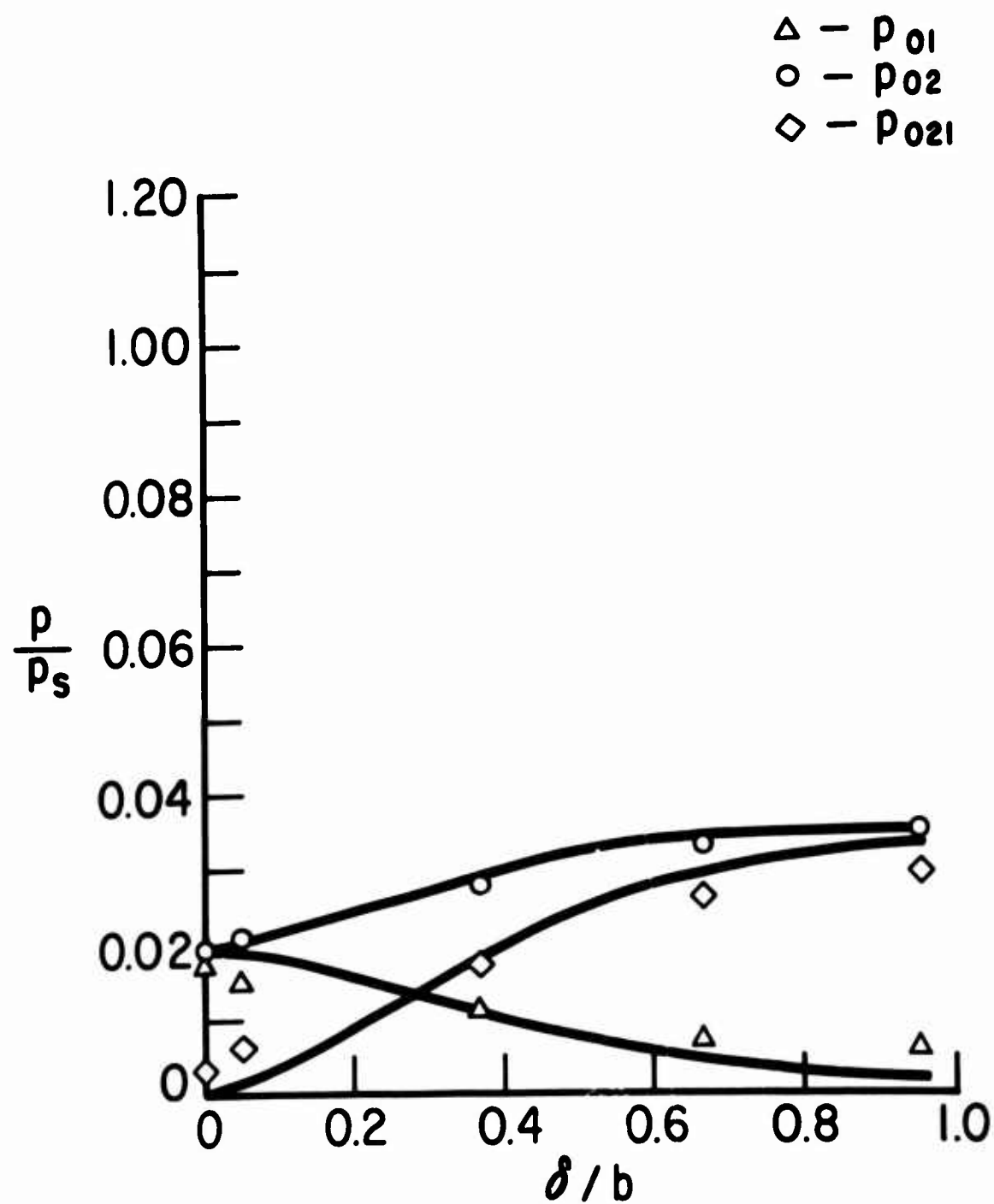
23. Effect of Center Dump on Blocked Load Pressure Recovery.



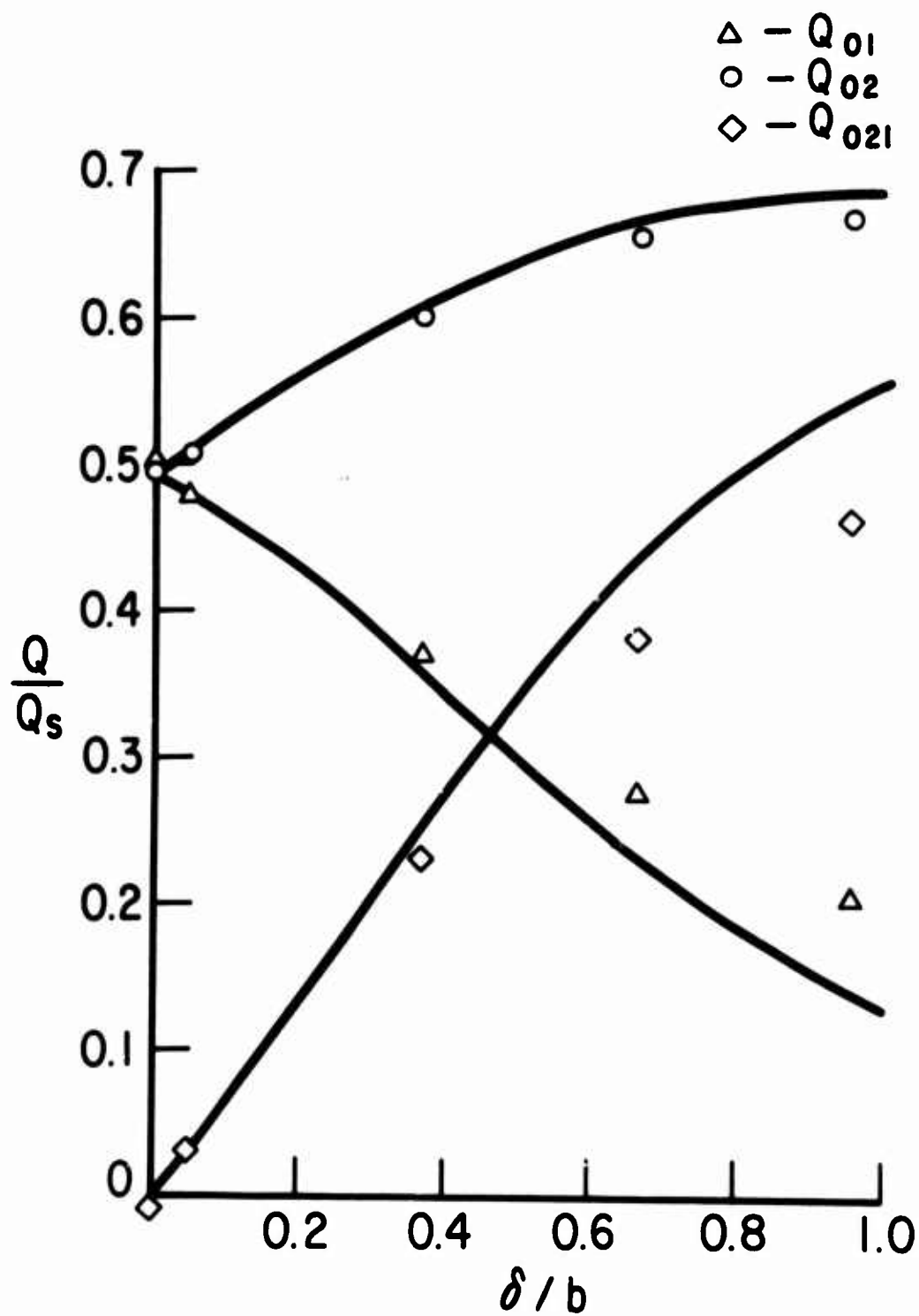
24. Illustration of Dividing Streamlines in the Calculation of Signal Recovery in Multiple Receiver Systems.



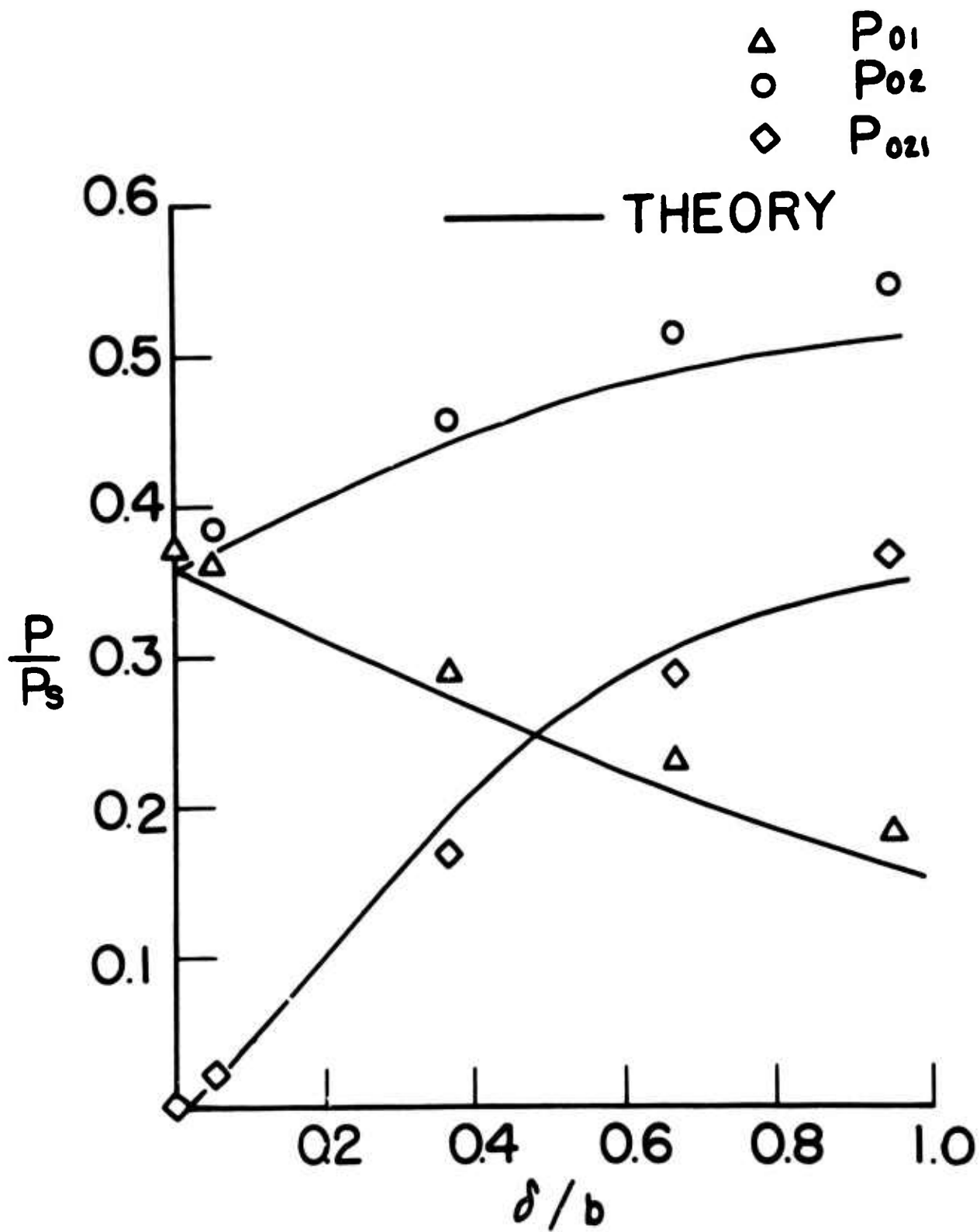
25. Comparison of Deflected and Undeflected Jet Profiles at plane of Receivers.



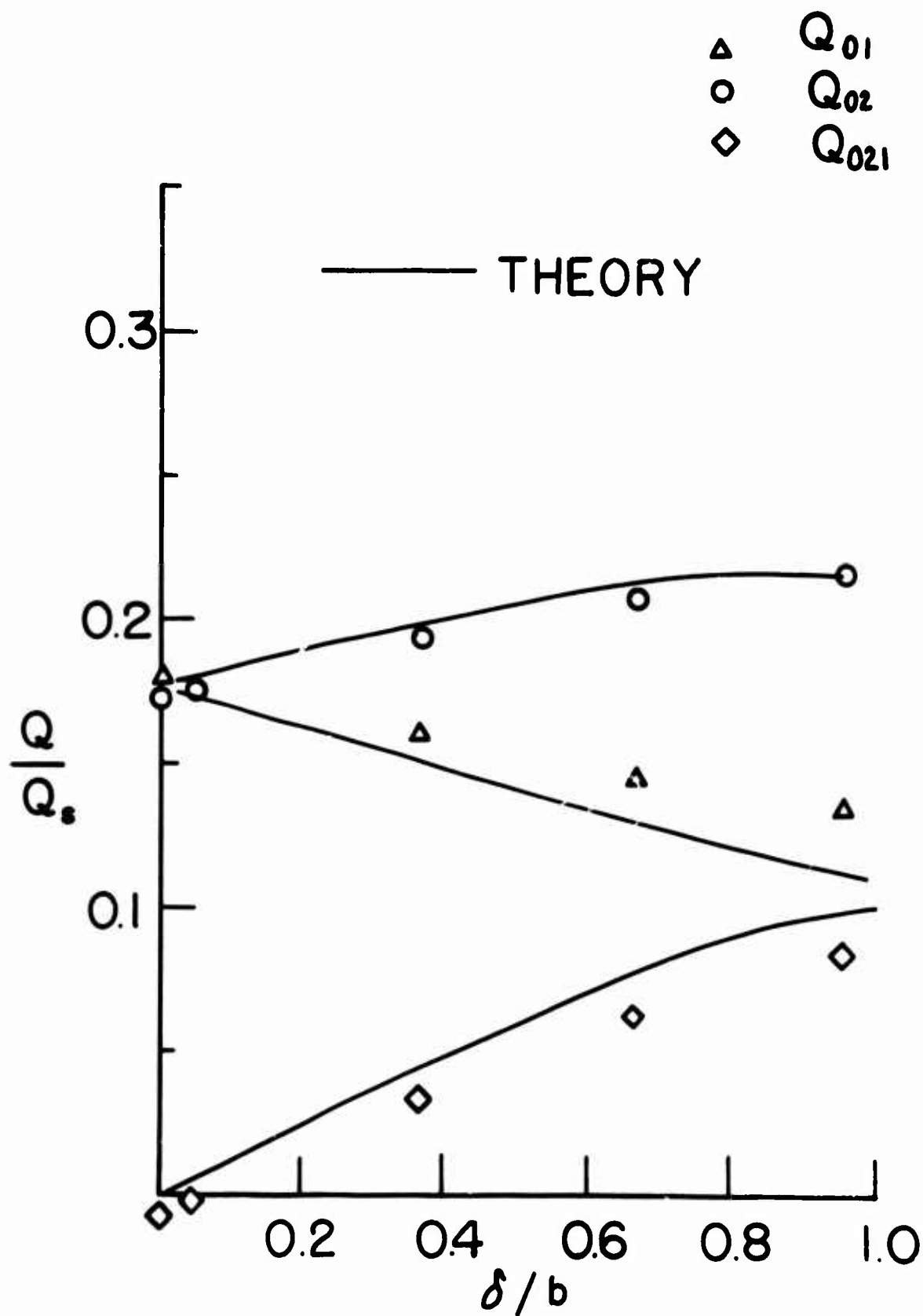
26. (a) Pressure and Flow Recovered versus Deflection. Open Receivers.



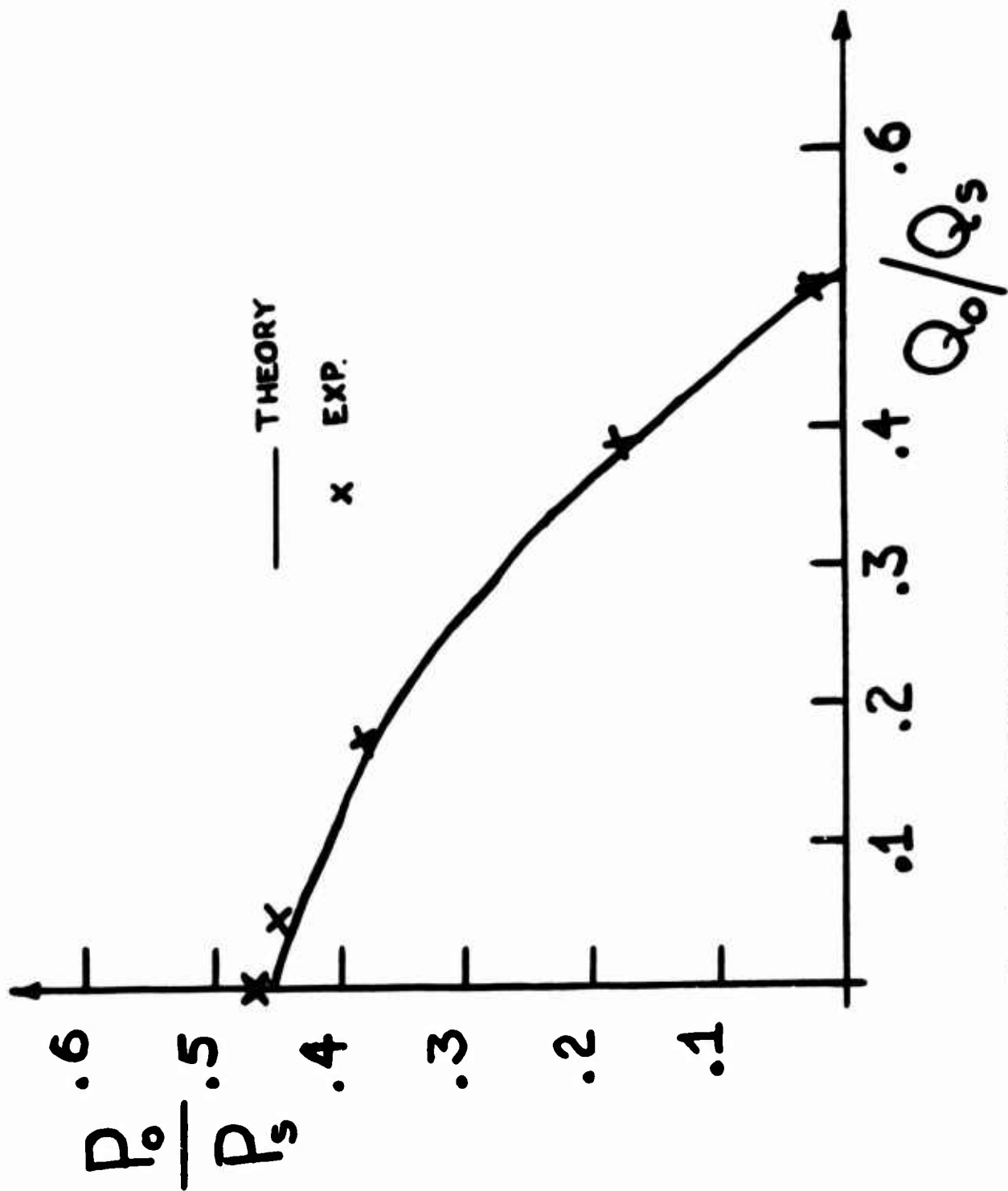
26. (b) Pressure and Flow Recovered versus Deflection. Open Receivers.



27. (a) Pressure and Flow Recovered versus Deflection. 69% Blocked.

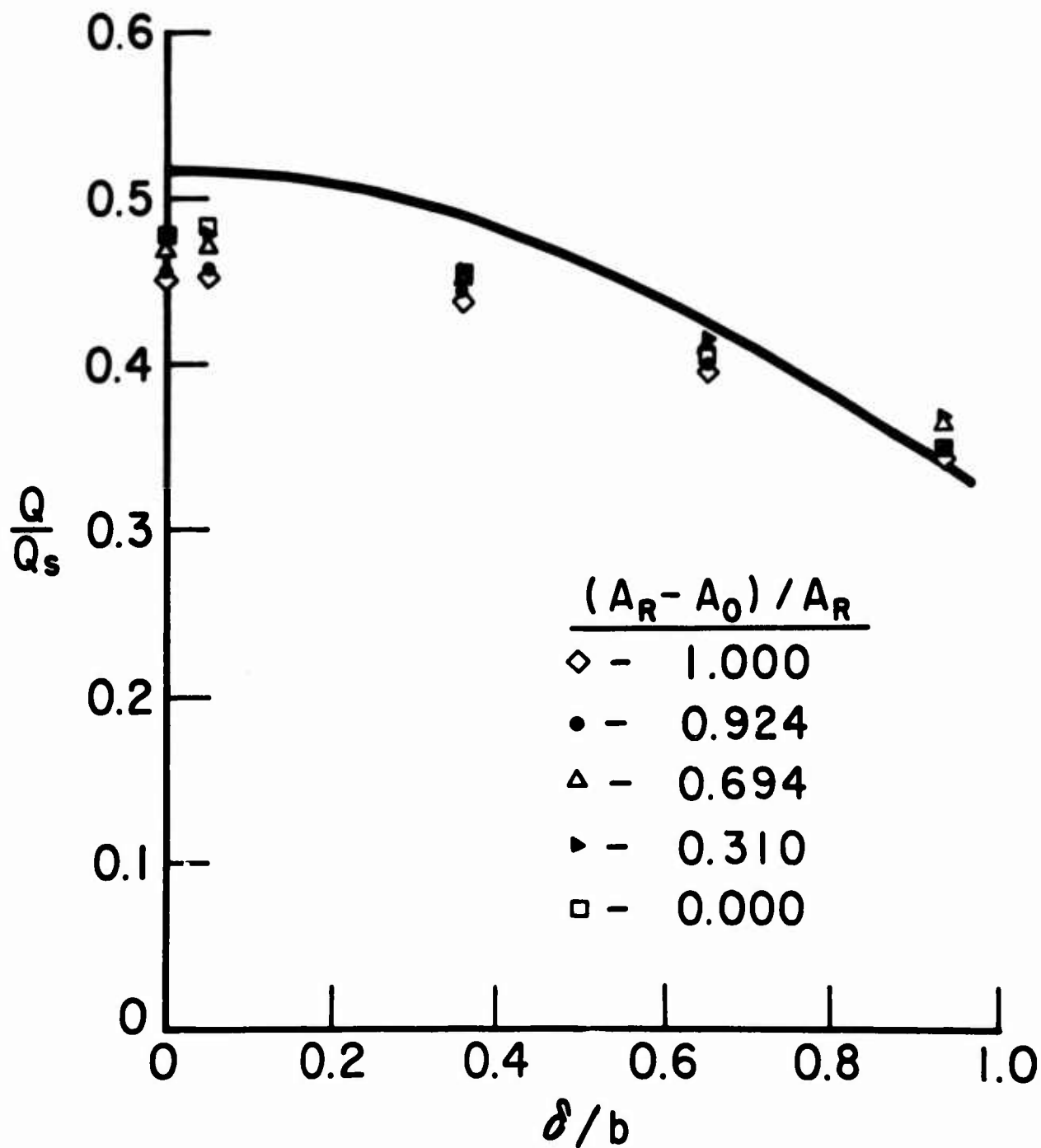


27. (b) Pressure and Flow Recovered versus Deflection. 69% Blocked.

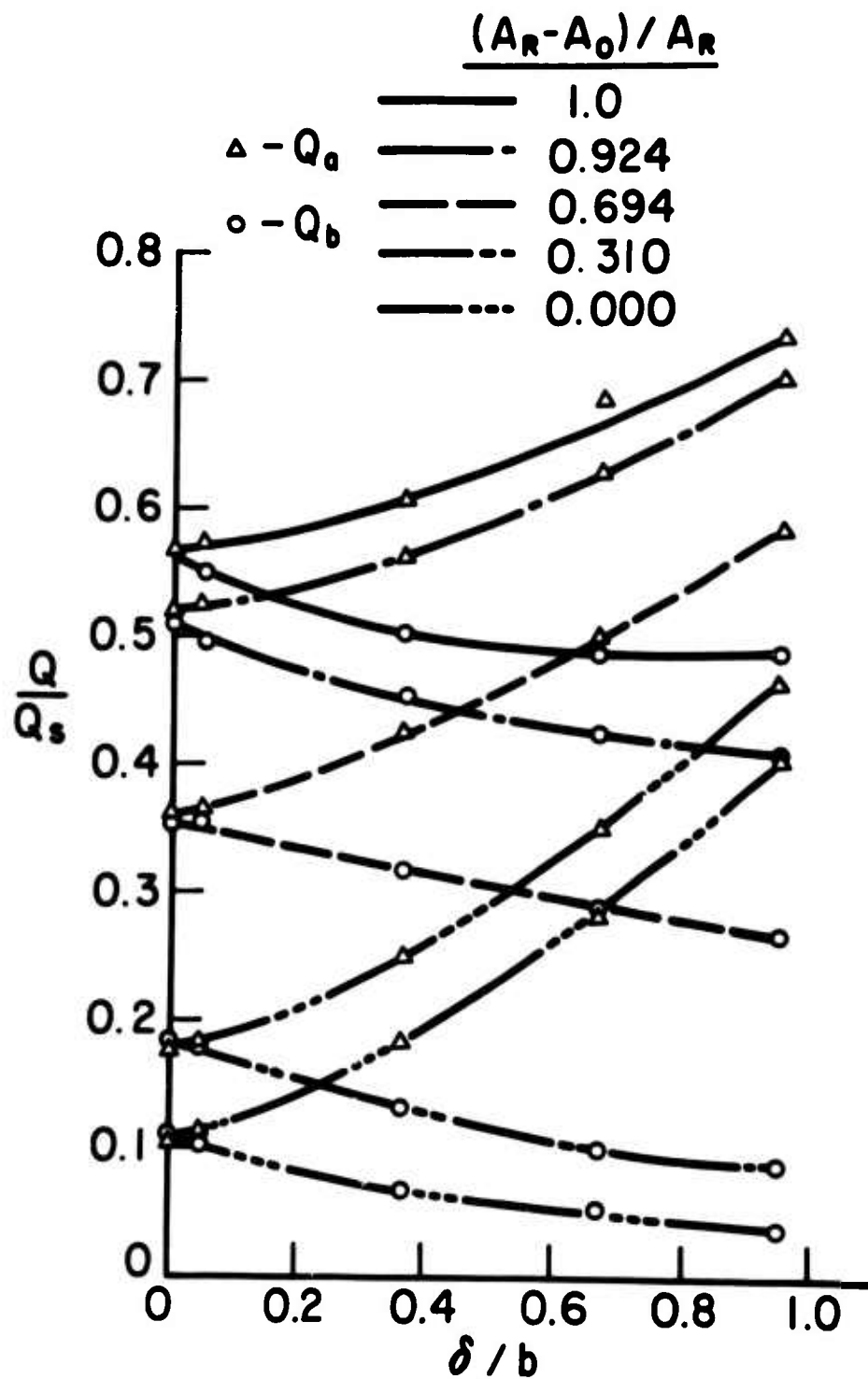


28. Centered Jet Output Characteristic.

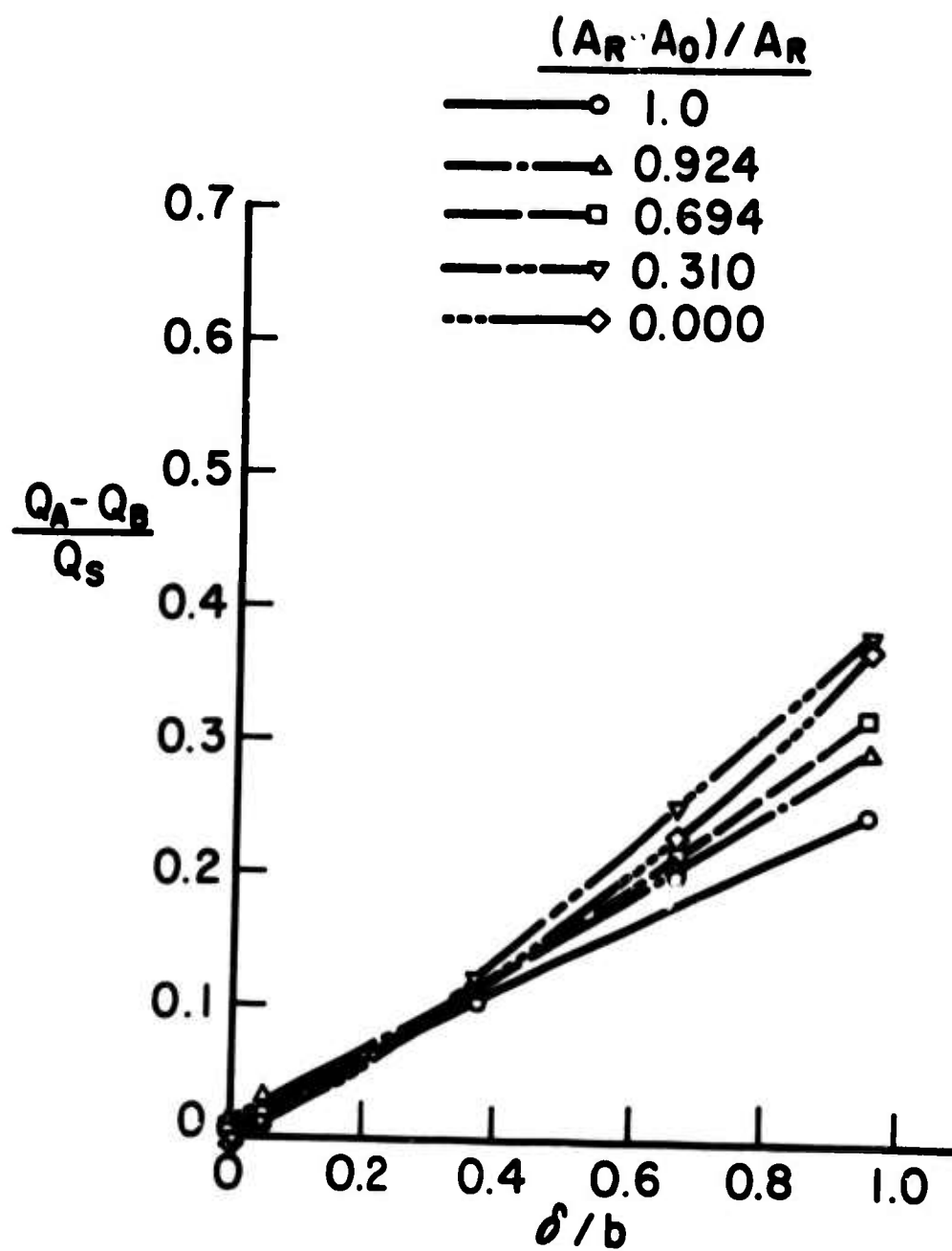




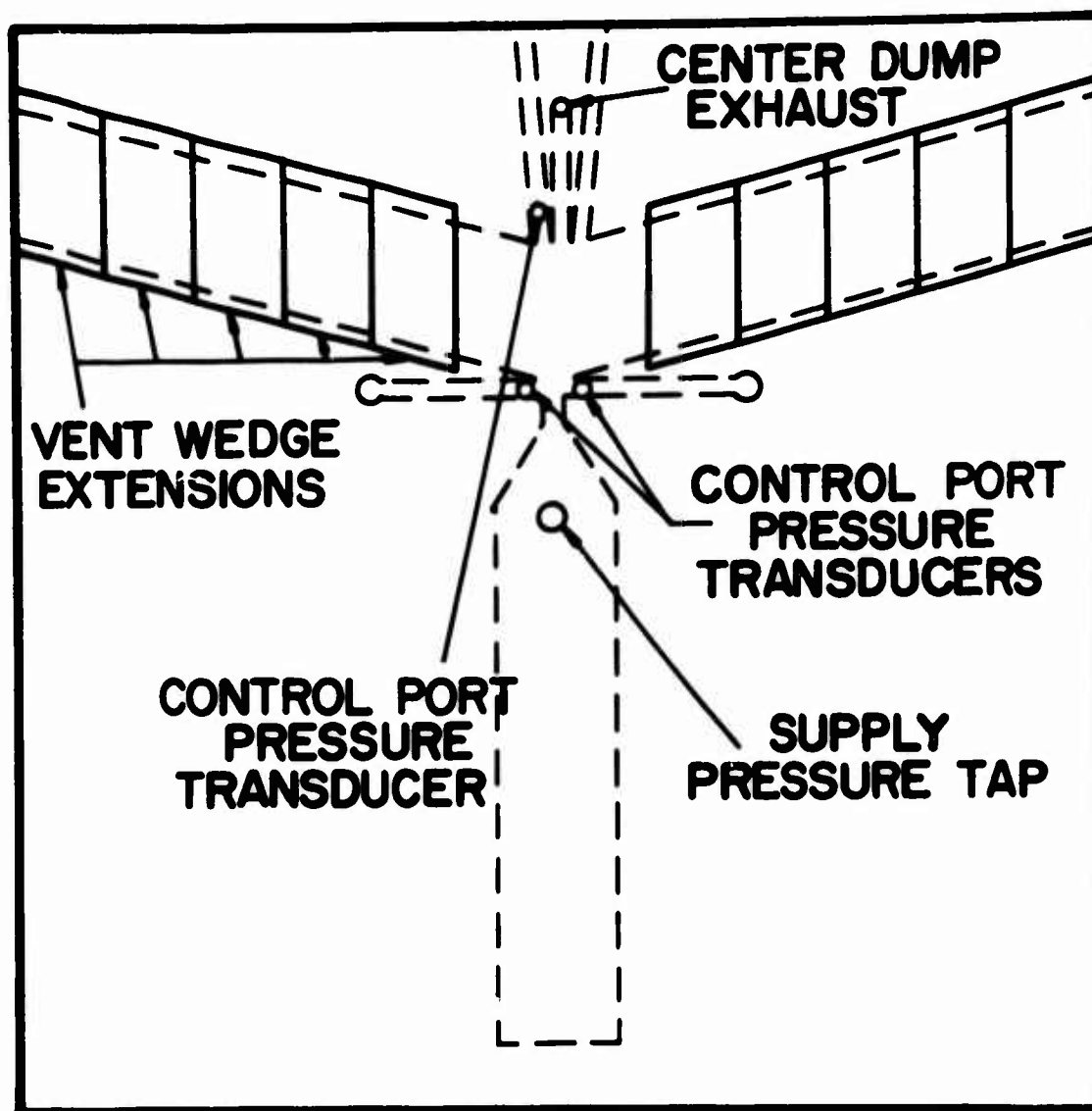
29. Center Dump Flow versus Deflection.



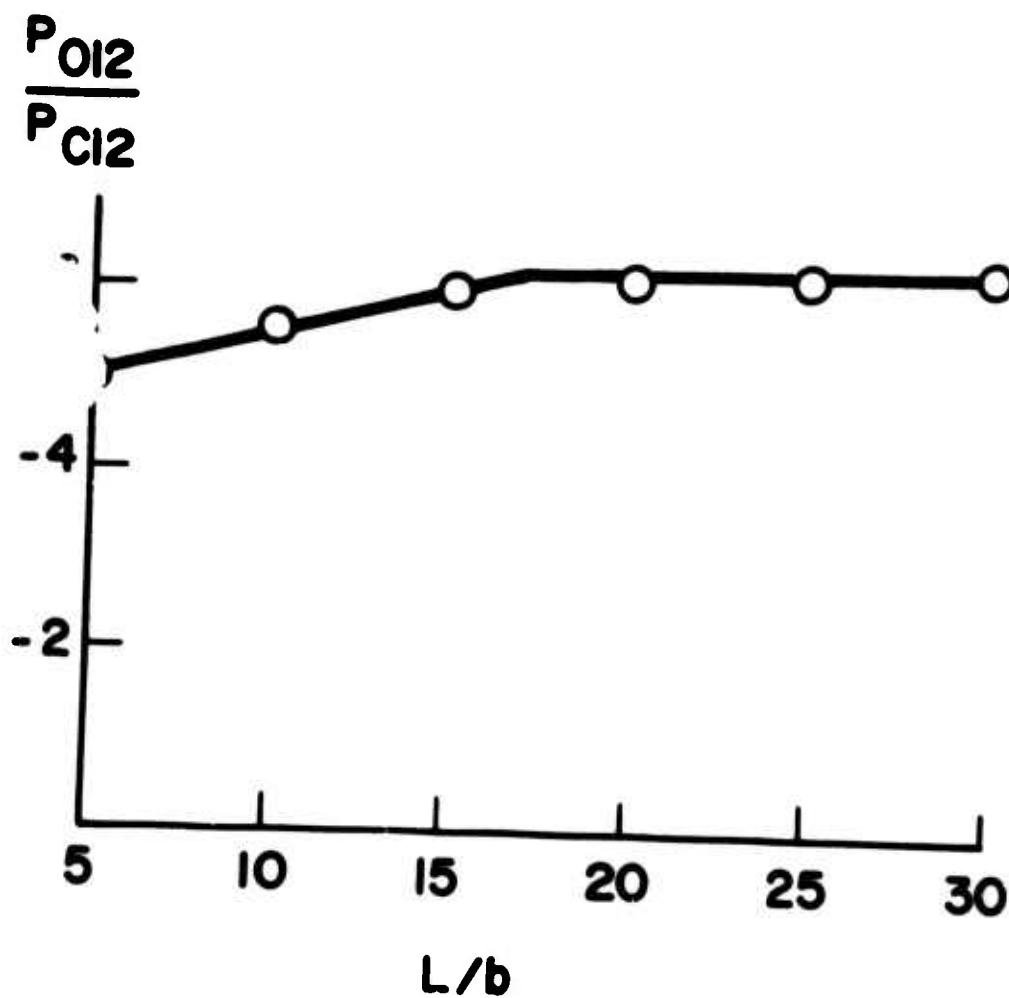
30. Vent Spillover Flows versus Jet Deflection.



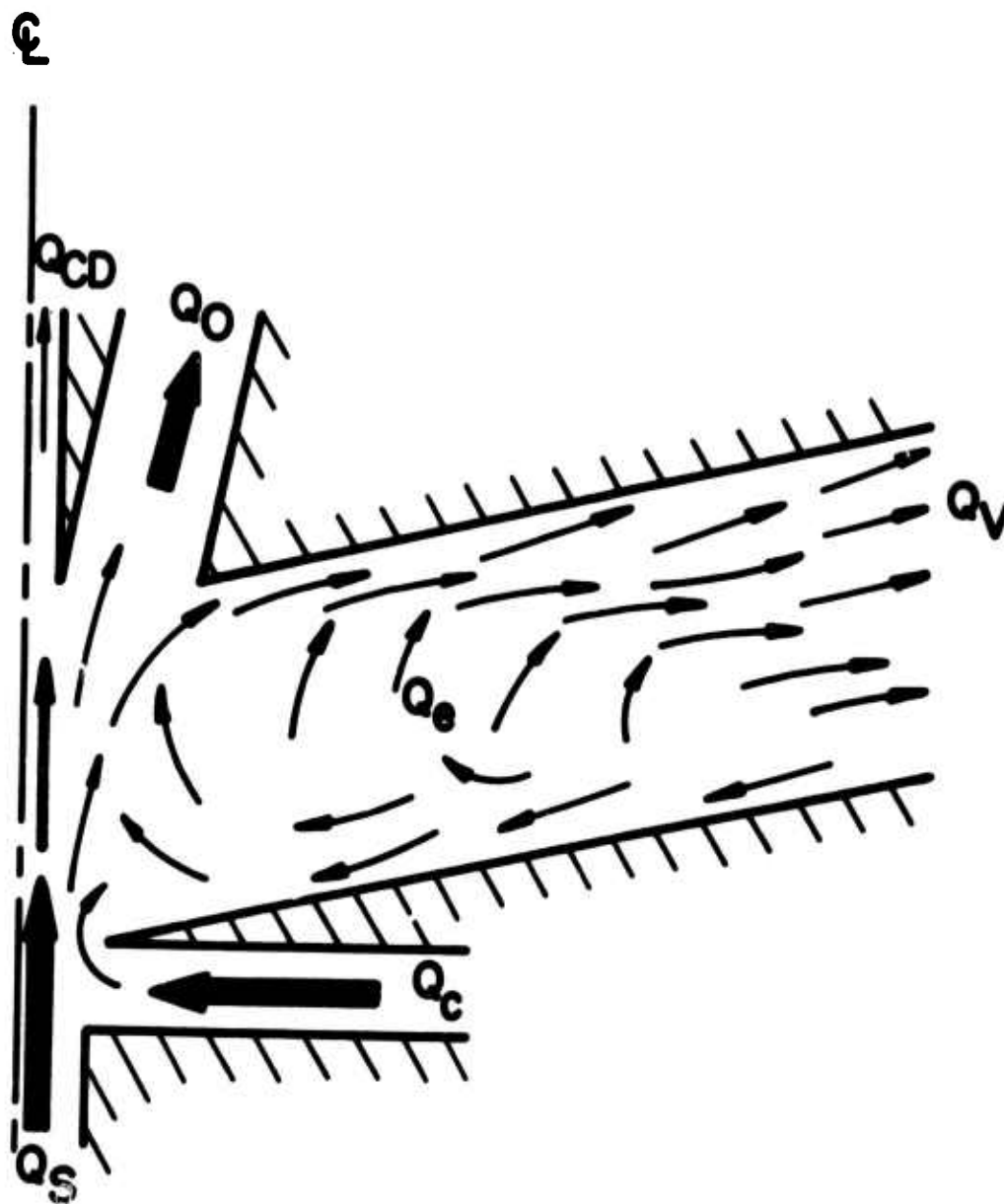
31. Differential Vent Spillover versus Jet Deflection.



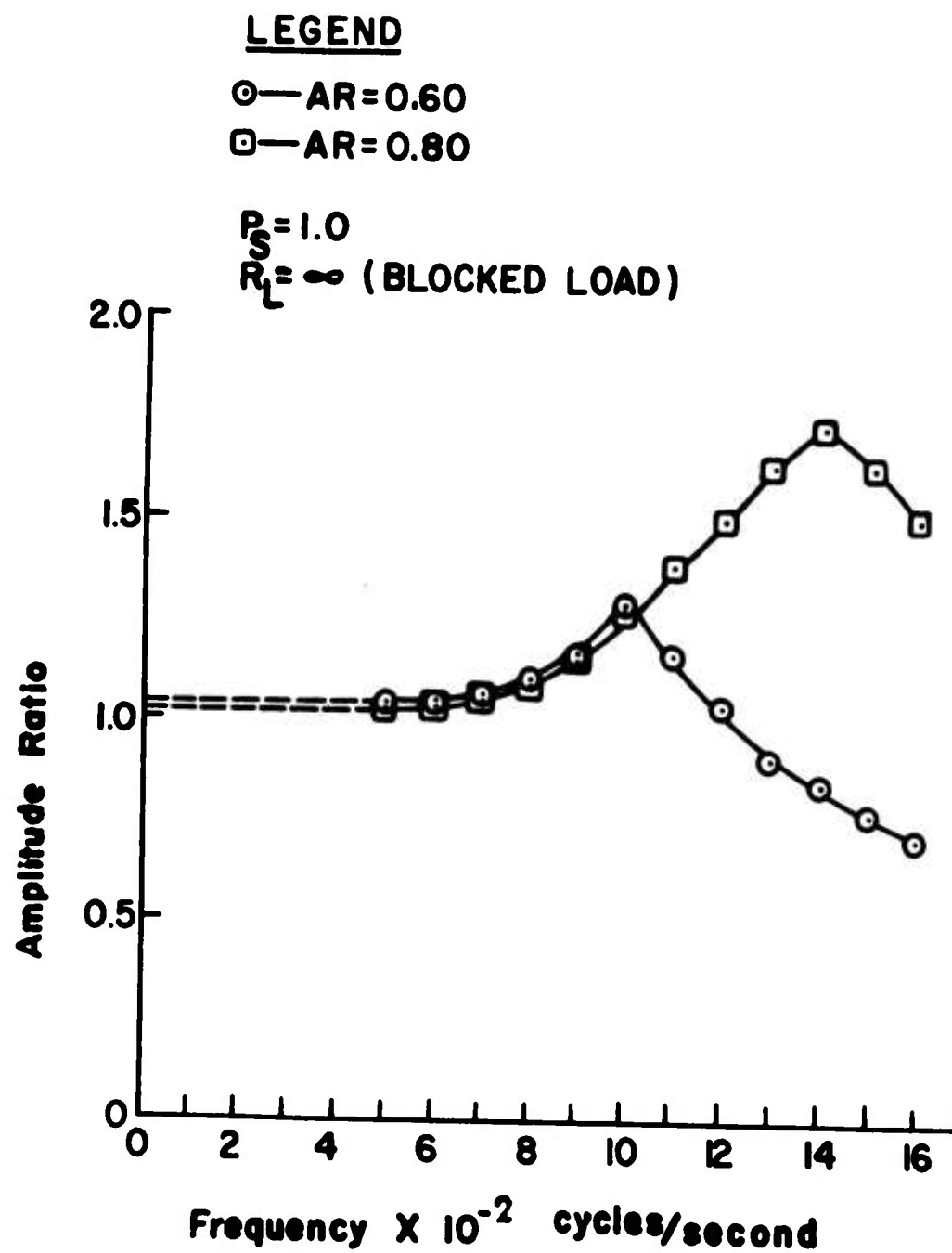
32. Variable Vent Length Amplifier of Shipp [31].



33. Blocked Load Pressure Gain versus Vent Length [31].



34. Diagram of Flow Pattern in Parallel Wall Vent Illustrating Entrained Atmospheric Flow [31].

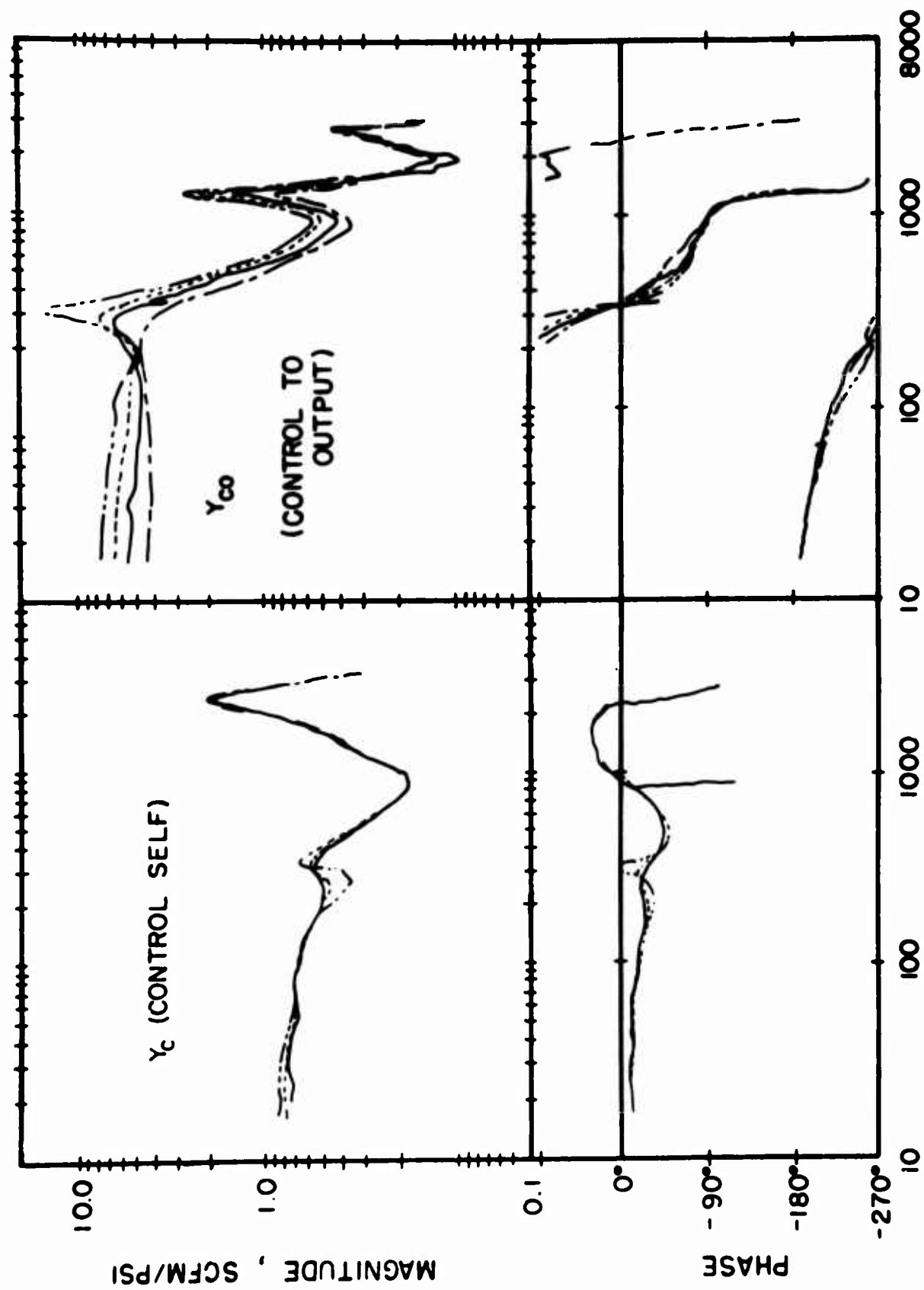


35. Frequency Response of a Fluidic Rectifier with Blocked Receivers.

C

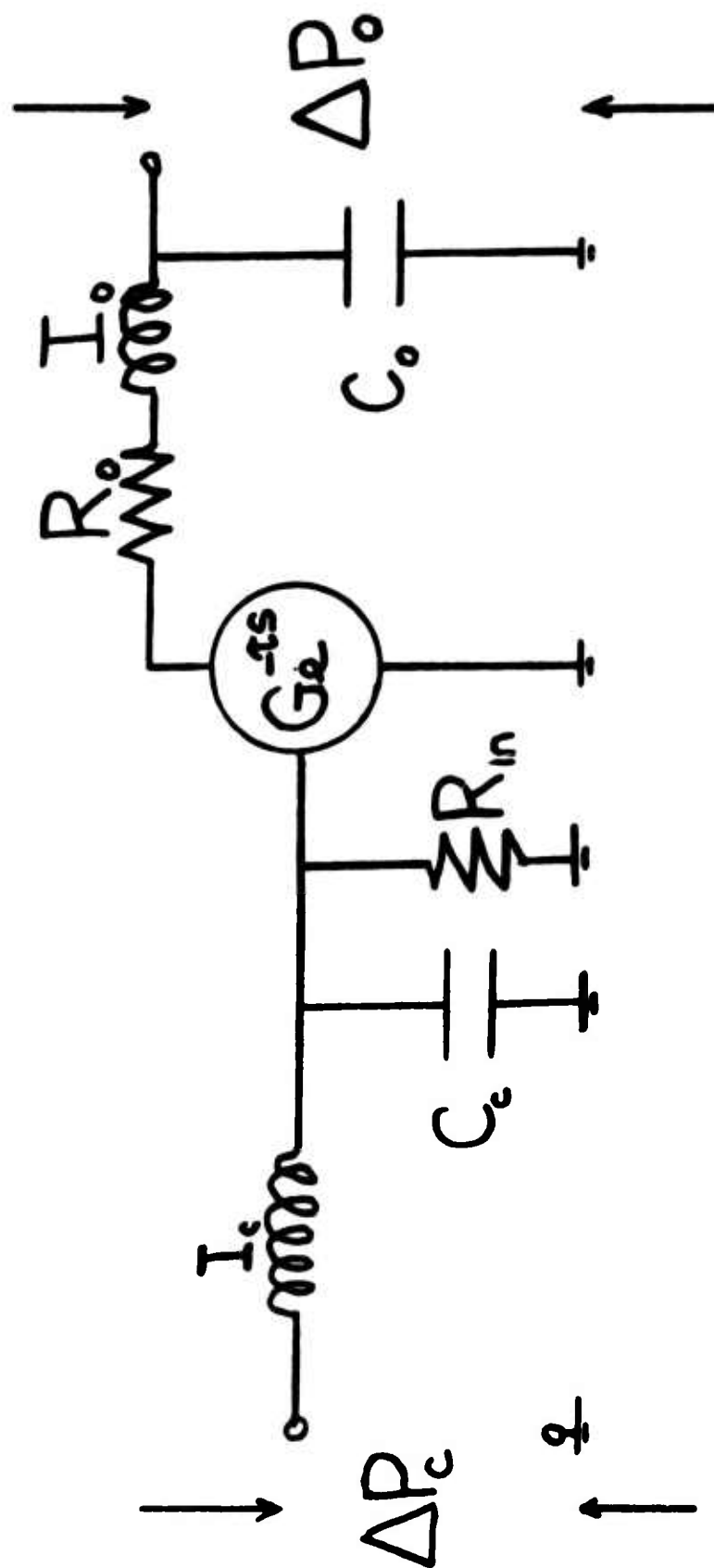
C

C

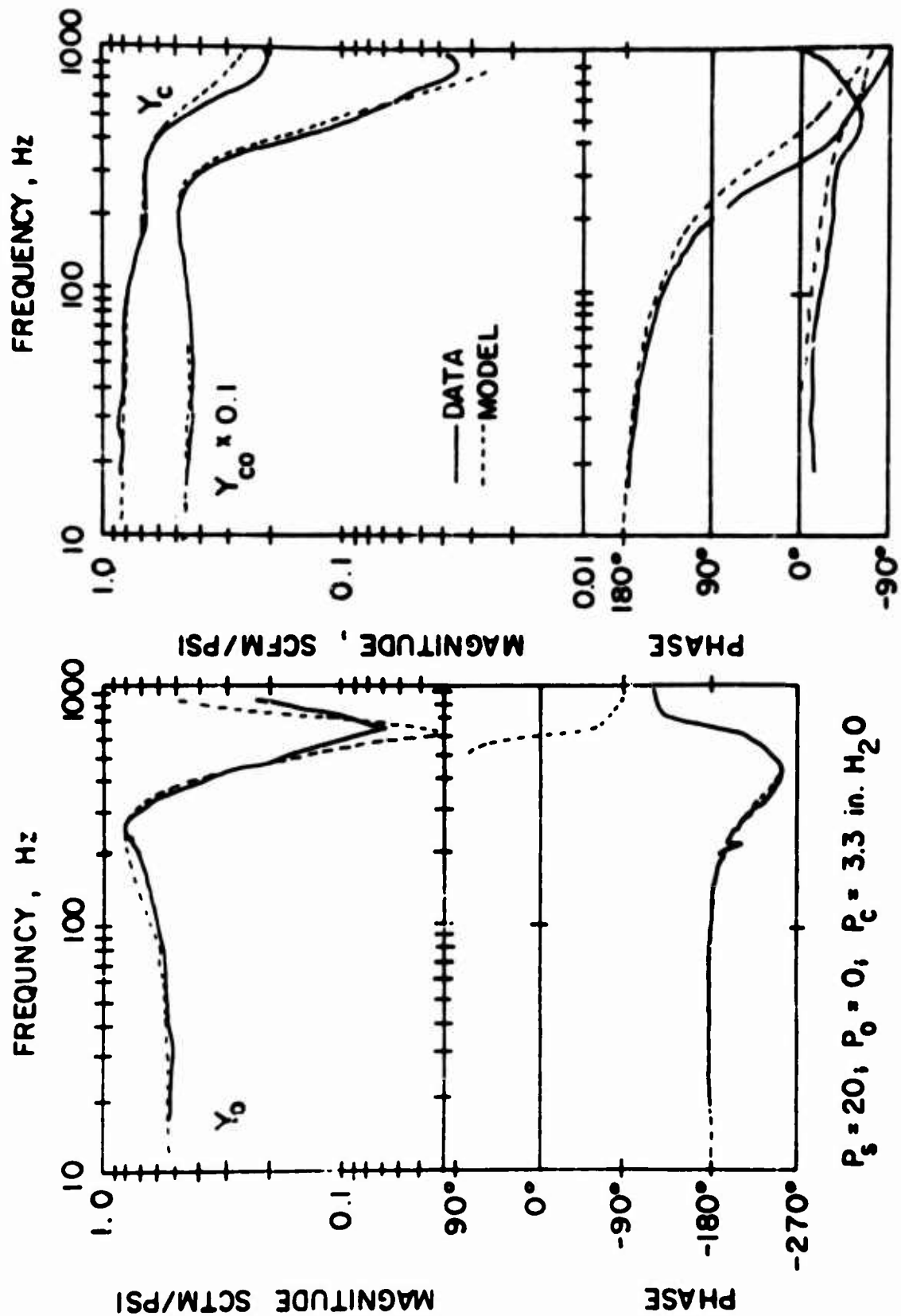


36. Control to Output Admittance Frequency Response [34].



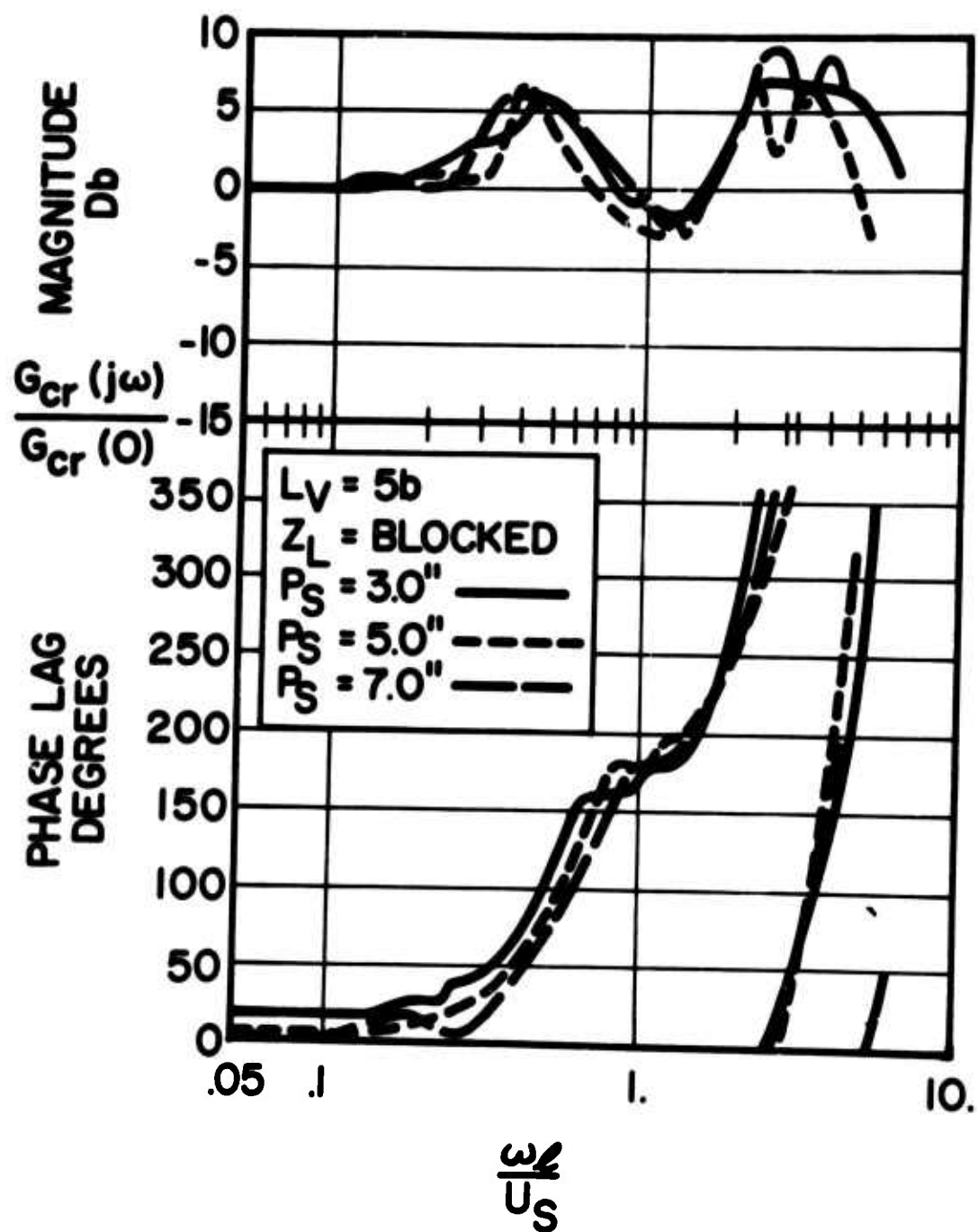


37. Electric Circuit Model of a Perfectly Vented Amplifier after Belsterling [35].

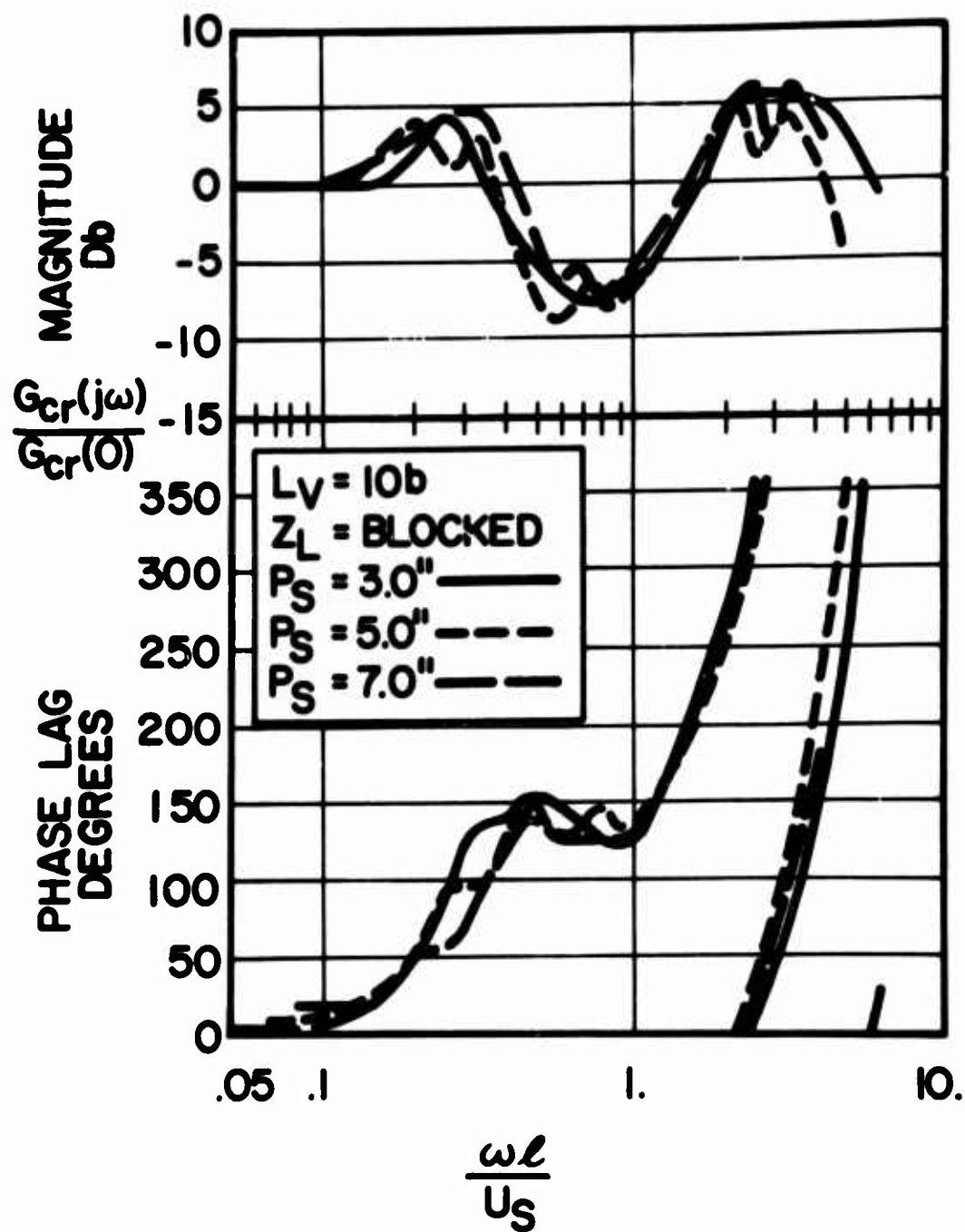


$P_s = 20; P_o = 0; P_c = 3.3 \text{ in. H}_2\text{O}$

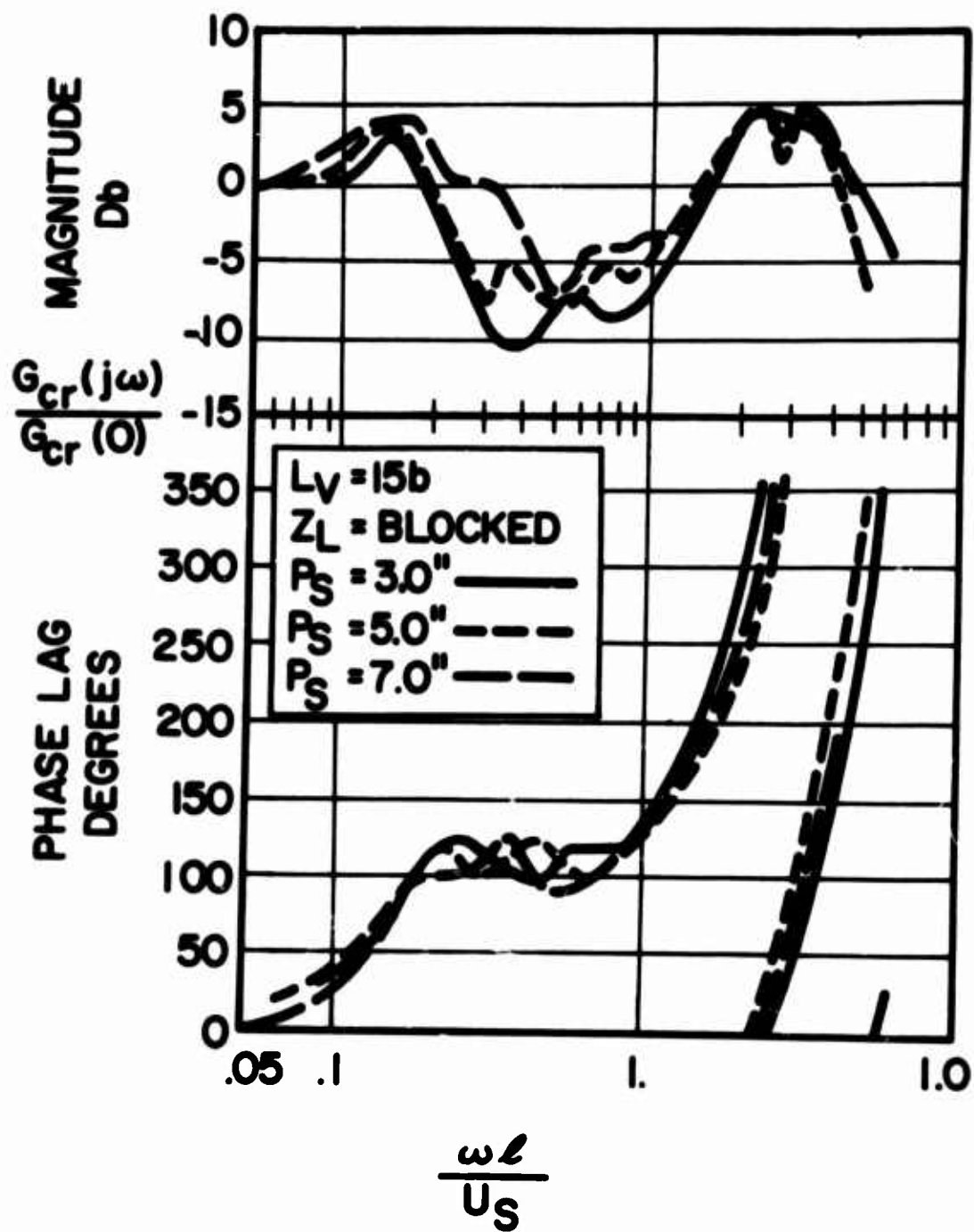
38. Comparison of Predicted and Measured Frequency Response for Control to Output Admittance from [33].



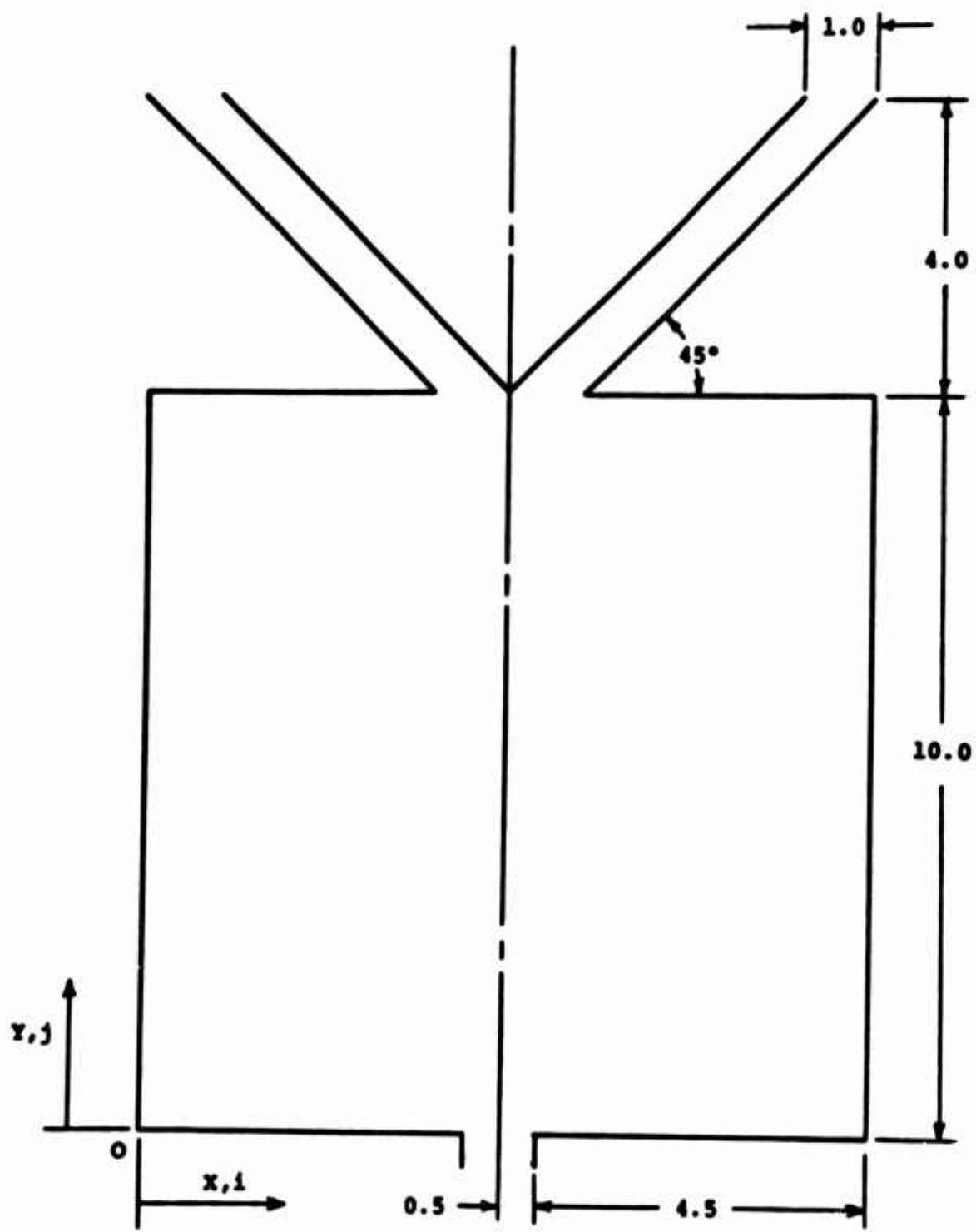
39. Blocked Load Frequency Response  $L_V^* = 5$  from [31].



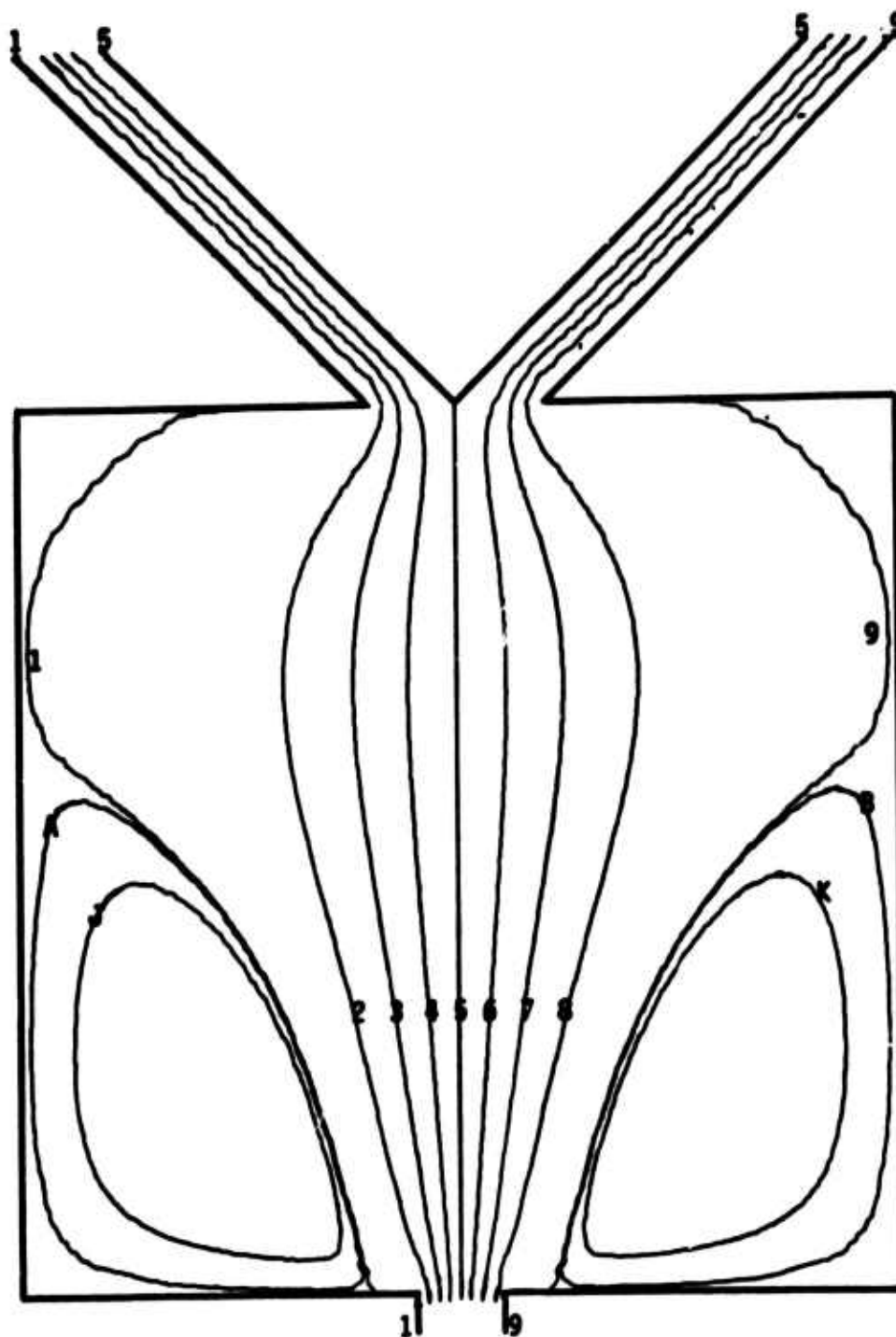
40. Blocked Load Frequency Response  $L_V^* = 10$  from [31].



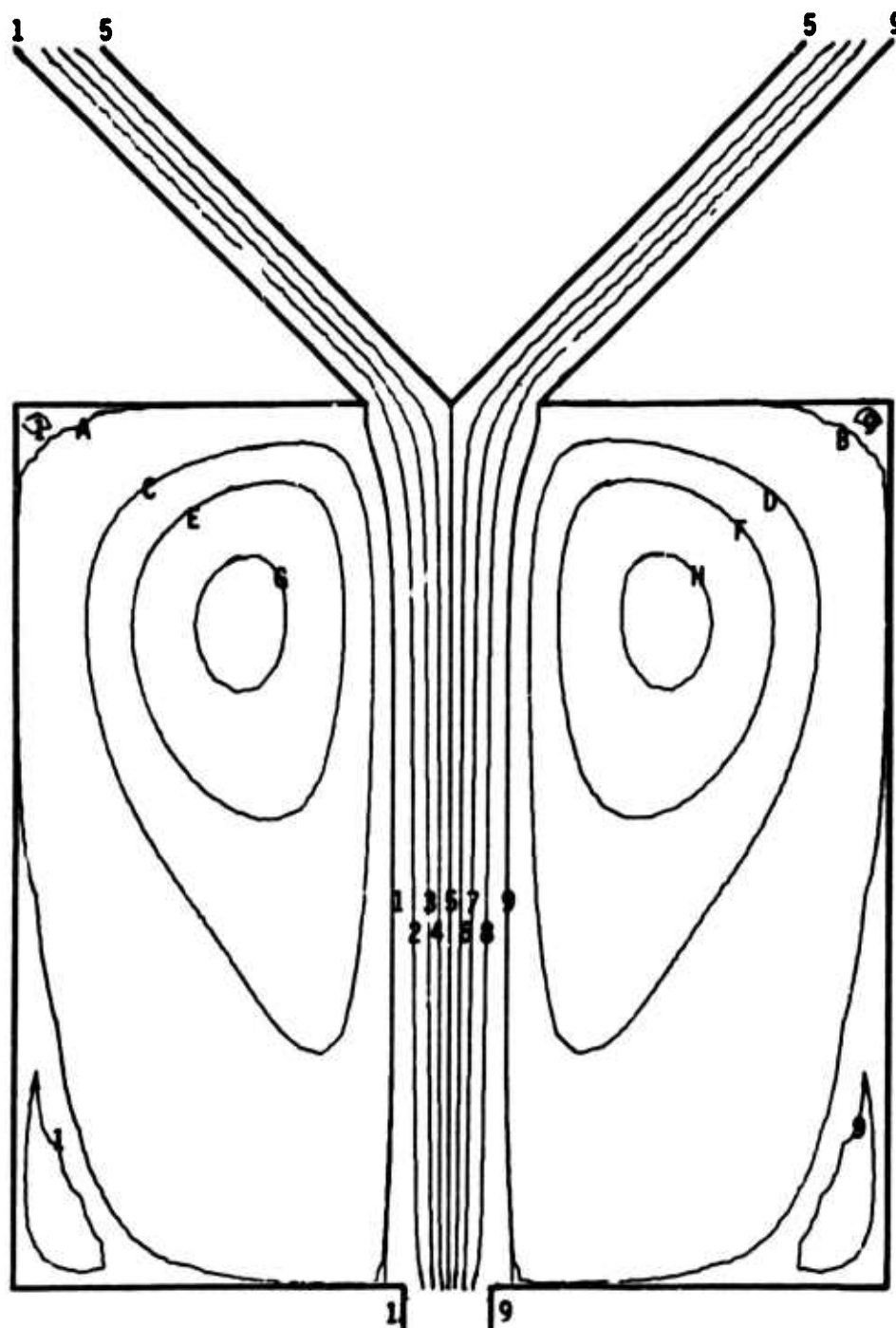
41. Blocked Load Frequency Response  $L_V^* = 15$  from [31].



42. Geometry Considered for Field Solution.

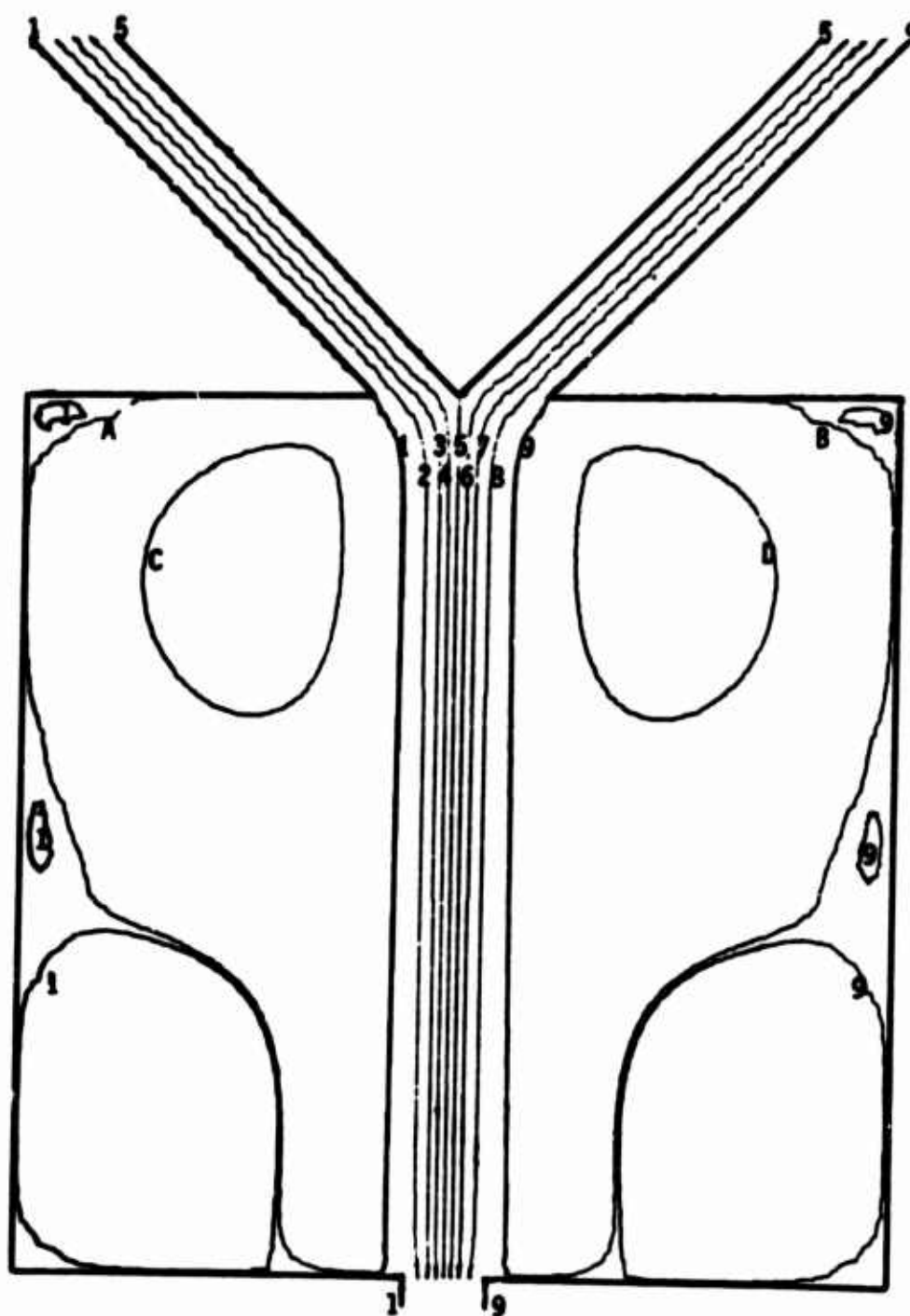


43. Stream Function Solution  $Re = 10$ .



44. Stream Function Solution  $Re = 100$ .





45. Stream Function Solution  $Re = 1,000$ .

FLUIDIC PROPORTIONAL AMPLIFIERS  
FOR VERY LOW REYNOLDS NUMBERS

BY ROBERT H. BELLMAN

## TABLE OF CONTENTS

- I. Introduction
- II. Problem definition
- III. Approximation of the viscous losses in the power nozzle
- IV. Results
- V. Conclusions

### SYMBOLS

A	area
P	Pressure
Q	Flow rate
V	Velocity
X, Y, Z	Cartesian coordinate directions
a	nozzle dimension in Y direction
b	nozzle dimension in Z direction
c	subscript for control
e	mathematical constant
l	nozzle dimension in X direction
n	$\frac{Z}{Y}$ of the nozzle
o	subscript for output
s	subscript for supply
t	subscript for the supply nozzle throat
u	velocity in X direction
v	velocity in Y direction
w	velocity in Z direction
x, y, z	distances in cartesian coordinate directions
$\rho$	fluid density
$\Delta$	difference
$\mu$	fluid viscosity
$\pi$	mathematical constant

## I. INTRODUCTION

This paper represents work performed in trying to find small proportional fluidic amplifiers which would function on the available pressures in high velocity air conditioning ducts. The normal high velocity air conditioning ducts can supply pressures of  $3/4$ "  $H_2O$  to 6"  $H_2O$ . The conventional fluidic amplifiers began to lose efficiency (gain and maximum pressure recovery) at about 3"  $H_2O$  and were considered useless at below 1"  $H_2O$ . The aim of the work performed was to keep the amplifiers useful at supply pressures of  $1/2$ "  $H_2O$  and less, to keep the devices small enough to be economically packaged and to have the devices use less than .1 watt supply power.

## II. PROBLEM DEFINITION

The amplifier geometry started with is shown in figure 1. Briefly the amplifier functions by emitting a jet from the power supply nozzle which is reconverted into pressure at the amplifier receivers. Control jets emitted from the amplifier control nozzles deflect the power jet thru momentum summing and pressure deflection to cause a difference in the recovered pressures at the receivers.

Experimental data was taken on the basic amplifier using the test set-up shown in figure 2. Pressure calibration was based upon a Dwyer incline manometer filled with red oil with a specific gravity of .86. Flow calibration was based upon a Fischer Porter volume displacement flow meter with a Fisher Scientific barometer and a mercury thermometer used to correct all flows to the standard conditions of  $59^{\circ}F$  and 14.7 psia. The room temperatures during testing were kept at 70 to  $75^{\circ}F$  to keep viscous effects constant.

The experimental data is summarized in figures 3 through 5. Figure 3 shows how the maximum recovered

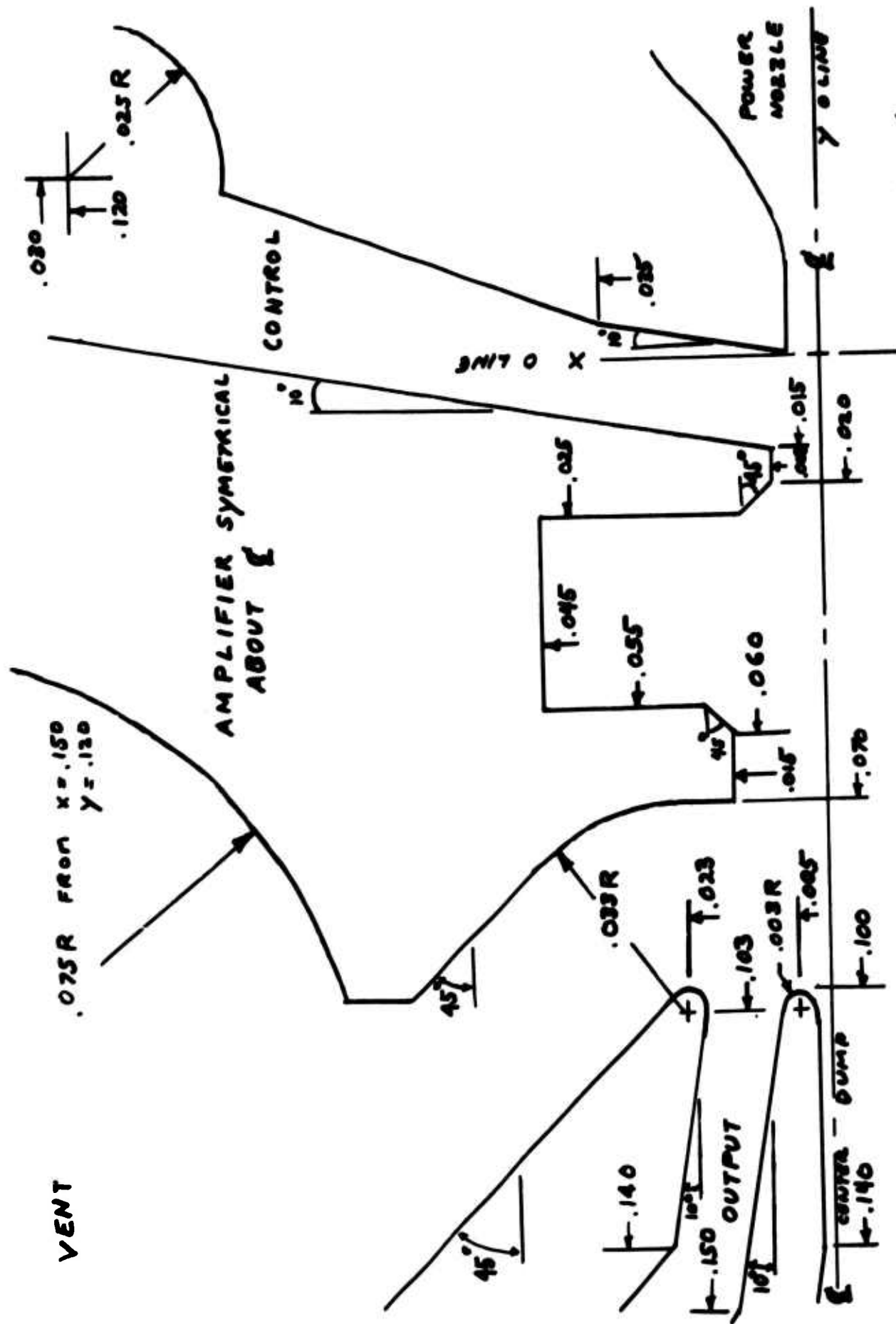
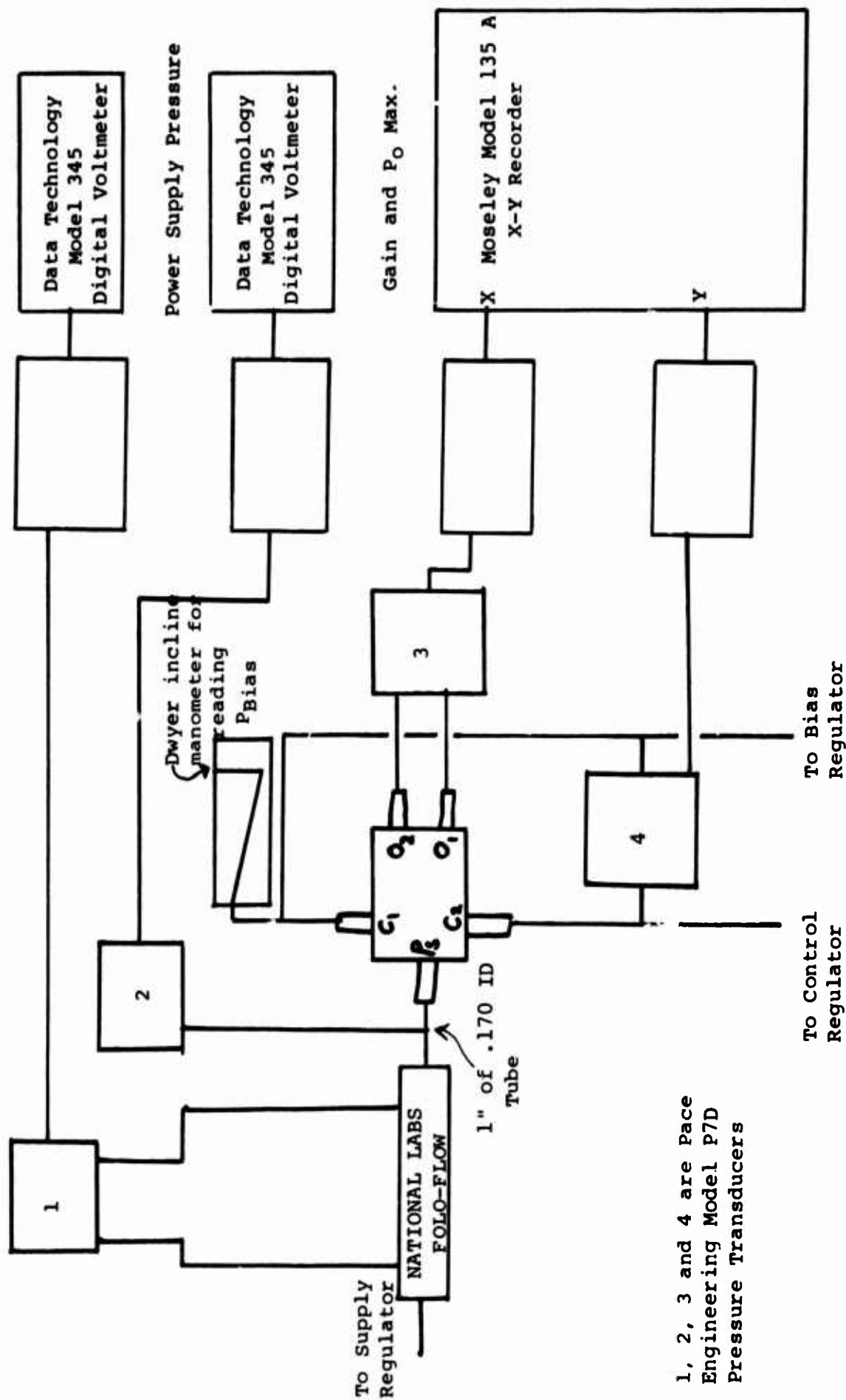


FIGURE 1

Dyna Sciences Corp.  
Carrier Demodulators  
Model CD10

Flow Rate



1, 2, 3 and 4 are Pace  
Engineering Model P7D  
Pressure Transducers

FIGURE 2

WAK OUTPUT RECOVERY

VS

SUPPLY PRESSURE

WAK SUPER AMP  
BLOCKED OUTPUTS

.010  $P_n$   $R = 2.0$

MAXIMUM OUTPUT PRESSURE RECOVERY

$P_{o \max} / P_s$

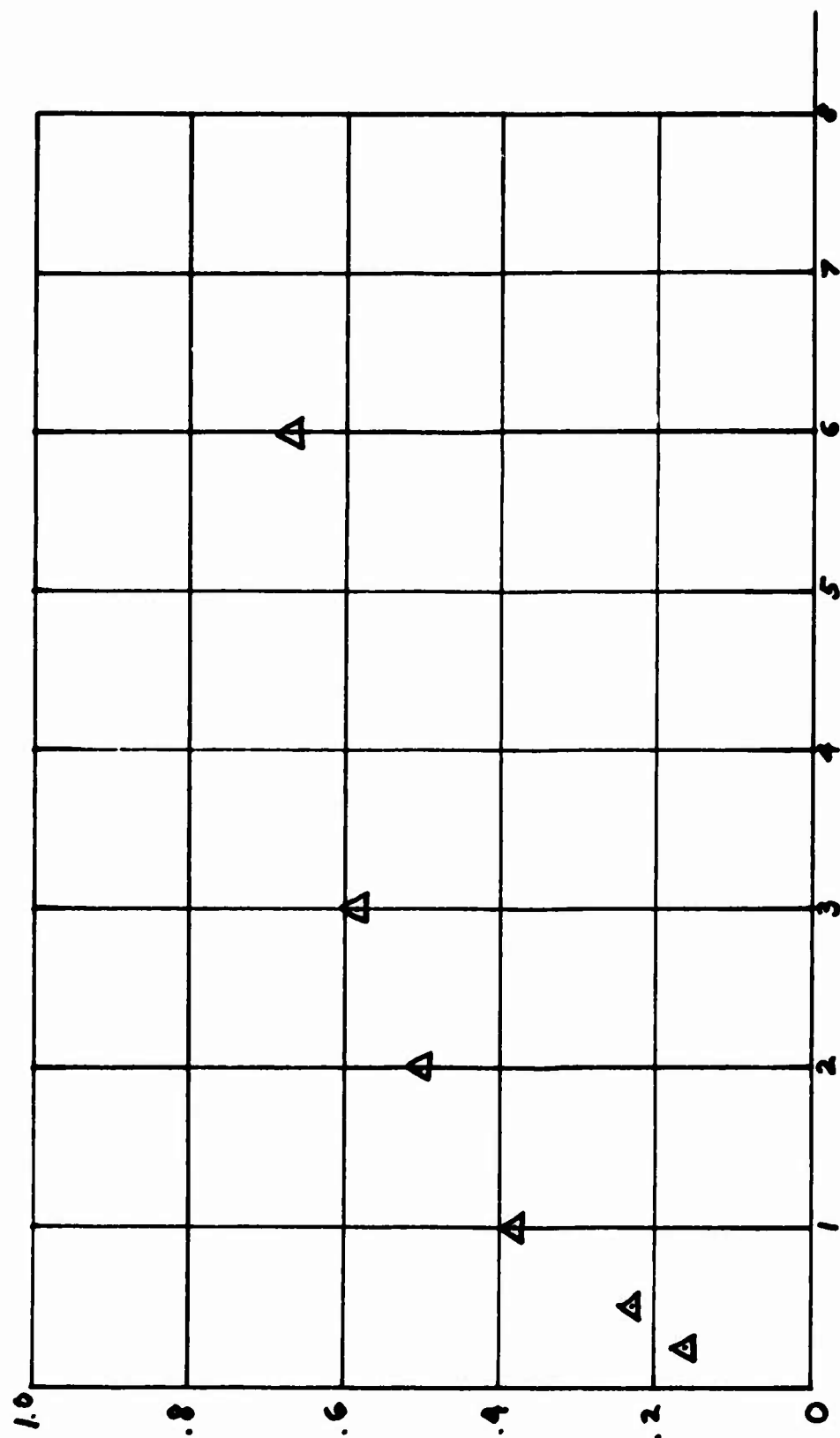


FIGURE 3

INCH H<sub>2</sub>O

POWER SUPPLY PRESSURE



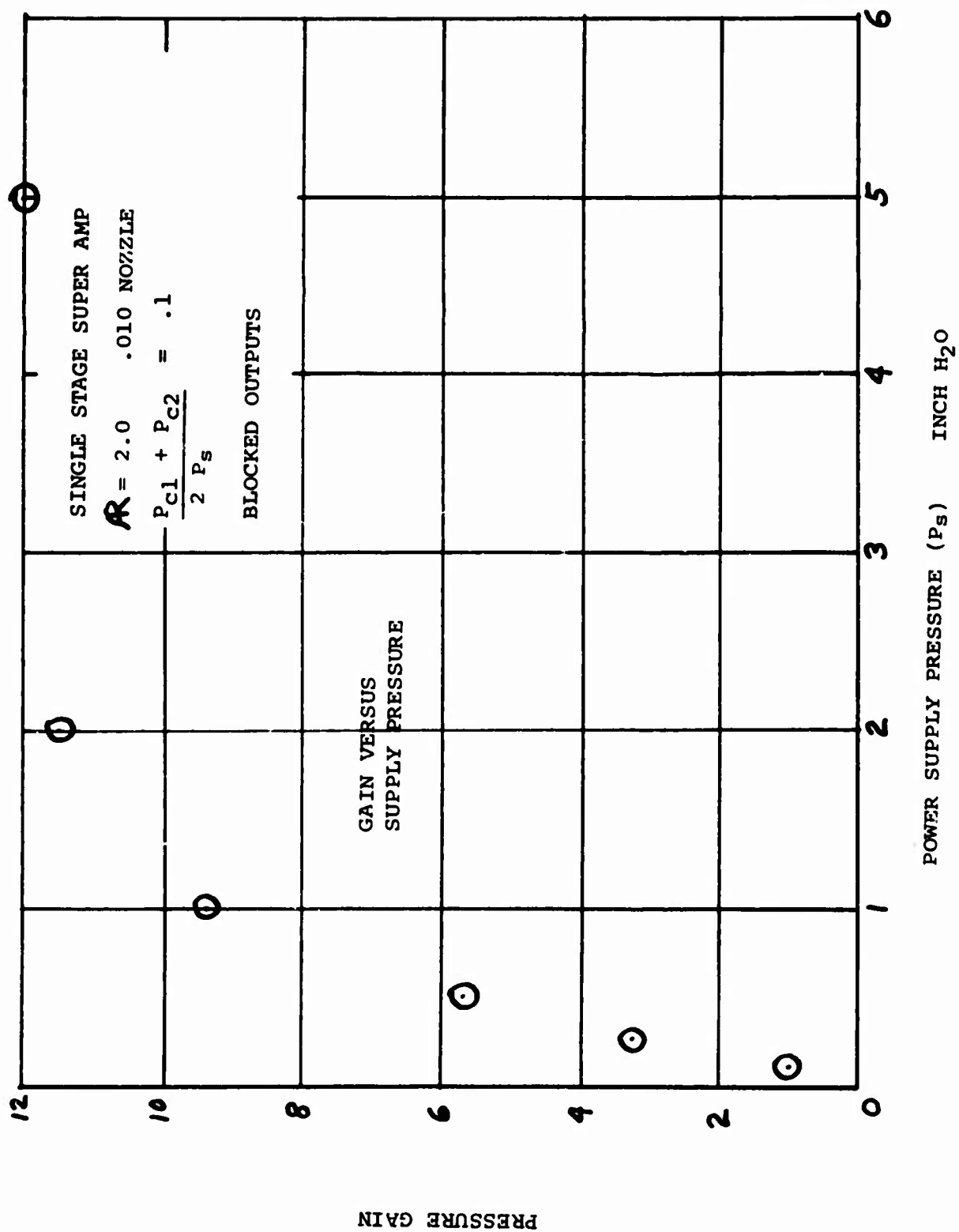


FIGURE 4

PRESSURE GAIN

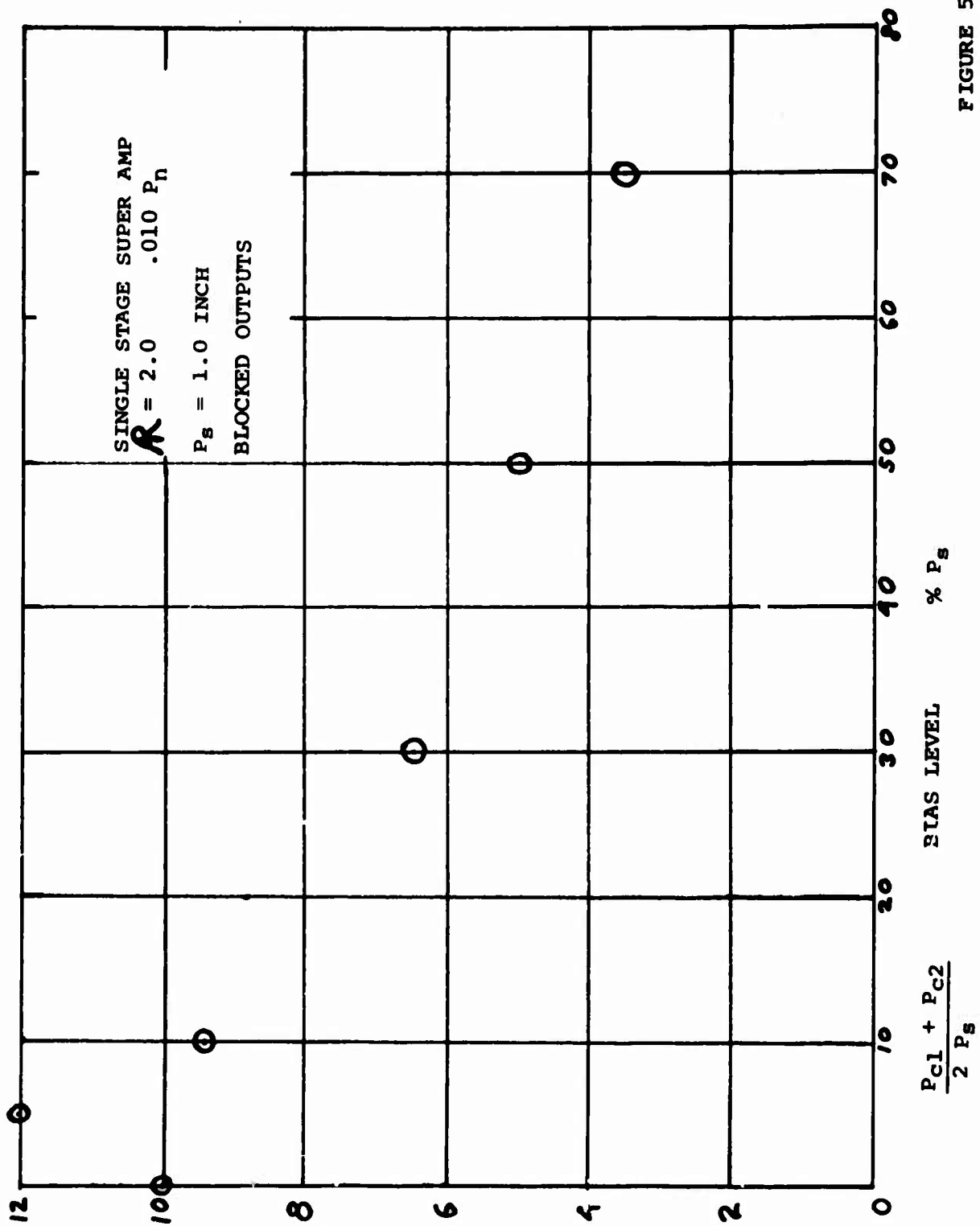


FIGURE 5

output pressure ( $P_o$  max.), in percentage of supply pressure, falls off as the supply pressure ( $P_s$ ) decreases. Figure 4 shows how the pressure gain ( $\frac{\Delta P}{\Delta R}$ ) falls off as the supply pressure decreases and figure 5 shows how the pressure gain decreases with increasing control pressure bias level ( $\frac{P_c + P_s}{2}$ ) at a constant supply pressure.

The curves plotted on figures 3 through 5 indicated that viscous losses might be causing the loss in amplifier efficiency at low supply pressures. Additional data was taken on amplifiers of various supply nozzle sizes with geometrically scaled planforms. The additional data allowed the Reynolds Number to be varied while the supply pressure was held constant so as to give a stronger indication of viscous losses being the problem. Figure 6 shows the maximum recovered output pressure plotted against Reynolds Number. The curve in figure 6 does show that the maximum recovered output pressure is dependent upon Reynolds Number and not the supply pressure, confirming that the efficiency loss of proportional amplifiers at low supply pressures is due to viscous losses.

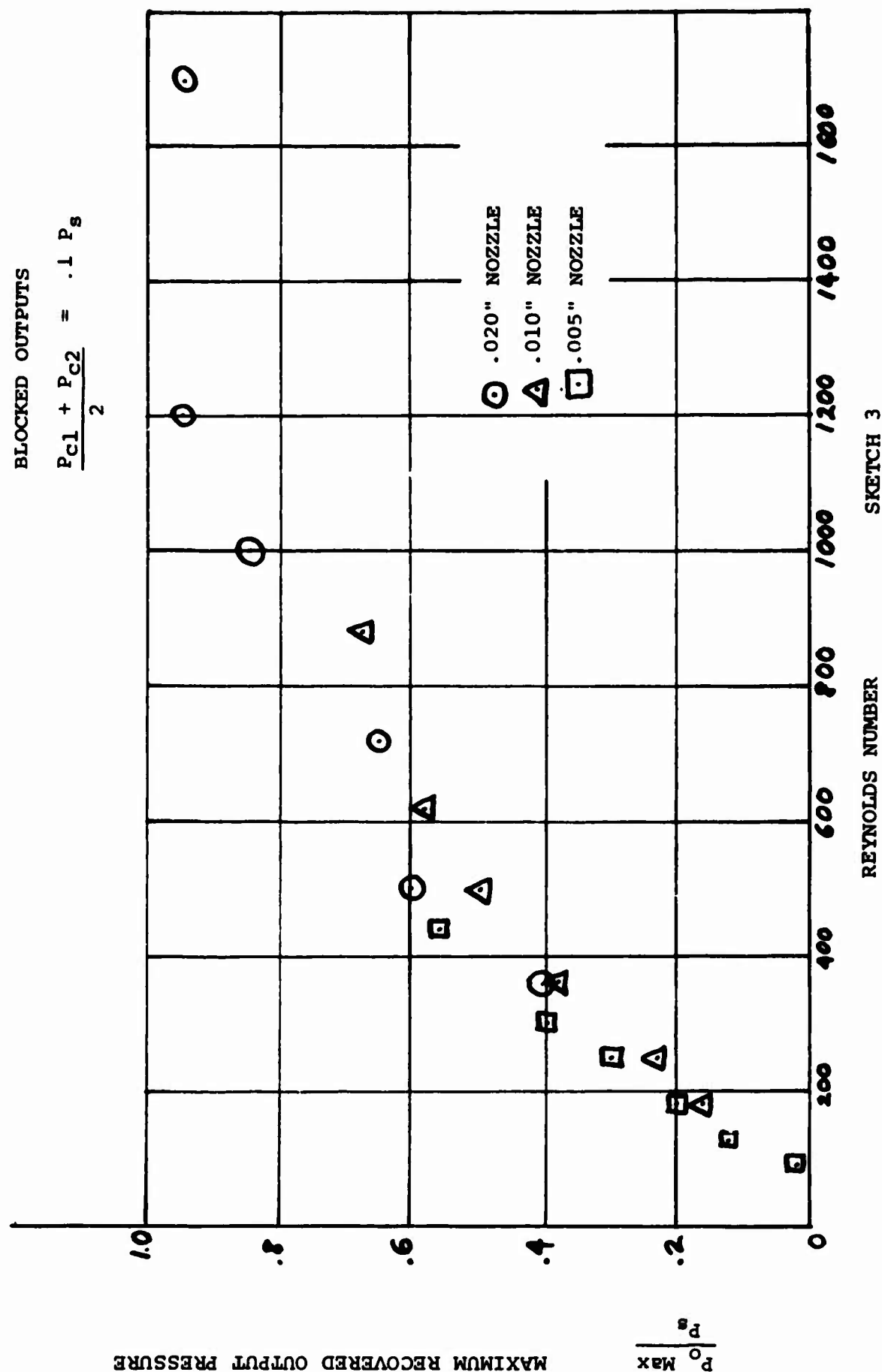
The problem of identifying where the main source of viscous losses occurs has yet to be solved. Two main sources of losses need to be considered. One source of losses would be in the power nozzle itself and the other source of losses would be in the submerged jet after it leaves the nozzle. Allen Werbow indicated in reference 1 that at the Reynolds Numbers involved and the jet length traveled the viscous losses in the jet would not cause a significant slowing of the jet centerline velocity. Therefore the loss was thought to be in the power nozzle itself.

The source of viscous losses was further pinpointed by taking experimental pressure versus flow data on the amplifiers supply nozzle and comparing the

SUPER AMP  
 $AR = 2$

BLOCKED OUTPUTS

$$\frac{P_{C1} + P_{C2}}{2} = .1 P_s$$



SKETCH 3

FIGURE 6

experimental flow data with inviscous calculated flows. Figure 7 shows the calculated flow and the experimental flow plotted against the supply pressure. The inviscous flow was calculated using the equation:

$$Q = A \sqrt{\frac{2 P_s}{\rho}} \quad \text{where the area } A \text{ is the nozzle throat area}$$

The experimental flow through the nozzle is clearly less than the calculated flow at low supply pressures indicating again that the viscous losses hampering fluidic amplifier operation at low supply pressures originate in the supply nozzle. A way of indicating where the losses occur and what their magnitude is, will be needed to minimize the losses and improve amplifier performance at the desired supply pressures.

### III. APPROXIMATION OF THE VISCOUS LOSSES IN THE POWER NOZZLE

The power nozzle, as shown in figure 1, can be considered in three sections. The flow in all three sections can be considered incompressible.

ZONE 1 The flow in the straight approach section of the nozzle is channel flow and can be solved using the pressure flow equation based upon Rouse's velocity profile (Reference 2) as integrated in Appendix A. The entrance effects at the channel entrance are neglected. The resulting equation:

$$\frac{P_s - P'_s}{Q} = \frac{\mu l}{u_s^2 D_s}$$

can predict the modified supply pressure ( $P'_s$ ) if the supply pressure, the flow rate, the fluid, and the channel dimensions are known. The modified supply pressure  $P'_s$  is the pressure available to accelerate the flow in the converging section of the nozzle.

ZONE 3 The flow in the narrow, straight, throat section of the nozzle is again channel flow. The

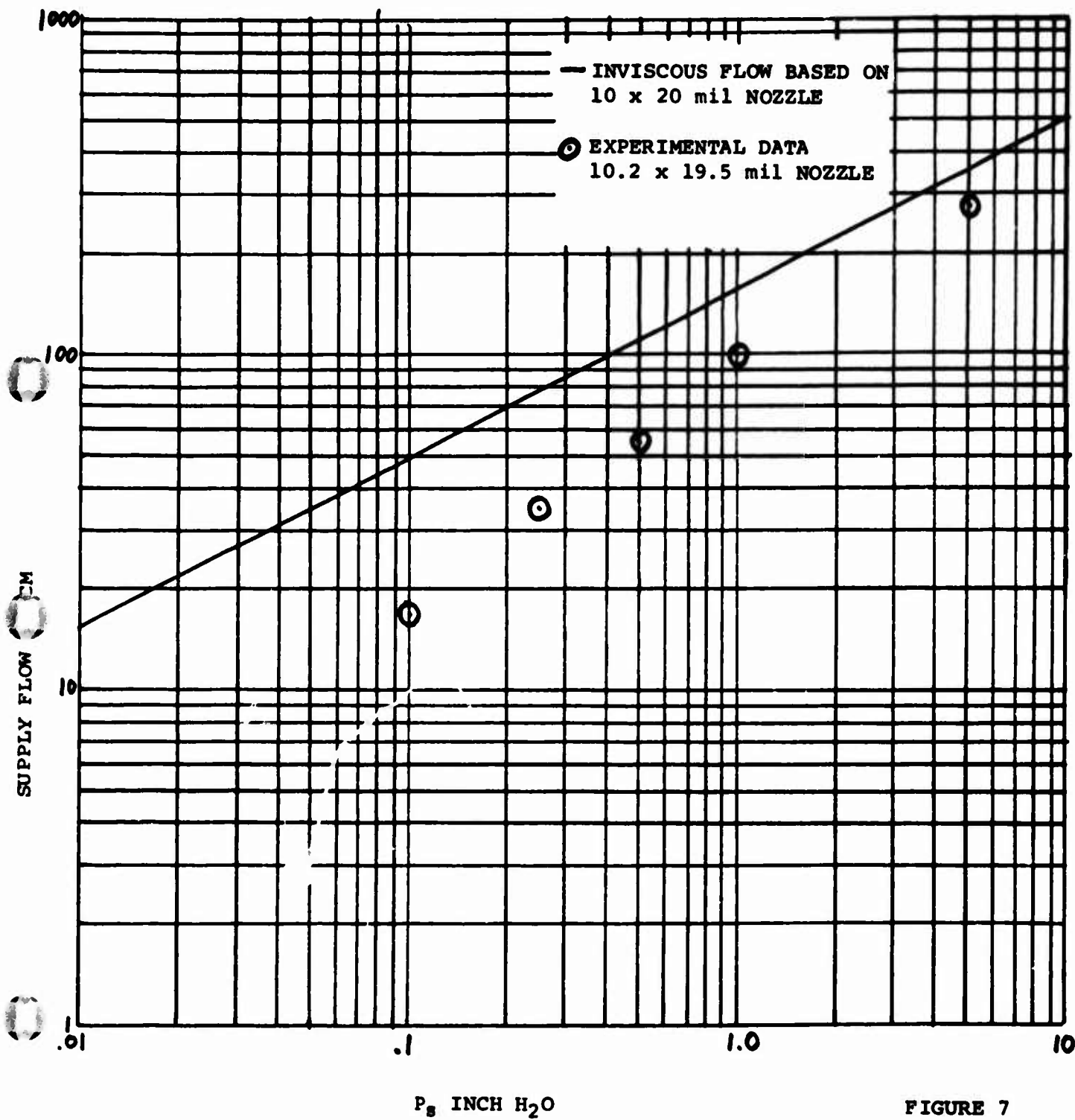


FIGURE 7

resulting equation:

$$\frac{P_s''}{Q} = \frac{\mu \ell_3}{a_s^4 D_3}$$

can predict the pressure drop in the nozzle throat  $P_s'$  if the flow rate, the fluid, and the throat dimensions are known. The pressure drop in the throat modifies the exit pressure of the converging section of the nozzle so that the pressure available to accelerate the flow and overcome the viscous losses in the converging section of the nozzle is:

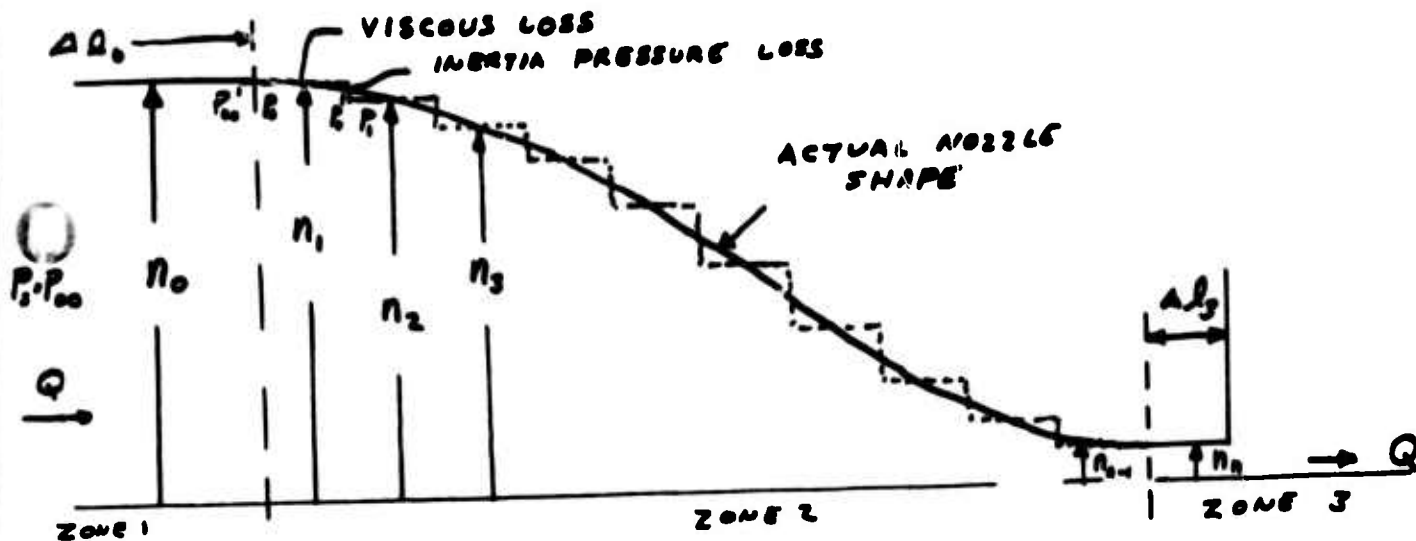
$$P_s - P_s' - P_s'' \quad \text{or:} \quad P_s - \frac{\mu \ell_1}{a_s^4 D_1} Q - \frac{\mu \ell_3}{a_s^4 D_3} Q$$

ZONE 2 The flow in the converging section of the nozzle is complicated by the curvature of the channel walls in the Z plane. A simplified approximation of the flow was made on the assumption that the boundary layer in the Y direction was dominant ( $1/Y$ ) and the boundary layer in the Z direction would remain approximately parabolic (Reference 5, page 90). The converging section of the nozzle could then be approximated by a series of short viscous flow channels with inviscous flow converging sections between to account for the inertia pressure drops. The approximate nozzle is shown in figure 8.

The total pressure drop across the converging section of the nozzle can then be predicted by the sum of the viscous pressure drops in the short channels plus the sum of the inertia pressure drops (Bernoulli's equation) needed to accelerate the flow so as to satisfy the conservation of mass. The sum of the viscous pressure drops is:

$$Q \sum \frac{\Delta P_{v,i}}{Q} = Q \sum_{i=1}^m \frac{\mu \Delta \ell_i}{a_i^4 D_i}$$

so the viscous pressure drop can be calculated if the



ZONE 1 VISCIOUS LOSS

$$\frac{P_0 - P_0'}{Q} = \frac{\mu \Delta l_0}{a^4 D_0(n_0)} \quad \text{OR} \quad P_0' = P_0 - \frac{\mu \Delta l_0}{a^4 D_0(n_0)} Q$$

1ST APPROXIMATE BLOCK INERTIA PRESSURE DROP

$$P_{00}' = P_0 + \frac{1}{2} \rho \frac{Q^2}{a^5 n_1^2} = P_0' + \frac{1}{2} \rho \frac{Q^2}{a^5 n_1^2}$$

COMBINE TO GIVE

$$P_0 = P_3 - \frac{\mu \Delta l_0}{a^4 D_0(n_0)} Q - \frac{1}{2} \rho \frac{Q^2}{a^5} \left( \frac{1}{n_1^2} - \frac{1}{n_0^2} \right)$$

CONTINUE:

$$P_3 = \frac{\mu Q}{a^4} \left\{ \frac{\Delta l_0}{D_0(n_0)} + \frac{\Delta l_1}{D_1(n_1)} + \Delta l \sum_{n=1}^{n-1} \frac{1}{D_n(n_n)} \right\} + \frac{1}{2} \rho \frac{Q^2}{a^5} \left( \frac{1}{n_n^2} - \frac{1}{n_0^2} \right)$$

FIGURE 8



flow rate, the converging section shape, the number of increments the nozzle is to be divided into, and the fluid are known. The inertia pressure drop is:

$$\frac{1}{2} \rho \frac{Q^2}{a^2} \left( \frac{1}{n_1^2} - \frac{1}{n_2^2} \right)$$

so the inertia pressure drop can be calculated if the flow rate, the nozzle area at the entrance and the exit of the converging section, and the fluid are known.

Table II and III give the results of applying this equation to the standard nozzle. Figure 9 compares the estimated pressure versus flow to the experimental data. Only a fair comparison was obtained with the viscous losses being only half what they were measured to be. Part of the problem was found to be in the fabrication of the parts themselves. The parts were undersized (19.6 deep instead of 20 mil deep) and slightly distorted in the wide part of the channel (19.0 deep in the center and 19.6 on the edge). However this could only account for 10% of the error at most. The rest of the error was attributed to the approximation used in zone 2.

The theory did point where the losses were occurring and pointed the way to what could be done about them. The nozzle was redesigned to reduce the viscous losses by increasing the contraction ratio of the nozzle, increasing the rate of convergence and decreasing the throat length. The rate of convergence of the nozzle and the throat length were limited to values which were known to give good amplifier performance - Reference 3. The contraction ratio was limited by the process used to fabricate the nozzles (only two-dimensional shapes could be used and the wider the channel the more "sag" - center of channel shallower than edges). The new nozzle was called #15 for a 15 to 1 contraction ratio. The calculated pressure losses are shown in Tables IV and V. Figure 10 shows a comparison of calculated inviscous,

TABLE II

#11 NOZZLE

a = .020 INCH

$$-\frac{\Delta P}{Q} = 4.37 \times 10^{-4} \frac{\Delta X}{B}$$

X	Y	$\Delta X$	n	B	$-\frac{\Delta P}{Q}$	$\sum \frac{\Delta P}{Q}$
0	.010	0	1/2	.017	.000	0
.030	.010	.030	1/2	.017	.00077	.00077
.055	.014	.025	.7	.0245	.000445	.001215
.080	.0166	.025	.83	.029	.000387	.00160
.105	.026	.025	1.3	.068	.000180	.00176
.130	.0384	.025	1.92	.136	.0000805	.00184
.155	.0527	.025	2.63	.1667	.0000655	.00191
.180	.0675	.025	3.375	.2286	.0000478	.00196
.205	.0823	.025	4.11	.2899	.0000377	.00200
.230	.0945	.025	4.725	.3412	.000032	.00203
.255	.1035	.025	5.175	.379	.000029	.00205
.280	.1088	.025	5.44	.401	.000027	.00208
.580	.110	.300	5.5	.406	.000323	.00241

TABLE III

#11 NOZZLE

THEORY

P VS. Q

$$P_T = .00241 Q + .394 \times 10^{-4} Q^2$$

Q SCCM	P <sub>V</sub> IN H <sub>2</sub> O	P <sub>IV</sub> IN H <sub>2</sub> O	P <sub>T</sub> IN H <sub>2</sub> O
5	.012	.00098	.013
10	.024	.00394	.028
20	.048	.01575	.064
50	.120	.09820	.218
100	.241	.394	.635
200	.482	1.575	2.057
500	1.203	9.820	11.023

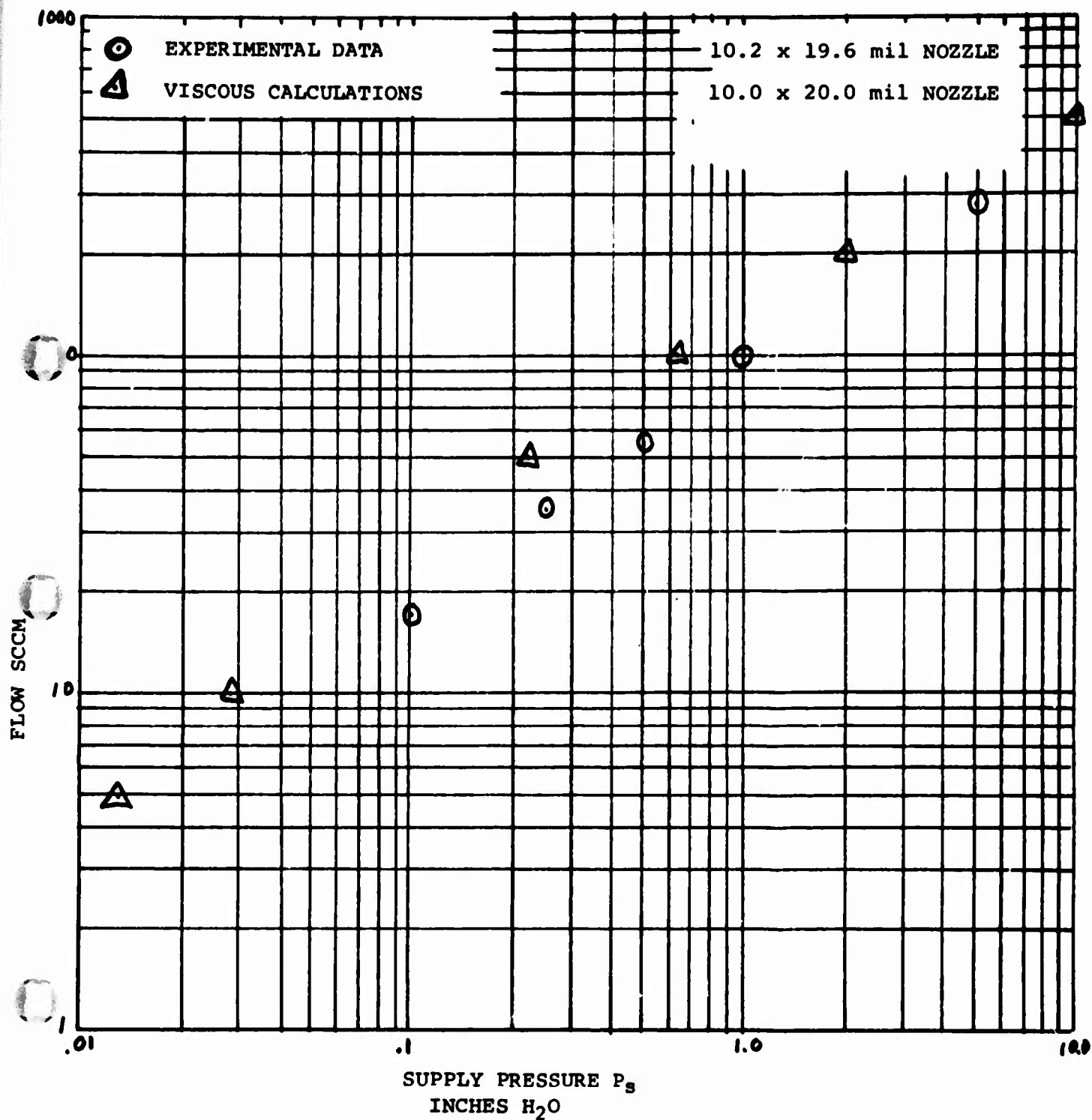


FIGURE 9

TABLE IV

#15 NOZZLE

$$-\frac{P}{Q} = 4.37 \times 10^{-4} \frac{X}{B}$$

$$a = .020$$

<u>X</u>	<u>Y</u>	<u>X</u>	<u>n</u>	<u>B</u>	<u><math>\frac{P}{Q}</math></u>	<u><math>\frac{P}{Q}</math></u>
0	.010	0	.50	.017	0	0
.010	.010	.010	.50	.017	.000257	.000257
.020	.017	.010	.85	.030	.000146	.000403
.030	.044	.010	2.2	.131	.0000334	.000436
.040	.0800	.010	4.0	.281	.0000155	.000452
.050	.118	.010	5.9	.439	.0000099	.000462
.060	.143	.010	7.15	.543	.0000080	.000470
.070	.150	.010	7.5	.573	.0000076	.000477
.580	.150	.510	7.5	.573	.000388	.000865

TABLE V

THEORY

P VS. Q

#15

$$P_T = .000865 Q + .394 \times 10^{-4} Q^2$$

<u>Q</u>	<u>P<sub>V</sub></u>	<u>P<sub>IV</sub></u>	<u>P<sub>T</sub></u>
5	.00433	.00098	.0053
10	.00865	.00394	.0126
20	.01730	.01575	.03305
50	.0433	.0982	.1415
100	.0865	.394	.480
200	.1730	1.575	1.648
500	.433	9.820	10.253

NEW NOZZLE  
ACTUAL SIZE .0012 x .0203

- EXPERIMENTAL
- △ VISCOUS THEORY
- INVISCID THEORY

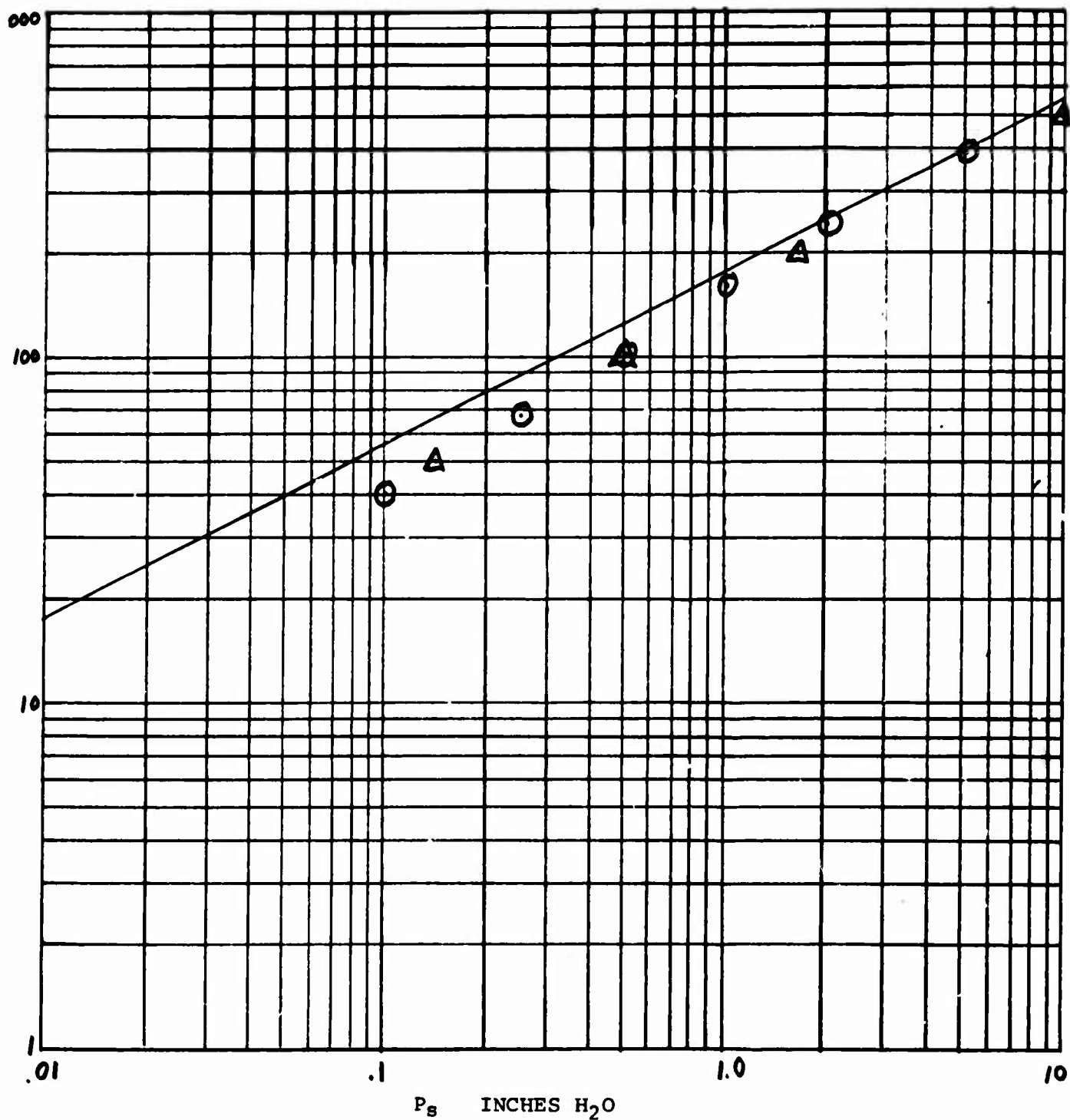


FIGURE 10

experimental and calculated viscous pressure versus flow. Very good agreement was obtained. The good agreement was attributed to the small contribution of zone 2.

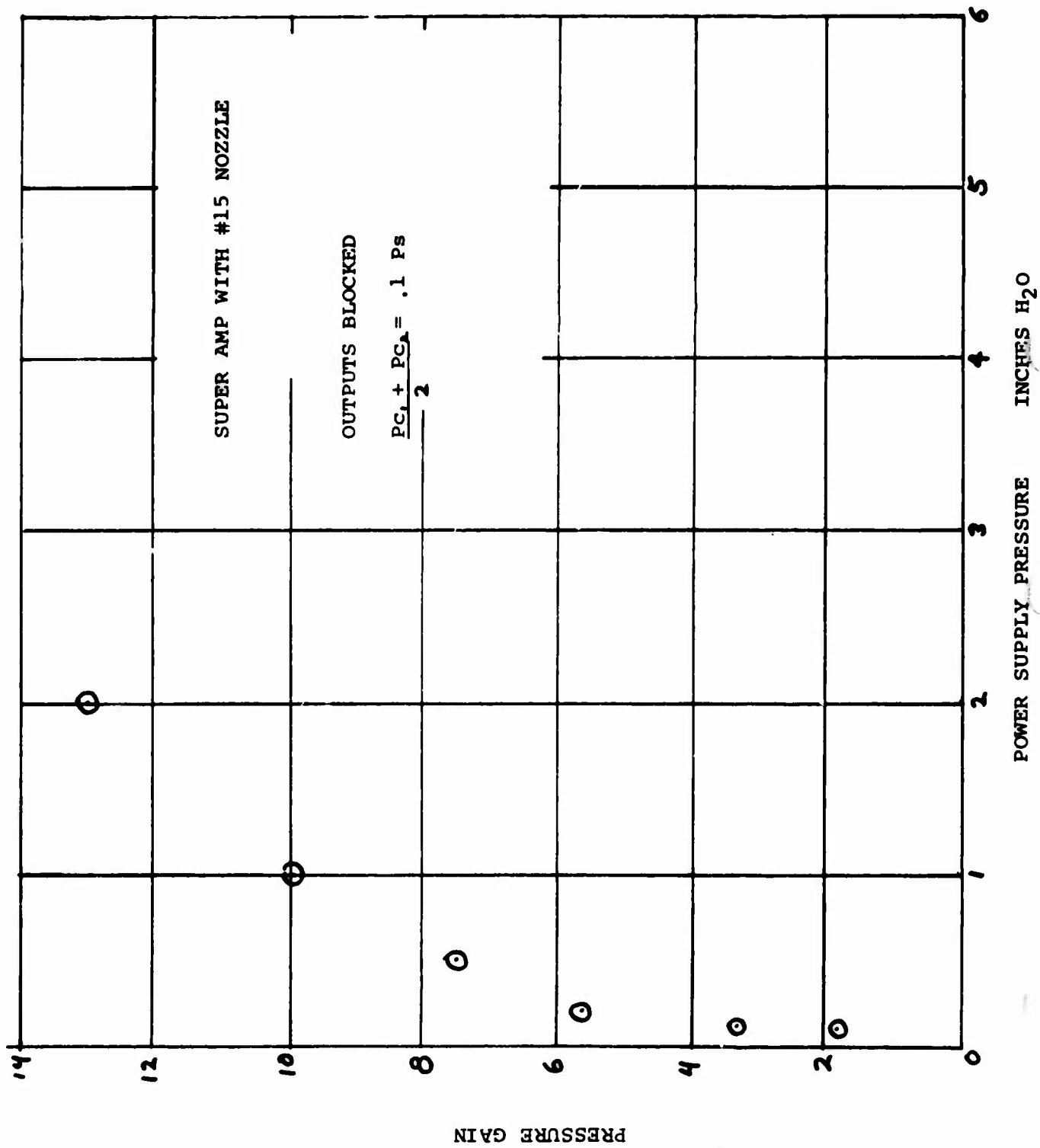
#### IV. RESULTS

The addition of the #15 power nozzle to the super amplifier resulted in improved pressure gain (figure 11) and improved peak recovery (figure 12). The pressure gain versus bias curve (figure 13) also shows some improvement. The modified amplifier allowed the fluidic air conditioner circuits to be built as described in reference 4.

#### V. CONCLUSIONS

The work performed in this paper indicates that the main cause of poor pressure recovery and poor gain in low pressure proportional amplifiers is the viscous losses in the power nozzle. The work also indicates that the viscous losses can be approximated by using the integrated form of Rouse's viscous flow solution for channel flow.





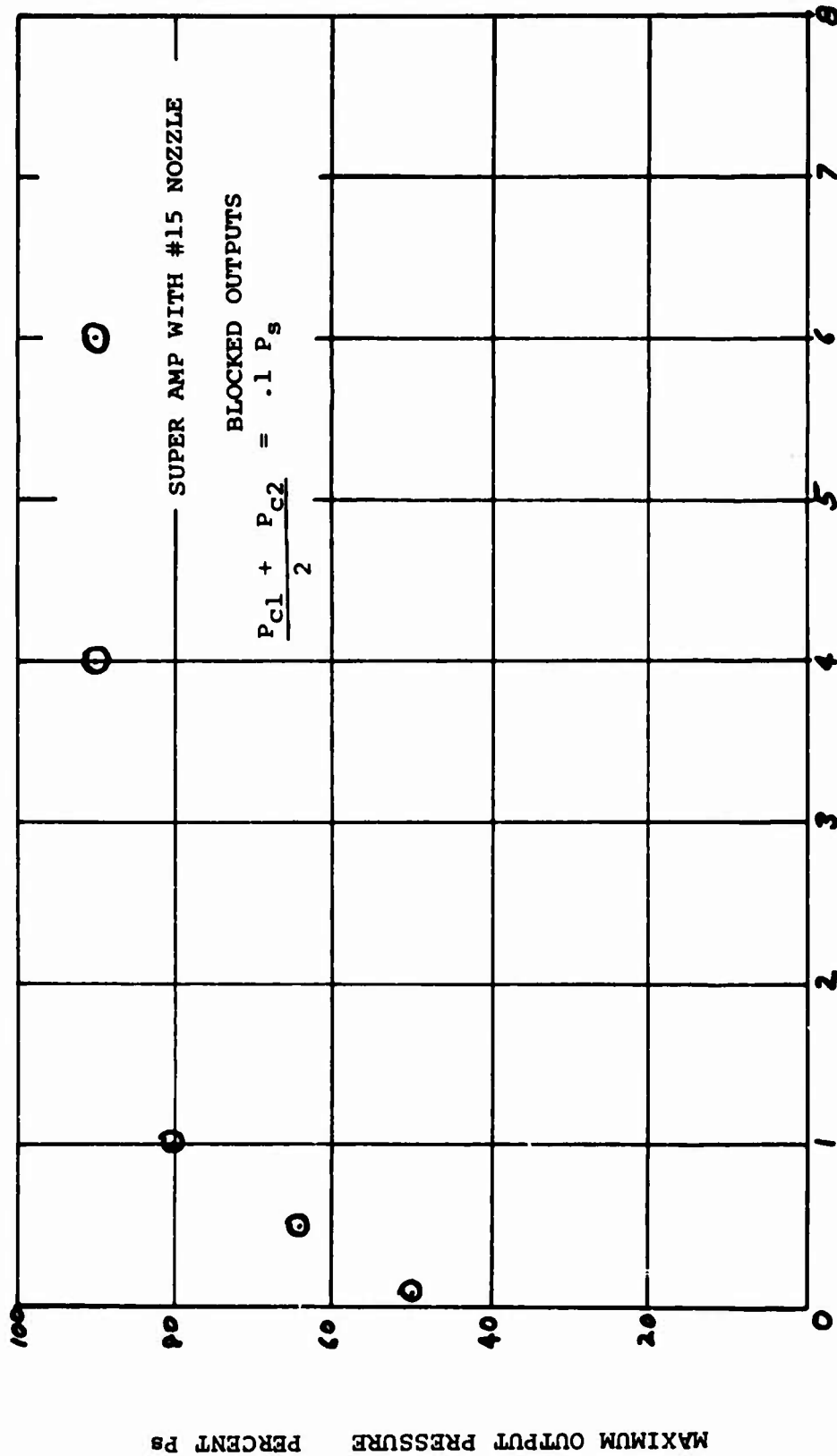


FIGURE 12

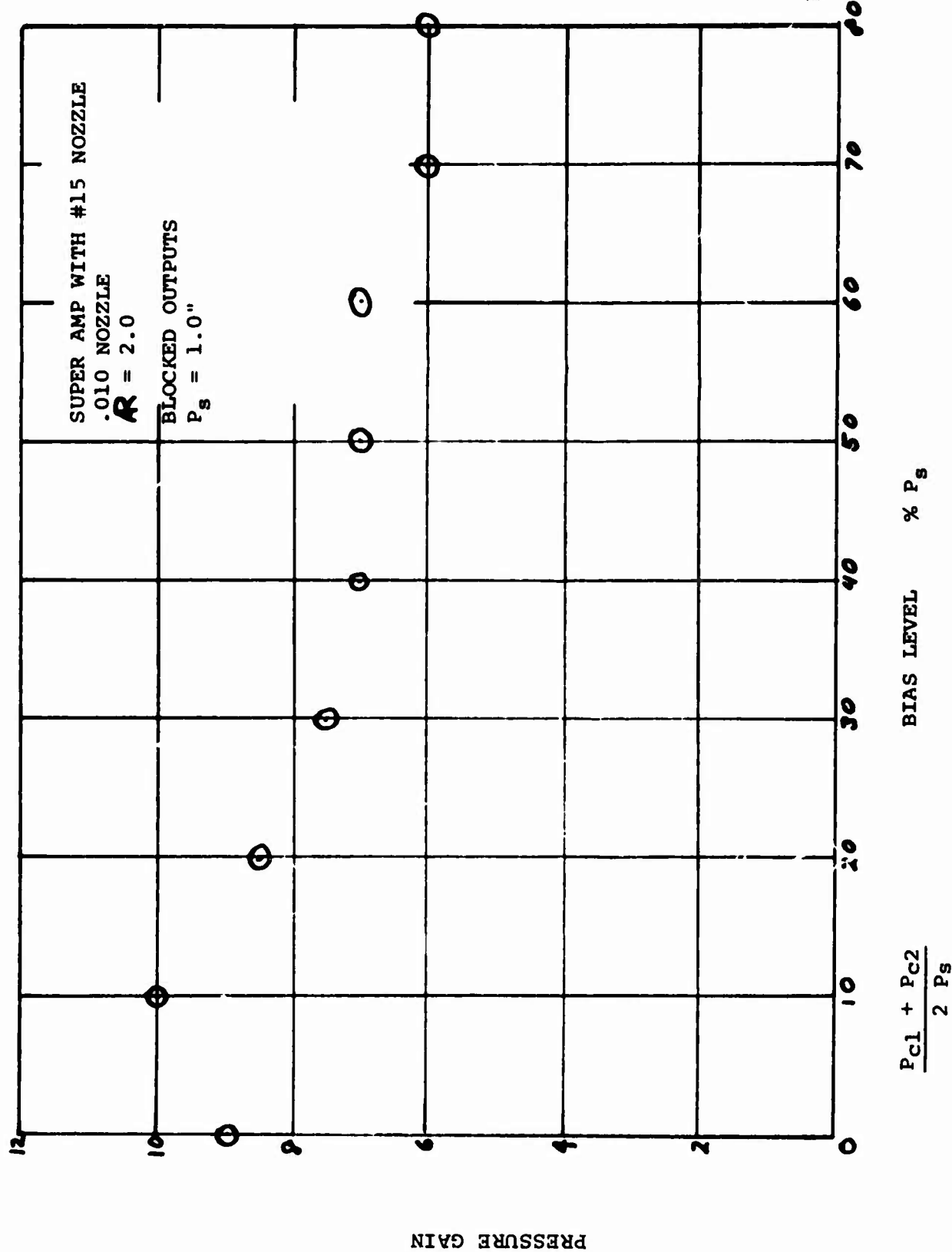


FIGURE 13

## REFERENCES

REFERENCE 1 - Effect of Reynolds Number and Nozzle Geometry on the  
Non-Turbulent Length of Free Axisym and Rectangular Jets.

by Allan Ross Werbow  
December 1966 - V.P.I.  
Master's Thesis

REFERENCE 2 - Advanced Mechanics of Fluids, .

Hunter Rouse  
John Wiley & Sons, 1959

REFERENCE 3 - Effects of the Inlet and Nozzle Geometries on the  
Performance of a Fluidic Power Nozzle

Abdulaziz Nurmohamed  
V.P.I.  
Master Thesis  
September 1973

REFERENCE 4 - Air Distribution with Fluidic Logic Control

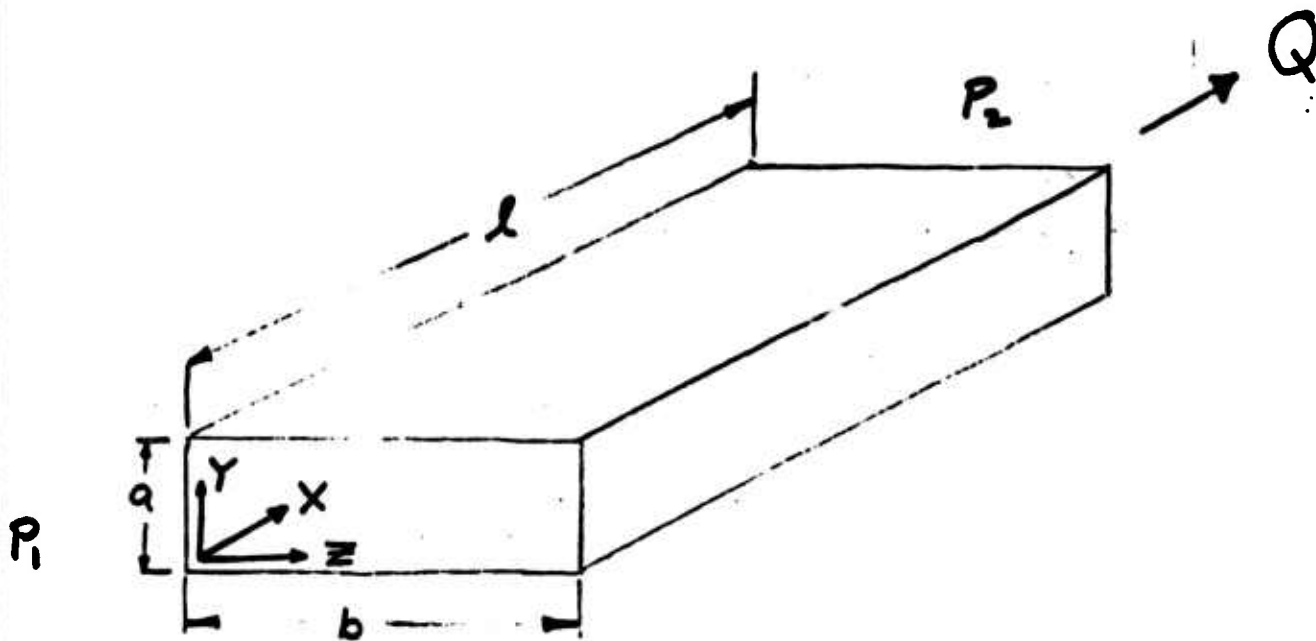
Bill Harris  
ASME Symposium of the JACC A7  
Ohio State University  
J8ne 1973

REFERENCE 5 - Boundary Layer Theory

Hermann Schlichting  
McGraw-Hill  
1960

## APPENDIX A

### CALCULATION OF VISCOUS LAMINAR FLOW LOSSES IN A RECTANGULAR CHANNEL



START NAVIER-STOKES INCOMPRESSIBLE CHANNEL FLOW

$$\frac{\partial^2 u}{\partial y^2} + \frac{\partial^2 u}{\partial z^2} = \frac{1}{\mu} \frac{dP}{dx}$$

$$n = \frac{b}{a} \quad \begin{matrix} 0 \leq y \leq a \\ 0 \leq z \leq b \end{matrix}$$

USE ROUSE'S SOLUTION - EQ 137 Page 219

$$u = \frac{1}{2\mu} \frac{dP}{dx} y(y-a) + \sum_{m=1}^{\infty} \sin \frac{m\pi y}{a} \left( A_m \cosh \frac{m\pi z}{a} + B_m \sinh \frac{m\pi z}{a} \right)$$

$$A_m = -\frac{2a^2}{\mu m^3 \pi^3} \frac{dP}{dx} (\cos m\pi - 1)$$

$$B_m = -\frac{A_m (\cosh m\pi - 1)}{\sinh m\pi}$$

INTEGRATE THE VELOCITY  $u$  OVER THE CHANNEL CROSS SECTION TO OBTAIN FLOW  $Q$

$$Q = \int_0^b \int_0^a u \, dy \, dz$$

$$Q = -\frac{a^3 b}{12\mu} \frac{dP}{dx} + \int_0^b \int_0^a \sum_{m=1}^{\infty} \sin \frac{m\pi y}{a} \left( A_m \cosh \frac{m\pi z}{a} + B_m \sinh \frac{m\pi z}{a} \right) dy \, dz$$

$$Q = -\frac{a^3 b}{12\mu} \frac{dP}{dx} + \sum_{m=1}^{\infty} \frac{a}{m\pi} (1 - \cos m\pi) \left[ \frac{a A_m}{m\pi} \sinh m\pi + \frac{a B_m}{m\pi} (\cosh m\pi - 1) \right]$$

$$Q = -\frac{a^3 b}{12\mu} \frac{dP}{dx} - \frac{2a^4}{\mu \pi^5} \frac{dP}{dx} \sum_{m=1}^{\infty} \frac{(1 - \cos m\pi)^2}{m^5} \left[ \frac{(\cosh m\pi - 1)^2}{\sinh m\pi} - \sinh m\pi \right]$$

$$Q = -\frac{a^4}{\mu} \frac{dP}{dx} \left\{ \frac{n}{12} + \frac{2}{\pi^5} \sum_{m=1}^{\infty} \frac{(1 - \cos m\pi)^2}{m^5} \left[ \frac{(\cosh m\pi - 1)^2}{\sinh m\pi} - \sinh m\pi \right] \right\}$$

COMPUTER CAN'T HANDLE  $(\cosh m\pi - 1)^2$   
SO LOOK AT

$$\left[ \frac{(\cosh m\pi - 1)^2}{\sinh m\pi} - \sinh m\pi \right]$$

OR

$$\left[ \frac{\left( \frac{e^{m\pi} + e^{-m\pi}}{2} - 1 \right)^2 - \frac{e^{m\pi} - e^{-m\pi}}{2} \left( \frac{e^{m\pi} - e^{-m\pi}}{2} \right)}{\frac{e^{m\pi} - e^{-m\pi}}{2}} \right]$$

$$= \frac{-2e^{m\pi} - 2e^{-m\pi} + 4}{e^{m\pi} - e^{-m\pi}}$$

COMPUTE

$$D = \frac{n}{12} + \frac{2}{\pi^5} \sum_{m=1}^{\infty} \frac{(1 - \cos m\pi)^2}{m^5} \left[ \frac{-2e^{m\pi} - 2e^{-m\pi} + 4}{e^{m\pi} - e^{-m\pi}} \right]$$

WHERE

$$Q = -\frac{a^4}{\mu} \frac{dP}{dx} D$$

Then

$$\frac{dP}{dx} = \frac{Q\mu}{a^4 D} \text{ or } \frac{P_1 - P_2}{L} = \frac{Q\mu}{a^4 D}$$

<u>n.</u>	<u>D</u>
1	.03503
2	.11421
3	.19736
4	.28068
5	.36402
6	.44737
7	.53070
8	.61403
9	.69737
10	.78092
11	.86425
12	.94758
13	1.03091
14	1.11425
15	1.19758
16	1.28091
17	1.36425
18	1.44758
19	1.53091
20	1.61425



DESIGN CHARACTERISTICS OF A NEW LIQUID LAMINAR

JET FLUIDIC ELEMENT

S.B. Friedman, M.Sc., Ph.D., P.Eng.  
William Rainey Harper College, Illinois

H.R. Martin, M.Sc., Ph.D., P.Eng.  
University of Waterloo, Canada

A B S T R A C T

The use of deflected laminar air jets has been avoided in fluidics because of the difficulty of maintaining laminar condition when the jet is deflected and the difficulty of satisfactory reattachment. However, a liquid laminar jet is unsubmerged and is found to have some unusual characteristics indicating excellent potential as a fluidic device.

The most significant observation is that when the main jet is interacted with a low flow control jet, it is deflected towards the control jet. This is quite the opposite action to current air jet interaction. The resultant device exhibits great stability, very high gain, and high fan out numbers. The paper describes the device and how its characteristic curves are used in circuit design.

## Introduction

When compared with conventional hydraulic control devices, fluidic elements, using liquid as the fluid medium, have significant potential advantages in that,

- (a) They have greater reliability and faster response than conventional control units.
- (b) Both size and weight are small, with no precision machining required.
- (c) Integration of fluid computing functions is feasible so eliminating electronics, i.e. in the conventional electro-hydraulic system.
- (d) Insensitivity to dust, radiation, and vibration.

The use of liquid as a fluid medium is more expensive than air, so it is important to achieve better economic return. Most air fluidic devices operate under turbulent flow conditions, and the resultant diffusion of the jet results in a poor pressure recovery. A laminar jet gives much better pressure recovery since the diffusion of the jet is much less. On the other hand both kinds of devices do require continuous power consumption and tend to be sensitive to temperature.

An investigation into the operation of a proportional fluidic device operating on oil was carried out by Kelley and Boothe (1). They introduced the concept of Reynolds coefficient

$$C_R = \mu / \sqrt{p} \quad (1)$$

as a measure of the relationship between supply pressure and Reynolds number flows. It was shown that while water and air were comparable, hydraulic oil had a very much higher Reynolds coefficient. Since this was the result, it is most desirable to operate hydraulic fluidic systems at low Reynolds numbers. The gain of such devices was shown to be a function of Reynolds number, becoming essentially constant at Reynolds numbers in excess of 1000. It was concluded that oil-operated devices were comparable to air-operated devices as far as staging and operating in circuits.

## Laminar Liquid Jet Device

The normal impingement of two jets, and the resultant deflection can be readily predicted by means of jet momentum flux interchange. However, it has been found that momentum interchange does not adequately predict the behaviour of liquid jets operating at low Reynolds numbers (2).

For the arrangements shown in Figures 1 and 2, it was discovered that when an axisymmetric emitter jet operates in the laminar region, the jet could not only be deflected away from the control jet, Fig. 1, but using low control jet flow rates, it could be deflected towards the control jet, Fig. 2.

The following explanation is offered for this unusual jet deflection technique. Consider that for the condition shown in Fig. 2, an additional force system is present to overcome the momentum flux of the control flow  $J_c$ . As hypothesized by Lighthill (3) and Keller (4), this force system must result from pressure differences across the jet in the interaction region. Douglas and Neve (5), and Sarpkaya, et al. (6) both identified the fact that within the interaction region, and for a distance of approximately four diameters downstream, the control and emitter jets maintain their individual integrities. Brown and Belen (7) verified this and showed that a low total pressure region of the profile represented the control flow within the interaction region. The photograph shown in Fig. 3 seems to support this view. It can be seen that the flow path of the main jet appears to be longer on the control side than on the atmospheric side, resulting in higher velocity and lower pressure. This seems to substantiate Lighthill's and Keller's hypotheses.

It has been shown in (2) that the control equation is

$$\tan \theta = \frac{(K_1 - R_c^2)}{R_s^2} \quad (2)$$

The value of  $K_1$  is found experimentally. This concept was used to design a liquid jet fluidic NOR gate operating in the Reynolds number range 1000 to 1800 for the emitter jet and 50 - 150 for the control jet. This results in a device with extremely high gain, efficiency, and low power consumption. The final design arrangement is shown in Fig. 4.

It has been stated in (2) that the switching time of a laminar jet device should be function of the velocity of the main jet and the distance from the interaction region to the receiver mouth.

$$t = K_2 (L d / v R_s) \quad (3)$$

Pressure recovery is also an important factor, and it has been shown in (3), that the pressure recovery of an undeflected jet is

$$p_r = K_3 (\mu_s^2 / \rho_s) (R_s / d)^2 \quad (4)$$

While the pressure in the receiver is an important consideration in itself, the ratio of the pressure in the receiver to that required to assure control flow is at least as important, since this gives an indi-

cation of the number of elements that may be driven by one master element. Fan out may be based on the pressure in a receiver and the pressure required in the controls of the next elements,  $p_r/\Delta p_c$ . Since the flow required in the control passages is extremely low, it is reasonable to assume that it would be fully or very nearly fully developed laminar flow, hence

$$\Delta p_c = f \frac{1}{d} \frac{\rho_c \bar{u}_c^2}{2} = \frac{32L}{d_c} \left(\frac{\mu_c}{d_c}\right)^2 \left(\frac{R_c}{\rho_c}\right) \quad (5)$$

giving

$$\frac{p_r}{\Delta p_c} = K_3 \left(\frac{d_c}{L_c}\right) \left(\frac{R_c}{\rho_c}\right)^2 \quad (6)$$

if the flow passages are of common diameter.

The ideal fluidic element should have minimum input power requirements, minimum size, fastest switching speeds and highest pressure recovery; coupled with the highest insensitivity to contamination and the broadest possible operating range of Reynolds number. For constant diameters of flow passages, the first five of these parameters may be expressed

$$p \propto R_s^3 \quad (7)$$

$$L \propto (R_s/R_c)^2 \quad (8)$$

$$t \propto R_s^{-1} \quad (9)$$

$$p_r/\Delta p_c \propto R_s^2/R_c \quad (10)$$

$$c \propto \text{diameter of particle}/d \quad (11)$$

Unfortunately, these parameters, when considered together, result in a typical engineering paradox. The larger the size of the flow passage, the lower the power requirement for an equivalent Reynolds number and the lower the susceptibility to contamination of the working fluid. However size, speed, and pressure recovery are adversely affected.

It is therefore clear that there does not appear to be a single combination that will permit the maximization of all parameters. It

therefore becomes necessary to assign priorities to operating characteristics and optimise the design so as to produce the best combination. These results are presented in subsequent graphs.

#### Operational Characteristics

The angular deflection of the laminar jet is defined in equation 2, while the experimental results are shown in Fig. 5. The experimental set up is shown schematically in Fig. 6. This results in a value for  $K_1$  of  $2.97 \times 10^5$  for water. It was felt that for design purposes, the data could be presented in a much more useful form by plotting control and main jet Reynolds numbers for various deflection angles. These experimental results are shown in Fig. 7.

Switching times plotted against main jet Reynolds number or various angular deflections required to switch the device OFF, are shown in Fig. 8. The fluid used was water at 60°F with element passage diameters of 0.020 in. Repeating this experiment with hydraulic oil (MIL-H-5606) Fig. 9, indicates that the switching speed of the device, when operated on oil 100°F is at least as fast as most conventional air fluidic devices. In relation to equation (3),  $K_2$  can be approximated to  $0.5 S_c$ .

It is convenient to express pressure recovery characteristics as shown in Fig. 10. Analysis of these results show that in relation to equation (4)

$$K_3 = \frac{11.22 (L_s/d)^{0.14}}{R_s^{0.8}} \quad (12)$$

The pressure factor characteristics are shown in Fig. 11.

#### Application of Operational Characteristics to Design

Consider a logic control system. The specification requires that the working fluid be water and that the switching time be equal or less than 8 milliseconds.

The design procedure would be:

(a) Examination of Fig. 8 shows that a switching time of 8 ms. using a device with passage diameters of 0.02 in. requires a main jet Reynolds number of 1670 for a 6° deflection at the design line. The design line indicates the boundary of usable control flow Reynolds number.

(b) From Fig. 7, a  $6^\circ$  deflection at Reynolds number of 1670 results in a control Reynolds number requirement of less than 95. This is the minimum acceptable for reliable operation.

(c) From Fig. 11 for

$$R_c = 90, d = 0.02, L/d = 10 \text{ and } R_s = 1670$$

a pressure factor of around 150 results.

(d) In determining the size of the device reference is made to Fig. 4

$$d = 0.02 \text{ in.}, L_s = L_c = 0.2 \text{ in.}, m = 0.04 \text{ in.}$$

$$n = 0.030/0.035, \ell = d \cot \theta = 0.191 \text{ in.}$$

The receiver length,  $L_r$ , should be as short as possible and should expand quickly and smoothly to minimize pressure losses.

### Conclusions

This research has resulted in a fluidic device, with many unique features in its performance. In particular the high gain, high fan out and low power consumption in relation to other attempts to build liquid fluidic elements. Table 1 shows a comparison of its performance with the conventional air turbulence amplifier.

Table 1

	Turbulence Amplifier	Laminar Device
Function	NOR	NOR
Fluid	AIR	Water
Supply nozzle area	$23 \times 10^{-5} \text{ in.}^2$	$31 \times 10^{-5} \text{ in.}^2$
Supply pressure ( $P_s$ )	$1-1.6 \text{ lbf/in.}^2$	$1-4 \text{ lbf/in.}^2$
Supply flow ( $Q_s$ )	$0.01 \text{ scfm at } P_s = 1.25$	$0.002 \text{ cfm at } P_s = 2.0$
Fan out	$1-4^*$	18
Minimum input	$0.09 \times P_s$	$0.05 \times (Q_s)$
Minimum output	$0.15 \times P_s$	$0.98 \times (Q_s)$
Response <sup>+</sup>	500 for $1^*$ ; 150 for $4^*$	100 $H_z$
Size (in)	$1.4 \times 0.8 \times 0.1$	$0.88 \times 0.5 \times .31$

\* Element response varies with fan out

<sup>+</sup> Liquidic device gains significantly on circuit response

The devices that have been in operation have varied in size from 0.14 in<sup>3</sup> (comparable with the smallest air fluidic unit) to 14.6 in<sup>3</sup>. No doubt even larger units are feasible. When operated using hydraulic oil, the device compares favourably with air fluidics, with respect to speed of response. A water medium results in an order of magnitude slower response. However since the device does not usually operate in isolation, but rather with groups of elements, signal transmission times must be considered. Therefore, with respect to systems, liquid fluidics can have a faster operating time than equivalent air units

While no production models have been designed, the device lends itself to both a low cost stamped fram and tubing construction, as well as a planar version which could be moulded using a rigid plastic. Prototypes were machined at labor costs of less than \$0.50 each, with tooling amounting to less than \$200.00. While both stamping and forming dies, and injection moulds are not cheap, they are certainly reasonable if adequate sized production runs are considered.

#### Acknowledgements

The authors wish to acknowledge the financial support of the National Research Council of Canada, under grant number A7729.

### Symbols

C	=	Contamination factor
$c_R$	=	Reynolds coefficient
d	=	Tube diameter (in)
J	=	Momentum flux
K	=	Constant (as required)
L	=	Passage length (in)
$\ell$	=	Free jet length from control to receiver (in)
n	=	Distance from control nozzle to main jet (in)
P	=	Power
p	=	Pressure lbf/in
R	=	Reynolds number, based on average velocity
$S_t$	=	Strouhal number
t	=	Switching time (sec)
$\bar{u}$	=	Mean axial jet velocity (in/sec)
$\theta$	=	Jet deflection angle (deg)
$\nu$	=	Kinematic viscosity (in <sup>2</sup> /sec)
$\rho$	=	Density (lbf sec <sup>2</sup> /in <sup>4</sup> )
$\mu$	=	Absolute viscosity

### Subscripts

c	=	control
o	=	output
r	=	receiver
s	=	supply



### References

1. Kelley, L.R. and Boothe, W.A., "Hydraulic Fluidics", Paper 68WA/FE26, ASME Winter Meeting, December 1968.
2. Friedman, S.B., "An Experimental Approach to the Design of a New Control and Instrumentation Device using Liquids Operating at Low Reynolds Numbers", Ph.D. Thesis, University of Waterloo, Ontario, 1973.
3. Lighthill, M.J., "Notes on the Deflection of Jets by Insertion of Curved Surfaces, and on the Design of Bends in Wind Tunnels", Aeronautical Research Council Reports and Memoranda, No. 2105, September 1945.
4. Keller, J.B., "Teapot Effect", Journal of Applied Physics, Vol. 28, No. 8, August 1957, pp. 859-864.
5. Douglas, J.F. and Neve, R.S., "Investigation into the Behaviour of a Jet Interaction Proportional Amplifier", Paper C3, 2nd Cranfield Fluidics Conference, Cambridge, 1967.
6. Sarpkaya, T., Weeks, S.B. and Hiriart, G.L., "A Theoretical and Experimental Investigation of the Interaction of Jets in Beam-Deflection Type Fluidic Elements", Paper B3, 4th Cranfield Fluidics Conference, Coventry, 1970.
7. Brown, E.F. and Belen, F.C., "Jet Interaction in a Simplified Model of a Bistable Fluid Amplifier", Paper 72-WA/Flcs-6, ASME Winter Meeting, November 1972.

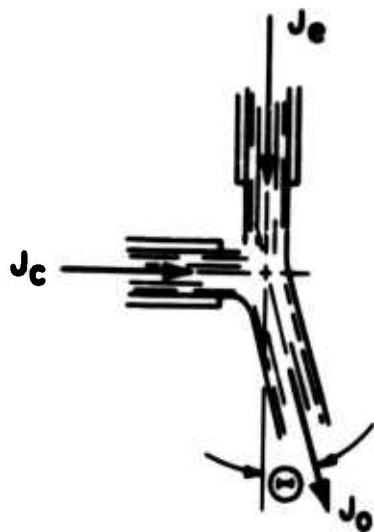


**Fig. 1 CONVENTIONAL MOMENTUM  
FLUX INTERCHANGE**

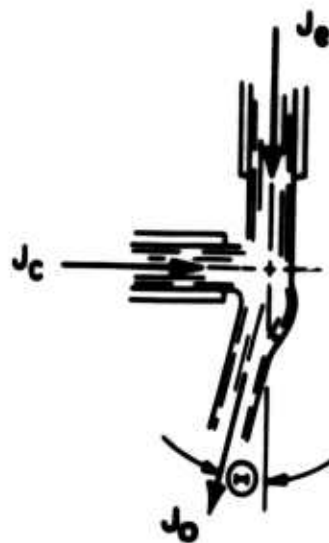


**Fig. 2 APPARENT MOMENTUM  
FLUX INTERCHANGE**



Figure 3 Interaction region of laminar jets.

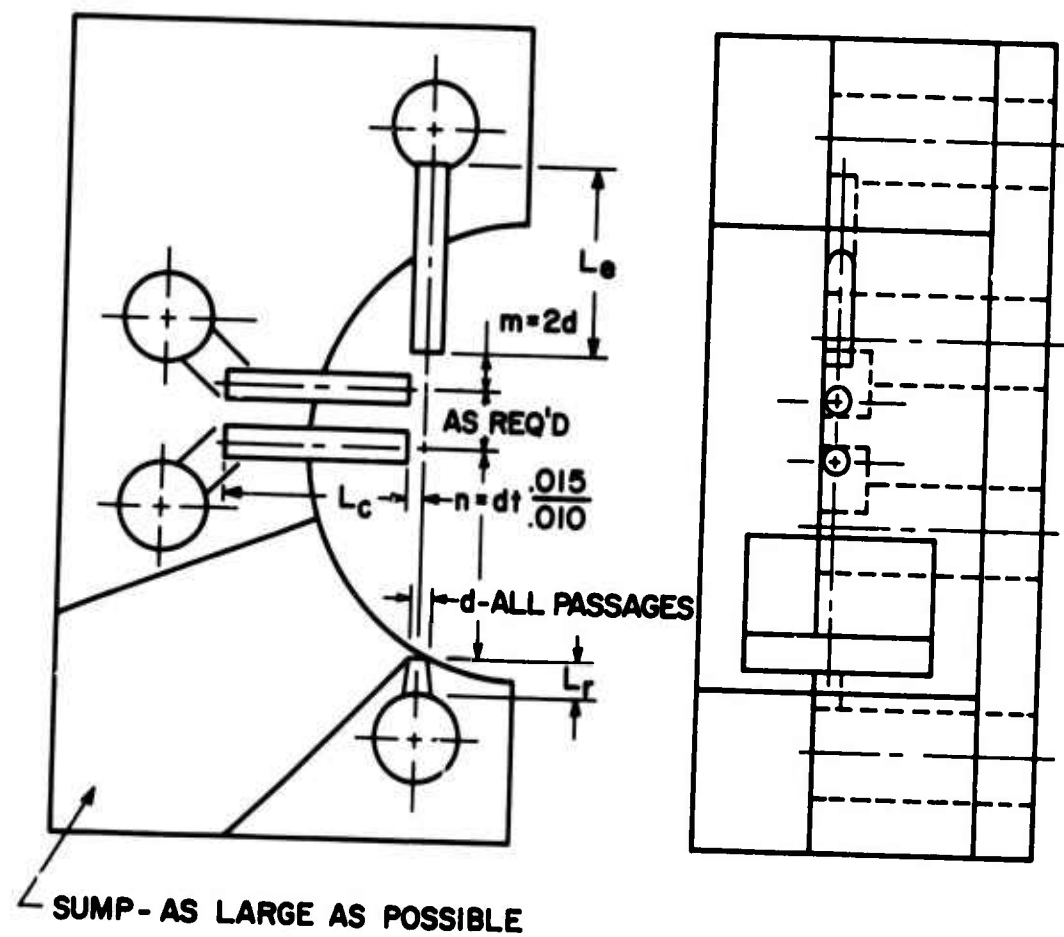


Fig. 4 DETAILS OF THE LIQUID FLUIDIC DEVICE

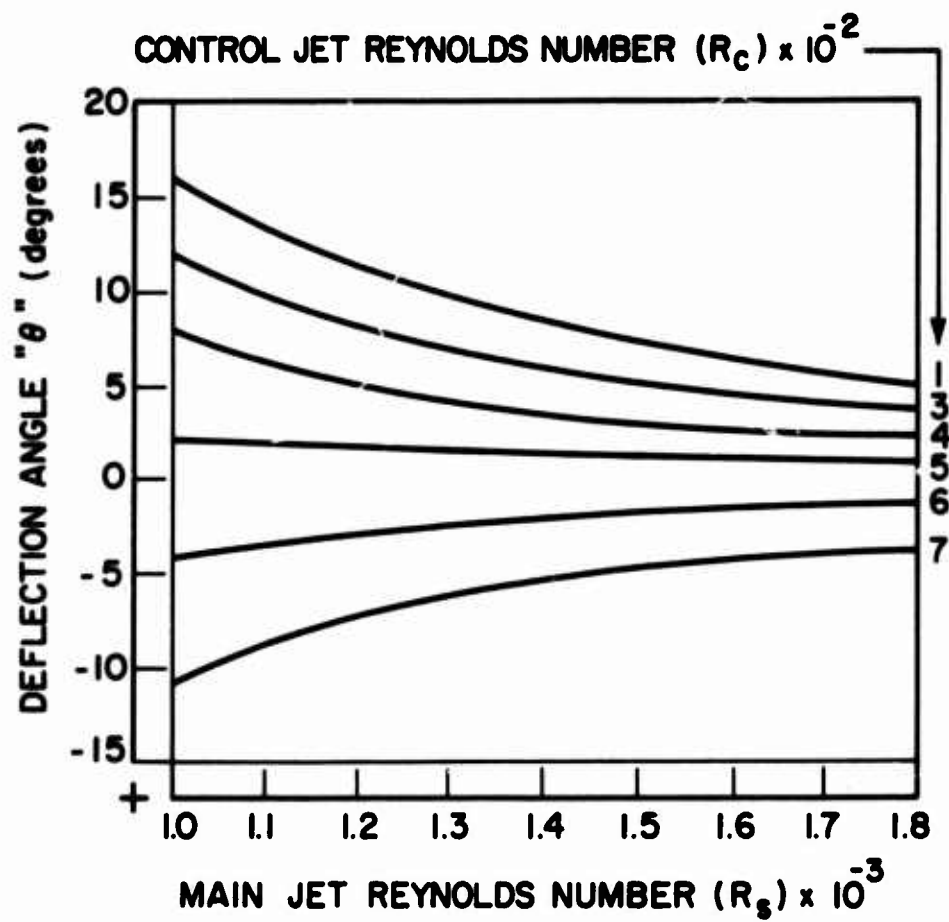
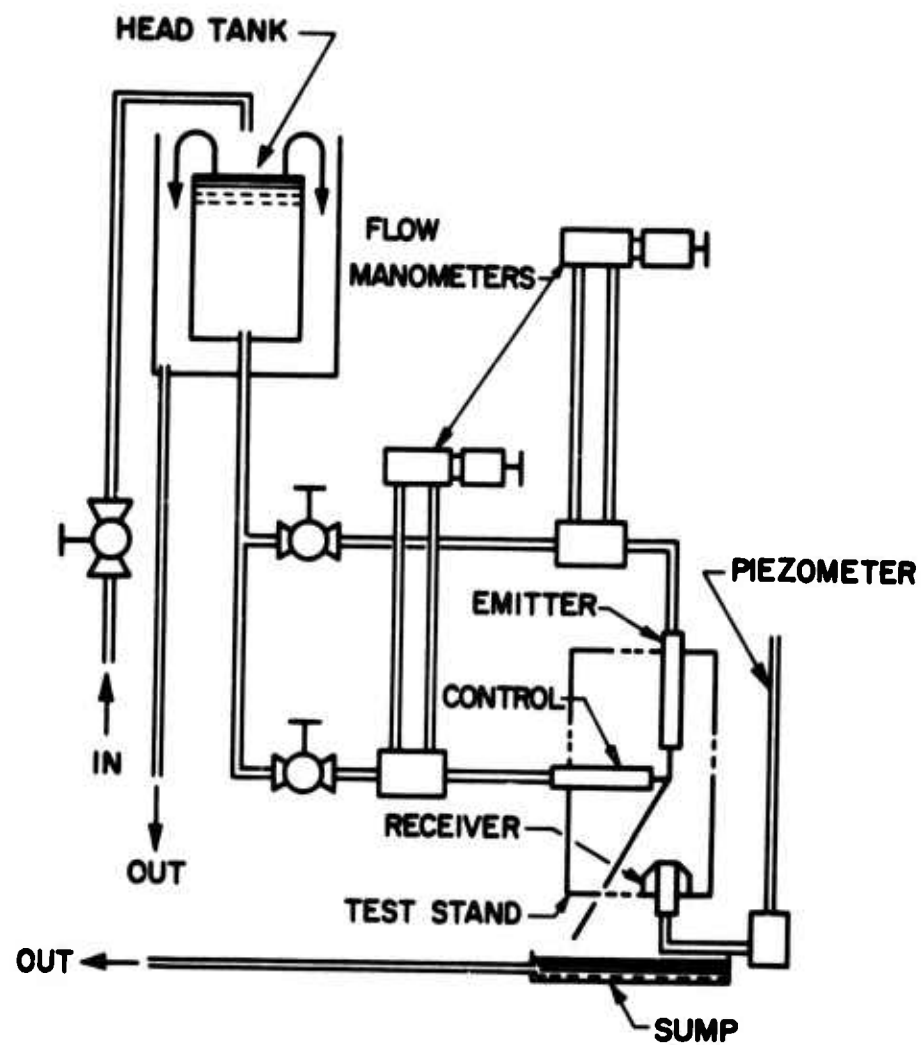


Fig. 5 DEFLECTION CURVES FOR LIQUID FLUIDIC DEVICE



**Fig. 6** SCHEMATIC OF EXPERIMENTAL SET UP FOR DETERMINATION OF ANGLE OF DEFLECTION OF LIQUID FLUIDIC DEVICES

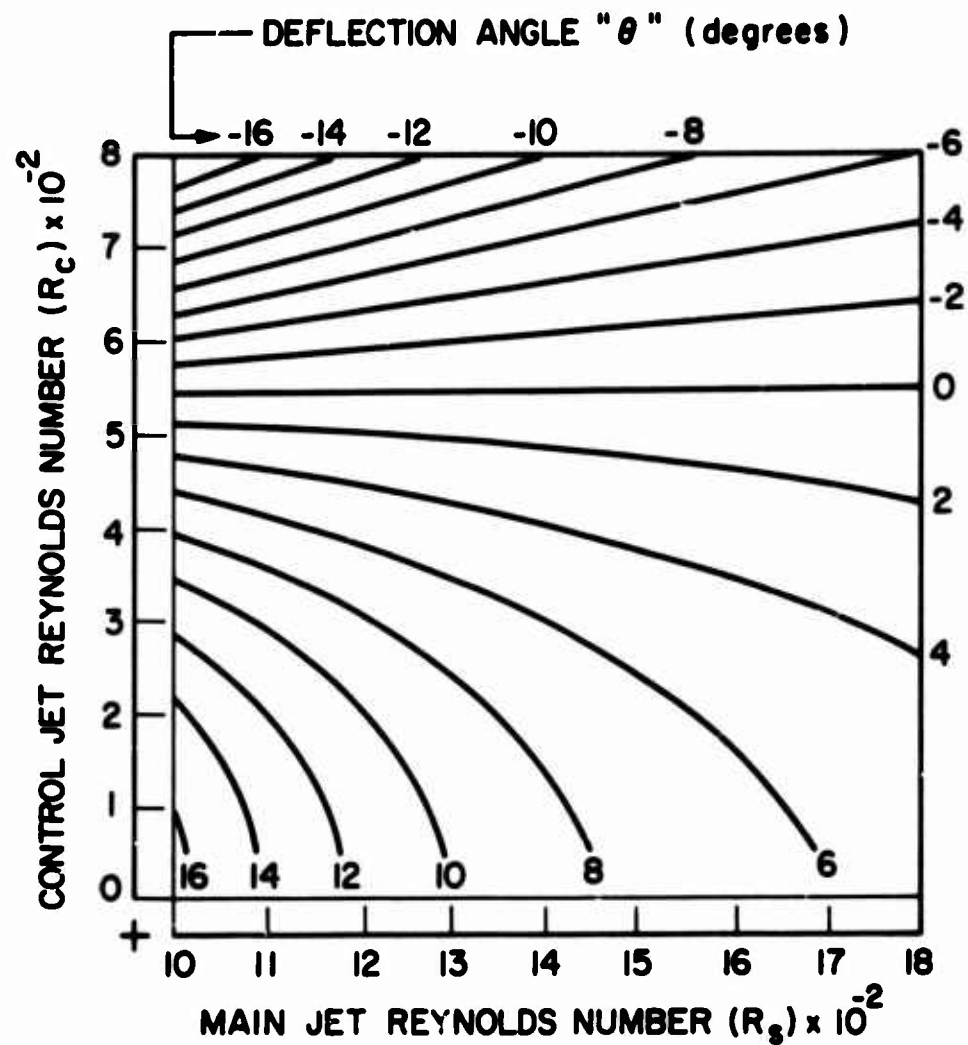
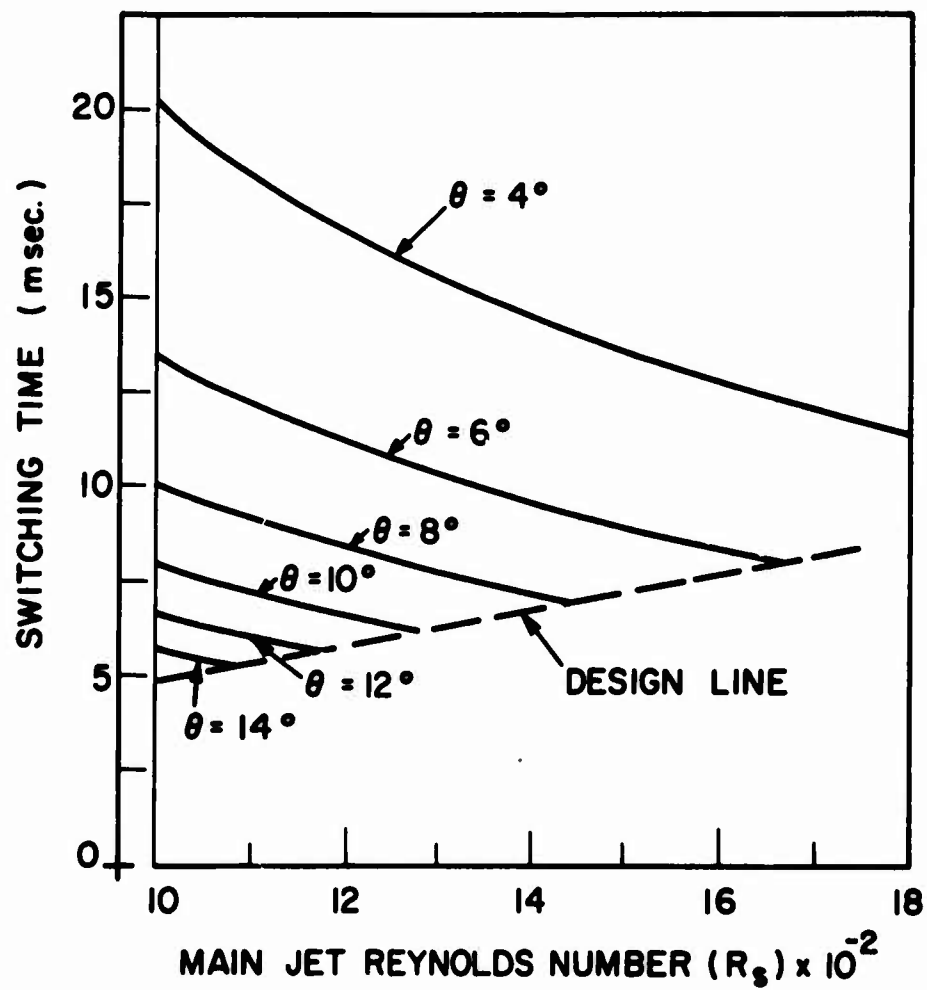


Fig. 7 CONTROL AND EMITTER FLOWS REQUIRED TO DEVELOP GIVEN DEFLECTION ANGLES IN LIQUID FLUIDIC DEVICES



**Fig. 8 INTERNAL SWITCHING TIMES FOR VARIOUS ANGULAR DEFLECTIONS USING WATER AS THE FLUID.**



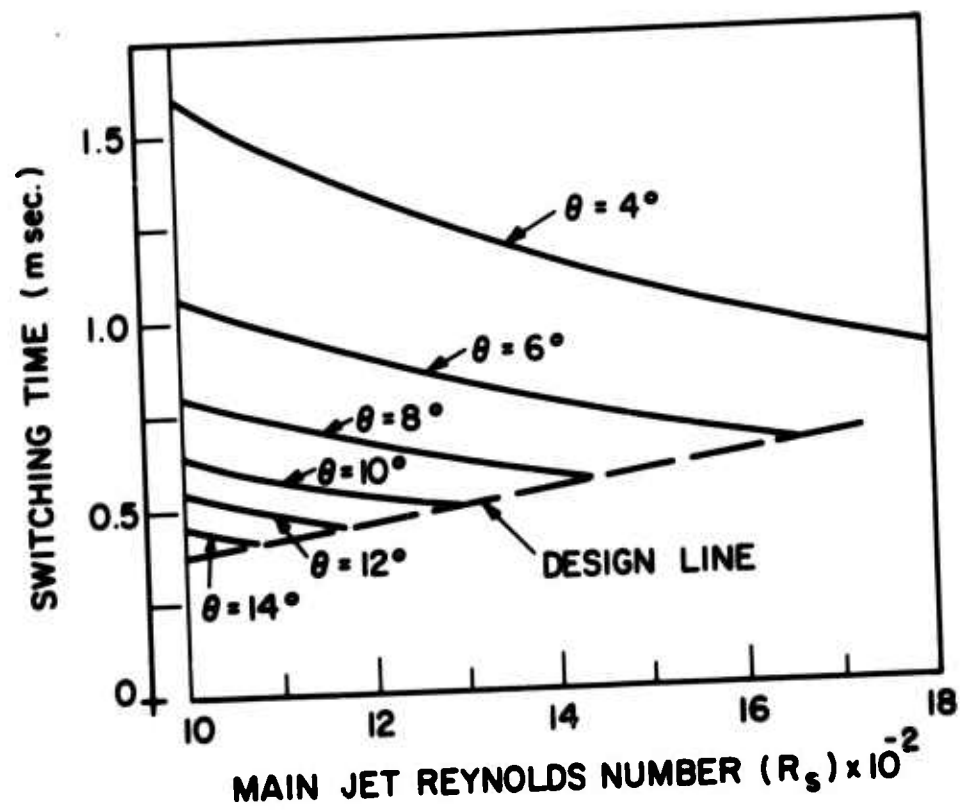


Fig. 9 INTERNAL SWITCHING TIMES FOR VARIOUS ANGULAR DEFLECTIONS USING MIL-H-5606 HYDRAULIC OIL AS THE FLUID.

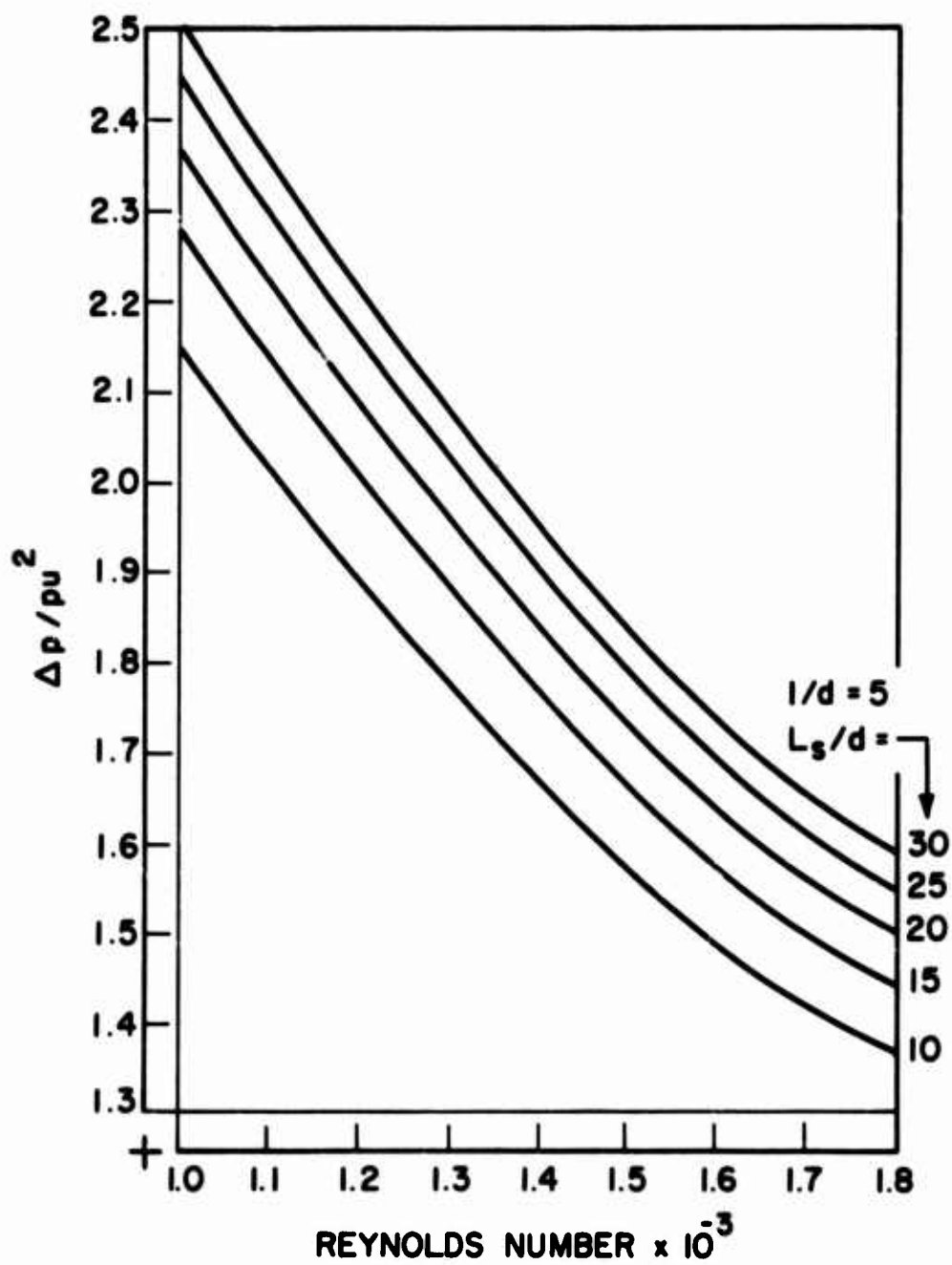


Fig. 10 ADMITTANCE CURVES FOR PRESSURE RECOVERY  
USING FREE JET LENGTH OF 5 JET DIAMETERS

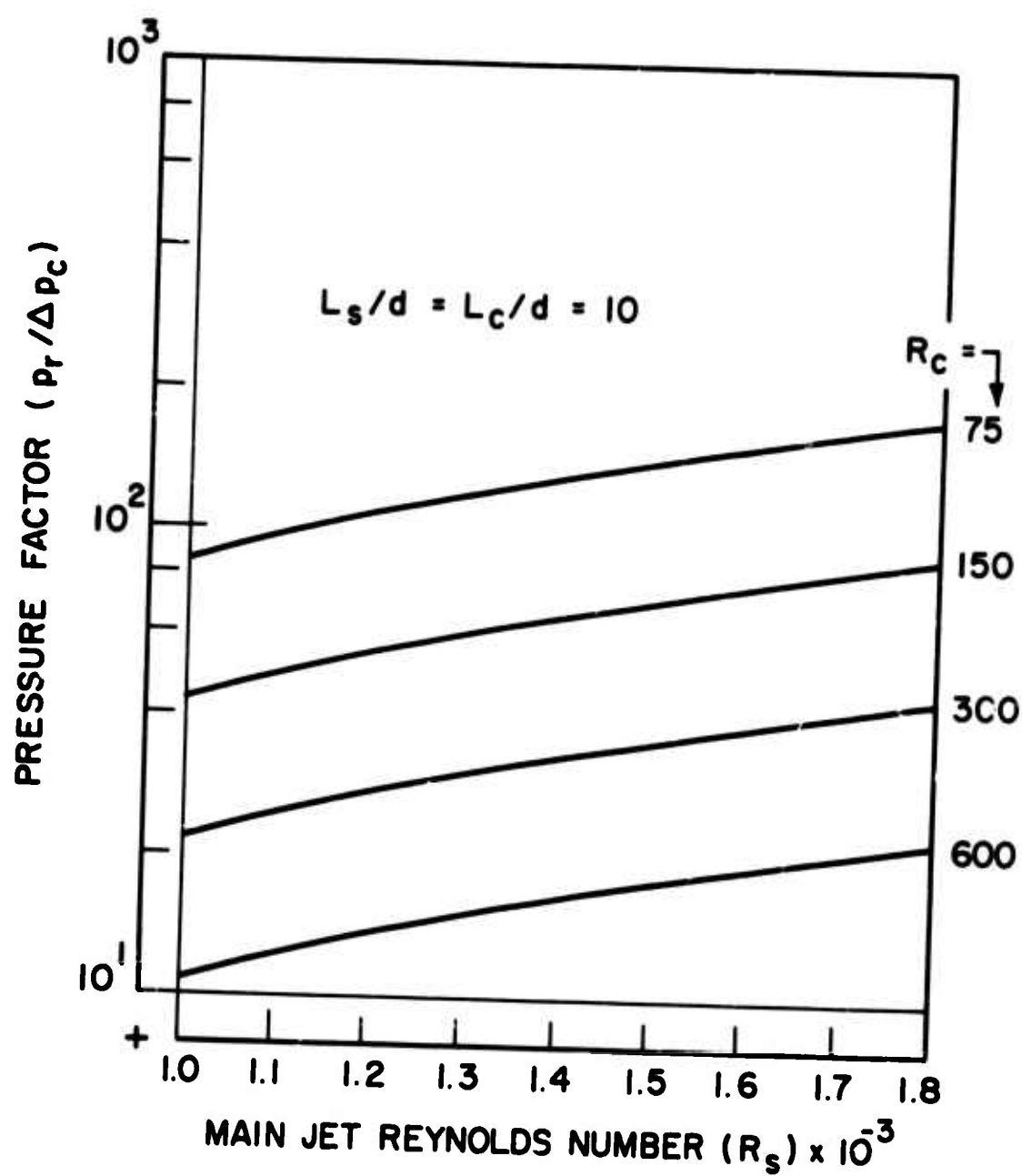


Fig. II PRESSURE FACTOR (GAIN) OF LIQUID FLUIDIC DEVICE FOR CONTROL PASSAGE LENGTH OF 10 JET DIAMETERS

**THE EFFECT OF GEOMETRIC AND FLUID PARAMETERS ON STATIC  
PERFORMANCE OF WALL-ATTACHMENT-TYPE FLUID AMPLIFIERS**

**H. L. Mozes**

**Department of Mechanical Engineering  
Virginia Polytechnic Institute and State University**

**R. A. Comparin**

**Department of Mechanical Engineering  
Newark College of Engineering**

The current state-of-the-art in relating the geometry and fluid parameters to the static performance characteristics of wall-attachment-type fluid amplifiers is reviewed. The basic concepts involved in available analytical approaches are outlined with some experimental results. The effect of these parameters on amplifier performance is summarized, with reference to the analyses and experiments.

# SYMBOLS

$A_n$	Nozzle area
$A_{eff}$	Effective area for flow
$b_c$	Control nozzle width
$b_o$	Receiver width
$b_s$	Power nozzle width
$b_{sp}$	Splitter width
$b_v$	Vent width
$c$	Distance to virtual origin of jet
$c_p$	Specific heat at constant pressure
$C_d$	Discharge coefficient
$d$	Attachment wall offset
$h$	Amplifier depth
$J$	Jet momentum flux per unit depth
$J_r$	Momentum returned upstream at attachment
$k$	Ratio of specific heats for a gas
$N_r$	Reynolds number based on nozzle width
$M$	Mach number
$L_n$	Overall nozzle length
$\dot{m}$	Mass flow rate
$p_a$	Pressure outside of attached jet
$p_b$	Pressure in separation bubble
$p_c$	Control pressure
$p_{c'}$	Pressure at control nozzle exit
$p_s$	Supply pressure
$p_l$	Pressure at nozzle exit
$Q$	Volume flow rate
$Q_c$	Control flow
$Q_e$	Flow entrained by jet from separation bubble
$Q_r$	Flow returned to separation bubble at attachment
$Q_s$	Supply flow
$Q_l$	Volume flow at nozzle exit

$Q_2$	Volume flow at attachment
$R$	Radius of jet centerline
$s$	Distance along jet centerline
$s_2$	Distance along jet to attachment
$T_s$	Supply temperature
$u$	Velocity at any point in jet
$u_m$	Maximum velocity in jet
$V_1$	Jet exit velocity
$x$	Distance parallel to power nozzle centerline
$x_2$	Attachment distance
$x_L$	Attachment wall length
$x_s$	Splitter distance
$y$	Distance normal to jet
$\alpha$	Attachment wall angle
$\beta$	Initial angle of jet
$\eta$	Similarity parameter
$\theta$	Attachment angle
$\nu$	Fluid kinematic viscosity
$\rho$	Fluid density
$\sigma$	Aspect ratio, $h/b_c$
$\sigma_E$	Jet spread parameter
$\phi$	Diffuser angle

## INTRODUCTION

The fluid amplifier is usually described as a relatively simple device with no moving parts. From a fluid dynamics point of view, however, the relation between the geometry of the device and its performance is not at all simple. Many of the basic fluid mechanics problems, such as turbulent, three-dimensional, and separated flow, are involved. Since the performance of the device is affected by these phenomena, a complete analysis of the flow, starting from the fundamental equations of motion, is practically impossible. On the other hand, because there are a large number of variables involved, many of which are not independent, a completely experimental approach is also extremely difficult.

The relation between gate geometry and performance is important in design, manufacture, and, to some extent, in intelligent use of fluidics. Although there are a number of quite satisfactory fluidic components available, further design work will always be needed for new and improved devices. For example, existing designs can be improved for manufacturability and resistance to environmental conditions, such as contamination. Even with established designs, a knowledge of the effect of dimensional variations is important to the manufacturer. Furthermore, the basic problems associated with fluidics are not completely unique, and a better understanding of these problems is important in the design of any device that involves fluid flow.

In the early development of fluidics, like most new devices, the design approach was primarily trial and error with, at best, a qualitative understanding of the phenomena involved. During this development, however, a large amount of research has been devoted to fluidics, making use of years of research in related areas of fluid mechanics. As a result, a much better understanding of the relation between geometry and performance has been developed, and effective designs can be achieved with a small amount of trial and error. However, experience is still an important factor in design, and further research is definitely of value.

The purpose of this paper is to review the present understanding of the relation between the geometry, fluid parameters, and static characteristics of the wall-attachment type, digital fluid amplifier. It is not intended as a complete bibliography of all of the past work in this area, but rather as a summary of the current state-of-the-art. With this objective in mind, the basic ideas involved in the analytical approaches are reviewed along with some experimental results, and finally the effects of fluid and geometric variables on static performance are summarized.

## ANALYSIS

A number of analyses have been developed for various aspects of the flow in fluid amplifiers, including approximate models for the complete device. These analyses involve some empiricism, but are based on fundamental concepts and do correlate experimental data. The extent to which they are used directly in design depends on the individual designer, but in any case they are useful in understanding the flow and in interpreting the experimental results.

Since several analytical models have been developed that differ mainly in the approximations used, only the basic concepts are outlined here. Specific details are intended as examples, not recommended procedures. Furthermore, the discussion is limited to the static characteristics of typical wall-attachment-type devices such as those shown in Fig. 1.

### Nozzle Characteristics

The nozzle is an essential element in many fluidic devices. It forms the main jet as well as determining the power consumption and control impedance.

The flow is usually assumed one-dimensional and inviscid except along the walls, or boundary layers. Then, for incompressible flow, the exit velocity is given by

$$v_1 = \sqrt{\frac{2(p_s - p_1)}{\rho}} \quad (1)$$

For compressible, isentropic flow

$$v_1 = \sqrt{2c_p T_s \left[ 1 - \left( \frac{p_1}{p_s} \right)^{\frac{k-1}{k}} \right]} \quad (2)$$

The flow rate is

$$Q = C_d A_n v_1, \quad (3)$$

and

$$\dot{m} = \rho Q.$$

Equations 1 and 2 give approximately the same result for a gas, such as air, at low pressures. For the results shown in Fig. 2a, the density in equation 1 is based on downstream conditions.



For the power nozzle in a wall-attachment device, the exit pressure is usually assumed atmospheric, but it is slightly less with no control flow and increases with control flow to approximately five percent of the supply pressure at switch. Control nozzles are usually vented, as shown in Fig. 1, and the assumption of atmospheric exit pressure is valid in this case. (For choked compressible flow, the exit pressure is fixed by the sonic condition.)

The discharge coefficient  $C_d$  can be estimated as a function of the Reynolds number  $N_R$  and aspect ratio  $\sigma$  as described in reference 1. However an approximate value of 0.85-0.90 is usually sufficient.

The Reynolds number is usually based on the nozzle width  $b$ .

$$N_R = \frac{V_1 b}{\nu} \quad (4)$$

Some authors have chosen other lengths, such as nozzle height  $h$ , as being more significant. However, Reynolds similarity only holds for geometrically similar devices with similar boundary conditions and incompressible flow.

Although some devices operate at lower Reynolds numbers, a lower limit for typical wall-attachment gates is approximately 1500. The upper limit in the nozzle is set by choking (approximately 7000 for a 0.25 mm nozzle with air) but higher values are achieved in the jet with further expansion.

Power consumption is usually calculated at the nozzle. For low pressures (incompressible flow),

$$\text{Power} = A_n V_1 p_s \propto A_n V_1^3.$$

This result leads to the conclusion that for similar devices with a minimum Reynolds number, power consumption decreases with increasing size (references 2 and 3). However, power required by the system is determined by the compressor output pressure, which is usually much higher than the fluidic supply pressure. With a fixed compressor output, the power is proportional to the flow rate and increases with size, and it is actually flow consumption that is most important.

Because the above simple analysis gives satisfactory results for the exit velocity and flow rate, the nozzle is often assumed unimportant in design. However, it is known that three-dimensional flows exist in planar nozzles that can affect performance, particularly with short nozzles (see reference 4, for example). Otherwise good designs have failed because of this effect. The main difficulty is that unsymmetrical flow into the nozzle can cause a slightly unsymmetrical jet, which can appreciably affect the switch pressure. Although shorter devices can be made with symmetrical inlets, to insure that the entrance conditions do not affect the jet and switch pressure, the total length  $L_n$  (Fig. 2b)

should be approximately  $40b_s$  for a 10 to 1 contraction ratio (reference 5).

## Jet Flow

### a) Free Jet

The analysis of fully developed, two-dimensional, free jet flow is well established (see reference 6, for example). For turbulent flow, a number of analyses have been developed which agree well with the experimental data. The approach outlined below is that of Görtler (as presented in reference 7).

With a suitable approximation for the turbulent shear stress and the introduction of a similarity variable  $\eta$ , the equation of motion reduces to an ordinary differential equation which can be solved for the velocity distribution

$$\frac{u}{u_m} = 1 - \tanh^2 \eta \quad (5)$$

where

$$\eta = \sigma_E \frac{y}{s+c} .$$

The spread parameter  $\sigma_E$  is related to the turbulent shear stress and determines the rate at which fluid is entrained by the jet. For a free jet, a value of 7.67 for  $\sigma_E$  gives good agreement with experiments. In most wall attachment analyses, the spread parameter is used as an empirical constant to correlate experimental data.

The maximum velocity is determined from the conservation of momentum in the jet.

$$u_m = \frac{1}{2} \sqrt{\frac{3 \sigma_E J}{\rho (s+c)}} \quad (6)$$

where  $J = \rho b_s v_1^2$  for a uniform velocity profile at the nozzle exit.

The volume flow rate, which increases in the downstream direction, is found by integration of equation 5.

$$Q = v_1 b_s \sqrt{\frac{3(s+c)}{\sigma_E b_s}} \quad (7)$$

The distance  $c$  from the virtual origin of the jet to the nozzle exit (Fig. 3a) is usually found by assuming that the flow in the hypo-

thetical, fully developed jet at  $s = 0$  is the actual nozzle flow.

$$c = \frac{\sigma_E b}{3} \quad (8)$$

Other analyses of jet flow consider the developing section in more detail (reference 6). In fact, if an approximation is made for the turbulent viscosity in this region, the resulting equation, which is parabolic in nature, can be solved in a stepwise procedure as accurately as desired. In the Reynolds number range of most interest, however, the jet is laminar for 3-5 nozzle widths downstream of the exit and any analysis is likely to be somewhat approximate.

Although the free jet forms the basis of most wall attachment analyses, it is realized that the jet is affected by confining walls and curvature (reference 8, for example). The effect of confining walls has been investigated experimentally (references 9 and 10), but the three-dimensional flow offers a fundamental difficulty in the usual analytical approach. The pressure is usually assumed known and the two velocity components are determined from the streamwise momentum equation and continuity. The three-dimensional, or secondary flow, effects introduce an additional unknown velocity component.

#### b) Wall Jet

When the jet attaches to the wall in a fluidic device, a wall jet is formed as indicated in Fig. 3b. In the two-dimensional case with no pressure gradients, the wall jet reaches a fully developed state, but the velocity near the wall depends on the Reynolds number (reference 11). A number of analyses have been developed for the two-dimensional case, including the effects of varying outer velocity and pressure gradient (reference 12, for example).

In a typical fluidic device, the wall jet is not fully developed and is affected to some extent by confining walls and corners. Experimental studies related to fluidics have been conducted (reference 4 and 13), but the analysis is, at best, difficult. Problems of this type can be treated with three-dimensional methods such as reference 14, but depend on an approximation for the turbulent shear stress.

#### Jet Attachment

The jet attachment phenomena is basic to the operation of the fluid amplifiers considered here and is a fundamental problem related to separated flow in general.

The difficulty in the analysis of this kind of problem stems from the different methods of treating shear layers and the outer flow. The

equation of motion for the shear layer (jet, in this case) is parabolic in nature and can be solved in a stepwise procedure, independent of downstream conditions. The pressure field is determined by an elliptic equation (for subsonic flow) and is usually assumed independent of the shear layer. With separated flow there is a strong interaction between the two, and the solutions cannot be carried out independently.

A large number of analyses have been developed for the jet attachment problem, most of which refer to the basic approach of Borque and Newman (reference 15). The above difficulty is avoided by assuming the jet development in parametric form and solving simultaneously with the pressure field. Since this approach has become reasonably standard, it will be outlined in its simplest form here.

The jet is assumed to develop as a free jet (except that the spread parameter  $\sigma_j$  is left as an empirical constant) with a curved centerline. For simplicity, the jet centerline is usually assumed to follow a circular arc of radius  $R$ , and the bubble pressure  $p_b$  is thus assumed constant. Then the complete jet geometry can be described as a function of device geometry, the attachment angle  $\theta$ , and the jet exit angle  $\beta$  which is zero for no control flow. (Refer to Fig. 4a for notation).

$$R = (d + \frac{b}{2}) \frac{\cos \alpha}{\cos(\alpha + \beta) - \cos \theta} \quad (9)$$

$$x_2 = \frac{d + \frac{b}{2}}{\cos(\alpha + \beta)} \frac{\cos \alpha \cos(\frac{\theta + \alpha + \beta}{2})}{\sin(\frac{\theta - \alpha - \beta}{2})} + \sin \alpha \quad (10)$$

$$s_2 = R(\theta + \alpha + \beta) . \quad (11)$$

The total jet flow, and thus the flow entrained from the separation bubble can be determined from equations 7, 9 and 11.

$$Q_e = \frac{1}{2}(Q_2 - v_1 b_s) . \quad (12)$$

The momentum returned into the separation bubble at attachment is determined by a momentum balance at that point (Fig. 3c).

$$\frac{J_r}{J} = \frac{1 - \cos \theta}{2} \quad (13)$$

The flow returned is related to the momentum by integrating the velocity profile, equation 5. A simple approximation was found in

reference 16 for this result.

$$\frac{Q_r}{Q_2} = 0.302 \theta \left[ 1 + \frac{10.3}{\sigma^{3/2} N_R^{1/3}} \right] \quad (14)$$

The last term in equation 14 is an empirical factor to account for three-dimensional effects with small aspect ratio. These effects are usually neglected, but experiments (reference 16) indicate that they are definitely important at low Reynolds numbers and small aspect ratios of interest in fluidics.

With no control flow the jet angle  $\beta$  is zero. The solution is then completed by equating the flow entrained from the separation bubble to that returned at attachment and solving for the attachment angle  $\theta$ .

With the addition of control flow, the jet forms an angle  $\beta$  near the nozzle exit. (Assuming an angle  $\beta$  on the circular arc centerline at the nozzle exit is an approximation for the actual case when control flow causes a change in curvature.) This angle can be estimated by equating the pressure forces to the change in momentum (Fig. 4b). For small  $\beta$ ,

$$\rho \frac{Q_1^2}{b_s} \tan \beta = \rho \frac{Q_c^2}{a} + (p_{c'} - p_a) b_c \quad (15)$$

and

$$p_{c'} = p_c - \rho \frac{Q_c^2}{2b_c^2} \quad (16)$$

The pressure outside of the attached jet is usually assumed atmospheric, but it is determined in reference 17 by conservation of mass in the complete interaction area. The control flow is related to the control pressure and the bubble pressure by an effective area between the jet and the attachment wall.

$$A_{eff} = D + b_c (\tan \alpha + \tan \beta) \quad (17)$$

and

$$p_c - p_b = \frac{\rho}{2} \frac{Q_c^2}{A_{eff}^2} \quad (18)$$

For large offset the effective area is limited by the control nozzle area.

The bubble pressure is related to the jet curvature  $R$  by the radial momentum equation.

$$p_a - p_b = \frac{J}{R} \quad (19)$$

Equations 15-19 determine the exit angle  $\beta$  as a function of the control pressure and attachment angle  $\theta$ . Thus by equating the control flow plus the flow returned at attachment to that entrained by the jet, the solution can be completed by solving for the angle  $\theta$ .

#### Low Frequency Switching

Low frequency switching considered here refers to the case where the control pressure is slowly increased until the gate switches. This control pressure is the minimum switch pressure. It is assumed that in the bistable devices discussed here the jet reaches a point of instability and switches to the opposite output in a digital manner, as opposed to a proportional switch.

In reference 18 the switching process was classified into three types: 1) terminated-wall or bleed, 2) contacting-both-walls, and 3) splitter switching (Fig. 5). In an actual fluidic device, the process is probably affected by all three factors, and is not complete until the jet reaches the opposite output. Furthermore, if the flow is completely and correctly modeled including the effect of the opposite wall, splitter, vents, and loads, a classification of this type is not necessary--an instability will be determined by the analysis. However, it appears that different factors are predominant with different geometries, and it is helpful when considering the analysis or the experimental results to discuss the switching process in these terms.

#### a) Terminated-Wall Switching

With relatively short attachment walls and large offsets, the control pressure drives the jet off the end of the wall, where it reaches an unstable position and switches. The above analysis can be used to estimate this condition by relating the attachment point to the end of the wall. However, the attachment point model as given above is not valid as the point approaches the end of the wall. In fact, this model predicts a latching effect (reference 19) which does occur under some conditions. An empirical relation between the wall length and the theoretical attachment point at switch was developed in reference 20. This approach correlated the data, but might be limited in generality.

A continuous calculation was carried out in reference 17 until the

jet reached the opposite output. When the jet passed the end of the wall, vent flow was allowed into the separation bubble. The effective area for this flow was assumed to be that between the attaching streamline and the upstream edge of the vent.

#### b) Contacting-Both-Walls Switching

With relatively long walls and small offsets, the jet contacts the opposite wall before it reaches the end of the attachment wall. Just what condition causes an instability is not clear, however. With a short pulse duration, the jet can return to the attached wall (reference 21). At some point the jet does appear to reach an instability with a sustained control pressure. This conclusion is based on experiments (reference 20, discussed later in this paper) which show that above a certain length the switch pressure is independent of wall length. An empirical relation was developed in reference 20 for this type of switching, but it was not considered as a separate mode in reference 17.

#### c) Splitter Switching

In most fluid amplifiers of the type considered here, the jet reaches the end of the wall or contacts both walls before it crosses the splitter. In some devices, however, it crosses the splitter first (Fig. 5c) and can switch in this manner, but the switching is usually not completely digital. Even when this is not the primary cause of switching, the flow is affected to some degree by the splitter, particularly at low output flow. The above analytical approach can be used to predict the jet position relative to the splitter, but should be modified for a wide or cusped splitter that causes a stabilizing vortex to be established.

#### Flow and Pressure Recovery

The output characteristics of a bistable fluid amplifier (Fig. 6) are similar to those of a pump. In fact, the operation of the device is very similar to a jet pump, but the geometry is more difficult to analyze with a simple flow model. The difficulty stems from spillover of the jet before it enters the receiver, which is a complex flow interaction with the vent and splitter.

Some approximate analyses of this problem have been presented, which give the correct trends and agree with some experiments. Reference 22, for example, describes a simple, inviscid approach. In reference 17 the analysis is based on a dynamic pressure at the receiver entrance determined by averaging the momentum over the area. The momentum is assumed to be that in the downstream direction from the attachment point. Two approximations are discussed in reference 23, but both require a knowledge of the wall jet velocity profile.



## EXPERIMENTAL RESULTS

Since it is not feasible to completely analyze the flow in fluid amplifiers starting from the basic equations of motion, experimentation has played an important role in their development. (This is, in fact, the case with most devices that involve fluid flow.) Although some experiments are mainly trial and error, productive experimental research is no less of a science than a purely analytical approach. Analyses, however, are important in guiding and interpreting as well as applying the experimental work. Thus it is the combination of approximate analyses and careful experimentation, along with a good physical understanding of the flow, that is mainly responsible for advancements in the state-of-the-art.

There has been a large amount of experimental work in the fluidics area, conducted for a number of purposes and on a variety of devices. Objectives of this work have varied from basic studies on certain aspects of the flow, such as wall attachment, to the determination of performance characteristics of new devices. Several different fluidic devices with different operating principles (wall attachment, beam deflection, vortex, turbulence, etc.) have been proposed, and experiments have been conducted on a number of basically different designs of each of these. Much of this work has been published, but much more simply makes up the experience of the individual investigator.

The purpose of this paper is, again, to review the relation between geometry and static performance of wall-attachment-type devices. Only a limited set of experiments, which were conducted for this specific purpose, will be considered in detail here. Furthermore, only one basic configuration (Fig. 7), which is typical in a fundamental sense, at least, to many devices of this type, is considered. It should be emphasized that a number of variations of this basic configuration have been developed (curved walls, cusped splitters, etc.) which result in interesting devices. However, with the number of variables involved, it is perhaps best to limit this discussion to the basic configuration.

The objective of the first experiments considered here was to determine the relation between the wall angle, length, and offset and the switch pressure (reference 20). These experiments were conducted on a large-scale device with a control nozzle width equal to the power nozzle width and an aspect ratio of two. The device was similar to that shown in Fig. 7 except that the downstream sections (splitter and output channels) were removed for most of the tests. Air at low pressures was used as a working fluid, except for some visual studies with water, and tests were conducted at Reynolds numbers of 8000 and 12000. The results of these experiments are shown in Fig. 8. As the wall length was increased, the switch pressure increased until a certain length was reached. Above that value, wall length had little effect on the minimum switch pressure. This result, along with the fact that the addition of a splitter had little effect under these conditions, led to the con-



clusion that the jet reached an unstable position due to the presence of the opposite wall before it reached the end of the attachment wall. For the two values considered, the Reynolds number had no effect on switching.

The next experiments (not previously published) were conducted on a complete, large-scale device with the basic dimensions given in Fig. 7. Air, again, was used as a working fluid, but with Reynolds numbers more typical of actual fluid amplifiers. Tests were run with three values of each of several geometric variables, keeping the other more significant variables constant whenever possible. The results of these tests are given in Table 1. For most loading conditions, the control nozzle size had the most significant effect on the switch pressure. With blocked outputs the device was quite sensitive to the receiver configuration, particularly the position of the vent relative to the splitter. In the range tested, all other variables had a surprisingly small effect on performance.

The final experiments included here were conducted to determine the effect of aspect ratio on performance. The experimental devices had a power nozzle width of 0.51 mm and the basic configuration given in Fig. 7. They were cut in plastic with a milling machine to different depths and all were made from the same master. Results from these tests are given in Table 2. It was concluded that aspect ratio definitely had an appreciable effect. In fact, this configuration was not bistable with an aspect ratio of one.

## SUMMARY OF EFFECTS OF GEOMETRIC AND FLUID PARAMETERS ON STATIC PERFORMANCE

As a result of the experimental and analytical efforts of many investigators, the effect of geometric changes on gate performance can be understood and, to some extent, predicted. Although the quantitative results given here refer to one basic configuration, the summary is as general as possible, qualitatively at least, for the wall-attachment-type fluid amplifier.

### a) Amplifier Size and Reynolds Number

It is usually assumed, by similarity arguments, that the non-dimensional gate characteristics ( $p_c/p_s$ ,  $p_o/p_s$ ) are not affected by a change in the device size or fluid properties if the Reynolds number is held constant. When compressibility is not important, this similarity holds very well for a change of fluid properties in the same device. When the size is changed, however, it is difficult to maintain identical inlet conditions and exact geometric similarity, because of such factors as wall roughness and rounded corners. (This is true for different manufacturing processes.) Large devices, particularly experimental models, can have different performance characteristics, even with the same Reynolds Number. In the experiments considered here, a size increase by a factor of 12.5 resulted in approximately the same switch pressure but higher recovery pressure. Above some minimum value, an increase in the Reynolds number usually results in lower switch pressure and higher recovery. This minimum value and the effect on switch pressure depend on the geometry.

### b) Supply Pressure and Compressibility

When the supply pressure to a fluid amplifier is increased, both the Reynolds number and the Mach number increase. Fluidic devices often operate under conditions where there is an appreciable change in fluid density ( $M > 0.20$ ), and some operate with supersonic flow. However, most wall-attachment-type devices operate with subsonic flow, and the compressibility effect is small. For the geometry considered here with a small (0.25 mm) device, an increase in supply pressure results in a slight decrease in the switch and output pressure.

### c) Nozzle Geometry

Nozzle size determines the power consumption and the control impedance, and other dimensions are related to the power nozzle width. With a reasonable contour, the exact shape is not critical. However, an overall length of approximately  $40b_g$  is needed to ensure that flow conditions at the inlet to the power nozzle do not affect the switching characteristics.

d) Attachment Wall Length, Angle, and Offset

The length, angle, and offset of the attachment walls are important design parameters and are all related. For the configuration considered here the switch pressure increases sharply with wall length up to a value of approximately 9-10b, depending on the angle and offset. The output pressure decreases with an increase in wall length, particularly at low output flow where recovery depends more on maximum wall jet velocity than on total momentum. The effect of angle and offset on switch pressure depends on the wall length, or switching mode. An increase in either angle or offset decreases the recovery, but this effect is small in typical devices.

e) Control Nozzle Size

The size of the control nozzle relative to the power nozzle is one of the most important design parameters. Since the effect of this size on the switch pressure is reasonably consistent and predictable, it is often used to make final adjustments in new designs. An estimate of the effect of a change in control nozzle size can be obtained from Table 1 or by assuming that the control flow required to switch is approximately constant. An increase in control nozzle size decreases the output pressure, but this effect is usually secondary.

f) Aspect Ratio

For the low values ( $\sigma \leq 4$ ) of interest in most fluid amplifiers, the aspect ratio has a significant effect on switch pressure, particularly at low Reynolds numbers ( $N_R \leq 3000$ ). It also affects the recovery, but to a lesser degree. An estimate of the magnitude of this effect can be obtained from Table 2.

g) Receiver Geometry

The size and location of the vents relative to the splitter can have an important influence on the stability of the device, depending on the load. This geometry is related to the switch pressure in a complex manner, probably through recirculating flow, and is not accounted for in the analyses. Although there are many others, some satisfactory (and unsatisfactory) designs can be determined from Table 1.

## REFERENCES

1. McRee, D. I., and Moses, H. L., "The Effect of Aspect Ratio and Offset on Nozzle Flow and Jet Reattachment", pp. 142-161, Advances in Fluidics, Brown, F. T., ed., ASME, 1967.
2. Comparin, R. A., Mitchell, A. E., Müller, H. R., and Glättli, H. H., "On the Limitations and Special Effects in Fluid Jet Amplifiers", Symposium on Fluid Jet Control Devices, ASME, 1962.
3. Small, D. A., "Optimizing Fluidic Element for Speed and Power Consumption", ASME Paper No. 67-WA/FE-39, 1967.
4. Wagner, W. B., and Owczarek, J. A., "An Experimental Study of Flow Fields in Bistable Fluid Amplifiers", ASME Paper No. 72-WA/Flcs-9, 1972.
5. Nurmohamed, A. R., "Effects of the Inlet and Nozzle Geometrics on the Performance of a Fluidic Power Nozzle", M.S. Thesis, Dept. of Mechanical Engineering, VPI & SU, Sept. 1973.
6. Kirshner, J. M., "Jet Flows", Fluidics Quarterly, Vol. 1, No. 3, 1968.
7. Schlichting, H., "Boundary-Layer Theory", Sixth Edition, McGraw-Hill, 1968.
8. Sawyer, R. A., "Two-Dimensional Reattaching Jet Flows Including the Effects of Curvature on Entrainment", Journal of Fluid Mechanics, Vol. 17, 1963, pp. 481-498.
9. Foss, J. F., and Jones, J. B., "Secondary Flow Effects in a Bounded Rectangular Jet", Trans. ASME, Journal of Basic Engineering, Vol. 90, Series D, No. 2, June 1968, pp. 241-248.
10. Trapani, R. D., "An Experimental Study of Bounded and Confined Jets", Harry Diamond Laboratories, Washington, D.C., Fluidics 22, AD 644737, 1966.
11. Glauert, M. B., "The Wall Jet", Journal of Fluid Mechanics, Vol. 1, 1956.
12. McGahan, W. A., "The Incompressible, Turbulent Wall Jet is an Adverse Pressure Gradient", MIT Gas Turbine Laboratory Report No. 82, 1965.
13. Sarpkaya, T., and Richardson, D. C. "Turbulent Jet Over an Inclined Wall", ASME Paper No. 69-WA/Flcs-1, 1969.
14. Patankar, S. V., and Spalding, D. B., Heat and Mass Transfer in Boundary Layers, 2nd Edition, Intertext Books, 1970.

15. Borque, C. and Newman, B. G., "Reattachment of a Two-Dimensional Incompressible Jet to an Adjacent Flat Plate", The Aeronautical Quarterly, Vol. 11, 1960, pp. 201-231.
16. McRee, D. I., and Edwards, J. A., "Three-Dimensional Turbulent Jet Reattachment", ASME Paper No. 70-WA/Flcs-5, 1970.
17. Goto, J. M., and Drzewiecki, T. M., "An Analytical Model for the Response of Fluoric Wall Attachment Amplifiers", Harry Diamond Laboratories, HDL-TR-1598, 1972.
18. Kirshner, J. M., Editor, "Fluid Amplifiers", McGraw-Hill Book Company, New York, 1966, pp. 187-203.
19. Brown, F. T., "Pneumatic Pulse Transmission with Bistable-Jet-Relay Reception and Amplification", Sc.D. Thesis, Massachusetts Institute of Technology, 1962.
20. Moses, H. L., and McRee, D. I., "Switching in Digital Fluid Amplifiers", ASME Paper No. 69-Flcs-31, 1969.
21. Müller, H. R., "Wall Reattachment Device with Pulsed Control Flow", 2nd Fluid Amplification Symposium, HDL, Vol. 1, 1964.
22. Sarpkaya, T., and Kirshner, J. M., "The Comparative Performance Characteristics of Vented, Unvented, Cusped, and Straight and Curved Walled Bistable Amplifiers", 3rd Cranfield Conference, Paper F3.
23. Moses, H. L., and Comparin, R. A., "Flow and Pressure Recovery in Wall-Attachment Fluid Amplifiers", ASME Paper No. 70-WA/Flcs-9, 1970.

TABLE 1 EXPERIMENTAL RESULTS FOR LARGE-SCALE FLIP-FLOP

 $(\alpha = 4.0, N_R = 6000 \text{ except as noted})$ 

Geometry	Load (nozzles)	Switch		Output	
		$P_c/P_s$	$Q_c/Q_s$	$P_o/P_s$	$Q_o/Q_s$
Basic geometry	0	.09	.17	.62	0
	1	.10	.17	.55	.68
	3	.11	.16	.38	1.33
Basic geometry ( $N_R = 4250$ )	0	.12	.19	.64	0
	1	.12	.18	.55	.68
	3	.13	.18	.36	1.35
Control nozzle $b_c = 1.25 b_s$	0	.05	.19	.58	0
	1	.07	.18	.53	.66
	3	.07	.18	.37	1.34
Control nozzle $b_c = 1.50 b_s$	0	.03	.21	.58	0
	1	.04	.19	.52	.66
	3	.06	.19	.38	1.36
Wall length $x_L = 10 b_s$	0	.12	.19	.56	0
	1	.13	.18	.53	.66
	3	.13	.18	.37	1.32
Wall length $x_L = 11 b_s$	0	.11	.17	.51	0
	1	.11	.17	.50	.65
	3	.12	.18	.36	1.32
Wall offset $d = 0.25 b_s$	0	.11	.22	.58	0
	1	.15	.23	.52	.65
	3	.14	.22	.38	1.33
Wall offset $d = 0.50 b_s$	0	.07	.24	.54	0
	1	.15	.27	.49	.63
	3	.14	.26	.37	1.33
Splitter distance $x_s = 10 b_s$	0	.10	.17	.52	0
	1	.10	.17	.52	.64
	3	.10	.17	.38	1.35
Splitter distance $x_s = 12 b_s$	0	0	.14	.58	0
	1	.10	.17	.60	.70
	3	.10	.16	.37	1.30
Splitter width $b_{sp} = 1.0 b_s$	0	.10	.18	.61	0
	1	.09	.16	.55	.67
	3	.11	.16	.36	1.30

TABLE 1 (continued)

<u>Geometry</u>	<u>Load (nozzles)</u>	<u>Switch</u>		<u>Output</u>	
		<u><math>P_c/P_s</math></u>	<u><math>Q_c/Q_s</math></u>	<u><math>P_o/P_s</math></u>	<u><math>Q_o/Q_s</math></u>
Splitter width $b_{sp} = 2.0 b_s$	0	.10	.19	.64	0
	1	.10	.17	.58	.71
	3	.10	.17	.38	1.34
Vent width $b_v = 2.0 b_s$	0	0	-	-	-
	1	.10	.17	.60	.71
	3	.10	.16	.38	1.34
Vent width $b_v = 4.0 b_s$	0	.11	.17	.51	0
	1	.11	.17	.50	.65
	3	.12	.18	.36	1.32

TABLE 2 ASPECT RATIO EXPERIMENTS  
( $b_s = 0.51$  mm)

$\sigma$	$N_R$	Load (nozzles)	Switch		Output	
			$P_c/P_s$	$Q_c/Q_s$	$P_o/P_s$	$Q_o/Q_s$
2	4000	1	.089	.185	.413	.715
		2	.083	.173	.295	1.203
		4	.082	.173	.115	1.515
2	6000	1	.061	.178	.404	.728
		2	.055	.167	.289	1.235
		4	.052	.163	.111	1.531
3	4000	1	.105	.202	.451	.748
		2	.102	.190	.338	1.273
		4	.098	.184	.126	1.663
3	6000	1	.065	.195	.424	.745
		2	.058	.185	.329	1.306
		4	.054	.182	.128	1.651
4	4000	1	.111	.198	.452	.737
		2	.103	.189	.343	1.311
		4	.098	.188	.157	1.778
4	6000	1	.078	.190	.432	.756
		2	.071	.183	.337	1.334
		4	.066	.177	.150	1.783



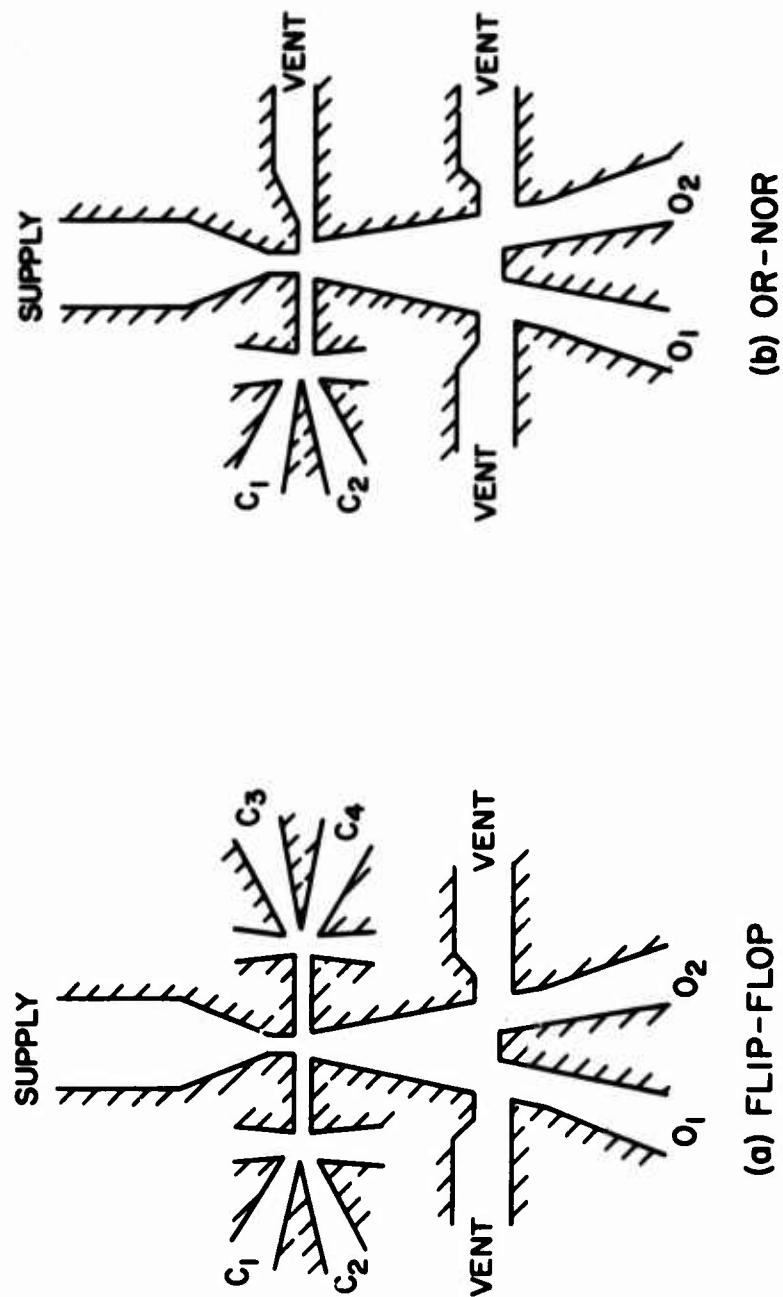
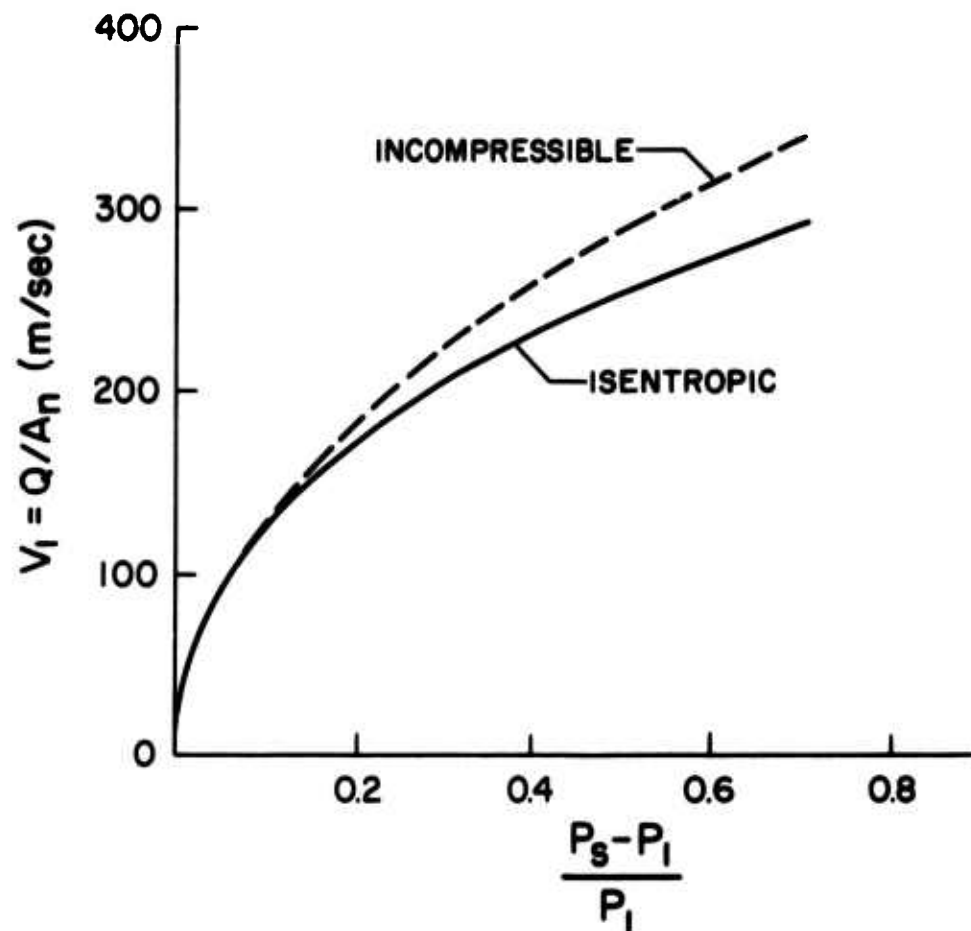
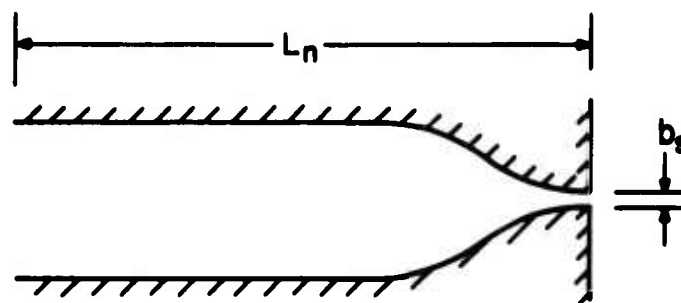


FIG. 1 TYPICAL WALL-ATTACHMENT DEVICES

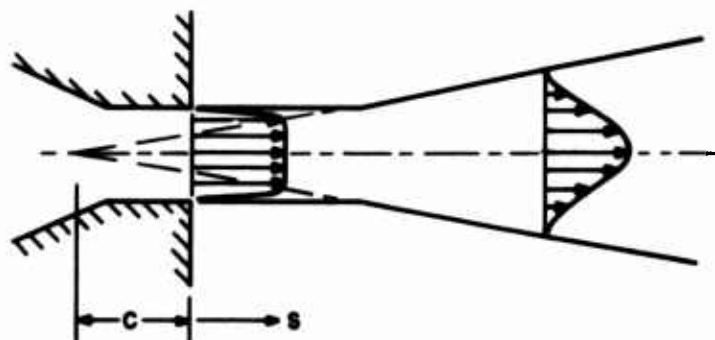


(a) FLOW-PRESSURE CHARACTERISTICS (AIR AT STANDARD CONDITIONS)

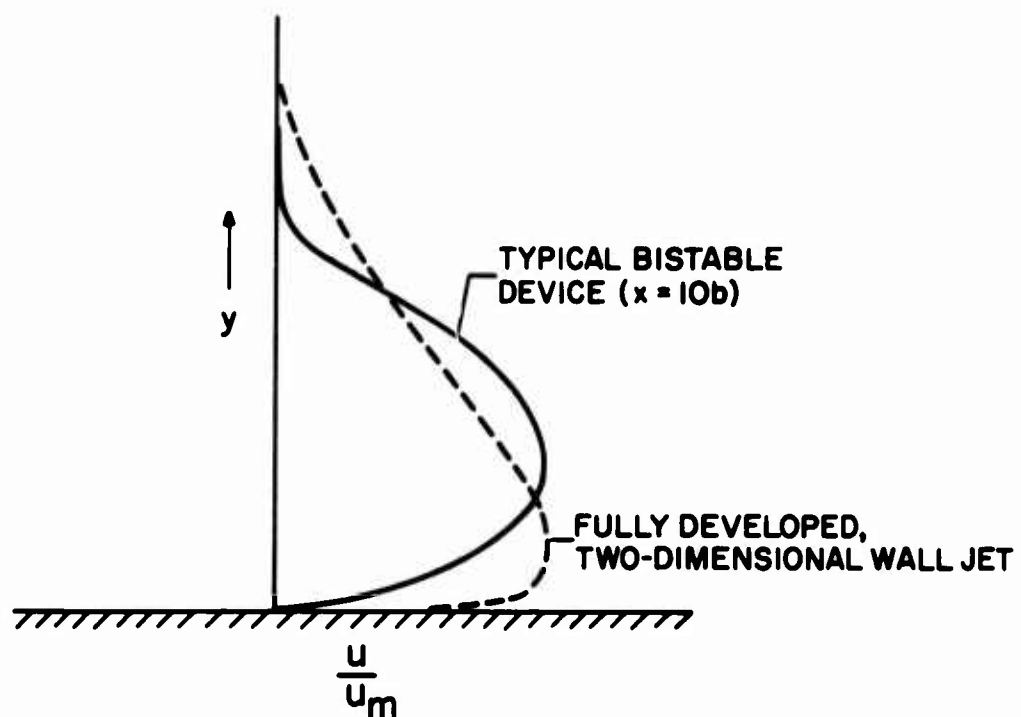


(b) TYPICAL NOZZLE GEOMETRY

FIG. 2 NOZZLE CHARACTERISTICS

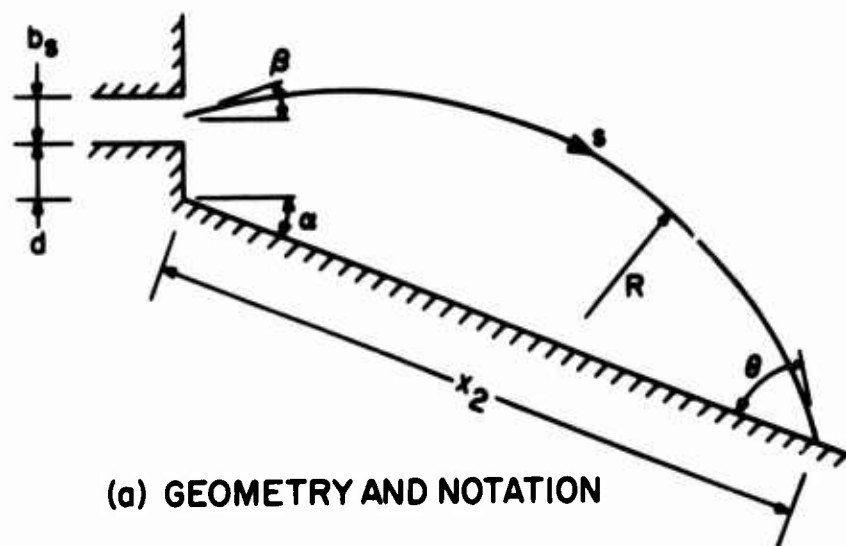


(a) FREE JET

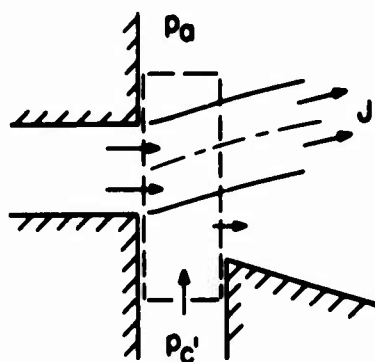


(b) WALL JET

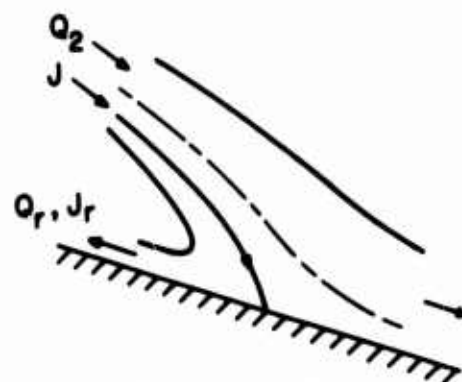
FIG. 3 JET FLOW



(a) GEOMETRY AND NOTATION

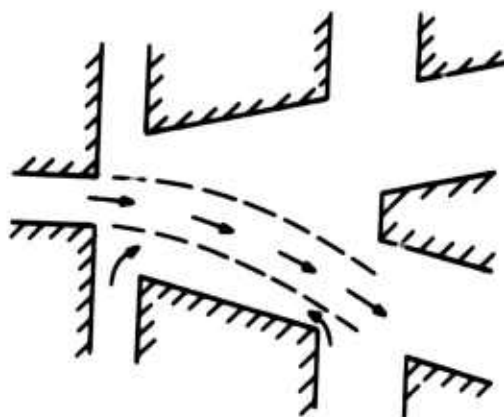


(b) JET DEFLECTION

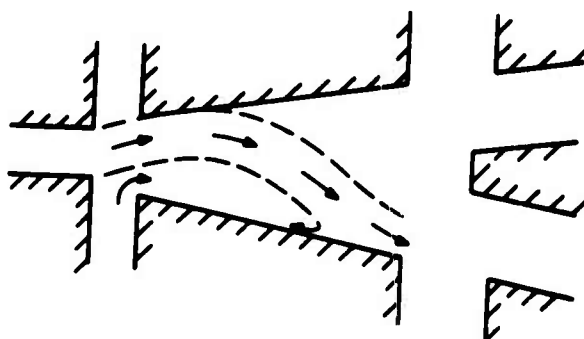


(c) ATTACHMENT POINT

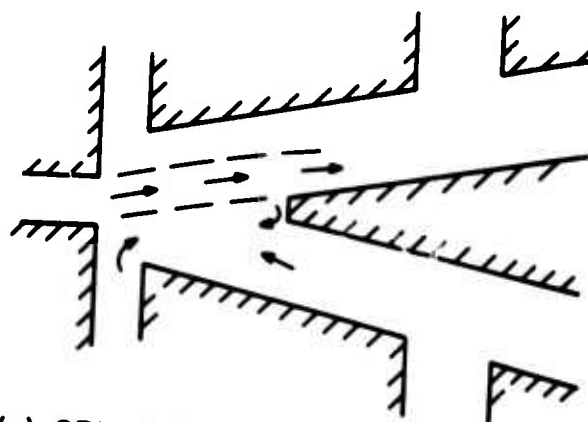
FIG. 4 JET ATTACHMENT MODEL



(a) TERMINATED WALL

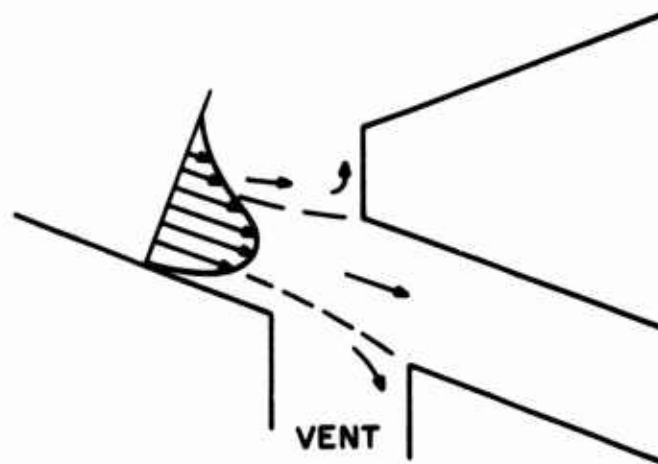


(b) CONTACTING-BOTH-WALLS

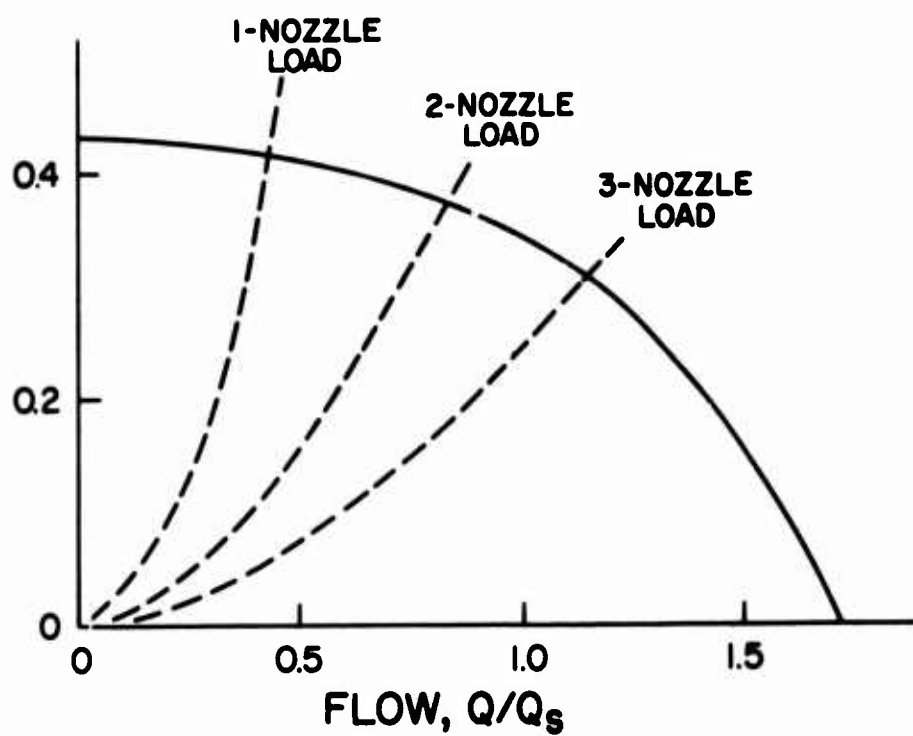


(c) SPLITTER

FIG. 5 SWITCHING MODES (REFERENCE 18)

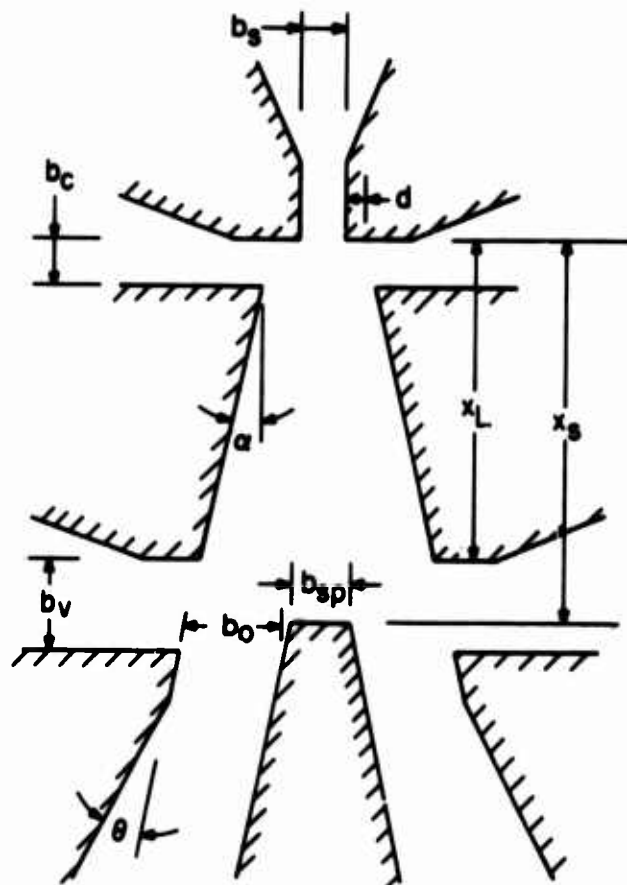


(a) RECEIVER GEOMETRY



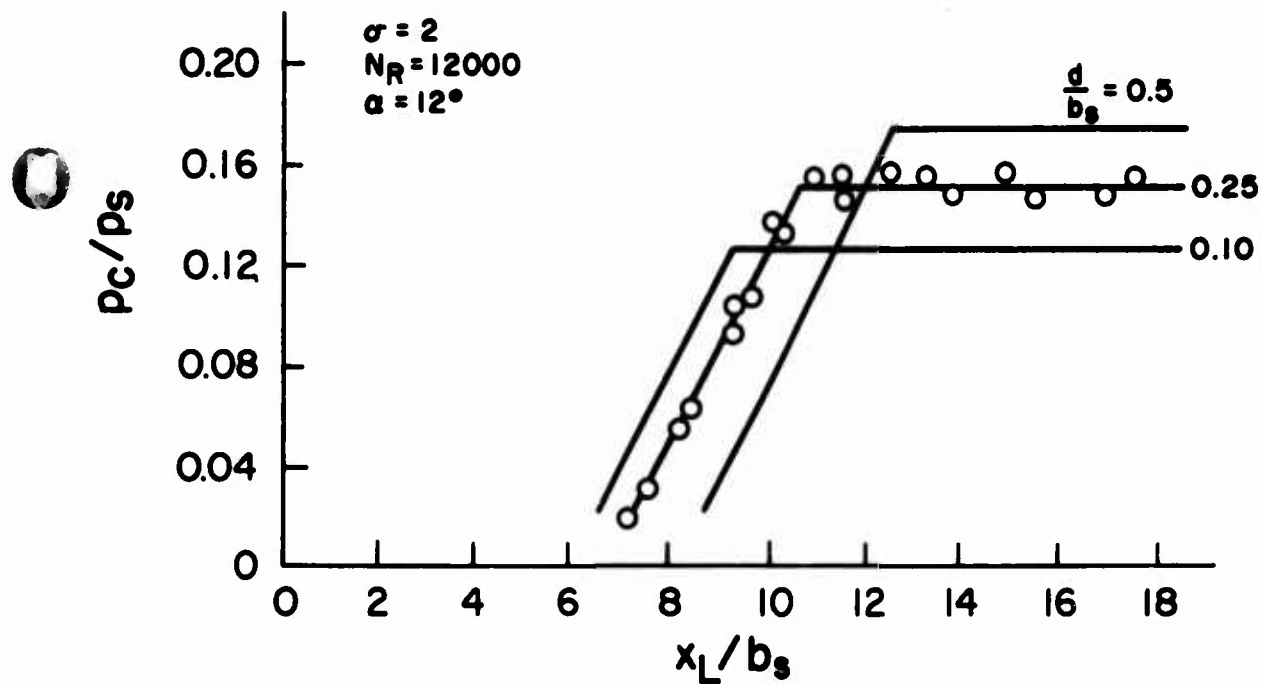
(b) OUTPUT CHARACTERISTICS

FIG. 6 FLOW AND PRESSURE RECOVERY

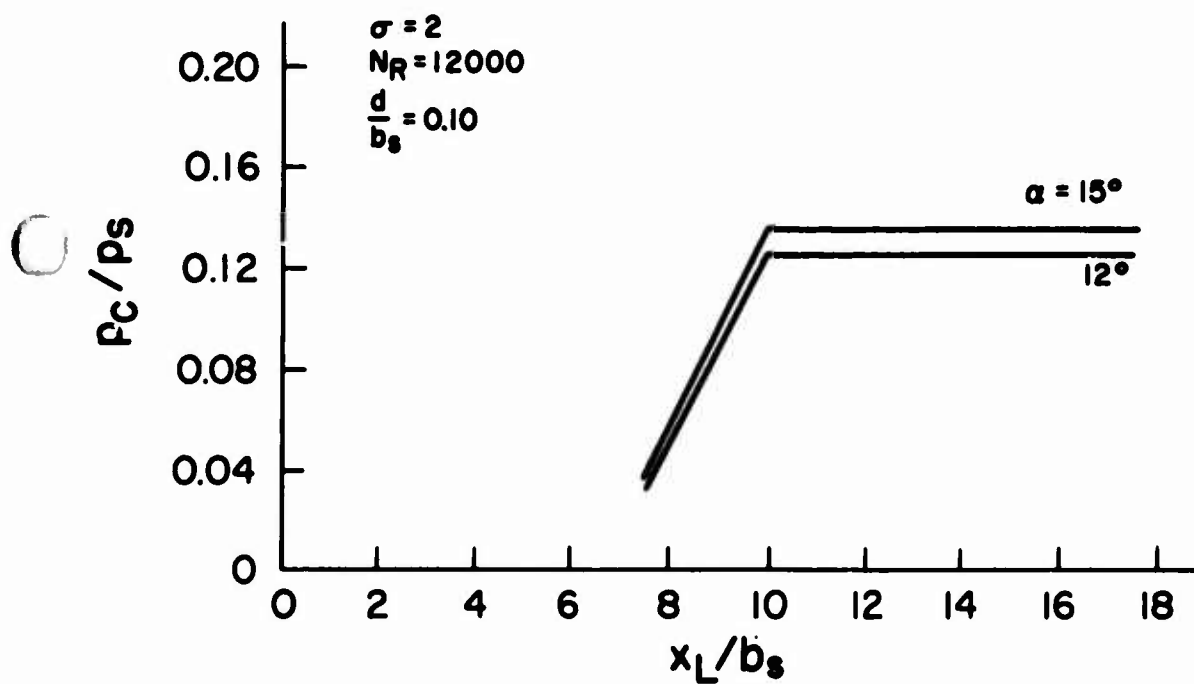


<u>PARAMETER</u>		<u>BASIC GEOMETRY</u>
$b_s$	POWER NOZZLE WIDTH	$b$
$b_c$	CONTROL NOZZLE WIDTH	$b$
$d$	OFFSET	$0.1b$
$\alpha$	WALL ANGLE	$12^\circ$
$x_L$	WALL LENGTH	$9b$
$x_s$	SPLITTER DISTANCE	$11b$
$b_{sp}$	SPLITTER WIDTH	$1.5b$
$b_v$	VENT WIDTH	$3b$
$b_o$	RECEIVER WIDTH	$2.5b$
$\theta$	DIFFUSER ANGLE	$7^\circ$
$\sigma$	ASPECT RATIO	$4$

FIG. 7 EXPERIMENTAL CONFIGURATION



(a) WALL LENGTH AND OFFSET



(b) WALL LENGTH AND ANGLE

FIG. 8 EFFECT OF WALL LENGTH, OFFSET, AND ANGLE ON SWITCH PRESSURE



THE DESIGN OF FLUERIC, TURBULENT,  
WALL ATTACHMENT FLIP-FLOPS

by

TADEUSZ M. DRZEWIECKI

Submitted for presentation

The Harry Diamond Laboratories Fluidic State-of-the-Art Symposium

30 Sep - 4 Oct 1974

## CONTENTS

	Page
ABSTRACT .....	435
FOREWORD .....	436
NOMENCLATURE .....	437
LIST OF FIGURES .....	439
1. INTRODUCTION .....	440
2. GEOMETRY OF A FLUERIC WALL ATTACHMENT FLIP-FLOP .....	441
3. FLIP-FLOP STATIC DESIGN .....	441
3.1 Standard Characteristics .....	442
3.1.1 Power Consumption .....	442
3.1.2 Pressure Recovery .....	442
3.1.3 Output Characteristics .....	442
3.1.4 Blocked-Pressure Static Transfer Characteristic .....	442
3.1.5 Input Characteristics .....	443
3.2 Computed Parameters .....	443
3.2.1 Dimensionless Switching Pressure .....	443
3.2.2 Pressure Gain .....	443
3.2.3 Flow Gain .....	443
3.2.4 Fanout .....	444
3.2.5 Flow Recovery .....	444
3.3 Some Approximations .....	444
3.4 Analytical Static Design Curves .....	445
4. FLIP-FLOP DYNAMIC DESIGN .....	448
4.1 Response Time .....	449
4.2 Maximum Frequency Response .....	450
4.3 Other Dynamics .....	450
4.4 Dynamic Design Conclusions .....	451
5. OTHER DESIGN CONSIDERATIONS .....	452
5.1 Supply Pressure .....	452
5.2 Nozzle Dimensions .....	454
5.3 Aspect Ratio .....	454
5.4 Nozzle Design .....	454
6. THE FAST FLIP-FLOP .....	455
7. SUMMARY OF DESIGN EQUATIONS .....	460
8. DESIGN SPECIFICATIONS .....	461
9. DESIGN EXAMPLE .....	462
9.1 Statement of the Problem .....	462
9.2 Flip-Flop Specifications .....	463
9.3 Step-by-Step Design .....	465
9.4 Flip-Flop Geometry and Characteristics .....	467
10. SUMMARY AND CONCLUSIONS .....	468
11. ACKNOWLEDGEMENTS .....	469
12. REFERENCES .....	470
13. FIGURES .....	471

# ABSTRACT

This report is a guide for the design of turbulent, wall attachment flip-flops with straight walls and sharp splitters. The analysis provides the steady state and transient characteristics, and is presented graphically in this report to facilitate design. Fabrication techniques are discussed where they may compromise design criteria. In addition to presenting the material necessary to design flip-flops in general, a specific design for minimum response time is followed from conception to final component status and then a typical design example is considered.

## FOREWORD

This report is a culmination of four years intensive work, and many years of basic research, into the operation of wall-attachment devices. The name "flip-flop" is used here to differentiate this from an analog device called the amplifier. Although amplification occurs in the sense that a greater power is recovered or switched than that impressed on the controls, the primary function is that of switching. The report is intended to be used by the fluidic designer who has to satisfy specific system requirements. All the basic theoretical work is embodied in the references, so that this should be a "cook-book" for the designer. Some knowledge and understanding of the basic operation of bistable wall attachment devices and fluid transmission lines is required.

Except for certain angular units the system of units used is the Systems International, SI. This is basically the MKS system for those unfamiliar with it and is in accordance with the military standards set for reporting of fluidics data and with the ASME guidelines (Mechanical Engineering Vol. 95, No. 11, Nov. 1973). The unit of pressure is the pascal, Pa, and has the basic units of  $\text{kg}/(\text{ms}^2)$ . One kilopascal ( $\text{kPa} = 10^3 \text{ Pa}$ ) is equal to roughly 6.89 psi, and one atmosphere is roughly 101 kPa. Where convenient for ready understanding, the units of angles are given in degrees, such as wall angles and splitter angles.

# NOMENCLATURE

a	- speed of sound, (m/s)
A	- cross-sectional area, (m <sup>2</sup> )
b	- nozzle width, (m)
c <sub>d</sub>	- discharge coefficient, (dimensionless)
C	- capacitance, (m <sup>3</sup> /Pa)
D	- offset, (m)
f	- frequency, (Hz)
F	- force, N
F <sub>o</sub>	- fanout, (dimensionless)
G <sub>p</sub>	- pressure gain, (dimensionless)
h	- fluid height, (m)
ℓ	- length, (m)
L	- inductance, (kg/m <sup>4</sup> )
m	- mass, kg
N <sub>R</sub>	- Reynolds number, (dimensionless), $\frac{b_s}{\nu} \sqrt{\frac{2P_s}{\rho}}$
P	- pressure, (Pa)
Q	- flow, (m <sup>3</sup> /s)
R	- fluid resistance, (Pa/m <sup>3</sup> /s, kg/m <sup>4</sup> s)
t	- time (s)
T	- switch time, (s)
V	- volume, (m <sup>3</sup> )
W	- power, (Pa · m <sup>3</sup> /s)
X	- attachment point location, (m)
α	- attachment wall angle, (degrees, radians)
ζ	- damping coefficient, (dimensionless)
ν	- kinematic viscosity, (m <sup>2</sup> /s)
ρ	- density, (kg/m <sup>3</sup> )
σ	- aspect ratio, h/b <sub>s</sub> , (dimensionless)
τ	- time, (s)
ψ	- splitter angle, (rad)
ω	- angular frequency, (rad/s)

## Subscripts

a	- acoustic
A	- amplifier
abs	- absolute
c	- control
FET	- fully established turbulence
ℓ	- line
LR	- inductive-resistive
max	- maximum
n	- natural
o	- output
p	- pressure
per	- period
r	- rise time

s - supply or reference condition  
sp - splitter  
sw - switch point  
t - transport  
th - throat  
v - vent

# LIST OF FIGURES

	Page no.
Figure 1. The geometry of a flueric bistable wall attachment flip-flop .....	473
Figure 2. Input characteristics of a commercial flip-flop showing loading effects .....	474
Figure 3. Flip-flop characteristic curves .....	475
Figure 4. The construction of an input characteristic .....	476
Figure 5. The construction of a blocked-pressure static transfer characteristic .....	477
Figure 6. Static design curves for $\alpha = 10^\circ$ .....	478
Figure 7. Static design curves for $\alpha = 12^\circ$ .....	479
Figure 8. Static design curves for $\alpha = 15^\circ$ .....	480
Figure 9. Static design curves for $\alpha = 30^\circ$ .....	481
Figure 10. Geometry of control nozzle used for static design curves .....	482
Figure 11. Geometry of decoupler used in calculating gain and fanout .....	483
Figure 12. Switching pressure versus offset for $\alpha = 10^\circ$ , $12^\circ$ , $15^\circ$ .....	484
Figure 13. Switching flow versus offset for $\alpha = 10^\circ$ , $12^\circ$ , $15^\circ$ .....	485
Figure 14. Pressure gain and fanout versus offset for $\alpha = 10^\circ$ , $12^\circ$ , $15^\circ$ .....	486
Figure 15. Motion of the attachment point in response to a sharp input pressure signal .....	487
Figure 16. Switching times for various geometries .....	488
Figure 17. Output pressure response of flip-flop .....	489
Figure 18. Equivalent circuit for the outlet .....	490
Figure 19. Geometry of the initial fast flip-flop .....	492
Figure 20. Geometry of the final version of the fast flip-flop .....	493
Figure 21. Photograph of the fast flip-flop and its interior laminations .....	494
Figure 22. Comparison of predicted static characteristics with actual x-y data .....	495
Figure 23. Maximum operating frequency response versus element size with supply pressure as a parameter .	497
Figure 24. Corner frequency as a function of control amplitude .....	498

## 1. INTRODUCTION

Since fluidics was first conceived in 1959, the design of fluidic digital components has been almost entirely relegated to trial-and-error procedures, with some design guides in the form of experimental curves of attachment point, pressure recovery versus, say, offset or some other geometrical variable. No dynamic design information other than transport time existed for the switching of actual devices. It is true that some theoretical switching information existed [1 - 4]\* for some very simplified geometries, or input signals, but none for actual devices with outlet channels, splitters and so forth or for realistic input signals. Work on steady-state wall attachment, starting with Bourque and Newman [5] up through the present [6 - 14] ending with the work of Brown and Belen [15], has been similarly limited to very simple configurations. In 1972, however, Goto and Drzewiecki [16], [17] published their papers on the model for the response of wall attachment flip-flops. By combining the existing theoretical treatments of the wall-attachment problem and adding the effects of time-varying-control nozzle discharge coefficients, the resistive-inductive effects of all the channels, the effect of lowered opposite wall pressure and the "peeling off" of momentum by a sharp splitter, the authors arrived at a fairly accurate composite picture of the dynamics of the wall attachment flip-flop. Further work, recently reported by Drzewiecki [18], showed that very long rise time signals could be applied to the numerical model [16] and that the static characteristics of any geometrically-shaped bistable device, under the restrictions of straight walls and sharp splitter, could be a priori predicted to within engineering accuracy. These characteristics include such standard specified quantities as, pressure recovery, pressure gain, fan-out, flow recovery and power consumption [18, 19].

When one has an analytical model, one specifies a geometry and obtains the response; whereas, in designing one specifies a desired response or set of characteristics and the solution desired is a geometry. In order, then, to provide such a design scheme the responses to many geometries are obtained, parameterized and are presented, so that a choice of geometry may be made on the basis of an a priori knowledge of the desired characteristics or response. The static information is presented in parameterized graphical form for ease in visualization. The dynamic information is presented in part graphically, but for the most part on a phenomenological basis as a result of knowledge and insight gained from the dynamic model. Other design information obtained from experience and experimental work as presented by Drzewiecki [20] will be used where necessary for clarification or the definition of impossibilities, etc. Where possible, fabrication limitations are also discussed.

The optimization of the response time of a flip-flop is also

\*Numbers in brackets refer to similarly numbered references listed in section 11.



presented. The design of a "fast" flip-flop [21] is followed from its inception to the presentation of an actual final component along with many of its characteristics. A sample design problem is presented and solved.

## 2. GEOMETRY OF A FLUERIC WALL ATTACHMENT FLIP-FLOP

The general geometry and operating principles of flueric bistable switches is adequately described by Kirshner [22]. In figure 1 a general geometry of a flip-flop is shown defining the terms in this report. It should be noted this design pertains to output decoupled devices in particular, and in some cases to input and output decoupled devices. Flueric devices can effectively be output decoupled by exhausting the output across a vent and catching this "output jet" with a receiver wider than the outlet. This results in a jet-pumping action increasing the output flow. The inputs may also be decoupled in this manner; however, space restrictions usually allow only a one-sided vent, shown in (fig. 1).

Without going into any great detail on the merits of decoupling, suffice it to say that if the output is not decoupled, then loading the output changes the interaction region flow field, often quite drastically. Drzewiecki's [20] measurements have shown this quite graphically. As a consequence of output or input loading the switch point may change as much as 100%, although more realistically about 50%. Therefore to make an analysis of a non-decoupled device requires the analysis of an infinite number of flow fields, one for each possible load. Decoupling obviates the necessity of such numerous analyses of flow-fields because for all loads on the catcher output the flow field is the same in the interaction region since all the flow field "sees" is ground (the decoupler vent). A graphic example of the effects of both output and secondary input loading on a non-decoupled element is shown in figure 2. As shown the switch pressure varies 40% while the switch flow varies up to 35% depending on the blockage of the outputs. In addition the slopes change drastically with secondary input loading. This particular data is representative of non-decoupled, commercial, off-the-shelf flip-flops. It is estimated that to adequately describe the static operation of a two-input, two-output, non-decoupled, flip-flop, would require 85 curves at just one operating supply pressure.

Decoupling prevents spurious signals from entering the interaction region, and hence allows one to design a device to operate on the edge of stability, resulting in a very sensitive (high gain) device.

## 3. FLIP-FLOP STATIC DESIGN

In order to design a fluid flip-flop, one must be aware of its characteristics. A flip-flop is a device that has two stable states, with a signal at either of the two outlets and if there is a signal at one there isn't at the other. The signal may be pressure, flow, or power (a combination of the two). The signal required to initiate the output

change is less than the change in signal at the output. MIL-STD 1306A and 1361 [23], [24] are available, but 1361 is being rewritten, and in accordance with the new proposed standards, the five characteristics describing a fluoric flip-flop are as follows: (1) power consumption, (2) pressure recovery, (3) output, (4) block-pressure static transfer and (5) input.

### 3.1 Standard Characteristics

#### 3.1.1 Power Consumption, W

The power consumed by a fluoric device,  $W$ , is defined as the product of the supply stagnation pressure  $P_s$ , and the associated volume flow through the supply nozzle  $Q_s$ . A power curve, or supply characteristic, is plotted with the supply volumetric flow as the ordinate and the supply stagnation pressure as the abscissa. A typical curve is shown in figure 3a.

#### 3.1.2 Pressure Recovery

The pressure recovery of a fluoric device is the ratio of the pressure at the end of a blocked output  $P$  to the supply stagnation pressure,  $P_s$ . To determine this ratio, a curve is generated with the blocked-output pressure as the ordinate and the supply stagnation pressure as the abscissa. The slope of a line extending from the origin to a point on the curve is the pressure recovery for the supply pressure and indicates losses sustained in the unit. A typical curve is shown in figure 3b.

#### 3.1.3 Output Characteristics

The operating point of a fluoric device is determined by the pressure-flow relation at the output, and the input characteristic of a succeeding unit which represents a load on the output. For a loadline having a flow-pressure relation starting at the origin and increasing, there is a unique point in pressure and flow that is matched by the output. To this end, the output volumetric flow  $Q_{OA}$  is plotted against the output pressure  $P_{OA}$  when the supply stagnation pressure  $P_s$  is at some nominal preset value. Data is obtained by loading down the output until it is completely blocked, while measuring the pressure and flow (fig. 3c).

#### 3.1.4 Blocked-Pressure Static Transfer Characteristic

A static transfer characteristic is the steady-state plot of the output pressure  $P_{OA}$  with the active outlet blocked versus the control stagnation pressure  $P_c$ . The plot then represents the DC function of output against input and gives the switching pressure for the blocked-output. A typical transfer curve is shown in figure 3d.

### 3.1.5 Input Characteristics

It is not only important to know what load can be driven by a device (obtainable from the output characteristic), but how much control it takes to drive it must also be known. This is the input characteristic where the input (or control) volumetric flow  $Q_c$  is shown as a function of the control stagnation pressure  $P_c$ . This also determines the input or control power required to initiate operation. An input characteristic with hysteresis (non-decoupled inputs) is shown in figure 3e.

### 3.2 Computed Parameters

Several parameters can be computed from the information in the standard characteristics in addition to the ones mentioned.

#### 3.2.1 Dimensionless Switching Pressure, $P_{sw}/P_s$

Dimensionless switching pressure is the minimum control stagnation pressure required to change the state of the outputs of a digital fluoric device divided by the supply stagnation pressure  $P_{sw}/P_s$ . The switching pressure may be obtained from the input characteristic at the point of an abrupt change in the upward-going curve. In some devices, the switching pressure point is not defined and the state of the outputs must be monitored simultaneously. The switching pressure is the control pressure that produces a positive constant signal in the initially off output.

#### 3.2.2 Pressure Gain, $G_p$

The pressure gain of a digital fluoric device is defined [23] as the blocked static pressure  $P_o$  at the active outlet port of a fluoric device at the point of incipient switching, divided by the control stagnation pressure required to initiate switching  $P_{sw}$ . The latter pressure is the switching pressure for a blocked output and should be differentiated from the dimensionless switching pressure above.

#### 3.2.3 Flow Gain

The flow gain is the ratio of active output volumetric flow,  $Q_o$ , at ambient output pressure to control volumetric flow at the point of switching  $Q_{sw}$ . This latter value must be obtained from the input characteristic operated with ambient pressure at the outputs (no external load).

### 3.2.4 Fanout

Fanout is one of the most important parameters related to digital circuitry and is defined as the number of like units operating at the same supply pressure that can be simultaneously switched by the output of one unit. The measurement of fanout is complicated when many units operate from the output of one, since the closest units may be switched on a pressure wave (from the output) and the input impedance of the switched units then increases, allowing the excess flow from the driving output to switch additional elements. Another occurrence is a "slaving" effect where a wave from the controls of a just-switched amplifier causes another element to switch. Thus, determining the elements that switch simultaneously is complicated by the dynamic matching characteristics of the transmission lines used and the terminations on the ends, in a basically quasi-static test, and the measurement requires identifying the elements switched by the original output wave. In principle this can be done, but a practical alternative is to define ideal fanout as the integer number ratio of the volumetric flow from a unit (at an output pressure equal to the switching pressure) to the input volumetric flow required to initiate switching. The flow out of a unit is determined from the output characteristic and is the output flow at the switching pressure. The control flow at switching pressure is obtained from the switching point on the input characteristic. The value obtained for ideal fanout should be a reasonably conservative approximation to actual fanout. Steady-state losses caused by interconnections act as additional loads and tend to decrease the actual fanout.

### 3.2.5 Flow Recovery

The flow recovery is defined as the ratio of the output volumetric flow at ambient pressure  $Q_o$  to the supply volumetric flow  $Q_s$ , indicating losses and venting in a unit. If the flow recovery is less than unity and the unit is small, there should be no danger of contamination from the ambient atmosphere since no flow enters, but is expired through auxiliary ports. However, units having a flow recovery greater than unity entrain flow through the vents and aspirate ambient fluid and there may be a higher fanout. If contamination is of no concern, this type may be advantageous.

### 3.3 Some Approximations

Several rules of thumb can be applied to some of the characteristics.

If the controls are not vented so that there is a hysteresis loop in the input characteristic, the characteristic can be approximated, knowing three points on the curve; the blocked-control pressure, the nozzle dimensions and the switching pressure or flow. In general the characteristic prior to switching is relatively linear in the direction of increasing control pressure as seen in figure 3e. The off portion

of the curve after switching follows the known nozzle pressure-flow characteristics [19]. The off-value of flow immediately after switching is roughly 2/3 of the flow required to initiate a switch. If the zero-pressure-control flow is known, this gives yet another point. If the control is vented, then the characteristic is just the orifice relation for the nozzle [19]. The portion of the input characteristic, for increasing pressure and flow prior to switch, is referred to as the "switch-on". Switchback results from a suction on the control when the jet is on the other side. Figure 4 shows the construction of a switch-on input characteristic. (The switchback point and curve can only be obtained from the complete analysis [18]).

The blocked-pressure-transfer characteristic may be approximated by knowing the pressure recovery and the switch pressure. If a unit is output-decoupled, the switch pressure will not depend on the state of the output loading; hence, there is only one value of switch pressure. The construction of the on portion of the transfer curve is shown in figure 5. If the switchback pressure is known, the off portion can also be constructed. Input decoupled (vented) units generally do not have switchback points, since suction will just draw flow from ambient and not the interaction region.

The supply, pressure recovery, and output characteristics are determined from the analysis, although the output can be approximated if the flow and pressure recoveries are known. Then a quadratic may be fitted between the two points, whose equation is simply

$$\frac{P_{oA}}{P_s} = \frac{P_o}{P_s} \left[ 1 - \left( \frac{Q_{oA}/Q_s}{Q_o/Q_s} \right)^2 \right] \quad (1)$$

Equation 1 may not be a good fit if the outlets are very long, and in this case (e.g. when  $L_o/b_s > 50$  where  $L_o$  is the output length and  $b_s$  is the supply nozzle width) a straight-line fit is probably better, as in equation 2.

$$\frac{P_{oA}}{P_s} = \frac{P_o}{P_s} \left[ 1 - \frac{Q_{oA}/Q_s}{Q_o/Q_s} \right] \quad (2)$$

### 3.4 Analytical Static Design Curves

The static design of a flueric flip-flop results from a set of specifications. Static specifications are generally in the form of minimum pressure or flow to initiate a switch, minimum fanout (number of elements to be driven), and/or a minimum, (or maximum) pressure, or flow available at the output, in the case of an actuator device which must drive, a piston or some other mechanical device.

The trends of important variables that should be noted are as follows:

1. Attachment point location,  $X$  increases with increase in:
  - a. Wall angle,  $\alpha$
  - b. Splitter distance,  $\ell_{sp}$
  - c. Offset,  $D$  for values larger than one-half nozzle width. (see fig. 1)
2. Pressure recovery decreases with increases in:
  - a. Wall angle,  $\alpha$
  - b. Splitter distance,  $\ell_{sp}$
  - c. Offset,  $D$
3. Pressure and flow to switch decreases with:
  - a. Increase in wall angle,  $\alpha$
  - b. Increase in offset for  $D/b_s > .5$
  - c. Decrease in offset for  $D/b_s < .5$
  - d. Decrease in splitter distance,  $\ell_{sp}$

Figures 6 to 9 graphically present the computed values of various parameters from the general analytic theory presented by Drzewiecki [18]. The myriad combination of geometries precludes the presentation of sufficient curves to cover every possible case. Curves are presented, however, from which design is possible for those configurations which fall into the general area of conventional devices. The curves given cover wall angles,  $\alpha$ , from  $10^\circ$  to  $30^\circ$ , splitter locations,  $\ell_{sp}$  from 6 to 15 nozzle widths, vent locations  $\ell_v$  from 8 to 20 nozzle widths, and wall offsets  $D$  from 0 to 1.0 nozzle widths. Figures 6 to 9 present the attachment location, pressure recovery, blocked-control pressure, and open-port control flow, as a function of offset for four different wall angles and two different control nozzle widths.

When considering the static design of a flip-flop, one of the first design considerations is the point of attachment. The walls must be long enough so that when the control ports are both open to ambient pressure, the attachment point of the jet should be on the upstream side of the sidewall vent. Experience has shown that at least one-to-two nozzle widths should be allowed for a margin of stability. Therefore,

$$\begin{aligned} \text{wall length} &= \text{attachment location} + 2b_s \\ \ell_v &= X + 2b_s \end{aligned} \tag{3}$$

The attachment-point locations, shown in figures 6 to 9 for the open controls, have to be used with care. The attachment location is a function of the flow entering through the controls and therefore of the

control impedance. If there is a highly restrictive control (i.e. long channel), then the flow is less and so the attachment point is closer to the blocked case, and if there is control-area modulation by the jet ( $D/b_s < 0.5$ ), the effective input impedance is higher and the attachment distance is shorter. This phenomenon (area modulation) occurs when the control impedance is determined by the area between the edge of the jet and the downstream edge of the control port. For small off-sets ( $D$  usually less than half a supply nozzle width), the distance from the jet edge to the control edge is less than the control nozzle width, hence is the limiting restriction. The control nozzle used for the analytical determination of the attachment location is shown in figure 10.

While it may be instructive to provide curves of attachment point against control flow, as in Brown and Belen [15], the designer does not *a priori* know what that flow will be and will not know until he has designed the geometry. The attachment curves presented are representative and the safety factor used will generally cover most control geometries that will be designed. Since the zero control pressure (open control) flow is given with the attachment point, a linear interpolation (or even extrapolation) between the blocked (zero flow) case can be made. The curves for attachment point versus control flow are fairly linear (for example see Brown and Belen [15]) therefore a linear interpolation is valid. Thus, a choice of a different nozzle with a different impedance can be made and the resulting attachment point can be checked to see if the device will be bistable (e.g. the attachment point is upstream of the sidewall vent).

Certainly, there may be occasions when the device is to operate from zero flow rather than zero pressure, and in this case the blocked-control attachment-point location may be used.

The pressure recovery shown in figures 6 to 9 is the total head at the output which then exits across the decoupler vent and is captured. In general, there is a slight loss of head across the vent and a marked increase in the flow due to entrainment. For example, a commonly used decoupler configuration as shown in figure 11 has recovery characteristics so that the blocked-pressure recovery is 75% and the flow recovery at zero-back pressure is 210%. The pressure recovery from figures 6 to 9 is determined from the output flow so that

$$\frac{P_o}{P_s} = \left( \frac{Q_o}{Q_s} \right)^2 \left( \frac{b_s}{b_o} \right)^2 \quad (4)$$

Hence, for a known performance decoupler geometry, the amplifier pressure, and flow recovery can readily be determined. For example,



$$\left. \frac{P_o}{P_s} \right|_A = 0.75 \frac{P_o}{P_s} \quad (5)$$

$$\left. \frac{Q_o}{Q_s} \right|_A = 2.1 \frac{Q_o}{Q_s} \quad (6)$$

for the decoupler in figure 11.

Figure 12 shows static-switching pressures while figure 13 shows static-switching flows. The values obtained from the theory satisfy Keto's [25] "bubble-venting condition" which specifies that the necessary condition for a self-sustaining switch is that the attachment bubble be vented or ruptured. While it is not always necessary to "vent" the bubble to initiate switching, as in the case when the attachment angle is large enough to cause bubble instability, in the geometries chosen here, venting occurs before the bubble instability.

Figure 14 shows the computed parameters of pressure gain  $G_p$  and fanout,  $F_o$ . It must be noted that the values presented are only representative since amplifier fanout and pressure recovery depend on a choice of splitter locations and decoupler design, to name but a few of the possibilities. Values are for a splitter location of  $6b_s$ , and the decoupler of fig. 11. Moving the splitter downstream will decrease the gain. The gain and fanout for other geometries may be obtained from the switching flows and pressures and the respective flow and pressure recoveries.

Figures 6 to 9, and 12 to 14 present a set of curves that are sufficient for the engineering design of a turbulent wall-attachment flip-flop with a sharp splitter and specific decoupled output, but without consideration of any dynamic effects.

#### 4. FLIP-FLOP DYNAMIC DESIGN

The design specifications for bistable devices, in general, may include either frequency-response or response-time requirements. The HDL analytical model [18] allows the determination of many internal flow phenomena, in that it gives the complete temporal history of all the pressures and flows in response to a given applied signal. In this manner one can make a judicious choice of the geometric parameters other than those which have been statically determined. The good agreement of experiment with the analysis of references [16] and [18] indicates that a valid assumption is that all channels leading to or away from interaction region of the device are resistive and inductive. The capacitance of a flip-flop is therefore attributed to the predominance of the attachment bubble.



#### 4.1 Response Time

Some dynamic features were noted in reference [16] and [18]. One of the more important effects of inductance of the channels is the increasing of response time of a switching jet. In figure 15 the motion of the attachment point is shown, in time, in response to a sudden control pressure. The attachment initially moves slowly due to the lag of control flow behind the control pressure, caused by the control line inductance. Then the point starts to move quickly. During this time the flow entering the interaction region through the "inactive" outlet approaches zero. As the splitter diverts flow to that outlet the inductance of that channel is felt, and the pressure on the opposite side of the jet increases until the flow in the outlet starts to move. This increase in pressure on the opposite side is evidenced by the slowdown of the attachment point motion as the flow in the "inactive" outlet becomes positive. Eventually, of course, the bubble is ruptured by the splitter and the jet switches to the other side. A reduction of the inductance

$$L = \frac{\rho \ell}{A} \quad (7)$$

where

- L - inductance
- $\rho$  - fluid density
- $\ell$  - channel length
- A - minimum channel cross-section area

in both the control and the outlet will speedup the switching. Although not shown, a similar inductive effect occurs as the flow enters the bubble through the sidewall vent. However, the vent does not have as dominant an effect as the other two channels. Thus, the first rule, when response time is at a premium, is to minimize the quantity  $\ell/A$  for any channel.

The response time of a flip-flop is strongly dependent on the strength of the input signal and on its shape. The response to a "step" of a finite rise time is illustrated in figure 15. In general, the response time diminishes with increased amplitude of a signal for the same rise time. References 1 to 4, and 16 to 17 show this effect. Ozgu and Stenning [26] show some response times for cusped splitter devices. In figure 16 response times for various geometries are given in response to finite rise-time input pressure signals.

As demonstrated, the response time of the flip-flop is made up of the responses of the control lines and the jet and the output lines; hence, the fastest response can only be attained when the line dynamics are negligible and when the jet does not have to move far before the bubble becomes unstable. This can be achieved by making the attachment wall, control ports and outputs short and by the placing of the splitter in such a location that it just starts to intercept the jet when the jet

is initially attached to one wall. Clearly this arrangement is just barely stable, so care must be exercised in the use of such a device.

#### 4.2 Maximum Frequency Response

The response curves shown in figure 16 are based on non-dimensional times. Frequency response certainly can be normalized; however, it is much clearer to the user/designer to speak of hertz frequency. The minimum time for the switching of a jet, from attachment to reattachment, is the time it takes the jet to swing past the splitter, reattach to the opposite side and then reach equilibrium in a newly reattached state. On an output-pressure versus time plot, this time would be the rise-time of the inactive pressure as shown in figure 17. The maximum frequency then will be the reciprocal of twice this time. This frequency represents the maximum number of times in one second that the output pressure of a device can reach 63% of the pressure recovery. It is clear that, while a higher frequency may be obtained with the jet still attaching to each wall in its turn, the output channel cannot respond fast enough; hence, the output pressure will be degraded. On a Bode plot one would see a dropoff in amplitude. Maximum frequency response is a function of input amplitude so that when choosing the frequency response, care must be taken that the required input-pressure amplitude does not exceed the amplifier-pressure recovery or the pressure gain will be less than one and there no longer will be any amplification.

Frequency response increases when the element size is made smaller since the transport time through the device is decreased.

In general, the jet cannot be expected to switch at a speed faster than the transport time between the splitter and the control. For turbulent devices the theory predicts and experiment verifies (see section 6) that about 3.0 transport times is the shortest response time for reasonable control signals. Katz, et al., [27] found experimentally that, even with huge signals, the switch time only approached the transport time to the splitter.

#### 4.3 Other Dynamics

When the dynamic output of a flueric flip-flop is measured, the circuitry used to make the measurement often imposes its own dynamics so that the response picture is not exactly as predicted. The experimental blocked-pressure response usually exhibits "ringing". References 16 and 17 show this. The ringing is directly due to the response of the additional lines and fittings required to mount transducers. Here the compressibility of a gas, or the compliance of a transducer in any fluid, acts as a capacitor. The outlet channel of the flip-flop (in a decoupled device, the catcher) and the associated transmission lines, to the transducer, act as a series resistance and inductance. Their volume and the volume of the transducer, or the transducer compliance, act as a capacitance to ground. The equivalent circuit is shown in figure 18. The response then has a natural frequency,  $\omega_n$

$$\omega_n = \frac{1}{\sqrt{LC}} \quad (8)$$

and a damping factor,  $\zeta$ ,

$$\zeta = R/\sqrt{L/C} \quad (9)$$

where

- L - inductance
- C - capacitance
- R - resistance

The capacitance of a fixed volume such as the volume of the channels or the internal volume of a transducer, may be approximated by  $C = V/(n \cdot P_{abs})$  where  $V$  is the volume and  $n$  is the polytropic constant.

For high frequencies  $n = 1.4$ , the process is adiabatic, for low frequencies  $n = 1$ , isothermal process.

Further loading may be added with a consequent change in the response. The case of long lines with a high impedance on the end, as in a feedback line in an oscillator, may be treated as an LR circuit with a time constant,  $\tau$ , characterized by the rise time,  $\tau = L/R$ . The circuit response is shown in figure 18c also, which shows the difference between adiabatic and isothermal response.

The flip-flop model's theoretical response [16] does not consider the external dynamics hence the response is always flat. When considering a circuit with interconnections, the resonant frequency and damping factor must be determined as it is conceivable that the overshoot could switch an upstream device when not desired, as might be visualized from the response shown in figure 18.

#### 4.4 Dynamic Design Conclusions

In general, any response of a digital device is limited by the response of the channels within it and the transmission lines, fittings and coupling, without. Optimizing the response of a particular component may often be wasted effort, especially if the response of the associated circuitry is below that desired. Furthermore, if the optimization of the response time of a device is at the expense of some desired static characteristics then it is undesirable. To give an example, if it desired to activate a circuit in a hazardous environment, where the fluidic signal from the flip-flop must be transmitted a distance  $\ell = 1$  meter, using standard plastic tubing to transmit the signal, immediately it is apparent there will be an acoustic delay

$$\tau_a = \frac{\ell}{a} = \frac{1\text{m}}{325 \text{ m/s}} = 3 \times 10^{-3}\text{s}$$

where

$a$  = speed of sound (in air  $a \sim 325$  m/s)

In addition, there will be an  $L/R$  rise time. If the load at the end of the tubing is a typical  $0.5 \times 1.0$  mm nozzle then the resistance, in air, for a maximum signal of 5 kPa will be approximately  $10^8$   $P_a/m^3/s$ , and if the tubing ID is 3.125 mm then the inductance is

$$L = \rho \ell / A = \frac{1.2059 \frac{\text{kg}}{\text{m}^3} \times 1 \text{ m} \times 4}{(3.125 \times 10^{-3})^2 \text{ m}^2} = 1.57 \times 10^5 \frac{\text{kg}}{\text{m}^4}$$

and so the rise time  $\tau = L/R$  is  $1.57 \times 10^{-3}$  s. Hence the total time for a signal to propagate, one-way is 4.57 ms. Considering twice that time for two-way operation, or any function that requires a feedback from the output to initiate the next cycle, results in the maximum frequency of this simple circuit being less than 110 Hz. The optimization of a flip-flop to switch from say  $10^{-4}$  s for a switch to  $10^{-5}$  s is obviously immaterial. If the device were very large, such that the switch time were in the order of milliseconds then it might pay to optimize to at least hold a 100 Hz frequency system response.

Any presentation of response data must be inadequate for many reasons. The multitude of geometries is one reason; however, the most important is that the response is a function of the shape of and amplitude of the input so that an additional infinity of possible signals adds to the problem. However, in fluidic circuits, transmission lines and other passive components, often are the limiting factors so that if estimates of the frequency response of these other parts can be made, this can often suffice. Where integrated circuits, stacking or staging, is used, the connections can be very short and the device's response can play a significant part. For this reason the results presented become important.

## 5. OTHER DESIGN CONSIDERATIONS

### 5.1 Supply Pressure

The application of the design criteria presented in the previous sections applies when fully established turbulent flow exists in the flueric device. From experimental evidence it is known that under certain conditions all devices exhibit Reynolds number dependence. When the flow reaches a high enough Reynolds number, such parameters as attachment length, gain and fanout reach a constant value. This is because at high values of Reynolds number, the entrainment becomes constant. From the experimental work of McRee and Moses [10] and McRee and Edwards [14] on jet attachment, the attachment point is found to be constant when the modified Reynolds number,  $N_R'$  is a given constant value for all aspect ratios,  $\sigma$ .

$$N_R' = N_{Rs} / [(\ell_{th}/b_s + 1)(1 + 1/\sigma)^2] = 1000 \quad (10)$$

where

$$\begin{aligned} N_{Rs} &= b_s \sqrt{2P_s/\rho/\nu} \\ \ell_{th} &- \text{length of supply nozzle throat} \\ \sigma &- \text{aspect ratio} \\ \rho &- \text{fluid density} \\ \nu &- \text{fluid kinematic viscosity} \end{aligned}$$

This form of modified Reynolds number comes from the derivation of the discharge coefficient, [19], where it can be shown that the discharge coefficient is only dependent on the modified number; hence, at one value of  $N_R'$  the properties of the supply flow are probably constant.

Measurements performed at HDL on gain and fanout on several flip-flops verifies this value of modified Reynolds number. For example for an aspect ratio of 2, and a nozzle width  $b_s$  of 0.5 mm, the gain and fanout are within 3% of the final value at a supply pressure of 6 kPa, or  $N_R' = 996$ .

From measurements performed on other digital logic elements, both commercial and in-house, of various geometries, including latching vortex type devices, values for the modified Reynolds number, above which constant normalized operation occurs, range from a low of 807 to a high of 1090. Considering the uncertainties i.e. exact values of  $\sigma$ ,  $\ell_{th}/b_s$ , this is felt to be sufficiently close to 1000.

Muller's [28] data on switching control flow,  $Q_{sw}$ , shows that  $Q_{sw}$  becomes constant at  $N_{Rs} = 8000$  for  $\sigma = 1$ . For his nozzle geometry  $\ell_{th}/b_s = 1$  and  $\sigma = 1$ . This gives a  $N_R' = 1000$ . The operating pressure (or nozzle width, or aspect ratio) can be obtained from Eq. 10 or 11, which expands Eq. 10 into its basic parts.

$$P_s = \left[ \left( \frac{\ell_{th}}{b_s} + 1 \right) (1 + 1/\sigma)^2 \frac{\nu}{b_s} \right]^2 \frac{\rho}{2} \times 10^6 \quad (11)$$

Furthermore, if the device is expected to operate in the incompressible flow range, the supply gage pressure should not exceed half an atmosphere.

It should be noted, however, that many characteristics are considerably improved (pressure gain  $G_p$ , fanout  $F_o$ ) if the flow is not fully turbulent. Advantage may be taken of this if care is taken not to operate in an unstable region. If a device is designed to be

marginally stable from the curves presented here (based on fully-established turbulence) then there is not margin for reducing the minimum operating pressure. Since only a few scattered experimental results for a limited number of geometries exist for the change of the various parameters with Reynolds number, no design curves can be specifically generated, and all that can be stated is that gain and fanout can be substantially improved. However, if the problem is that of varying environments, insensitivity to Reynolds number is desirable to achieve constancy of operation, so the gain or fanout presented here must be settled for.

## 5.2 Nozzle Dimensions

In general, the narrowest channels in a flip-flop will be either the supply or control nozzles. Fabrication technology at present can probably make a channel to about 0.025 mm wide; however, such regions as corners can usually be held to only 0.050 mm radii in metal etch or fine blanking processes. These radii can adversely affect the flow field. In a supply nozzle the effect would be to add a diffuser at the end (e.g. with an expansion ratio of 5, for a 0.025 mm nozzle). A general rule of thumb for nozzles is that the exit corner radius should be kept to less than one-half the nozzle width. In that case, the minimum-width nozzle that can be made is 0.1 mm. This is a practicable size and metal etching of 0.1 mm thickness laminates is an easy matter. The tolerance held by the manufacturing process becomes very crucial when it is observed that gain (and fanout) changes very rapidly as a function of offset at low values of offset (see fig. 14). Inadvertently making the nozzle too large decreases offset and vice versa so that such devices may not function properly.

## 5.3 Aspect Ratio

Although the theoretical model [16] incorporates aspect ratio and its effects, it is a good rule of thumb, in order to preserve pressure and flow recovery and strong attachment, to use an aspect ratio of at least two. The model allows for any aspect ratio in the nozzles; however, it does not consider the retarding effect of the proximity of the downstream bounding surfaces which begin to have some significant influence when  $\sigma < 1.0$ . When  $\sigma < 1$  the effect is deleterious in that recovery decreases as does gain for bistable turbulent devices. Actual devices usually are designed to have  $\sigma > 1.0$ .

## 5.4 Nozzle Design

In accordance with the specifications [19], nozzles should be smooth, have a contraction ratio and length in excess of 5, and should have as short a throat as possible commensurate with the rest of the design specifications. This is to ensure minimum losses in the nozzle so that the recovery, and hence gain, will not be adversely affected.

## 6. THE FAST FLIP-FLOP

During the time that the analytical model for the response of bistable devices was being completed, the problem was posed as to how one would design a flip-flop with acceptable static characteristics for a minimum response time.

Such a device has to be designed with extremely short inlet and outlet channels since the motion of the attachment point is retarded by the inductance (inductance) of these channels.

In addition, when the response of the inlet line to a step in control pressure,  $P_c$ , is analyzed as a series L-R circuit, the flow response  $Q(t)$  can be approximated by

$$Q(t) = P_c/R_c (1 - \exp(-R_c t/L_c)) \quad (12)$$

where  $t$  = time

The dynamic model has shown that the total volume of flow supplied to the control  $V_{sw}$  is roughly constant when switching occurs, independent of the amplitude of the control pressure  $P_c$ . Integrating the control flow to some switch time,  $T$ , results in Eq. (13)

$$V_{sw} = P_c T/R_c + L_c/R_c (\exp(-R_c T/L_c) - 1) \quad (13)$$

It can be seen that for constant switch volume  $V_{sw}$  and control pressure amplitude  $P_c$ , to minimize the switch time  $T$  one must also minimize input impedance  $R_c$ . Physically, this means that if the input resistance is higher it will take longer to push in a given total volume of fluid. Hence, in addition to decreasing the inductance, one must also decrease the resistance.

Looking at conventional devices, it is not immediately obvious how this can be achieved. Of course, the nozzle itself should be of an optimum efficiency design, but in close-wall devices (where high gain, fanout and recovery exist, see section 3.4) the limiting impedance is the spacing between the attaching jet and the attachment wall at the downstream corner of the control nozzle. This corner, however, may be cut away, leaving only the nozzle as the limiting impedance. Therefore, in designing the device, a rounded corner was used. The width of the nozzle was chosen so that the device would have a stable attachment with the control ports open (or decoupled) and with the splitter as close-in as allowable. The marginal safe-splitter distance is about 6 supply-nozzle widths, so 8 was chosen to be completely stable. Note that if the splitter is too close in, it will intercept the attaching



jet and make it oscillate. For a wall angle of  $12^\circ$  (see design curve of fig. 7), an offset of zero, the attachment length for open ports is just under 6 nozzle widths if the control width is 0.75 of a supply nozzle. This means that the attachment point is about  $2b_s$  from the splitter. Using the vent location criterion, Eq. 3, a side-wall vent should be located at about  $8b_s$ . The value of wall angle,  $12^\circ$ , was chosen as a compromise between weaker attachment (for faster switching) and higher recovery characteristics (for good steady-state operation).

The consideration of short lines now becomes a fabrication problem. Ideally, the design would have output channels only 1 or  $2b_s$  long, so that the decoupler-vent area becomes a wide gap right across the device. To illustrate the fabrication problem, figure 19 shows the planview of a flip-flop that had very short channels by the splitter and had been panto-milled into a block of plexiglas. It can be seen that a problem would arise if the planview were to be fabricated by some process using laminates, where the interior is cut completely through the material, in that the splitter could not be fixed relative to the geometry since it is an island. Many years of experience in the fabrication of fluidic elements has shown that to avoid asymmetry, devices must be made in laminates, alternate elements of which can be inverted. Up to this time, metal etching, has proven the most acceptable fabrication process with respect to, cost, quality, and availability for low-and-high volume production. In spite of this, however, the device was made, as stated, by panto-milling because it was the only way to make the island splitter, with the result, which was foreseen, that the characteristics were asymmetrical and the characteristics could not be adequately duplicated from one device to another. A further compromise was then made - in order to obtain reproducibility and symmetry - the island was eliminated, the splitter was lengthened and the outputs flared out, so that the decoupler vents were no longer common (see fig. 20).

It was desired that the device be both input and output decoupled. The output decoupler chosen had a pressure recovery of 70% and a flow recovery of 125% and the input decoupling vent had a 90% pressure recovery and a 100% flow recovery.

The steady state characteristic can now be computed. For a normalized switch pressure  $P_{sw}/P_s$  of 0.075 (estimated from fig. 11,  $P_{sw}/P_s = 0.042 \times (1/.75)^2 = .0747$ , where the switch pressure at  $b_c = b_s$  is multiplied by the square of the ratio of the control areas) and a normalized pressure recovery  $P_o/P_s$  of .364 (from fig. 7) the gain,  $G_p$ , is

$$G_p = \frac{P_o/P_s}{P_{sw}/P_s} \times \frac{P_A/P_o}{P_{cA}/P_c} = \frac{.364}{.0765} \times (.7)(.9) = 3.071$$



For a normalized switch flow of 0.266 (from fig. 11, switch flow is relatively independent of control width) and a normalized output flow  $Q_o/Q_s$  of 0.905 the fanout  $F_o$  is

$$F_o = \frac{Q_{oA}}{Q_{sw}} = \frac{\frac{Q_o}{Q_s} \times \frac{Q_{oA}}{Q_o}}{\frac{Q_{sw}}{Q_s}} = \frac{0.905 \times 1.25}{.266} = 4.25 \approx 4$$

These values compare exceptionally well to the measured values where  $G_p = 3.5$  and  $F_o = 4$ . The final device is shown in its planview in figure 20 and a photograph in figure 21. Table I shows a comparison of some of the parameters including others not calculated above.

Table I. Comparison of Computed and Measured Steady State Parameters

	Computed	Measured
Pressure Recovery	0.26	0.28
Flow Recovery	1.26	1.25
Gain	3.07	3.5 - 4.3
Fanout	4	3-4
Switch Pressure	0.07	.065 - .078
Switch Flow	0.265	0.303

The computed data is sufficient to approximately construct all the steady-state characteristic curves in the manner described in section 3. Figure 22 shows these constructions, the theory, and the comparison with actual x-y recorder data for the output and the transfer characteristics. The equation for the discharge coefficients  $c_d$  for the supply and control nozzles are given by equation (14) which can be obtained from reference [19] and is

$$c_d \approx 1 - 3.5/\sqrt{N_R'} \quad (14)$$

where

$N_R'$  - modified Reynolds number, equation 10.

The validity of the theory for the discharge coefficient was established by its good agreement with the data [19]. The theoretically predicted values of the flip-flop characteristics are well within any experimental spread with which workers in turbulent fluidics are familiar.

Experimental measurement of the actual jet switch-time is difficult. The switch time, defined as the time it takes the jet to move across the device after separating from the initial wall, can be estimated from a fairly simple experiment. If the unit is connected as a feedback

oscillator of a low enough frequency to insure stable attachment each half period, and the output pressure is monitored, the following calculations can be made. The output signal, generally, will look like an underdamped second order RLC response. This is the result of the output jet impinging on the decoupler catcher which acts as a second order system resonator. The second order response to an input whose rise time is less than one quarter of the output rise time is essentially the same as for a step, so that the input signal to the catcher is about a quarter of the output rise time. This is then the rise time for the flow out of the receiver from the moment the jet starts to move across the amplifier to the time it is completely reattached. Measurements made at three different frequencies (61, 213, and 320 Hz) for two supply pressures (10 kPa and 20 kPa) indicated an average switch time of  $2.9 \pm 1.2$  transport times to the splitter. Transport time  $\tau_t$  to the splitter is defined as the average jet-exit velocity  $c_d \sqrt{2P_s/\rho}$  divided into the splitter distance,  $\ell_{sp}$

$$\tau_t = \ell_{sp} / c_d \sqrt{2P_s/\rho} \quad (15)$$

Computations made with the numerical model with an input pressure signal equal to the pressure recovery for various rise-time signals show that the time for the jet to move across the device is relatively constant at an average of 4.5 transport times. Considering the approximation assumed, and the experimental scatter, this is a good verification.

Lowering the supply pressure, as indicated before, tends to make the attachment weaker. Goto and Drzewiecki [16] have shown theoretically that the laminar jet switches faster (in normalized time). This is further verified here in that at supply pressures of 5 and 2.5 kPa, the experimental switch times were found to be 1.5 and 1.1 transport times to the splitter. Below 2.5 kPa, the unit was proportional. The response of the entire unit was estimated at 1.15 transport times through the device at 5 kPa. The response time is estimated by assuming that the period of oscillation is twice the response time, twice the input rise time to switch pressure, and the acoustic delay. The first is the quantity in question, the second can be measured but is simply estimated by the L/R rise time  $\tau_{LR}$  of the output feedback line inductance  $L_o$  and the average control resistance  $R_c$  as in section 4.4 so that

$$\tau_{LR} \Big|_{P_c = P_{sw}} \approx (L_o/R_c)/G_p \quad (16)$$

If one assumes that the pressure recovery is reached in time  $L_o/R_c$ , then the switch pressure  $P_{sw}$  is reached in the fraction of time  $P_{sw}/P_o$  (which is the reciprocal of the gain,) hence eq. 16. The acoustic delay is merely twice the distance around the feedback lines through the flip-

flop divided by the speed of sound. The period is simply measured, thus the response time  $\tau_r$  is

$$\tau_r = \frac{\tau_{\text{per}} - \tau_a - 2\tau_{\text{LR}}}{2} \quad (17)$$

where

- $\tau_{\text{per}}$  - period
- $\tau_a$  - acoustic delay
- $\tau_{\text{LR}}$  - inductive-resistive delay

In simple terms, this is the time it takes the device to respond with an output signal after enough pressure has been imposed on it to initiate switching. Since flow lags the pressure, and not only switch pressure but switch flow must be satisfied, then eq. 17 should generally be a conservative estimate for the flip-flop response time. For the device operating with fully established turbulent flow, a response time  $\tau_r$  of about three (3) transport times has been observed.

The maximum operating frequency response  $f_{\text{max}}$  of this unit, for no degradation of output signal can then be estimated as

$$f_{\text{max}} = \frac{1}{2\tau_r} \Big|_{\text{min}} \approx \frac{1}{6\tau_t}$$

$$f_{\text{max}} \approx 0.17 c_d \sqrt{\frac{2P_s}{\rho}} / \ell_{\text{unit}} \quad (18)$$

where

$\ell_{\text{unit}}$  - length of the device

Using the criteria for minimum supply pressure and eq. 18 results in a chart for maximum frequency response as a function of element size and supply pressure, shown in figure 23, and a resultant zone of operation, for this particular supply nozzle shape. Decreasing  $c_d$  shifts the  $N_R$  line to the right, further decreasing the operation zone.

The corner frequency  $f$  is a function of control amplitude in a bistable device. In general, it has been found that the corner frequency as a function of input amplitude is a straight line passing through the minimum switch pressure (no response below minimum switch pressure) up to the maximum operating frequency response at a control amplitude equal to the pressure recovery. This results in eq. 19.

$$f/f_{\max} = (P_c/P_s - P_{sw}/P_s)/(P_o/P_s - P_{sw}/P_s) \quad (19)$$

Figure 24 shows a comparison of some data with eq. 19, and the agreement is good. The rationale for using the frequency in response to a control pressure amplitude equal to the pressure recovery as the maximum frequency point is simple. In figure 16, at the value shown, the flip-flop switching time is within 5% of the minimum, or in other words, amplitudes greater than the pressure recovery, do little to speed it up. The data of figure 24 shows the frequency response of both the first design (fig. 19) and of the final design (fig. 20). For a device with  $b_s = .1 \text{ mm}$  ( $\ell_{\text{unit}} \sim 4 \text{ mm}$ ) operating at about 70 kPa, a maximum attainable frequency response (in air) is about  $10^4 \text{ Hz}$ .

The flip-flop designed here is probably not the optimum design. The static characteristics, for example, could probably be enhanced somewhat, but that was not the object. The maximum frequency response at 20 kPa for  $b_s = 0.5 \text{ mm}$  is about 1300 Hz. This exceeds by a factor of five the quoted specifications of similar sized commercial off-the-shelf devices. The static characteristics compare favorably with the commercial elements in that they fall within the large range of quoted characteristics.

#### 7. SUMMARY OF DESIGN EQUATIONS

The equations which are felt to be important to the designer are briefly summarized in this section.

- Eq. 1 - Output Characteristic based on known pressure and flow recovery - short outputs  $< b_s$ .

$$P/P_s = P_o/P_s [1 - ((Q/Q_s)/(Q_o/Q_s))^2]$$

- Eq. 2 - Output Characteristic based on known pressure and flow recovery - long output  $> 50 b_s$ .

$$P/P_s = P_o/P_s [1 - (Q/Q_s)/(Q_o/Q_s)]$$

- Eq. 3 - Attachment wall length criterion  
Wall length = Attachment point with open ports +  $2 b_s$

$$\ell_v = X + 2 b_s$$

- Eq. 4 - Relationship between no loss blocked pressure recovery and flow recovery before decoupling

$$P_o/P_s = (Q_o/Q_s)^2 (b_s/b_o)^2$$

Eq. 7 - inductance of a channel

$$L = \rho \ell / A$$

Eq. 11 - Minimum pressure for supply pressure independent operation (e.g. fully established turbulent flow)

$$P = 0.5 [(\ell_{th}/b_s + 1)(1 + 1/\sigma)^2 v/b_s]^2 \rho \times 10^6$$

Eq. 15 - Definition of transport time to the splitter

$$\tau_t = \ell_{sp} / (c_d \sqrt{2P_s/\rho})$$

Eq. 16 - Inductive delay time due to signal transmission through an inductive - resistive line

$$\tau_{LR}|_{P=P_{sw}} \approx (L/R)/G_p$$

Eq. 17 - Definition of flip-flop response time from an oscillator

$$\tau_r = (\tau_p - \tau_a - 2\tau_{LR})/2$$

Eq. 18 - Maximum frequency response of a fast flip-flop

$$f_{max} \approx 0.17 c_d \sqrt{2P_s/\rho} / \ell_{unit}$$

Eq. 19 - Frequency response of a fast flip-flop

$$f/f_{max} = [(P_c/P_s) - (P_{sw}/P_s)] / [(P_o/P_s) - (P_{sw}/P_s)]$$

## 8. DESIGN SPECIFICATIONS

There is a practical limit to the number of specifications which can be required of a flip-flop design, *a priori*. Assuming that any quantity or parameter specified by itself can be met, then it follows that there are only a finite number of other specifications which can (also) be arbitrarily set. In other words, one can over-specify requirements so that it is impossible to arrive at a design meeting all requirements.

In general there are nine possible specifications. They are listed below showing the parameters upon which they depend.

### 1. Output pressure

$$P_o = P_o(D, \alpha, \ell_{sp}, Q_o, b_o)$$

2. Output flow

$$Q_o = Q_o(D, \alpha, l_{sp})$$

3. Switch flow

$$Q_{sw} = Q_{sw}(D, \alpha, l_v, l_{sp})$$

4. Switch pressure

$$P_{sw} = P_{sw}(D, \alpha, l_{sp}, l_v, b_c, Q_{sw}, b_o)$$

5. Pressure gain

$$G_p = G_p(D, \alpha, l_{sp}, l_v, b_c, P_{sw}, Q_{sw}, Q_o, b_o)$$

6. Fanout

$$F_o = F_o(D, \alpha, l_{sp}, Q_o, b_o, Q_{sw}, l_v)$$

7. Maximum frequency response

$$f_{max} = f_{max}(P_s, b_s, h, l_o, l_c, l_v, l_{sp})$$

8. Power Consumption

$$W = W(P_s, Q_s, b_s, h)$$

9. Switching time

$$\tau_{sw} = \tau_{sw}(f_{max}, P_c, \tau_r)$$

Of these nine, only four do not depend strongly on any other; hence, it is reasonable to say that three conditions may be specified at will, and under exceptional conditions sometimes four. Common sets of specifications are power consumption, gain and fanout; or gain, frequency response, and pressure recovery.

9. DESIGN EXAMPLE

In section 6 the design of a "fast" flip-flop was considered. In the following section a set of typical flip-flop specifications are given and a flip-flop design is determined in a step-by-step fashion.

9.1 Statement of the Problem

A fluidic flip-flop is required to activate a reject actuator at

the end of a fluidic-logic sequence that determines acceptance of a product. The fluidic-logic gates are standard commercial devices with a nominal final gate output power of 100 mW ( $Q_o = 3 \times 10^{-5} \text{ m}^3/\text{s}$  at  $P_o = 3.3 \text{ kPa}$ ), a 45% pressure recovery and a 125% flow recovery at a nominal power flow of  $5.5 \times 10^{-5} \text{ m}^3/\text{s}$  at 10 kPa. The mechanical actuator is an air cylinder with a 25.0 mm diameter bore that must push a 5 kg box off a conveyor belt whose coefficient of friction is 0.1. The length of the box is 20 cm and the conveyor moves at 50 cm/s.

## 9.2 Flip-Flop Specifications

The problem stated above made three requirements of a fluidic flip-flop: (1) nominal input (control) power in terms of the available output from the gates; (2) pressure recovery, in terms of the force requirements on the air cylinder; and (3) response time, in terms of the allowable time the air cylinder can be in contact with the product.

The specifications are examined separately.

Starting with the minimum control signal to switch, it can be determined that if the most rapid operation is desired, or a safety factor is added to the minimum control signal, about 62% of the nominal signal, should be used, hence, the minimum control signal for the flip-flop, or the switching power, must be 62 mW.

The second specification is the pressure recovery. To slide a 5 kg mass off a 0.1 coefficient of friction belt requires 0.5 kg, or 5N. Assuming a "stiction" force in the cylinder of 1.0 N then the minimum pressure required to oppose 6N, the flip-flop blocked output pressure is:

$$P_{OA} = \text{Force/Area} = 6\text{N}/((25 \times 10^{-3} \text{ m})^2 \pi/4) = 12.2 \text{ kPa}$$

The last specification is the minimum response time. Assuming that the logic sequence or function is done far enough down the line so that the reject signal comes to the actuator flip-flop just as the box is lined up with the air cylinder, then the cylinder must be fully extended in 0.4s, the duration of the passing of a 20 cm box on a 50 cm/s conveyor. The time constant of the air-cylinder volume in series with the flip-flop outlet is:

$$\tau = RC$$

and the compressibility capacitance of the air cylinder, with a retracted length of 25 mm is:

$$\begin{aligned} C &= V/nP = (25 \times 10^{-3} \text{ m})^2 (\pi/4) (25 \times 10^{-3} \text{ m})/1 \times (12.2 + 101) \times 10^3 \\ &= 1.08 \times 10^{-10} \text{ m}^3/\text{Pa} \end{aligned}$$

The resistance will not be known until a geometry is chosen but the final design must meet the requirement that the switch time, plus the cylinder pressure rise time, plus the cylinder extension time, is less than 0.4 seconds. The extension time can be estimated simply by applying Newton's Second Law to the piston-mass system. The governing equation is

$$\ddot{x} = \Sigma F/m$$

where  $\Sigma F$  is the net force acting on the piston and mass, e.g. the sliding friction, the cylinder "stiction", and the pressure force on the piston end. The mass,  $m$ , is composed of the piston and the box but since the box is fairly large,  $m$  can be considered to be the box mass alone. Noting that the initial  $x$ -displacement and  $x$ -velocity are zero, the time required to extend the cylinder is simply

$$t = \sqrt{\frac{x \cdot m}{\Sigma F}}$$

To get an idea of the order of magnitude of this extension time for a 10 cm extension, assume an excess force of 1.0N. Then:

$$t = \sqrt{\frac{10 \times 10^{-2} \text{ m} \times 5 \text{ kg}}{1.0 \text{ kg m/s}^2}} = \sqrt{.5} \sim .7 \text{ seconds}$$

It is clear then that 1.0 N excess force is not sufficient to meet the requirement that the total time be less than 0.4s. An excess force of 4N will bring the extension time down to 0.35s. This corresponds now to increasing the required amplifier output pressure to about 20 kPa. Experience dictates that switching times can be kept low to the order of milliseconds hence the outlet resistance must be low enough to allow a cylinder pressure-rise time of less than 0.05s, (50 ms), or

$$R_o = \tau/C = 0.05 \text{ s} / 1.08 \times 10^{-10} \text{ m}^3/\text{Pa}$$

$$R_o < 5 \times 10^8 \text{ kg/m}^4\text{s}$$

The flip-flop specifications therefore are:

1.  $W_{sw} \leq 62 \text{ mW}$  ( $P_{sw} \leq 3.3 \text{ kPa}$ )
2.  $P_{oA} \geq 20 \text{ kPa}$  ( $G_p = P_{oA}/P_{sw} \geq 6.6$ )
3.  $R_o < 5 \times 10^8 \text{ kg/m}^4\text{s}$  ( $\tau_{sw} \sim 0$  (1 ms))

In addition, the energy required to move the piston is roughly 1 watt ( $W = \frac{FL}{t}$ ); hence, the output power recovery should be in excess of this value.



### 9.3 Step-by-Step Design

Since the primary concern is output pressure level, a high pressure recovery device with fairly high gain is required. If we assume that the final device is to be in the conventional design area with outlets decoupled by the device shown in figure 11, then we can use figure 14 to start with. Assuming a design specification for  $G_p$  at 7.0, we pick three combinations, of the figure, of attachment angle and wall offset:

$$\alpha_1 = 10^\circ, D_1 = 0; \alpha_2 = 12^\circ, D_2 = 0.1; \alpha_3 = 15^\circ, D_3 = 0.275$$

Upon examination of figures 6 to 8 one sees that for high-pressure recovery, the splitter location should be at  $6 b_s$ . Noting the 25% decoupler pressure loss, we find now that for each combination with  $\ell_{sp} = 6 b_s$

$$P_{oA}/P_{s1} = 0.405 \text{ (fig. 6)}$$

$$P_{oA}/P_{s2} = 0.33 \text{ (fig. 7)}$$

$$P_{oA}/P_{s3} = 0.255 \text{ (fig. 8)}$$

Since high recovery is a desirable characteristic let us examine the first choice.

$$\alpha_1 = 10^\circ, D_1 = 0.0, \ell_{sp} = 6 b_s$$

From figure 6 the open port ( $b_c = b_s$ ) attachment point location is about  $5.2 b_s$ . Applying the wall length criterion, Eq. 3, the wall length must be at least  $7.2 b_s$  so  $8 b_s$  is used complying with the gain from figure 11. This puts the vent downstream of the leading edge of the splitter. The switching pressure is obtained from figure 12 and is

$$P_{sw}/P_s = 0.058$$

or from the gain,  $G_p = P_{oA}/P_{sw} = 7$ , and the pressure recovery

$$P_{sw}/P_s = P_{oA}/P_s / G_p = .405/7 = 0.058$$

The supply pressure is now obtained from the pressure recovery

$$P_s = P_{oA} / (P_{oA} / (P_{oA}/P_s)) = 20 \text{ kPa} / 0.405 = 49.4 \text{ kPa}$$

or rounding off  $P_s = 50 \text{ kPa}$  and the switch pressure is  $P_{sw} = 0.058 (50) =$

2.9 kPa, which is within the specifications. The input-power specification is 62 mW so that the flow to switch can be estimated as,

$$Q_{sw} = W_{sw}/P_{sw} = 0.062 \text{ watts}/3 \times 10^3 \text{ Pa} \\ \dot{=} 2.0 \times 10^{-5} \text{ m}^3/\text{s}$$

Using a conservative estimate of the control nozzle-discharge coefficient as 0.6, the nozzle area can be determined from the Bernoulli equation:

$$P = \frac{\rho}{2} \left( \frac{Q}{C_d A} \right)^2$$

where  $\rho$  is the density of air so that

$$A = \sqrt{\frac{\rho}{2P}} \frac{Q}{C_d} = \sqrt{\frac{1.2059 \text{ kg/m}^3}{2 \times 3 \times 10^3 \text{ kg/ms}^2}} \frac{2 \times 10^{-5} \text{ m}^3/\text{s}}{.6} \\ A = 4.7 \times 10^{-7} \text{ m}^2$$

Using an aspect ratio of 2, as recommended, the area is simply twice the nozzle width squared, so that

$$b_s \sqrt{A/2} = 0.00048 \dot{=} 0.5 \text{ mm}$$

Assuming a short supply nozzle (again to minimize losses)  $\ell_{th} = 0.5 b_s$ , using the above values of nozzle width and aspect ratio the minimum supply pressure is obtained from Eq. 11

$$P_s = 0.5 [\ell_{th}/b_s + 1] (1 + 1/\sigma)^2 v/b_s]^2 \rho \times 10^6 \\ P_s = 0.5 [(1.5)(1.5)^2 1.486 \times 10^{-5} \frac{\text{m}^2}{\text{s}} / .0005 \text{ m}]^2 1.2059 \frac{\text{kg}}{\text{m}^3} \times 10^6 \\ P_{s_{min}} = 12.139 \text{ kPa} < 50 \text{ kPa (spec)}$$

Since this value is less than the value required by the specs, it is assured that the flow is Reynolds number independent.

The response time of this device can be estimated as being faster than the times given in figure 16, since  $\ell_{sp}$  is only  $6b_s < 8b_s$ . Assuming a final amplitude control signal of 3.3, kPa yields a normalized signal  $P_c/P_s = 0.066$ . This yields a normalized response time of approximately 350 or in real time

$$t = \tau / (\sqrt{2P_s/\rho}/b_s) = 350 / \left( \frac{2 \times 50 \times 10^3 \text{ kg/ms}^2}{1.2059 \text{ kg/m}^3} / .5 \times 10^{-3} \text{ m} \right) \\ t = 0.0006 \text{ s} = 0.6 \text{ ms}$$

An estimate of the decoupler outlet impedance can be obtained from Eqs. 4, 5 and 6

$$R_o = \frac{P_{oA}}{Q_{oA}} = \frac{P_s}{Q_s} \frac{.75 P_o/P_s}{2.1 Q_o/Q_s} = \frac{P_s}{Q_s} \frac{P_{oA}/P_s}{2.1 (\sqrt{P_o/P_s}/(b_s/b_o))}$$

Assuming  $c_{ds} = 0.9$ , and applying Bernoulli's equation, again one can find the supply flow

$$Q_s = c_d \sqrt{\frac{2P}{\rho}} b_s^2 \sigma = 1.3 \times 10^{-4} \text{ m}^3/\text{s}$$

The output leg width is  $b_o = 1.53 b_s$ , from geometry

The outlet impedance is therefore,

$$R_o = \frac{50 \times 10^3 \text{ kg/ms}^2}{1.3 \times 10^{-4} \text{ m}^3/\text{s}} \frac{.405}{2.1 (\sqrt{.54}/0.66)}$$

$$R_o = 6.5 \times 10^7 \text{ kg/m}^4\text{s}$$

This value is an order of magnitude less than the maximum allowed by the specifications; hence, the total of the flip-flop response time and the cylinder rise time is about 5.6 ms. This, coupled with a 0.35s extension time, is less than the maximum 0.4s allowed for the reject mechanism to operate.

#### 9.4 Flip-Flop Geometry and Characteristics

The problem stated in section 9.1 can be satisfied by a flip-flop with the following dimensions, characteristics, and operating conditions:

$b_s$	=	0.5 mm	}	Dimensions
$D/b_s$	=	0		
$\alpha$	=	$10^\circ$		
$\ell_v/b_s$	=	8.0		
$b_o/b_s$	=	1.53	}	Characteristics
$P_{oA}/P_s$	=	0.405		
$P_{sw}/P_s$	=	0.058		
$G_p$	=	7	}	Operating Conditions
$W_s$	=	6.5 watts ( $W_{oA} \sim 1.3w$ )		
$P_s$	=	50 kPa		
$Q_s$	=	$1.3 \times 10^{-4} \text{ m}^3/\text{s}$		

It is worth noting that this design is not unique. Other less efficient designs could have been arrived at using the other two geometric choices. There are no commercially available devices that could do the job alone.

#### 10. SUMMARY AND CONCLUSIONS

This report has presented graphically, and in simple closed form, the results of a theoretical model for the operation of a turbulent wall attachment flip-flop with straight walls, a sharp splitter and decoupled outputs, so that a rational design of such a device can be made to satisfy both static and dynamic specifications. These results are in the form of parametric graphs of pressure recovery, attachment point location, blocked control pressure, switch pressure, switch flow, pressure gain, fanout and response time. They are also in the form of simple closed form relations for output characteristics, frequency response, and maximum frequency response. In addition, rules of thumb for the construction of the steady state characteristics, input and transfer, are given and illustrated, and intuitive insight into the transient response is given by identifying the transient processes.

The optimization of response time of a flip-flop was followed through from initial to final design, compromised by fabrication problems. A frequency response in the order of 1000 Hz for a device with a nozzle width of 0.5 mm is obtained and experimentally verified. From the analytic model a maximum attainable frequency response (with present fabrication technology) is estimated to be about  $10^4$  Hz. Higher frequencies can be achieved; however, there would be an attenuation of the output greater than -3db. For instance, if an ultra-high frequency oscillator is desired with the jet moving from attachment to detachment, with no concern about the attenuation due to the outputs, then a frequency could be expected of the order of  $10^5$  Hz.

A brief recapitulation of the design curves indicates that, from a static view-point, pressure gains and fanouts of the order of ten are not unreasonable along with pressure recoveries in excess of 50%. Compromises of these figures occur when decoupling or when fabricating by a specified process.

A design example is given for what is hoped might be a typical case. The design is followed through step-by-step resulting in a geometric configuration.

In conclusion, then, this report can be used as a comprehensive design guide for a fluidic wall-attachment flip-flop to meet both static and dynamic requirements.

## 11. ACKNOWLEDGEMENTS

The theoretical work could not have come to a successful conclusion had it not been for the collaboration of John Goto with whom I co-authored references [4], [16], and [17].

J. Iseman's help in solving, numerically, some of the lumped parameter output circuits is deeply appreciated.

The manufacture of all the in-house fast-flip-flop models by J. Delawter and R. Brown is appreciated.

The manufacture of the final devices was by McDonnell-Douglas Astronautics Co., and thanks are extended to Dr. Westerman whose great pains with the drawing are evident in the excellent quality of the end product.

Finally, thanks are extended to Al Freiling who put all the elements together, and who made the original technical drawings.

## 12. REFERENCES

1. Lush, P. A., "The Development of a Theoretical Model for the Switching Mechanism of a Wall Attachment Fluid Amplifier," Ph.D. Thesis, U. of Bristol, Dept. of Aero. Eng., Sept., 1968.
2. Wilson, M. P., Jr., "The Switching Process in Bistable Fluid Amplifiers," ASME Publication 69-FLCS-28, June 1969.
3. Epstein, M., "Theoretical Investigation of the Switching Mechanism in a Bistable Wall Attachment Fluid Amplifier," J. Basic Eng., March 1971.
4. Goto, J. M. and Drzewiecki, T. M., "Reattached Jet Response to Input Pressure in a Non-Loaded Fluidic Bistable Configuration," Proc. 5th Cranfield Conf., Uppsala, Sweden, June 1972.
5. Bourque, C. and Newman, B. G., "Reattachment of a Two-Dimensional, Incompressible Jet to an Adjacent Flat Plate," The Aero. Quart., V. XI, Aug. 1960.
6. Levin, S. G. and Manion, F. M., "Jet Attachment Distance as a Function of Adjacent Wall Offset and Angle," HDL-TR-1087, Dec 1962.
7. Sher, H. C., "Jet Attachment and Switching in Bistable Fluid Amplifiers," ASME Publication No. 64-FE-19, NY, 1964.
8. Comparin, R. A., Moore, R. B. and Jenkins, W., "Jet Reattachment at Low Reynolds Numbers and Moderate Aspect Ratios," ASME Publication, 67-FE-25, NY 1967.
9. Perry, C. C., "Two Dimensional Jet Attachment," Advances in Fluidics, ASME Publication, 1967.
10. McRee, D. I. and Moses, H. L., "The Effect of Aspect Ratio and Offset on Nozzle Flow and Jet Reattachment," Advances in Fluidics ed. F. Brown, ASME, 1967.
11. Kimura, M. and Mitsuoka, T., "Analysis and Design of Wall Attachment Devices by a Jet Model of Unsymmetrical Velocity Profile," Proc. IFAC Symp. on Fluidics, London 1968.
12. Moses, H. L. and McRee, D. I., "Switching in Digital Fluid Amplifiers," ASME Publication No. 69-FLCS-31, 1969.
13. Fahnestock, M. R., "A Theoretical Study of Laminar Jet Wall Reattachment," Research Report 12, Sys. and Controls Lab., Penn. State U., Oct. 1970.
14. McRee, D. I. and Edwards, J. A., "Three Dimensional Jet Reattachment," ASME paper 70-WA/FLCS-5, Nov. 1970.
15. Brown, E. F., and Belen, F. C., Jr., "Jet Interaction in a Simplified Model of a Bistable Fluid Amplifier," ASME Publication 72-WA/FLCS-6, Nov., 1972.
16. Goto, J. M. and Drzewiecki, T. M., "Fluidics 32. An Analytical Model for the Response of Fluoric Wall Attachment Amplifiers," HDL-TR-1598, Harry Diamond Labs, Wash., DC, June 1972, (AD-747761).
17. Drzewiecki, T. M. and Goto, J. M., "An Analytical Model for the Response of Fluoric Wall Attachment Amplifiers," Fluidics Quarterly, Vol. 5, no. 1, Jan., 1973.
18. Drzewiecki, T. M., "Prediction of the Dynamic and Quasi-Static Performance Characteristics of Fluoric Wall Attachment Amplifiers," Fluidics Quarterly, Vol. 5, no. 2, April, 1973.

19. Drzewiecki, T. M., "Planar Nozzle Discharge Coefficients," Proc. 13th Midwestern Mechanics Conf., Pittsburgh, PA, Aug. 1973.
20. Drzewiecki, T. M., "Interpretation of Surface Static Pressure Distributions in Fluid Amplifier Applications," HDL-TR-1627, Harry Diamond Labs, Wash., DC, 1973.
21. Drzewiecki, T. M., "High Speed Decoupled Fluidic Switching Device," U.S. Patent 3,720,218, April 1973.
22. Kirshner, J., Editor, Fluid Amplifiers, McGraw-Hill, NY, 1966.
23. MIL-STD 1306A, "Military Standard, Fluidics, Terminology and Symbols," 8 Dec 72.
24. MIL-STD 1361, "Military Standard, Fluidics, Test Methods and Instrumentation," 5 Nov 1971.
25. Keto, J. R., "Transient Behavior of Bistable Fluid Elements," Proc. 2nd Fluid Amplification Symposium, Harry Diamond Labs, Vol. III, May 1964.
26. Ozgu, M. R. and Stenning, A. H., "Switching Dynamics of Bistable Amplifiers with Low Setbacks," Trans. ASME, J. of Dynamic Systems, Measurement and Control, March 1972.
27. Katz, S., Winston, E. T. and Hawes, P., "The Response of a Bistable Fluid Amplifier to a Step Input," Proc. Fluid Amp. Symp., Vol. I Harry Diamond Labs, Wash., DC, May 1964.
28. Müller, H. R., "A Study of the Dynamic Features of a Wall-Reattachment Fluid Amplifier," ASME paper, 64-FE-10, May 1964.

13. FIGURES



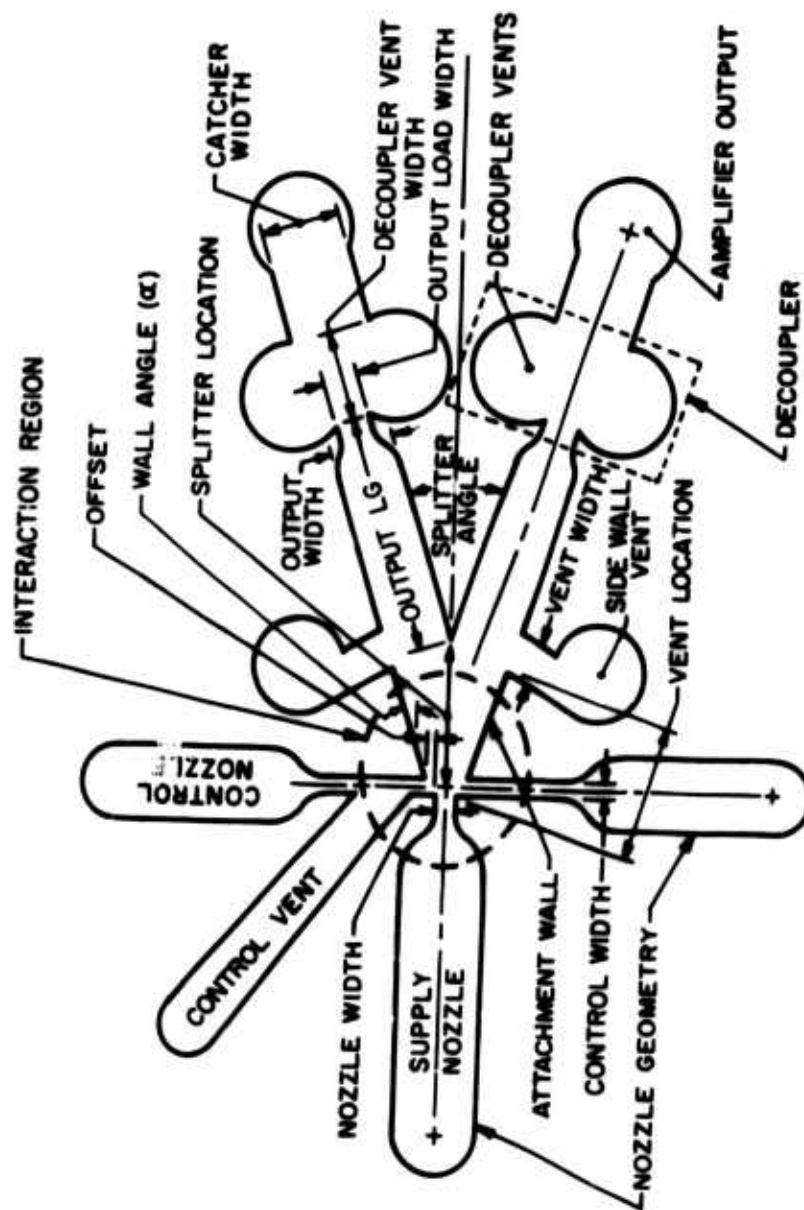


Figure 1. The geometry of a fluoric bistable wall attachment flip-flop

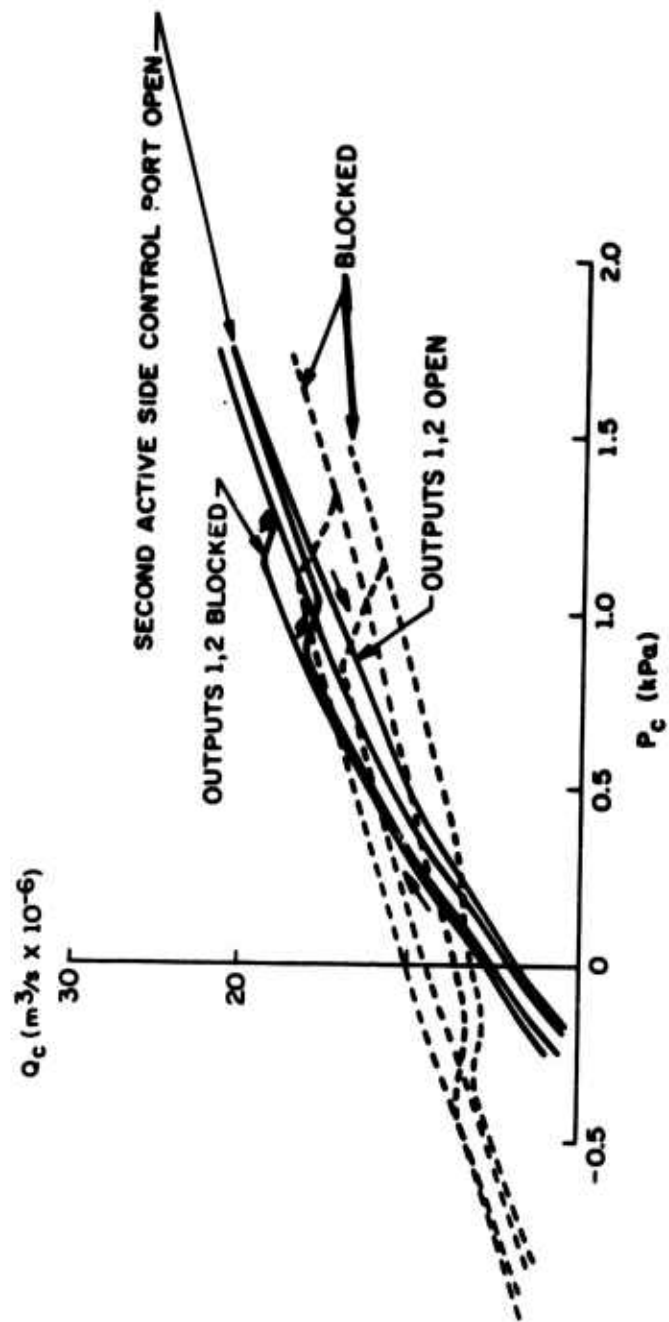
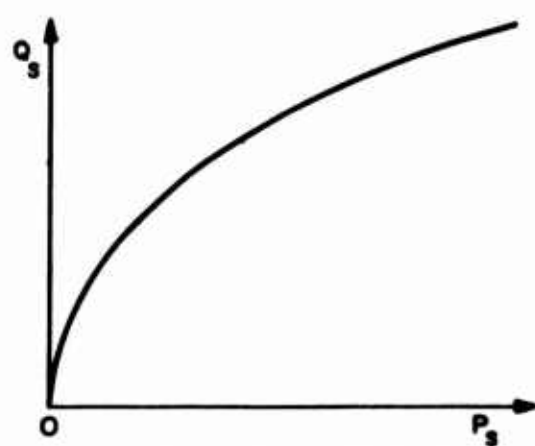
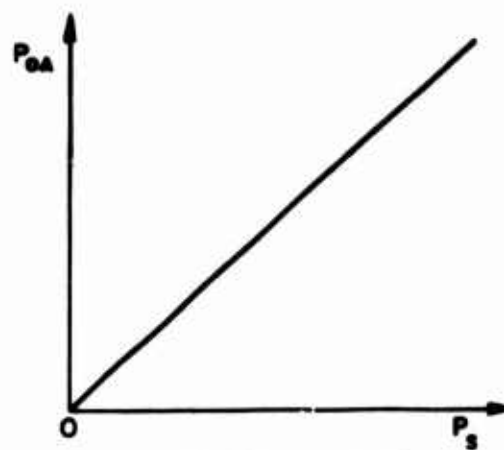


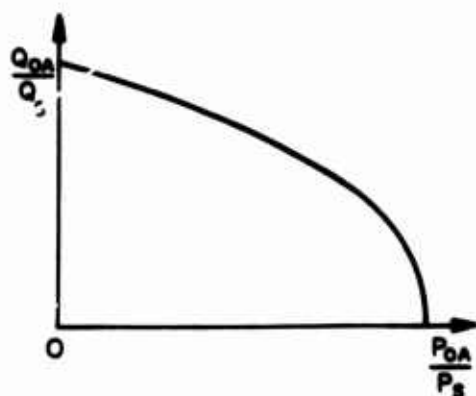
Figure 2. Input Characteristics of a commercial flip-flop showing loading effects



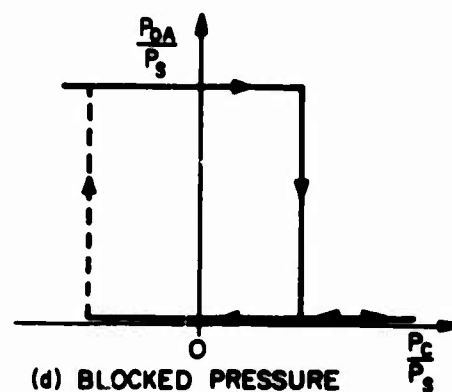
(a) SUPPLY CHARACTERISTIC



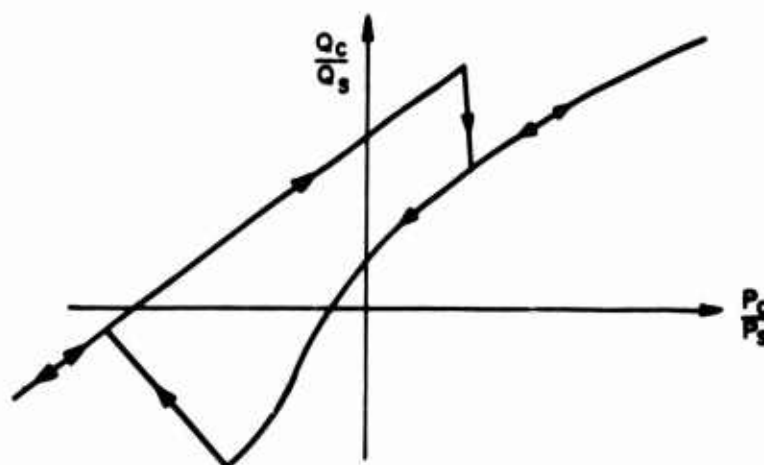
(b) PRESSURE RECOVERY



(c) OUTPUT CHARACTERISTIC



(d) BLOCKED PRESSURE TRANSFER CHARACTERISTIC



(e) INPUT CHARACTERISTIC

Figure 3. Flip-Flop characteristic curves

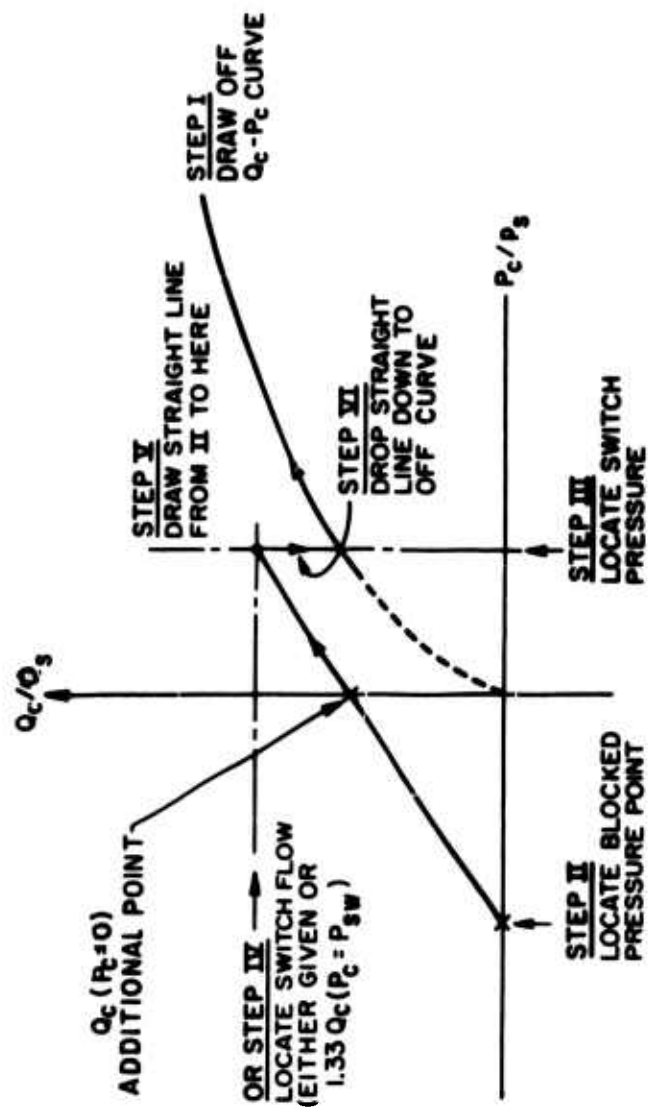


Figure 4. The construction of an input characteristic

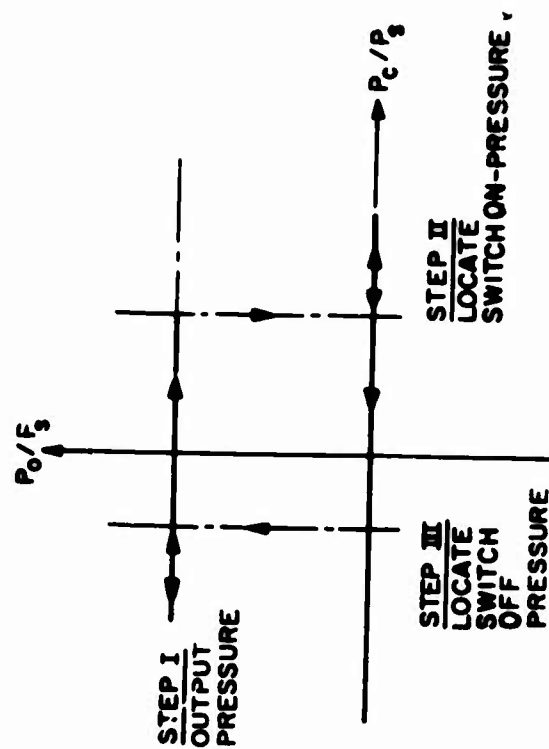


Figure 5. The construction of a blocked-pressure static transfer characteristic

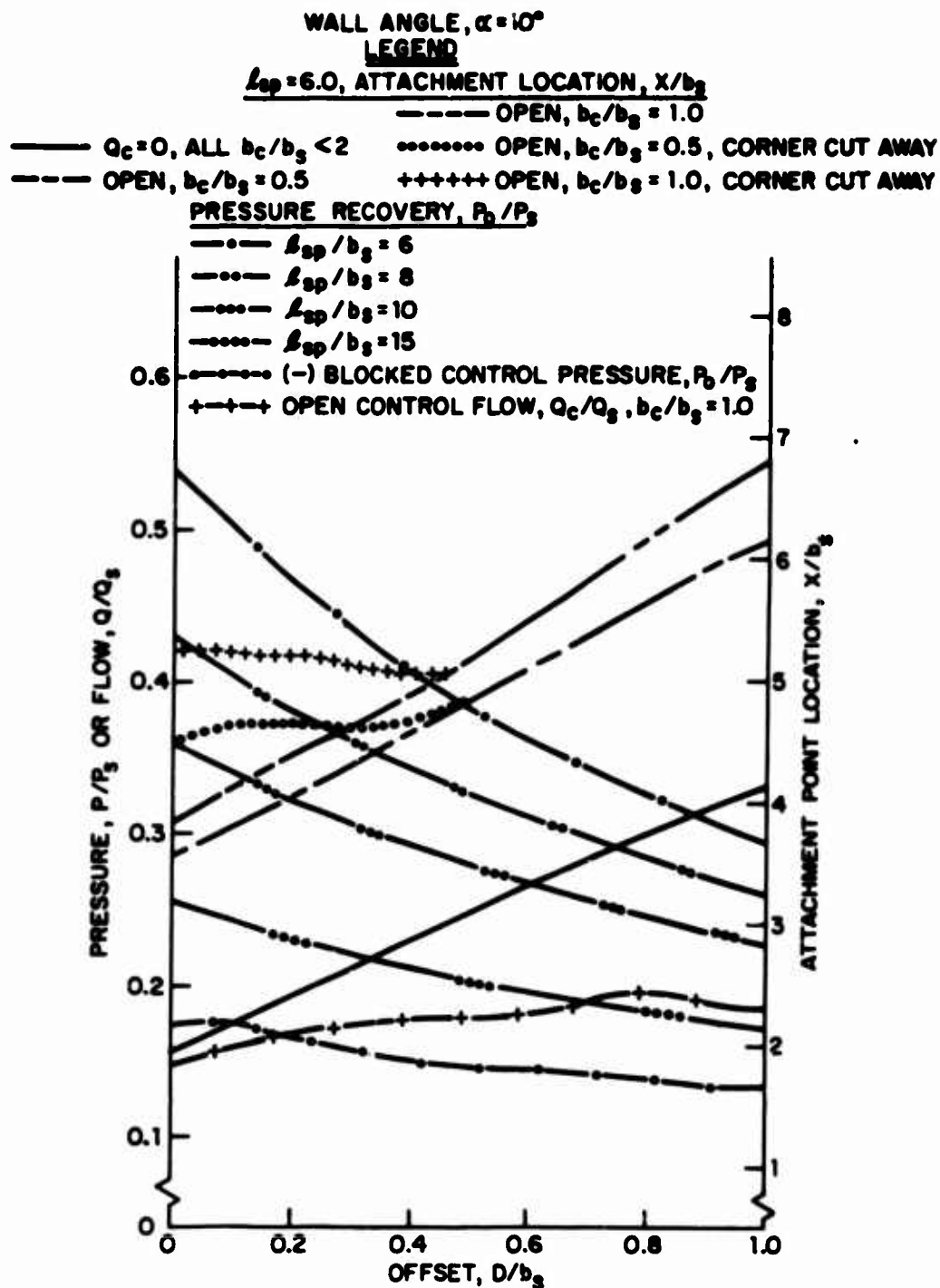


Figure 6. Static design curves for  $\alpha = 10^\circ$

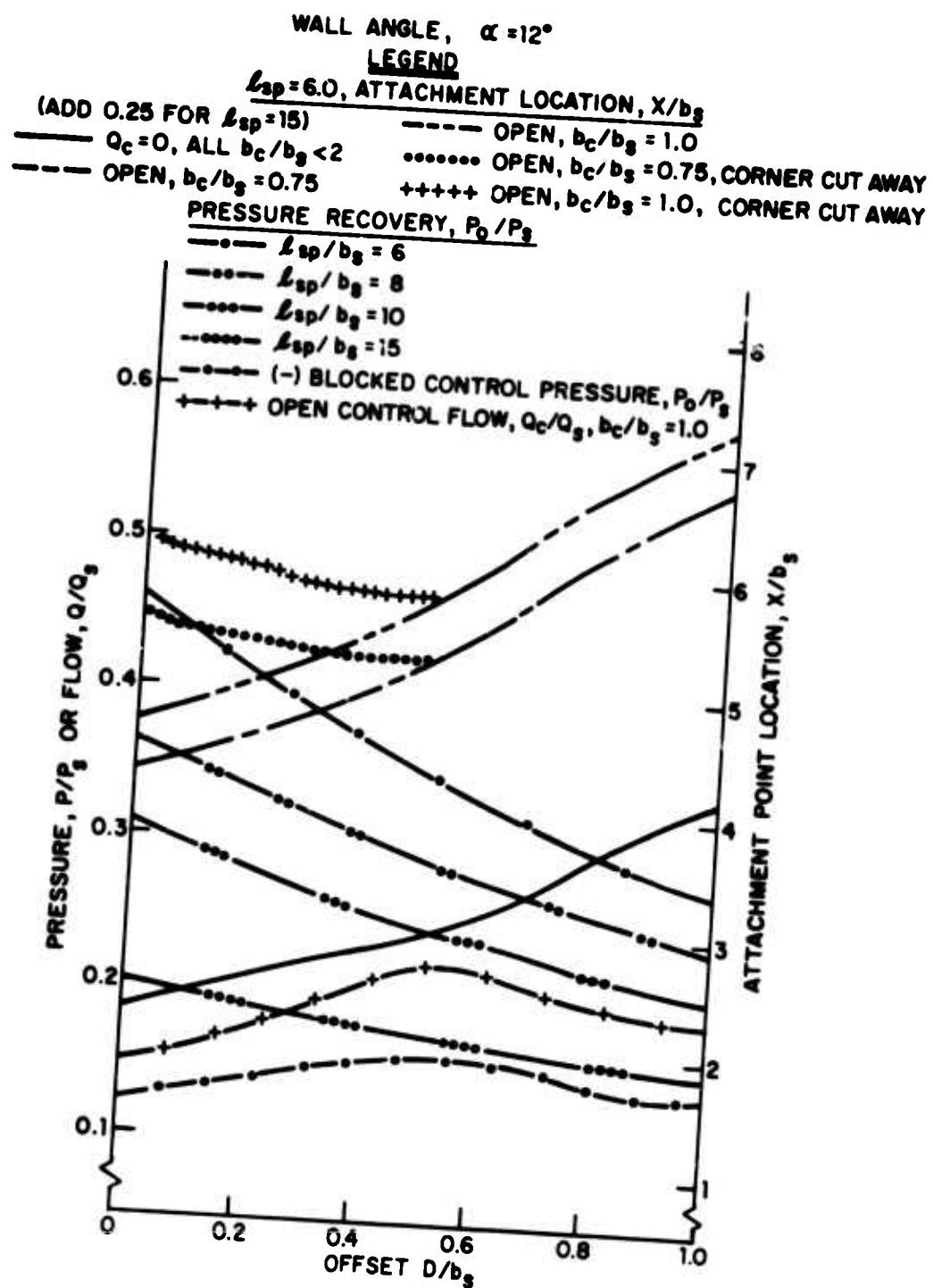


Figure 7. Static design curves for  $\alpha = 12^\circ$

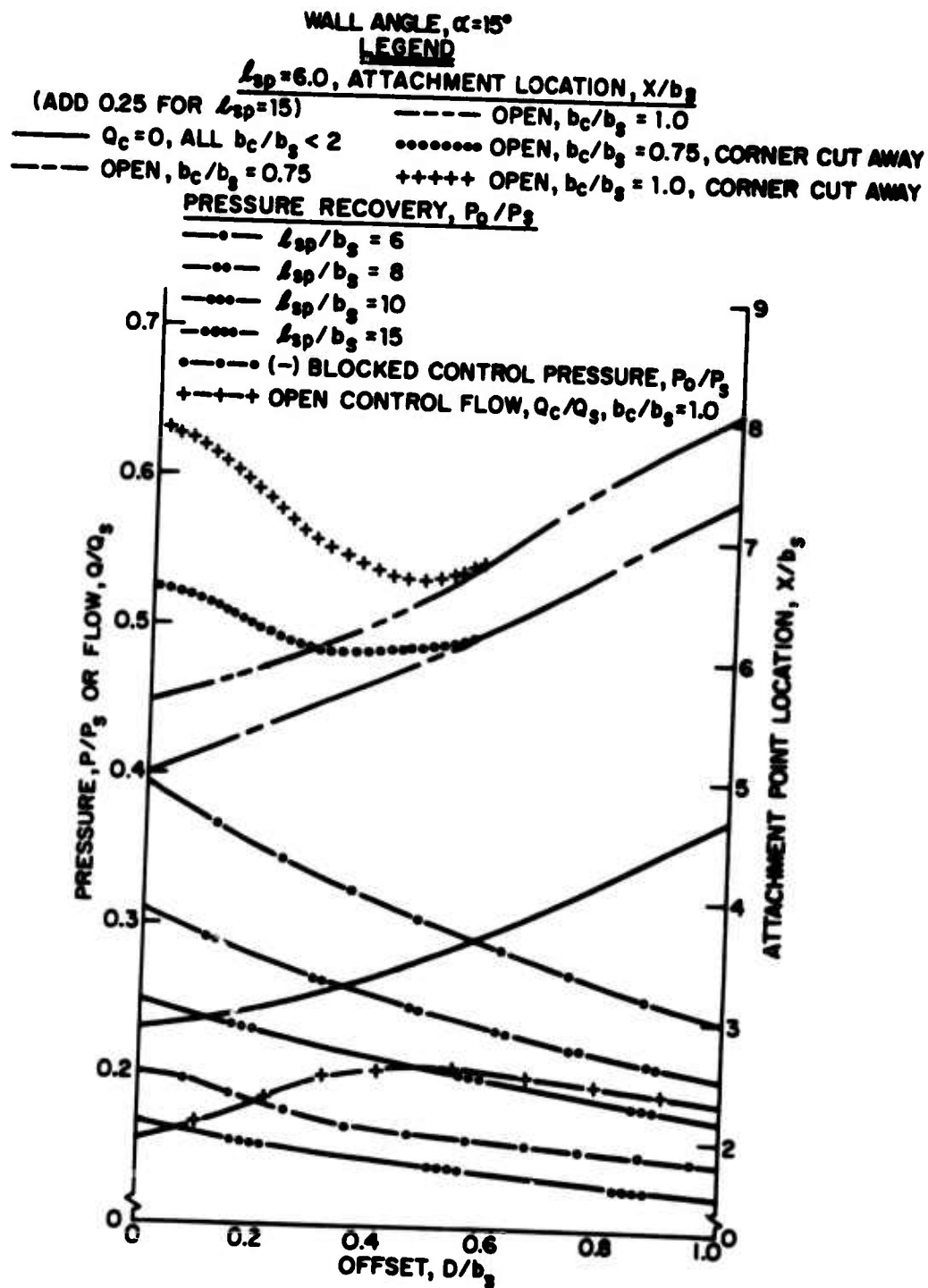


Figure 8. Static design curves for  $\alpha = 15^\circ$



WALL ANGLE,  $\alpha = 30^\circ$

LEGEND

$l_{sp} = 6.0$ , ATTACHMENT LOCATION,  $x/b_s$

(ADD 1.25 FOR  $l_{sp} = 15$ ,  $D = 0$ , 2.00 FOR  $D = 1.0$ )

—  $Q_c = 0$ , ALL  $b_c/b_s < 3$

--- OPEN,  $b_c/b_s = 0.5$

OUTPUT PRESSURE RECOVERY,  $P_o/P_s$

—•—  $l_{sp}/b_s = 6$

—••—  $l_{sp}/b_s = 8$

—•••—  $l_{sp}/b_s = 10$

—••••—  $l_{sp}/b_s = 15$

—•••••— (-) BLOCKED CONTROL PRESSURE,  $P_o/P_s$

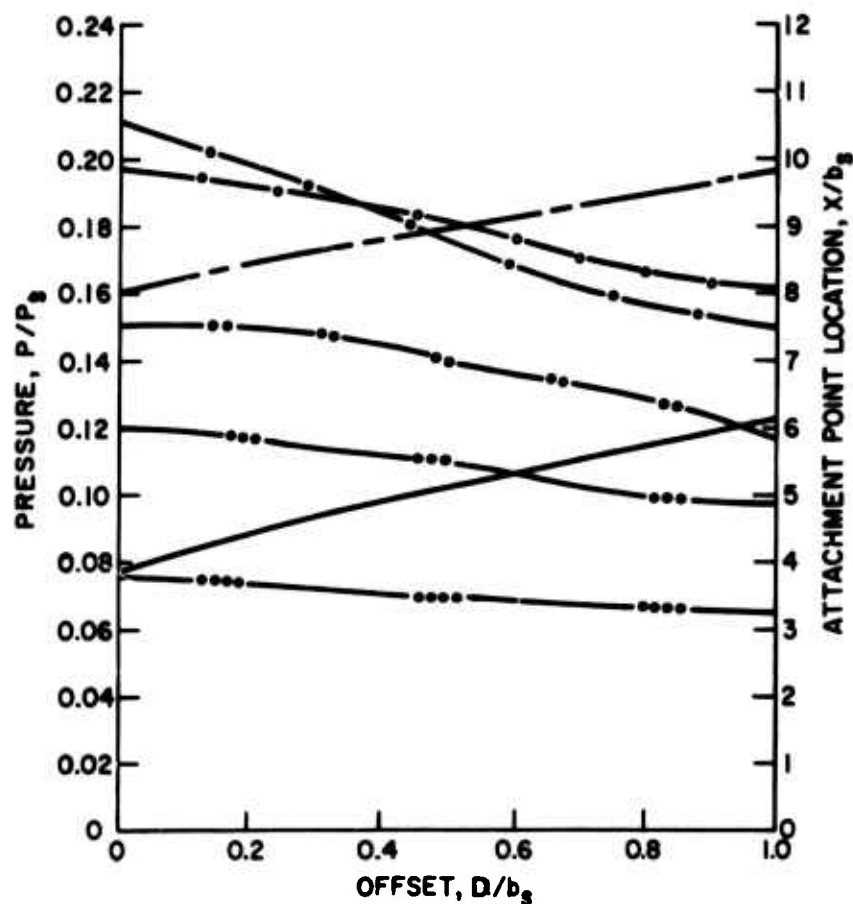
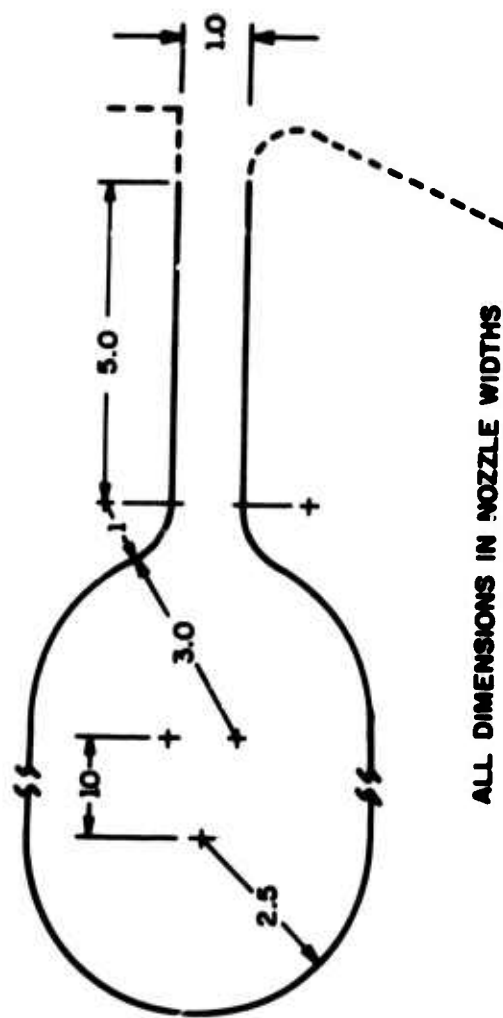


Figure 9. Static design curves for  $\alpha = 30^\circ$



ALL DIMENSIONS IN NOZZLE WIDTHS

Figure 10. Geometry of control nozzle used for static design curves

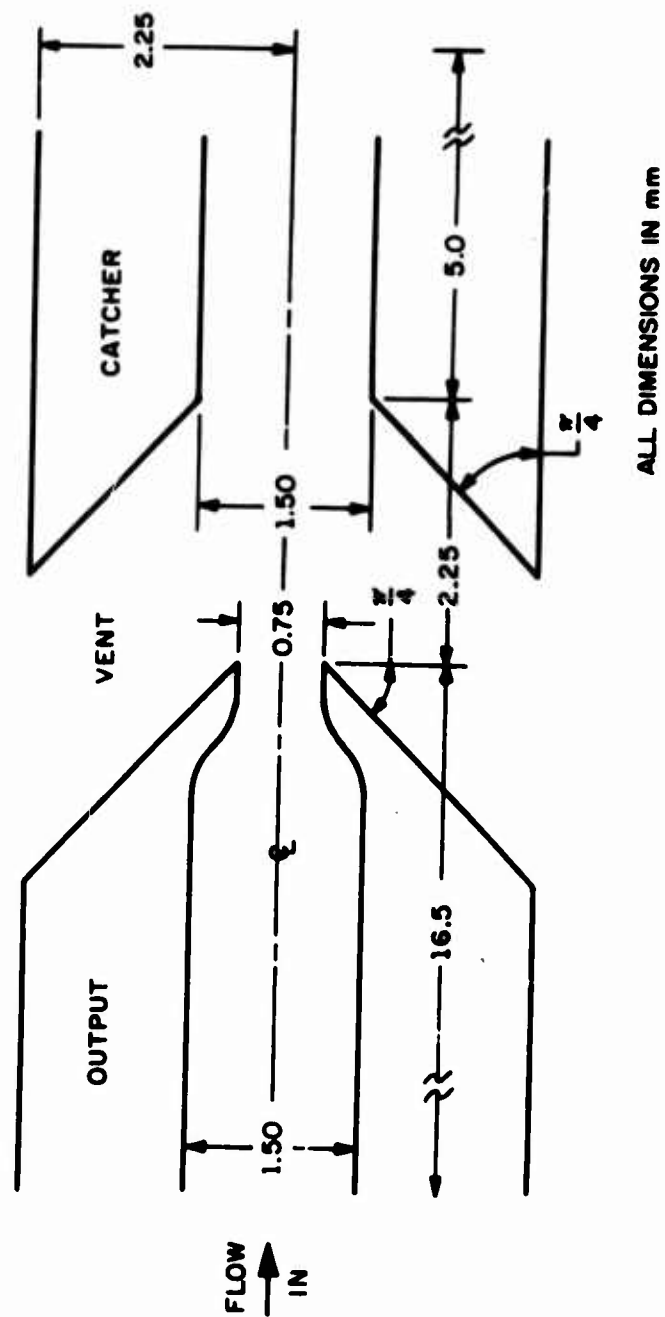


Figure 11. Geometry of decoupler used in calculating gain and fanout

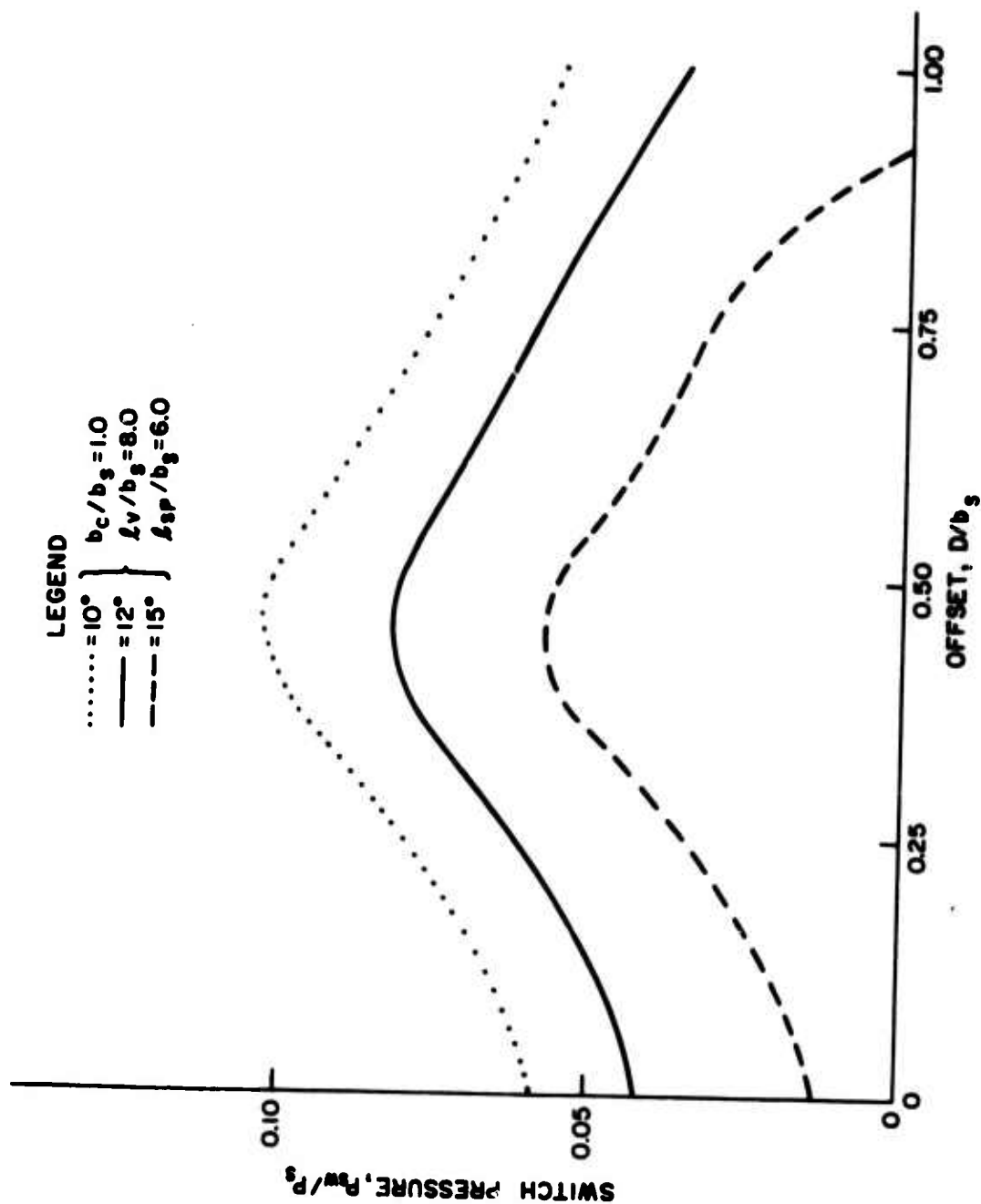


Figure 12. Switching pressure versus offset for  $\alpha = 10^\circ, 12^\circ, 15^\circ$

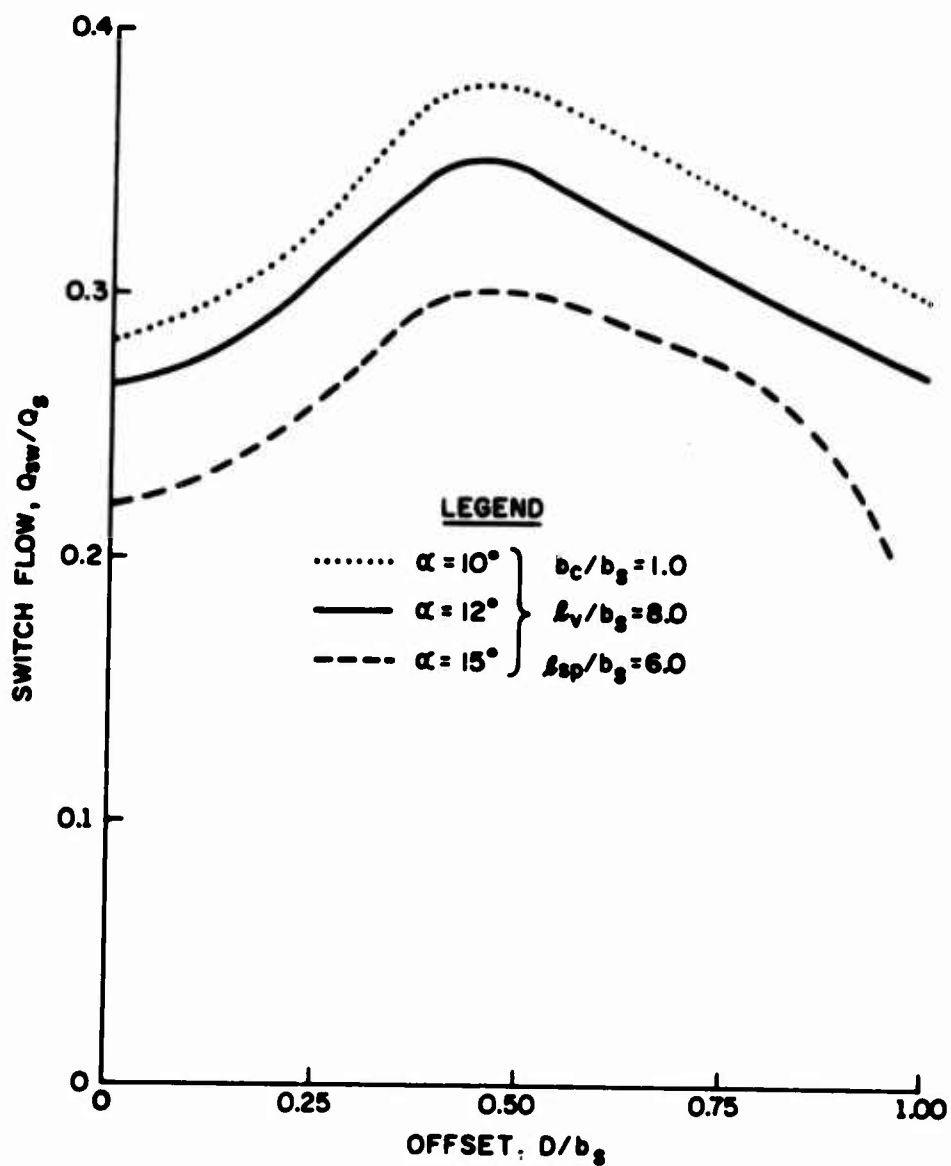


Figure 13. Switching flow versus offset for  $\alpha = 10^\circ, 12^\circ, 15^\circ$

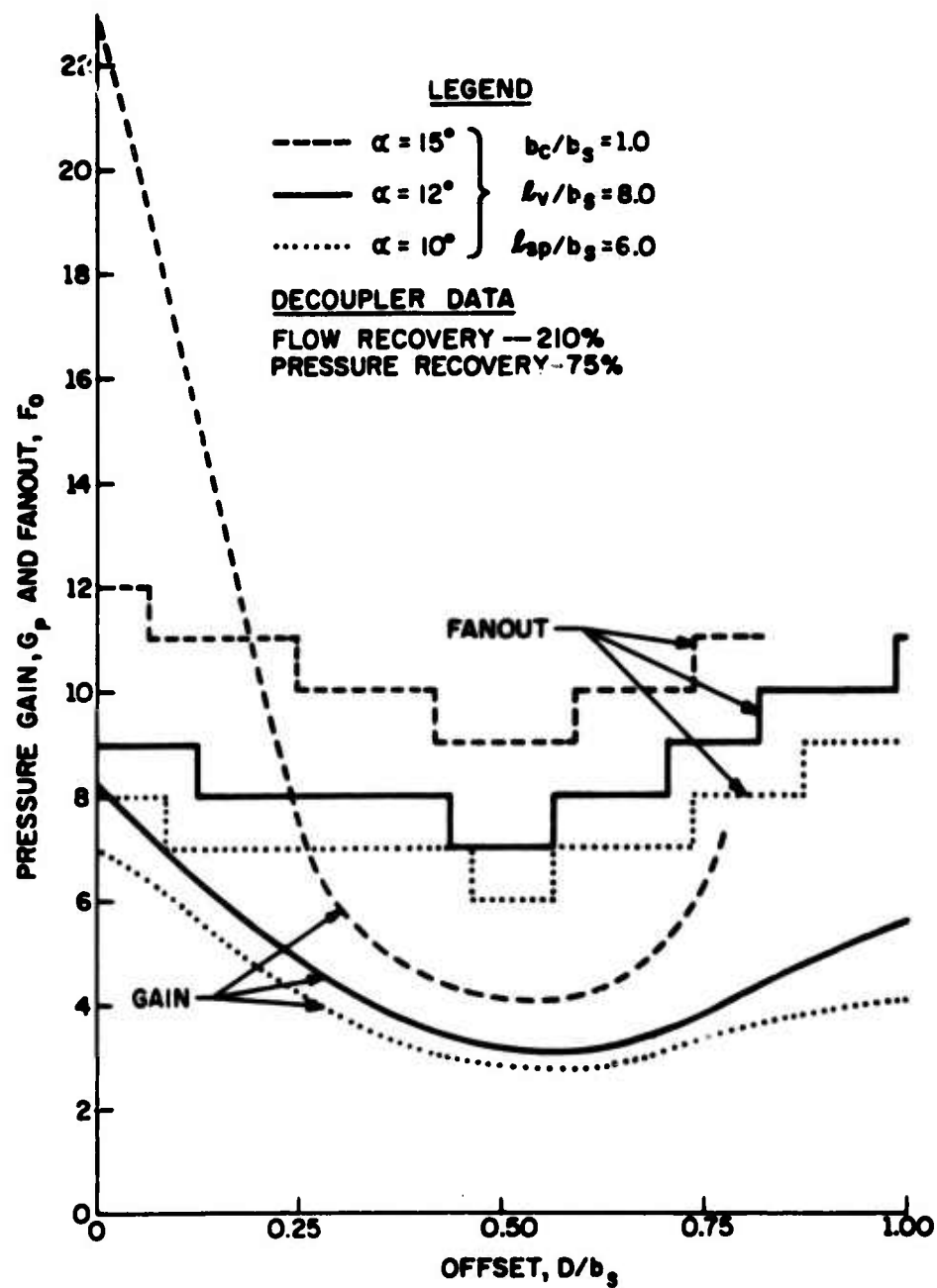


Figure 14. Pressure gain and fanout versus offset for  $\alpha = 10^\circ, 12^\circ, 15^\circ$

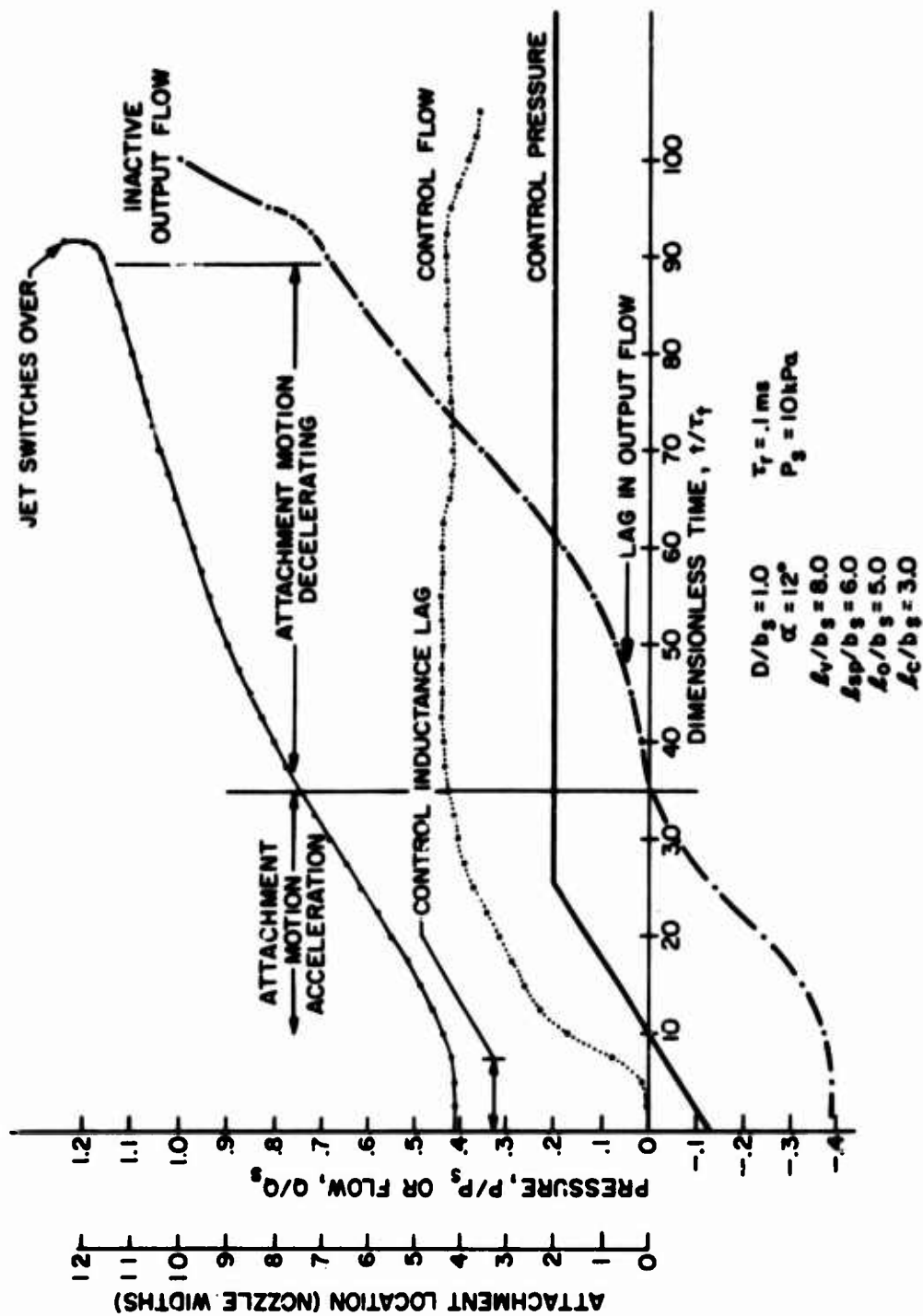


Figure 15. Motion of the attachment point in response to a sharp input pressure signal

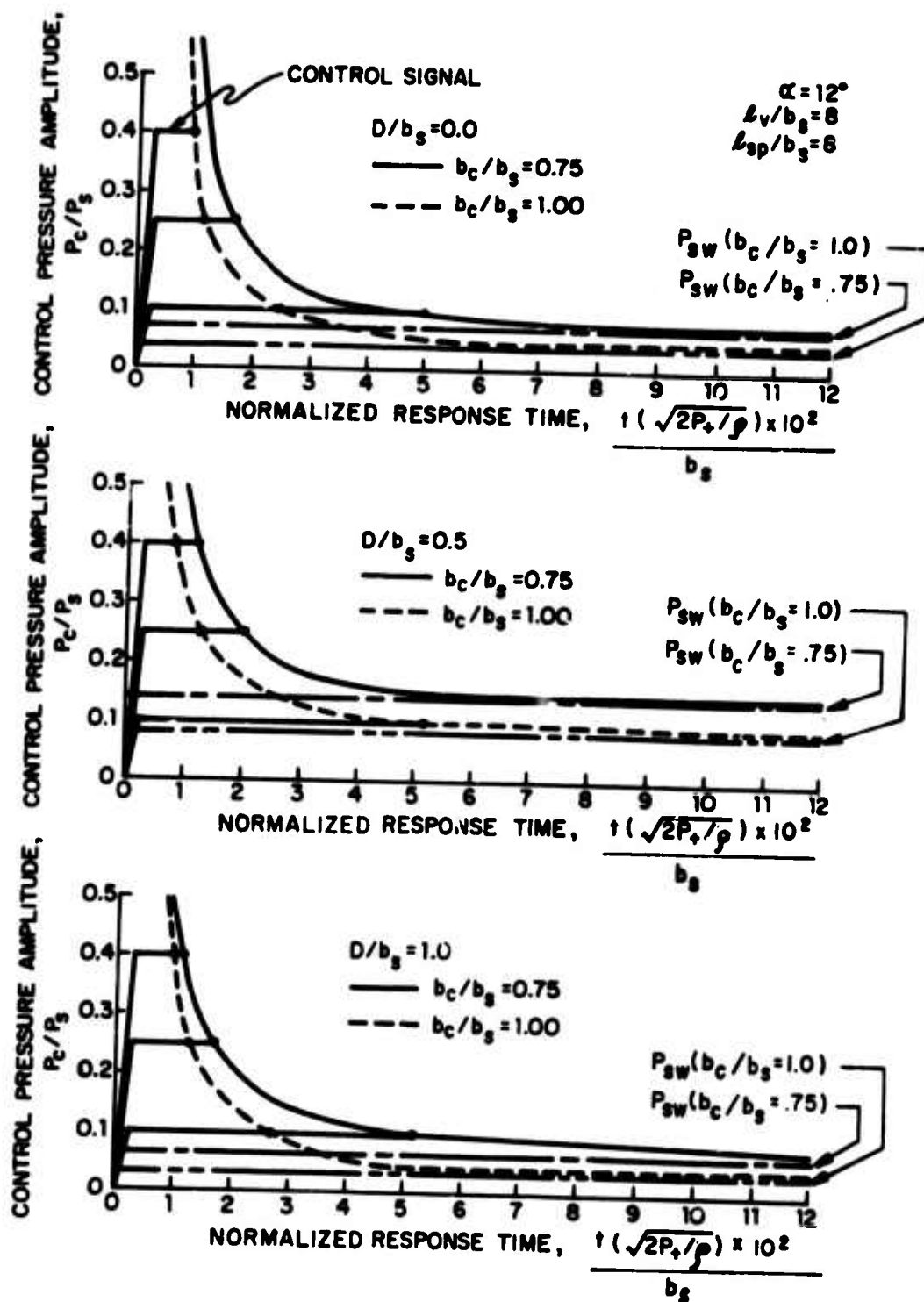


Figure 16. Switching times for various geometries



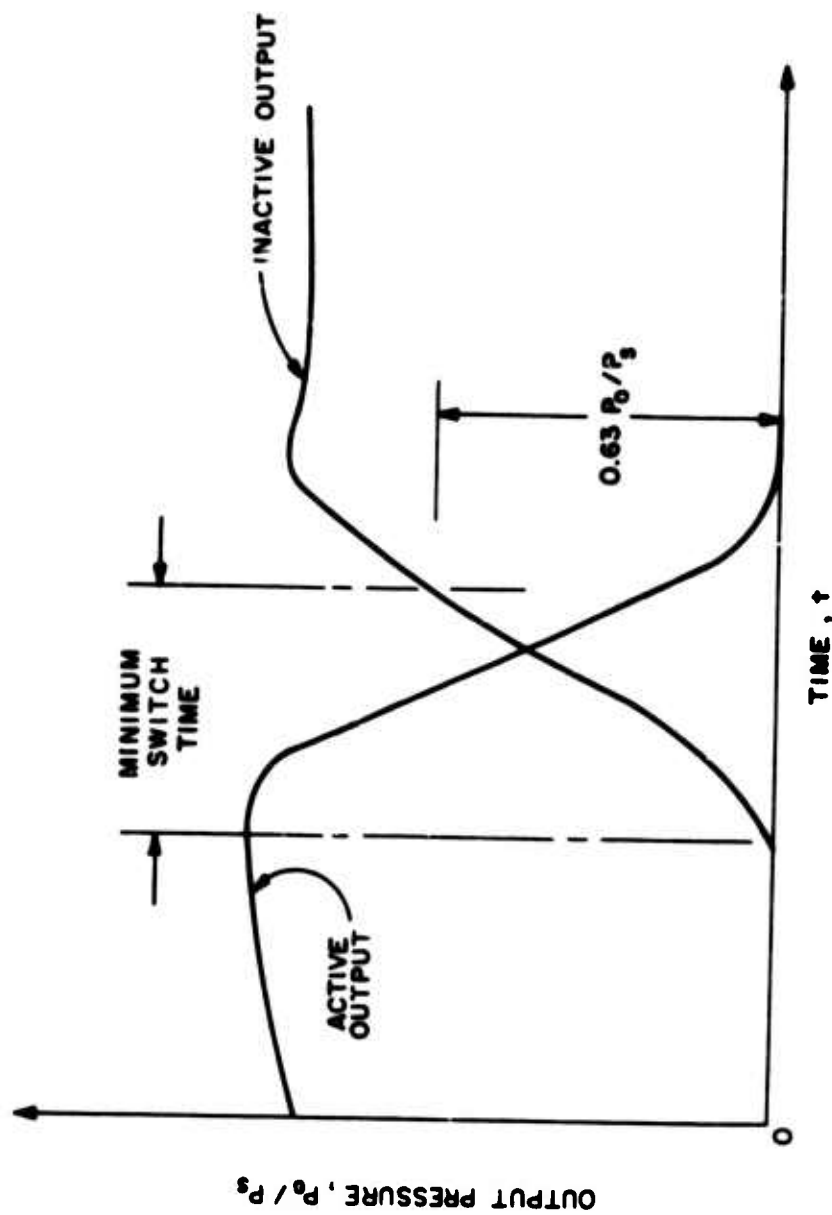
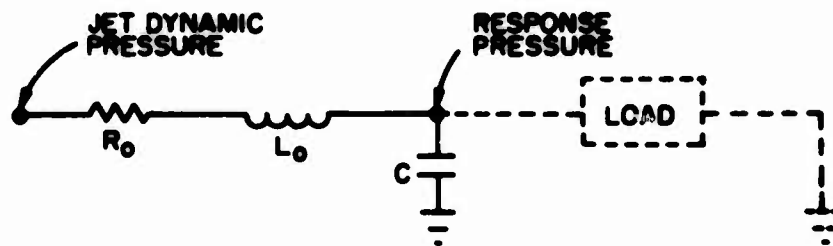
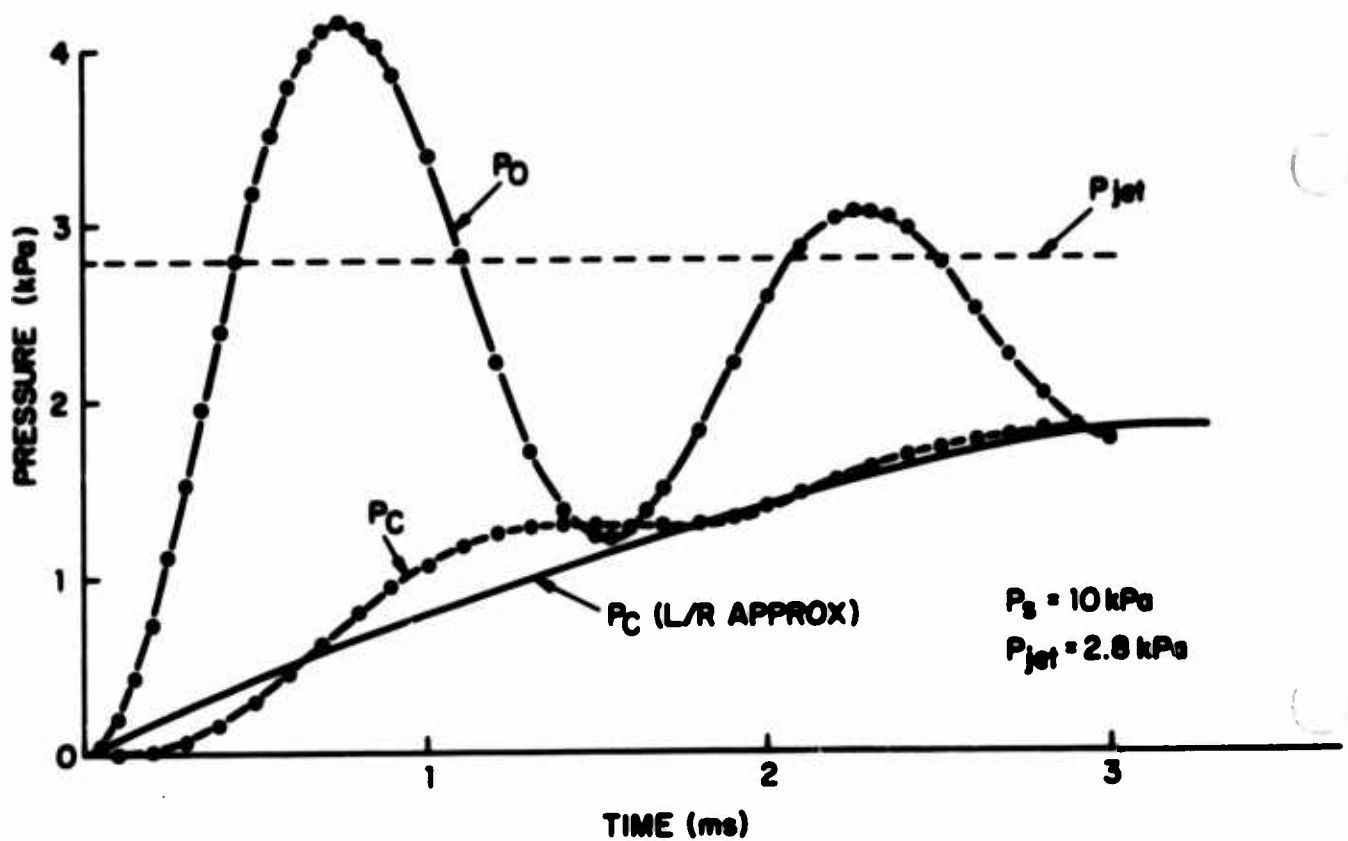
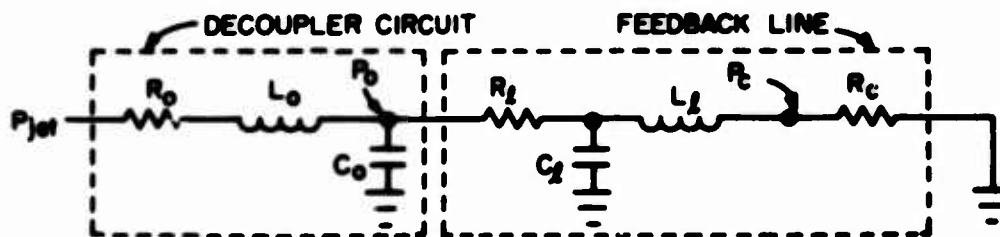


Figure 17. Output pressure response of flip-flop

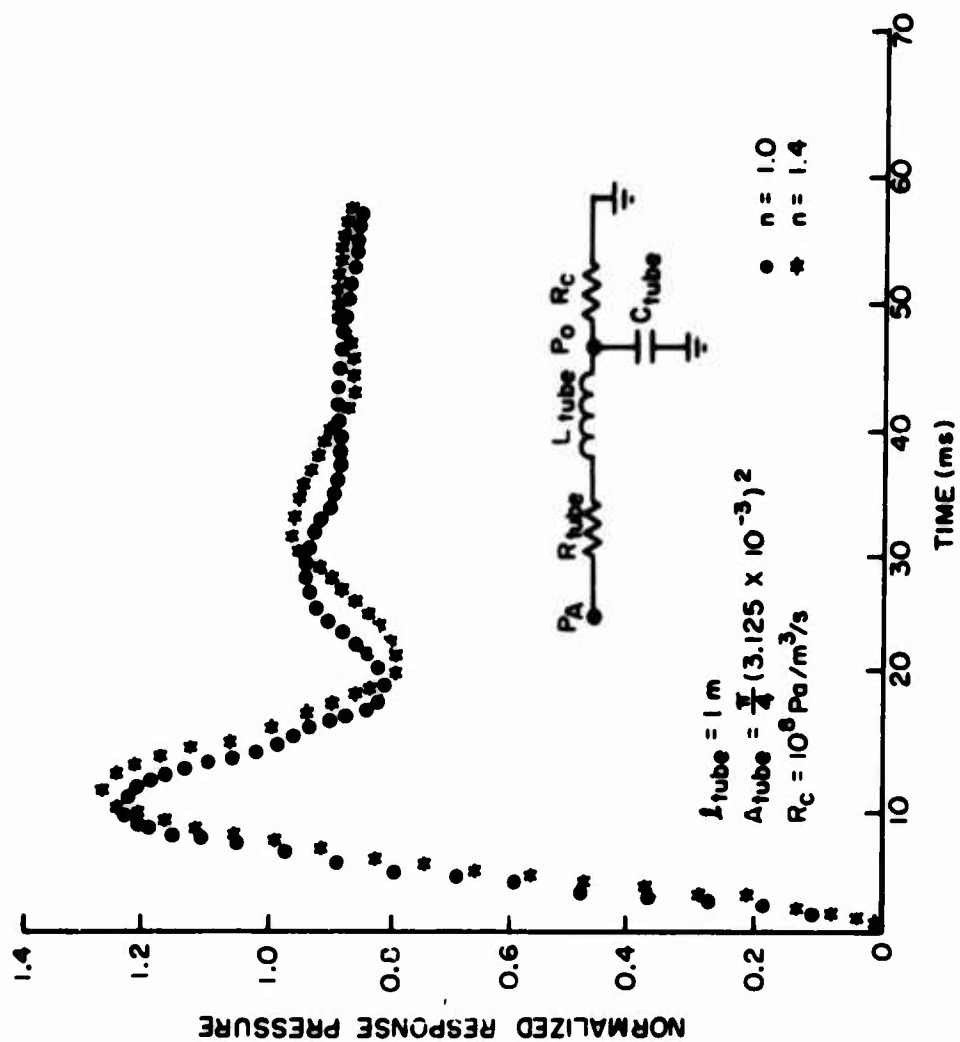


(a) PARASITIC CIRCUITRY DURING MEASUREMENT



(b) PARASITIC CIRCUITRY FOR FEEDBACK OSCILLATION

Figure 18a, b Equivalent circuits for the outlet



(c) TYPICAL RESPONSE SHOWING DIFFERENCE OF ADIABATIC AND ISOTHERMAL CAPACITANCE

Figure 18c Equivalent circuit for the outlet

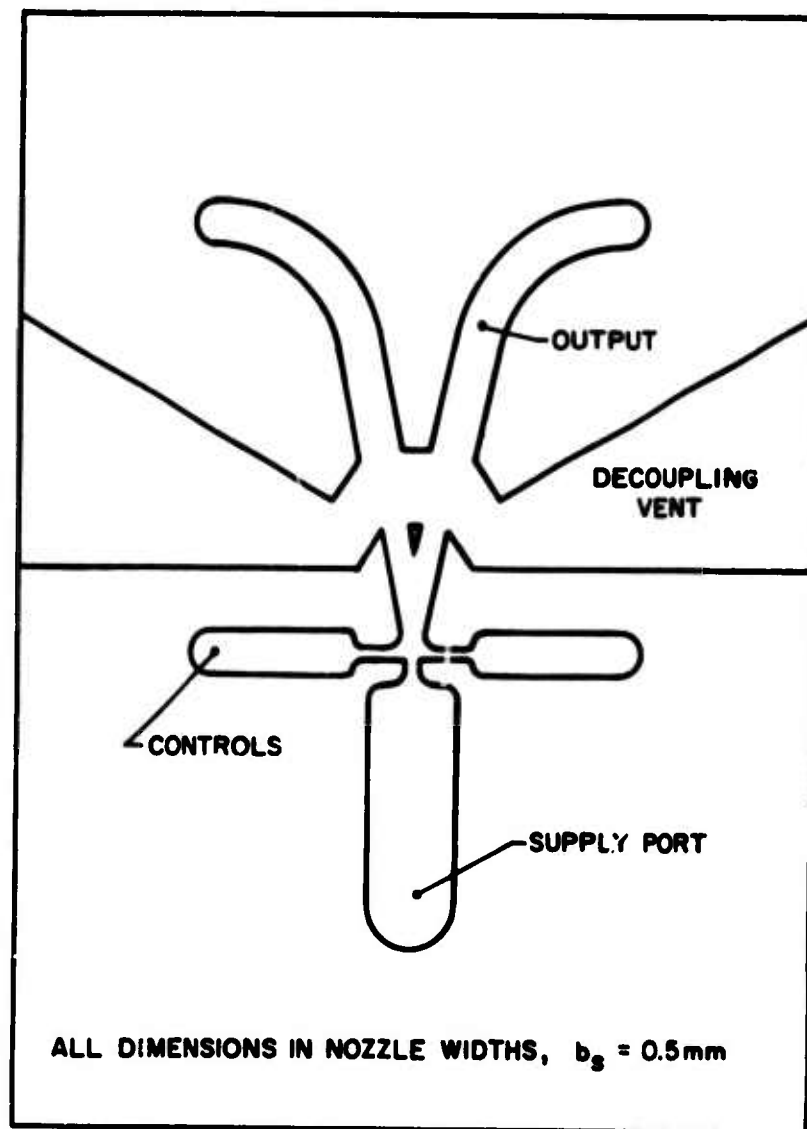
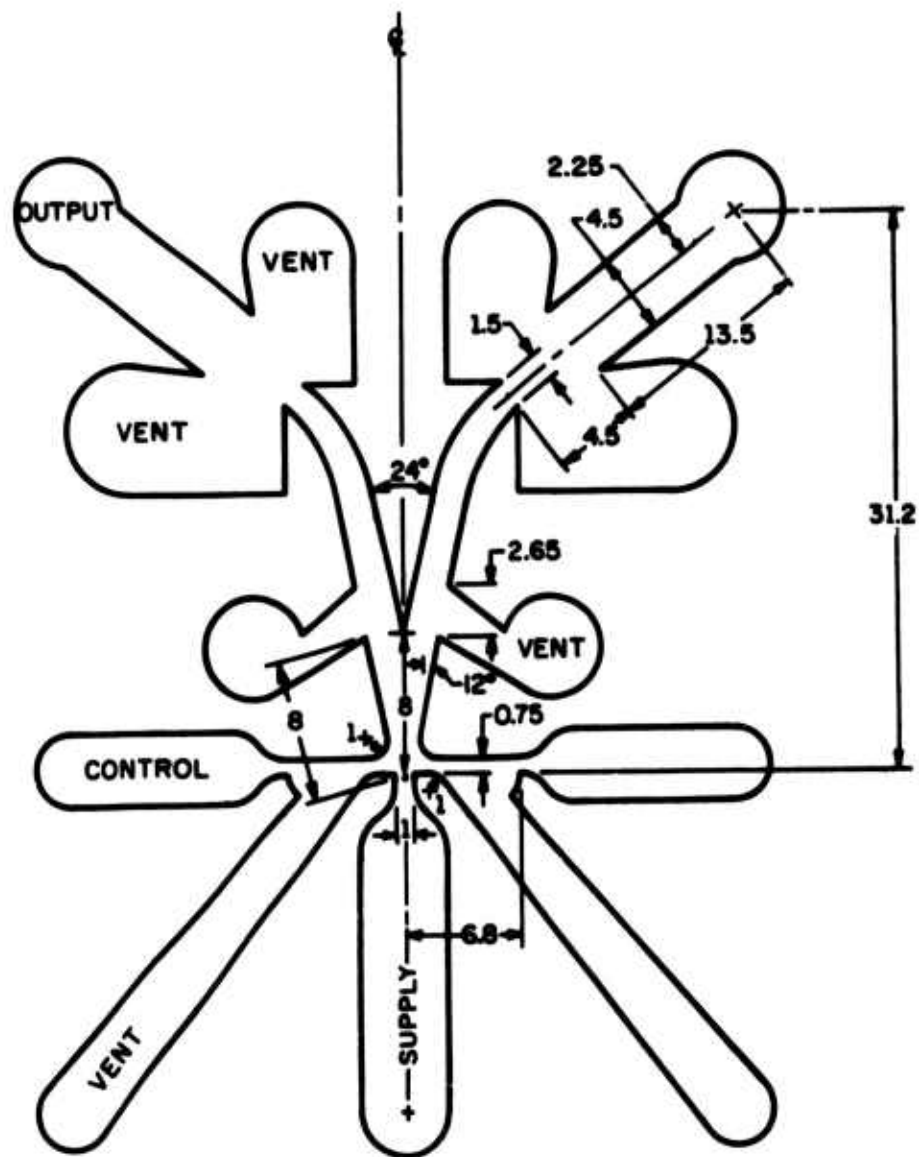


Figure 19. Geometry of the initial fast flip-flop



ALL DIMENSIONS IN NOZZLE WIDTHS,  $b_g = 0.5 \text{ mm}$

Figure 20. Geometry of the final version of the fast flip-flop



Figure 21. Photograph of the fast flip-flop and its interior laminations

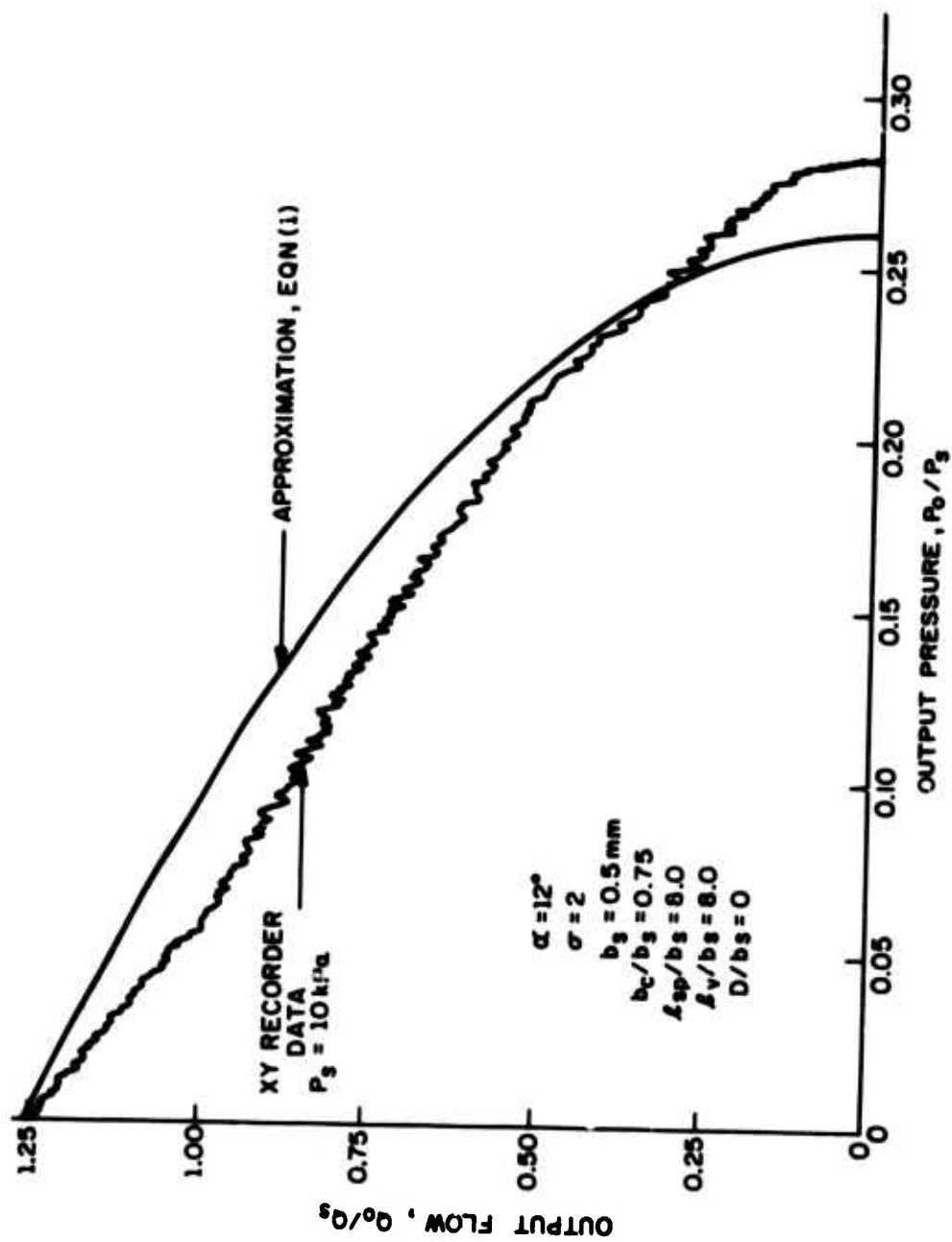


Figure 22a. Comparison of predicted static characteristics with actual x-y data - Output Characteristic

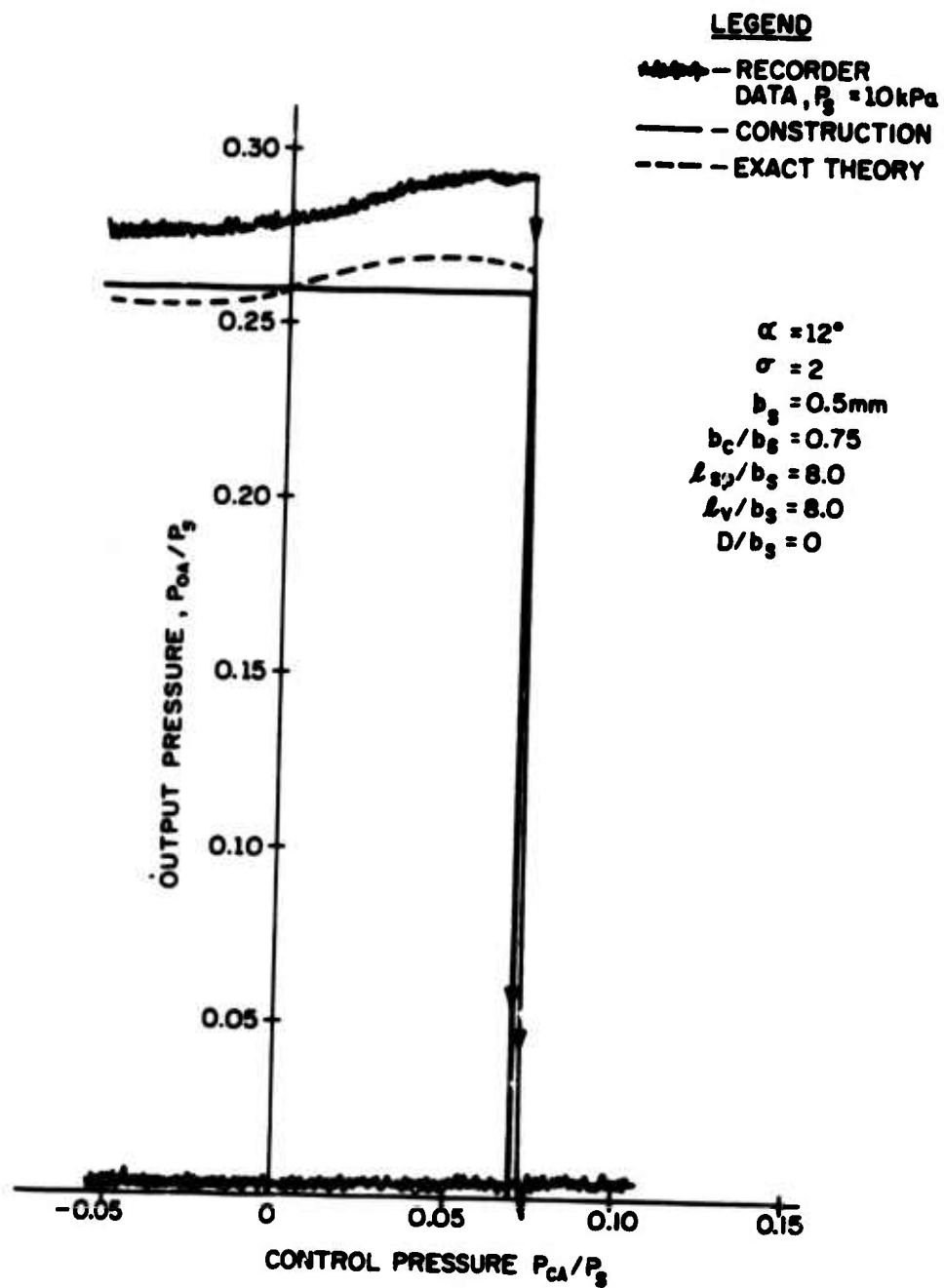


Figure 22b. Comparison of predicted static characteristics with actual x-y data - Transfer Characteristic



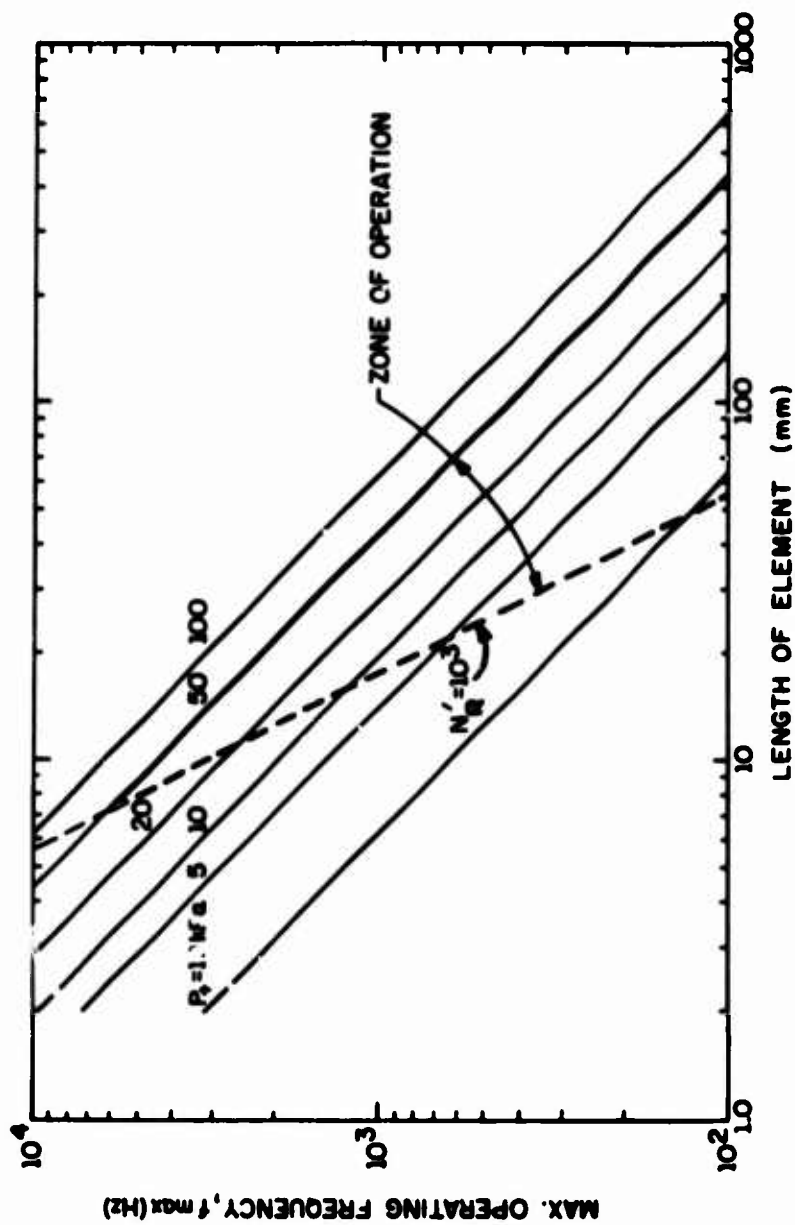


Figure 23. Maximum operating frequency response versus element size with supply pressure as a parameter

# THEORY

— EQ.18 - EARLY UNIT  
 - - - EQ.19 - FINAL UNIT

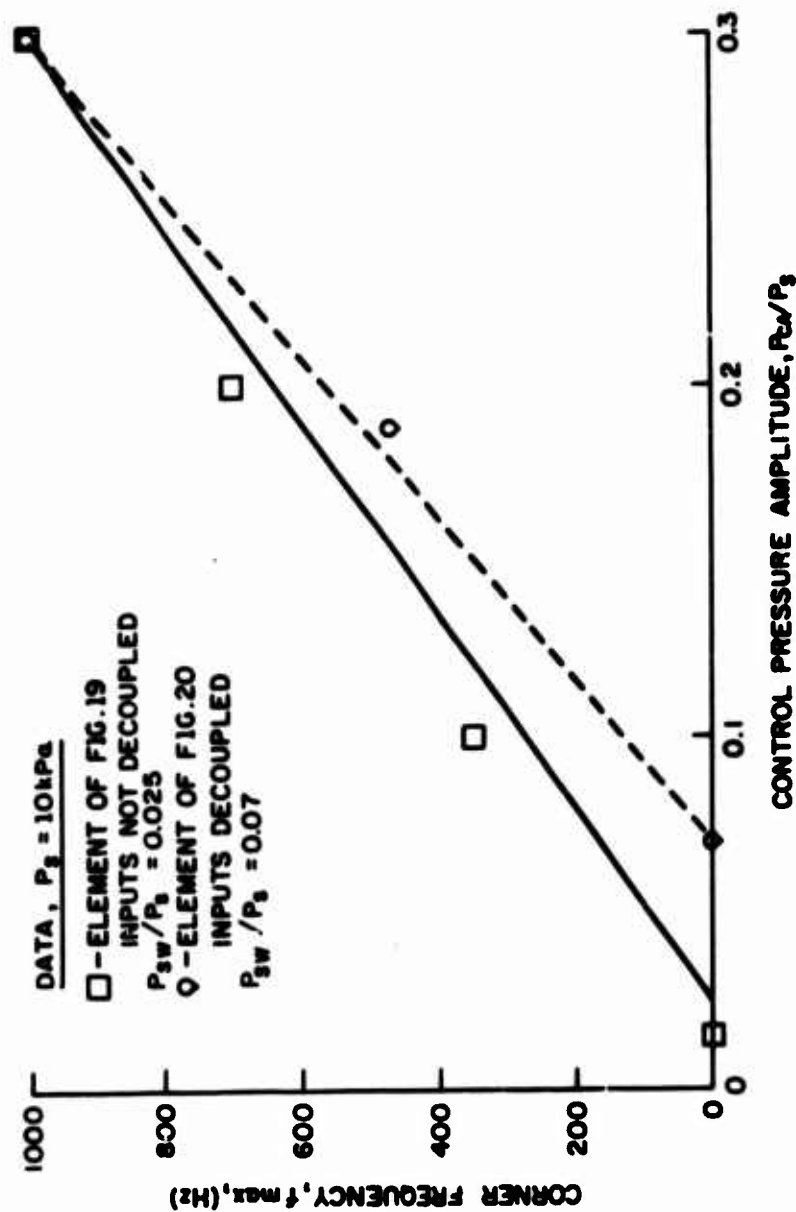


Figure 24. Corner frequency as a function of control amplitude

Effects of a Splitter and Vents  
on a Reattaching Jet and Its Switching  
in Wall Reattachment Fluidic Devices

T. Wada, A. Shimizu, and M. Takagi  
(Okayama University, Okayama, Japan)

1. Introduction

When one tries to design a wall reattachment fluidic device by using results that have been obtained from models without an end to the reattaching wall or without a splitter, or a vent, careful reconsideration may be required. When a device has a splitter, for outputs, and vents, for decoupling cascaded devices, the splitter and vents may have considerable effects on the behavior of jet. Such a jet, affected by the splitter and the vents, may be called an *Affected Jet*.

If the splitter distance is less than some critical value, the jet is affected by the splitter. In such an event, the pressure in reattaching bubble decreases and the reattachment point of jet moves upstream, as compared to the case where the splitter is faraway[1]. That is, the bubble shrinks. In addition, when the reattachment point is near the vent or the side wall end and a part of the jet flows out through the vent or the jet flows away at an angle to the wall plane, the jet is then affected by the vent or the wall end. Bourque-Newman have shown that the reattachment point of a jet on a short wall is less than that on a long wall[2]. We also have investigated such phenomena, in more detail[3]. These facts indicate that the movement of the reattachment point, due to the application of control flow, will be suppressed by the presence of a splitter or vent.

Furthermore, the presence of a vent causes a discontinuous expansion of the bubble at some control flow rate. This occurs when the jet jumps over the vent to attach to the wall downstream of the vent and vent flow enters the bubble.

The above behavior of the jet may have an effect on the characteristics of a device. The existing literature does not discuss to any great extent the effects of the splitter on the characteristics of a device, and in light of the above discussion the published models may not necessarily be applicable to the jet affected by the vent. For example, the end wall type models[4,5,6], where the jet switching is directly related with inflow to the bubble through the vent, must be used with care in some cases[3].

In the above discussion, the jet is separately affected by the splitter and the vent. However, when the jet is affected simul-

taneously by both the splitter and the vent, the phenomena may be very complex. It is these phenomena that must be understood in order to get a general model for the wall reattachment device.

It is the intent of this paper, therefore, to phenomenologically clarify the behavior; the switching, and the pressure recovery of an affected jet. At the same time, a discussion is presented of applicability of existing results to the design of devices and some conceptual suggestions are made for any analytical model of the affected jet.

## 2. Experimental Setup and Procedure

The experiments are carried out on the large scale model shown in Fig.1. The model is made of transparent plastic, and the blocks making up the side walls, the control nozzle, the splitter, and the vent are movable in order to obtain the various desired geometric configurations. These blocks are sandwiched between two flat plates, sealed completely by white vaseline, and fixed by C-clamps.

The main nozzle width and the control nozzle width of the model are both 8.0 mm, and the aspect ratios are 6 and 5 for the operating fluids of air and water, respectively. In water, the flow is visualized by means of fine polystyrene grain tracers, and only the behavior of the jet and the switching mechanism is investigated. Quantitative investigations of the jet flow are performed using the air model. The jet Reynolds number is equal to  $1.4 \times 10^4$  in air and  $8.3 \times 10^3$  in water, where the characteristic dimension is the main nozzle width. It is thus believed that the effects of Reynolds number and secondary flow are negligible[2,7]. Further, since the turbulence intensity of the main nozzle in the plenum chamber may affect the jet characteristics[8], the turbulence in this chamber is suppressed by a honeycomb core flow straightener.

In the experiments, the flow rate from the main nozzle  $Q_{SO}$  is evaluated by the following equation:

$$Q_{SO} = C_d b_s \sqrt{2(P_s - p_\infty)/\rho} \quad (1)$$

where  $P_s$ : main nozzle total pressure

$p_\infty$ : ambient pressure (nozzle exit static pressure in free jet)

$\rho$ : fluid density

$C_d$ : discharge coefficient defined by  $1 - 2\delta^*/b_s$

$\delta^*$ : displacement thickness at nozzle exit.

The control flow rate  $Q_c$  is measured by a float type flow meter.

In this investigation, switching of the jet is effected by applying a step-wise incremental control flow rate to the jet in critical static equilibrium due to the control flow. This type of switching is described as static switching in a later section.

## 3. Results and Discussion

One purpose of the investigation is to get an understanding of the effects of the splitter and the vent on jet behavior, hence to isolate these effects from the other the experimental model in some

cases does not use an opposite side wall.

### 3.1. Effects of Splitter

#### 3.1.1. Behavior of the Reattached Jet

In this part of the study the vent width  $b_v$  is equal to zero. Fig.2 shows an example of the effects of the splitter distance  $L_s$  on the reattaching wall pressure distributions. For values of  $L_s$  less than a critical distance  $L_{sc}$  the pressure in the bubble decreases. That is, the jet is affected by the splitter : the radius of jet curvature  $R$  decreases, and the bubble volume shrinks and the reattachment point moves upstream in comparison to an unaffected jet ( $L_s > L_{sc}$ ). The decrease in bubble pressure may be explained in the following way: the pressure drop in a flow passage or a duct, consisting of the splitter and the side wall, affects the upstream bubble pressure by effectively increasing the pressure difference. However, it seems that no theoretical explanations for this phenomenon have yet been presented.

Experimental data for the above-mentioned critical splitter distance  $L_{sc}$  without control flow is shown in Fig.3(a). For offset  $D/b_s = 1$  and inclined wall angle  $\alpha = 15^\circ$ , this distance  $L_{sc}/b_s$  is equal to 8.6. Fig.3(b) shows the distance from the nozzle exit to the outer edge of jet on the nozzle axis and the critical splitter distance for some offsets with a constant wall angle  $\alpha = 15^\circ$ . As can be seen, even when the jet outer edge is located for upstream from the tip of splitter, the jet can still be affected by the splitter. Some flow patterns showing the splitter effects are shown in Photo.1. As the splitter distance decreases, the bubble shrinks considerably for  $Q_c = 0$ .

For the jet with control flow, as a matter of course, the critical splitter distance increases over the no control flow case.

For  $D/b_s = 1.0$  and  $\alpha = 15^\circ$ , some wall pressure distributions showing the critical distances  $L_{sc}/b_s$  are given in Fig.4 and 5.  $L_{sc}/b_s$  for control flow rate  $Q_c/Q_{so} = 0.1$  and  $0.2$  is about 1.25 and 1.5 times that of  $Q_c/Q_{so} = 0$ , respectively.

For the same splitter distance, therefore, the degree to which the splitter effects the jet is very dependent on control flow rate. The more the flow rate becomes, the more the effect, generally. As the splitter distance decreases and becomes less than critical, the bubble shrinks and the jet is suppressed by the splitter. Such a shrinkage has a certain limit for the geometry and the control flow rate. As this limit is approached, the jet begins to run out along the opposite surface of splitter. This run-out is also closely related to switching, and will be discussed later on.

In order to evaluate the run-out, a concept of run-out intensity is introduced. The *Run-Out Intensity* is defined as the ratio of the total pressure of the flow over the opposite surface of splitter,  $P_R$  to the main jet supply total pressure  $P_s$ . If the jet flow is incompressible and has a sufficiently high Reynolds number, the characteristics of jet may not depend on Reynolds number. In that case then,  $P_R/P_s$  can be considered as a nondimensional quantity independent of  $P_s$ .

Fig. 6 shows the relationship of control flow rate  $Q_c/Q_{so}$  to splitter distance  $L_s/b_s$  for constant run-out intensity and  $D/b_s = 1.0$  and  $\alpha = 15^\circ$ . This particular relation is called the *Run-Out Characteristic*. In this figure, it can be seen that for  $L_s/b_s = 10$  the jet cannot run-out at a control flow rate  $Q_{c1}/Q_{so}$  where the run-out intensity is zero. As the flow rate increases, the jet run-out increases. When the control flow rate reaches  $Q_{c2}/Q_{so}$ , the intensity increases to 0.2.

Fig. 7 shows jet velocity profiles in the model without a splitter for  $Q_c/Q_{so} = 0.2$ . If it is assumed that the splitter does not affect the jet, the jet for  $L_s/b_s = 10$  must begin to run-out, when  $Q_c/Q_{so}$  attains to about 0.2. In fact, however, due to the suppressive effects of the splitter on the attachment point the control flow rate necessary for run-out to start (critical run-out control flow rate) is about 0.4. Since the critical splitter distance depends strongly on the control flow rate, the effects of splitter distance on the characteristic of device may depend on the control flow rate level,  $Q_{cs}/Q_{so}$  necessary for switching. For example, as the switching level  $Q_{cs}/Q_{so}$  becomes larger, the splitter distance must increase if the characteristic is to be unaffected.

### 3.1.2. Switching

Fig. 8 shows the relationship between switching control flow rate  $Q_{cs}/Q_{so}$  and splitter distance  $L_s/b_s$  for various opposite side wall offsets  $D_N/b_s$ . In the figure, the dashed line indicates the above-mentioned run-out characteristics. Considering, for an example, the results of  $D_N/b_s = 1.0$ , as  $L_s/b_s$  is decreased from about 20  $Q_{cs}/Q_{so}$  increases gradually due to the suppressive effects of splitter. This is because for the same control flow rate, the jet with smaller  $L_s/b_s$  shrinks more than that with a large  $L_s/b_s$ , and when the splitter distance  $L_s/b_s$  is larger than 10, the jet does not run-out. Thus the switching pattern is a so-called *Contacting Both Walls Switching*, since the switching flow is always less than the amount of flow required to cause run-out, and so the jet switches before any jet-splitter interaction. The degree of approach of the jet to the opposite side wall also becomes an important factor. If the same degree of the jet approach is required for switching, the more the jet suppressed, and so the more the control flow is required.

Decreasing, further, the distance  $L_s/b_s$ , the switching control flow rate corresponds to the flow rate of constant run-out intensity for very short splitter distances ( $L_s/b_s < 6$ ). In this region, the degree of jet approach to the opposite side wall does not apparently have an important effect on the switching, but the run-out intensity is an important factor.

As a matter of course, there is a region of splitter distance where both the run-out intensity and the degree of jet approach to the opposite wall have comparable effects on the switching. In the present example, this region is  $6 \leq L_s/b_s \leq 10$ . A simple illustration of this characteristic is given in Fig. 9. In the region AB

the mode of switching is contacting both walls, though the jet is affected by the splitter, and the region ED results in switching that requires a constant run-out intensity. In practice, an intermediate area, shown by EB, also exists.

For the case of  $D/b_s = 1.0$ ,  $D_N/b_s = 2.0$  and  $\alpha = \alpha_N = 15^\circ$ , the switching patterns are shown in Photo.2, 2(a) shows the patterns in area ED and 2(b) the patterns in area AB.

Although, as mentioned above, the switching patterns depend on the splitter distance, the substance of switching may be discussed by the pressure condition in the space bounded by the jet and the opposite side wall. We can assume that switching occurs, if and only if the pressure equilibrium in the space is broken down. This equilibrium is broken down by the jet approach in the area AB, and by the run-out flow of jet in the area ED. The run-out intensity necessary to break down the pressure equilibrium may increase, as the opposite space expands. In Fig.9, this state exists in the area BC.

As seen before in Fig.6, the control flow rate necessary to increase the run-out intensity from 0 to 0.2 changes by large extent in the area BD of Fig.9. It must be noted then that the switching flow rate is greatly affected by the opposite wall offset  $D_N/b_s$ . If the control flow change to the run-out intensity is small, the switching flow rate may not be affected by the opposite wall offset.

### 3.2. Effects of the Side Wall Vent

#### 3.2.1. Behavior of the Jet

In this case the splitter is not installed in the experimental model. The distance  $L_s/b_s$  is infinite. The discussion begins with the results from the model with infinite vent width  $b_v/b_s = \infty$ , that is, the model has a fixed length of reattachment side wall,  $L_w$ , that terminates at that point.

In Fig.10, the pressure distributions on the wall for various control flows are shown for  $D/b_s = 0.5$ ,  $\alpha = 15^\circ$ , and  $L_w/b_s = 12.0$ , in comparison with that for  $L_w/b_s = \infty$  (long compared with the reattachment distance). For the control flow rate  $Q_c/Q_{s0} = 0.27$ , the reattachment point is located slightly upstream of the wall end. The pressure distribution in bubble is not affected by the presence of the terminated wall. Increasing the control flow rate, however, to  $Q_c/Q_{s0} = 0.33$ , where the reattachment distance  $L_R/b_s = 12.0$  for  $L_w/b_s = \infty$ , the  $L_w/b_s = 12$  reattachment point may locate in the vicinity of the wall end. The pressure distribution in bubble is then affected by the end and consequently the pressure drops. That is, the radius of jet curvature decreases. In the affected jet, the reattached state is maintained for  $Q_c/Q_{s0}$  up to 0.4, due to the bubble shrinkage. Bourque-Newman[2] have given one explanation for this phenomenon, wherein the jet momentum direction downstream of the reattachment point is considered. The above phenomenon can be explained in a similar way.

Let the radius of jet curvature for the very long wall length be  $R_\infty$  and for the finite length short wall,  $R_{end}$ . From the momentum equation along the wall for the control volume EFGHE in Fig.11(a) and



the relation  $J/R = -p_B$  for  $R \gg b_s$ , the next two equations are obtained:

$$R_{\infty} = \frac{D^* \cos \alpha}{\cos(\alpha + \beta) - J_d/J} \quad (2)$$

$$R_{\text{end}} = \frac{D^* \cos \alpha}{\cos(\alpha + \beta) - J_d \cos \beta / J} \quad (3)$$

These equations show that the radius of jet  $R$  decreases if the flow downstream from the reattachment point cannot flow along the wall. Hence the bubble pressure drops and the bubble shrinks, compared with the jet for  $L_w/b_s = \infty$ .

Fig.12 shows data for some jet centerlines (locus of maximum velocity point measured by hot wire anemometer) for  $L_w/b_s = 12$  and 15 in comparison with that for  $L_w/b_s = \infty$ . For the control flow rates  $Q_c/Q_{s0}$  given, the reattachment distance is  $L_R/b_s = 12$  and 15 for  $L_w/b_s = \infty$ , respectively. Effects of the wall end on the jet can be easily recognized by the change in radius of curvature. The flow patterns in Photo.3 clearly show the effects of the wall end on the flow direction of the jet. In Photo.3(a), the flow is in the direction of the wall, so that the effects of the wall end may be negligible. In Photo.3(b) and (c), however, the flow direction makes a certain angle to the wall, and so the effects of wall end are marked.

For the case of small wall offset  $D/b_s$  and wall length  $L_w/b_s$ , the control flow rate necessary to detach the jet from the wall is comparatively small. In that case the attachment angle  $\theta$  becomes small, and the jet is practically unaffected by the wall end (Fig.13).

Next, the results from the model with a wall vent width  $b_v/b_s$  of order about 1 are discussed. Here, the wall length downstream from the vent is very long.

Fig.14 shows the pressure distributions for the wall length upstream from the vent  $L_v/b_s = 12$ ,  $D/b_s = 0.5$ , and  $\alpha = 15^\circ$ . When the control flow rate  $Q_c/Q_{s0}$  applied is 0.33, the reattachment point is located just upstream from the wall end. The upstream pressure distribution from the vent is not affected. By increasing  $Q_c/Q_{s0}$  to 0.40, the wall end effect can be seen; the bubbles for  $b_v/b_s = 1.5$  and 3.0 shrink in comparison with that for  $L_v/b_s = \infty$ . However, for the vent width  $b_v/b_s = 0.5$ , the wall end effect is not as predominant in comparison with the jet with large vent width because the reattachment point jumps over the vent and attaches to the downstream part of the wall. At the same time, the bubble is expanded with the pressure increase in bubble, due to inflow through the vent to the bubble.

As mentioned above, the vent has two effects on the jet: one is the shrinkage of bubble, the other is the large expansion of the bubble due to the jump of the reattachment point over the vent. These effects can be explained as follows: for the upstream section, the flow agrees with a model as in Fig.11(a), but in the downstream section the flow must be modified as in Fig.11(c), then the radius of jet curvature



$R_V$  is given by the same procedure for  $b_V/b_S = \infty$  :

$$R_V = \frac{D \cos \alpha}{\cos(\alpha + \beta) - \{J_d - J_V(1 - \cos \theta)\}/J} \quad (4)$$

and considering  $J_d = J_V + \tilde{J}_d$ ,

$$R_V = \frac{D \cos \alpha}{\cos(\alpha + \beta) - (J_V \cos \theta + \tilde{J}_d)/J} \quad (5)$$

Thus, as the vent width  $b_V/b_S$  decreases, and  $J_V$  becomes small, it means that the decrease of  $R_V$  becomes small with  $b_V/b_S$  or the wall end effect on jet becomes weak. Further, this means that the control flow rate necessary to make the reattachment point jump is affected by  $b_V/b_S$  and decreases with  $b_V/b_S$ . Photo.4 shows this phenomenon.

In this case, the shrinkage effect due to the wall end or vent is negligible when compared to the small angle  $\theta$  case. Then, the control flow rate necessary to jump is practically unaffected by the vent width  $b_V/b_S$ . Fig.15 demonstrates this phenomena. However, after the jet has jumped, the attachment point depends strongly on the vent width due to the inflow through the vent. The larger the vent width, the more the bubble expands.

### 3.2.2 Switching

Consider first the case of switching for a terminated wall, or an infinite vent width  $b_V/b_S = \infty$ , that is, finite wall length  $L_W/b_S$ . The switching control flow rate is that necessary to detach the jet from the reattachment wall. For a reattached side offset  $D/b_S = 1.0$  and  $0.5$ , and an inclined wall angle  $\alpha = 15^\circ$ , the opposite side inclined wall angle  $\alpha_N = 15^\circ$ , the relationship of switching control flow rate  $Q_{CS}/Q_{S0}$  to the opposite side offset  $D_N/b_S$  are shown in Fig. 16, for several wall length  $L_W/b_S$ . The switching characteristic for  $L_W/b_S = \infty$  is described by a solid line. In that case, the switching pattern shows a typical *Contacting Both Walls Switching* (Refer to Photo.5).

As an example, the switching mechanism for the case of  $D/b_S = 1.0$ , is discussed. When the wall length  $L_W/b_S$  is very short,  $L_W/b_S = 8.0$ , then the switching mechanism is the so-called *End Wall Switching*. That is, after the jet detaches from the initial wall the jet is then reattaches to the opposite wall. By increasing the wall length, two switching mechanisms appear depending on the offset  $D_N/b_S$ . The contacting both walls switching occurs for small  $D_N/b_S$ , and the end wall switching for large  $D_N/b_S$ . For a wall length  $L_W/b_S = 10$ , it seems that the end wall effect is negligible. For the  $L_W/b_S = 12$ , however, the end wall effect is marked. Then, the switching control flow rate  $Q_{CS}/Q_{S0}$  for small  $D_N/b_S$  increases due to the wall end effect, that is, there is bubble shrinkage in comparison with that of the  $L_W/b_S = \infty$  case.

A schematic representation of such a switching characteristics is

shown in Fig.17. In this figure, the switching mechanism in the area, described by the dashed line, is the end wall switching. Up to this point, the effect of the opposite wall on the jet behavior has not been considered. In actual fact, the opposite wall can affect the pressure in the flow field in a manner such that the pressure drops uniformly in the whole flow field. For small offsets  $D_N/b_S$ , the decrease may become quite large. Thus the pressure in the vicinity of the wall end tends to drop, so the jet tends to detach from the initial wall with a smaller control flow rate in comparison with that of large offset  $D_N/b_S$ . It seems that this tendency is more prominent due to the following condition, also. When the flow downstream from the reattachment point enters a free space, the jet whose reattachment point is near the end of the wall, undergoes large fluctuations.

For  $L_w/b_S = 15$ , the switching mechanism for all values of  $D_N/b_S$  is the contacting both walls switching, while the effect of wall end becomes marked for large  $D_N/b_S$ .

Photo.6 shows the switching patterns for  $D/b_S = 1.0$ ,  $\alpha = \alpha_N = 15^\circ$  and  $D_N/b_S = 1.5$ . The end wall switching can be observed for  $L_w/b_S = 10$  and 12, while for  $L_w/b_S = 15$  the contacting both walls switching like that of  $L_w/b_S = \infty$  is recognized. As mentioned above, if the offset  $D/b_S$  and the wall length  $L_w/b_S$  are smaller than 1 and 10, respectively, the jet is almost unaffected by the wall end. The existing formulations of switching[4,5,6], therefore, may be reasonable. For the vent width  $b_v/b_S$  of the order about unity, however, the direct application of existing formulations may not be reasonable. It is noted that the jet attaches on the downstream wall, even if the bubble is released to ambient through the vent, for sufficiently long wall downstream of the vent.

Since vent width is an important parameter, switching for definite vent width is discussed next. Fig.18 shows the switching characteristics for several vent width  $b_v/b_S$ ; 18(a) shows the characteristics for the small control flow rate necessary to jump the vent (low jump level); and 18(b) large control flow rate to initiate a jump (high jump level).

For the low jump level, the jet behavior after jump is greatly affected by the inflow through the vent. Thus, the switching in such a condition is very much a function of the vent width. The switching mechanism is contacting both walls. On the other hand, as the vent width increases, the jump control flow is almost the same as the switching flow. For example, the switching in the area  $D_N/b_S < 1$  for  $b_v/b_S = 1$  and  $D_N/b_S < 2$  for  $b_v/b_S = 2$  shows such a characteristic. Even under such conditions, however, the switching is substantially contacting both walls. In the case when the jump flow corresponds to the switching flow, the analytical formulation of end wall switching may be approximately applied.

For the high jump level, the switching mechanism for small  $D_N/b_S$  is contacting both walls switching before the jump, although the end wall effect is fairly dominant. Here the characteristic that the jump agrees with the switching is observed even in the area of large

$D_N/b_S$  due to the large expansion of the bubble because of the jump in comparison with that of the low jump level. In this case the jump level is very dependent on the vent width  $b_V/b_S$  as mentioned in the previous section, and this level increases with the vent width in the region  $b_V/b_S < 5$ . However, for large vent width the condition agrees with the case of  $b_V/b_S = \infty$ . In such a condition, the jump level drops due to the fluctuation of the jet (Refer to Fig.19).

Furthermore, for high jump level, since the jet, before the jump, can come sufficiently close to the opposite wall, the pressure in flow field decreases in comparison with the low jump level case. Also, since the vent is open to ambient, when the reattachment point is near the upstream wall end, this pressure decrease may aid in the switching. The schematic representation of this characteristic is shown in Fig.17, provided *End Wall Switching* is replaced by the *Jump Level*. The various flow patterns of this switching are shown in Photo.7; 7(a) shows switching before jump, 7(b) shows the switching just after jump, and 7(c) shows the switching after jump. In case 7(c), the switching flow rate is equal to the jump level plus an additional flow rate. From these patterns, one can see that the switching mechanism for the configuration with a vent is essentially the contacting both walls switching.

### 3.3 Effects of Vent and Splitter

In the two previous sections, the effects of splitter and vent have been dealt with separately. Here, the case where the jet is affected by both splitter and vent is discussed.

#### 3.3.1 Behavior of the Reattached Jet

Using the previous results, the present problems are considered, qualitatively. Fig.20 and Fig.21 show characteristic effects of the splitter and vent, respectively. In each of these figures, the top figure shows the jet centerline and the bottom one shows the pressure distribution on the reattachment wall.

When these effects are superimposed, the following conditions can be guessed at: if the splitter is located near the vent or upstream of it, the pressure near the vent will drop. In addition to this, since the vent is open to ambient, the decreased pressure near the vent may help push the jump of the jet. This means that the shrinkage effect of splitter will be reduced by the presence of the vent. Here, the meaning of the words *push and reduce* is that the control flow rate necessary to cause a jump becomes smaller. In order to discuss such a tendency in a less abstract form, the results shown in Fig.22, are analyzed as an example. This figure shows the relationship between the pressure distributions on the wall and the relative position between vent and splitter. The upper figure indicates the existence of a certain splitter distance  $L_S^*/b_S$  in relation to the upstream wall length  $L_V/b_S$ , where the splitter and the vent have the same effect on the pressure distribution in bubble. The lower figure shows that the splitter effect is marked when the splitter distance  $L_S/b_S$  is smaller

than the boundary distance  $L_s^*/b_s$  and for  $L_s/b_s$  larger than  $L_s^*/b_s$  the vent effect is predominant.

Thus, in the case of  $L_s < L_s^*$  the jump may be pushed almost certainly due to the pressure drop near the vent. This indicates that the splitter has the same effect as an opposite wall for the jump. On the other hand, for the case of  $L_s > L_s^*$  the relation of the splitter effect to the vent effect to jump becomes important. When splitter effects dominate, the control flow rate necessary to jump (jump level) increases by some degree. It has been experimentally determined that the limiting splitter distance  $L_s^*$  can be given as in Fig.23 for many configurations.

After the jet jumps across the vent it is affected by the splitter and the vent. The vent effect is determined by the inflow rate to the bubble through the vent. This inflow rate increases and the bubble expands in proportion to the vent width  $b_v$  to some degree. Therefore, for a configuration with the same splitter distance  $L_s$ , the jet with a larger vent width is affected more by the splitter, then the jet may begin to run-out along the opposite surface of splitter with a smaller control flow rate, as we can guess from the data of Fig.6. For a configuration with a constant vent width, the qualitative effect of splitter agrees with the results in Fig.5, as shown in Fig.24.

In order to understand more quantitatively the above discussion, the above phenomena are discussed by making use of the concept of the run-out intensity which was introduced in section 3.1.

Fig.25 and Fig.26 show the run-out characteristics as defined in previous section. For large vent width, as in this example, the characteristics differ quite a bit from that of the no vent case  $b_v/b_s = 0$ . In Fig.25, the jump level is low due to small vent distance  $L_v/b_s$ , while in Fig.26 this level is high due to a long vent distance. In the area of  $L_s/b_s < L_s^*/b_s$ , the jump level however drops due to the splitter effects.

The difference here, in comparison with that of  $b_v/b_s = 0$  case, is that the jump has a large effect on the run-out characteristics. When the vent width is narrow, however, the jump may be suppressed by the splitter if the splitter distance is short, and the bubble, even just after jump, is not allowed to expand. Thus, for this case the run-out characteristics become similar to that of the zero vent width case.

Now, in the case of large vent width  $b_v/b_s = 2$ , the dominant tendency that may be observed in relation to the splitter distance, as shown in two figures, is that in the region of small splitter distance, the control flow rate of the limiting run-out ( $P_R/P_S = 0$ ) agrees with the jump level. This means that the jet just after jump is beyond the state of the run-out limit. In the region of splitter distance, where the jet just after jump is not beyond this limit, additional control flow is necessary to produce run-out.

For example, keeping a constant control flow rate smaller than that at this limit and decreasing the splitter distance  $L_s/b_s$  from the

area of large  $L_s/b_s$ , the jet gets to the limit at a smaller  $L_s/b_s$  than that when  $b_v = 0$ , due to the large expanded bubble after the jump. By further, decreasing  $L_s/b_s$ , the run-out intensity increases even at fairly low control flow levels, since the jet which has jumped cannot return to the before-jump state. Unlike the case when  $b_v = 0$ , the range of control flow rate necessary to increase the run-out intensity, for example, from 0 to 0.2 becomes remarkably narrow with the decrease of  $L_s/b_s$ . Such a range does not appear in practice, so then the run-out is markedly increased with the jump.

As mentioned in previous section, the jet just after jump is very much affected by the vent width, therefore for large  $b_v/b_s$ , the range of  $L_s/b_s$ , where the jump level agrees with the control flow rate of run-out limit, extends to even large  $L_s/b_s$ . By comparing these run-out characteristics to that of the  $b_v/b_s = 0$  case, the reduction of the splitter effect due to the presence of the vent can be quantitatively understood.

As a matter of course, the strong reduction of the splitter effect may be obtained for smaller  $L_v/b_s$  and larger  $b_v/b_s$ . In practice, however, we can get  $L_v/b_s$  as small as possible and  $b_v/b_s$  as large as possible. These quantities also have a direct bearing on the recovery pressure of a device. Thus, an optimal values of these parameters must exist for optimal performance.

Now, the run-out characteristics relate directly to the switching as shown later. One method, therefore by which the switching characteristics may be roughly approximated, is presented here.

Fig.27 is a schematic representation of the run-out characteristics. A difference exists between two jets: one where the inflow to the bubble is the sum of control flow and flow through the vent, and the other where the inflow is the control flow only. Ignoring this difference, however, the effects of the vent and splitter on the run-out characteristics can be roughly approximated. If the run-out characteristics for  $b_v/b_s = 0$ , the jump level for sufficient large  $L_s/b_s$ , and the about inflow rate through the vent are known, the rough characteristic can be presented as shown in Fig.27.

### 3.3.2 Switching

Typical examples for the relationship of switching control flow rate  $Q_{cs}/Q_{so}$  to the splitter distance  $L_s/b_s$  are shown in Fig.28 and Fig.29, with low jump level and high jump level, respectively. In each figure, the run-out characteristic is superimposed with dashed lines. In the following paragraphs the switching in relation to the run-out characteristics is discussed.

First, the results presented in Fig.28 are discussed. In the region of  $L_s/b_s$ , where the range of control flow rate necessary to increase  $P_R/P_s$  from 0 to 0.2 is sufficiently narrow, the effects of the opposite offset  $D_N/b_s$  are negligible on the switching flow rate  $Q_{cs}/Q_{so}$ . This means that the run-out, sufficient to break down the pressure equilibrium on opposite side, is applied by the jump. By increasing  $L_s/b_s$  beyond this region,  $Q_{cs}/Q_{so}$  is affected by  $D_N/b_s$  due to the above range for control flow rate. Then, the wider the

opposite space becomes, the higher the run-out intensity necessary to switch the jet. The opposite space becomes wide, when the opposite offset is large and the splitter distance is short, due to the splitter effect.

For a low jump level, for large values of  $D_N/b_s$ , even just after jump the jet may still remain attached. Then, the jet is very much affected by the splitter. As  $L_s/b_s$  becomes larger, however, the splitter effects reduce, the jet can come closer to the opposite wall, and the run-out intensity necessary to switch decreases. In the region of splitter distance longer than a certain distance, run-out cannot be observed and the switching mechanism in this area is almost the same as that when only a vent is present as shown in section 3.2.

Further, when the jump level is fairly low, the jet even just before jump has considerable space on the opposite side, even for  $D_N/b_s = 0.5$ . Then, the pressure drop due to the opposite wall is not large, so the jump level is practically unaffected by  $D_N/b_s$ .

Next, the results presented in Fig.29 for higher jump level are discussed. In the area of  $L_s/b_s$ , where the switching characteristics almost agree with the run-out, the discussion is quite similar to that of the low jump level. An important difference is that the jet just after jump detaches and switches even for  $D_N/b_s = 6$ , so that the switching when the run-out intensity becomes important can be observed for large  $L_s/b_s$ , unlike that for the low jump level.

By considering the difference between jump levels, one can make the following explanation: the bubble of the attached jet with high jump level can expand so much just before the jump in comparison with that of jet with low jump level that the jet can come sufficiently close to the opposite wall to be switched. In that case run-out is not necessary to switch the jet. At the same time, however, the jump level is affected very much by the opposite offset  $D_N/b_s$ . The switching flow level for  $D_N/b_s = 2.0$  is 0.1 less than the  $D_N/b_s = 6.0$  case. For small  $D_N/b_s$ , switching can occur before the jump. Except for small  $D_N/b_s$ , switching occurs just after jump, but, while the switching for large  $L_s/b_s$  is independent of the run-out, for small  $L_s/b_s$  switching depends substantially on the run-out intensity.

Photo.8 shows flow patterns of switching: 8(a) switching where the run-out intensity is substantial, and 8(b) switching just after jump.

As mentioned above, by introducing the run-out intensity, it has been shown that the effects of the splitter and vent on the behavior and switching of a reattached jet can be explained more clearly.

### 3.4 Effects of vent and Splitter on Recovery Pressure

The previous three sections have concerned themselves with the input characteristics of device. However, as stated in the introduction the configurations of the vent and splitter are to be considered not only from the standpoint of the input characteristics but also output pressure recovery.

Here, the effects of the configurations of the vent and splitter on the pressure recovery for a completely blocked output duct (maximum recovery pressure) are discussed. Fig.30 shows the relationship of



the maximum recovery pressure  $P_{rec}/P_s$  to the splitter distance  $L_s/b_s$ . In the case of small vent width the load cannot be decoupled for a splitter distance  $L_s/b_s$  smaller than about  $L_s^*/b_s$ . This means that the pressure on the wall upstream of the vent increases due to the blockage, so the jet detaches from the initial wall. For the large vent width, even though the load at small splitter distances  $L_s/b_s$  can be decoupled to some degree, the recovery pressure drops somewhat.

When the splitter distance is fairly large compared to  $L_s^*/b_s$ , the pressure recovery does not depend much on the distance  $L_s/b_s$ . Now, since this pressure depends somewhat on the output duct width, it seems that the momentum into the duct rather than the pressure is the proper variable with which to discuss the effects of splitter and vent on the jet. The net momentum into the duct  $J_d$  is described by  $P_{rec}B$ , where  $P_{rec}$  is the recovery pressure and  $B$  is the duct width. Non-dimensionalizing this by means of the main jet momentum  $J_s = 2C_d^2 P_s b_s$ , the expression for the momentum  $J_d$  is :

$$\bar{J}_d = \bar{P}_{rec} \bar{B} / 2 \quad (6)$$

where  $\bar{P}_{rec} = P_{rec}/P_s$ ,  $\bar{B} = B/b_s$ .

Fig.31 and 32 show the relationship of this momentum  $\bar{P}_{rec} \bar{B} / 2$  to the splitter distance  $L_s/b_s$ . From these results, it should be noted that the vent width does not affect the recovered momentum much for a considerably large range of  $L_s/b_s$  greater than  $L_s^*/b_s$ , but the minimum distance of splitter to be able to decouple depends very much on the width  $b_v/b_s$ . The minimum splitter distance decreases, as the vent width  $b_v/b_s$  becomes large. This means that the pressure near the upstream side of vent is not affected even by the blocked load, for large vent widths. When the distance  $L_s/b_s$  becomes small, the momentum decreases significantly. This means that outflow through the vent to ambient exists and the effective momentum into the duct is decreased.

Fig.33 shows the relationship of this momentum to the splitter distance  $L_s/b_s$  for a constant vent width  $b_v/b_s = 2.5$ , and for various vent distances  $L_v/b_s$ . In these configurations, the maximum momentum is obtained at the splitter distance  $L_s/b_s \approx L_v/b_s + 5$ . For splitter distances smaller than this, the momentum decreases so much that the pressure recovery may drop, even if the outlet width  $B/b_s$  decreases. For the larger distances  $L_s/b_s$ , the momentum does not depend much on the distance  $L_s/b_s$  so that the pressure recovery does drop due to the effect of the increasing width  $B$ .

Photo.9 shows flow patterns for a completely blocked duct. The configurations are  $D/b_s = D_N/b_s = 1.0$ ,  $\alpha = \alpha_N = 15^\circ$ ,  $L_v/b_s = 10$ , and  $b_v/b_s = 2.0$ , and the distance  $L_s/b_s$  changes from 18 to 10. In order to relate these patterns to the momentum into the duct, consider the approximate model shown in Fig.34. In the case where the splitter is located slightly downstream from the vent, the flow does not separate, but rather the flow separation is suppressed by the vent. Then, referring Fig.34(a) the momentum into the duct is approximated by the next

equation:

$$\bar{P}_{ec} B/2 = J (1 + \cos\phi). \quad (7)$$

On the other hand, when the splitter is located near the vent, the pressure rises near the vent, so the flow may separate upstream of the vent. Referring to Fig.34(b), the momentum into the duct is given by next equation:

$$\bar{P}_{ec} B/2 = J(1 + \cos\phi) - J_v(\cos\phi + \cos\theta) \quad (8)$$

This equation shows that for such a vent and splitter configuration the outflow through the vent decreases the momentum into the output duct.

Ignoring the differences between the vent widths in Fig.33 and Photo.9, one may conclude from the above discussions that the momentum change for  $L_v/b_s = 10$  in relation to the splitter distance can be directly related to the flow patterns shown in Photo.9.

#### 4. Conclusion

The effects of a vent and splitter on the behavior of a reattached jet and its switching to an opposite wall were experimentally investigated. In order to explain these effects, the concept of run-out intensity was introduced and was found to describe the ensuring phenomena quite well.

The results obtained are as follows:

- (1) The effects of a vent and splitter on a reattached jet were clearly related to the run-out intensity.
- (2) When the effects of a vent were superimposed on the effects of a splitter, the splitter effects were greatly reduced. Phenomenological explanations for this have been presented in the paper.
- (3) The applicability of the present results to a reattached jet was made clear, and the basic concepts have been tied into an analytical model that includes the effects of vent and splitter.

#### References

- 1) T.Wada et al., Trans. SICE, Vol.6, No.3, pp.214-220 (in Japanese) (1970)
- 2) C.Bourque and B.G.Newman, The Aeronautical Quarterly, Vol.XI, pp. 201-232 (1960)
- 3) T. Wada et al., Trans. SICE, Vol.9, No.5 (in Japanese) (1973)
- 4) P.A. Lush, Proc. IFAC Symposium on Fluidics, A3 (1968)
- 5) D.I. McRee and H.L. Moses, ASME Paper, 69-Flcs-31 (1969)
- 6) M. Kimura, Proc. 2nd IFAC Symposium on Fluidics, A8 (1971)
- 7) D.I. McRee and H.L. Moses, Advances in Fluidics, ASME, pp.142-161 (1967)
- 8) R.W. Gray and J.L. Shearer, Trans. ASME, Series G, Vol.93, No.1, pp.53-60 (1971)



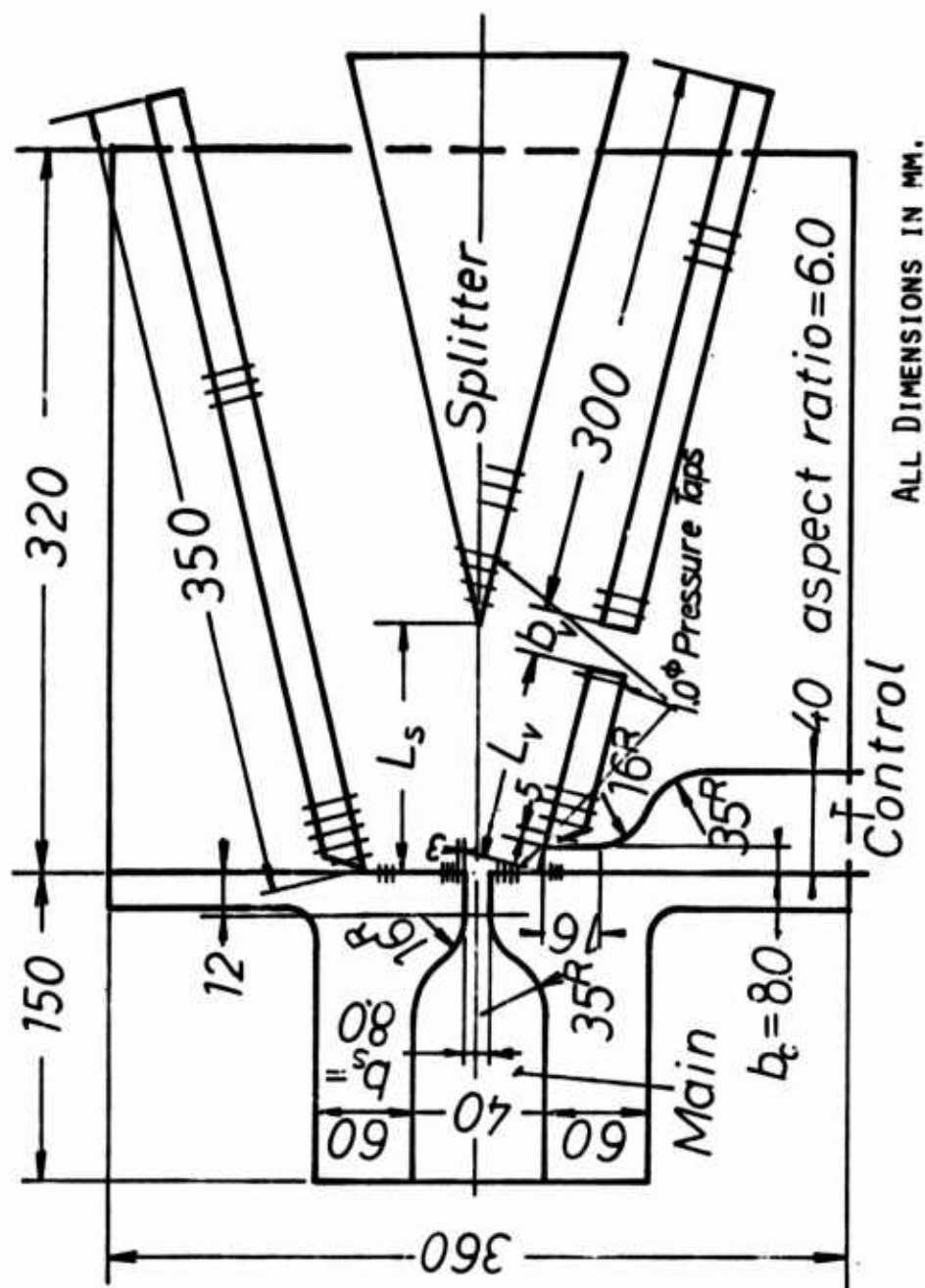


FIG.1 EXPERIMENTAL MODEL OF DEVICE

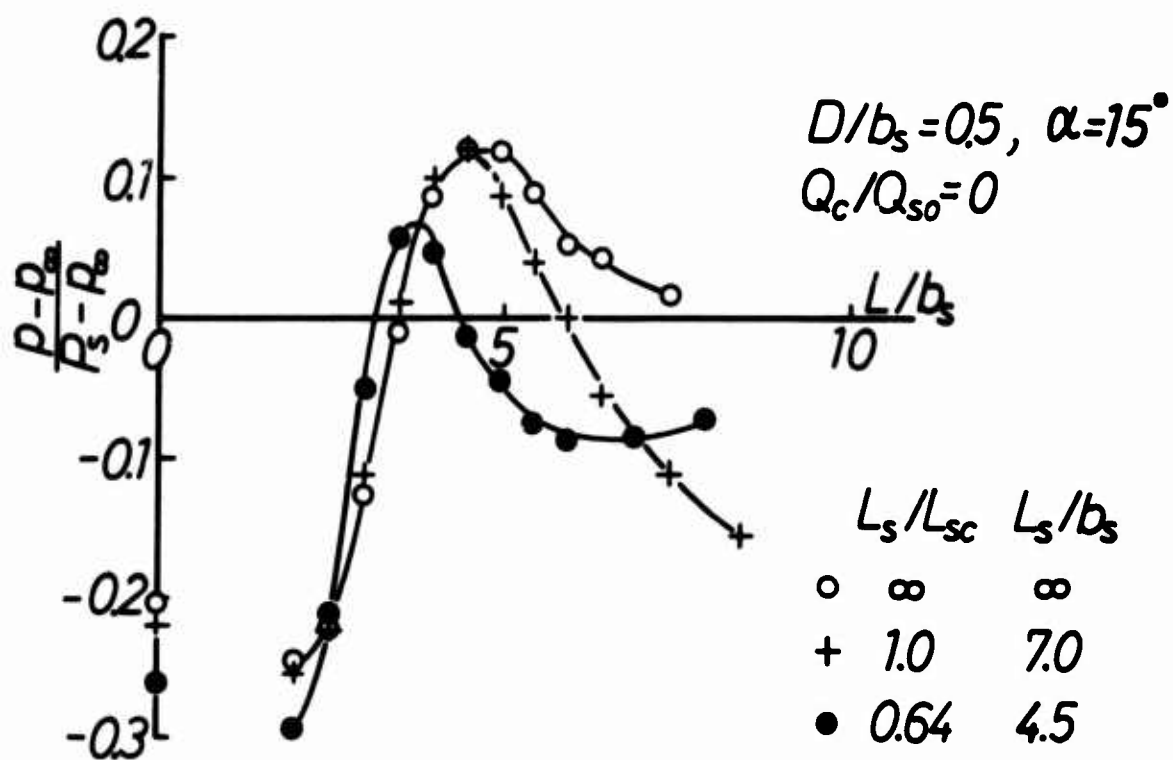
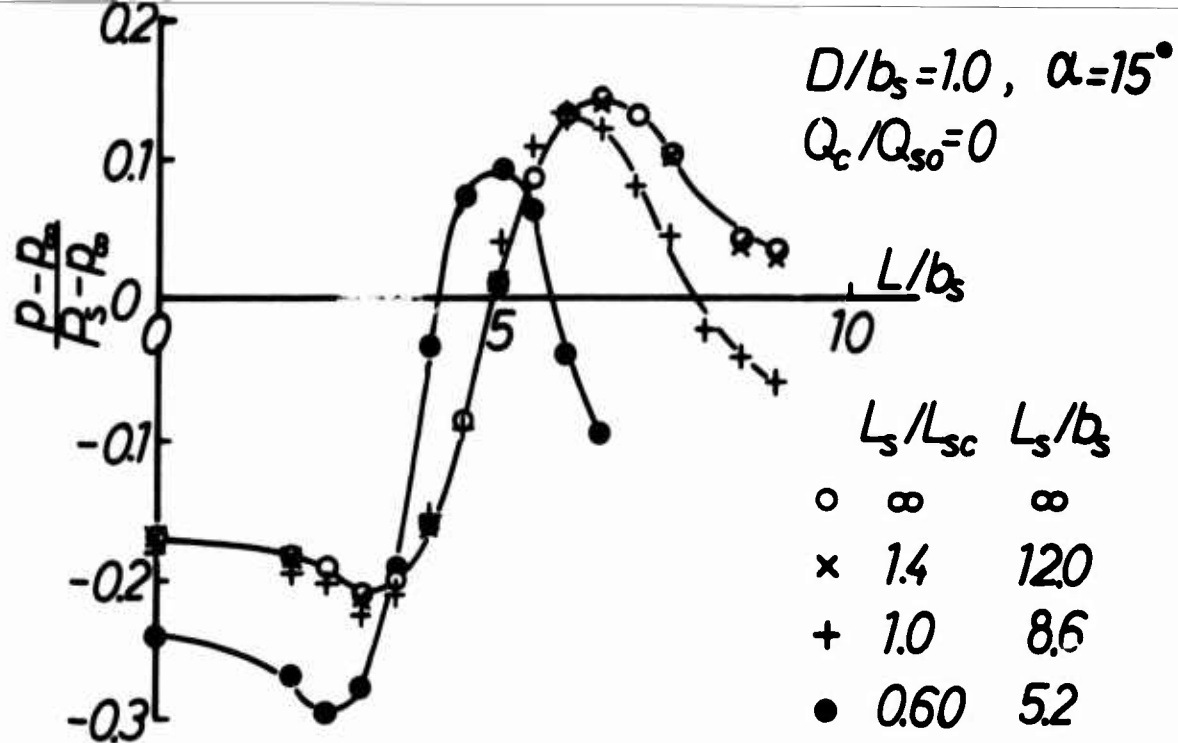


FIG.2 EFFECTS OF SPLITTER DISTANCE ON REATTACHMENT WALL PRESSURE DISTRIBUTIONS

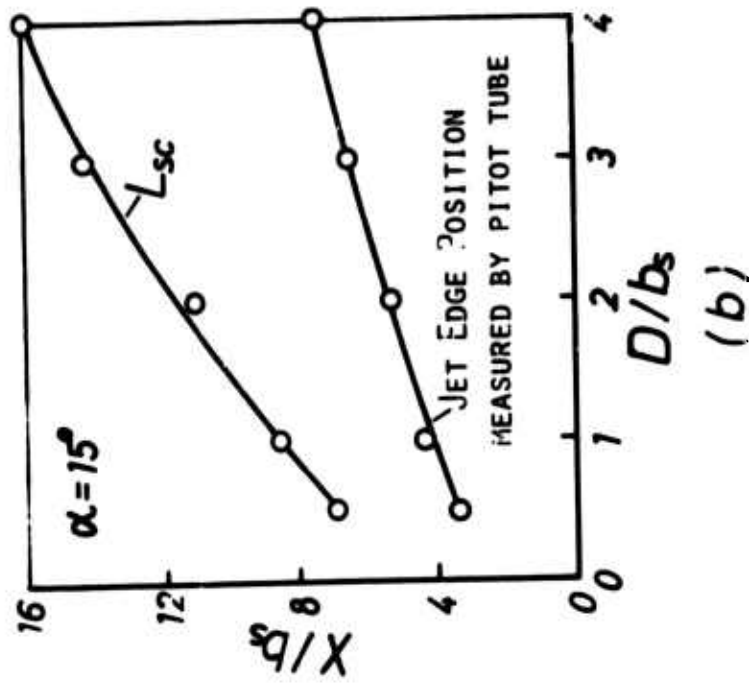
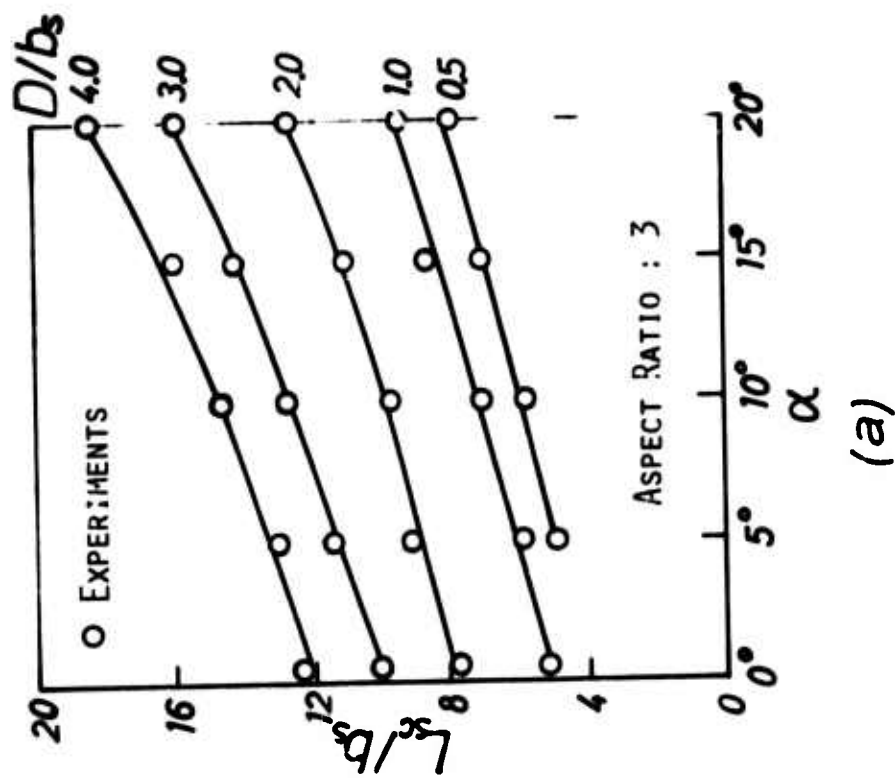


FIG.3 CRITICAL SPLITTER DISTANCE WITHOUT CONTROL FLOW

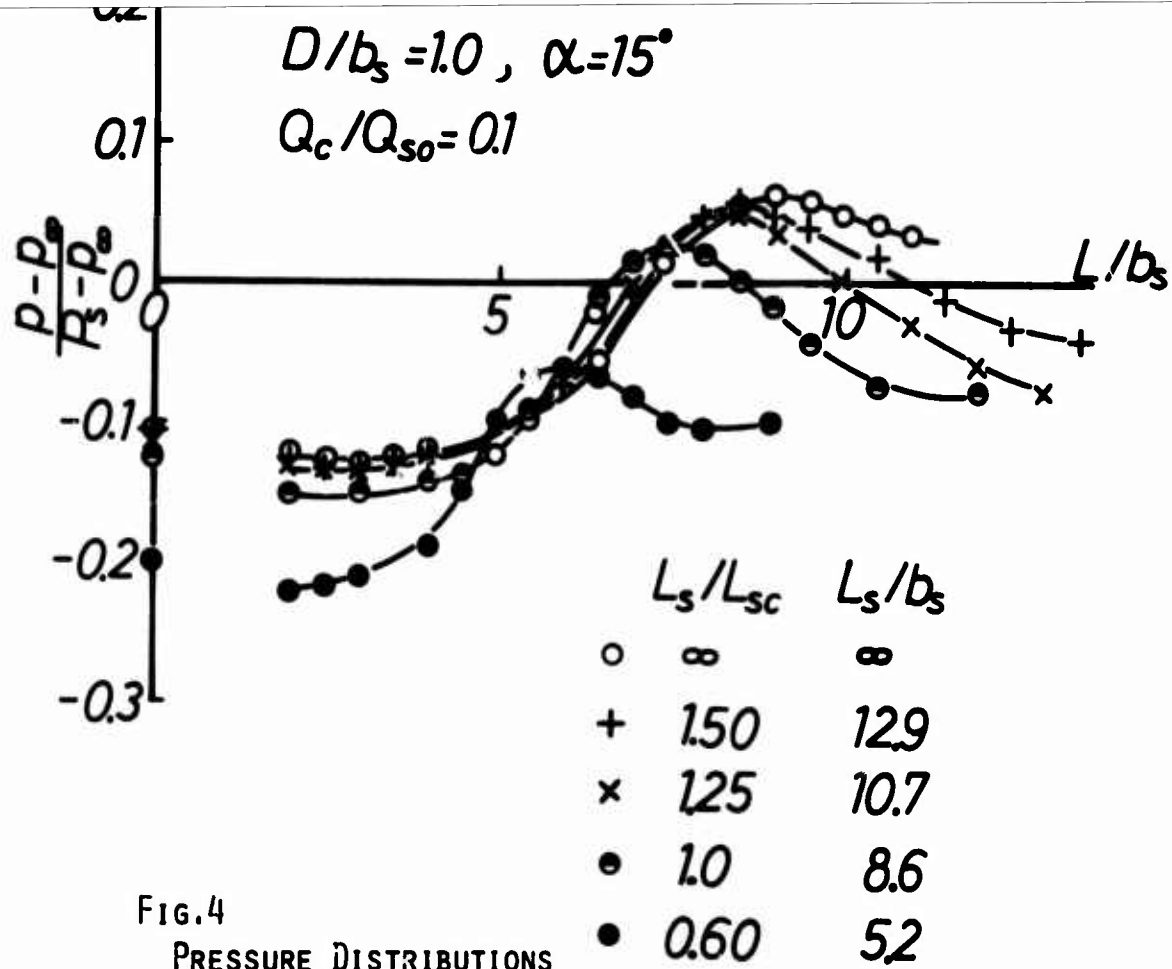


FIG.4  
PRESSURE DISTRIBUTIONS

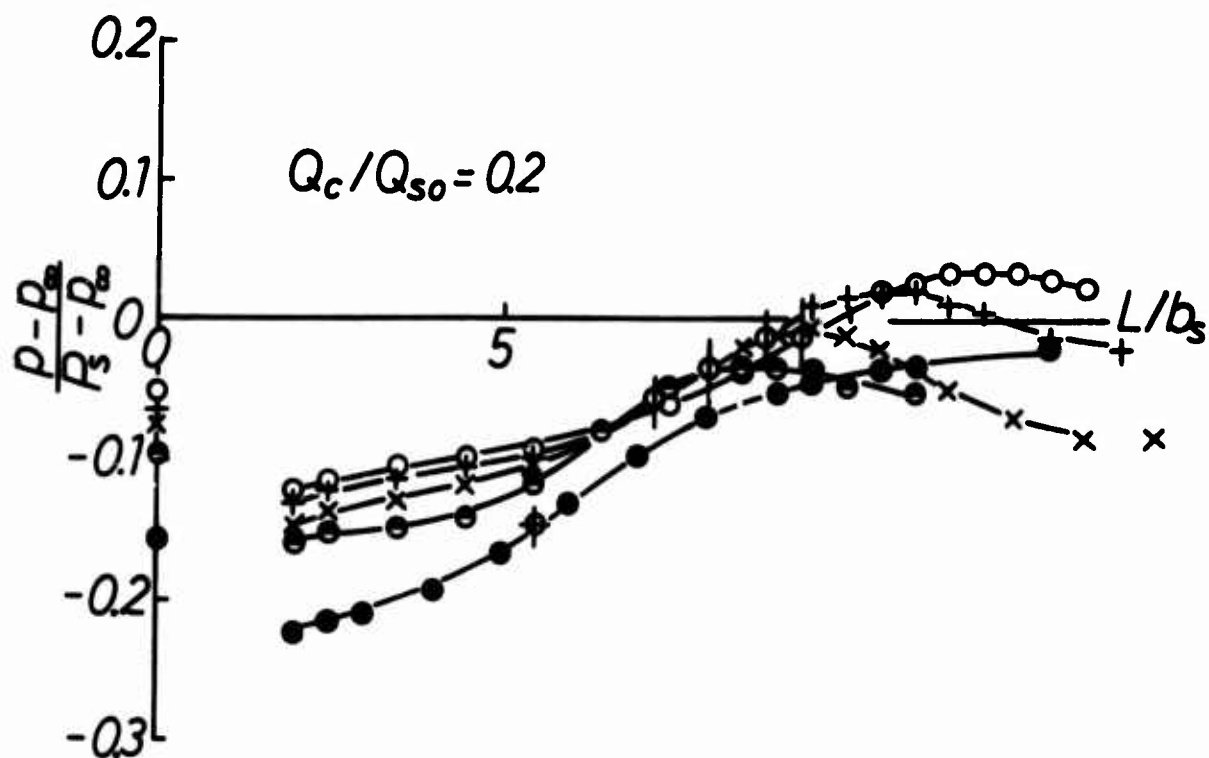


FIG.5 EFFECTS OF SPLITTER DISTANCE ON REATTACHMENT  
WALL PRESSURE DISTRIBUTIONS

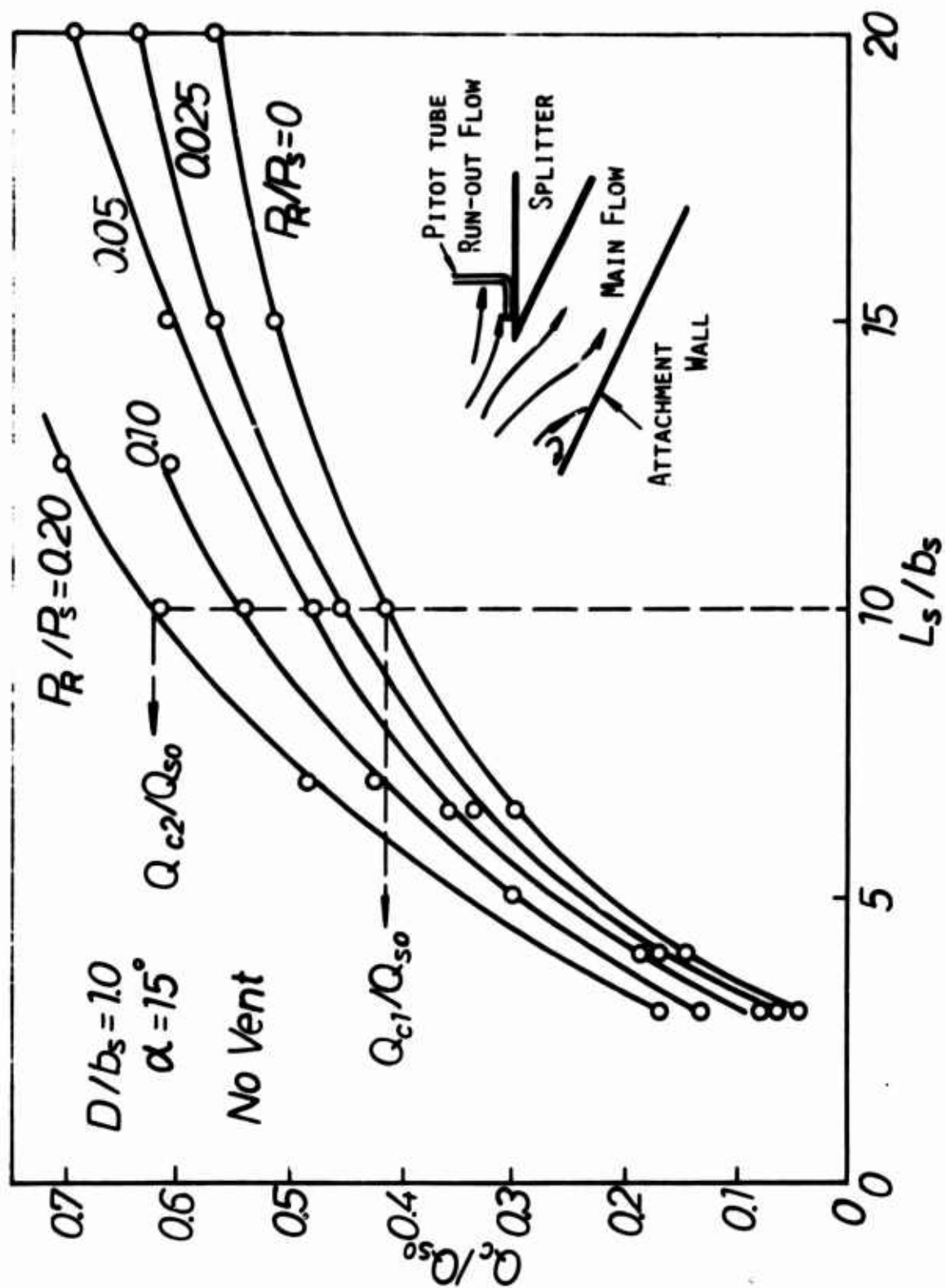


FIG. 6 RUN-OUT CHARACTERISTICS

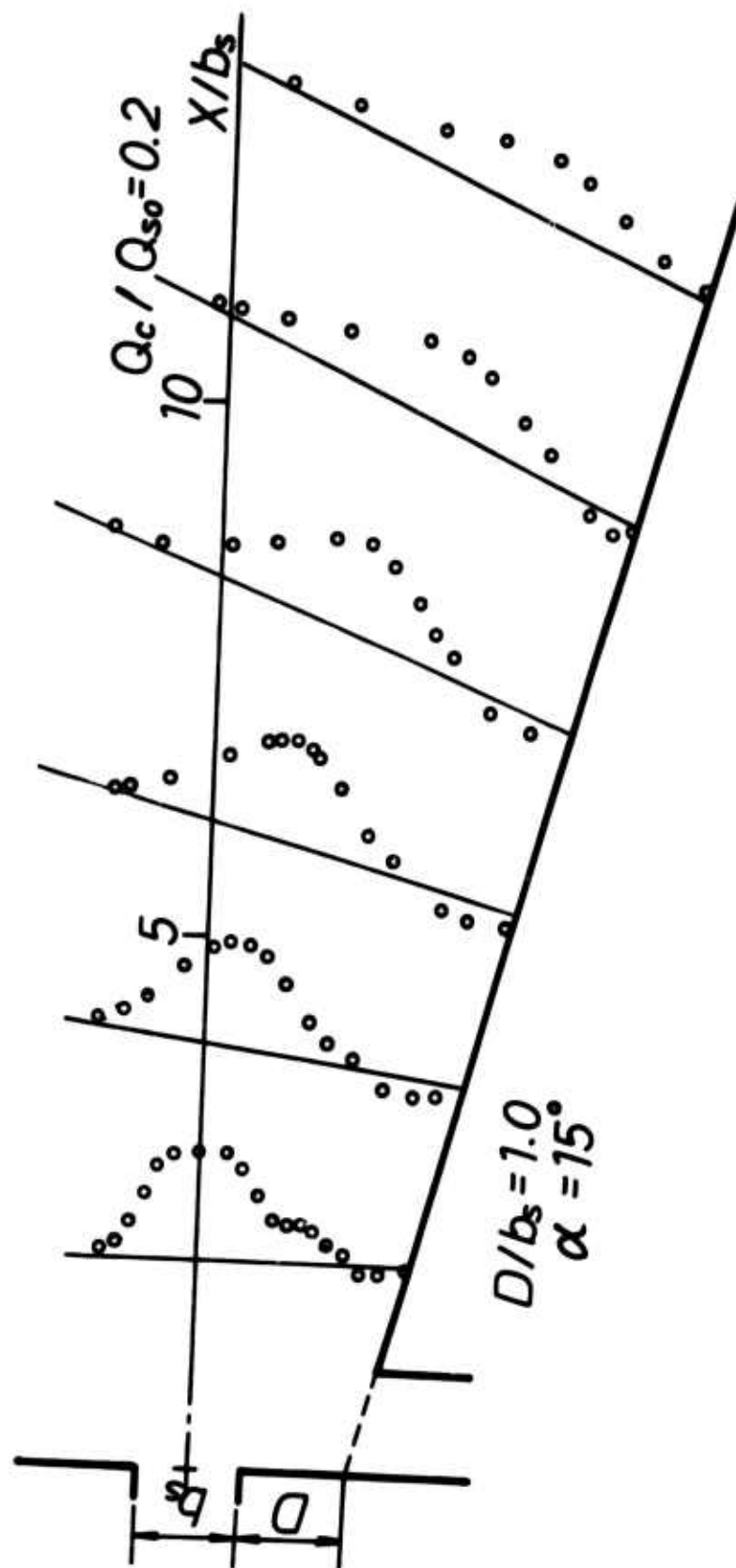


FIG.7 REATTACHED JET VELOCITY PROFILE

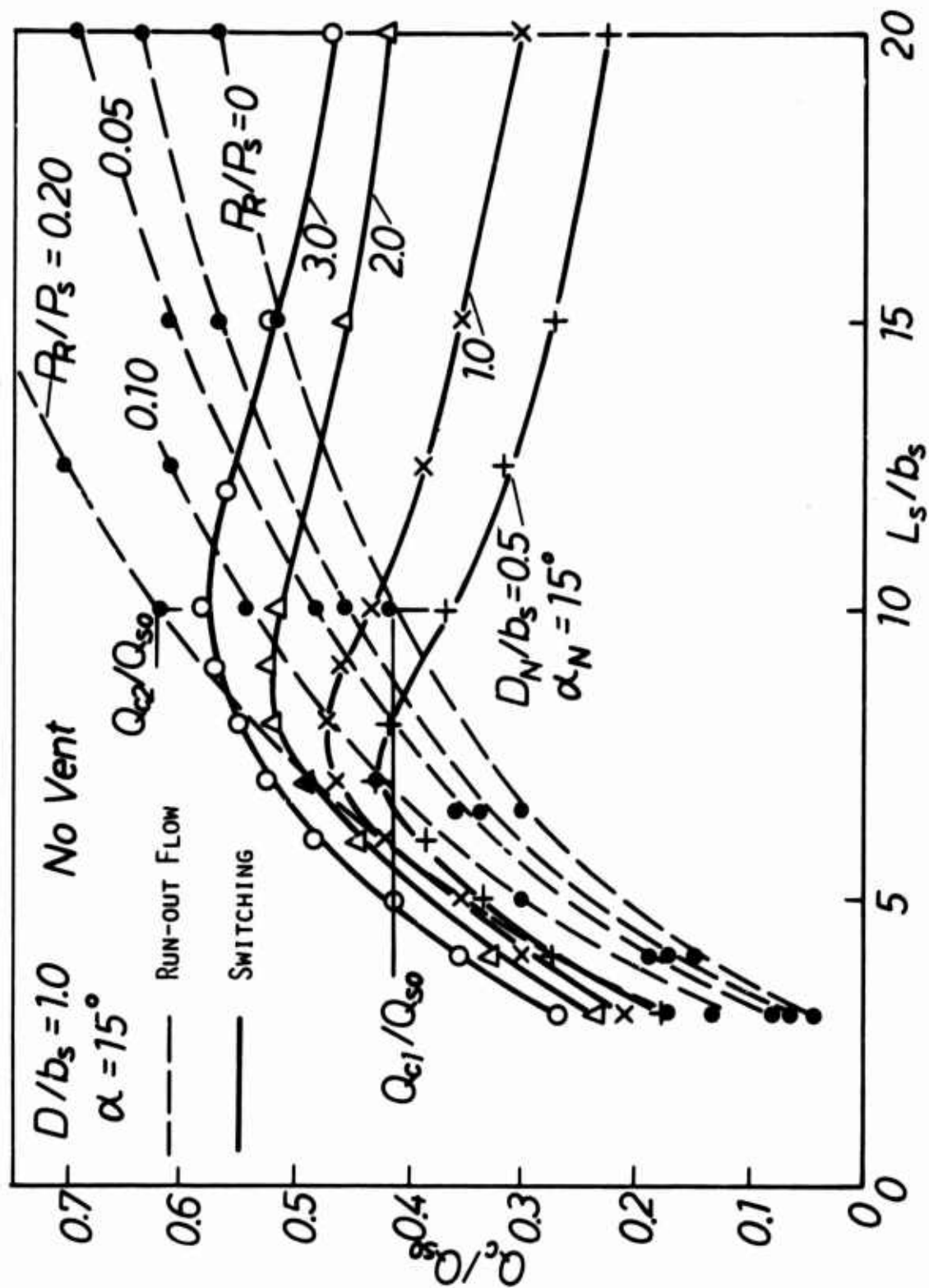


FIG.8 RUN-OUT AND SWITCHING CHARACTERISTICS FOR DEVICE WITH SPLITTER ONLY

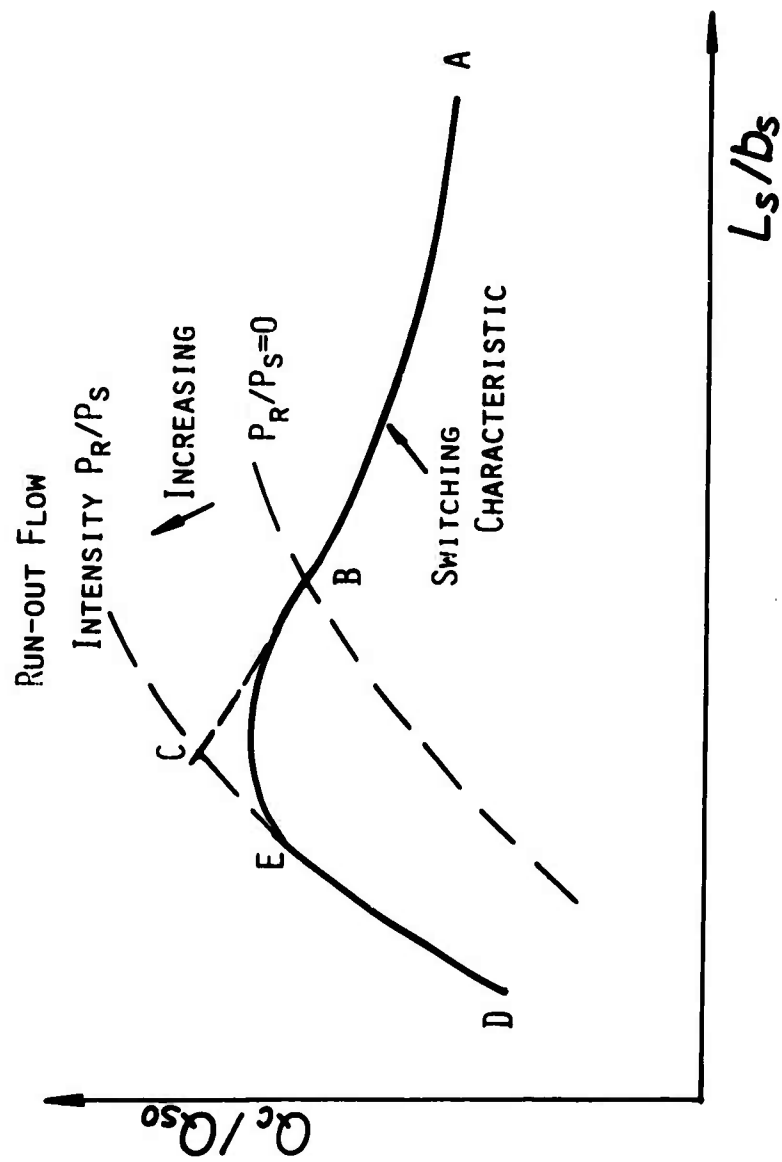


FIG.9 TYPICAL SWITCHING CHARACTERISTICS, RELATED TO RUN-OUT FLOW INTENSITY



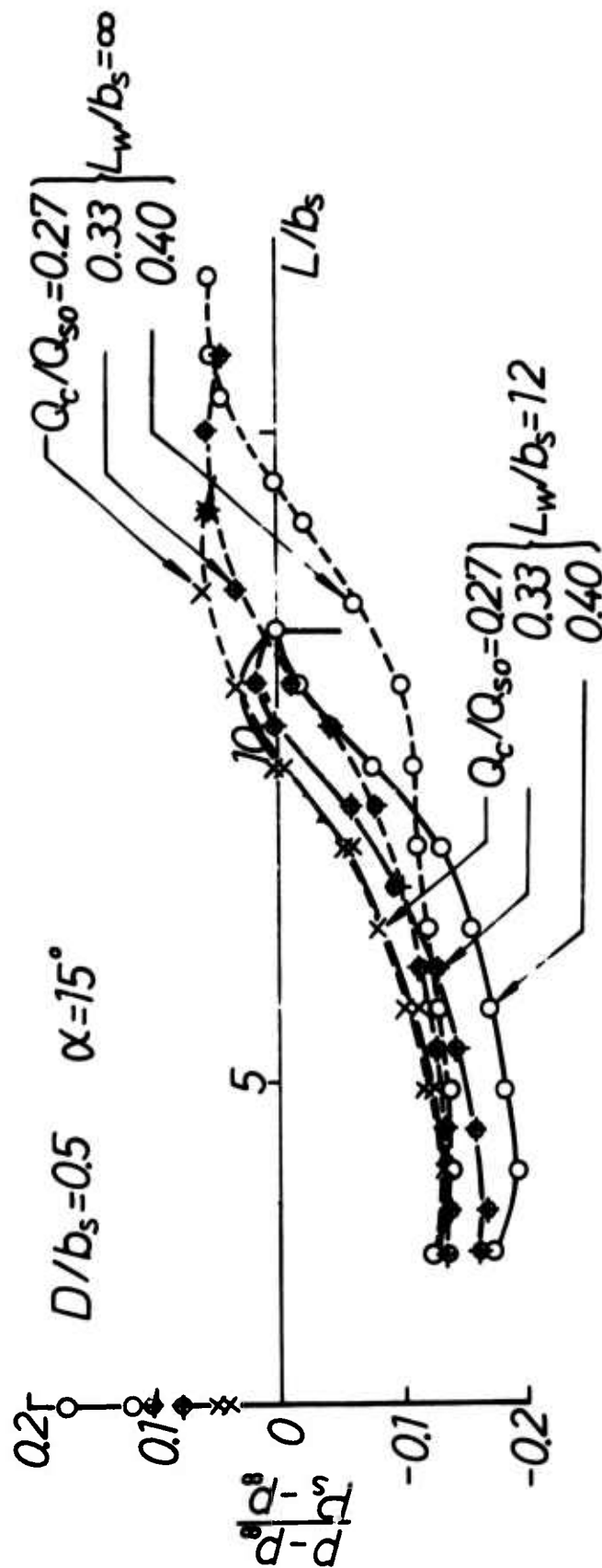


FIG.10 PRESSURE DISTRIBUTIONS FOR FINITE WALL LENGTH, COMPARED WITH THAT FOR INFINITE WALL LENGTH

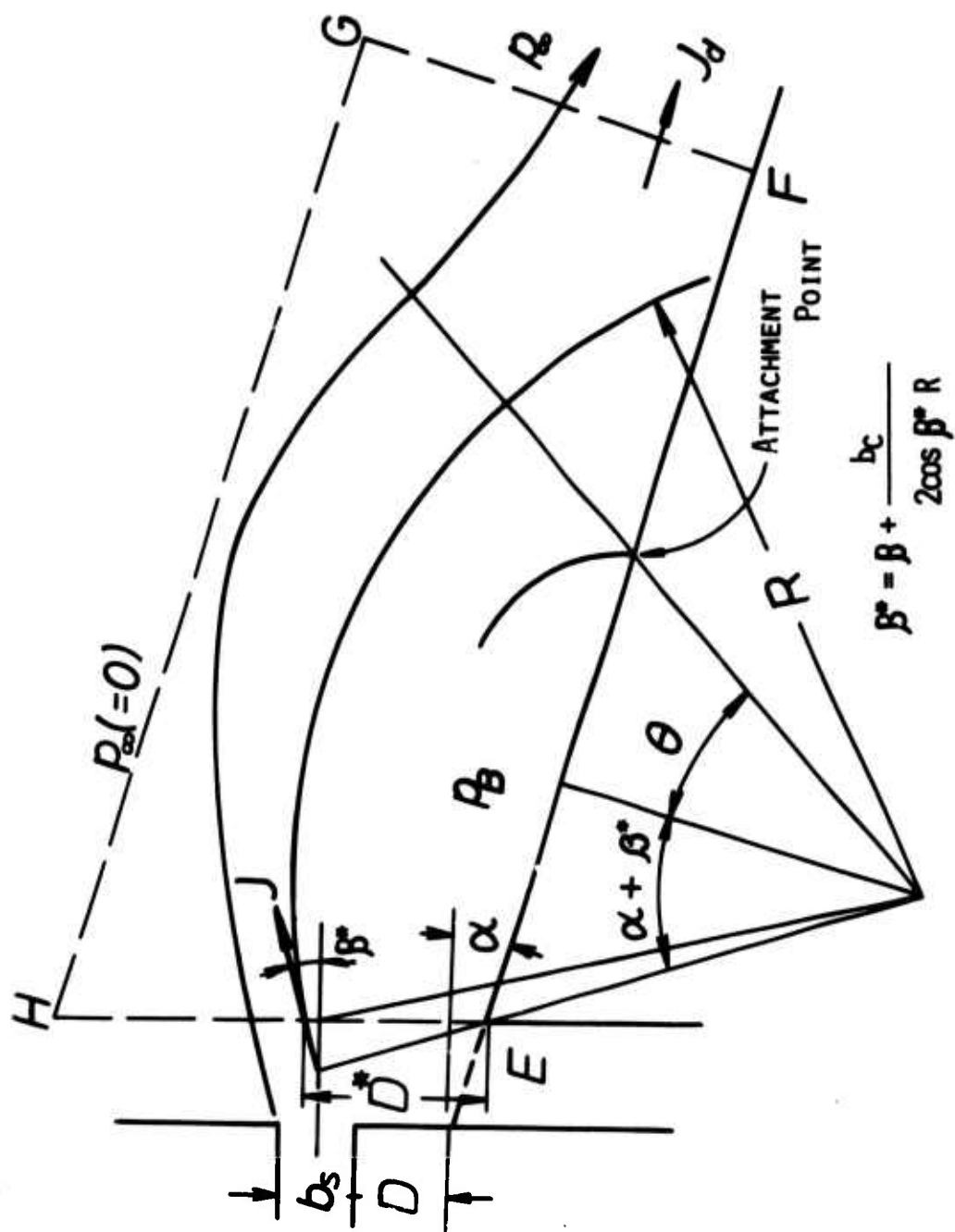


FIG.11(a) MODEL FOR NO SPLITTER AND NO VENT CONFIGURATION

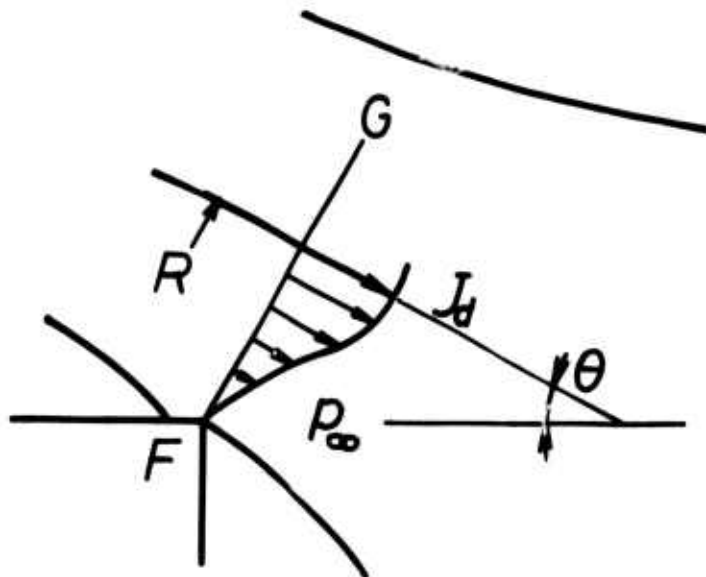


FIG.11(b) MODEL FOR END WALL CONFIGURATION

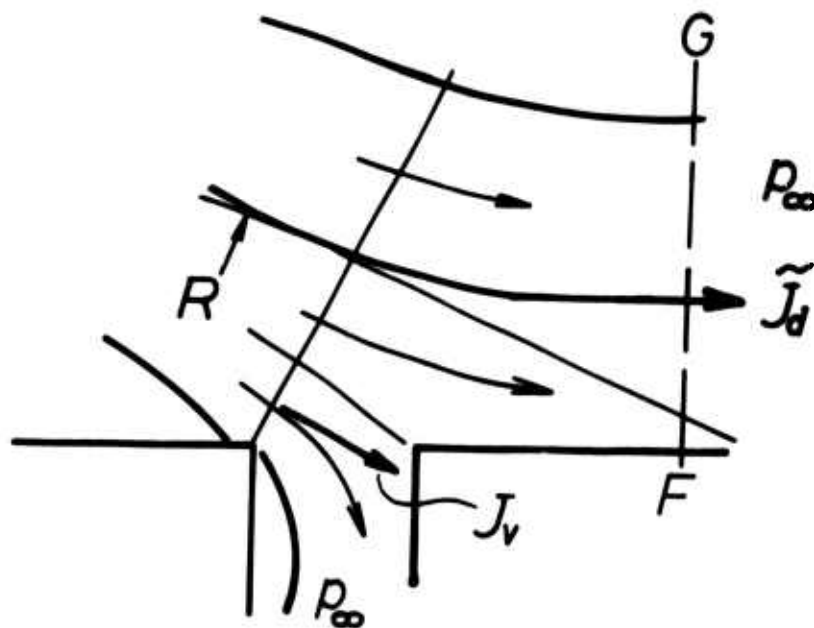


FIG.11(c) MODEL FOR VENT CONFIGURATION



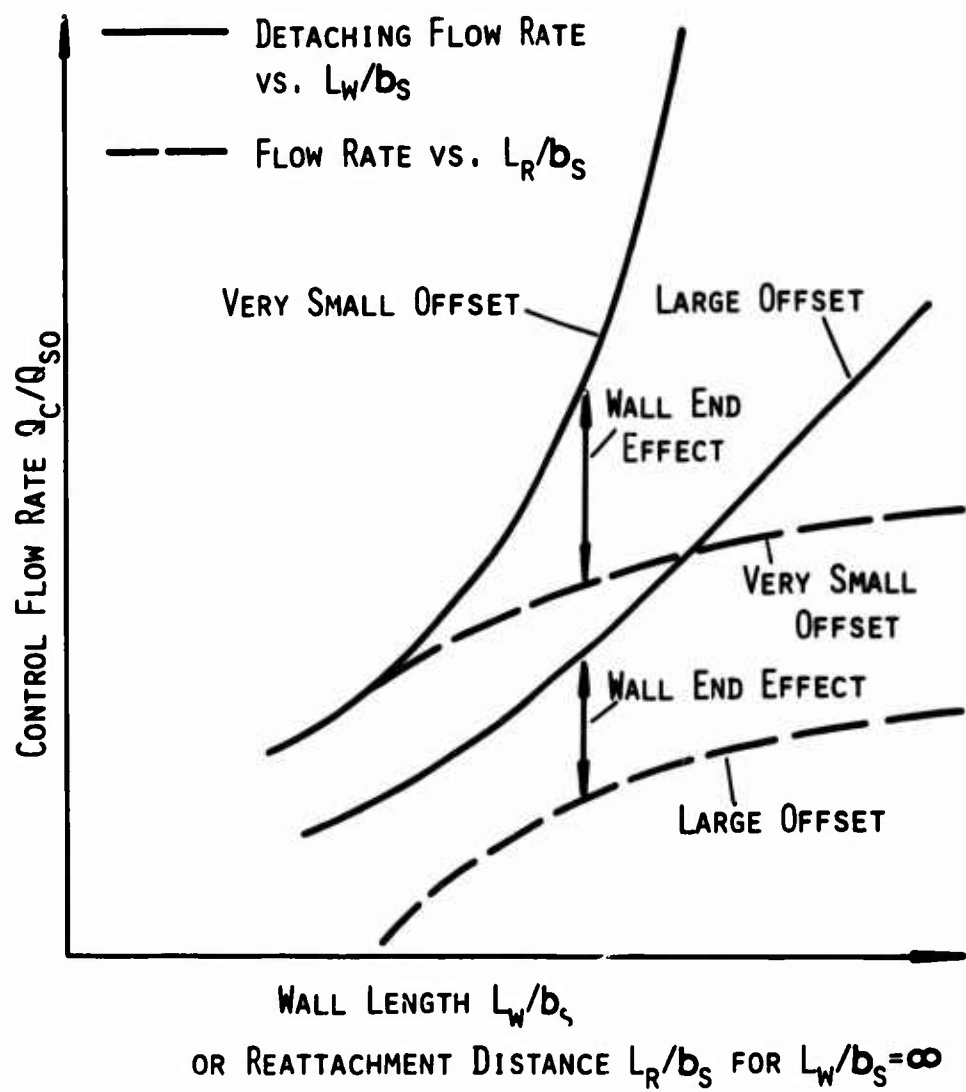


FIG.13 SCHEMATIC REPRESENTATION OF CHARACTERISTICS

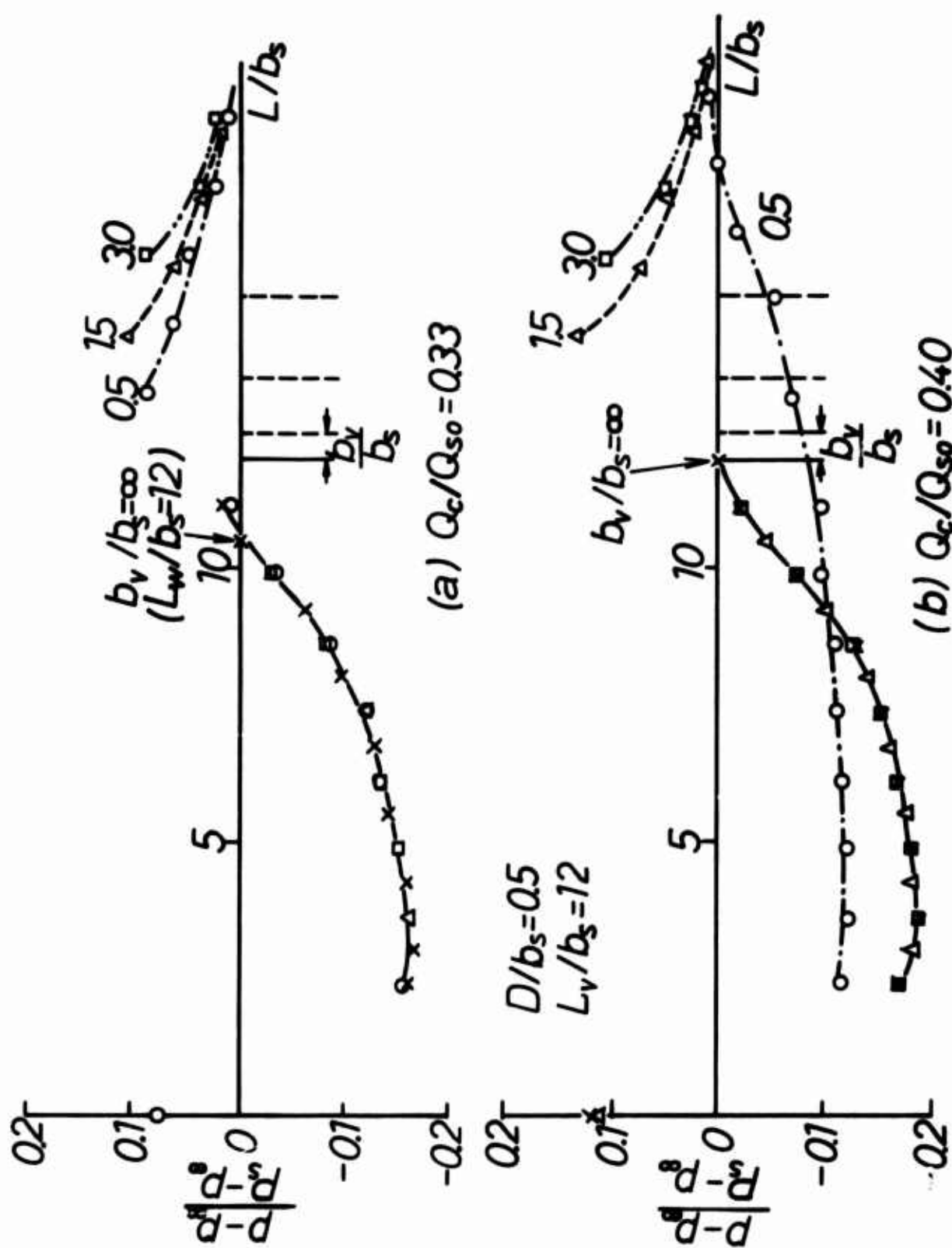


FIG.14 PRESSURE DISTRIBUTIONS FOR VARIOUS VENT CONDITIONS

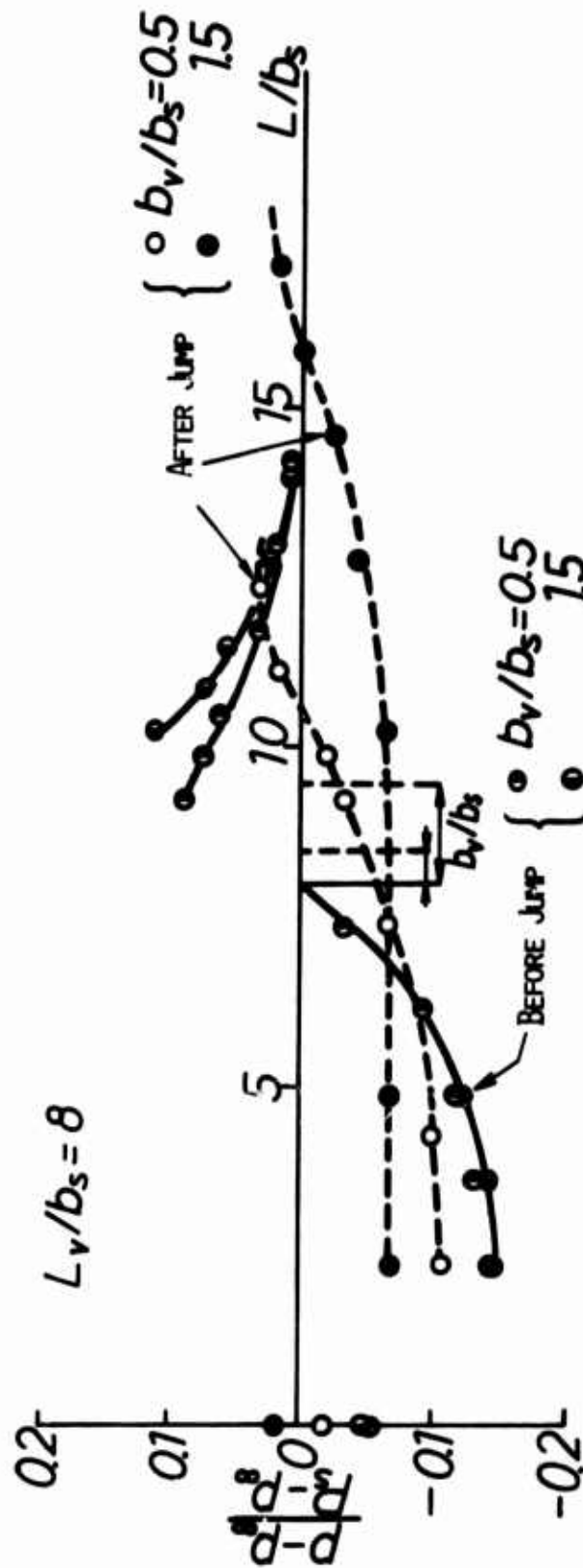


FIG.15 PRESSURE DISTRIBUTIONS FOR SOME VENT CONDITIONS,  
JUST BEFORE JUMP OF ATTACHMENT POINT AND AFTER THE JUMP

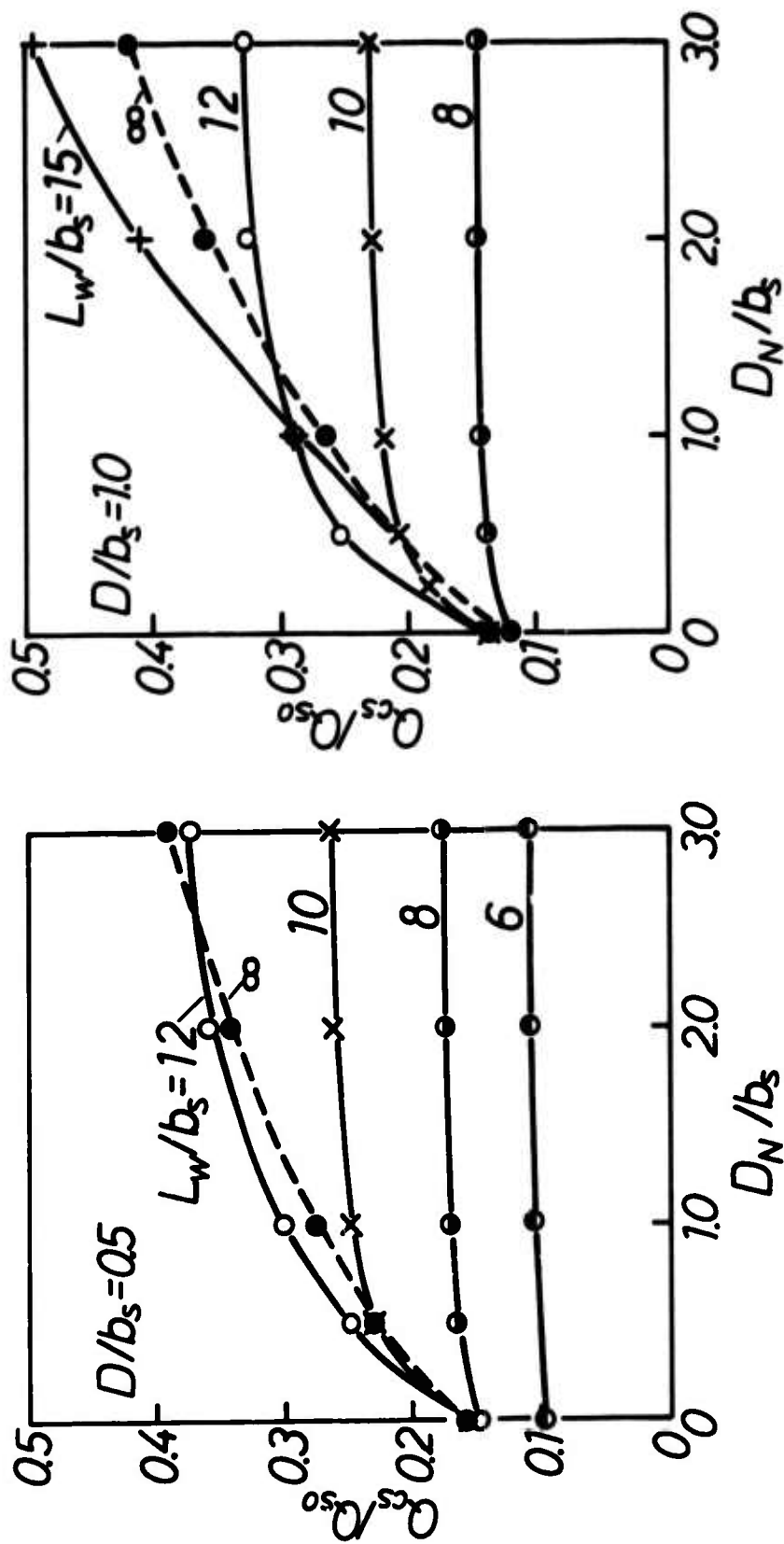


FIG.16 SWITCHING FLOW RATE VS. OPPOSITE SIDE WALL OFFSET  
FOR END WALL TYPE DEVICES ( $\alpha = \alpha_N = 15^\circ$ )



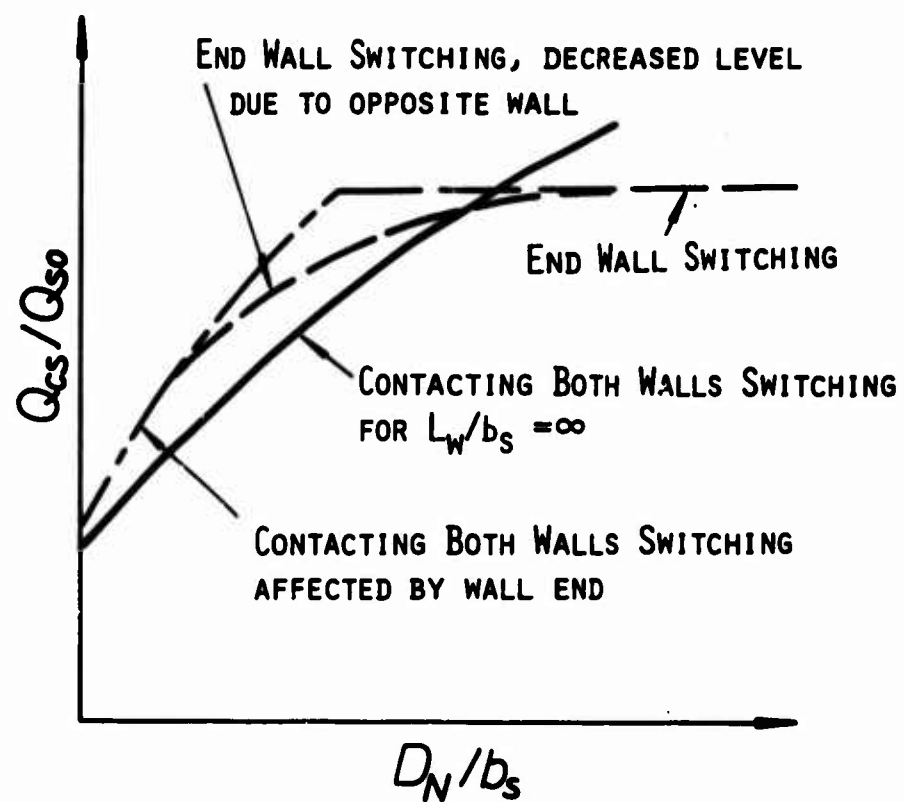


FIG.17 SCHEMATIC REPRESENTATION OF CHARACTERISTICS

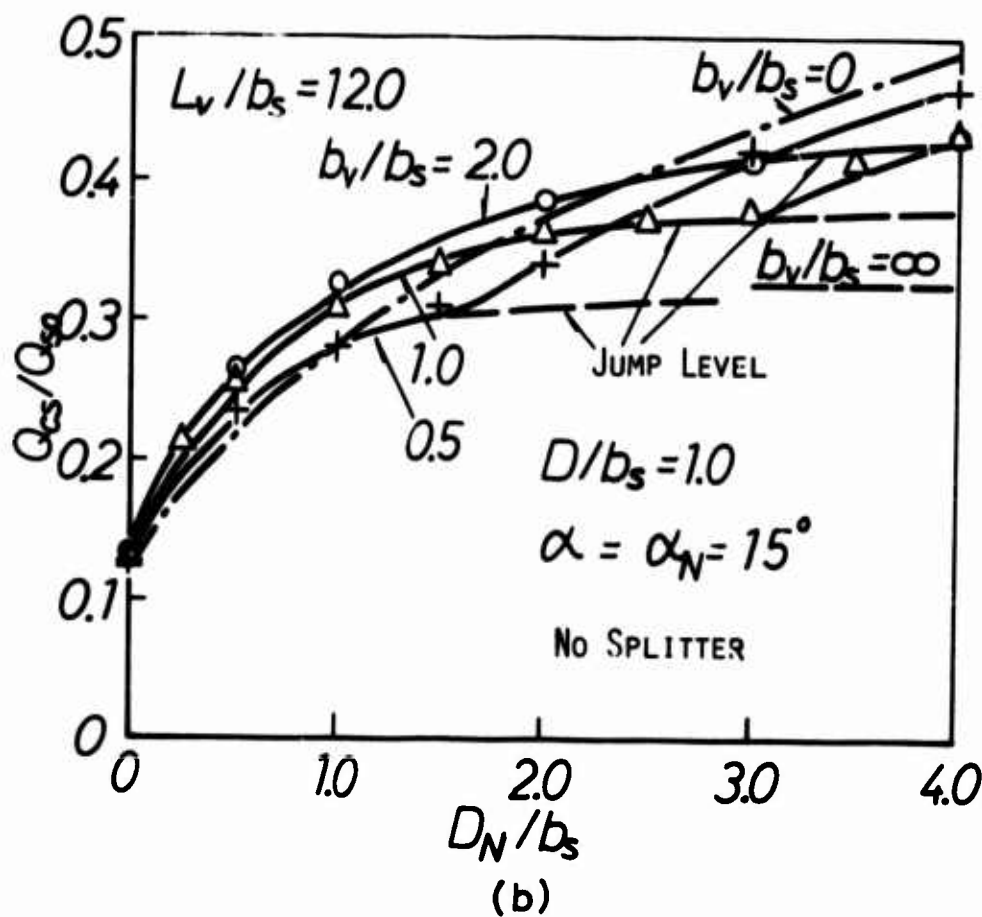
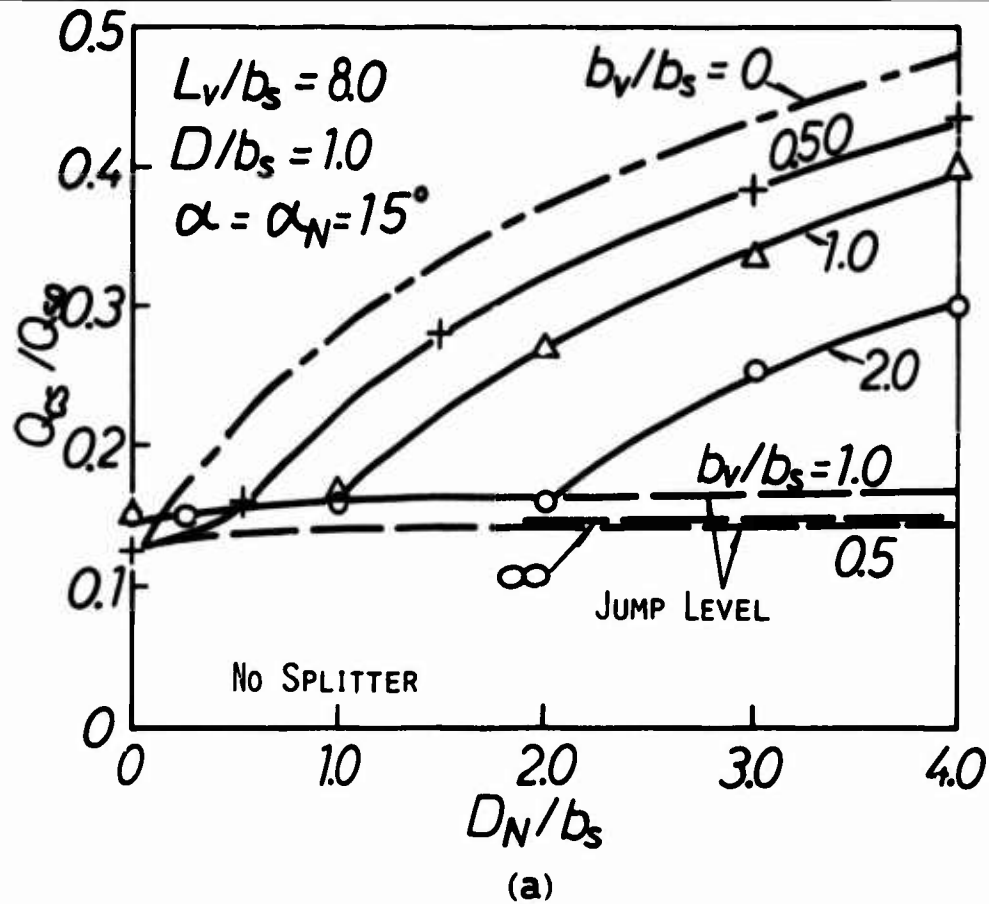


FIG.18 EFFECTS OF VENT ON SWITCHING

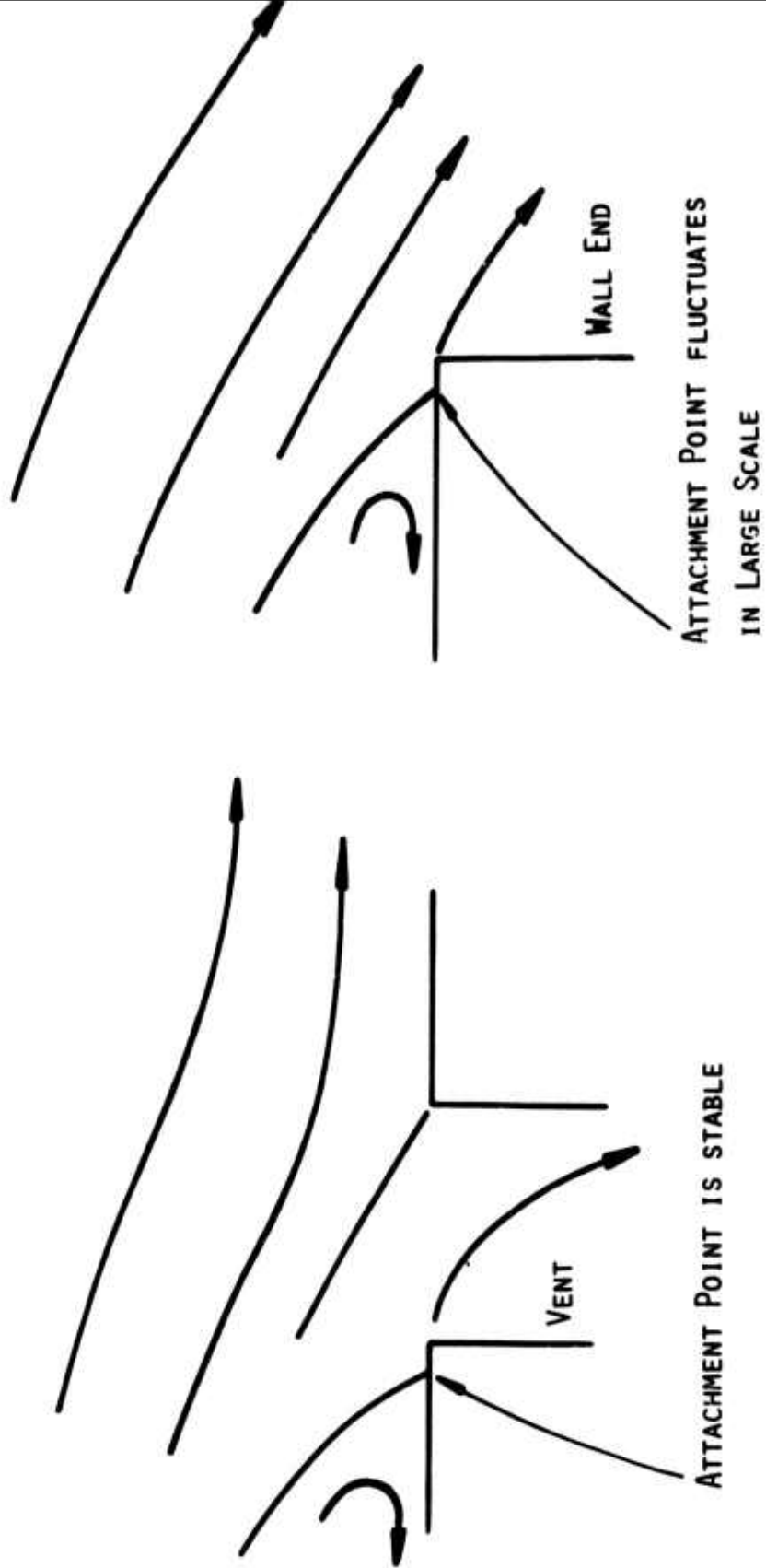


FIG.19 EFFECTS OF WALL CONDITIONS ON JET STABILITY

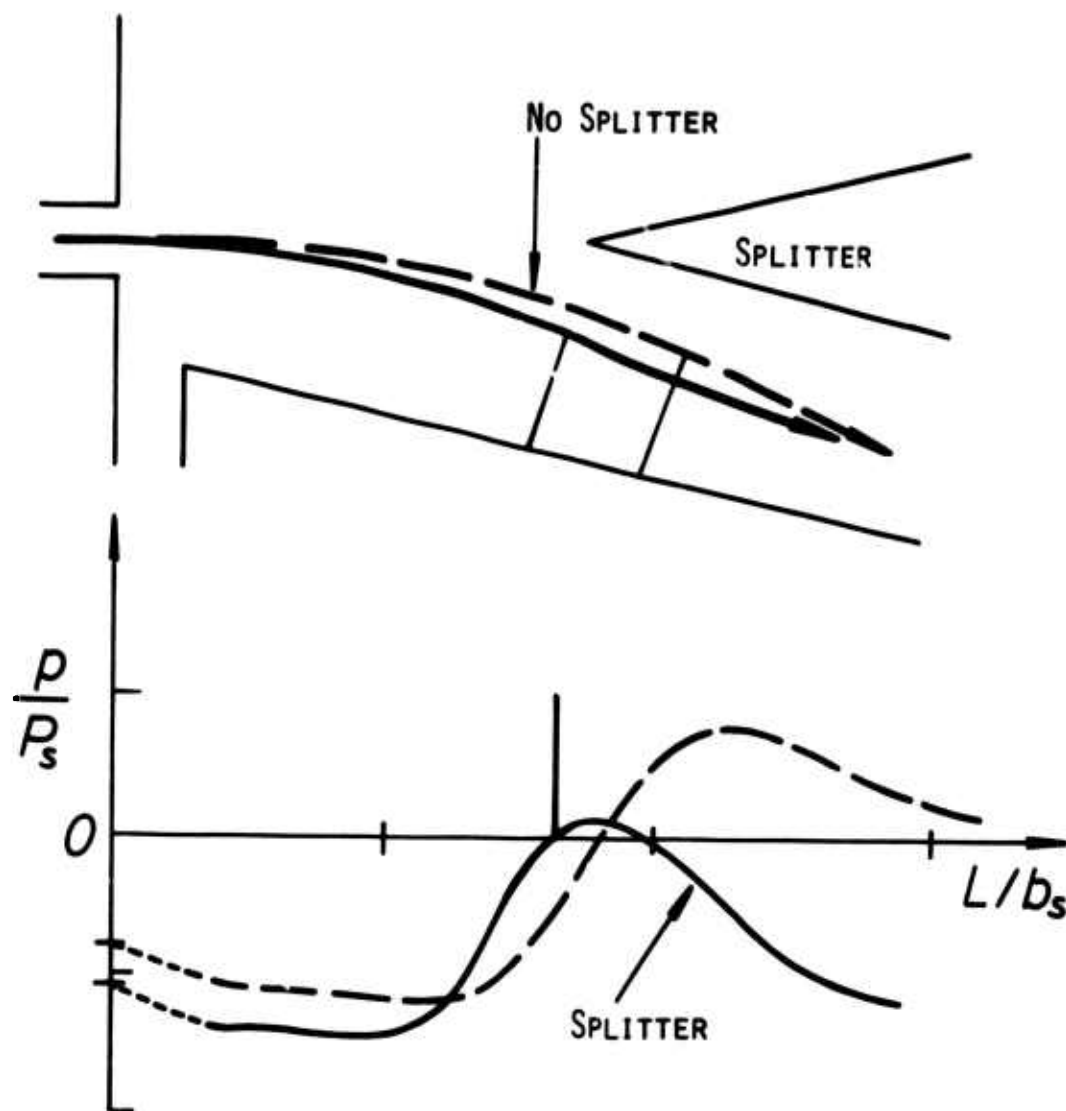


FIG.20 SPLITTER EFFECT

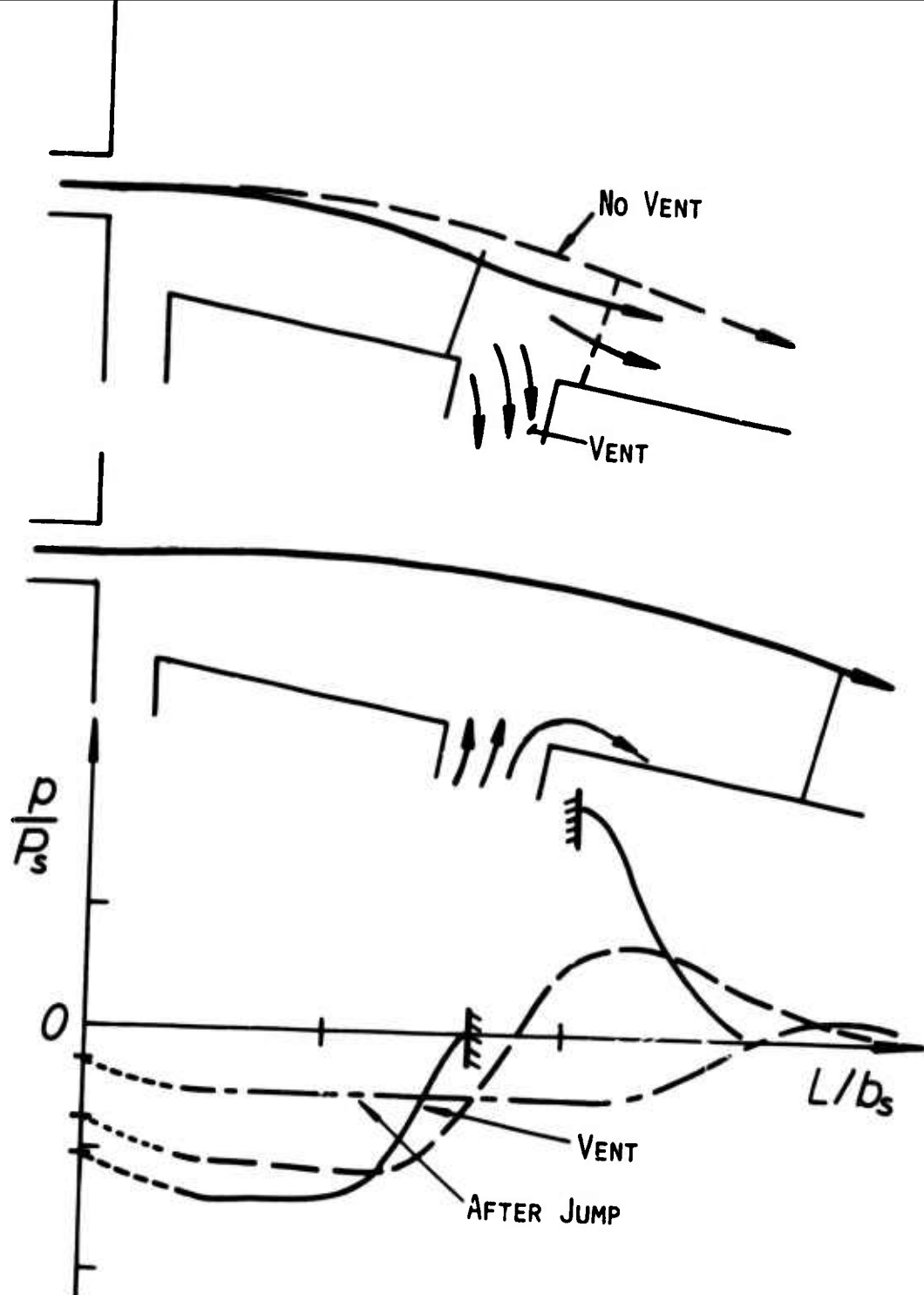


FIG.21 VENT EFFECT

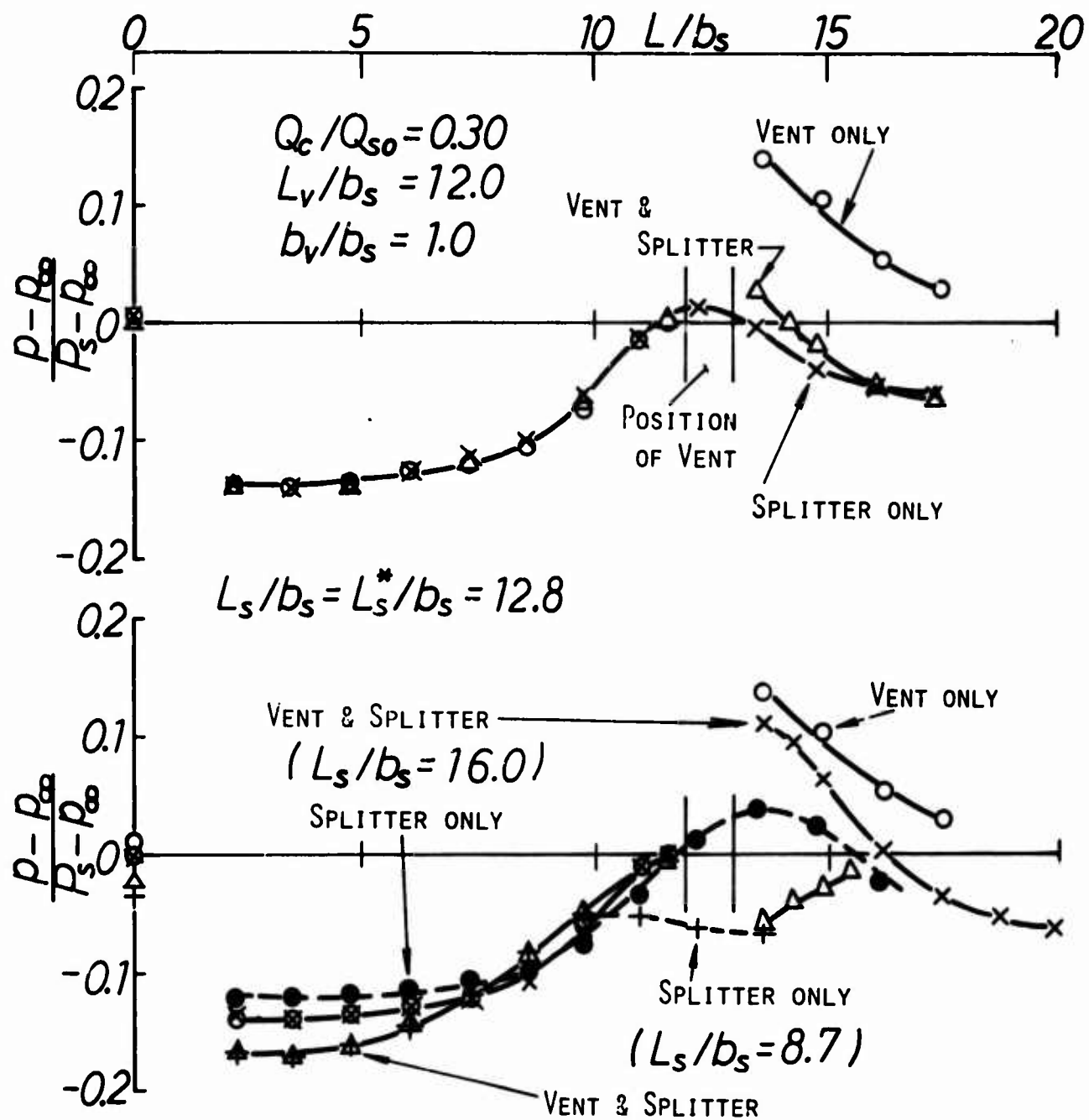


FIG.22 PRESSURE DISTRIBUTIONS ON ATTACHED WALL,  
RELATED TO VENT AND SPLITTER POSITION

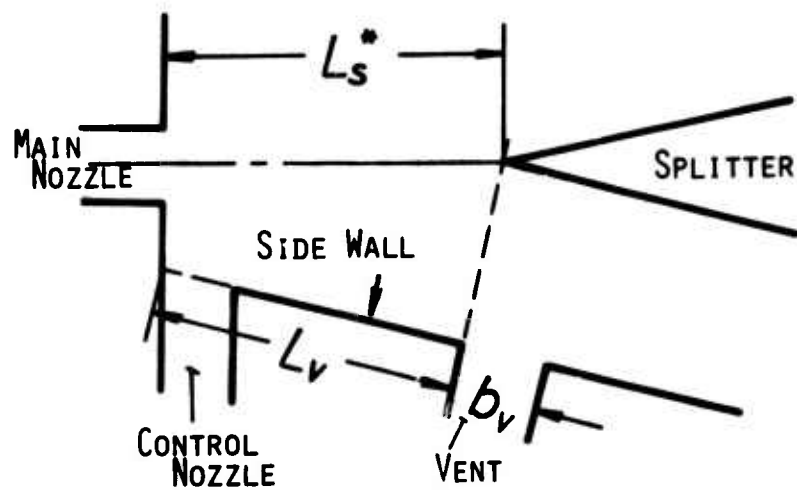


FIG.23 SPLITTER DISTANCE  $L_s^*$  , RELATED TO  $L_v$  AND  $b_v$

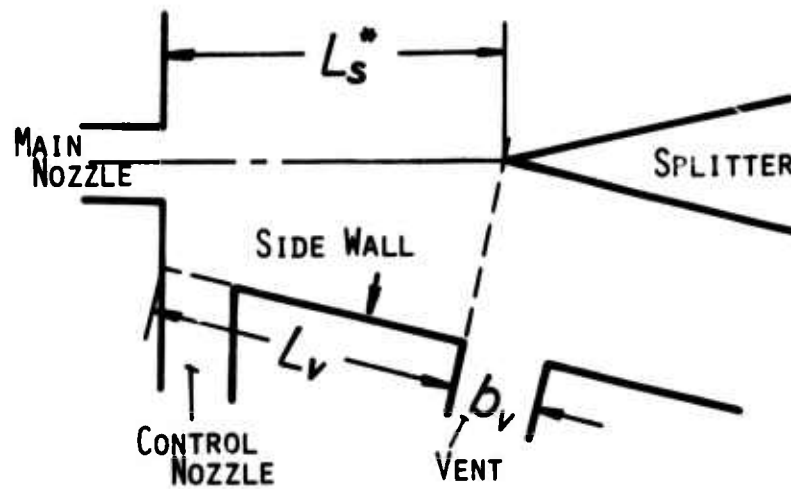


FIG.23 SPLITTER DISTANCE  $L_s^*$  , RELATED TO  $L_v$  AND  $b_v$



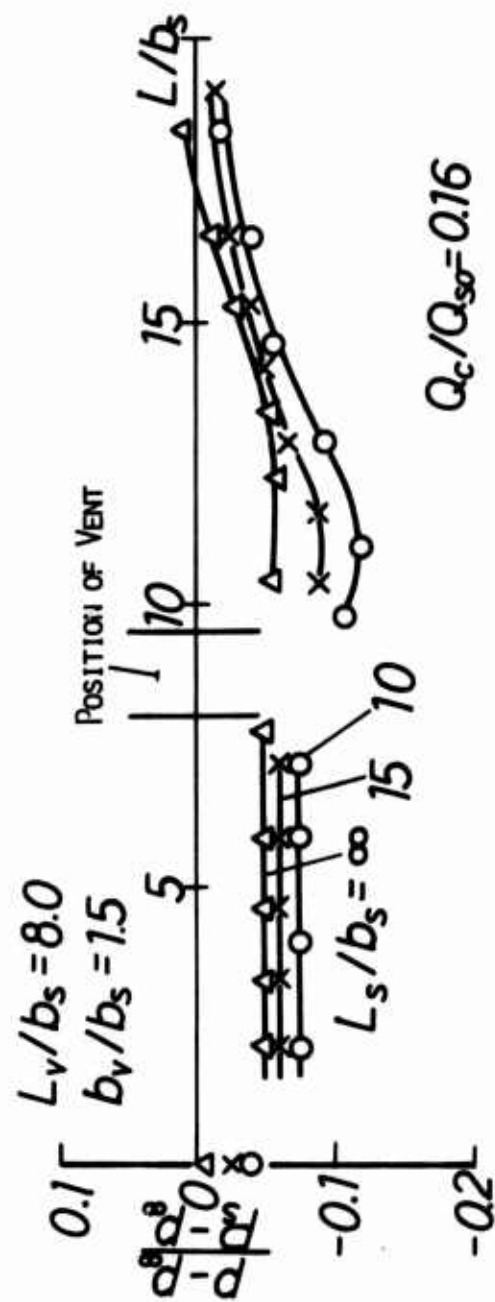


FIG.24 PRESSURE DISTRIBUTIONS ON ATTACHED WALL FOR JUMPED JET, RELATED TO SPLITTER POSITION

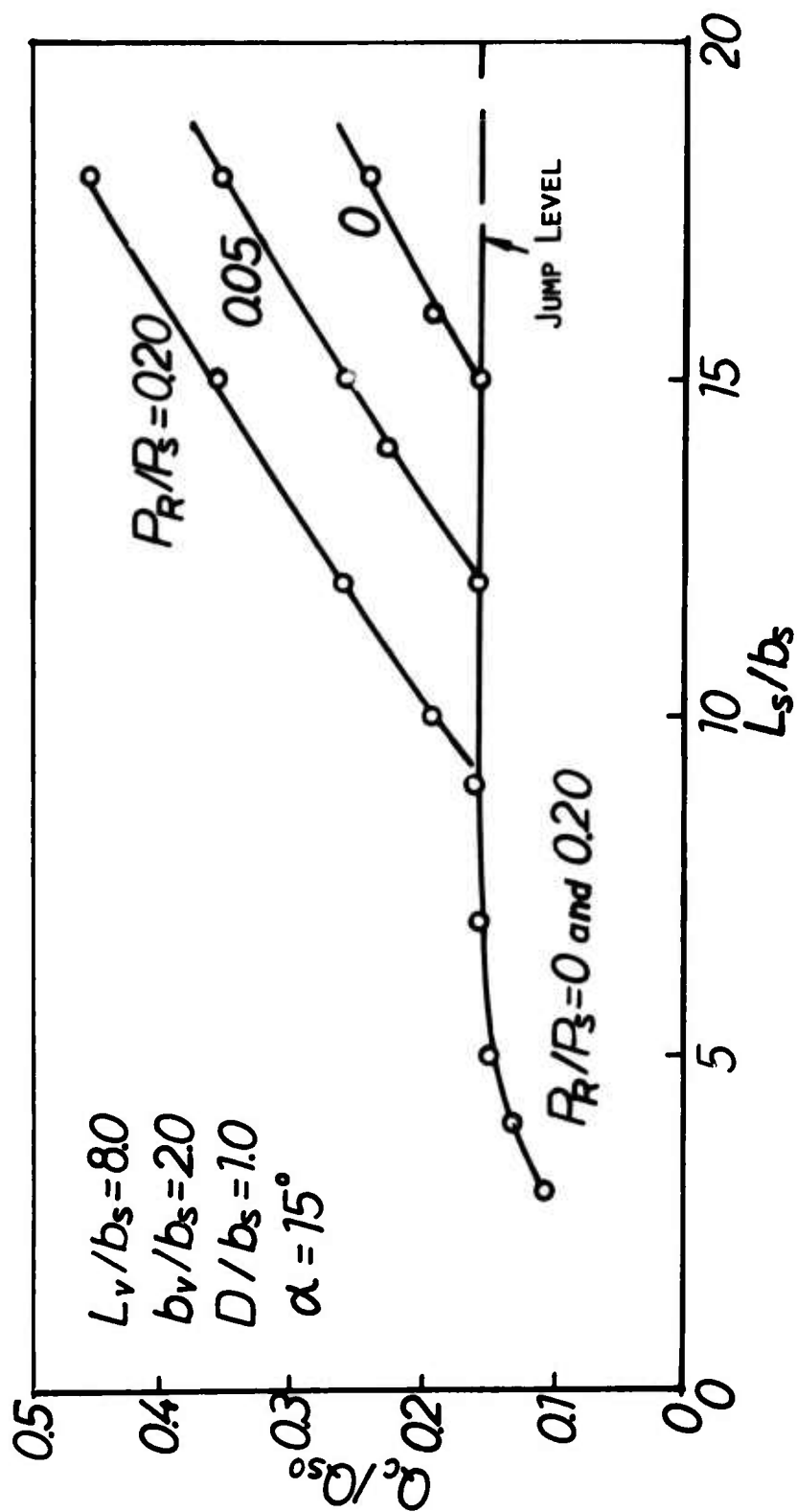


FIG.25 RUN-OUT CHARACTERISTICS

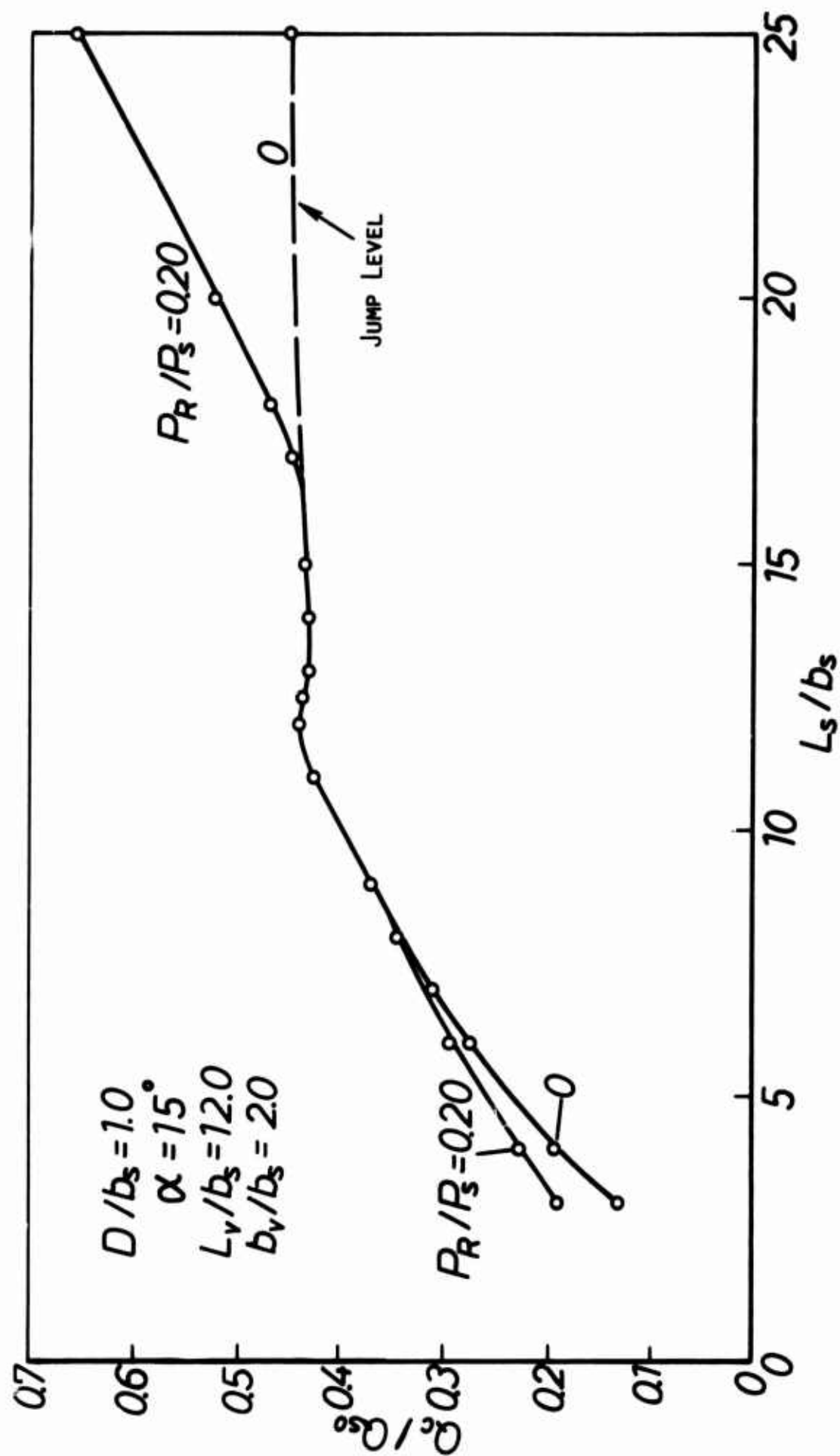


FIG.26 RUN-OUT CHARACTERISTICS



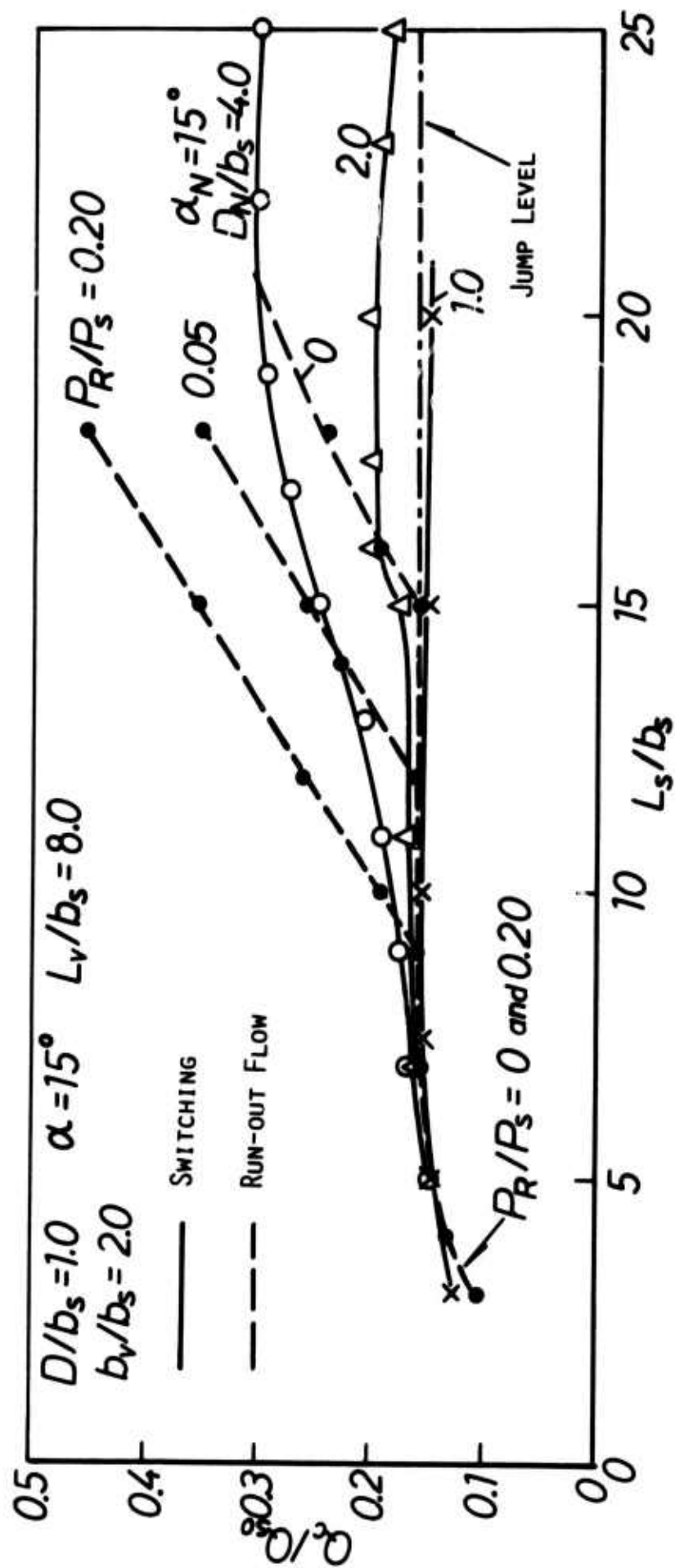


FIG.28 RUN-OUT AND SWITCHING CHARACTERISTICS FOR DEVICE WITH VENT AND SPLITTER

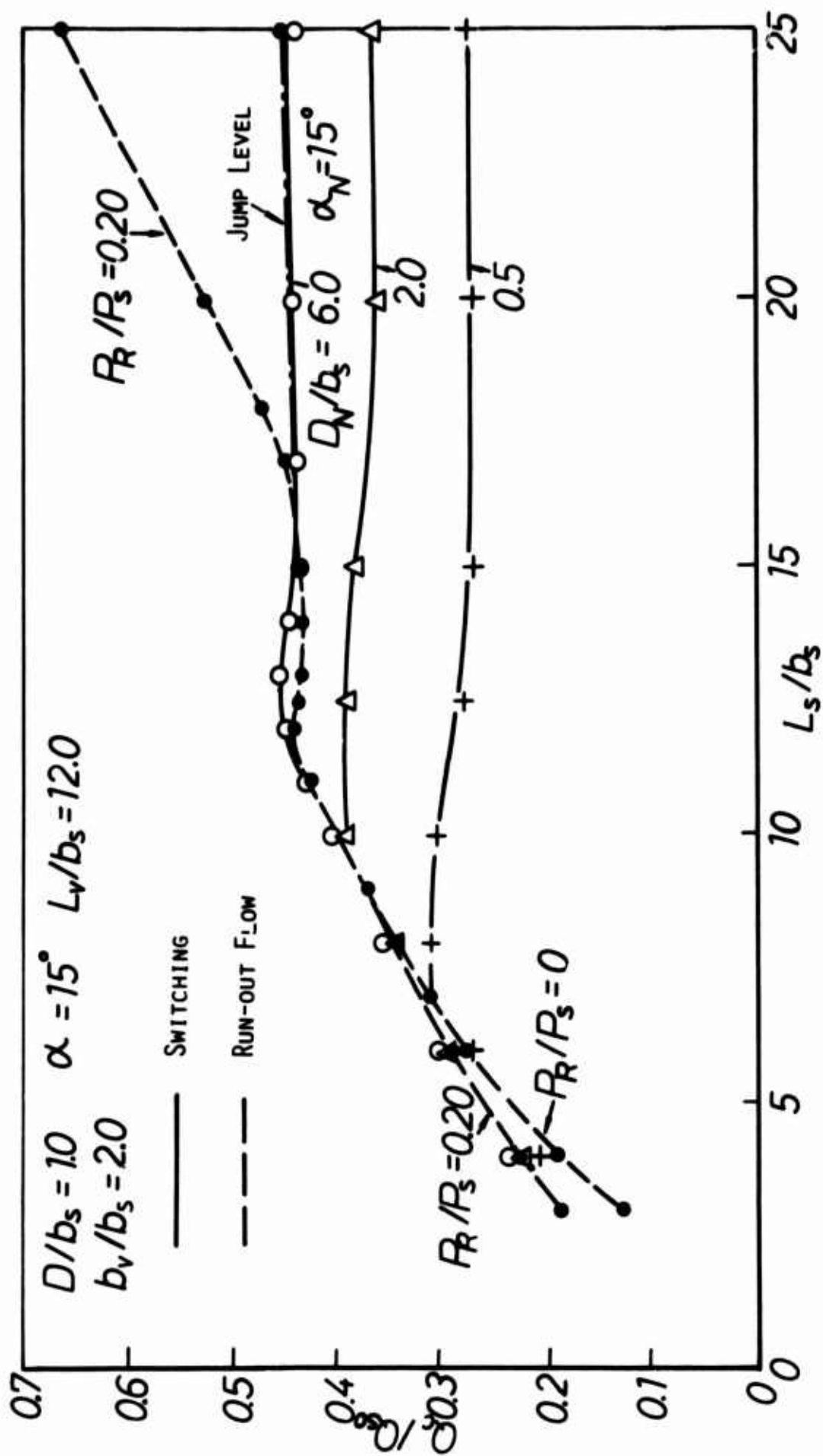


FIG.29 RUN-OUT AND SWITCHING CHARACTERISTICS FOR DEVICE WITH VENT AND SPLITTER

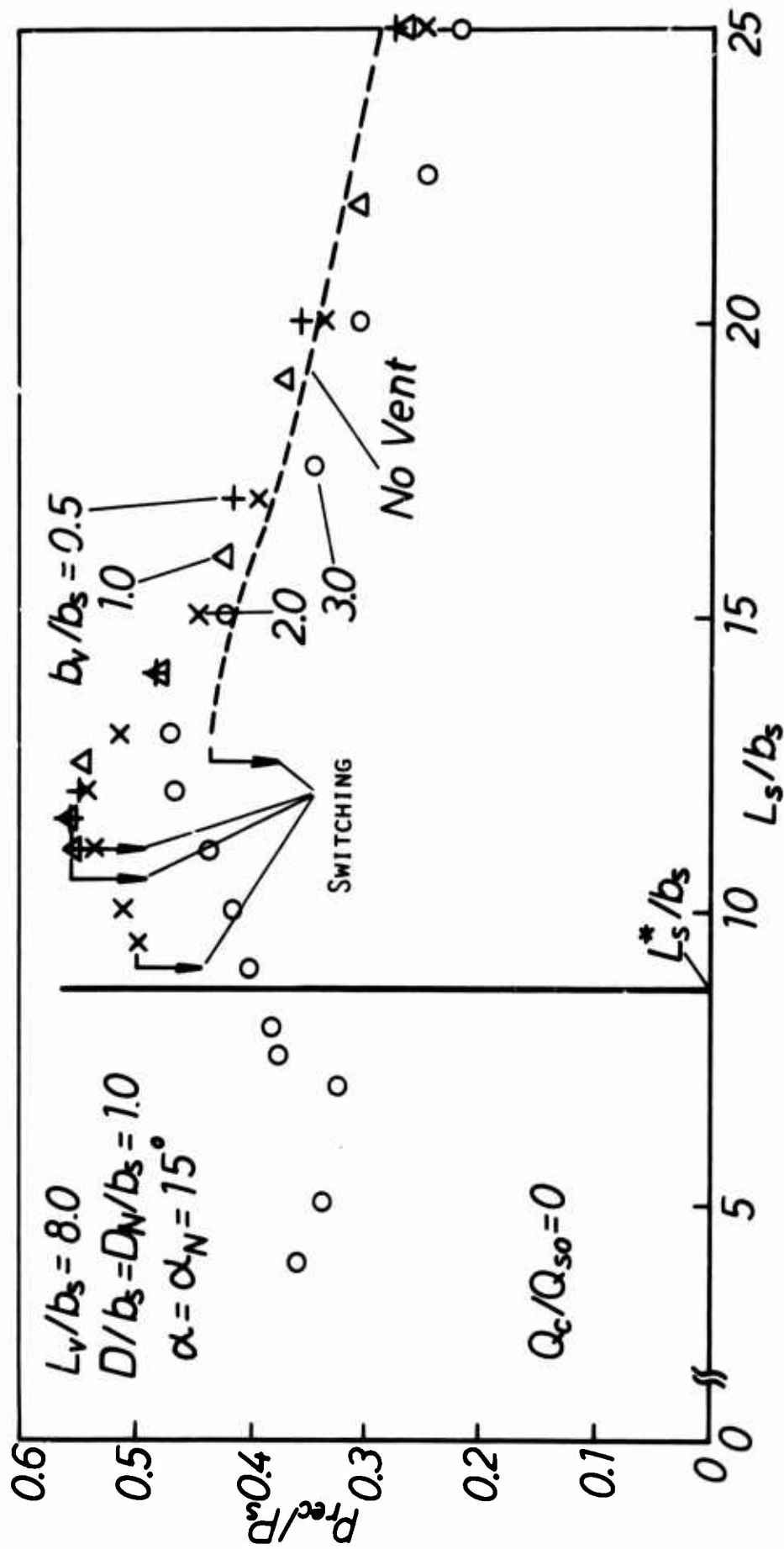


FIG.30 RECOVERY PRESSURE VS. SPLITTER DISTANCE

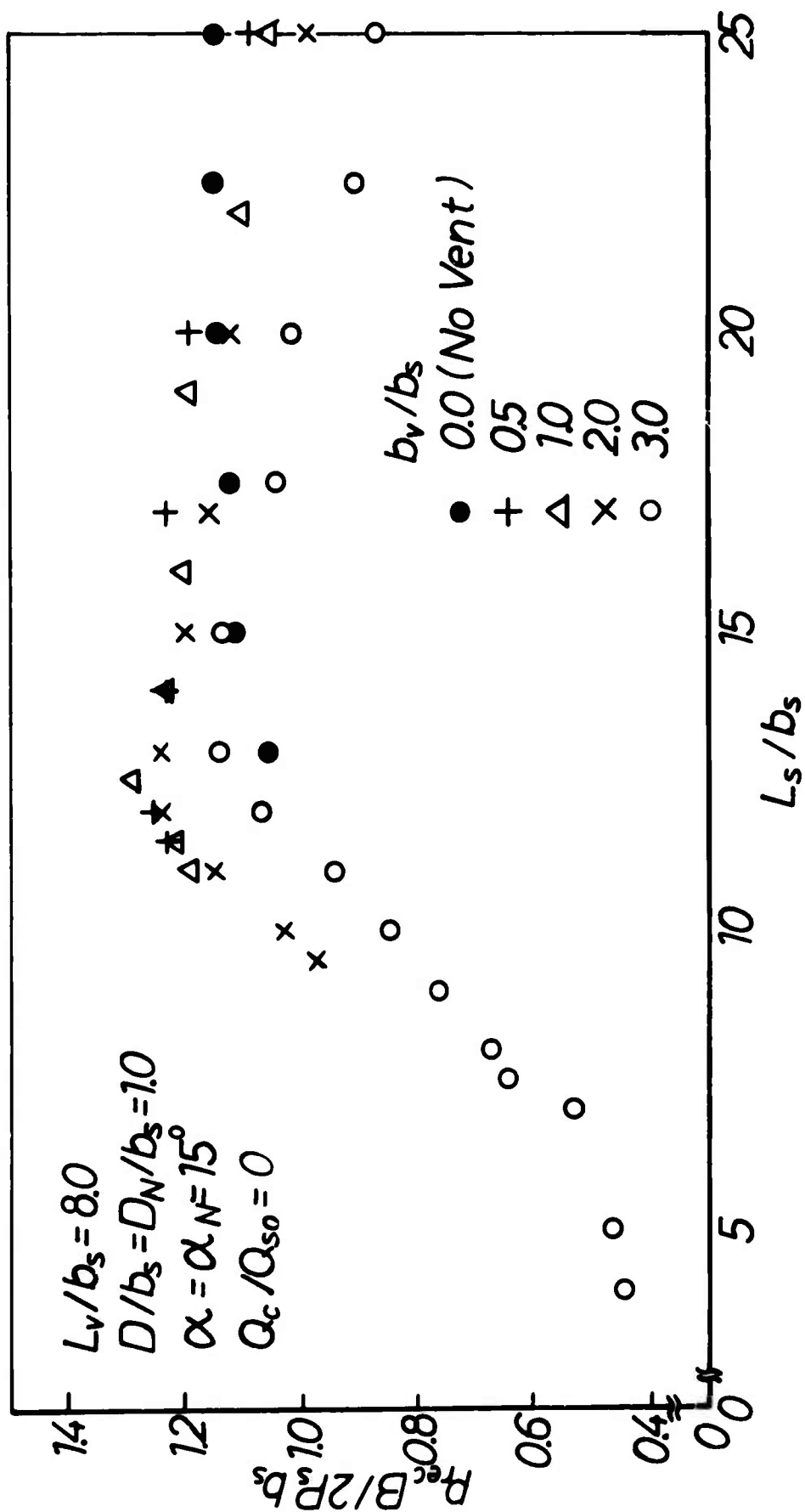


FIG.31 MOMENTUM INTO DUCT FOR  $L_v/b_s = 8$



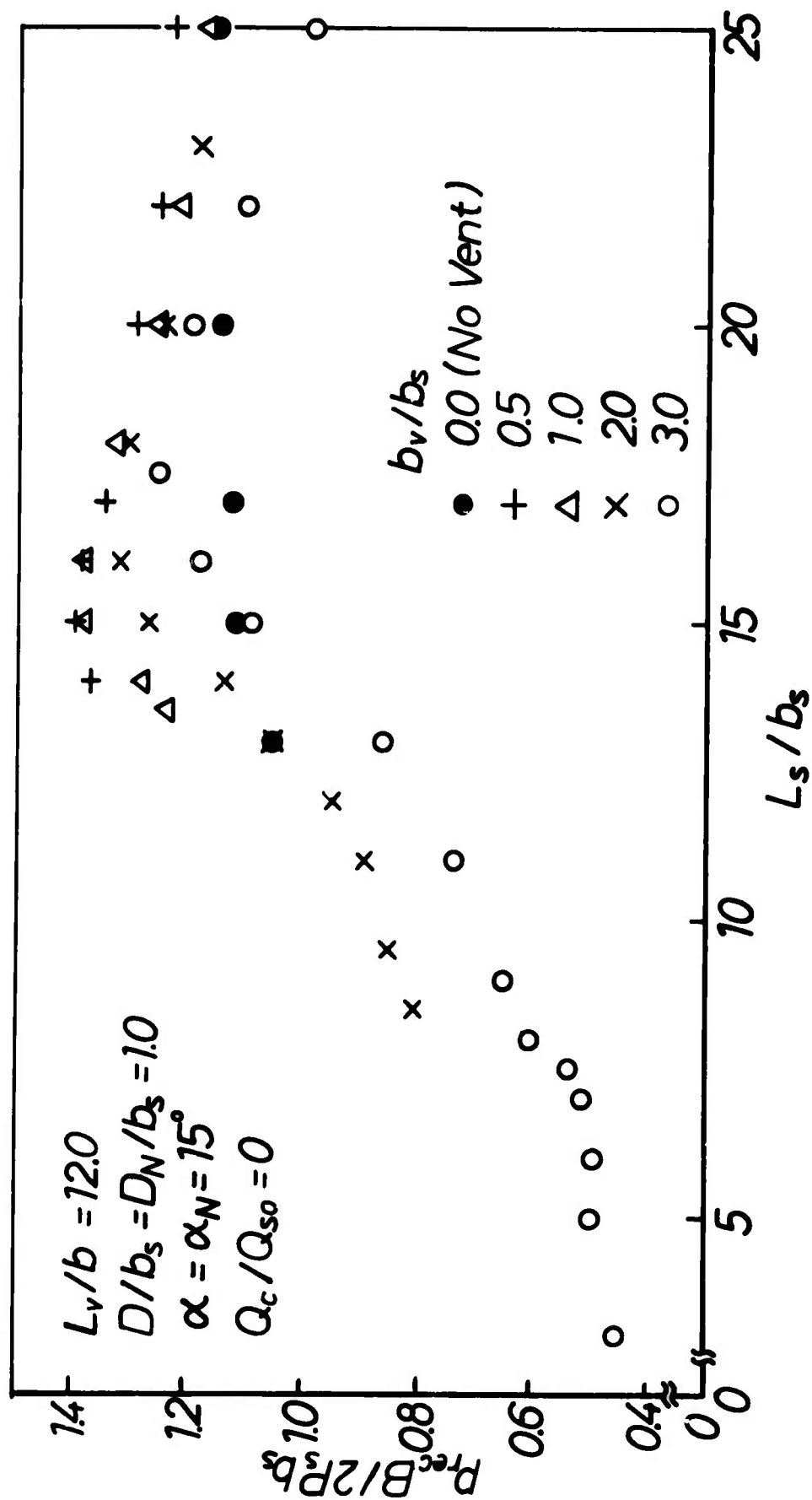


FIG. 32 MOMENTUM INTO DUCT FOR  $L_v/b_s = 12$

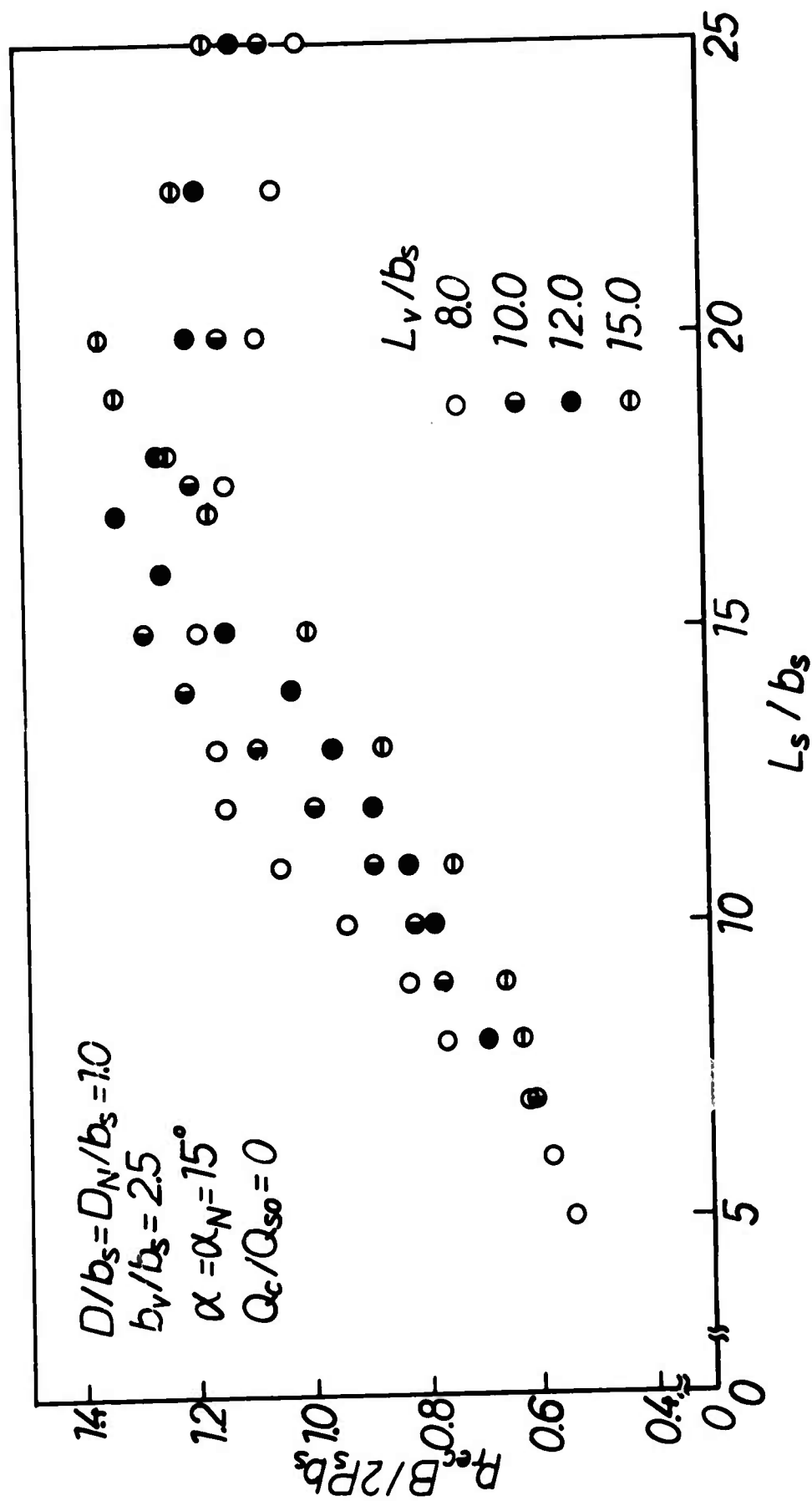


FIG.53 MOMENTUM INTO DUCT FOR SOME  $L_v/b_s$

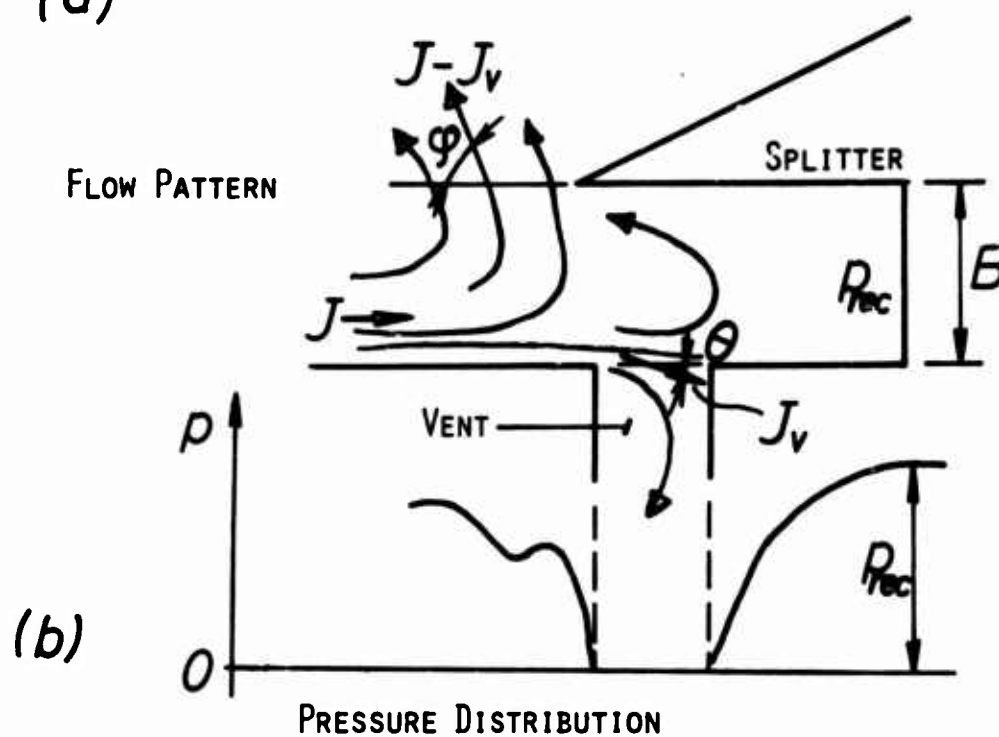
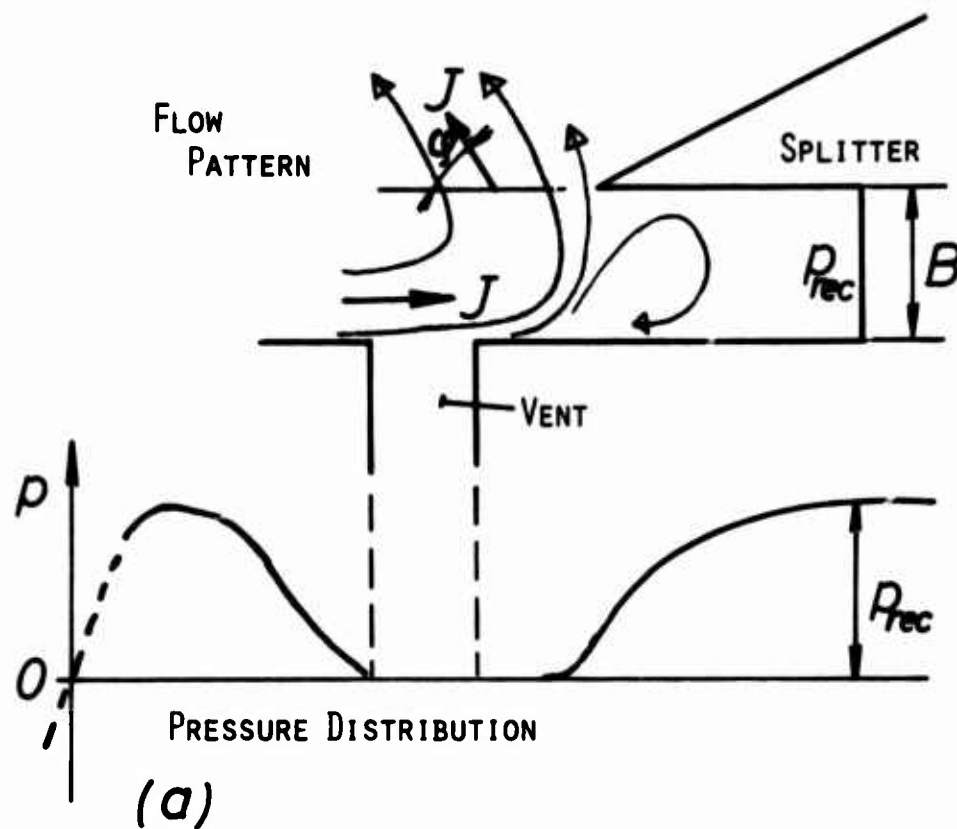


FIG.34 MOMENTUM INTO DUCT AND FLOW PATTERNS

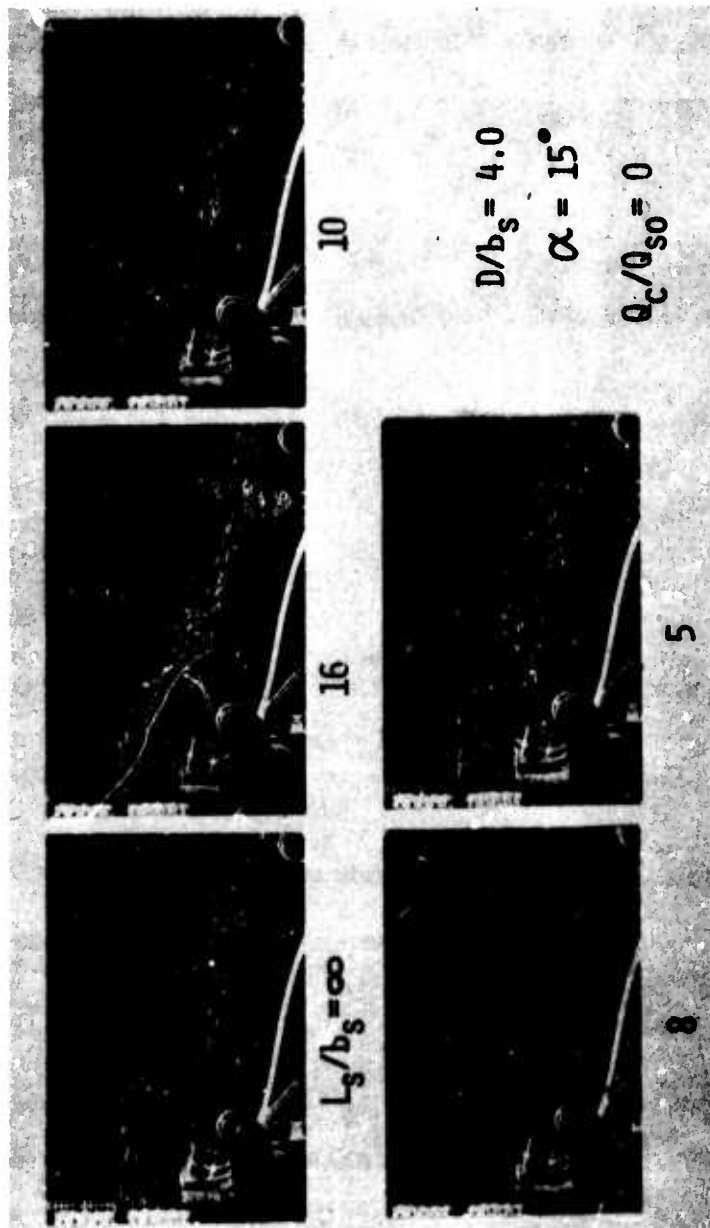


PHOTO.1 FLOW PATTERNS SHOWING SPLITTER EFFECTS

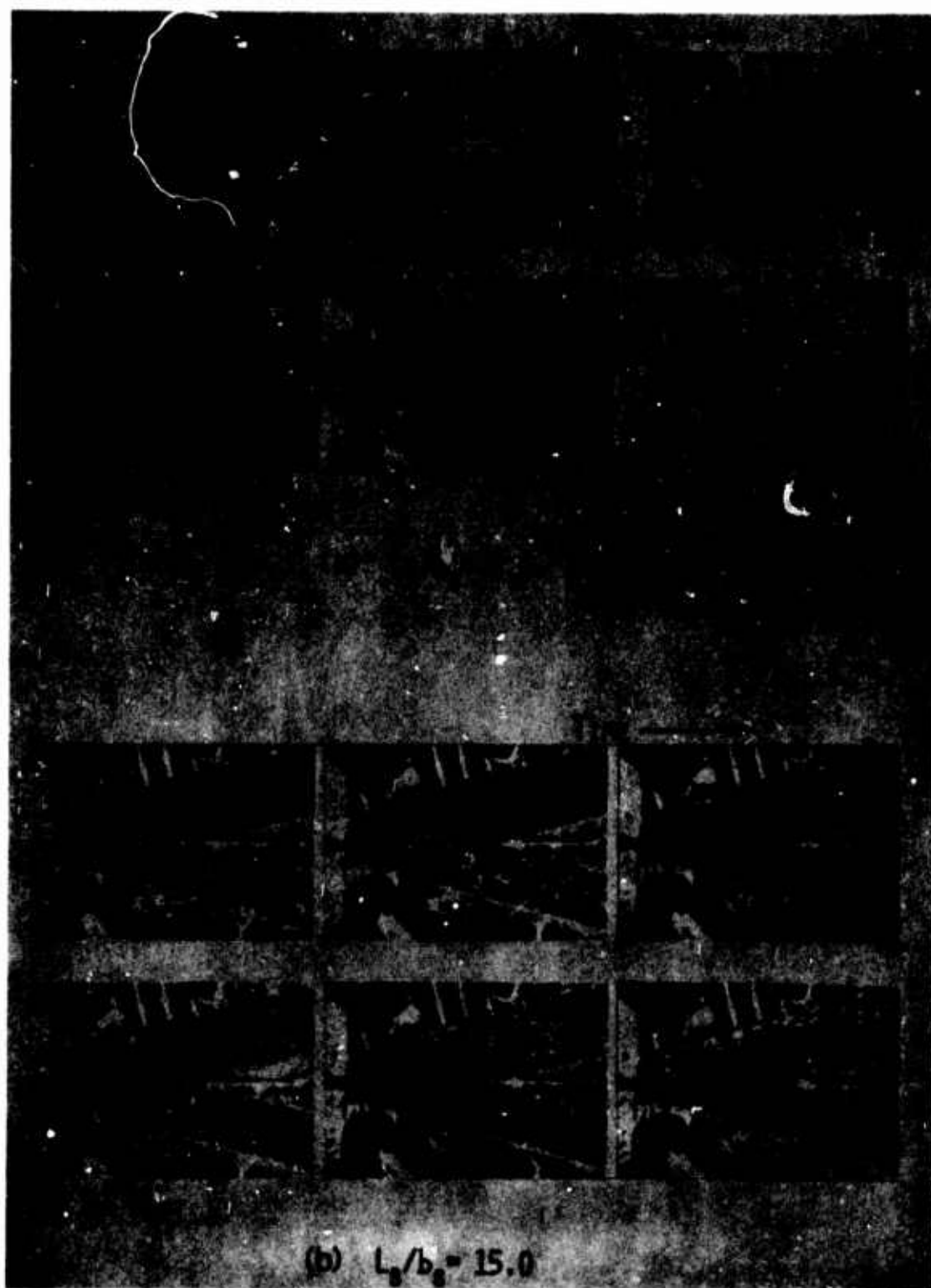


PHOTO.2 SWITCHING PROCESS, AFFECTED BY SPLITTER DISTANCE



PHOTO.3 FLOW PATTERNS FOR SHORT WALL LENGTH AND SUFFICIENTLY LONG WALL, IN SOME CONTROL FLOW CONDITIONS

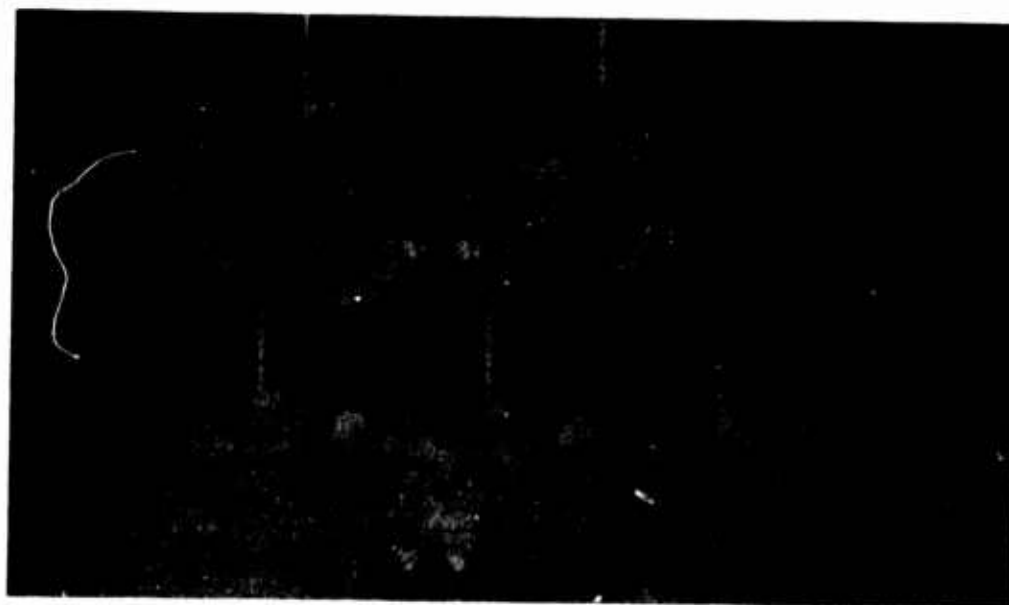


PHOTO.4 FLOW PATTERNS, AFFECTED BY VENT WIDTH ( $D/b_s = 2$ ,  $L_v/b_s = 12$ )



PHOTO.5 CONTACTING BOTH WALLS SWITCHING

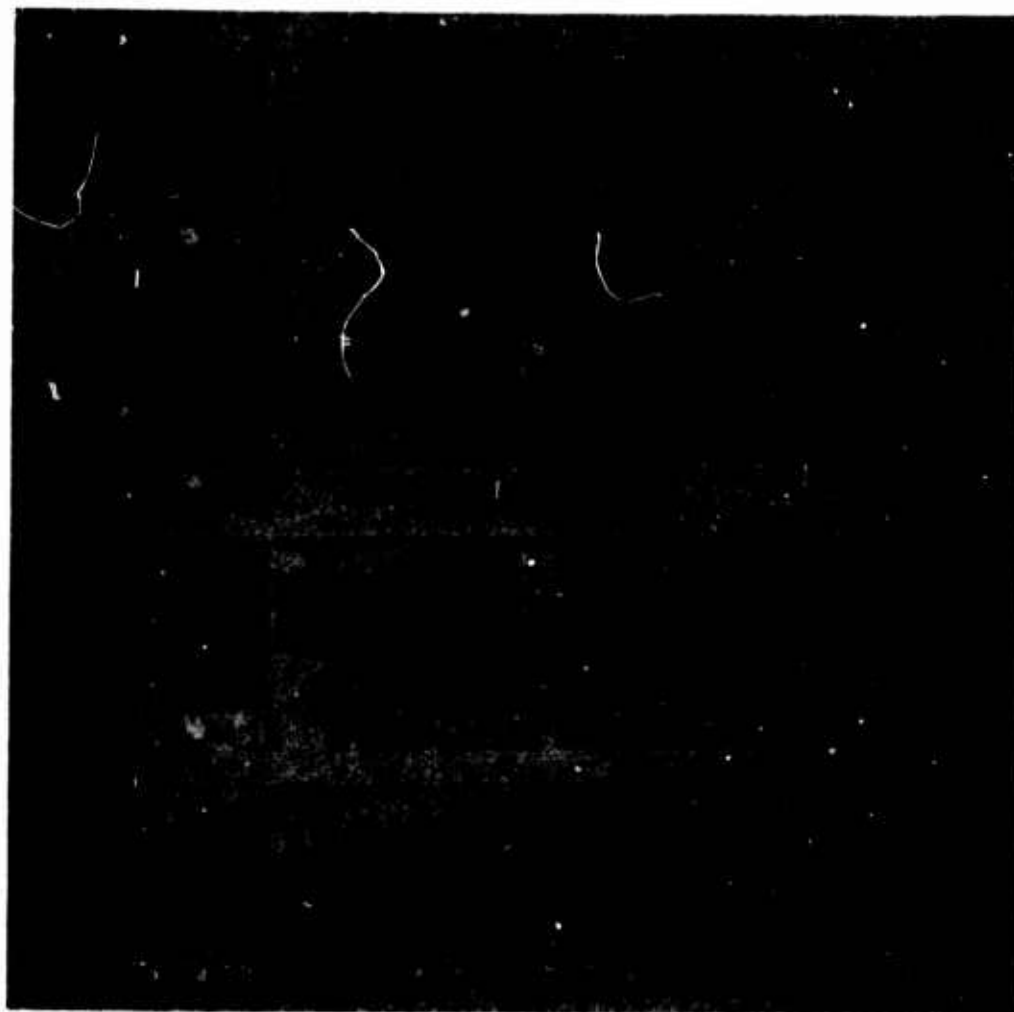


PHOTO.6 SWITCHING MECHANISM, AFFECTED BY WALL LENGTH

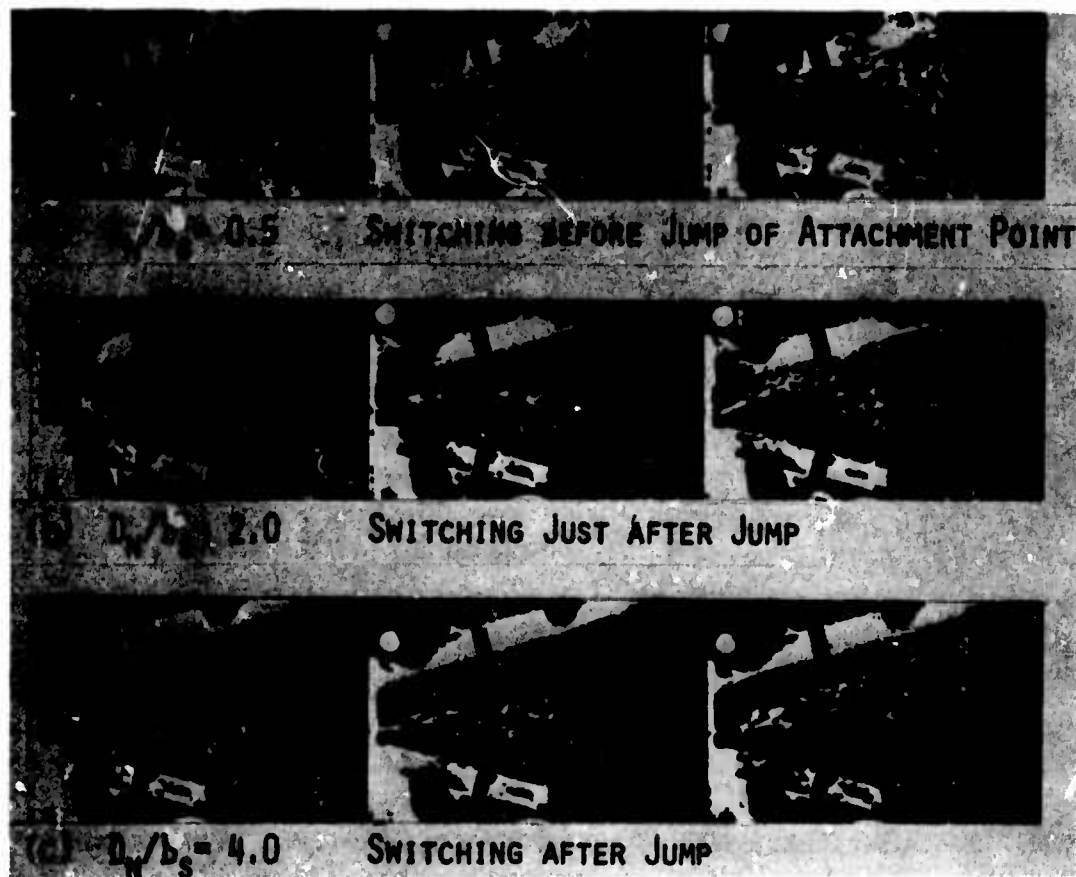


PHOTO.7 FLOW PATTERNS OF SWITCHING FOR VENT TYPE DEVICES  
 ( $D/b_s = 0.5$ ,  $L_v/b_s = 10.0$ ,  $b_v/b_s = 1.5$ )





PHOTO.8 FLOW PATTERNS OF SWITCHING, AFFECTED BY  
 SPLITTER DISTANCE



PHOTO.9 FLOW PATTERNS FOR COMPLETE LOAD

# SPLITTER SWITCHING IN BISTABLE FLUIDIC AMPLIFIERS

by C.J. WILLIAMS<sup>1</sup> and W.G. COLBORNE<sup>2</sup>

## ABSTRACT:

A brief history of the investigations into switching in bistable fluid amplifiers is presented. This includes a description of all important switching mechanisms as well as the two switching theories currently available.

In the new research described in this paper, hot wire measurements were made of the velocity profiles of attached jets similar to those found in bistable fluidic amplifiers. Using the Simson velocity profiles, and the experimentally determined jet centre line, a universal description of the flow from three scaled nozzles was found for a variation in nozzle velocity and offset of the attachment wall. A new probe was developed to measure the size of the separation bubble.

From these results an original theory was formulated to describe the splitter switching mechanism. Also the optimum position of the splitter, for maximum gain and minimum switching time, can be predicted.

---

1 Graduate Student, Department of Mechanical Engineering, University of Windsor, Ontario, Canada.

2 Head, Dept. of Mechanical Engineering, University of Windsor, Ontario, Canada.

# NOMENCLATURE

- $A_c$  - control channel area
- $A_d$  - area of the main jet leaving the control volume  
used in the main jet/control jet momentum study
- $A_o$  - supply nozzle area
- $b$  - supply nozzle width
- $b_c$  - control channel width
- $D$  - setback or offset distance
- $D/b$  - setback or offset ratio
- $F$  - distance between nozzle exit and attachment point
- $J$  - momentum per unit depth of the main jet
- $J_L$  - momentum per unit depth of the main jet passing  
downstream of the attachment point
- $J_R$  - momentum per unit depth of the supply jet  
returned upstream from the attachment point
- $K$  - a constant in the Simson velocity profile, where  
 $Y_c = KS$
- $L_w$  - attachment length measured along the attachment  
wall (including the control channel width)
- $P_a$  - atmospheric pressure
- $P_c$  - control channel static pressure
- $Q_c$  - control flowrate per unit depth
- $q_c = Q_c/Q_o$  - non-dimensional control flowrate
- $Q_E$  - flow entrained from the separation bubble  
per unit depth
- $q_E = Q_E/Q_o$  - non-dimensional entrained flowrate

- $q_N$  - net flowrate into the separation bubble (non-dimensionalized)
- $Q_O$  - main flow rate per unit depth
- $Q_R$  - flow returned upstream from the attachment point per unit depth
- $q_R = Q_R/Q_O$  - non-dimensional returned flowrate
- $R$  - separation bubble radius
- $S$  - distance measured along jet centreline from nozzle exit
- $S_O$  - potential core length
- $V$  - local velocity
- $V_c$  - control channel velocity
- $V_d$  - velocity of the main jet leaving the control volume used in the main jet/control jet momentum study
- $V_O$  - main jet velocity at the nozzle exit
- $W$  - separation bubble volume per unit depth
- $X$  - distance measured along the nozzle centreline from the nozzle exit plane
- $Y$  - distance measured normal to the jet centreline
- $Y_c$  - perpendicular distance measured from the edge of the potential core
- $Y_R$  - distance measured normal to the nozzle centreline
- $Y_W$  - value of  $Y_c$  terminating at attachment point
- $\alpha$  - attachment wall angle
- $\gamma$  - reattachment angle
- $\theta$  - see Fig. 11

$\psi$  - deflection of main jet by control jet  
 $\eta$  -  $Y/KS$   
 $T$  - time

#### SUBSCRIPTS

1 - initial conditions for phase I of switching theory  
2 - final conditions of phase I and initial conditions of phase II  
3 - conditions after moving jet a small distance along the attachment wall  
max - maximum value

## INTRODUCTION

Fluid amplifiers are devices in which a high energy power jet is controlled by a low energy control signal. There are various types of fluidic amplifiers one of which is the bistable type. This amplifier is a digital device with two stable operating conditions. It is called a digital device because the two output conditions are, full flow of the power jet at an outlet of the amplifier, or zero flow at the outlet. A control signal is used to switch the amplifier from one stable condition to the other.

A typical bistable amplifier showing the standard notation used to describe its components is presented in Fig. (1). The main stream of fluid, which is to be controlled, enters the main nozzle where the main jet is formed. Entrainment of the surrounding fluid into the main jet results in the main jet being attracted to, and subsequently attaching to one of the adjacent attachment walls. These walls are symmetrically offset from the edges of the main nozzle, and are inclined to form a diverging channel as shown in Fig. (1). The splitter divides this diverging channel into two output legs. The output channel in which the jet is flowing is referred to as the active output leg, whereas the other output channel is called the passive output leg. After attachment the main flow will therefore flow along one of the attachment walls and through the corresponding output leg. Output leg vents may

be included to ensure that the main jet remains attached to the wall in the event of the output leg being blocked. Control ports are positioned at the main nozzle exit, perpendicular to the main nozzle axis. The main jet can be switched from one output leg to the other by supplying a pulse of fluid into the control port on the same side as that to which the main jet is attached.

The switching of bistable fluid amplifiers has been experimentally studied by many workers, while the analysis of switching has received a relatively small amount of attention. The analyses which do exist enable one to predict the switching times of large scale bistable fluid amplifiers.

This paper reviews the various ways in which an amplifier switches and also reviews the existing theories which describe certain switching mechanisms. The paper also presents a theory which describes splitter switching. Switching time is predicted by the use of this theory and compared to experimental results.

#### LITERATURE SURVEY

This section provides a brief history of the analysis of switching in bistable fluid amplifiers. Only those papers which give information directly applicable to the understanding of the operation of bistable fluid amplifiers will be described. Literature containing refinements which would tend to detract from the central theme of the survey, will be only briefly mentioned. All switching mechanisms of practical



importance are described and, in addition, material is presented which will assist with the understanding of the two switching theories currently available.

#### I STEADY STATE OPERATION OF BISTABLE FLUID AMPLIFIERS

The phenomenon which causes a jet to attach to a nearby surface has been called the Coanda effect, after Dr. Henry Coanda [1]. Figure (2) shows how the Coanda effect causes attachment in a bistable amplifier. The main jet, issuing from the main nozzle, entrains the stationary fluid existing on both sides of the jet. This entrainment results from the turbulent interaction between the main jet and the surrounding fluid. The entrainment causes an acceleration of the surrounding fluid and therefore a reduction in pressure on both sides of the jet. As the turbulent entrainment is a random process the entrainment, and hence the pressure reduction on both sides of the jet will not be exactly equal. If the entrainment is slightly higher on, say, the lower side of the jet, then the acceleration of surrounding fluid and reduction in pressure will be greater on this side of the jet. The pressure differential across the jet will then bend the jet towards the lower attachment wall, Fig. 2(b). This will have the effect of increasing the velocity of the entrained fluid and hence further reducing the pressure on this side of the jet. If the attachment wall is long enough and close enough to the main nozzle, then the main jet will eventually attach to it, as shown in

Fig. 2(c). A low pressure region, called the separation bubble, is formed between the main jet and the attachment wall. At the point where the jet strikes the wall, called the attachment point, a quantity of fluid from the main jet is returned into the separation bubble. The main jet also entrains fluid from the separation bubble. At the time when the jet first attaches to the wall the entrained flow is greater than the returned flow. This causes the bubble volume to decrease. This decrease causes the attachment point to move upstream thereby increasing the attachment angle. With a greater attachment angle, the return flow becomes larger while the entrained flow becomes smaller due to the shorter bubble. A steady state condition is attained when the returned flow equals the entrained flow, Fig. 2(d).

Bourque and Newman [2] were among the first to provide a theoretical analysis of a reattached two-dimensional jet. They presented two theories to analyse the Coanda effect, with the most important of these being, as far as this paper is concerned, the attachment point model. This theory demonstrates how a momentum balance at the attachment point can be used to determine a relationship between the attachment angle and the momentum of the flow returned into the separation bubble. It is then possible, if the velocity profile of the main jet is known, to determine the actual value of the returned flow. This is discussed in further detail in the

next section.

This initial theory has been improved by many workers. Sawyer [3] allowed for the different rates of entrainment on either side of the curved jet. Levin & Manion [4] proposed a modification of the attachment point model which would remove the necessity of assuming that the attachment angle is equal to the wall angle, as assumed by Bourque and Newman. Bourque [5] showed that a better agreement between theory and experiment is obtained, if a nonconstant separation bubble pressure assumption is used in Shear's [6] modification of the Bourque & Newman theory. A fairly comprehensive list of the many other modifications of the Bourque & Newman attachment theory can be found in the introduction to McRee & Edwards paper [7].

The power jet in all of the above theories is described by the Goertler free jet profile [8]. Simson [9] suggested the use of a modified form of the Albertson profile [10] to describe the jet formed at the exit of a nozzle similar to the main nozzle of a bistable fluid amplifier.

## II SWITCHING MECHANISMS OF BISTABLE FLUID AMPLIFIERS [11] - [15]

The switching mechanism in bistable fluid amplifiers can be divided into two main categories:- slow switching and rapid switching.

- i) Slow Switching: This occurs when a low control flow to main flow ratio is used. Longer switching

times will result, but less control flow has to be used than in rapid switching. All of the slow switching mechanisms are characterized by a bubble filling process. When a control flow is applied to the amplifier, fluid enters the separation bubble through the control channel. This upsets the equilibrium between the returned flow and entrained flow which existed during steady state attachment, as shown in Fig. 3(a). The separation bubble will now expand because the net flow into the bubble is positive due to the addition of control flow as shown in Fig. 3(b). As the bubble expands the power jet will be forced towards the passive output leg. Switching will then continue in one of the three modes of slow switching described below. It is necessary to identify these three modes because the method of analysis is different in each case.

a) End Wall Switching: This type of switching results when small control jet to main jet momentum ratios are used in amplifiers with short attachment walls. The position of the vents in the output legs, shown in Fig. 4, determine the length of the attachment wall. The jet remains attached to the initial wall while the bubble grows and moves the attach-

ment point downstream. When the attachment point passes over the output leg vent, the jet begins to separate from the wall, and the bubble filling process is augmented by a flow of ambient air through the vent into the bubble. This is shown in Fig. 4.

b) Opposite Wall Switching: One of the requirements for opposite wall switching is that an amplifier has its attachment walls positioned to give a small offset. Also a large splitter distance and a slightly larger control jet to main jet momentum ratio are required. The main jet attaches to the opposite wall, following the application of control flow, but also remains attached to the initial wall as shown in Fig. 5. The separation point on the opposite wall and the attachment point on the initial wall both move downstream as the bubble expands by the bubble filling process.

c) Splitter Switching: Correct positioning of the splitter and selection of a large enough offset, will result in splitter switching. The bubble filling process causes the bubble to expand forcing the main jet over the splitter into the new output leg. This is illustrated in Fig. 6.

ii) Rapid Switching: Rapid switching, sometimes called momentum switching, can occur with any of the above amplifier geometries if a high enough value of control jet momentum ratio is used. The main jet is forced across the splitter almost instantaneously. This mechanism produces the shortest switching time since there is no extended bubble filling process.

The switching process in any of the above mechanisms can be aided by critical attachment angle switching. If the angle between the power jet and the attachment wall exceeds a certain value then the returned flow into the bubble will be greater than the entrained flow from the bubble. At this point the control flow may be discontinued, whereas in all of the above mechanisms the control flow is applied during the complete switching process.

Switching may also occur by load switching which arises in unvented amplifiers by blocking the active output leg. Under certain conditions, if the passive control port is restricted sufficiently while the active control port is open then the amplifier will switch. This is called vacuum switching and occurs because the entrainment to the passive side of the jet is reduced, forming a low pressure region on that side of the jet.

### III SWITCHING MECHANISM ANALYSES

When the present work was started only two of the above

switching mechanisms had been analysed in detail. The first was end wall switching which has been theoretically described by Epstein [16]. The steady state condition of the main jet in his analysis was described by Bourque's theory [5], which used a Goertler free jet profile to give the velocity profiles in the main jet. Epstein divided the switching process into three phases, which were similar to those used by Lush [17]. Phase I began when the control flow was started. A combined jet, of main flow and control flow, was assumed to be formed. The momentum interaction between these two jets rapidly deflected the main jet away from the initial attachment wall. While this occurred the reattachment point of the main jet on the initial wall was assumed to remain at its initial steady state position. Phase I ended when the combined jet had deflected to its maximum angle, which was calculated from the momentum ratio of the main jet to control jet. Phase II then began and consisted of a bubble filling process which expanded the bubble and moved the reattachment point downstream. This phase ended when the reattachment point reached the edge of the vent in the initial wall. The deflection angle of the combined jet in this phase and phase III remained constant at the maximum as found at the end of phase I. The beginning of phase III was defined as the point when it was possible for flow to enter the separation bubble through the vent. Phase III ended when a specified portion of the main jet had passed over

the splitter. This was a convenient way of stating that the flow had reached a certain value in the passive leg. Expressions were derived which permitted calculations of the bubble volume and the net flow rate into the bubble to be made at any time during the switching process. Hence the time taken for switching to occur could be calculated.

To compare his theory with Lush's experimental results Epstein assumed the following: 1) a value for the output leg vent discharge coefficient, which enabled the flow in the vent during phase III to be calculated; 2) the portion of the main jet which had passed over the splitter at the end of phase III and 3) a value for the jet spread parameter which was used in the Goertler free jet profile. Good agreement on switching times was found between his theory and the experimental results of Lush. By plotting the bubble volume, with respect to time, Epstein showed that the bubble did not grow at a constant rate. In fact the bubble volume was found to remain almost constant in the middle of the switching process.

The only other switching mechanism which had been examined was opposite wall switching, which was analysed by Ozgu and Stenning [18]. One of the important contributions of this work was the discussion of the merits of the Goertler and the Simson profile representations to describe the main jet. They found that the Simson profile gave a better description of the flow immediately downstream of the nozzle exit, since it in-



cluded the potential core. The profile developed by Simson [9] showed good agreement with the experimental profiles, provided by Albertson [10], for a two dimensional submerged jet. Ozgu & Stenning therefore decided to use this profile to describe the main jet of a bistable fluid amplifier. They also divided the complete switching process into three phases. The first phase began with the application of control flow. This phase ended when the main jet touched the opposite wall.

In order to calculate the time required for this phase, two assumptions had to be made. The first was that the flow entrained from the bubble was equal to the flow returned into the bubble at the attachment point. The second was that the steady-state bubble volume was negligible.

Phase II started when the main jet touched the wall of the passive leg. An empirical relationship was formed which allowed the bubble volume to be calculated at any time during this phase. Phase II was continued by increasing the attachment distance by small increments, and finding the bubble volume after each increment. This phase concluded when the inside edge of the jet reached the edge of the vent in the wall of the active leg.

The net rate of flow into the bubble at any instant in time during this phase was expressed as, the control flow plus the returned flow, minus the entrained flow. The returned flow was found by integrating the Simson profile at the re-

attachment point. The entrained flow was found using the fact that the increase in the width of a jet, at a given downstream location, is a measure of the surrounding fluid that it has entrained up to that point.

As the attachment point was moved along the wall in small increments, the volume of the bubble was increased also in small increments. The time required for each change in volume could be calculated knowing the rates of flow into the bubble. The total time to complete this phase was then found.

Estimates of the time taken to complete phases I and II was made based on flow visualization studies. A correction to allow for a variation of some of the quantities they had assumed constant during this phase gave a good agreement with their experimental values.

The total switching time was measured by recording the time interval between pressure signals transmitted from pressure transducers placed in the control channel and passive output leg. The time for the third phase was calculated by subtracting the time for phases I and II from the total switching time. The analytical expression to predict the time for this phase was derived from a relationship, based on the dynamics of a fluid in a channel, fitted to the experimental values. Ozgu & Stenning were therefore able to predict the total switching time of a bistable fluid amplifier, which had switched by the opposite wall switching mechanism.

#### IV SWITCHING TIME MEASUREMENTS

Experimental measurements of the switching time of bistable fluid amplifiers have received a relatively small amount of attention. Savkar et al. [13], Muller [19], Ozgu and Stenning [18] made measurements of the switching times of a bistable amplifier using water for the supply and control jets. Lush [17], Williams and Colborne [20], and Foster and Carley [21] made similar measurements using air. The results of all of these experiments agree qualitatively, but exact comparisons are difficult to make as the amplifier geometries were different in each case. There are also discrepancies in the definitions of switching times.

##### SPLITTER SWITCHING STUDY

A major objective was to experimentally determine the characteristics of the main jet in a bistable fluidic amplifier. This included the measurement of the velocity profiles at various distances downstream of the nozzle and the determination of the location of the centre line of the jet. Based on this information a theory was formulated to describe splitter switching which permitted the response time for this type of device to be estimated. In order to determine the effects of size on the velocity profile and splitter location, tests were also run on three different sized, geometrically similar amplifiers.

#### I EXPERIMENTAL APPARATUS AND PROCEDURE

The experimental apparatus consisted of three geometrically similar nozzles and attachment walls similar

to those found in bistable fluidic amplifiers. Similar entrance sections were also provided. Hot wire anemometer traversing means was provided to allow velocity profiles to be measured at any location in the flow field.

Compressed air was fed through a line containing a 5 micron filter and two pressure regulators. This line could be connected to one of three scaled settling chambers and power jet nozzles. Each settling chamber contained a baffle and screens, and was connected to the nozzle by a bellmouth contraction to assure smooth and uniform flow conditions at the power jet nozzle entrance.

A typical power jet nozzle, shown schematically in Fig. 7, was constructed by positioning the various components between plexiglass sidewalls. The three models had nozzle widths of 0.25, 0.125 and 0.50 inches with the aspect ratio being 4 to 1 in all cases. The set-back ratio defined as  $D/b$  as shown in Fig. 7 was set at one of two values 0.06 or 0.50. In each nozzle, three flow rates were investigated. These flow rates resulted in Reynolds numbers of  $4.0 \times 10^3$ ,  $13.3 \times 10^3$ , and  $26.5 \times 10^3$  based on nozzle width. The splitter and opposite wall normally found in bistable fluid amplifiers were removed to produce an undisturbed attached bounded jet.

It was found by Sher [6] for setback ratios from 0 to 1.2 and Perry [22] for setback ratios greater than 1.0 that

removal of these components had little or no effect on the distance of the reattachment point from the nozzle exit. Wada and Shimizu [23] in their paper showed the values for critical splitter distance for setback ratios greater than 0.5. This was defined as the distance between the splitter and the nozzle exit which resulted in a 5% reduction in the attachment distance measured without the splitter. It was also found that moving the splitter from infinity toward the nozzle exit did not affect the pressure within the separation bubble until the critical splitter distance was reached. We assumed that there would be no change in the velocity profiles within the bubble when the splitter was located at any point beyond the critical.

We therefore have confidence that velocity profiles measured without the splitter or the opposite wall will be representative of those found in a bistable fluid amplifier with the splitter located beyond the critical position.

Velocities were measured using a Disa 55 A 53 hot wire with a 55 D 05 constant temperature anemometer. Velocity traverses were made in the  $X_R$ - $Y_R$  plane at various values of  $X_R$  from zero to  $20b$  downstream. In order to reduce the effects of the hot wire supports, the standard hot wire was modified by bending the supports 90 degrees as shown in Fig. 7. The voltage output from the anemometer was recorded for 5 seconds at each location on a paper chart recorder. A mean voltage was obtained from this 5 second trace. The calibration curve

of velocity versus voltage was produced by placing a pitot tube and the hot wire in the same horizontal plane at the nozzle exit. The calibration curve was checked at the beginning and end of each series of traverses.

Within a separation bubble there is a circulating flow. A boundary region exists in the centre of the bubble with fluid on one side flowing upstream and the fluid on the other side flowing downstream. Because of the turbulence in this region, the precise location of a line of zero velocity is impossible to determine with a single hot wire.

An opposite facing double total pressure probe was developed which permitted a fairly accurate measure of the location of the line of zero velocity. This probe consisted of two 0.056" diameter tubes soldered along side each other. The lower ends were plugged and two 0.010" diameter holes were drilled one on each side. The upper unblocked ends were connected to an inclined 'U' tube manometer. A null position occurred when the total pressures on either side of the tubes were equal. Traversing this probe through the separation bubble at various downstream positions located the line of flow reversal.

## II EXPERIMENTAL RESULTS

One of the initial requirements was to determine whether the measured velocity profiles could be adequately described in all three nozzle sizes by an analytical expression. It was found that the expression developed by Simson [9] agreed

very closely with the experimentally determined velocity profiles. The expressions developed by Simson to provide the velocity distributions in a jet, identify two regions. The first region is that containing a potential core with velocities given by

$$\frac{V}{V_0} = \left[ 1 - \left( \frac{y_e}{y_{e_{\max}}} \right)^{7/4} \right]^2$$

The second region downstream of the potential core has velocities given by

$$\frac{V}{V_0} = \sqrt{\frac{S_0}{S}} \left[ 1 - \left( \frac{Y}{Y_{\max}} \right)^{7/4} \right]^2$$

The Simson profile was developed for a straight jet with the velocities given along lines perpendicular to the centreline of the jet at various locations downstream. To compare these profiles with those of a curved jet, the centreline of the curved jet must be found. The centreline is considered to be the locus of the points at the centre of the potential core, and the points of maximum velocity in the flow region downstream of the potential core.

Centreline points were found for all three nozzle widths with Reynolds numbers of  $26.5 \times 10^3$  and  $13.3 \times 10^3$ , setback ratios of 0.5 and 0.06 and non dimensional distances downstream  $X_R/b$  equal to 0, 0.5, 1.0, 1.5, 2.0, 2.5 and 3.0. All of these points fell close to a single line and a least squares analysis

gave the equation of this line in rectangular coordinates as

$$Y_R/b = 0.067 + 0.097 (X_R/b)^{1.56}$$

Points in the flow field have been located, either on rectangular coordinates by  $(X_R, Y_R)$  see Fig. 7, or from the curved centreline of the jet by coordinates  $(S, Y)$ .  $S$  is the distance measured along the curve of the centreline from the nozzle exit and  $Y$  is the distance measured perpendicular from the curved centreline.

The Simson profile also requires that the end point of the potential core be specified. For the above range of variables the average length of the potential core was found to be  $X_{R/b} = 6.58$ .

The next step was to compare the measured velocity profiles with the profiles as calculated from the Simson expression. Since the measured profiles were on a curved centreline, the Simson velocity at each point had to be calculated using the  $S$  and  $Y$  coordinates.

A typical plot of the experimental and theoretical results for the variables stated above is given in Fig. 8.

The velocity profile on the side of the centreline closest to the wall was accurately described by the Simson profile. The agreement on the side away from the wall was not as good as seen in Fig. 8. However this lack of agreement is of



little concern since only the approximate location of the outer edge is required in the splitter switching theory. In future work it would be possible to modify the expression for the outer edge shape to provide a better description of the jet if this was justified. The non dimensional velocity in the potential core is seen to vary from 1.05 to 1.00. The local increase in velocity, above the nozzle exit value, is caused by the low static pressure in the separation bubble. Again the expression for the profile could be modified to account for this increased velocity, however the additional complication was not justified. The wall side of the jet is described well by the Simson expression until the point of flow reversal in the separation bubble is reached. Beyond this point an assumption concerning the shape of the velocity profile is made as described below.

Figure 9 shows a typical comparison of the Simson profile with experimental profiles for a setback ratio of 0.06. The principal difference between this and Fig. 8 is the apparent lack of a flow reversal close to the wall. For this setback the separation bubble is very small. It is interesting to note that changing the offset does not change the location of the jet centreline or the shape of the jet, but only the size of the separation bubble.

The remaining portions of the flow field to be described are the separation bubble and the attachment point.

The centre of the separation bubble was located during

each hot wire traverse by noting the position of the point of minimum velocity. These points are plotted for  $D/\delta = 0.50$  in Fig. 10 together with the values obtained from the double probe. Since there is a circulation within the separation bubble, the mass flow on each side of the centre will be equal and opposite. Two assumptions were made concerning the separation bubble. The first specified that the velocity profiles on each side of the centre were identical and secondly that the static pressure along any line perpendicular to the wall is constant. The distance from the wall to the centre is therefore half the total width of the bubble.

The steady state flow field in the separation bubble region of a bistable fluidic amplifier can now be confidently predicted for the range of variables used using the derived expression for the centreline of the jet and the Simson velocity profile.

In order to develop a theory on splitter switching it is necessary to locate the splitter in a specified position. Wada and Shimizu [23] working with a similar amplifier with a setback ratio of 0.5 found the critical splitter distance from the nozzle exit to be  $6.0b$ . Velocity profiles were measured for the nozzles used in this study for values of  $X_R/b$  of 3.5, 4.0, 5.0, 6.0, 10.0 and 20.0, in order to confirm the conclusion of Wada and Shimizu. It was found with the splitter located at a distance  $6.0b$ , that there was a very low flow in the passive leg of the amplifier as indicated by flow visualization using smoke. The small amount of

flow separated from the main jet by the splitter was mostly returned to satisfy the entrainment requirements of the main jet. This indicates that this splitter position was very close to the optimum.

### III SPLITTER SWITCHING THEORY

The splitter switching mechanism is considered to take place in two phases. In phase I the main jet is assumed to remain attached at the same point on the attachment wall, while being deflected through an angle,  $\psi$ . The value of this angle is obtained by solving the momentum equations in the  $X_R$  and  $Y_R$  directions. This process is not one of bubble filling but involves an expansion of the separation bubble to satisfy the new geometry caused by main jet deflection. It has been shown that that attachment point remains at the same location during the time taken for this bubble expansion [24], [18]. This portion of the switching process corresponds to our Phase I. Our own calculations have shown that Phase I occurs in a time that could be considered negligible. We have therefore used Phase I only as a means to calculate the initial conditions for Phase II and not as a part of the total switching time. In Phase II the bubble volume increases by a bubble filling process. The net flowrate into the bubble is the control flowrate plus the flow returned from the attachment point, minus the flow entrained from the top of the bubble. With this net flow rate, the times required to produce incremental changes in the bubble volume can be found. By defining the end point of Phase II the time required

for Phase II is the sum of the times for the incremental changes.

#### PHASE I ANALYSIS

From experimental observations, at a setback ratio of 0.5, the points indicating the boundary between the separation bubble and the main jet are shown in Fig. 10. In order to determine a bubble boundary a uniform static pressure in the bubble was assumed. This resulted in a constant curvature arc which was drawn tangent to the edge of the nozzle. The points outside of the region of interference caused by the control channel were considered more significant in fitting the curve. The intersection of this curve with the attachment wall gave a location for the attachment point of  $Lw/b = 2.56$  as shown in Fig. 10.

To find the geometry of the bubble at the end of Phase I the main jet is deflected through an angle  $\psi$  as shown in Fig. 11. This angle will be dependent on the ratio of control jet to main jet momentum and on the pressure differential existing across the jet. Writing the momentum equation in the  $X_R$  direction, with reference to Fig. 12, gives:

$$\rho A_o V_o^2 - \rho A_d V_d^2 \cos^2 \psi + (P_a - P_c) A_c \tan \psi = 0$$

Similarly in the  $Y_R$  direction:

$$\rho A_c V_c^2 - \rho A_d V_d^2 \sin \psi \cos \psi + (P_c - P_a) A_c = 0$$

The two equations can be solved for  $\psi$  by substituting the values of control channel static pressure, area and velocity, as well

as supply nozzle area and velocity.

The new value of  $\theta$  resulting from a change of main jet direction by  $\psi$  is:

$$\theta_2 = \theta_1 - \psi$$

The attachment angle,  $\gamma$ , becomes

$$\gamma_2 = \gamma_1 + \psi.$$

The radius of curvature for the separation bubble boundary is given by:

$$R_2 = \frac{F_2}{2 \cos(\theta_2)}$$

The volume per unit depth of the separation bubble is given by:

$$W_2 = \frac{180 - 2\theta_2}{360} \pi R_2^2 - \frac{F_2 R_2}{2} \sin(\theta_2) + \frac{(D - b_c \tan \alpha) F_2 \sin(\theta_2 + \psi)}{2}$$

#### PHASE II ANALYSIS

The values of  $\theta$ ,  $\gamma$ ,  $R$  and  $V$  found at the end of phase I are used as initial conditions for phase II. See Fig. 11 and 13.

Moving the jet down the attachment wall increases  $F_2$  by  $\delta F$  giving:

$$F_3 = F_2 + \delta F$$

$$\theta_3 = \cos^{-1} \left( \frac{F_2}{F_3} \cos(\theta_2 + \alpha + \psi) \right) - \alpha - \psi$$

$$\gamma_3 = 180 - 2\theta_3 - \alpha - \psi$$

$$R_3 = \frac{F_3 \sin(\theta_3)}{\sin(180 - 2\theta_3)}$$

and

$$W_3 = \frac{(180 - 2\theta_3)}{360} \pi R_3^2 - \frac{F_3 R_3}{2} \sin \theta_3 + \frac{(D - b_c \tan \alpha) F_3 \sin(\theta_3 + \psi)}{2}$$

The change in bubble volume for this first step of phase II is  $W_3 - W_2$ .

The net flow into the separation bubble is given by:

$$q_N = q_C + q_R - q_E$$

The value of  $Q_E$ , the flow entrained into a jet which has a Simson profile, is given by the expression

$$Q_E = \int_0^{Y_e} V dY - \frac{V_o b}{2}$$

where  $Y_e$  is the distance along the  $Y$  axis from the jet centre-line to the edge of the profile at the attachment point.

Williams [25] outlines the details of this integration and calculation and finds

$$Q_E = 0.182 \frac{S}{S_o}$$

The returned flow is that flow between the theoretical outside edge of the jet and the attachment wall at the attachment point. This is given by

$$Q_{\text{ret}} = \int_0^{Y_e} v \, dY - \int_0^{Y_w} v \, dY$$

which results in:

$$q_R = Y \left[ 0.495 - \left[ \eta - \frac{8}{11}(\eta)^{11/4} + \frac{2}{9}(\eta)^{9/2} \right] \right]$$

where

$$Y = \frac{KS}{b} \quad \text{and} \quad \eta = Y_R / KS$$

Now the momentum equation at the attachment point gives

$$J \cos \gamma = J_L - J_R$$

and assuming no loss of momentum at attachment

$$J_L + J_R = J$$

$$\therefore J \cos \gamma = J - 2J_R$$

$$\cos \gamma = 1 - \frac{2J_R}{J}$$

Now

$$J_R = \int_{Y_R}^{Y_e} \rho v^2 \, dY \quad \text{and} \quad J = \rho v_o^2 b$$

which results in

$$\cos \gamma = 1 - 0.7276 \bar{Y} + 2\bar{Y} \left[ \eta - \frac{16^{11/4}}{11^\eta} + \frac{12^{9/2}}{9^\eta} - \frac{16^{25/4}}{25^\eta} + \frac{1^8}{8^\eta} \right]$$

$\eta$  can therefore be found for any value of  $\gamma$ .

The attachment point was moved downstream in steps by increasing  $F$  by increments indicated by  $\delta F$ . The time for one of these steps from  $F_2$  to  $F_3$  is given by

$$T_{2-3} = \frac{2(W_3 - W_2)}{q_{N_2} + q_{N_3}}$$

A computer program was written to calculate the time intervals required to increment  $F$  by  $\delta F$ . The position and geometry of the jet can therefore be determined at any instant in time.

The program was run for control flow ratios of  $q_c = 0.06$  to  $q_c = 0.1$  and setback ratios of 0.5 and 0.20. The results show that the switching time does not alter appreciably with varying setback, even though a much larger separation bubble exists with a setback ratio of 0.50. One would expect that the larger separation bubble would lead to a longer switching time. However, the larger bubble volume resulted in a larger reattachment angle in all cases and as a result the returned flow into the bubble was greater. This assisted in the bubble filling process and gave a total switching time nearly the same as that for a



smaller volume bubble.

#### IV DETERMINATION OF THE END POINT OF PHASE II

The response times of a model bistable fluid amplifier were experimentally measured to assist in the determination of the end point of phase II. These values of response time were measured by recording the time interval between a change in output of a hot wire placed in the control channel and the change in output of a hot wire placed in the output leg of the amplifier. In both cases the change in output of the hot wire indicated the initiation of flow over the hot wire. Complete details of the experimental method of measuring the response time can be found in reference [20]. The points plotted in Fig. 14 show the experimental values of response time, for various values of the non-dimensional control flow ratio, for a bistable amplifier having a nozzle width of 0.25 inches, a splitter distance of  $6b$  and a setback ratio of 0.2.

The upper portion of the response time curve ( $Q_c/Q_o > 0.13$ ) is a straight line and represents the region of momentum switching. The response time in this region is assumed to be the time taken for the deflection of the jet plus the transport time in the control and outlet channels. It was further assumed that by extrapolation of this straight line into the region  $Q_c/Q_o < 0.13$ , a close estimate of the time of momentum interaction and transport time could be obtained. It was concluded that the difference in time between the straight line and the experimental curve could be attributed to the bubble filling process. Therefore at values of  $Q_c/Q_o < 0.13$  the bubble filling process is required to complete switching since the initial main jet deflection is not sufficient

to achieve switching.

This paper directs its attention to the bubble filling process. The theory which is proposed permits the calculation of the time required for this bubble filling to take place. This portion of the switching process is referred to as Phase II.

The times required, expressed as Strouhal numbers, for the bubble filling process have been extracted from Fig. 14 and are replotted on Fig. 15. These values are considered as experimental, based on the assumption that the momentum switching line can be extrapolated as mentioned above. The values of the time for bubble filling, calculated from the switching theory are shown on Fig. 15. The calculated results are shown for two end conditions, one when 22% of the jet has passed over the splitter, and the second, when 24% of the jet has passed over the splitter. This method of defining when switching has occurred is consistent with the definition of switching as used in the experimental determination of response time.

As can be seen from Fig. 15 the agreement between experiment and theory is very good for values of  $Q_c/Q_0 < 0.85$ . It is therefore concluded that this region represents splitter switching caused by the bubble filling process. In the region immediately above  $Q_c/Q_0 = 0.85$  the switching time is less than that predicted by the bubble filling theory. It is assumed that in this region the interaction between the main jet and the opposite wall begins.

In using this splitter switching theory to predict the switching time for a bistable amplifier it is recommended that the end

point of Phase II be selected as that point when 22% to 24% of the width of the jet has passed over the splitter tip.

#### CONCLUSIONS

1. The Simson profile was found to give a good description of the curved main jet. This was found to be true for a range of Reynolds numbers from  $26.5 \times 10^3$  to  $13.3 \times 10^3$ , a setback ratio from 0.5 to 0.06 and for non-dimensional downstream distances from 0 to 3.5.
2. An equation defining the centreline of the main jet was found for the range of variables given above. This equation was

$$\frac{Y_R}{b} = 0.067 + 0.097 \left( \frac{X_R}{b} \right)^{1.56}$$

3. A theory describing splitter switching has been developed and switching time calculations have been made for a range of variables.
4. Comparisons between the calculated switching time and the measured response time in an actual amplifier allowed a rational determination of the end point of Phase II. This end point has been defined as that point when 22 - 24 percent of the width of the main jet has passed over the splitter.

#### ACKNOWLEDGEMENTS

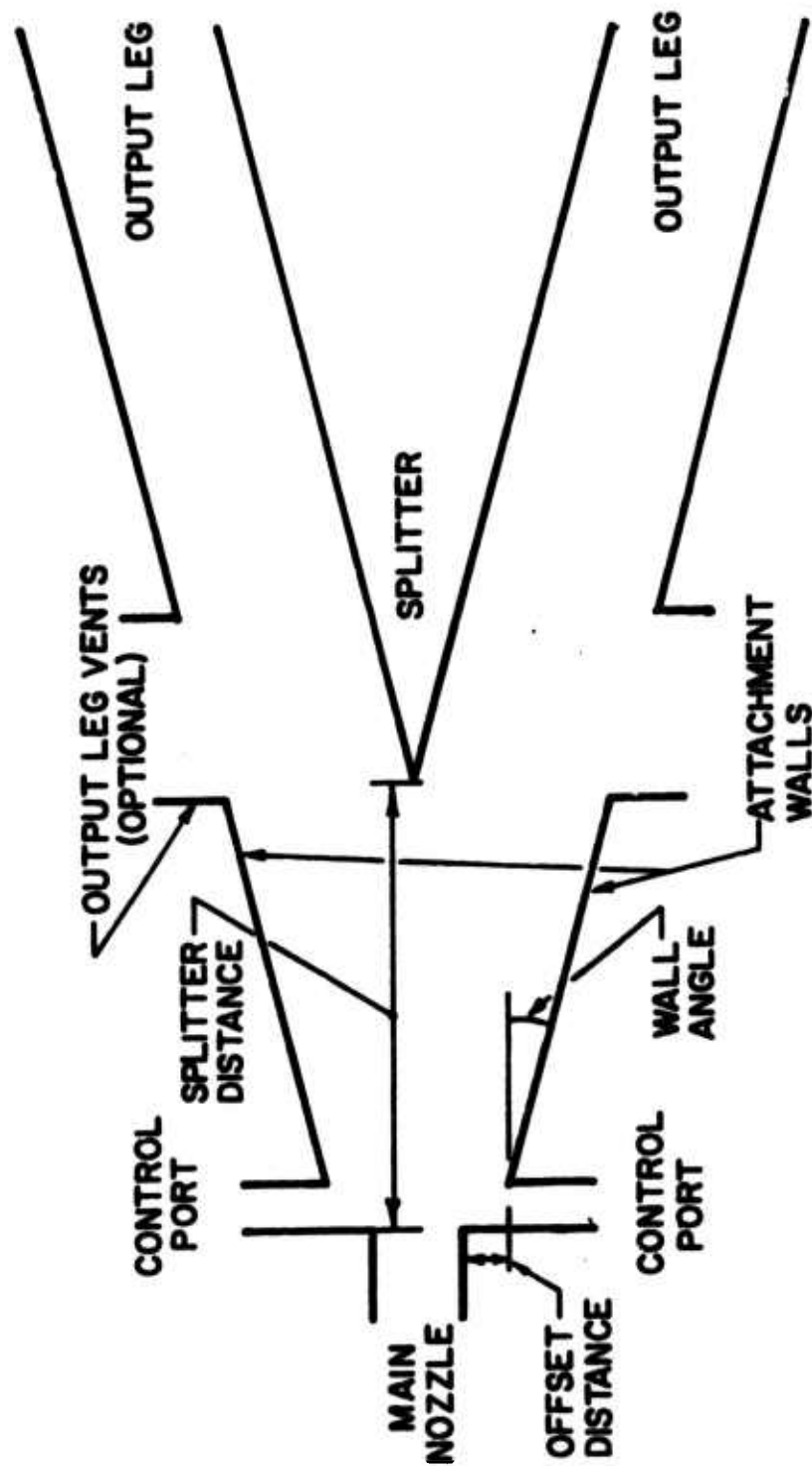
The authors acknowledge the financial assistance received from the National Research Council of Canada under grant number

A-1522 and a grant-in-aid awarded for 1971-72 from the American Society of Heating, Refrigerating and Air Conditioning Engineers.

## REFERENCES

1. Kirshner, J.M., "Fluid Amplifiers", McGraw-Hill Book Company 1966.
2. Bourque and Newman, "Reattachment of a Two-Dimensional Jet to an Adjacent Flat Plate", Aero. Quarterly, Vol. 11, Pg. 201, 1960.
3. Sawyer, R.A., "Two-Dimensional Reattaching Jet Flows Including the Effects of Curvature on Entrainment", J. Fluid Mech., Vol. 17, Pg. 481, 1963.
4. Levin and Manion, "Jet Attachment Distance as a Function of Adjacent Wall Offset and Angle", Fluid Amplification 5, December 31, 1962.
5. Bourque, C., "Reattachment of a Two-Dimensional Jet to an Adjacent Flat Plate", Advances in Fluidics, Pg. 192, 1967.
6. Sher, N.C., "Jet Attachment and Switching in Bistable Fluid Amplifiers," ASME Paper No. 64-FE-19, May 1964.
7. McRee and Edwards, "Three-Dimensional Turbulent Jet Reattachment", ASME Paper No. 70-WA/Flcs-5, July 1970.
8. Schlichting, H., "Boundary-Layer Theory", McGraw-Hill Book Company, 1968.
9. Simson, A.K., "A Theoretical Study of the Design Parameters of Subsonic Pressure Controlled Fluid Jet Amplifiers", Ph.D. Dissertation, Massachusetts Institute of Technology, Department of Mechanical Engineering, July 1963.
10. Albertson, M.L. et al., "Diffusion of Submerged Jets", Transactions of the ASCE, Vol. 115, 1950.
11. Warren, R.W., "Some Parameters Affecting the Design of Bistable Fluid Amplifiers", ASME Symposium on Fluid Jet Control Devices", Nov. 1962.
12. Comparin et al., "On the Limitations and Special Effects in Fluid Jet Amplifiers", ASME Symposium of Fluid Jet Control Devices, Nov. 1962.
13. Savkar et al., "Experimental Study of Switching in a Bistable Fluid Amplifier", ASME Paper No. 67-WA/FE-37.

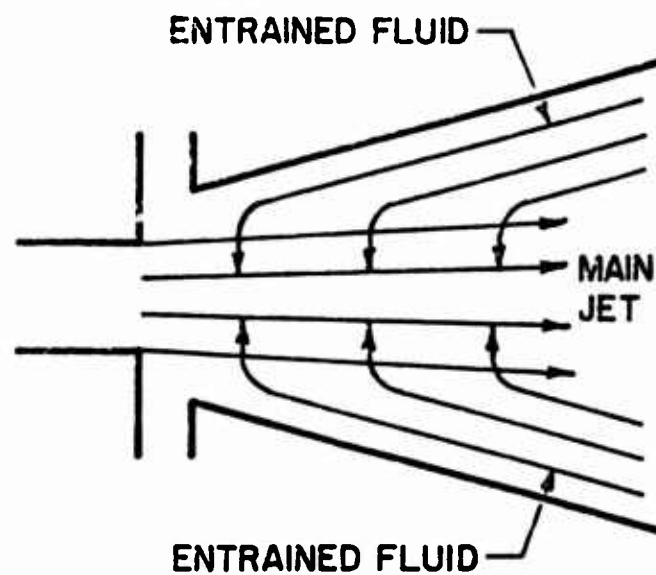
14. Sarkaya, T., "Steady and Transient Behaviour of a Bistable Fluid Amplifier to a Step Input", Proceedings of the Fluid Amplification Symposium, MDL, Vol. 1, May 1964.
15. Wilson, M.P., "The Switching Process in Bistable Fluid Amplifiers", ASME Paper No. 69-FLCS-28, June 1969.
16. Epstein, M., "Theoretical Investigation of the Switching Mechanism in a Bistable Wall Attachment Fluid Amplifier", ASME Paper No. 70-Flcs-3, April 1970.
17. Lush, P.A., "A Theoretical and Experimental Investigation of the Switching Mechanism in a Wall Attachment Fluid Amplifier", Proceedings of the IFAC Symposium on Fluidics, Nov. 1968.
18. Ozgu and Stenning, "Switching Dynamics of Bistable Fluid Amplifiers", Lehigh University Technical Report No. 3, Submitted to the Office of Naval Research under Contract No. N00014-69-A-0417, March 1971.
19. Muller, H.R., "A Study of the Dynamic Features of a Wall-Reattachment Fluid Amplifier", ASME, J. Basic Engineering, 86 D(4), 1964.
20. Colborne and Williams, "Experimental Study of Switching in a Bistable Fluid Amplifier", ASME Paper No. 72-FE-11, November 1971.
21. Foster and Carley, "The Dynamic Switching of Fluidic Digital Elements and the Effect of Back Pressure", Paper obtainable from Fluidics Feedback, BHRA, Cranfield, Bedford, England. Paper No. 5.340F5.
22. Perry, C.C., "Two-Dimensional Jet Attachment", Advances in Fluidics, pg. 205, 1967.
23. Wada and Shimizu, "Experimental Study of Attached Jet Flow On Inclined Flat Plate with Small Offset", Fluidics Quart., 1,'72.
24. Ries, J.P., "Dynamic Modelling of the Bistable Fluid Amplifier", Lehigh University, Technical Report No. 8, Submitted to the Office of Naval Research under Contract No. N00014-69-A-0417, January 1972.
25. Williams, C.J., "An Experimental and Theoretical Study of Splitter Switching in Bistable Fluid Amplifiers", Ph.D. Thesis, University of Windsor, Department of Mechanical Engineering, to be submitted.



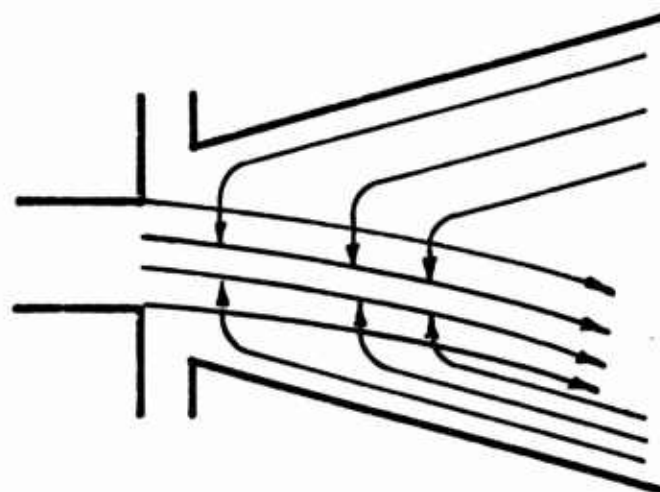
BISTABLE FLUID AMPLIFIER SCHEMATIC

FIG. I

- a) ENTRAINMENT PATTERN WHEN THE MAIN JET STARTS TO FLOW.



- b) BENDING OF THE MAIN JET DUE TO UNEVEN ENTRAINMENT.

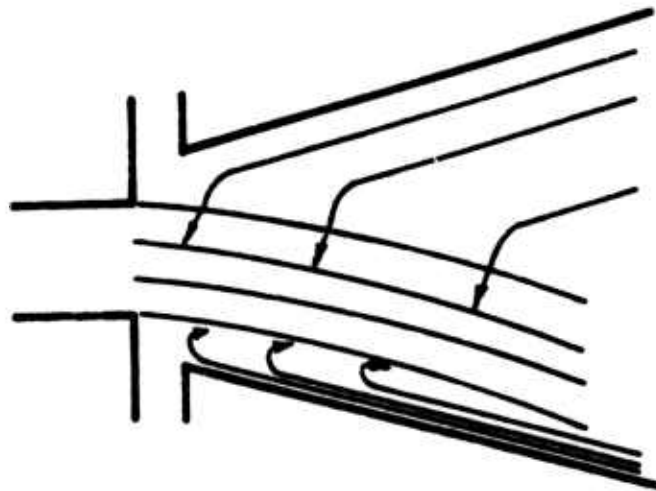


THE COANDA EFFECT.

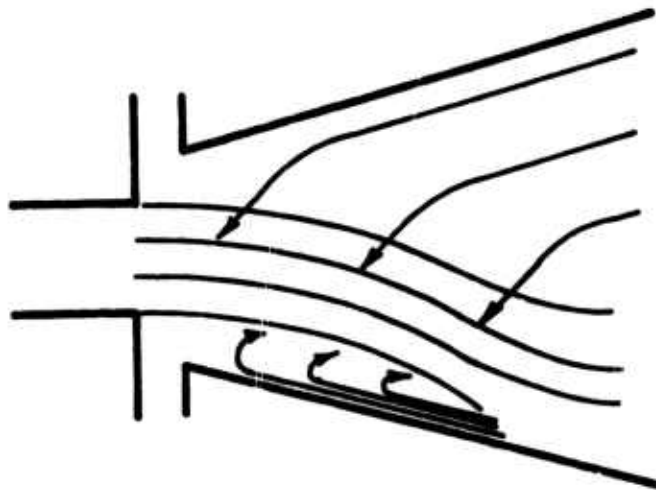
FIG.2



c) INITIAL ATTACHMENT.



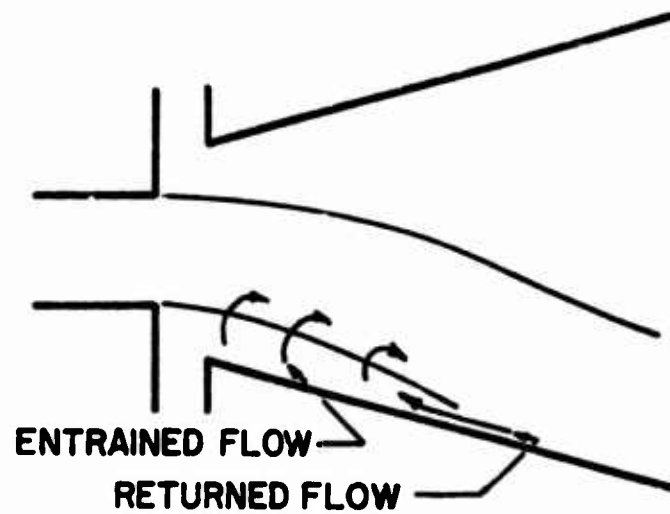
d) STEADY STATE ATTACHMENT.



THE COANDA EFFECT.

FIG.2

- a) STEADY STATE ATTACHMENT.  
ENTRAINED FLOW = RETURNED FLOW.



- b) BUBBLE FILLING  
 $\text{CONTROL} + \text{RETURNED} > \text{ENTRAINED}$

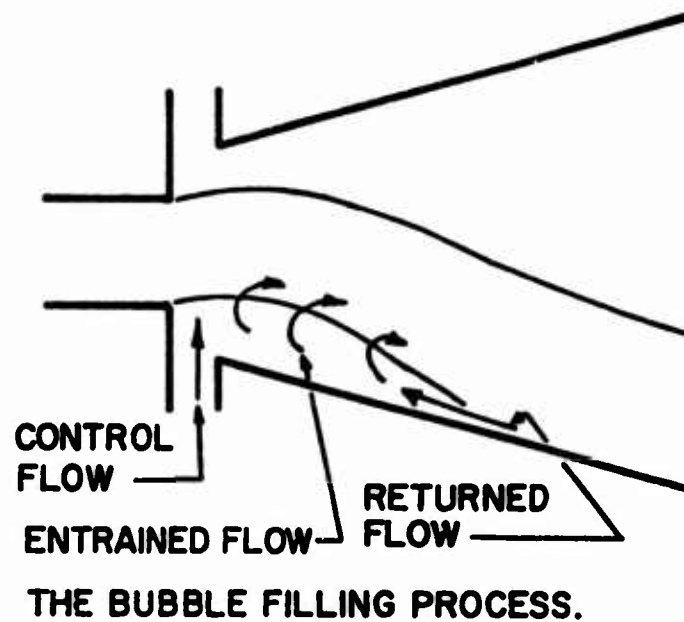
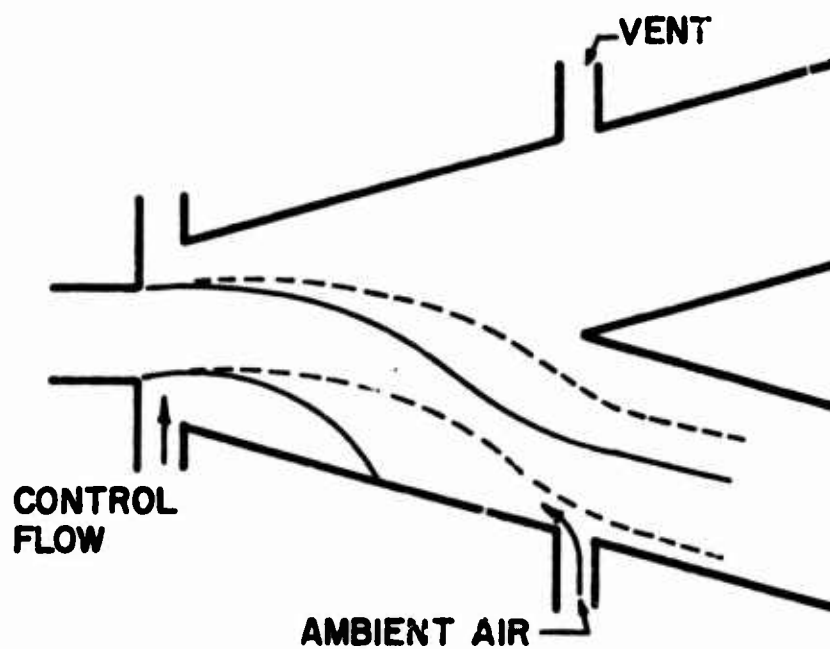


FIG.3

**MAIN JET LOCATION:**

— IMMEDIATELY AFTER THE CONTROL FLOW IS APPLIED.

--- DURING THE BUBBLE FILLING PROCESS.

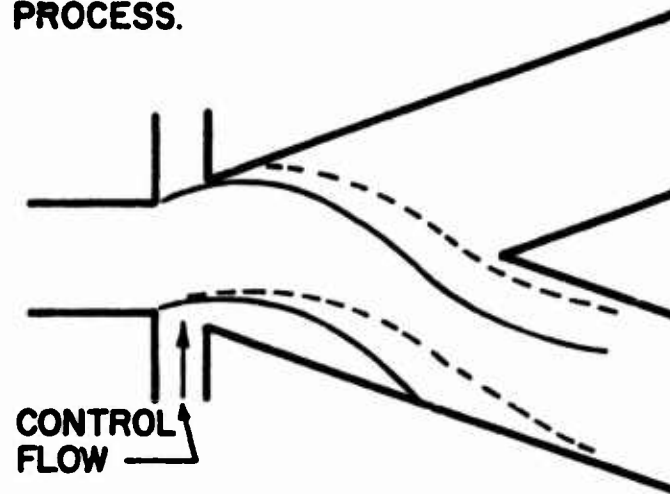


**END WALL SWITCHING.**

**FIG. 4**

**MAIN JET LOCATION:**  
— IMMEDIATELY AFTER THE CONTROL  
FLOW IS APPLIED.

--- DURING THE BUBBLE FILLING  
PROCESS.

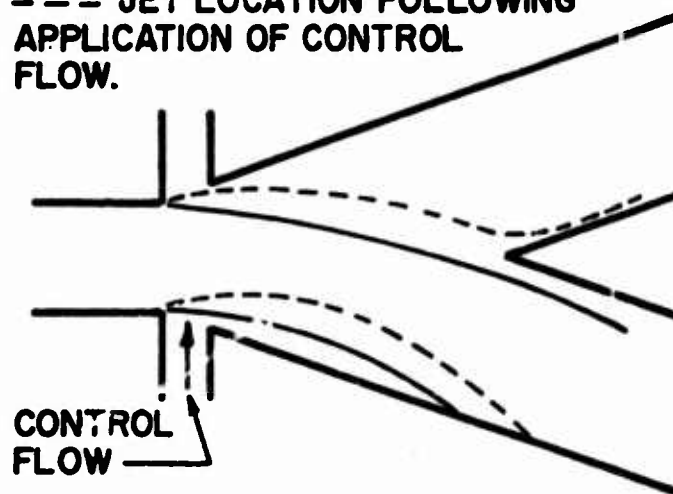


**OPPOSITE WALL SWITCHING.**

**FIG.5**

**MAIN JET LOCATION:**  
— STEADY STATE ATTACHMENT WITH  
NO CONTROL FLOW.

--- JET LOCATION FOLLOWING  
APPLICATION OF CONTROL  
FLOW.



**SPLITTER SWITCHING.**

**FIG.6**

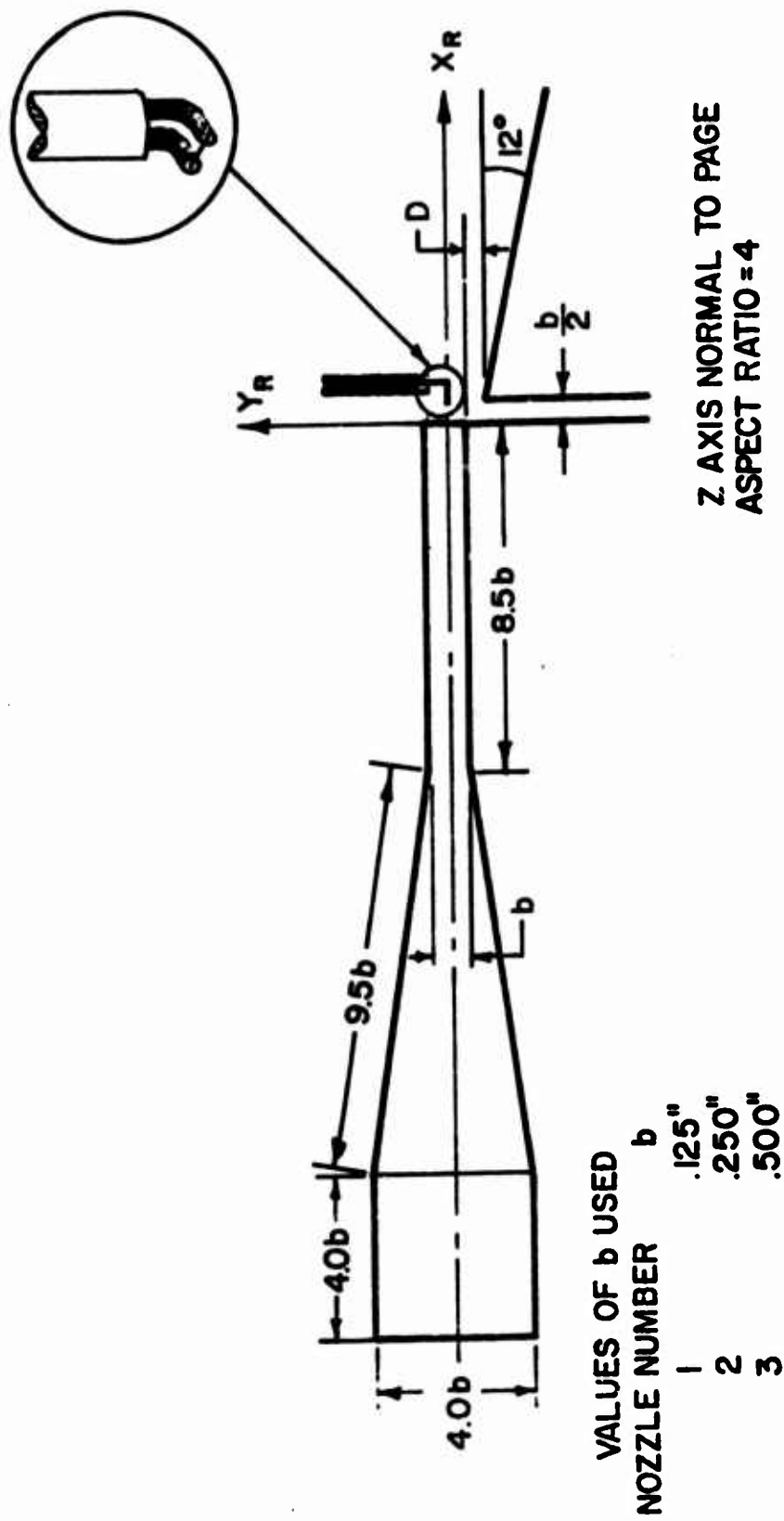
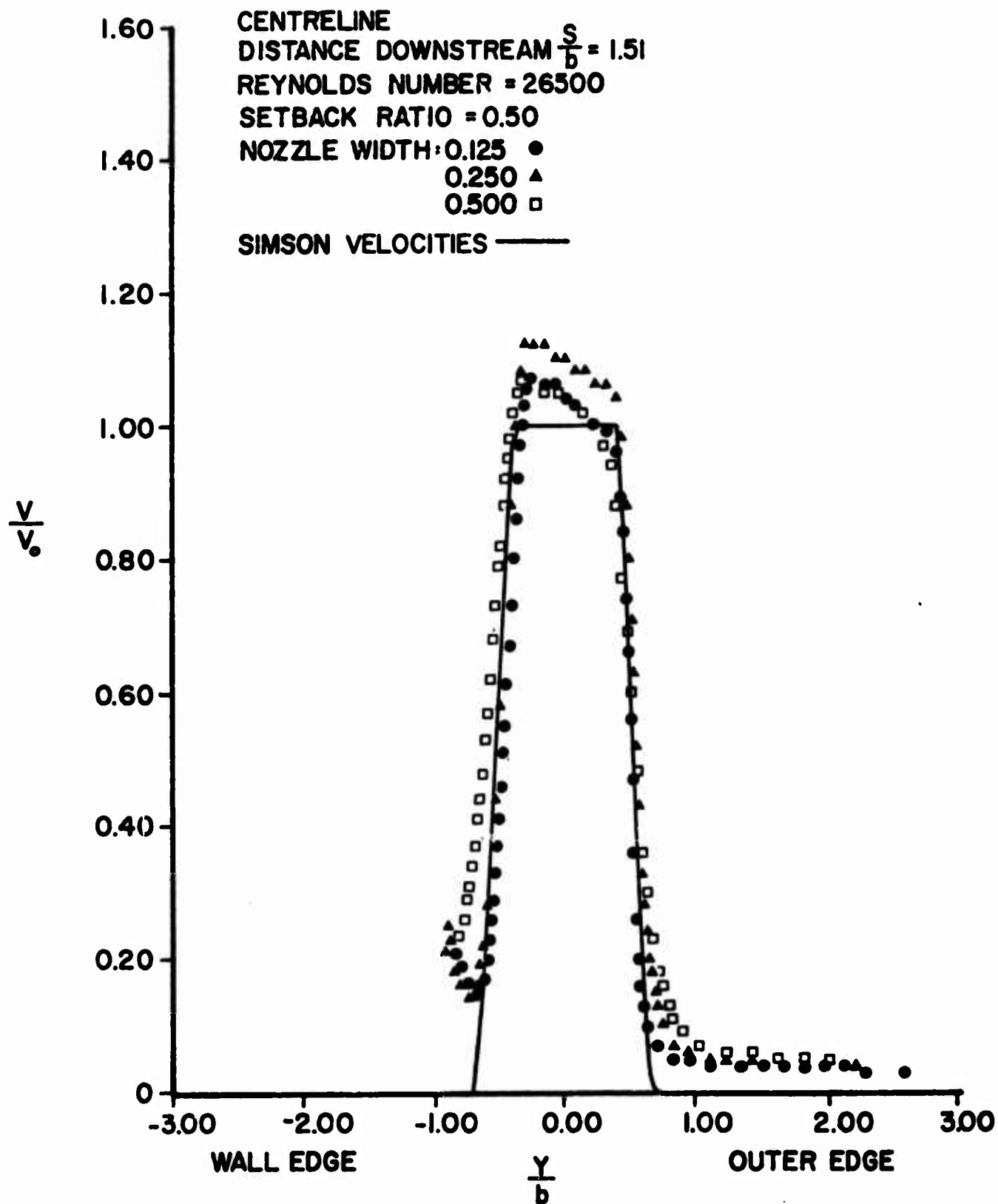


FIG. SCHEMATIC OF A TYPICAL POWER JET NOZZLE

FIG.7



THEORETICAL AND EXPERIMENTAL VELOCITY PROFILES

FIG. 8

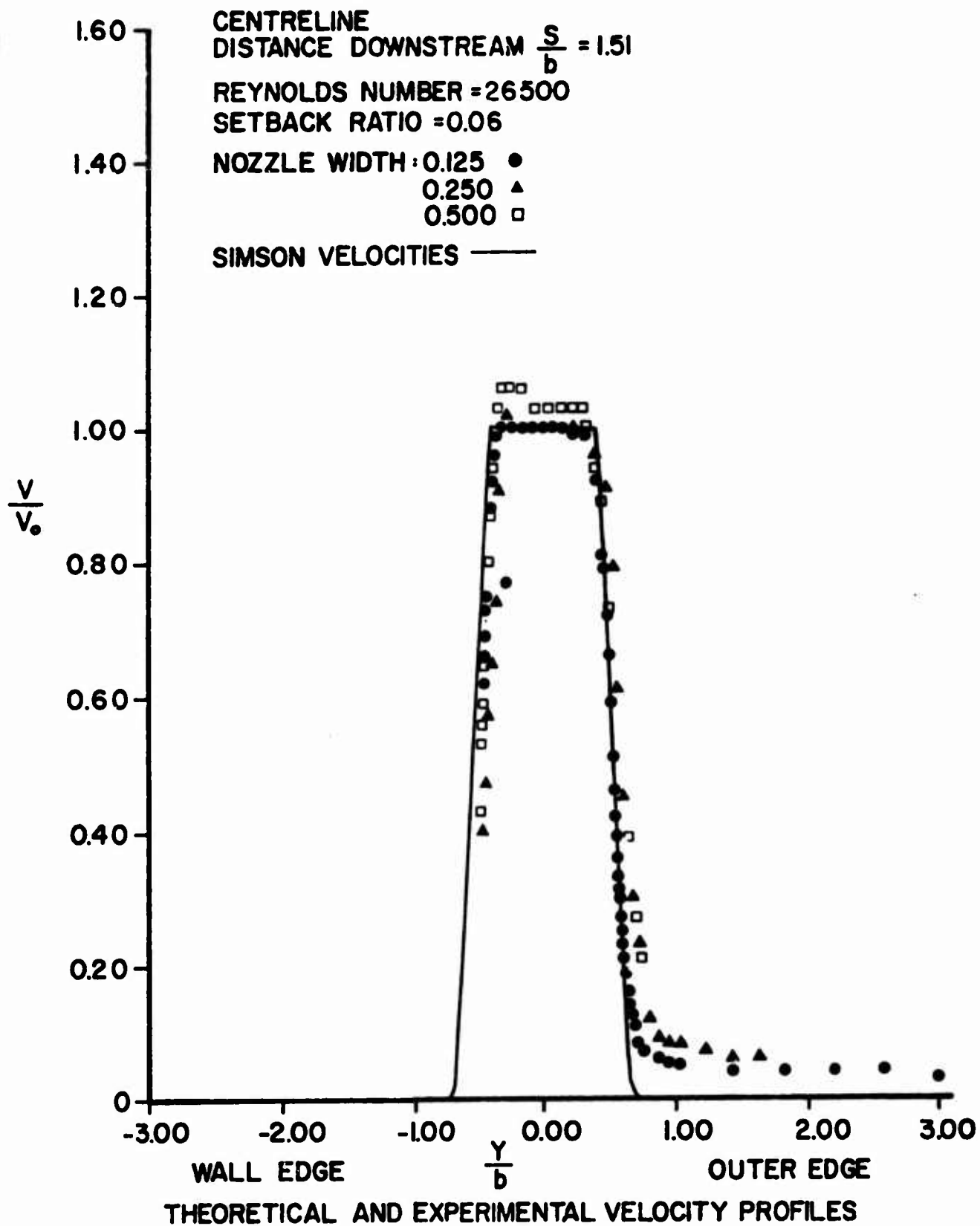


FIG. 9

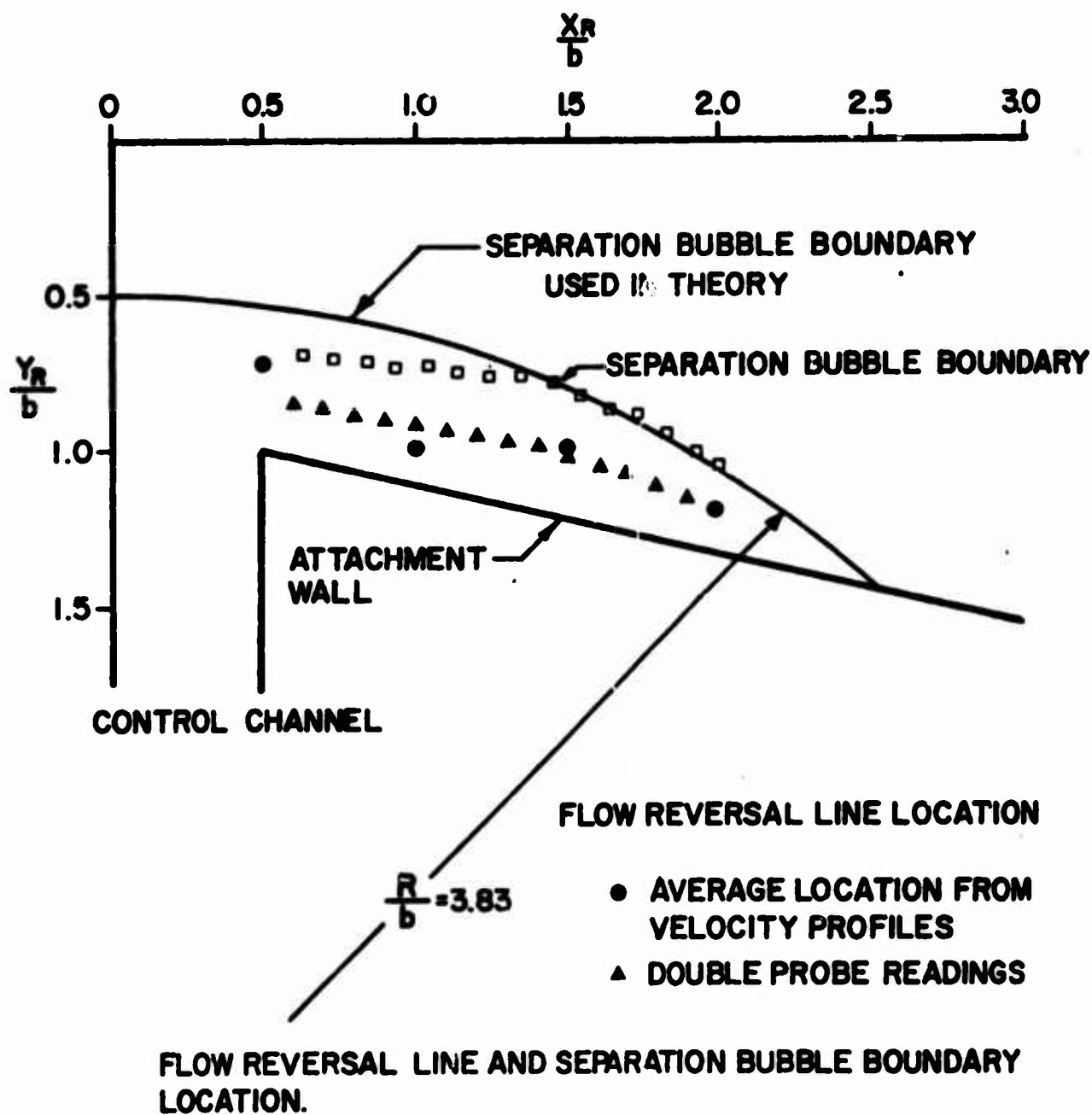
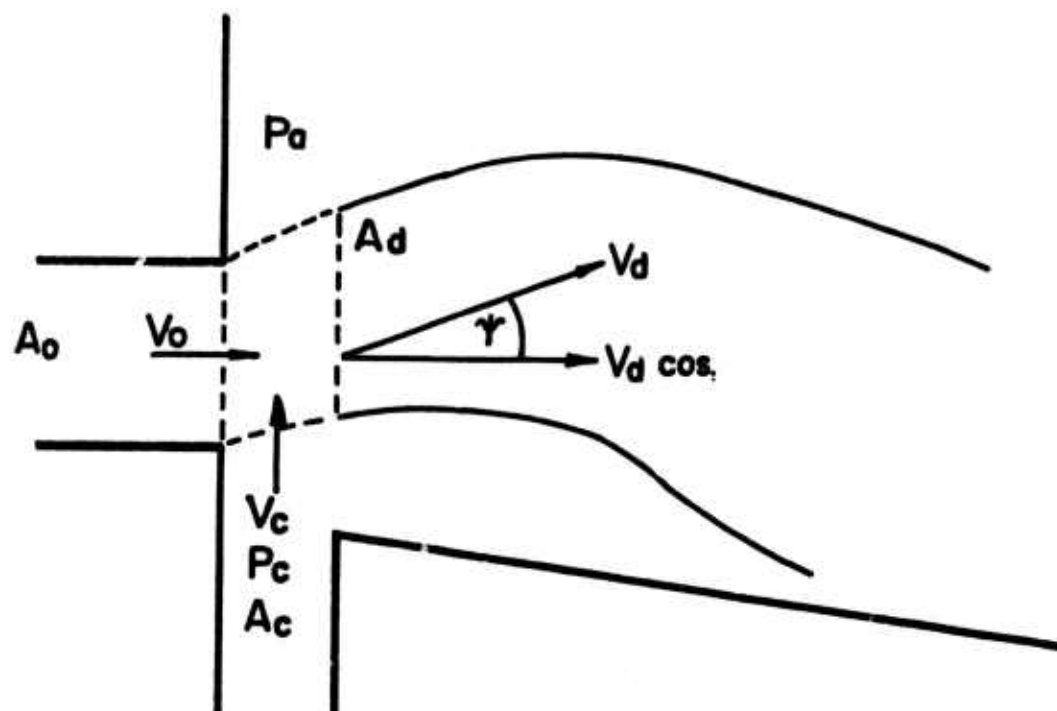


FIG. 10







--- CONTROL VOLUME.

CONTROL VOLUME USED IN MOMENTUM STUDY.

FIG.12



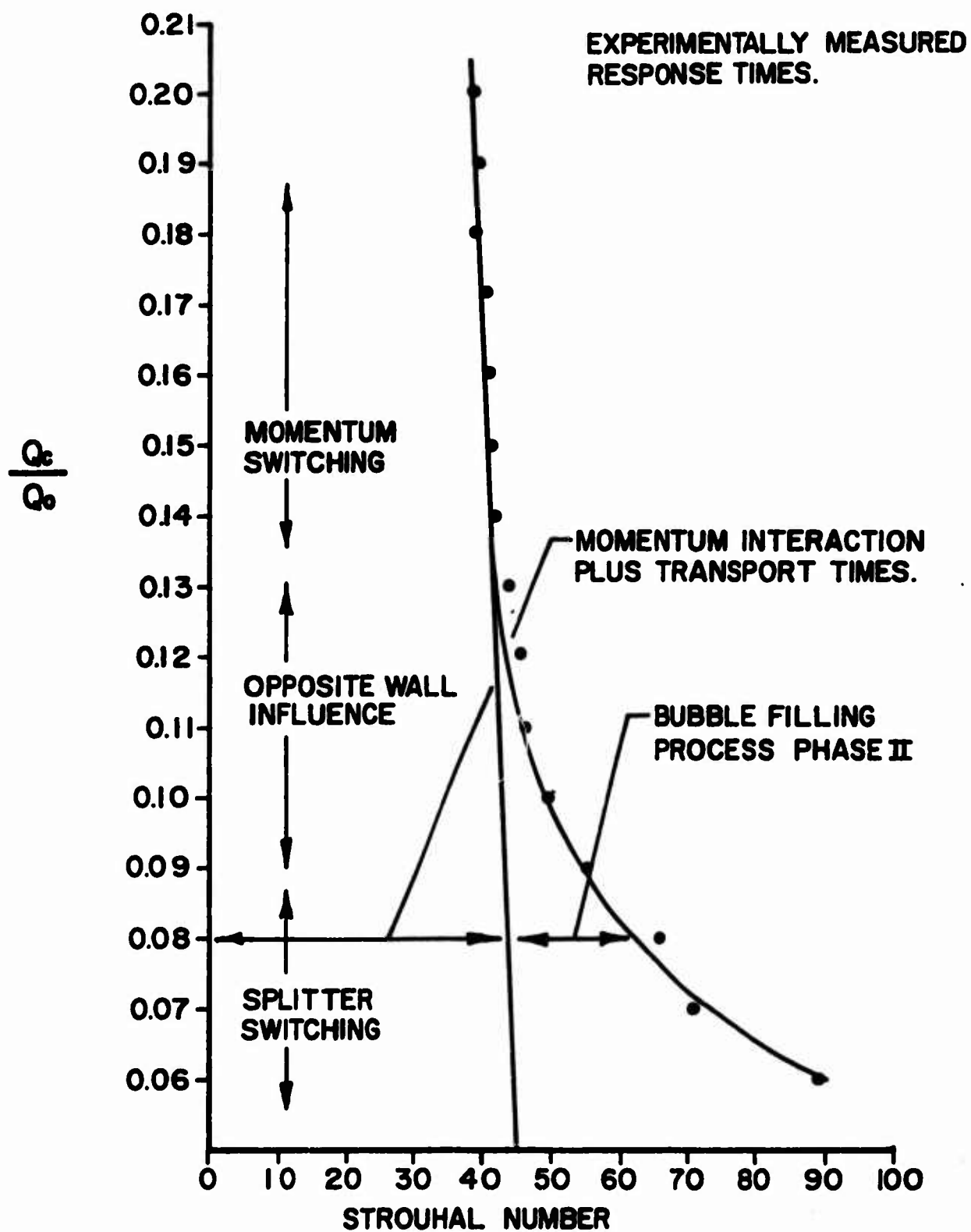


FIG.14

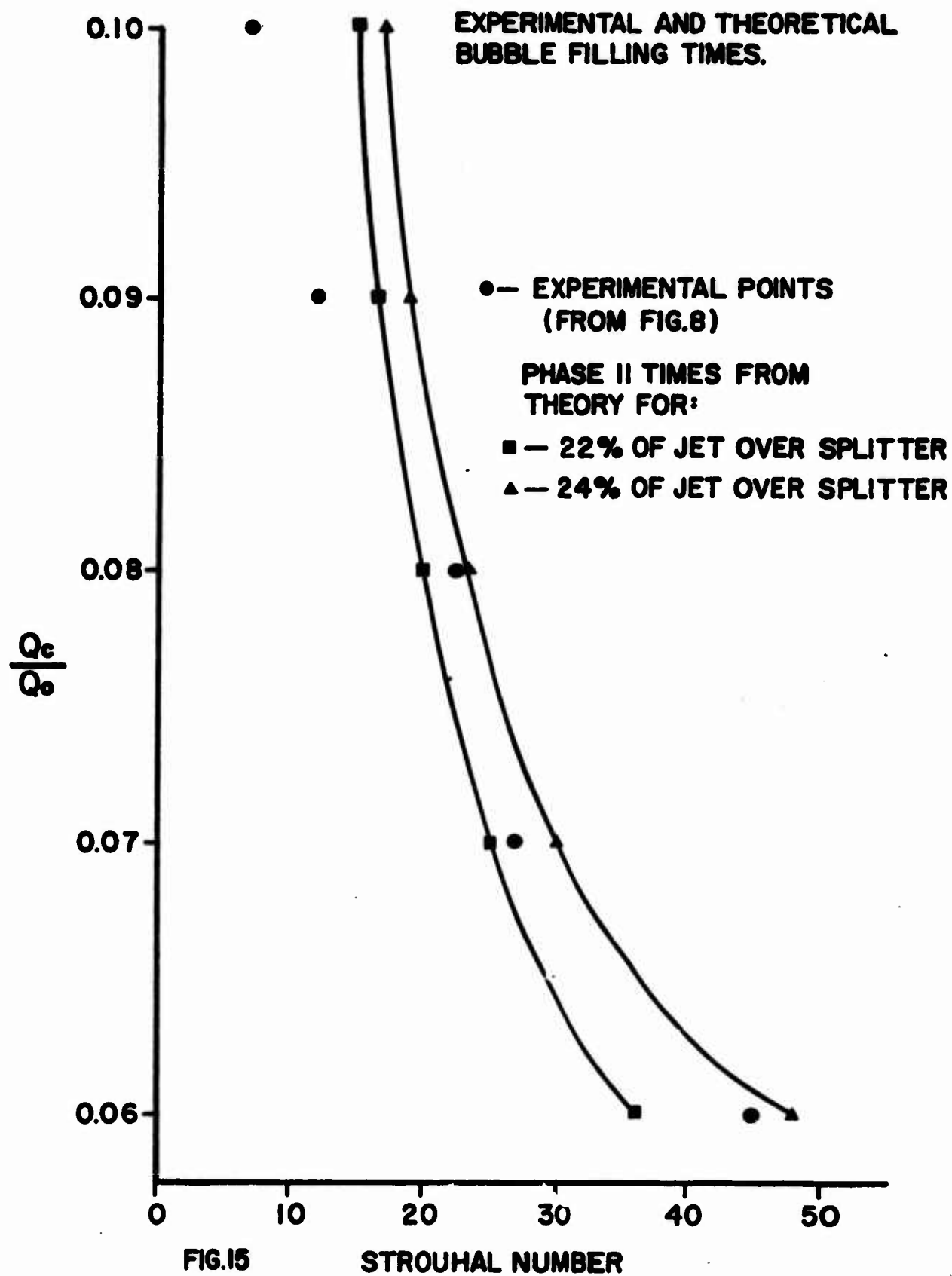


FIG.15

STROUHAL NUMBER